Heat Flow and Vibrations in Thin-Walled Structures with Temperature-Dependent Material Properties

(Värmeledning och vibrationer i tunnväggiga strukturer med temperaturberoende materialegenskaper)

av

Ulf Olsson

(tekn. lic.)

AKADEMISK AVHANDLING

som med tillstånd av Chalmers Tekniska Högskola framlägges till offentlig granskning för teknologie doktorsgrads vinnande fredagen den 10 september 1971 kl. 10 å Palmstedtsalen vid Chalmers Tekniska Högskola, Sven Hultins gata Göteborg.

Abstract

This thesis is a collection of works performed by the author at Volvo Flygmotor AB during the years 1969-1970. The aim of these works is to investigate, how the temperature dependence of the material properties influences the temperature fields and vibrations of thin-walled structures in modern jet engines.

The study begins with some works on heat conduction. The first one gives a variational method formulated in the internal energy. It is an alternative to Biot's method in which the temperature is varied. The second work shows that the application of perturbation analysis to heat conduction problems may be simplified through the introduction of certain substitutions. It also gives bounds on the successive approximating solutions. Lastly in the third work this perturbation method is used in investigating how the temperature dependence of the material properties influences the transient temperature field in a heated cylindrical shell.

The investigations on vibrations start with a study of the linear flutter stability of jet engine afterburners under various operating conditions. It is shown that the temperature dependence of the material properties may cause instability to occur at ignition of the afterburner.

The next work provides exact analytical solutions to the problem of free vibrations at linearly, exponentially and harmonically transient temperature fields. This is followed by an investigation of thermally induced deflections and a brief note on the influence of transient internal pressures.

Proceeding to nonlinear vibrations, three works have been performed. Thus, nonlinear equations for a circular cylindrical shell are derived taking care of temperature dependent material properties

Using Galerkin's method, these equations are then reduced to ordinary differential equations at transient, axially nonuniform temperature fields. Based on these two works, the last work in the thesis provides solutions to the linear and nonlinear flutter problems in circular cylindrical shells being heated convectively as in a jet engine afterburner.

In conclusion, the investigations performed show that the temperature dependence of the material properties have a large qualitative and quantitative influence on the heat conduction and vibrations in thin-walled structures.

Contents	Page

Introduction and Literature Review

In recent years the progress in areas such as space and aeronautical technology has made high temperature phenomena increasingly important. One problem then arisen is how to take care of the temperature dependence of the material properties, which at elevated temperatures makes the conventional linear-elastic theories insufficient. The mathematical difficulties involved have so far limited the research in this field to the analysis of a few rather specific problems.

Early investigations were made in the fifties by Hilton[1] and Nowinski[2]. Further progress was made by Trostel[3,4], who used perturbation techniques to solve the general stationary thermoelastic problem. Subsequent works have used the same methods in analyzing various one-dimensional and stationary problems such as e.g. the stress states in circular plates and thick-walled cylinders and spheres[5-10]. An extension to shell problems was given by Ismail and Nowinski[11], who treated stationary thermal stresses in thin shells of revolution using linear shell theory and a multiparameter perturbation method[12]. Ambartsumian et al.[13] derived nonlinear equations for shells of revolution at general temperature fields. However, in treating specific problems they considered temperatures varying only with time and applied the nonlinear theory only to free vibrations of plates. Later, Tang has analyzed stationary thermal stresses in plates[14] and in simply connected bodies[15] as well as the free vibrations of rectangular plates exposed to stationary temperature fields[16].

Parallell to the development of thermo-elasticity has gone that of heat conduction. At temperature dependent material properties Fourier's heat conduction equation is nonlinear and untractable to exact analytical solutions but for some special cases.[17,18] Thus, numerical or approximate methods of solution must be resorted to.

Perturbation methods have been used by many authors[4,11] in a rather straightforward way and Appl and Hung[19,20] have developed a method of successively converging bounds on the exact solution. However, it is the variational methods which have received most attention in the literature. Two important such methods are due to Goodman and Biot.

Goodman's method, the heat balance integral technique, has been applied to many problems involving nonlinear heat inputs and temperature dependent material properties.[21,22,23]

The variational principle introduced by Biot[24,25] were formulated in the temperature of the body and confined to problems involving prescribed surface temperature. This method has later been extended by various authors,[26,27] to include prescribed surface heat fluxes and radiation boundary conditions.

Of other variational principles may be mentioned one due to Glansdorf et al.[28], who studied the case in which the principle of minimum entropy production is not valid and introduced the concept of the local potential. This method has been applied to heat conduction in materials with temperature dependent material properties by Hays[29] and Hays and Curd[30].

An extensive review of variational methods appled to transport phenomena is given by Hiraoka and Tanaka.[31]

The aim of the present work is to investigate how the temperature dependence of the material properties influences the temperature fields and vibrations of thin-walled structures. In order to make the results applicable to e.g. jet engine afterburners, a finite circular cylindrical shell has been chosen as an object for the investigations. Besides, the circular cylindrical shell is a rather general structural element making the results representative also for beams and plates.

The vibration problems studied here include free and forced vibrations as well as flutter of cylindrical shells. In Ref. 13 investigations of this type have been carried out considering linear shell theory and geometrically uniform, linearly transient temperature fields. In the present work nonlinear shell theory and geometrically nonuniform transient temperature fields will be considered. This gives rise to such effects as thermally induced vibrations, prestability deformations and limit cycle oscillations not considered in previous studies on the present subject.

We begin by developing some new methods in heat conduction analysis, then choose one of them, a perturbation method, for the calculations of the transient temperature field in the shell wall. For such calculations see e.g. Ref. 11 and for temperature independent materials, Brull and Vinson[32] and Pfahl.[33] Proceeding to the vibration problems, we investigate free and thermally induced vibrations, derive nonlinear shell equations at temperature dependent material properties and proceed to nonlinear flutter problems. In solving these problems we shall make use of the methods developed in the literature for treating the nonlinear flutter and vibration of isothermal cylindrical shells. See e.g. Olson and Fung[34], Evensen and Olson[35], Dowell.[36] An extensive review of the literature in this field is given by Dowell.[37]

Qualitatively, the weakening of the structure with increasing temperature should result in larger amplitudes and lower frequencies. Especially at flutter this is of great importance because the stability limits may be passed during the heating up of the structure, causing instability to occur at a certain temperature. Transient analyses of such courses of events will be carried out in what follows.

1 ON A VARIATIONAL METHOD IN HEAT CONDUCTION FORMULATED IN THE INTERNAL ENERGY

In this paper a variational principle in heat conduction is formulated in the internal energy. The principle corresponds to that formulated in the temperature by Biot[24], the two formulations being identical at temperature independent materials.

The method is compared to that of Biot in a special case viz. heat conduction in a semi-infinite solid with prescribed surface temperature and temperature dependent specific heat. The results show no remarkable difference between the two methods but the one given here is considered to be a valuable alternative at temperature dependent material properties, because convective heat transports are directly included. For an application of Biot's method to such problems, see Ref. 38. The present paper is a rewriting of a former work[39] on the same subject.

2 APPLICATION OF A PERTURBATION METHOD TO HEAT FLOW ANALYSIS IN MATERIALS HAVING TEMPERATURE DEPENDENT PROPERTIES[40]

The perturbation method or the method of successive approximations has proved itself to be a valuable tool in the analysis of nonlinear boundary value problems. It is intended here to study the application of this method to heat flow problems from a more theroretical point of view.

The solutions are expanded in powers of one parameter, common for the various material properties, thereby splitting up the original nonlinear problem into a set of interdependent linear ones. It is shown that the difficulties arising because of the products of derivatives in these equations may be released through suitable transformations. In addition a method is given, which makes it possible to predict the convergence of the series solution.

This method may also be used to obtain bounds on the solutions to the classical linear heat flow problem. It is a generalization of a method given by Boley[41] to include transient conditions, internal heat generation and convective heat transfer to the surface of the body. The principle is to obtain the temperature bounds starting out from assumed bounds on the prescribed heat flows. This is contrary to the method used by e.g. Appl and Hung[19], who choose bounds on the temperature in such a way that the heat generated in the body is approximated as well as possible.

3 TRANSIENT HEATING OF A CYLINDRICAL SHELL WITH TEMPERATURE DEPENDENT MATERIAL PROPERTIES [42]

In the two previous works were developed two methods of solution to the heat flow problem when the thermophysical material properties depend on the temperature. Here, we shall use the perturbation method [40] in an investigation of the influence of this temperature dependence on the transient temperature field in a heated circular cylindrical shell.

At its inner surface the shell is supposed to be heated convectively and by a constant heat flux. Simultaneously, it is cooled convectively at its outer surface. The temperature of the outer gas stream is assumed to be a constant while that of the inner one varies axially as a first order cosine series. There are no tangential temperature variations, i.e. the problem is rotationally symmetric.

Under these conditions, the nonlinear heat flow equation is transformed to a set of linear equations which are then solved approximately. The transient temperature fields emanating from convective heating and constant heat flux are calculated separately. In the latter case a linear variation of the temperature through the wall is included in the analysis.

The results indicate that even large variations in the thermophysical material properties have a relatively moderate effect on the temperature in a convectively heated shell. If the shell is heated by a constant heat flux the effect is somewhat larger. In both cases, use of initial material properties throughout the calculations overestimates the temperature while a relatively exact approximation is obtained by using average values of those properties in the temperature interval considered.

It is also shown, that influence of the temperature variation through the wall on the average wall temperature is of any significance only during the first few moments of the heating up period.

4. SOME NOTES ON THE FLUTTER OF JET ENGINE AFTERBURNERS[43]

When a jet engine afterburner is ignited, the velocity and temperature of the gas stream flowing through it increase and its walls are gradually heated up. Because of the temperature dependence of the material properties such an increase of the wall temperature leads to a decrease in the stiffness of the structure. Together with the changes in the gas flow properties this leads to changes in the flutter boundaries of the system.

In order to study these effects a simply supported circular cylindrical shell is considered at various values of gas and wall temperatures and gas pressure. The corresponding critical gas velocity for flutter is calculated using linear theories and it is shown that the flutter sensitivity is increased by increasing the velocity and pressure of the gas stream. It also increases with increasing wall temperature and decreasing gas temperature. The net effect of this is that flutter may occur at ignition of the afterburner in which case it will remain until the afterburner is shut off.

5 ON FREE VIBRATIONS AT TEMPERATURE DEPENDENT MATERIAL PROPERTIES AND TRANSIENT TEMPERATURE FIELDS[44]

During the heating up period of structures exposed to high intensity heat fluxes, the material properties may undergo significant variations. As shown in Ref. 13 this temperature dependence introduces essential changes in the free vibrations of the structure.

It is intended here to analyze this problem more extensively, taking into account the temperature dependence of the material damping parameter and Poisson's ratio as well as the second derivative in the relation between Young's modulus and the temperature, all of which were neglected in Ref. 13. Furthermore, not only linear but also exponential and harmonic transient temperature variations are considered.

Mathematically, the problem reduces to the solution of the linear vibrational differential equation with transiently varying coefficients. It is shown herein that exact analytical solutions to this equation may be found through a series of different transformations in the various cases mentioned previously.

Proceeding from those solutions, it is shown through numerical examples how at a monotonic increase of the temperature, either linearly or exponentially, the amplitudes and vibrational periods grow against limits provided by the stationary temperature. This tendency is further emphasized by the second derivative in the relation between Young's modulus and the temperature. The temperature dependence of the damping parameter has a large influence on the amplitudes but leaves the frequencies largely uninfluenced.

At cyclic temperature variations parametric resonance may occur at certain relations between the eigenfrequency of the structure and the frequency of the temperature fluctuations and when the amplitudes of these fluctuations are large enough. The temperature dependence of the material properties has a large effect on the stability limits and tends to make conditions more critical. In practice, however, the stabilizing effect of the material damping secures the stability of the oscillations.

6 TRANSIENT THERMAL DEFORMATIONS OF CYLINDRICAL SHELLS WITH TEMPERATURE DEPENDENT MATERIAL PROPERTIES[45]

It is intended here to study how the thermally induced deflections of a circular cylindrical shell are influenced by the temperature dependence of the material properties. It is assumed that the outer surface of the shell is insulated and that the inner surface is exposed to a constant heat flux of high intensity. The corresponding transient temperature field is calculated using the perturbation technique of Ref. 40, assuming that the specific heat and the heat conductivity vary linearly with the temperature.

The deflections are then calculated neglecting the variations of the elastic material properties through the shell wall and assuming the shell to be simply supported. Linear shell theory and a Galerkin procedure are used.

It is shown through a numerical example, how the average deflections as well as the amplitudes and vibrational periods of the superposed oscillations increase with time.

7 PRESSURE-INDUCED DEFLECTIONS OF HEATED CYLINDRICAL SHELLS WITH TEMPERATURE DEPENDENT MATERIAL PROPERTIES[46]

Exact analytical solutions are given for the transient deflections of a circular cylindrical shell exposed to instationary internal pressure and a constant heat flux to the wall. Young's modulus is assumed to vary linearly with the temperature and linear shell theory is used together with a Galerkin procedure.

Numerical results are given for a pressure step and it is shown, that in this case the transient deflections may be expressed in Fresnel integrals of the time variable.

8 NONLINEAR THERMOELASTIC EQUATIONS FOR BEAMS AND CYLINDRICAL SHELLS HAVING TEMPERATURE DEPENDENT PROPERTIES[47]

Proceeding from the hypothesis of Kirchoff-Love, the problem of finding the nonlinear deformations and stresses in a cylindrical shell having temperature dependent properties is reduced to the solution of two coupled differential equations with the radial displacement and a stress function as dependent variables. Hooke's law is assumed to be applicable and the derivation follows that in Ref. 13 for general rotationally symmetrical shells. The resulting equations are valid for arbitrarily varying temperature fields, i.e. for general anisotropic shell materials. They include as a special case the well known Donnell equations for an isotropic cylindrical shell.

9 REDUCTION OF THE DIFFERENTIAL EQUATIONS FOR A CYLINDRICAL SHELL OF TEMPERATURE DEPENDENT MATERIAL PROPERTIES TO ORDINARY DIFFERENTIAL EQUATIONS[48]

The nonlinear shell equations derived in the previous work are reduced here to ordinary nonlinear differential equations through the application of a Galerkin procedure.

It is intended to produce equations suitable for the numerical investigation of vibrations, flutter and buckling of heated cylindrical shells. To this end the following cases have been treated.

1. Linear thermally induced and free vibrations with temperature uniform in the surface of the shell.
2. Nonlinear flutter and buckling with neglected prestability deformations. Generally varying temperature field.
3. Nonlinear flutter and buckling with circumferentially uniform temperature field.

Prestability deformations taken into account. The resulting nonlinear ordinary differential equations are presented in nondimensional form.

10 SUPERSONIC FLUTTER OF HEATED CIRCULAR CYLINDRICAL SHELLS WITH TEMPERATURE DEPENDENT MATERIAL PROPERTIES[49]

This paper presents a theoretical analysis on the supersonic flutter of thin circular cylindrical shells exposed to transient temperature variations of such magnitudes, that the temperature dependence of the material properties must be taken into account.

Nonlinear shell equations of Donnell's type are developed for arbitrarily varying material properties. With the help of Galerkin's method and a two-mode series assumption for the deformations, those equations are reduced to ordinary differential equations, which are then solved asymptotically according to the method of Krylov-Bogoliubov. Instationary, axially varying temperature fields are considered, corresponding to convective heating of the shell wall as in a jet engine afterburner.

The nonlinear first order differential equations which result from the method of Krylov-Bogoliubov have been solved numerically. It is found that at trânsient heating of the shell wall, instabilities may occur because the resulting weakening of the structure leads to an increase in flutter sensitivity. Thus, oscillations which are initially stable may change over to instable ones if the stability limits are passed during the heating up of the shell wall. In such cases, the amplitudes are first damped out with time then suddenly begin to grow to very large values. The conditions under which such courses of events may take place are investigated in this work.

It is shown, how the curves describing the limit cycle amplitudes are moved to lower gas velocities at increasing shell wall temperatures and that realistic axial temperature variations have a moderate effect on these conditions. Numerical results are given for the variation with time of the amplitudes, the frequency and the phase angle between the two modes assumed in the Galerkin procedure.

Neglecting nonlinear terms, the frequency and the amplitude of the principal mode of deformation may be solved exactly from the differential equations obtained from the method of Krylov-Bogoliubov. Through comparison to the results of the nonlinear problem, it is verified that these linear solutions give qualitatively correct results.

References

[1] Hilton, M.H., "Thermal Stresses in Bodies Exhibiting Temperature Dependent Properties", J. Appl. Mech., Vol. 19, 1952, p. 350.

[2] Nowinski, J.L., "Thermal Stresses in a Thick-Walled Cylinder with Variable Elastic Properties", Arch. Mech. Stos., Vol. 5, No. 2, 1953, p. 295.

[3] Trostel, R., "Wärmespannungen in Hohlzylindern mit temperaturabhängigen Stoffwerten", Ingenieur-Archiv, Vol. 26, 1958, p. 134.

[4] Trostel, R., "Stationäre Wärmespannungen mit temperaturabhängigen Stoffwerten", Ingenieur-Archiv, Vol. 26, 1958, p. 416.

[5] Nowinski, J.L., "Thermoelastic Problem for an Isotropic Sphere with Temperature Dependent Properties", ZAMP, Vol. 10, No. 6, 1959, p. 565.

[6] Nowinski, J.L., "A Betti-Rayleigh Theorem for Elastic Bodies Exhibiting Temperature Dependent Properties", Appl. Sc.Res., Vol. 9, No. 6, 1960, pp. 429-436.

[7] Sokolowski, M., "One-Dimensional Thermoelastic Problems for Elastic Bodies with Material Constants Depending on Temperature", Bull. Acad. Polonaise Sci., Ser.Sci.Tech., Vol. 8, No. 4, 1960, p. 153.

[8] Nowinski, J.L., "Transient Thermoelastic Problem for an Infinite Medium with a Sperical Cavity Exhibiting Temperature Dependent Properties", J.Appl.Mech., 1962, p.399.

[9] Stanisia, "The Steady-State Thermal Stress Field in an Isotropic Sphere with Temperature Dependent Properties", Ing.-Arch., Vol.31, No.4, 1962, p.241.

[10] Nowinski, J.L., "Axisymmetric Problem of the Steady-State Thermal Stresses in Elastic Media with Temperature Dependent Properties", Appl.Sci. Res., Vol.12, No.4/5, 1964, p.349.

[11] Ismail, I.A., Nowinski, J.L., "Thermoelastic Problems for Shells of Revolution Exhibiting Temperature Dependent Properties", Appl.Sci.Res., Vol.14, No.3, 1964/1965, p.211.

[12] Nowinski, J.L., Ismail, I.A., "Application of a Multiparameter Perturbation Method to Elastostatics", Proceedings of the Second Southeastern Conference on Theoretical and Applied Mechanics, 1963.

[13] Ambartsumian, S.A. et al., "Some Problems of Vibration and Stability of Shells and Plates", Int.J. Solids Structures, Vol.2, 1966, pp.59-81.

[14] Tang, S., "Thermal Stresses in Temperature Dependent Isotropic Plates", J. Spacecrafts Rockets, Vol.5, No.8, Aug. 1968, pp. 987-990.

[15] Tang, S., "Some Problems in Thermoelasticity with Temperature Dependent Properties", J. Spacecraft, Vol.6, No.2, Febr. 1969, pp.217-219.

[16] Tang, S., "Natural Vibration of Isotropic Plates with Temperature Dependent Properties", AIAA Jnl, Vol. 7, No. 4, 1969, pp. 725-727.

[17] Carslaw, H.S., Jaeger, J.C., "Conduction of Heat in Solids", Oxford University Press, 2nd Ed., 1959, p. 10.

[18] Cobble, M.H., "Non-Linear Heat Transfer of Solids in Orthogonal Coordinate Systems", Int. J. Non-Linear Mechanics, Vol. 2, 1967, pp. 417-426.

[19] Appl., F.C., Hung, H.M., "A Principle for Convergent Upper and Lower Bounds", Int. J. Mech. Sci., Vol. 6, 1964, pp. 381-389.

[20] Hung, H.M., Appl, F.C., "Heat Transfer of Thin Fins with Temperature Dependent Thermal Properties and Internal Heat Generation", J. Heat Transfer, May 1967, pp. 155-162.

[21] Goodman, T.R., "The Heat Balance Integral-Further Considerations and Refinements", ASME Paper No. 60-SA-9, 1960.

[22] Koh, J.C.Y., "One-Dimensional Heat-Conduction with Arbitrary Heating Rate and Variable Properties", J. Aerospace Sci., Dec. 1961.

[23] Yang K., "Calculation of Unsteady Heat-Conduction in Single-Layer and Composite Finite Slabs with and without Property Variations by an Improved Integral Procedure", International Developments in Heat Transfer Part.I, published by ASME, 1961.

[24] Biot, M.A., "New Methods in Heat Flow Analysis with Application to Flight Structures", J. Aeron. Sci., Vol. 24, No. 12, Dec. 1957, pp. 857-873.

[25] Biot, M.A., "Further Developments of New Methods in Heat Flow Analysis", J. Aero/Space Sci., Vol. 26, No. 6, June 1959.

[26] Lardner, T.J., "Biot´s Variational Principle in Heat Conduction", AIAA Jnl., Vol. 1, No. 1, 1963, pp. 196-206.

[27] Zyszkowski, W., "The Transient Temperature Distribution in One-Dimensional Heat-Conduction Problems with Nonlinear Boundary Conditions", J. Heat Transfer, Febr. 1969, p. 11.

[28] Glansdorff, P., et al., "Variational Properties of a Viscous Liquid at a Nonuniform Temperature", Physics Fluids, Vol. 5, No. 2, 1962, pp. 144-149.

[29] Hays, D.F., "Variational Formulation of the Heat Equation: Temperature Dependent Thermal Conductivity", Symp. on Non-Equilibrium, Variational Techniques and Stability, Univ. of Chicago Press, Chicago, 1965.

[30] Hays, D.F., Curd, H.N., "Heat Conduction in Solids: Temperature-Dependent Thermal Conductivity", Int. J. Heat Mass Transfer, Vol. 11, 1968, pp. 285-295.

[31] Hiraoka, M., Tanaka, K., "A Variational Principle for Transport Phenomena - I. Formulation of Principle", Memoirs of the Faculty of Engineering, Kyoto Univ., Vol. 30, Part I, Jan. 1968, pp. 235-263.

[32] Brull, M.A., Vinson, J.R., "Transient Temperature Distribution in Shells of Revolution", J. Aero/Space Sci., Dec. 1958, pp. 742-750.

[33] Pfahl, R.C., "Transient Radial Temperature Distributions in Cylindrical Shells", Int. J. Heat Mass Transfer, Vol. 12, 1969, pp. 1704-1706.

[34] Olson, M.D., Fung, Y.C., "Comparing Theory and Experiment for the Supersonic Flutter of Circular Cylindrical Shells", AIAA Jnl., Vol. 5, No. 10, Oct. 1967, pp. 1849-1855.

[35] Evensen, D.A., Olson, M.D., "Circumferentially Traveling Wave Flutter of a Circular Cylindrical Shell", AIAA Jnl., Vol. 6, No. 8, 1968, pp. 1522-1527.

[36] Dowell, E.M., "Modal Equations for the Nonlinear Flexural Vibrations of a Cylindrical Shell", Int. J. Solids Structures, Vol. 4, No. 10, 1968.

[37] Dowell, E.M., "Panel Flutter: A Review of the Aeroelastic Stability of Plates and Shells", AIAA Jnl, Vol. 8, No. 3, 1970, pp. 385-399.

[38] Nigam, S.D., Agrawal, H.C., "A Variational Principle for Convection of Heat", J. Math. Mech., Vol. 9, 1960, pp. 864-884.

[39] Olsson, U., "On a Variational Principle in Heat Conduction Formulated in the Internal Energy", Flygmotor Research, RF 5:3034, Nov. 1969.

[40] Olsson, U., "Application of a Perturbation Method to Heat Flow Analysis in Materials Having Temperature Dependent Properties", AIAA Jnl., Vol. 8, No. 10, Oct. 1970, pp. 1902-1903.

[41] Boley, B.A., Weiner, J.K., "Theory of Thermal Stresses", Ch. 6, p. 188, J. Wiley and Sons Inc., New York 1960.

[42] Olsson, U., "Transient Heating of a Cylindrical Shell with Temperature Dependent Material Properties", Flygmotor Research, RF 5:3358, Febr. 1971.

[43] Olsson, U., "Some Notes on the Flutter of Jet Engine Afterburners", Flygmotor Research, RF 5:3359, Febr. 1971.

[44] Olsson, U., "On Free Vibrations at Temperature Dependent Material Properties and Transient Temperature Fields", Flygmotor Research, RF 5:3258, Sept. 1970.

[45] Olsson, U., "Transient Thermal Deformations of Cylindrical Shells with Temperature Dependent Material Properties", Flygmotor Research, RF 5:3370, Febr. 1971.

[46] Olsson, U., "Pressure-Induced Deflections of Heated Cylindrical Shells with Temperature Dependent Material Properties", Flygmotor Research, RF 5:3369, Febr. 1971.

[47] Olsson, U., "Nonlinear Thermoelastic Equations for Beams and Cylindrical Shells Having Temperature Dependent Properties", Flygmotor Research, RF 5:3014, Oct. 1969.

[48] Olsson, U., "Reduction of the Differential Equations for a Cylindrical Shell of Temperature Dependent Material Properties to Ordinary Differential Equations", Flygmotor Research, RF 5:3155, April 1970.

[49] Olsson, U., "Supersonic Flutter of Heated Circular Cylindrical Shells with Temperature Dependent Material Properties", Flygmotor Research, RF 5:3395, March 1971.

Acknowledgement

The author wants to express his gratitude to Prof. J. Hult, head of the Division of Solid Mechanics at Chalmers University of Technology, for valuable support during the course of the work. The author is also obliged to Mr L. Mossberg for making the numerical solutions of Part 10, to Mr L. Persson and Dr B. Persson for discussions and to Miss G. Johansson and Mrs M. Karlsson for typing the manuscripts.

ON A VARIATIONAL METHOD IN HEAT CONDUCTION FORMULATED IN THE INTERNAL ENERGY

Ulf Olsson *

Svenska Flygmotor AB, Trollhattan, Sweden

Introduction

Variational methods in heat flow analysis were introduced by Biot,[1,2] formulated in the temperature of the body and confined to problems involving prescribed surface temperature. The methods were later extended by various authors,[3,4] to include prescribed surface heat fluxes and radiation boundary conditions.

In this paper a variational principle in heat conduction is formulated in the internal energy. The principle corresponds to that formulated in the temperature by Biot, the two methods being identical at temperature-independent materials.

Although this new method does not give particularly more accurate results than that of Biot, it is considered to be a valuable alternative at temperature-dependent materials mainly because convective heat flows are more naturally taken care of.

---

* Research Engineer

Biot's variational principle

Biot has formulated the variational principle:

$$\frac{\partial F}{\partial \ell_k} + \frac{\partial D}{\partial \ell_k} + S_k = 0 \qquad (1)$$

directly corresponding to the heat flow equation:

$$k\theta,_i + \dot{H}_i = 0 \qquad (2)$$

in a body of volume V and boundary B.

Here $\ell_k(t)$ is a set of generalized coordinates, and:

$$F = \int_V \int_0^\theta c\theta d\theta dV \qquad (3)$$

$$D = \frac{1}{2} \int_V \frac{1}{k} \dot{H}_i \dot{H}_i dV \qquad (4)$$

$$S_k = \int_B \theta \frac{\partial H_i}{\partial \ell_k} \nu_i dB \qquad (5)$$

The temperature field is defined by θ and the vector H_i by the relation:

$$H_{i},_{i} = -c\theta + \int_0^t \dot{Q} dt \qquad (6)$$

where $\dot{Q}$ is the heat generation per unit time and unit volume, c is the heat capacity per unit volume, k is the thermal conductivity, and ν_i denotes the i-component of the unit normal vector of the surface B taken positive outward.

Energy formulation

The energy balance for an incompressible continuum, neglecting work done by the body forces and the surface tractions, may be written:

$$\rho \dot{E} + \rho(Eu_i)_{,i} + q_{i,i} - \dot{Q} = 0 \tag{7}$$

Here ρ is the density of the material, E the internal energy per unit mass of the body, u_i a velocity vector component, and q_i the heat flux vector defined by:

$$q_i = -k\,\theta_{,i} \tag{8}$$

Introducing vector fields H_i and W_i, Eq. (7) may be rewritten as:

$$\dot{H}_i = \rho E u_i + q_i - \dot{W}_i \tag{9}$$

$$H_{i,i} = -\rho E \tag{10}$$

$$Q = W_{i,i} \tag{11}$$

The equations (8)-(11) are to be solved under the following boundary conditions:

$$\theta = \theta_b \text{ or } E = E_b \quad \text{on } B_1 \tag{12}$$

$$q_i = q_{ib} \qquad \text{on } B_2 = B - B_1 \tag{13}$$

$$u_i = 0 \qquad \text{on } B \tag{14}$$

The latter two conditions indicate that:

$$\delta H_i = 0 \qquad \text{on } B_2 \tag{15}$$

It may now be proved that Eqs. (9)-(10) together with the boundary conditions (12) and (15) are the necessary conditions for the following variational equation to hold for an arbitrary variation of the vector H_i:

$$\delta \int_V \frac{1}{2}\rho^2 E^2 dV + \int_B \rho E_b \delta H_i \nu_i dB +$$

$$+ \int_V \frac{\rho c}{k} (\dot{H}_i - \rho E u_i + \dot{W}_i)\, \delta H_i dV = 0 \tag{16}$$

Proof.

Using Eqs. (8) and (10) together with Gauss' theorem and the relation:

$$E_{,j} = c\,\theta_{,j} \tag{17}$$

Eq. (16) may be rewritten as:

$$\int_B \rho(E_b - E)\,\delta H_i \nu_i dB +$$

$$+ \int_V \frac{\rho c}{k}(\dot{H}_i - \rho E u_i + \dot{W}_i - q_i)\,\delta H_i dV = 0 \tag{18}$$

To satisfy this equation at arbitrary δH_i in V and B, the relations (9), (12) and (15) are necessary conditions.

Q.E.D.

Introducing:

$$D = \int_V \frac{1}{2}\frac{\rho c}{k}(\dot{H}_i - \rho E u_i + \dot{W}_i)(\dot{H}_i - \rho E u_i + \dot{W}_i)\ dV \tag{19}$$

$$F = \frac{1}{2}\int_V \rho^2 E^2 dV \tag{20}$$

$$S_k = \int_{B_1} \rho E_b \frac{\partial H_i}{\partial \ell_k}\nu_i dB + \int_{B_2} \rho E_b \frac{\partial H_i}{\partial \ell_k}\nu_i dB_2 \tag{21}$$

where $\ell_k(t)$ is a set of generalized coordinates, the Eq. (15) may be rewritten in the Lagrangian form, similar to Eq. (1):

$$\frac{\partial F}{\partial \ell_k} + \frac{\partial D}{\partial \dot{\ell}_k} + S_k = 0 \tag{22}$$

Comparison with Biot's method

In order to compare the variational principle given here to that of Biot a special case has been analyzed viz. the semi-infinite solid with prescribed surface temperature, whose specific heat varies linearly with temperature as:

$$c = c_o(1+\frac{\theta}{\theta_b}) \tag{23}$$

while its heat conductivity is independent of the temperature.

Let the surface temperature be θ_b and assume that the temperature field within the solid may be approximated by:

$$\theta = \theta_b(1-\frac{x}{\ell})^2 \tag{24}$$

where $\ell(t)$ is the "penetration depth" of the temperature rise.

After having calculated the internal energy, the one-dimensional vector H is obtained from Eq. (10), using the condition H=0 at $x=\ell$. Using ℓ as a generalized coordinate, D, F and S_k from Eqs. (19)-(21) are introduced into (22), which with the condition $\ell=0$ at t=0 gives a solution for ℓ and thus for the temperature field.
The result is:

$$\ell = 3{,}01\ (\frac{k_o}{\rho c_o}\ t)^{1/2} \tag{25}$$

while Biot[1], using the same assumed temperature profile, obtained:

$$\ell = 2.97\ (\frac{k_o}{\rho c_o}\ t)^{1/2} \tag{26}$$

The resulting temperature distributions have been compared to a perturbation solution[5]. As shown in Fig. 1, the agreement of the present method with that of Biot is quite satisfactory.

(Fig. 1)

References

[1] Biot, M.A., "New Methods in Heat Flow Analysis with Application to Flight Structures", Journal of the Aeronautical Sciences, Vol. 24, No. 12, Dec. 1957, pp. 857-873.

[2] Biot, M.A., "Further Development of New Methods in Heat Flow Analysis", Journal of the Aerospace Sciences, Vol. 26, No. 6, June 1959, pp. 367-381.

[3] Lardner. T.J., "Biot's Variational Principle in Heat Conduction", AIAA Journal, Vol. 1, No. 1, Jan. 1963, pp. 196-206.

[4] Zyszkowski, W., "The Transient Temperature Distribution in One-Dimensional Heat Conduction Problems With Nonlinear Boundary Conditions", Journal of Heat Transfer, No. 2, Feb. 1969, pp. 77-82.

[5] Persson, B., "Heat Conduction in A Semi-Infinite Solid With Temperature-Dependent Properties", Flygmotor Research, RF 5:1704, 1965.

Ulf Olsson

Fig. 1

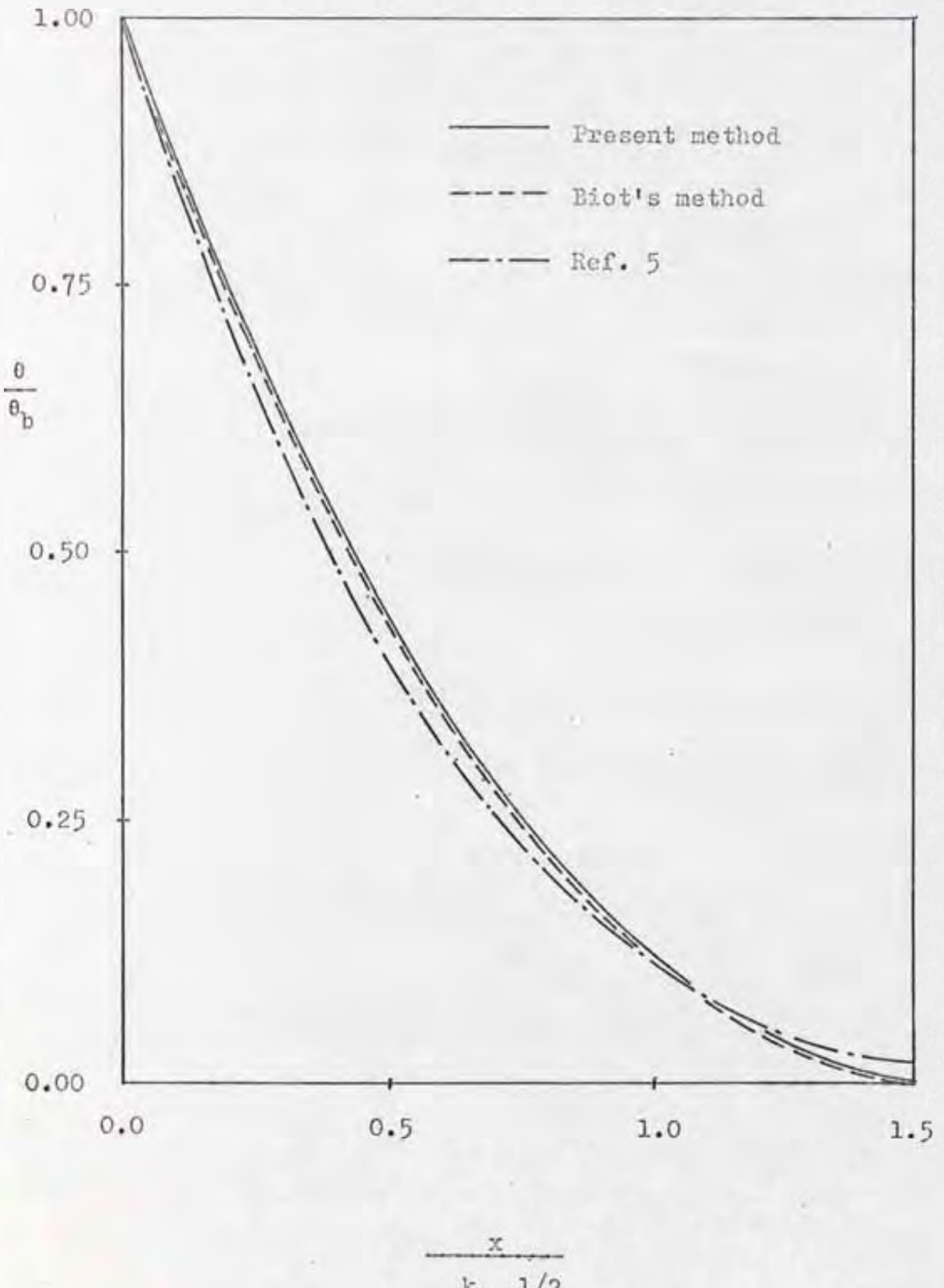

APPLICATION OF A PERTURBATION METHOD TO HEAT FLOW ANALYSIS IN MATERIALS HAVING TEMPERATURE-DEPENDENT PROPERTIES

Ulf Olsson *

Svenska Flygmotor AB, Trollhattan, Sweden

Introduction

In modern technology materials are often exposed to temperature ranges of such magnitudes that material property variations will be of great importance. The perturbation method or the method of successive approximations has proved itself to be a valuable tool in the analysis of the resulting non-linear boundary value problems[1,2]. It is intended here to study the application of this method to heat flow problems from a more theoretical point of view.

The solutions are expanded in powers of one parameter common for the various material properties, thereby splitting up the original non-linear problem into a set of interdependent linear ones. It is shown that the difficulties arising because of the products of derivatives in these equations may be released through a suitable transformation (Theorem 1, Eq. (10)). In addition a method is given (Theorem 2), which makes it possible to predict the convergence of the series.

---

* Scientist, Research Department

This method may also be used to obtain bounds on the solutions to the classical linear heat flow problem. It is a generalization of a method given by Boley[3] to include transient conditions, internal heat generation and convective heat transfer to the surface of the body. The principle is to obtain the temperature bounds starting out from assumed bounds on the prescribed heat flows. This is contrary to the method used by e.g. Appl and Hung[4], who choose bounds on the temperature in such a way that the heat generated in the body is approximated as good as possible.

Theory

Consider a continuum of volume V, boundary B and temperature T_s. At t=o this body is exposed to a heat load at the boundary and an in time and space varying temperature field is generated, described by the following boundary value problem:

$$(k(\theta)\ \theta_{,j})_{,j}+Q = \rho c(\theta) \frac{\partial \theta}{\partial t} \qquad \text{in V} \qquad (1)$$

$$-k(\theta)\ \theta_{,j} \nu_j - h(\theta)(\theta-\theta_a) = q_r \qquad \text{on B} \qquad (2)$$

$$\theta = T-T_s = 0 \qquad \text{at t=o} \qquad (3)$$

where k is the heat conductivity, c the specific heat, h the film heat transfer coefficient, θ_a the ambient temperature, Q the heat generated per unit volume of the body, q_r the surface heat flux and ν the normal to the boundary, which is taken positive in the outward direction.

Theorem 1.

Let the material properties k, c and h be written as:

$$f(\theta) = f_o + \varepsilon f_1 \theta + \varepsilon^2 f_2 \theta^2 \qquad (4)$$

where f stands for k, c or h.

Then using ε as a perturbation parameter, the nonlinear boundary value problem (1)-(3) may be reduced to the following set of linear problems:

$$k_o\ \psi_{m,ii} + Q_m - \rho c_o \frac{\partial \psi_m}{\partial t} = 0 \qquad \text{in V} \qquad (5)$$

$$-k_o\ \psi_{m,i} \nu_i - h_o \psi_m = q_m \qquad \text{on B} \qquad (6)$$

$$\psi_m = 0 \qquad \text{at t=0} \qquad (7)$$

$$m = 0, 1, 2 \ldots$$

where:

$$Q_m = Q\delta_{mo} - \frac{1}{2}\rho c_o \left(\frac{c_1}{c_o} - \frac{k_1}{k_o}\right)\frac{\partial \phi'_{m-1}}{\partial t} -$$

$$- \frac{1}{3}\rho c_o \left(\frac{c_2}{c_o} - \frac{k_2}{k_o}\right)\frac{\partial \phi''_{m-2}}{\partial t} \qquad (8)$$

$$q_m = q_r\,\delta_{mo} - h_o\left(\frac{1}{2}\frac{k_1}{k_o} - \frac{h_1}{h_o}\right)\phi'_{m-1} - h_o\left(\frac{1}{3}\frac{k_2}{k_o} - \frac{h_2}{h_o}\right)\phi''_{m-2} -$$

$$-h_o\theta_a - h_1\theta_a\theta_{m-1} - h_2\theta_a\theta_{m-2} \qquad (9)$$

$$\theta_m = -\frac{1}{2}\frac{k_1}{k_o}\phi'_{m-1} - \frac{1}{3}\frac{k_2}{k_o}\phi''_{m-2} + \psi_m \qquad (10)$$

$$\phi'_m = \sum_{n=o}^{m} \theta_{m-n}\,\theta_n \qquad (11)$$

$$\phi''_m = \sum_{n=o}^{m} \phi'_{m-n}\,\theta_n \qquad (12)$$

$$\theta = \sum_{n=o}^{\infty} \varepsilon^m\,\theta_m \qquad (13)$$

This theorem is proved through introducing Eqs. (4) and (13) into Eqs. (1)-(3) and singling out coefficients of ε, which give a set of linear equations, containing products of derivatives to the functions θ_m. These products are removed by introducing Eq. (10), which considerably simplifies the problem and leads to Eqs. (5)-(9), containing only time derivatives of the products of θ_m.

In order to predict the convergence of the series (13), consider the general heat flow problem:

$$k_o\, T,_{ii}+Q = \rho c_o \frac{\partial T}{\partial t} \qquad \text{in } V \qquad (14)$$

$$k_o\, T,_i v_i+h_o T+q = 0 \qquad \text{on } B \qquad (15)$$

$$T = 0 \qquad \text{at } t=o \qquad (16)$$

If $Q \geq 0$ and $q \leq 0$ then from energy considerations $T \geq 0$ and the following theorem can be stated:

Theorem 2.

Let T' be a solution to the heat flow problem (14)-(16) with Q' an arbitrary constant and $q'=o$, let T'' be the corresponding solution with $Q''=0$ and q'' an arbitrary constant,

If in Eqs. (14)-(16):

$$q_m \leq q \leq q_M \qquad (17)$$

$$Q_m+\rho c_o \frac{T'}{Q'}\frac{\partial Q_m}{\partial t}+\rho c_o \frac{T''}{q''}\frac{\partial q_M}{\partial t} \leq Q \leq Q_M+$$

$$+\rho c_o \frac{T'}{Q'}\frac{\partial Q_M}{\partial t}+\rho c_o \frac{T''}{q''}\frac{\partial q_m}{\partial t} \qquad (18)$$

then at all times $t \geq o$:

$$\frac{Q_m}{Q'}T'+\frac{q_M}{q''}T'' \leq T \leq \frac{Q_M}{Q'}T'+\frac{q_m}{q''}T'' \qquad (19)$$

The theorem is proved through the introduction of the fictitious temperatures:

$$T_M = \frac{Q_M}{Q'}T'+\frac{q_m}{q''}T''-T \qquad (20)$$

$$T_m = \frac{Q_m}{Q'}T'+\frac{q_M}{q''}T''-T \qquad (21)$$

into Eqs. (14)-(16). Using Eqs. (17)-(18) it follows that $T_{II} \geq o$ and $T_n \leq o$, which proves Eq. (19).

The theorem proved above, giving bounds on the solution to the linear heat flow problem, can be used to predict the magnitude of the function ψ_{m+1} once ψ_m has been solved from Eqs. (5)-(7) and the corresponding heat flows Q_{m+1} and q_{m+1} from Eqs. (8) and (9).

Example

The theory outlined above is applied to the problem of finding the transient temperature field in a convectively heated plate of inconel, having the following material properties, ($\theta = T - 273^{o}K$):

$$\rho = 8250 \quad kg/m^3$$

$$k = 14.7 + 0.015\ \theta \ W/m^{o}K$$

$$c = 430 + 0.265\ \theta \ Ws/kg^{o}K$$

The ambient temperature θ_a and the heat transfer coefficient h are taken as:

$$\theta_a = 700^{o}K$$

$$h = 190 + 0.029\ \theta \ W/m^2\ {}^{o}C$$

The thickness of the plate is taken to be $\delta = 3$ mm with no heat production within it and no heat flux at the surface i.e. $Q = q_r = o$.

The solution θ_o for temperature-independent material properties is derived first and introduced into Eqs. (8) and (9) to give the intermediate heat flows Q_1 and q_1. After having chosen bounds on these functions so that the relations (17) and (18) are satisfied, the corresponding bounds on the function ψ_1 are obtained from Eq. (19) once

ψ_1' and ψ_1'' have been solved from Eqs. (14)-(16). Lastly the function ψ_1 itself is derived from Eqs. (5)-(7) and a second approximation, m=1, of the temperature field obtained from Eqs. (10)-(13).

The calculations have been carried out for a chosen value of $\varepsilon=0.01$ and with the following bounds on the heat flows:

$$Q_m = 0 \qquad Q_M = Q_1$$

$$q_m = q_1 \qquad q_m = -10^6(1-e^{-0.035\ t})$$

The found time histories of the function ψ_1 and the temperature field in the middle of the plate are shown in Figs. (1) and (2) below, the solutions of the linear differential equations being taken from Ref. 5.

References

[1]Trostel, R., "Stationäre Wärmespannungen mit temperaturabhängigem Stoffwerten", Ing.-Archiv p.416, 1958.

[2]Ismail, I.A., Nowinski, J.L., "Thermoelastic Problems for Shells of Revolution Exhibiting Temperature-Dependent Properties", Appl. Sci. Res., 14, 3, p.211, 1964/1965

[3]Boley, B.A., Weiner, J.K., "Theory of Thermal Stresses", ch.6, p.188, John Wiley and Sons Inc., New York 1960.

[4]Appl, F.C., Hung, H.M., "A Principle for Convergent Upper and Lower Bounds", Int. J. Mech. Sci., vol. 6, p.381, 1964.

[5]Carslaw, H.C., Jaeger, J.C., "Conduction of Heat in Solids", ch. 3, 2nd ed., Oxford University Press, Oxford, 1959.

Ulf Olsson

Fig. 1

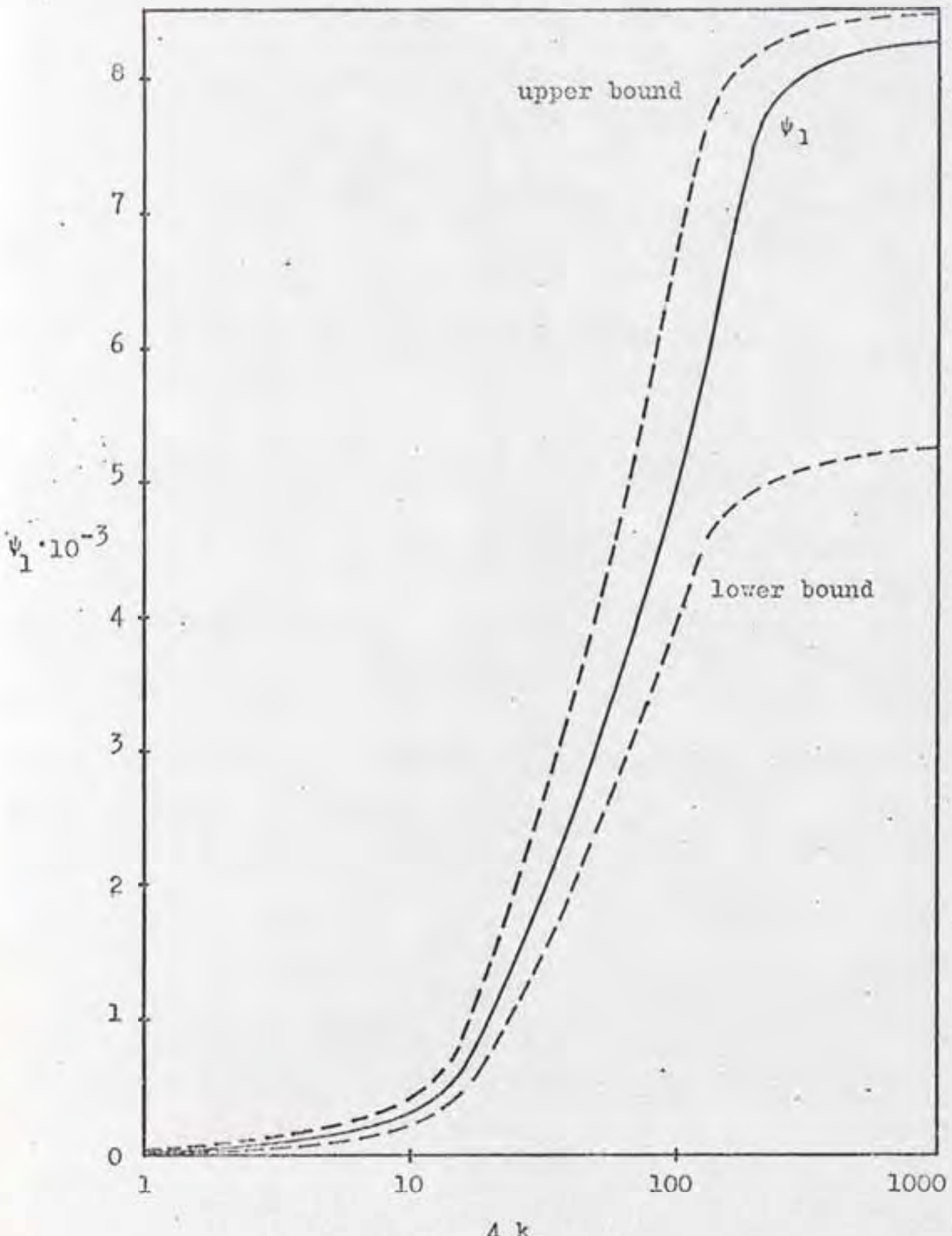

Ulf Olsson

Fig. 2

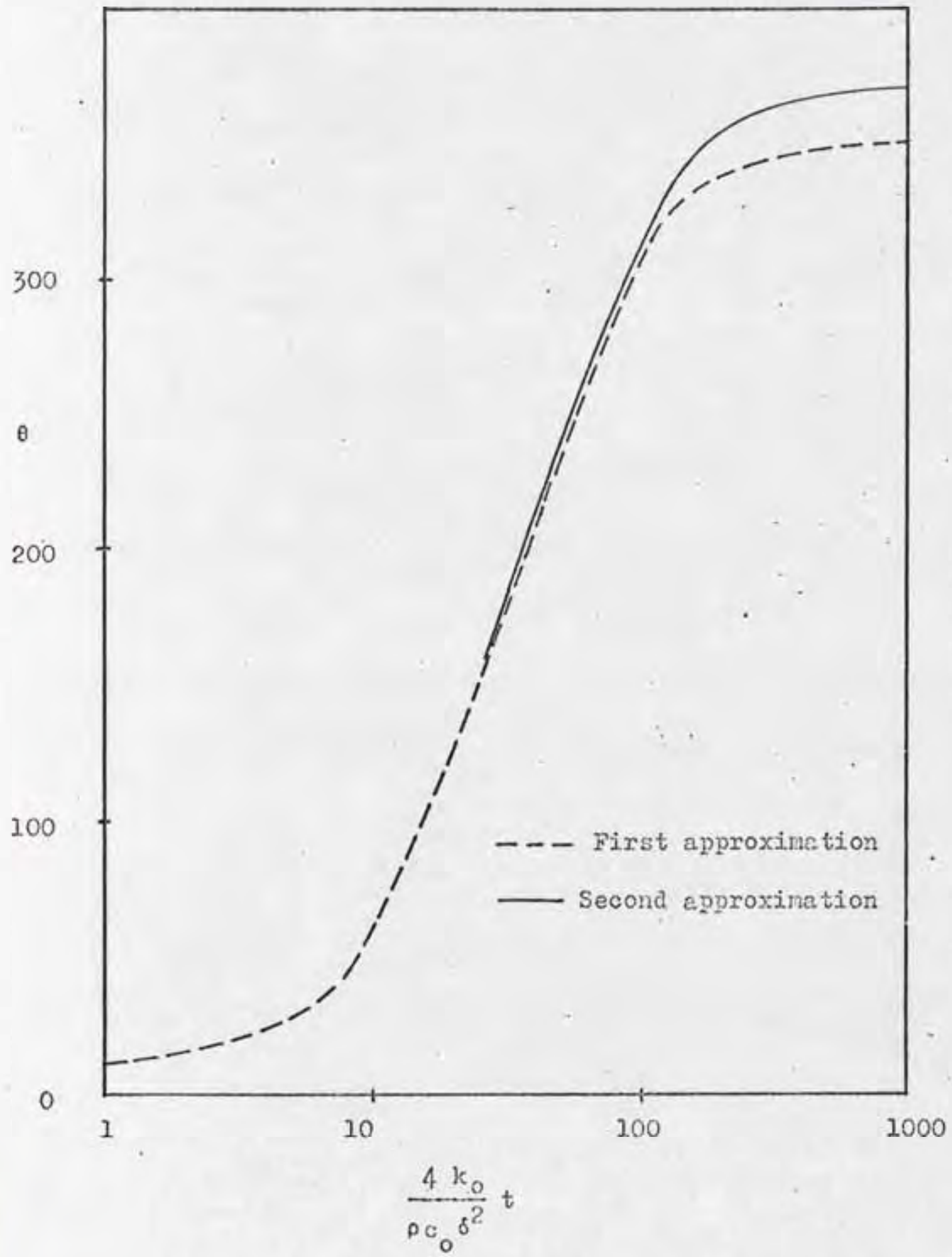

Figure captions

Fig. 1 The function ψ_1 with upper and lower bounds.

Fig. 2 First and second approximation of the temperature in the middle of the plate.

TRANSIENT HETATING OF A CYLINDRICAL SHELL WITH TEMPERATURE DEPENDENT MATERIAL PROPERTIES

Ulf Olsson [1]

Introduction

In Refs. 1 and 2 are developed two methods of solution to the heat flow problem when the thermophysical material properties depend on the temperature. Here, we will use the perturbational method[2] in an investigation of the influence of the temperature dependence on the transient temperature field in a cylindrical shell overflown by hot gas streams.

At its inner surface the shell is supposed to be heated convectively and by a constant heat flux. Simultaneously, it is cooled convectively at its outer surface. The temperature of the outer gas stream is assumed to be a constant while that of the inner one varies axially as a first order cosine series. There are no tangential temperature variations, i.e. the problem is rotationally symmetric.
Under these assumptions, the nonlinear heat flow equation will be transformed to a set of linear equations, which will then be solved approximately. The transient temperature fields emanating from convective heating and constant heat flux will be calculated separately and compared as regards the influence of the temperature dependent material properties.

---

[1]Scientist, Research Department, Volvo Flygmotor AB, Trollhattan, Sweden.

Theory and Solutions

We have to solve the following differential equation

$$\frac{\partial}{\partial \xi}\left(k \frac{\partial \theta}{\partial \xi}\right) + \frac{\partial}{\partial \zeta}\left(k \frac{\partial \theta}{\partial \zeta}\right) = \rho c \frac{\partial \theta}{\partial t} \tag{1}$$

with the boundary conditions

$$-k \frac{\partial \theta}{\partial \zeta} = h(\theta - \theta_c) \quad ; \quad \zeta = \frac{\delta}{2} \tag{2}$$

$$k \frac{\partial \theta}{\partial \zeta} = h(\theta - \theta_h) - q \quad ; \quad \zeta = -\frac{\delta}{2} \tag{3}$$

$$\frac{\partial \theta}{\partial \xi} = 0 \quad ; \quad \xi = 0 \text{ and } L \tag{4}$$

where the last condition, indicating that the heat flow at the ends of the shell vanishes, follows approximately if it is assumed that $L >> \delta$ and that the gas temperatures vary smoothly along the shell.

There is also an initial condition

$$\theta = 0 \quad \text{at} \quad t=0 \tag{5}$$

Now, using the methods outlined in Ref. 2, let the material properties k and c vary as

$$f(\theta) = f_o + \epsilon f_1 \theta \quad ; \quad f = k, c \tag{6}$$

Then using ϵ as a perturbation parameter, the nonlinear boundary value problem described by Eqs. (1)-(5) may be transformed to the following linear one[2]

$$k_o\left(\frac{\partial^2 \psi_m}{\partial \xi^2} + \frac{\partial^2 \psi_m}{\partial \zeta^2}\right) + Q_m - \rho c_o \frac{\partial \psi_m}{\partial t} = 0 \tag{7}$$

$$-k_o \frac{\partial \psi_m}{\partial \zeta} - h \psi_m = q_m^+ \quad ; \quad \zeta = \frac{\delta}{2} \tag{8}$$

$$k_o \frac{\partial \psi_m}{\partial \zeta} - h \psi_m = q_m^- \quad ; \quad \zeta = -\frac{\delta}{2} \tag{9}$$

$$\frac{\partial \psi_m}{\partial \xi} = 0 \quad ; \quad \xi = 0 \text{ and } L \tag{10}$$

$$\psi_m = 0 \qquad ; \qquad t = 0 \tag{11}$$

where for m = 0, 1, 2 ...

$$Q_m = -\frac{1}{2}\rho c_o \left(\frac{c_1}{c_o} - \frac{k_1}{k_o}\right) \frac{\partial\phi_{m-1}}{\partial t} \tag{12}$$

$$q_m^+ = -\frac{1}{2} h \frac{k_1}{k_o} \phi_{m-1} - h\theta_c \delta_{mo} \qquad ; \quad \zeta = \frac{\delta}{2} \tag{13}$$

$$q_m^- = -\frac{1}{2} h \frac{k_1}{k_o} \phi_{m-1} - h\theta_h \delta_{mo} - q\delta_{mo} \quad ; \quad \zeta = -\frac{\delta}{2} \tag{14}$$

$$\theta_m = -\frac{1}{2}\frac{k_1}{k_o} \phi_{m-1} + \psi_m \tag{15}$$

$$\phi_m = \sum_{n=0}^{m} \theta_{m-n}\,\theta_n \tag{16}$$

$$\theta = \theta_o + \varepsilon\theta_1 \tag{17}$$

Neglecting temperature variations through the wall and integrating Eq. (7) from $-\delta/2$ to $\delta/2$ according to Bolotin's method give

$$k_o \frac{\partial^2 \psi_m}{\partial \xi^2} - \frac{2h}{\delta} \psi_m - \rho c_o \frac{\partial \psi_m}{\partial t} + Q_m - q_m = 0 \tag{18}$$

$$\frac{\partial \psi_m}{\partial \xi} = 0 \qquad \xi = 0 \text{ and } L \tag{19}$$

$$\psi_m = 0 \qquad t = 0 \tag{20}$$

where

$$q_m = (q_m^+ + q_m^-)/\delta \tag{21}$$

If the temperature in the outer gas stream is a constant θ_c and that in the inner one is

$$\theta_h = \theta_{ho} - \theta_{h1} \cos \frac{\pi\xi}{L} \tag{22}$$

then Eq. (18) may be solved using Fourier series for Q_m, q_m and ψ_m in the form

$$\psi_m = \psi_{mo} + \psi_{m1} \cos \frac{\pi\xi}{L} + \psi_{m2} \cos \frac{2\pi\xi}{L} \tag{23}$$

which satisfies the boundary conditions Eq. (19).

Introducing the Fourier series into Eq. (18), singling out coefficients and solving the resulting equations under the initial condition Eq. (20) give

$$\psi_{mn} = e^{-\frac{t}{\tau_n}} \int_o^t e^{\frac{x}{\tau_n}} f_{mn}(x)\, dx \tag{24}$$

where

$$\tau_n = \rho c_o / \left(\frac{2h}{\delta} + k_o \frac{n^2\pi^2}{L^2}\right) \tag{25}$$

$$f_{mn} = (Q_{mn} - q_{mn})/\rho c_o \tag{26}$$

If there is no internal heat generation in the material one obtains after some calculations

$$\theta = \Phi_o + \Phi_1 \cos \frac{\pi\xi}{L} + \Phi_2 \cos \frac{2\pi\xi}{L} \tag{27}$$

where with q=0, i.e. for pure convective heating

$$\Phi_o = \psi_{oo} + \varepsilon\psi_{1o} - \frac{1}{2}\varepsilon\frac{k_1}{k_o}\left(\psi_{oo}^2 + \frac{1}{2}\psi_{o1}^2\right) \tag{28}$$

$$\Phi_1 = \psi_{o1} + \varepsilon\psi_{11} - \varepsilon\frac{k_1}{k_o}\psi_{oo}\psi_{o1} \tag{29}$$

$$\Phi_2 = \varepsilon\psi_{12} - \frac{1}{4}\varepsilon\frac{k_1}{k_o}\psi_{o1}^2 \tag{30}$$

$$\psi_{oo} = \frac{\theta_c+\theta_{ho}}{2}\ (1-e^{-\frac{t}{\tau_o}}) \tag{31}$$

$$\psi_{o1} = -\frac{h}{\rho c_o \delta}\ \theta_{h1}\ \tau_1 (1-e^{-\frac{t}{\tau_1}}) \tag{32}$$

$$\psi_{10} = b\tau_o \frac{(\theta_c+\theta_{ho})^2}{4} + \frac{b\tau_o h^2\ \theta_{h1}^2\ \tau_1^2}{2\delta^2\ \rho^2\ c_o^2}$$

$$+(\frac{a}{2}\ (\theta_c+\theta_{ho})^2 + \frac{h^2\ \theta_{h1}^2}{\delta^2\rho^2 c_o^2}\ \frac{a+b\tau_o}{(\frac{1}{\tau_o}-\frac{1}{\tau_1})(\frac{1}{\tau_o}-\frac{2}{\tau_1})}\ )\ e^{-\frac{t}{\tau_o}}$$

$$-\frac{a+b\tau_o}{2}\ (\theta_c+\theta_{ho})^2\ \frac{t}{\tau_o}\ e^{-\frac{t}{\tau_o}} - \frac{2a+b\tau_o}{4}\ (\theta_c+\theta_{ho})^2\ e^{-\frac{2t}{\tau_o}}$$

$$-(b+\frac{a}{\tau_1})\ \frac{h^2\ \theta_{h1}^2\ \tau_1^2}{\delta^2\rho^2 c_o^2}\ \frac{1}{\frac{1}{\tau_o}-\frac{1}{\tau_1}}\ e^{-\frac{t}{\tau_1}}$$

$$+(b+\frac{2a}{\tau_1})\ \frac{h^2\ \theta_{h1}^2\ \tau_1^2}{2\rho^2\delta^2 c_o^2}\ \frac{1}{\frac{1}{\tau_o}-\frac{2}{\tau_1}}\ e^{-\frac{2t}{\tau_1}} \tag{33}$$

$$\psi_{11} = -b\tau_1\ (\theta_c+\theta_{ho})\ \frac{h\,\theta_{h1}\ \tau_1}{\delta\rho\ c_o}$$

$$+\frac{\frac{a}{\tau_o}+b}{\frac{1}{\tau_1}-\frac{1}{\tau_o}}\ \frac{h\ \theta_{h1}\ \tau_1}{\delta\rho\ c_o}\ (\theta_c+\theta_{ho})\ e^{-\frac{t}{\tau_o}}$$

$$+\frac{b(1-\frac{\tau_1}{\tau_o}-\frac{\tau_o}{\tau_1})-a\ \frac{\tau_o}{\tau_1^2}}{\frac{1}{\tau_1}-\frac{1}{\tau_o}}\ \frac{h\,\theta_{h1}\ \tau_1}{\delta\rho\ c_o}\ (\theta_c+\theta_{ho})\ e^{-\frac{t}{\tau_1}}$$

$$+(\frac{a}{\tau_1}+b)(\theta_c+\theta_{ho})\ \frac{h\ \theta_{h1}\ \tau_1}{\delta\rho\ c_o}\ t\ e^{-\frac{t}{\tau_1}}$$

$$+(a(1+\frac{\tau_o}{\tau_1})+b\ \tau_o)(\theta_c+\theta_{ho})\ \frac{h\ \theta_{h1}\ \tau_1}{\delta\rho\ c_o}\ e^{-(\frac{1}{\tau_o}+\frac{1}{\tau_1})\ t} \tag{34}$$

$$\psi_{12} = \frac{b\tau_2}{2}\left(\frac{h\,\theta_{hl}\,\tau_1}{\delta\rho\, c_o}\right)^2 - \frac{\frac{a}{\tau_1}+b}{\frac{1}{\tau_2}-\frac{1}{\tau_1}}\left(\frac{h\,\theta_{hl}\,\tau_1}{\delta\rho\, c_o}\right)^2 e^{-\frac{t}{\tau_1}}$$

$$+\frac{\frac{a}{\tau_1}+\frac{b}{2}}{\frac{1}{\tau_2}-\frac{2}{\tau_1}}\left(\frac{h\,\theta_{hl}\,\tau_1}{\delta\rho\, c_o}\right)^2 e^{-\frac{2t}{\tau_1}}$$

$$+\frac{\frac{1}{\tau_2}-\frac{1}{\tau_1}-\frac{2\tau_2}{\tau_1^2}}{\left(\frac{1}{\tau_2}-\frac{1}{\tau_1}\right)\left(\frac{1}{\tau_2}-\frac{2}{\tau_1}\right)}\left(\frac{a}{\tau_2}+b\right)\frac{1}{2}\left(\frac{h\,\theta_{hl}\,\tau_1}{\delta\rho\, c_o}\right)^2 e^{-\frac{t}{\tau_2}} \qquad (35)$$

where in Eqs (33)-(35)

$$a = \frac{1}{2}\left(\frac{c_1}{c_o}-\frac{k_1}{k_o}\right) \qquad (36)$$

$$b = \frac{h}{\delta\rho c_o}\;\frac{k_1}{k_o} \qquad (37)$$

The corresponding results for a constant heat flux but with neglected convective heating, i.e. h=o, are

$$\psi_o = \frac{qt}{\rho c_o \delta} \qquad (38)$$

$$\psi_1 = -\frac{1}{2}\left(\frac{c_1}{c_o}-\frac{k_1}{k_o}\right)\frac{q^2t^2}{\rho^2 c_o^2 \delta^2} \qquad (39)$$

With Eqs. (15)-(17) this gives

$$\theta = \frac{qt}{\rho c_o \delta}\left(1-\frac{\varepsilon c_1}{2c_o}\;\frac{qt}{\rho c_o \delta}\right) \qquad (40)$$

The simplicity of this solution makes it convenient to use the case of a constant heat flux in order to investigate the influence of a temperature variation through the wall.

Assume the function ψ_m to vary linearly through the wall, i.e.

$$\psi_m = F_m + \frac{2\zeta}{\delta} G_m \tag{41}$$

Eq. (7) is then multiplied by 1 and ζ respectively and integrated from $-\delta/2$ to $\delta/2$ according to Bolotin's method. This gives two differential equations from which F_m and G_m may be solved in the form

$$F_m = \frac{1}{\rho c_o \delta} \int_o^t (q\delta_{mo} + \int_{-\delta/2}^{\delta/2} Q_m \, d\zeta) \, dx \tag{42}$$

$$G_m = \frac{\delta}{\rho c_o \delta} e^{-\frac{t}{\tau}} \int_o^t e^{\frac{x}{\tau}} (\int_{-\delta/2}^{\delta/2} Q_m \, \zeta d\zeta - \frac{\delta}{2} q\delta_{mo}) \, dx \tag{43}$$

where

$$\tau = \rho c_o \delta^2/12 \, k_o \tag{44}$$

and where Q_m is obtained from Eq. (12) with h=o.

Carrying out the calculations gives

$$F_o = \frac{q}{\rho c_o \delta} t \tag{45}$$

$$G_o = - \frac{q\,\delta}{4\,k_o} (1-e^{-\frac{t}{\tau}}) \tag{46}$$

$$F_1 = -\frac{1}{2}\left(\frac{c_1}{c_o} - \frac{k_1}{k_o}\right)\left(\frac{q^2}{\rho^2 c_o^{\,2} \delta^2}\, t^2 + \frac{\delta^2 q^2}{48 k_o^{\,2}} \left(1-e^{-\frac{t}{\tau}}\right)^2\right) \tag{47}$$

$$G_1 = \left(\frac{c_1}{c_o} - \frac{k_1}{k_o}\right)\left(\frac{q^2 \delta^2}{48 k_o^{\,2}} \left(1-e^{-\frac{t}{\tau}}\right) - \frac{q^2 t}{4\rho c_o k_o}\, e^{-\frac{t}{\tau}} + \right.$$

$$\left. \frac{3 q^2 t^2}{2\rho^2 c_o^{\,2} \delta^2}\, e^{-\frac{t}{\tau}}\right) \tag{48}$$

and from Eqs. (15)-(17)

$$\theta = \psi_o + \varepsilon \psi_1 - \varepsilon \frac{1}{2}\, \frac{k_1}{k_o}\, \psi_o^{\,2} \tag{49}$$

From Eq. (49) the average temperature in the wall is found to be

$$\theta = \frac{qt}{\rho c_o \delta}\left(1 - \frac{\varepsilon c_1}{2 c_o}\, \frac{qt}{\rho c_o \delta}\right) - \frac{\varepsilon c_1}{96 c_o}\, \frac{q^2 \delta^2}{k_o^{\,2}} \left(1-e^{-\frac{t}{\tau}}\right)^2 \tag{50}$$

If this is compared to Eq. (40), it is seen that the temperature variation through the wall does influence also the average wall temperature and that this influence is described by the last term in Eq. (50). This is in contrast to the case of temperature independent material properties, i.e. $\varepsilon = o$, where there is no such influence.

Results and Discussion

Calculations have been carried out for the following numerical values

$T_o=300^oK$, $\theta_{ho}=600^oC$, $\theta_{h1}=100^oC$, $\theta_c=100^oC$,

$q=10^5$ J/m^2 sec, $\delta=10^{-3}$ m, L=3 m,

$h=190$ J/m^{2}sec ^oC, $\rho=8150$ kg/m^3

$c=432+0.252\,\theta$ J/kg ^oC

$k=13.9+0.0231\,\theta$ J/m ^oC sec

For convective heating, only ϕ_o and ϕ_1 have been calculated and are shown in Figs. 1 and 2 with and without temperature dependence. The results indicate that even large variations in the thermophysical material properties have a relatively moderate effect on the temperature. In the temperature interval considered the specific heat changed with 20% and the heat conductivity with 60%. Still, the temperature at a given time did not differ more than 5% from the corresponding value if the material properties at θ=o had been used throughout the calculations. In this latter case the temperature would have been overestimated, see Fig. 1.

It is interesting to note. Fig. 1, that if the average values of the material properties in the actual temperature interval are used in the calculations, then the resulting temperature transient will be very near that found from perturbational theory. Thus, this would provide a simple and relatively exact approximation to the transient temperature field in a convectively heated thin-walled structure.

From Eq. (40) it is seen that at a constant heat flux to the wall the temperature dependence of the specific heat ($c_1 \geq 0$) tends to make the temperature rise less rapid. This is shown in Fig. 3. The temperature difference relative to the temperature independent case is half the variation of the specific heat i.e. maximum about 10% in the same temperature interval as for convective heating. Again, a calculation based on average material properties gives relatively exact results, Fig. 3.

Regarding the temperature variation through the wall, its influence on the average wall temperature is given by the last term in Eq. (50). In thin-walled shells this term has any significance only during the first few moments of the heating up period, Fig. 4. Thus, for the largest part of this period, Eq. (40) should provide a sufficiently accurate prediction of the average wall temperature.

Notations

$\theta = T-T_o$	increase in shell temperature
θ_c	temperature of the outer gas stream
θ_h	temperature of the inner gas stream
q	constant heat flux
k	heat conductivity
c	specific heat
h	heat transfer coefficient
ρ	density
ξ, ζ	axial and outside normal coordinates in shell median surface
δ	thickness of shell wall
L	length of shell
t	time

References

[1] Olsson, U., "On a Variational Principle in Heat Conduction Formulated in the Internal Energy", Flygmotor Research, RF 5:3034, Nov. 1969.

[2] Olsson, U., "Application of a Perturbation Method to Heat Flow Analysis in Materials Having Temperature Dependent Properties", AIAA Jnl., Vol. 8, No. 10, Oct. 1970, pp. 1902-1903.

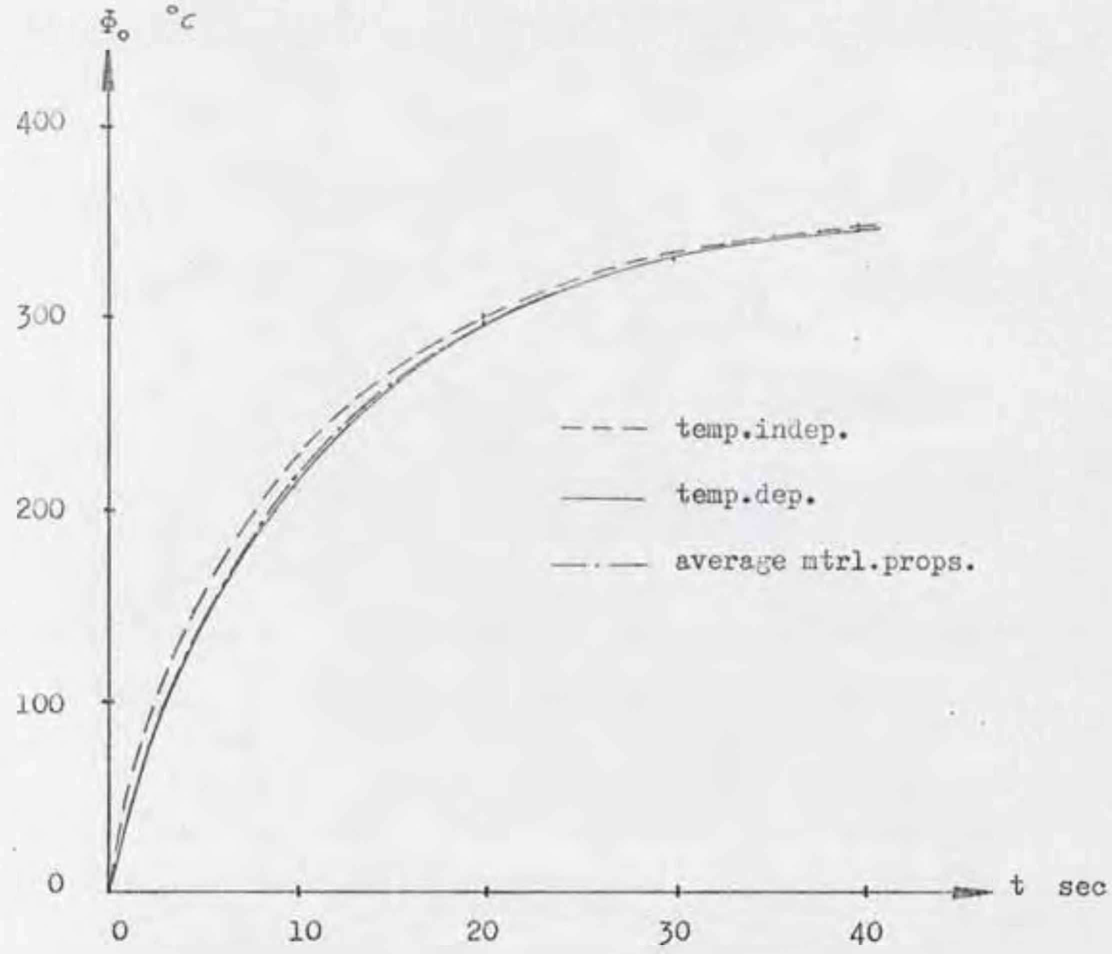

Fig. 1 Shell wall temperature Φ_o at convective heating

Fig. 2 Shell wall temperature Φ_1 at convective heating

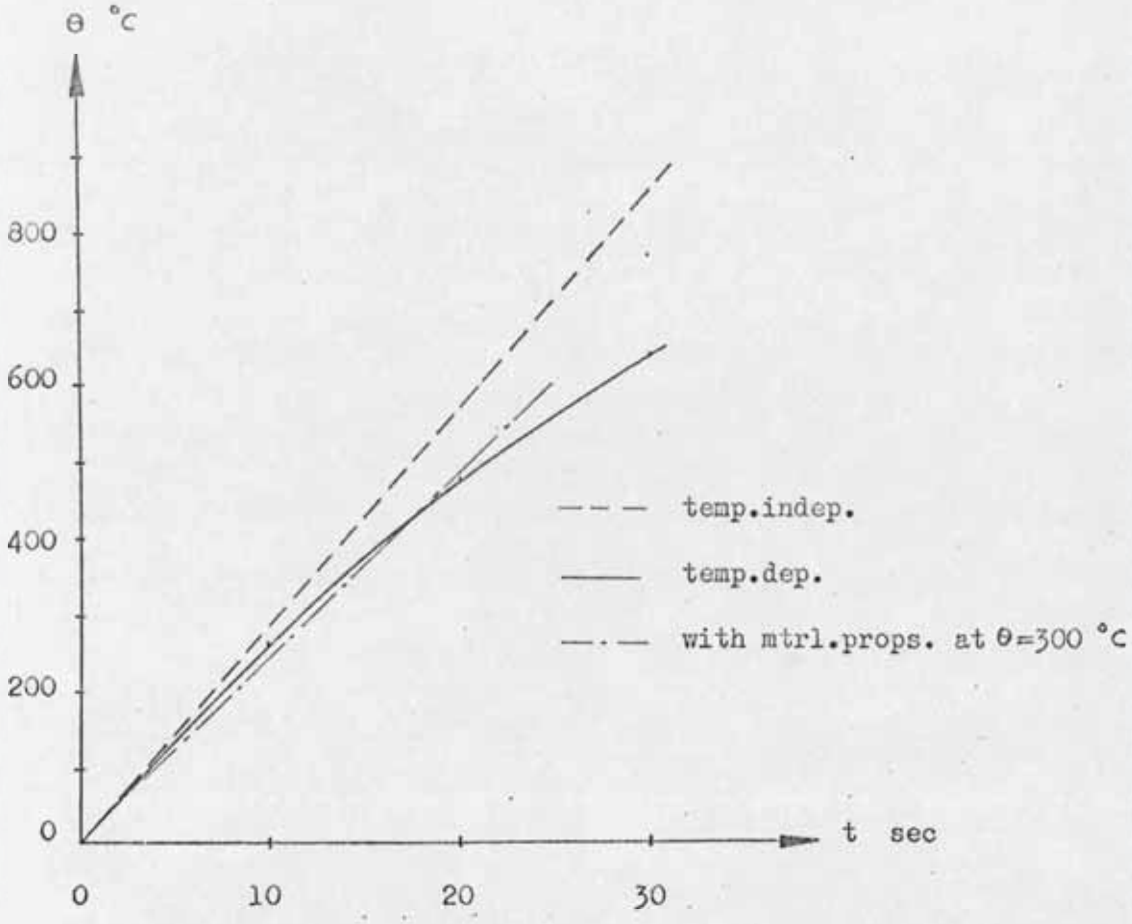

Fig. 3 Shell wall temperature a t constant heat flux to the wall

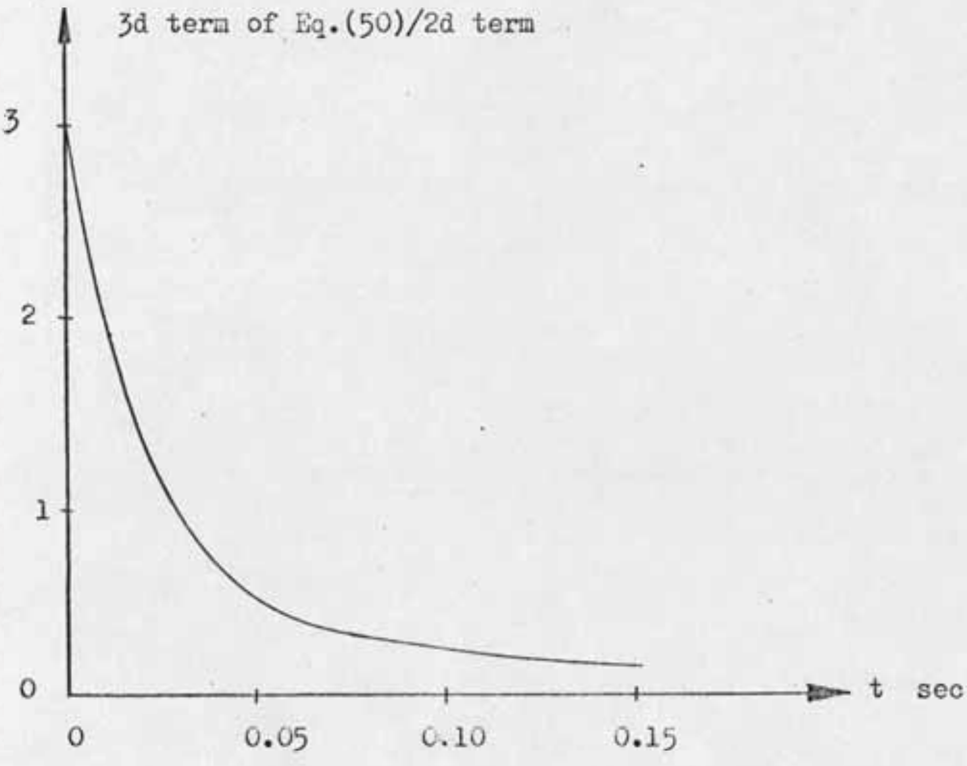

Fig. 4 Influence of temperature variation through the wall on average wall temperature

SOME NOTES ON THE FLUTTER OF JET ENGINE AFTERBURNERS

Ulf Olsson[1]

Introduction

A jet engine afterburner may be considered as a cylindrical shell exposed to a gas stream of high velocity and temperature. Such a shell may lose its stability and exhibit self-excited oscillations provided that certain critical conditions are fulfilled. At small amplitudes these conditions reduce to the demand that the velocity of the gas stream must be larger than a critical value for instability to occur. At larger amplitudes, when nonlinear effects must be taken into account, the critical conditions are more complicated and involve the amplitudes of the initial disturbances. However, at present we will concentrate on small deformations and neglect nonlinearities.

When the afterburner is ignited the velocity and temperature of the gas stream increase and the

[1]Scientist, Research Department, Volvo Flygmotor AB, Trollhattan, Sweden

shell is gradually heated up. Because of the temperature-dependence of the material properties such an increase of the wall temperature leads to a decrease in the stiffness of the shell. It is the purpose of the present work to investigate the influence of such effects on the stability of the afterburner.

Solutions

It is assumed in what follows that the temperature is uniform throughout the shell and that it varies so slowly with time that the transient coupling with the oscillations are negligible.

The well-known differential equations for a shallow cylindrical shell are

$$D\nabla^4 w + \frac{1}{R}\frac{\partial^2 \phi}{\partial x^2} + \rho_s \delta \frac{\partial^2 w}{\partial t^2} - N_x \frac{\partial^2 w}{\partial x^2} - Rp_m \frac{\partial^2 w}{\partial y^2} = p_a \quad (1)$$

$$\nabla^4 \phi = \frac{E\delta}{R}\frac{\partial^2 w}{\partial x^2} \quad (2)$$

If the aerodynamic loads on the shell wall are approximated by linear piston theory including a curvature correction term, the internal aerodynamic pressure will be [1]

$$p_a = -\rho_g\, a\, U \frac{\partial w}{\partial x} - \rho_g\, a \frac{\partial w}{\partial t} + \frac{\rho_g a^2}{2R}\, w \quad (3)$$

The shell is assumed to be simply supported.

Assuming the modal solution in the form

$$w = \delta\left(f \sin\frac{\pi x}{L} + g \sin\frac{2\pi x}{L}\right)\cos m\frac{y}{R} \quad (4)$$

and introducing it into Eq. (2) allows ϕ to be found as the particular solution to this equation. [2] Substituting ϕ, w and p_a into Eq. (1) and using a Galerkin procedure with $\partial w/\partial f$ and $\partial w/\partial g$ as weighting functions give two coupled equations

$$\frac{\partial^2 f}{\partial t^2} + \Delta\frac{\partial f}{\partial t} + \omega_{m_1}^2 f - \lambda g = 0 \quad (5)$$

$$\frac{\partial^2 g}{\partial t^2} + \Delta \frac{\partial g}{\partial t} + \omega_{m_2}^2 g + \lambda f = 0 \tag{6}$$

where

$$\Delta = \frac{a\rho_g}{\delta\rho_s} \tag{7}$$

$$\lambda = \frac{8aU\rho_g}{3\delta L\rho_s} \tag{8}$$

$$\omega_{mn}^2 = \frac{\mu\Omega^2}{12(1-\nu^2)}(1+n^2\beta^2)^2 + \frac{n^4\beta^4\Omega^2}{(1+n^2\beta^2)^2} - \frac{a^2\rho_g}{2\delta R\rho_s} + \frac{m^2 p_m}{\delta R\rho_s} \tag{9}$$

$$\Omega^2 = \frac{E}{\rho_s R^2} \qquad \mu = \frac{m^4\delta^2}{R^2} \qquad \beta = \frac{\pi R}{mL} \tag{10}$$

In order to investigate the possibilities of periodic solutions to Eqs. (5) and (6) we assume

$$f = F\cos\omega t \tag{11}$$

$$g = G\cos(\omega t + \psi) \tag{12}$$

introduce these into the equations and single out coefficients of sin ωt and cos ωt. We then find that a necessary condition for periodic solutions to exist is that

$$\lambda^2 = \Delta\frac{\omega_{m_2}^2 + \omega_{m_1}^2}{2} + \frac{(\omega_{m_2}^2 - \omega_{m_1}^2)^2}{4} \tag{13}$$

Since λ is directly proportional to U, Eq. (13) gives a critical gas velocity, U^*, above which the shell will exhibit self-excited oscillations with indefinitely growing amplitudes. Below we will study how this critical velocity depends on the operating conditions of the afterburner.

Results

As material we choose Hastelloy X whose temperature-dependence is known. With $p_m=0$ and fixed shell dimensions the important parameters are then p_g, T_g and T_w. p_g depends on the altitude of the aircraft, T_g and T_w on the burning conditions in the afterburner.

Calculations have been carried out for various sets of these parameters corresponding to an operating cycle of an arbitrary jet engine. For each such set the gas velocity is minimized with regard to the circumferential wave number thus giving both the mode of deformation and the critical gas velocity at which flutter begins. The results are shown in Table 1 below

T_g °K	T_w °K	p_g b	U^* m/sec	m
300	300	2	455	8
900	300	2	526	8
900	650	2	478	8
2000	650	2	573	8
2000	1200	2	455	8
900	1200	2	383	8
300	650	2	420	8
900	650	0.5	895	10
900	650	3.5	347	7

Table 1

Discussion

From the results given previously Figs. 1-4 have been constructed. As is seen from Fig. 1 the critical gas velocity decreases with increasing pressure in the gas stream. Thus the sensitivity to flutter could be reduced through climbing to higher altitudes. Figs. 2 and 3 show that an increase in T_g reduces the flutter sensitivity and that T_w has the opposite effect. For a working sequence of the engine this has the effect shown in Fig. 4.

When the engine is started, T_g and hence U^* increase very rapidly (0-1). This is followed by a relatively slow increase (during about 30 secs) of the wall temperature, which tends to decrease U^* (1-2). At ignition of the afterburner the course of events is the same (2-3-4). However, when the afterburner and the engine are shut off one obtains first a rapid decrease in U^* followed by a slow increase.

Now, the velocity U of the gas stream grows with T_g and realistic values show that it may be larger than the critical value U^* some time after ignition of the afterburner, a fictitious example being shown in Fig. 4.

Note also that it is the gas nearest to the wall that governs the wall temperature. Thus, if the afterburner may be ignited in steps it is at ignition of the flameholders nearest to the wall that flutter is most likely to occur. Lastly, see Table 1, the circumferential wave number tends to be larger at lower pressures.

References

[1] Krumhaar, H., "The Accuracy or Applying Linear Piston Theory to Cylindrical Shells". AIAA Jnl, Vol. 1, No. 6, p. 1448, June 1963.

[2] Olson, M.D., Fung, Y.C., "Comparing Theory and Experiment for the Supersonic Flutter of Circular Cylindrical Shells", AIAA Jnl, Vol. 5, No. 10, pp. 1849-1855, Oct. 1967.

Notations

D	= bending rigidity = $E\delta^3/(12(1-\nu^2))$
w	= shell radial displacement
R	= radius of cylindrical shell
x, y	= shell axial and circumferential coordinate
ϕ	= stress function
ρ_s	= shell material density
δ	= shell wall thickness
t	= time
N_x	= axial stress resultant due to loading
p_m	= pressure differential across shell wall
E	= Young's modulus
ρ_g	= gas stream density
a	= gas stream speed of sound
U	= gas stream velocity
F, G	= slowly varying average amplitudes
ω	= flutter frequency
ψ	= slowly varying average phase angle
p_g	= gas stream static pressure
m	= circumferential wave number

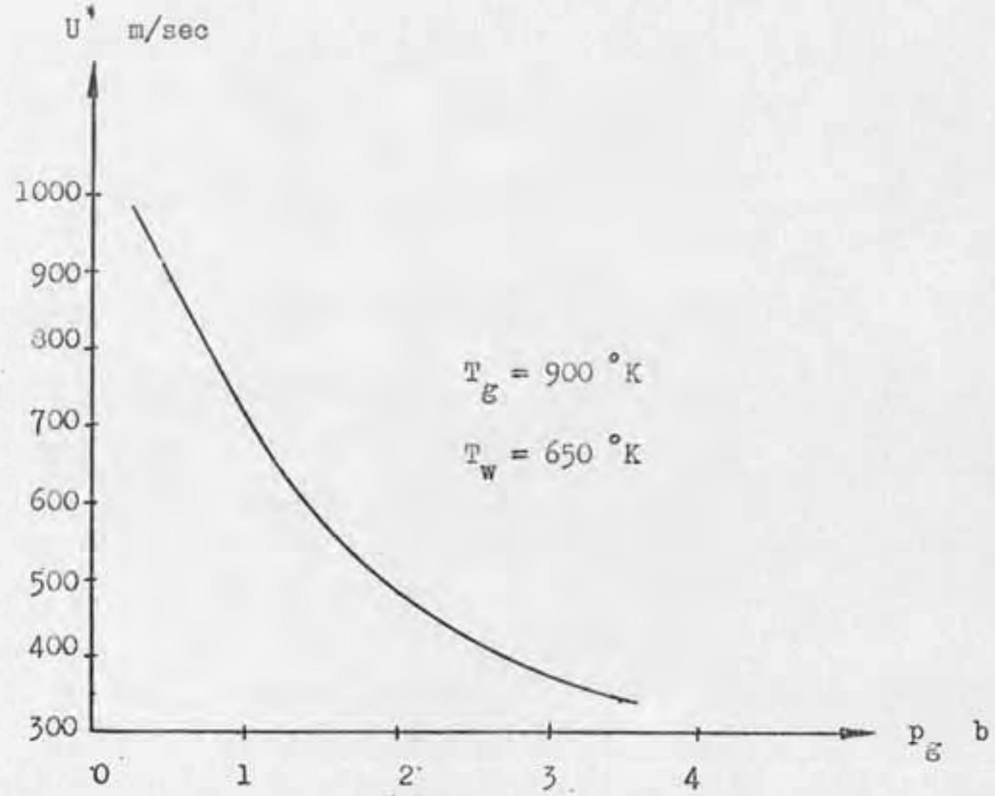

Fig. 1 Critical gas velocity U^* versus gas pressure p_g.

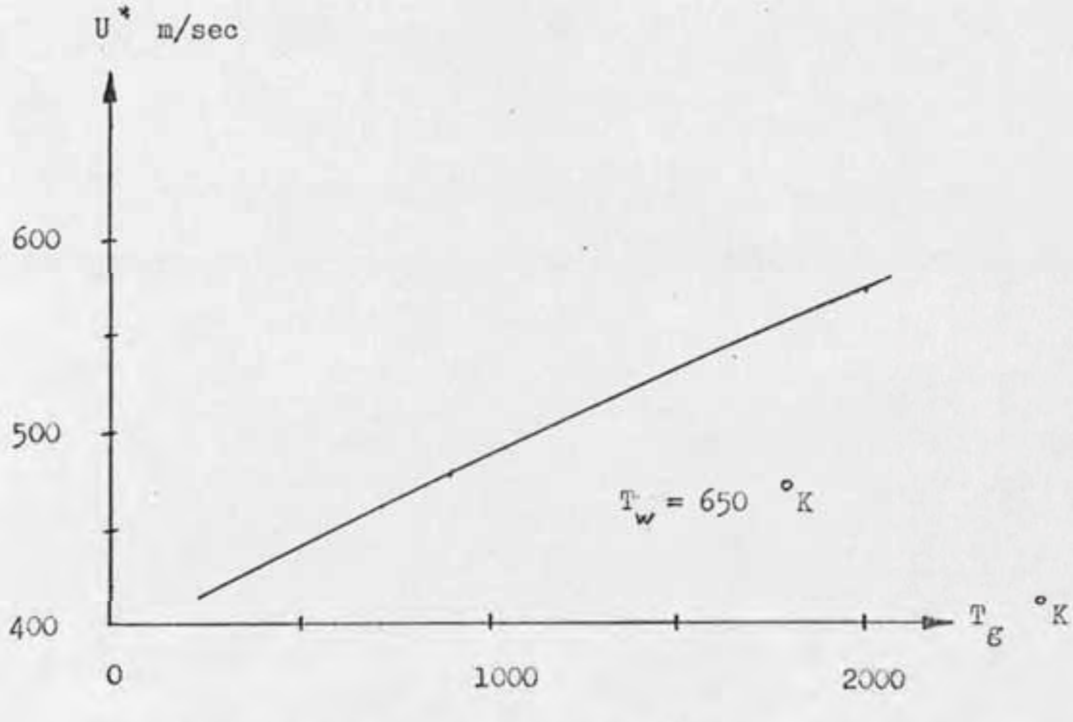

Fig. 2 Critical gas velocity U^* versus gas temperature T_g.

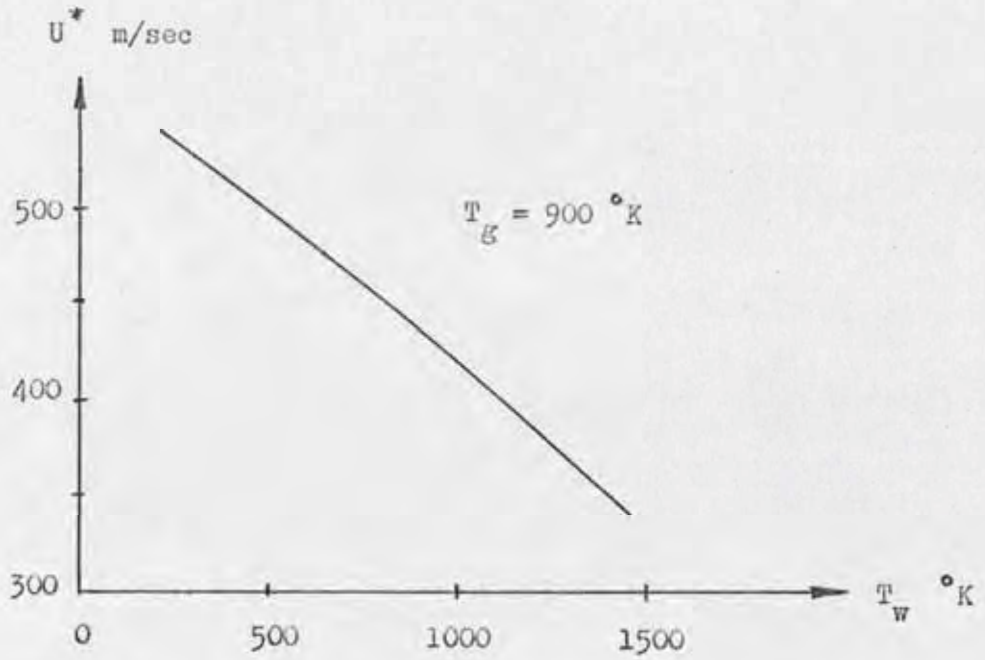

Fig. 3 Critical velocity U^* versus wall temperature T_w.

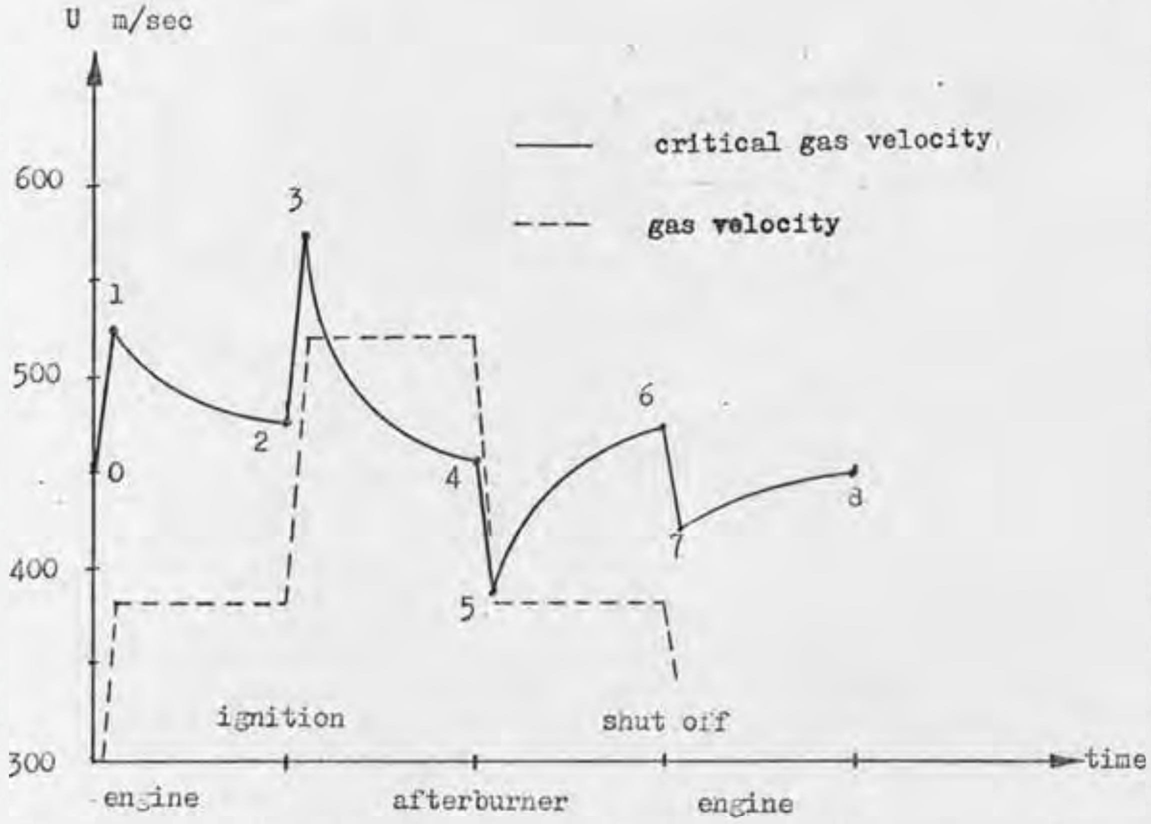

Fig. 4 Working sequence

ON FREE VIBRATIONS AT TEMPERATURE-DEPENDENT MATERIAL PROPERTIES AND TRANSIENT TEMPERATURE FIELDS

Ulf Olsson[1]

1. Introduction

During the heating up period of structures exposed to high intensity heat fluxes, the material properties may undergo significant variations. Ambartsumian et al. [1], on analyzing a cylindrical shell with temperature-dependent Young's modulus under a linearly transient temperature field, show that the temperature-dependence introduces essential changes in the free vibrations of the shell.

It is intended here to analyze this problem more extensively, taking into account the temperature-dependence of the material damping parameter and Poisson's ratio as well as the second derivative of the relation between Young's modulus and the temperature, all of which were neglected in Ref. 1. Furthermore, not only linear but also exponential and harmonic transient temperature variations are studied.

---

[1] Scientist, Research Department, Volvo Flygmotor AB, Trollhattan, Sweden

2. Basic Equations

The differential equation of motion is

$$\frac{\partial^2 w}{\partial t^2} + 2\varepsilon(t)\frac{\partial w}{\partial t} + \omega^2(t)\, w = o \qquad (1)$$

where w is the amplitude of the oscillations, ε the damping parameter, ω the natural angular frequency and t the time. For beams, plates and shells one has

$$\omega^2 = A_1 E + A_2 \frac{E}{1-\nu^2} \qquad (2)$$

Here ν is Poisson's ratio, E is Young's modulus, A_1 and A_2 are positive constants.

It will prove useful in what follows to introduce into Eq. (1) the transformation [2]

$$w = y(t)\ \exp\left(-\int_o^t \varepsilon(x)dx\right) \qquad (3)$$

to obtain

$$\frac{\partial^2 y}{\partial t^2} + \left(\omega^2 - \varepsilon^2 - \frac{\partial \varepsilon}{\partial t}\right) y = o \qquad (4)$$

3. Linear Temperature Variation

If a thin-walled structure is heated by a constant heat flux, the nondimensional wall temperature excess will be

$$\theta = \frac{T-T_o}{T_o} = \frac{t}{\tau}\ ; \qquad o \le t \le t_{max} \qquad (5)$$

Assume $\varepsilon = o$ and

$$\omega^2 = \omega_o^2\ (1 - a\theta) \qquad (6)$$

reflecting a linearized temperature-dependence of E and $E/(1-\nu^2)$ in Eq. (2). For most materials $E(\theta)$ decreases

with θ while $\nu(\theta)$ increases. Usually, e.g. for steel, the influence of $E(\theta)$ dominates so that $a>o$.
Now introducing the new independent variable

$$x = (1-\frac{a}{\tau}t)\left(\frac{\omega_o \tau}{a}\right)^{2/3} \tag{7}$$

Eq. (1) may be rewritten as [1]

$$\frac{\partial^2 w}{\partial x^2} + xw = o \tag{8}$$

having the general solution [3]

$$w = c_1 \, Ai(-x) + c_2 \, Bi(-x) \tag{9}$$

where c_1 and c_2 are arbitrary constants, $Ai(-x)$ and $Bi(-x)$ Airy functions, whose amplitudes and vibrational periods decrease with x [3]. It then follows, Eq. (7), that for $a>o$ the amplitude and vibrational periods of w increase with time.

The damping parameter $\varepsilon(\theta)$ has a maximum value at a certain temperature [4]. In temperature intervals not including such maxima, $\varepsilon(\theta)$ can be represented by a relation

$$\varepsilon = \frac{\varepsilon_o}{1-b\tau\theta} \tag{10}$$

Then assuming that $\omega=\omega_o$=constant and introducing the new independent variable

$$x = -\frac{\omega_o}{b} + \omega_o t \tag{11}$$

Eq. (4) may be rewritten

$$\frac{\partial^2 y}{\partial x^2} + \left(1-\frac{\varepsilon_o(\varepsilon_o+b)}{b^2 x^2}\right) y = o \tag{12}$$

This is again a Bessel differential equation, having the solution [3]

$$y = x^{1/2}\,(c_1 J_p(x)+c_2 N_p(x)) \tag{13}$$

where

$$p = \left(\frac{1}{4} + \frac{\varepsilon_o\,(\varepsilon_o+b)}{b^2}\right)^{1/2} \tag{14}$$

The solution for w is then found from Eq. (3).

Because the variations of $\varepsilon\,(\theta)$ are limited, a number $n>1$ may be found such that for $b>0$, $\varepsilon_{max}/\varepsilon_o < n$ and for $b<0$, $\varepsilon_o/\varepsilon_{min} < n$. It then follows from Eqs. (5), (10) and (11) that in both cases $|x|>\omega_o t_{max}/(n-1)$, where $\omega_o t_{max}$ is very large for real structures while n is limited. Thus, $|x| >> 1$ and it may be shown through using asymptotic expansions of the Bessel functions [3], that

$$w = A(c_1' \sin\phi + c_2' \cos\phi) \tag{15}$$

where c_1' and c_2' are arbitrary constants and where

$$A(t) \sim (1-bt)^{\varepsilon_o/b}\left(1+ \frac{\varepsilon_o(\varepsilon_o+b)}{4\omega_o^2(1-bt)^2} + ..\right) \tag{16}$$

$$\phi(t) \sim \left(1- \frac{\varepsilon_o(\varepsilon_o+b)}{2\omega_o^2(1-bt)} + ..\right)\omega_o t \tag{17}$$

Now, except perhaps in the immediate vicinity of the maximum of $\varepsilon(\theta)$, $(\varepsilon_o/\omega_o)<<1$ and $(1-bt)^{-1}<n$, why the second terms in the parathesis of Eqs. (16) and (17) have small significance. Thus, the temperature-dependence of ε, as expressed in Eq. (10), has but a small influence on the vibrational frequency, while its influence on the amplitude is described by the first term in Eq. (16),

which is obtained through directly introducing Eq. (10) into Eq. (3).

That the effect on the amplitude may be considerable is shown for aluminum in Fig. 1, the temperature-dependence of ε being taken from Ref. 4.

4. Exponential Temperature Variation

If the structure is heated convectively, the transient temperature field may be written

$$\theta = A+Be^{t/\tau} \tag{18}$$

It is assumed here that

$$\varepsilon = \varepsilon_o(1+b\theta) \tag{19}$$

$$\omega^2 = \omega_o^2(1-a_1\theta-a_2\theta^2) \tag{20}$$

Then introducing

$$c_1 = a_1A+a_2A^2+\frac{\varepsilon_o^2}{\omega_o^2}+2A\frac{\varepsilon_o^2b}{\omega_o^2}+\frac{\varepsilon_o^2b^2}{\omega_o^2}A^2 \tag{21}$$

$$c_2 = a_1B+2a_2AB+\frac{\varepsilon_ob}{\omega_o^2\tau}B+\frac{2\varepsilon_o^2b}{\omega_o^2}B+\frac{2\varepsilon_o^2b^2}{\omega_o^2}AB \tag{22}$$

$$c_3 = a_2B^2+\frac{\varepsilon_o^2b^2}{\omega_o^2}B^2 \tag{23}$$

$$\alpha = \frac{1}{2}+\frac{\omega_o\tau c_2}{2c_3^{1/2}}\pm i\omega_o\tau(1-c_1)^{1/2} \tag{24}$$

$$\gamma = 1 \pm 2i\omega_o\tau(1-c_1)^{1/2} \tag{25}$$

$$x = 2\omega_o\tau c_3^{1/2}e^{t/\tau} \tag{26}$$

$$z = y\,e^{x/2}x^{(1-\gamma)/2} \tag{27}$$

Eq. (4) is transformed to Kummer's differential equation

$$x \frac{\partial^2 z}{\partial x^2} + (\gamma - x) \frac{\partial z}{\partial x} - \alpha z = 0 \tag{28}$$

which has as its solution the confluent hypergeometric series

$$z = 1 + \frac{\alpha}{\gamma} x + \frac{\alpha(\alpha+1)}{2!\,\gamma(\gamma+1)} x^2 + \dots \tag{29}$$

After what the solution w is obtained from Eq. (3). When the temperature-dependence of ε and the second derivative of $\omega^2(\theta)$ are neglected, i.e. $a_2 = 0$, exchanging Eqs. (24)-(26) for

$$\alpha = \frac{\gamma}{2} \tag{30}$$

$$\gamma = 1 \pm 4\, i\omega_0\tau\, (1-c_1)^{1/2} \tag{31}$$

$$x = 4\omega_0 \tau\, c_2^{1/2}\, e^{t/2\tau} \tag{32}$$

gives again (28) and (29).

Observing that, except in the immediate vicinity of the maximum of $\varepsilon(\theta)$, $(\varepsilon_0/\omega_0) \ll 1$ while $b\theta$ is limited, it is seen that the terms including damping parameters have small significance in Eqs. (21)-(23). Thus, as for a constant heat flow (Section 3), the influence of the temperature-dependence of ε on the frequency is small, while the influence on the amplitude is obtained from Eqs. (19) and (3).

In order to investigate the influence of the temperature-dependence of ω^2 calculations have been carried out for a thin, straight beam of circular cross section. If such a beam is simply supported and convectively heated, then

$$\omega^2 = \frac{\pi^4}{16}\frac{D^2}{L^4}\frac{E}{\rho} \; ; \; \tau = -\frac{\rho c D}{4h} \tag{33}$$

where h is the heat transfer coefficient, ρ the density, c the specific heat, D the diameter and L the length of the beam. In the calculations, the real part of Eq. (29) was taken to represent the solution and the data used are representative for steel. A somewhat unrealistic value of $D/L=10^{-3}$ was chosen in order to obtain rapid convergence of the series Eq. (29). The damping was neglected i.e. $\varepsilon_o=o$.

The results are shown in Fig. 2. It is seen, that the amplitude and vibrational periods tend to increase with time and that the second derivative of $\omega^2(\theta)$ further emphasizes this tendency.

5. Harmonic Temperature Variation

With

$$\theta = \theta_m \cos \Omega t \tag{34}$$

$$\varepsilon = \varepsilon_o(1+b\theta) \tag{35}$$

$$\omega^2 = \omega_o^2(1-a\theta) \tag{36}$$

$$x = \Omega t \tag{37}$$

Eq. (1) will be

$$\frac{\partial^2 w}{\partial x^2} + \frac{2\varepsilon_o}{\Omega}(1+b\theta_m \cos x)\frac{\partial w}{\partial x} + \frac{\omega_o^2}{\Omega^2}(1-a\theta_m \cos x)w=o \tag{38}$$

If $\varepsilon_o=o$, Eq. (38) is Mathieu's differential equation, the stability of the solutions being described by the well-known Strutt's diagram [2].

In order to investigate the solutions of Eq. (38), w is assumed in the periodic series form

$$w = A_o + \sum_{n=1}^{\infty} \left(A_n \cos \frac{n}{2} x + B_n \sin \frac{n}{2} x\right) \tag{39}$$

Introducing this into Eq. (38) and evaluating coefficients give relations describing the conditions under which periodic solutions are possible. Neglecting terms of higher order than n=2, the following relations are obtained

$$\left(\alpha - \frac{1}{4}\right)^2 - \frac{1}{4}\beta^2 + \gamma^2 - \frac{1}{4}\delta^2 = o \tag{40}$$

$$\alpha\left((\alpha-1)^2 + 4\gamma^2\right) - \frac{1}{2}\beta^2(\alpha-1) + 2\beta\gamma\delta = o \tag{41}$$

where

$$\alpha = \frac{\omega_o^2}{\Omega^2} \tag{42}$$

$$\beta = \frac{\omega_o^2 a\theta_m}{\Omega^2} \tag{43}$$

$$\gamma = \frac{\varepsilon_o}{\omega_o}\alpha^{1/2} \tag{44}$$

$$\delta = b\theta_m \frac{\varepsilon_o}{\omega_o}\alpha^{1/2} \tag{45}$$

Introducing Eqs. (44) and (45) into Eqs. (40) and (41) gives two relations $\beta(\alpha)$, which together with the line $\beta = a\theta_m\alpha$ from Eq. (43) describe a modified Strutt's diagram as shown in Fig. 3. The possible states of vibration are situated on the line $\beta = a\theta_m\alpha$ and stability is secured as long as there are no intersections between this line and the curves $\beta(\alpha)$. From the general appearance of Strutt's diagram, such intersections seem most probable in the

The curve $\beta(\alpha)$ of this region is described by Eqs. (40), (44) and (45) and it may be seen that it is independent of $a\theta_m$ but depends on ε_o/ω_o and $b^2\theta_m^2$ so that β increases with increasing ε_o/ω_o and decreases with increasing $b^2\theta_m^2$. Thus, see Fig. 3, intersections between the curve and the line $\beta=a\theta_m\alpha$ become more possible with increasing $a\theta_m$ and $b^2\theta_m^2$. As mentioned in Section 3, $a>o$ for most materials, why it follows that an increase of the temperature-dependence of the material properties or of the temperature amplitude itself should have a destabilizing effect on the structure, while the damping has a stabilizing effect.

Solving for the intersection points, it is found that there are no intersections, i.e. stability is maintained, provided that

$$\theta_m^2 < \left(\left(\frac{\omega_o^4 a^2}{2\varepsilon_o^4 b^4} + \frac{2\omega_o^2}{\varepsilon_o^2 b^2} - \frac{4}{b^2}\right)^2 + \frac{16}{b^4}\left(\frac{\omega_o^2}{\varepsilon_o^2} - 1\right)\right)^{1/2}$$

$$-\left(\frac{\omega_o^4 a^2}{2\varepsilon_o^4 b^4} + \frac{2\omega_o^2}{\varepsilon_o^2 b^2} - \frac{4}{b^2}\right) \qquad (46)$$

E.g. for aluminium of Fig. 1 at $\omega_o=5.02\ \mathrm{sec}^{-1}$ and $T_o=498^\circ K$, giving $a=0.26$, $b=10.5$ and $\varepsilon_o/\omega_o=0.02$, the critical temperature amplitude is $80.7^\circ C$. At $a=o$ the corresponding value is $95.2^\circ C$ and at $b=o$ it is $152.4^\circ C$. Hence, the temperature-dependence of the material properties has a large influence on the stability limits.
In practice, however, it would be difficult to achieve temperature fluctuations of such amplitudes and frequencies ($\Omega \approx 10\ \mathrm{sec}^{-1}$).

This example was for a low frequency but the frequency-dependence of the material damping ε_o/ω_o, Ref. 4, seems not to be strong enough to change the conditions considerably at larger frequencies. Thus, in conclusion, although the temperature-dependence in itself has a destabilizing effect at cyclic temperature variations it is neutralized in practice by the damping of the material.

6. References

1 Ambartsumian, S.A., Bagdasarian, G.E., Durgarian, S.M., Gnuny, V.Ts., "Some Problems of Vibration and Stability of Shells and Plates", Int. J. Solids Structures, Vol. 2, 1966, pp. 59-81.

2 Stoker, J.J., "Nonlinear Vibrations", Interscience Publ. Inc., New York, 1950, p. 201, 221.

3 Abramowitz, M., Stegun, I.A., "Handbook of Mathematical Functions", Dover Publ. Inc., New York, 1965, pp. 446, 362, 365.

4 Zener, C.M., "Elasticity and Anelasticity of Metals", The Univ. of Chicago Press, 5th Ed., 1965, pp. 151, 55.

Fig. 1

U.Olsson

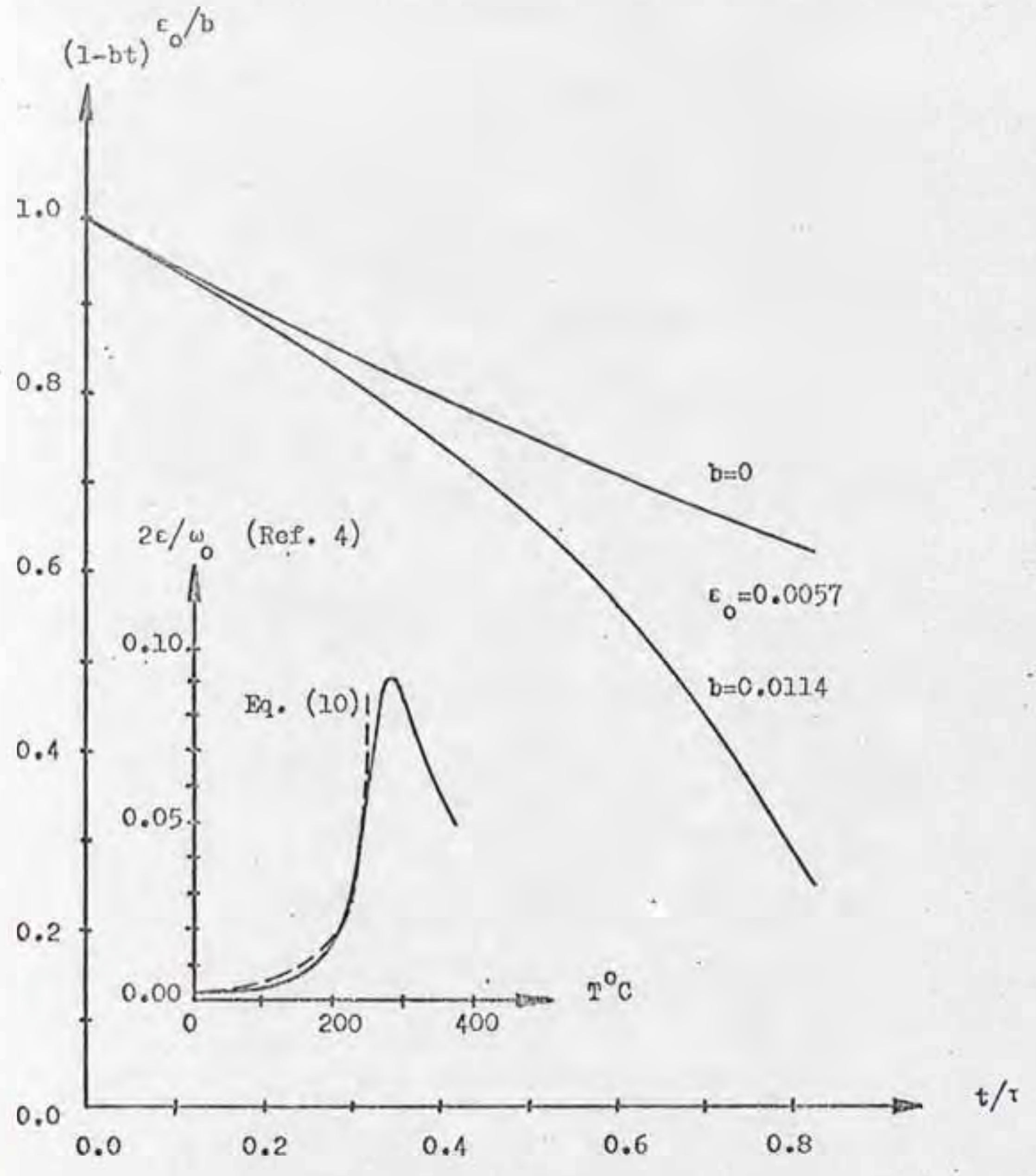

Fig. 2

U.Olsson

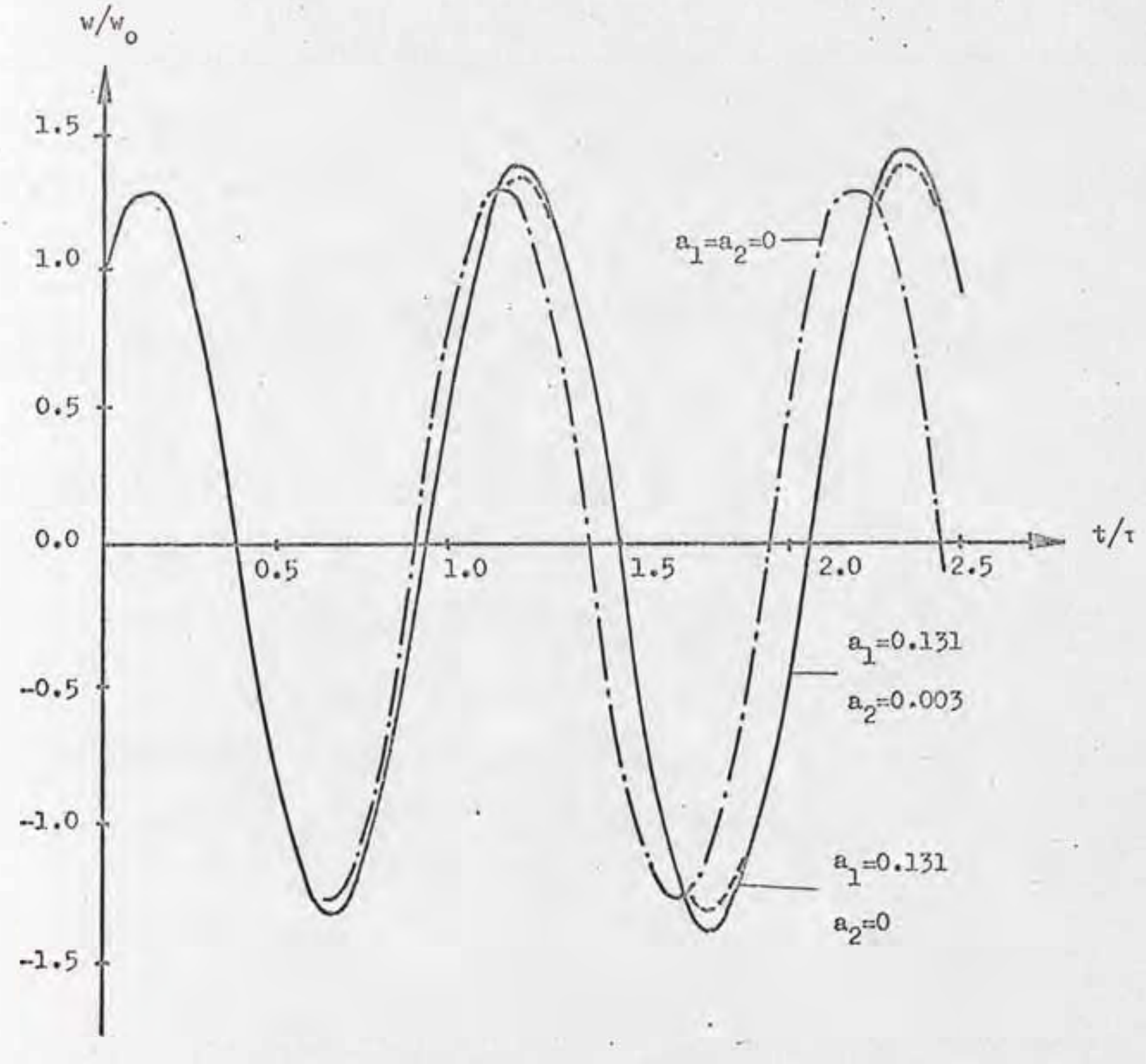

Fig. 3

U.Olsson

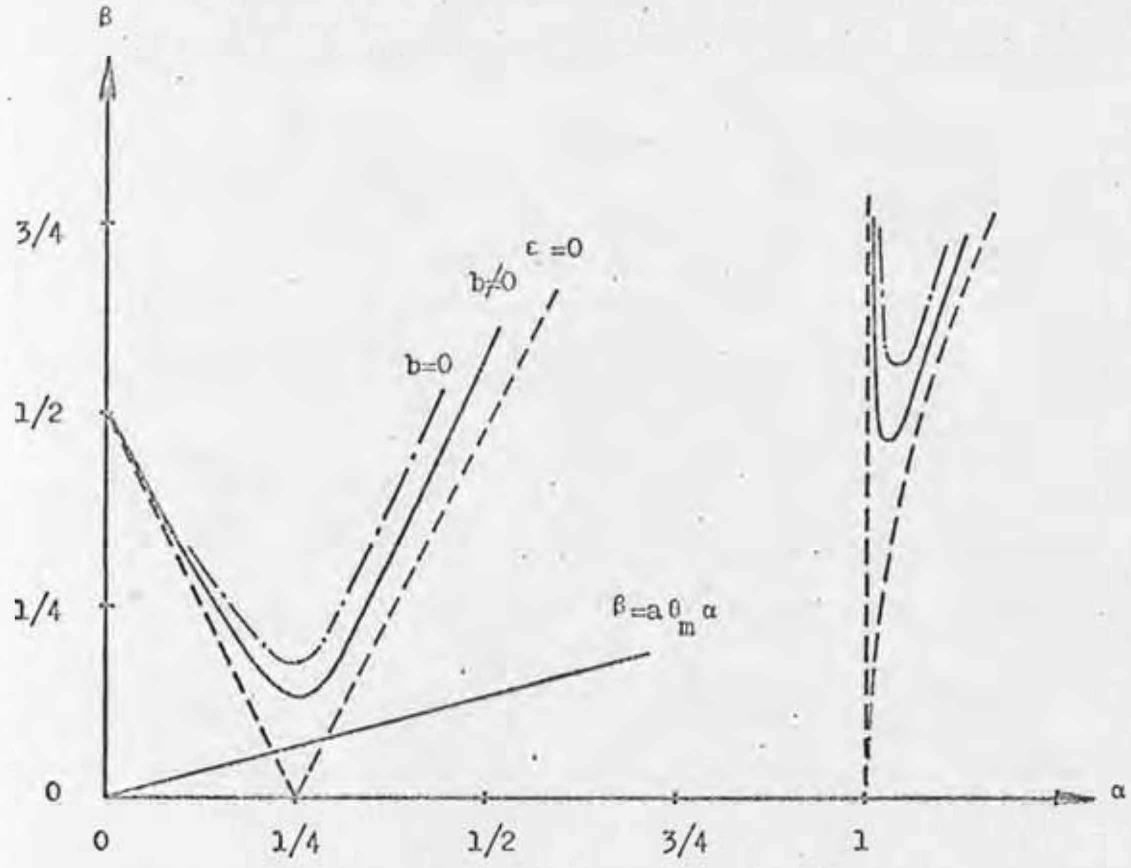

O. Olsson

Captions for figures

Fig. 1 Vibrational amplitudes with and without temperature dependent damping parameter; ω_o=5.02 sec^{-1}, τ =100 sec, T_o=273^{o}K, T_{max}=498^{o}K.

Fig. 2 Influence of temperature dependence on vibrations; E_o=2.06·10^{11} N/m^2, ρ =7850 kg/m^3, c=460 J/kg ^{o}C, h=190 J/m^2 sec, T_o=293 ^{o}K, A=-B=1.58.

Fig. 3 Modified Strutt's diagram.

TRANSIENT THERMAL DEFORMATIONS OF CYLINDRICAL SHELLS WITH TEMPERATURE DEPENDENT MATERIAL PROPERTIES

Ulf Olsson[1]

Introduction

A jet engine afterburner may be considered as a cylindrical shell through which flows a gas stream of high velocity and temperature. At ignition of the afterburner, the inner shell wall is exposed to a heat flux of high intensity inducing rapid deformations and subsequently following vibrations of the shell. Although the magnitude of the heat flux depends on the transient shell wall temperature it may be considered as invariant at least during the first moments after ignition. Under this assumption we will investigate here how the thermally induced deflections are influenced by the temperature dependence of the material properties.

---

[1]Scientist, Research Department, Volvo Flygmotor AB, Trollhättan, Sweden.

Temperature Field

The cylindrical shell wall is assumed to be exposed to a constant heat flux at the inside and to be insulated at the outside. Taking care of the temperature dependence of the thermophysical material properties, the nonlinear heat flow equation is transformed to a set of linear differential equations using the method given in Ref. 1. These equations are then solved approximately with Bolotin's method assuming a linear temperature variation through the shell wall. For linearly temperature dependent material properties

$$k = k_o + k_1 \Theta \tag{1}$$

$$c = c_o + c_1 \Theta \tag{2}$$

the solution for the temperature is in the first approximation[2]

$$\Theta = F_o + \frac{2\xi}{\delta} G_o - \frac{1}{2}\frac{k_1}{k_o}\left(F_o + \frac{2\xi}{\delta} G_o\right)^2 + F_1 + \frac{2\xi}{\delta} G_1 \tag{3}$$

where

$$F_o = \frac{q\,t}{\rho c_o \delta} \tag{4}$$

$$G_o = -\frac{\delta q}{4k_o}\left(1 - \exp\left(-\frac{12k_o t}{\rho c_o \delta^2}\right)\right) \tag{5}$$

$$F_1 = -\frac{1}{2}\left(\frac{c_1}{c_o} - \frac{k_1}{k_o}\right)\left(\frac{q^2\, t^2}{\rho^2 c_o^{\,2}\,\delta^2} + \frac{\delta^2 q^2}{48k_o^{\,2}}\left(1 + \exp\left(-\frac{24k_o t}{\rho c_o \delta^2}\right) - 2\exp\left(-\frac{12k_o t}{\rho c_o \delta^2}\right)\right)\right) \tag{6}$$

$$G_1 = \frac{\delta^2 q^2}{48k_o^{\,2}}\left(\frac{c_1}{c_o} - \frac{k_1}{k_o}\right)\left(1 - \exp\left(-\frac{12k_o t}{\rho c_o \delta^2}\right)\right) -$$

$$\left(\frac{c_1}{c_o} - \frac{k_1}{k_o}\right) \frac{q^2 t}{4 \rho c_o k_o} \exp\left(-\frac{12 k_o t}{\rho c_o \delta^2}\right) +$$

$$\left(\frac{c_1}{c_o} - \frac{k_1}{k_o}\right) \frac{3 q^2 t^2}{2 \rho^2 c_o{}^2 \delta^2} \exp\left(-\frac{12 k_o t}{\rho c_o \delta^2}\right) \tag{7}$$

Deflections

Because the temperature differences through the wall are small, their influence on the elastic material properties will be neglected. Furhermore it is assumed that the shell is simply supported and that there are no aerodynamic or other loads applied to it. Since both the loads and the boundary conditions of the shell are rotationally symmetric, the deflections will be so too. Then, proceeding from the usual linear equations for a cylindrical shell, we assume

$$w = \delta f \sin \frac{\pi x}{L} \tag{8}$$

and make use of Galerkin's method to obtain a differential equation for the nondimensional deflection f.

Splitting up f into one quasi-static and one dynamic part as

$$f = f_s + f_d \tag{9}$$

we obtain

$$f_s = \frac{4R}{\pi \delta \lambda} \varepsilon_{TO} + \frac{4 \pi R^2}{L^2 \lambda} \varepsilon_{T1} \tag{10}$$

where

$$\varepsilon_{Tn} = \int_{-1/2}^{1/2} \left(\int_o^{\theta} \alpha(\xi)\, d\xi \right) \left(\frac{\zeta}{\delta}\right)^n d\left(\frac{\zeta}{\delta}\right) \tag{11}$$

$$\lambda = 1 + \frac{\pi^4 \delta^2 R^2}{12L^4(1-\nu^2)} \tag{12}$$

and the following differential equation

$$\frac{d^2 f_d}{dt^2} + \frac{\lambda}{\rho R^2} E(t) f_d = - \frac{d^2 f_s}{dt^2} \tag{13}$$

For thin-walled shells, the influence of ν is very small, see Eq. (12). Therefore the temperature dependence of ν may be neglected so that λ will be a constant. Neglecting second order terms we assume a linear temperature dependence of Young's modulus, i.e.

$$E = E_o - E_1 F_o = E_o (1-\mu t) \tag{14}$$

where

$$\mu = \frac{\dot{q} E_1}{\rho c_o \delta E_o} \tag{15}$$

Then introducing a new independent variable

$$z = \left(\frac{E_o \lambda}{\rho R^2}\right)^{1/3} \left(\frac{1}{\mu}\right)^{2/3} (1 - \mu t) \tag{16}$$

Eq. (13) is transformed to

$$\frac{d^2 f_d}{d z^2} + z f_d = - \left(\frac{\rho R^2}{E_o \lambda}\right)^{\frac{2}{3}} \mu^{-\frac{2}{3}} \frac{d^2 f_s}{d t^2} = F(z) \tag{17}$$

whose general solution may be written as[3]

$$f_d = C_1 f_1(z) + C_2 f_2(z) + \frac{1}{W_o} \int_{z_o}^{z} F(\xi)(f_1(\xi) f_2(x) - f_1(x) f_2(\xi))\, d\xi \tag{18}$$

where C_1 and C_2 are arbitrary constants, $z_o = z(0)$ and

$$f_1(z) = z^{\frac{1}{2}} J_{\frac{1}{3}} \left(\frac{2}{3} z^{\frac{3}{2}} \right) \tag{19}$$

$$f_2(z) = z^{\frac{1}{2}} N_{\frac{1}{3}} \left(\frac{2}{3} z^{\frac{3}{2}} \right) \tag{20}$$

$$W_o = f_1(z_o) \frac{d f_2}{d z}(z_o) - f_2(z_o) \frac{d f_1}{d z}(z_o) \tag{21}$$

For $\alpha = \alpha_o + \alpha_1 \theta$, the quasi-static solution f_s may be obtained from Eqs. (10) and (11) and the dynamic solution f_d from Eq. (18). After having determined the constants C_1 and C_2 from the initial conditions

$$f(0) = \frac{df}{dt}(0) = 0 \tag{22}$$

the total solution f is obtained.

Results

As an example we take a shell with the following dimensions

$R = 0,5$ m $\quad L = 3$ m $\quad \delta = 10^{-3}$m

and the material properties

$\rho = 8150$ kg/m^3 $\quad \nu = 0,25$
$E_o = 2.07 \; 10^{11}$ N/m^2 $\quad E_1 = 7.35 \; 10^7$ N/m^2 ^{o}C
$c_o = 432$ J/kg^{o}C $\quad c_1 = 0.252$ J/kg^{o}C^2
$k_o = 13,9$ J/s m^{o}C $\quad k_1 = 2.31 \; 10^{-2}$ J/s m^{o}C^2
$\alpha_o = 12.4 \; 10^{-6}$ 1/^{o}C $\quad \alpha_1 = 5.9 \; 10^{-9}$ 1/^{o}C^2

The heat flux is assumed to be $q = 10^5$ J/m^{2}s.

For this example the influence of the temperature dependence of the material properties is shown in Figs. 1-3. As is seen from Fig. 1, the temperature rise will be slower than in the temperature independent case. This is directly reflected in the quasi-static deflection, Fig. 2. As regards the dynamic solution, it is much smaller than the quasi-static one and the temperature dependence makes the amplitude increase with time while the frequency decreases, Fig. 3. The influence of the temperature dependence manifests itself only a relatively long time after ignition of the afterburner. During the first few moments its influence is negligible.

Notations

k = heat conductivity

c = specific heat

ξ = coordinate along the outward normal of the shell median surface

Θ = temperature increase

ρ = density of shell material

q = heat flux to the inner shell surface

t = time

w = radial deflection

x = shell axial coordinate

L = shell length

R = shell radius

ν = Poisson's number

α = thermal expansion coefficient

E = Young's modulus

δ = shell wall thickness

ω = angular frequency

References

[1] Olsson, U., "Application of a Perturbation Method to Heat Flow Analysis in Materials Having Temperature-Dependent Properties", AIAA Journal, Vol. 8, No. 10, Oct, 1970, p. 1902.

[2] Olsson, U., "Transient Heating of a Cylindrical Shell with Temperature Dependent Material Properties", Flygmotor Research, RF 5:3358, Febr. 1971.

[3] Bellman, R., "Methoden der Störungsrechnung in Mathematik, Physik und Technik", R. Oldenbourg Verlag, München-Wien, 1967, p. 30.

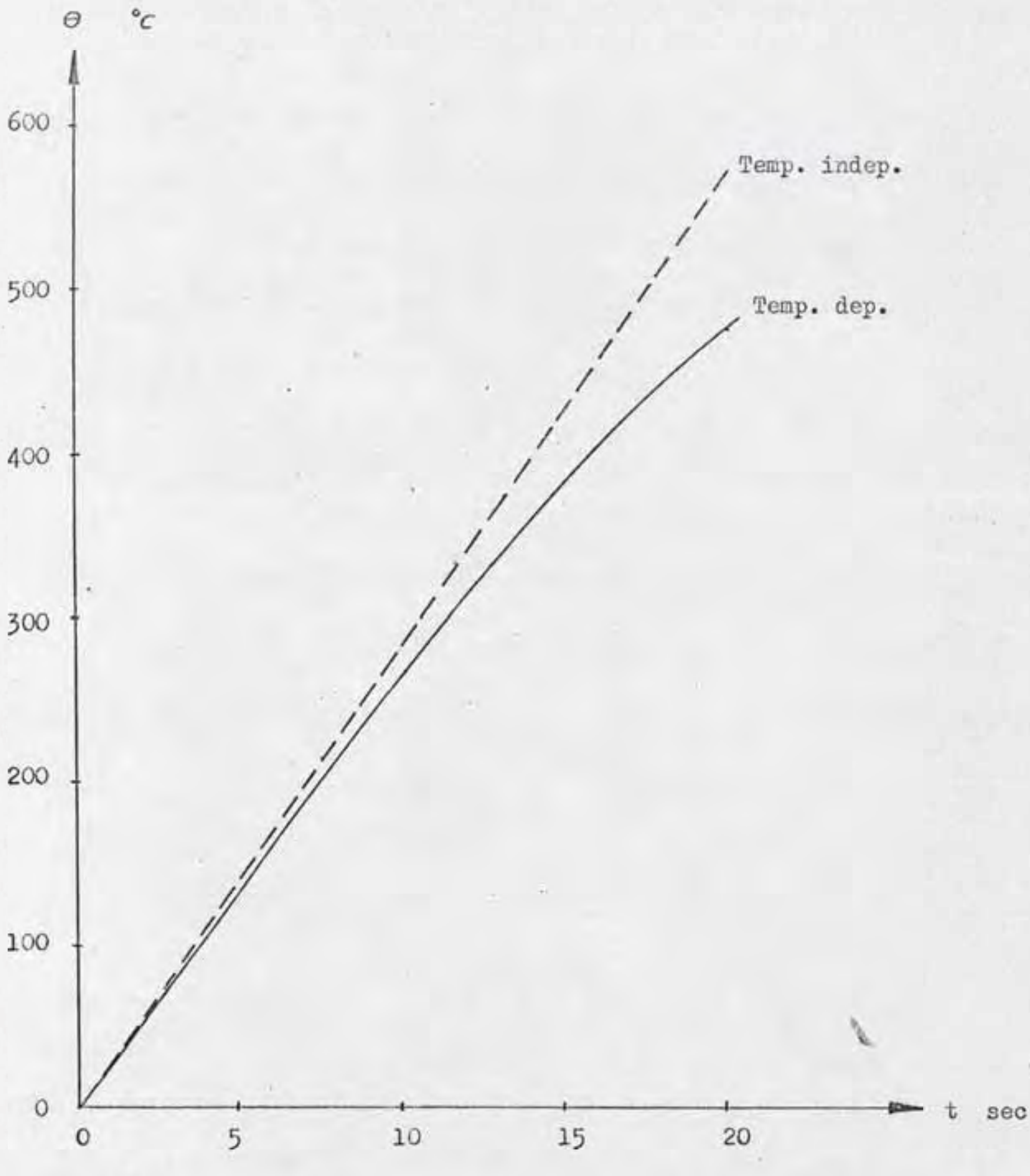

Fig. 1 Temperature variation with time

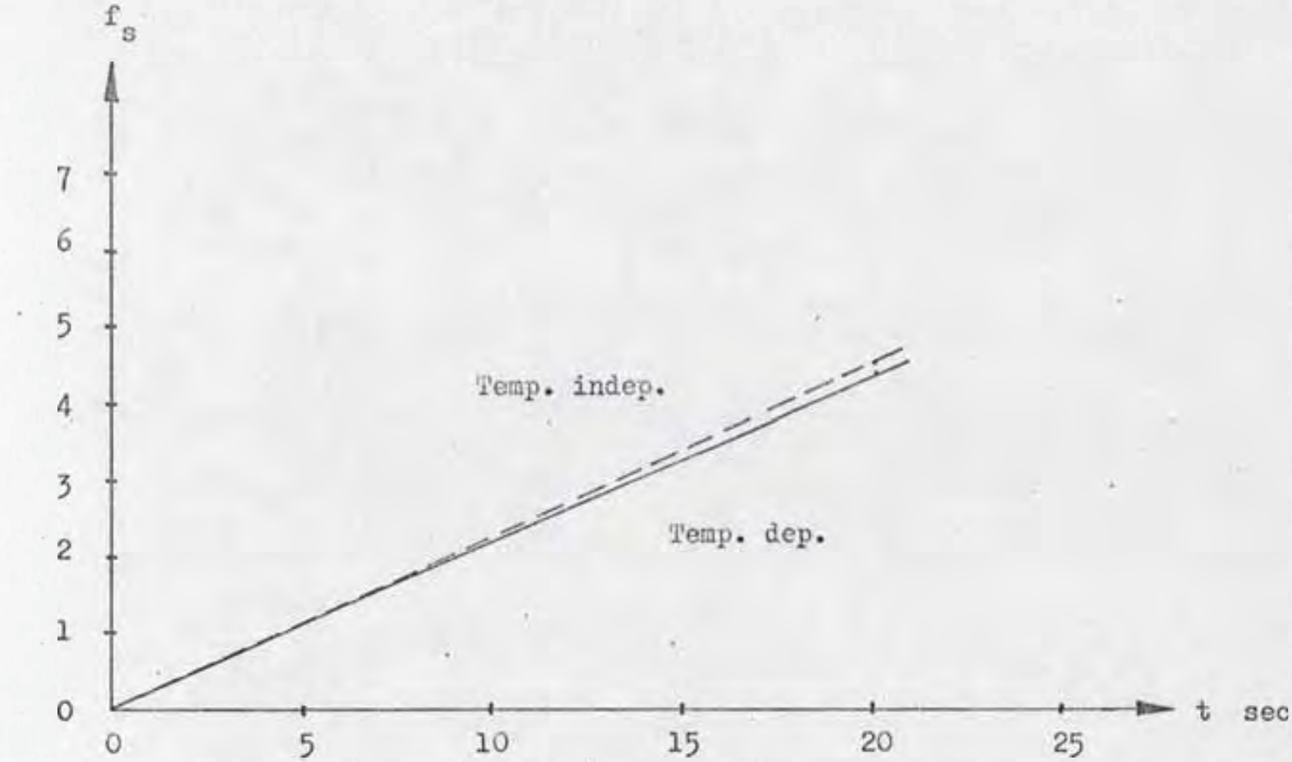

Fig. 2 Quasistatic deflection vs time

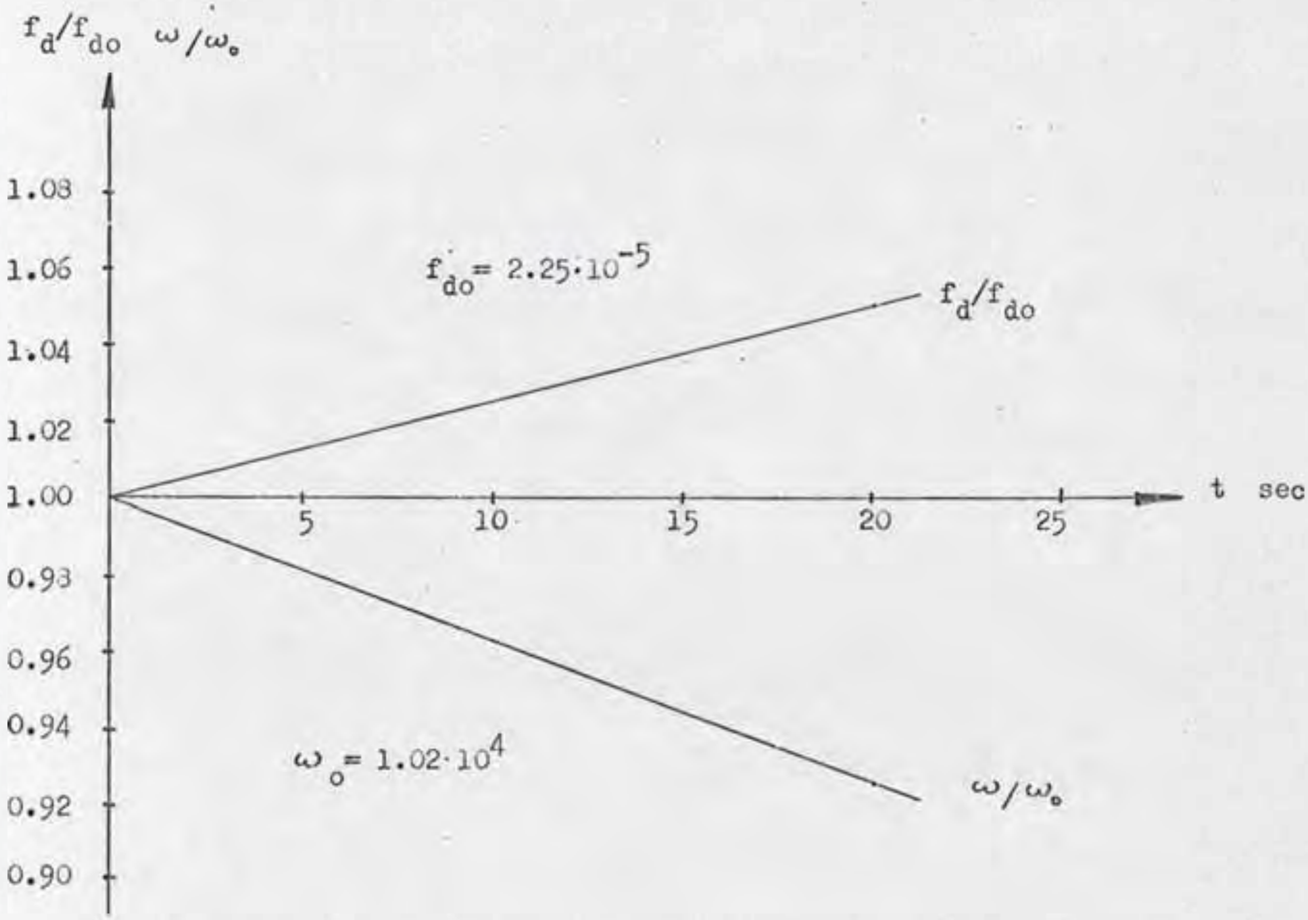

Fig. 3 Dynamic deflection and frequency vs time

PRESSURE-INDUCED DEFLECTIONS OF HEATED CYLINDRICAL SHELLS WITH TEMPERATURE DEPENDENT MATERIAL PROPERTIES

Ulf Olsson[1]

Introduction

Exact analytical solutions are given for the transient deflections of a circular cylindrical shell exposed to transient internal pressure and heated by a step heat flow to the wall. Young's modulus is assumed to vary linearly with the temperature and linear shell theory is used. Numerical results are given for a pressure step.

[1] Scientist, Research Department, Volvo Flygmotor AB, Trollhättan, Sweden.

Solutions

Because the temperature variations through the wall are small their influence on the elastic material properties will be neglected. It is assumed that the shell is simply supported and that there are no aerodynamic or other loads applied to it. Furthermore, the internal pressure is assumed to vary with time only, while the heat flux to the wall is constant. Thus, the problem is rotationally symmetric.

Proceeding from the usual linear equations for a circular cylindrical shell we assume

$$w = \delta f \sin \frac{\pi x}{L} \tag{1}$$

and make use of Galerkin's method to obtain the following differential equation for the nondimensional deflection f

$$\frac{\partial^2 f}{\partial t^2} + \omega^2 f = \frac{4}{\pi \rho \delta^2}\, p \tag{2}$$

where

$$\omega^2 = \frac{E\lambda}{\rho R^2} \tag{3}$$

$$\lambda = 1 + \frac{\pi^4 \delta^2 R^2}{12 L^4 (1-\nu^2)} \tag{4}$$

The initial conditions are taken to be

$$f(o) = \frac{\partial f}{\partial t}(o) = 0 \tag{5}$$

If the shell wall is heated by a constant heat flux q, the temperature excess may be written

$$\theta = \frac{t}{\tau} \qquad o \leq t \leq t_{max} \tag{6}$$

where

$$\tau = \frac{\rho c \delta}{q} \tag{7}$$

For thin-walled shells, $\delta \ll L$ so that $\lambda \approx 1$. Then, the influence of ν on the solutions is small and it is sufficient to assume that E alone depends on the temperature. Assuming a linear temperature dependence

$$E = E_o(1 - a\Theta) \tag{8}$$

and introducing a new independent variable

$$x = (1 - \frac{a}{\tau} t)\left(\frac{\omega_o \tau}{a}\right)^{2/3} \tag{9}$$

Eq. (2) is transformed to the form

$$\frac{\partial^2 f}{\partial x^2} + xf = F \tag{10}$$

where

$$F = \frac{\tau^2}{a^2}\left(\frac{a}{\omega_o \tau}\right)^{4/3} \frac{4}{\pi \varsigma \delta^2} \; p \tag{11}$$

The homogeneous solutions to this equation are

$$f_1 = x^{1/2} J_{1/3}\left(\frac{2}{3} x^{3/2}\right) \tag{12}$$

$$f_2 = x^{1/2} N_{1/3}\left(\frac{2}{3} x^{3/2}\right) \tag{13}$$

and those solutions to Eq. (10), which satisfy the homogeneous initial conditions[1]

$$f = \frac{1}{W_o} \int_{x_o}^{x} F(\xi)\left(f_1(\xi) f_2(x) - f_1(x) f_2(\xi)\right) d\xi \tag{14}$$

where the Wronski - determinant

$$W_o = f_1(x_o) \frac{\partial f_2}{\partial x}(x_o) - f_2(x_o) \frac{\partial f_1}{\partial x}(x_o) \tag{15}$$

Because $E > o$, it follows that $\frac{a}{\tau} t_{max} < 1$ why $\frac{\omega_o \tau}{a} > \omega_o t_{max}$. Since in reality $\omega_o t_{max} >> 1$, while the temperature-dependence, Eq. (8), is relatively weak, it also follows that $x >> 1$. Then asymptotic approximations may be used for the Bessel functions in Eqs. (12) and (13)[2] and with

$$y = \frac{2}{3} \xi^{3/2} \qquad z = \frac{2}{3} x^{3/2} \tag{16}$$

Eq. (14) may be rewritten as

$$f \sim \left(\frac{3}{2}\right)^{-2/3} z^{-1/6} \int_{z_o}^{z} F(y)\, y^{-1/2} \sin(z-y)dy \quad (17)$$

where

$$F(y) = \frac{\tau^2}{a^2} \left(\frac{a}{\omega_o \tau}\right)^{4/3} \frac{4}{\pi \varrho \delta^2}\, p(y) \qquad (18)$$

For $p = p_o \cdot H(t)$, Eq. (17) may be integrated directly to give

$$f \sim \left(\frac{3}{2}\right)^{-2/3} \frac{\tau^2}{a^2} \left(\frac{a}{\omega_o \tau}\right)^{4/3} \frac{4 p_o}{\pi \varrho \delta^2} (2\pi)^{1/2} z^{-1/6} \big((C_2(z)$$

$$- C_2(z_o)) \sin z - (S_2(z) - S_2(z_o)) \cos z\big) \quad (19)$$

where S_2 and C_2 are Fresnel integrals.

Calculations and results

Proceeding from Eq. (19), calculations have been carried out for the following values

$\varrho = 8150 \ \mathrm{kg/m^3}$	$c = 432 \ \mathrm{J/kg\,^oC}$
$\delta = 10^{-3} \ \mathrm{m}$	$R = 0.5 \ \mathrm{m}$
$E_o = 2.07 \ 10^{11} \ \mathrm{N/m^2}$	$a = 3.55 \ 10^{-4}\ {}^oC^{-1}$
$p_o = 10 \ \mathrm{b}$	$q = 10^5 \ \mathrm{J/m^2\,sec}$

The resulting deflections are shown in Fig. 1 divided by the corresponding static deflection of the shell at initial material properties, i.e.

$$f_s = \frac{4 p_o}{\pi \varrho \delta^2 \omega_o^2} \qquad (20)$$

As is seen, both the average deflection and the amplitude of the superposed oscillations increase with time. On the contrary, the frequency of the oscillations decreases with time as shown in Fig. 2.

Notations

w = shell deflection

δ = thickness of shell wall

x = axial coordinate of the shell

L = shell length

t = time

ρ = density of shell material

p = shell internal pressure

E = Young´s modulus

R = shell radius

ν = Poisson´s ratio

q = heat flux to shell wall

c = specific heat of shell material

References

[1] Bellman, R., "Methoden der Störungsrechnung in Mathematik, Physik und Technik", R. Oldenbourg Verlag, München-Wien, 1967, p. 30.

[2] Jahnke, E., Emde, F., "Tables of Functions", 4th Ed., Dover Publications, New York, 1958, p. 138.

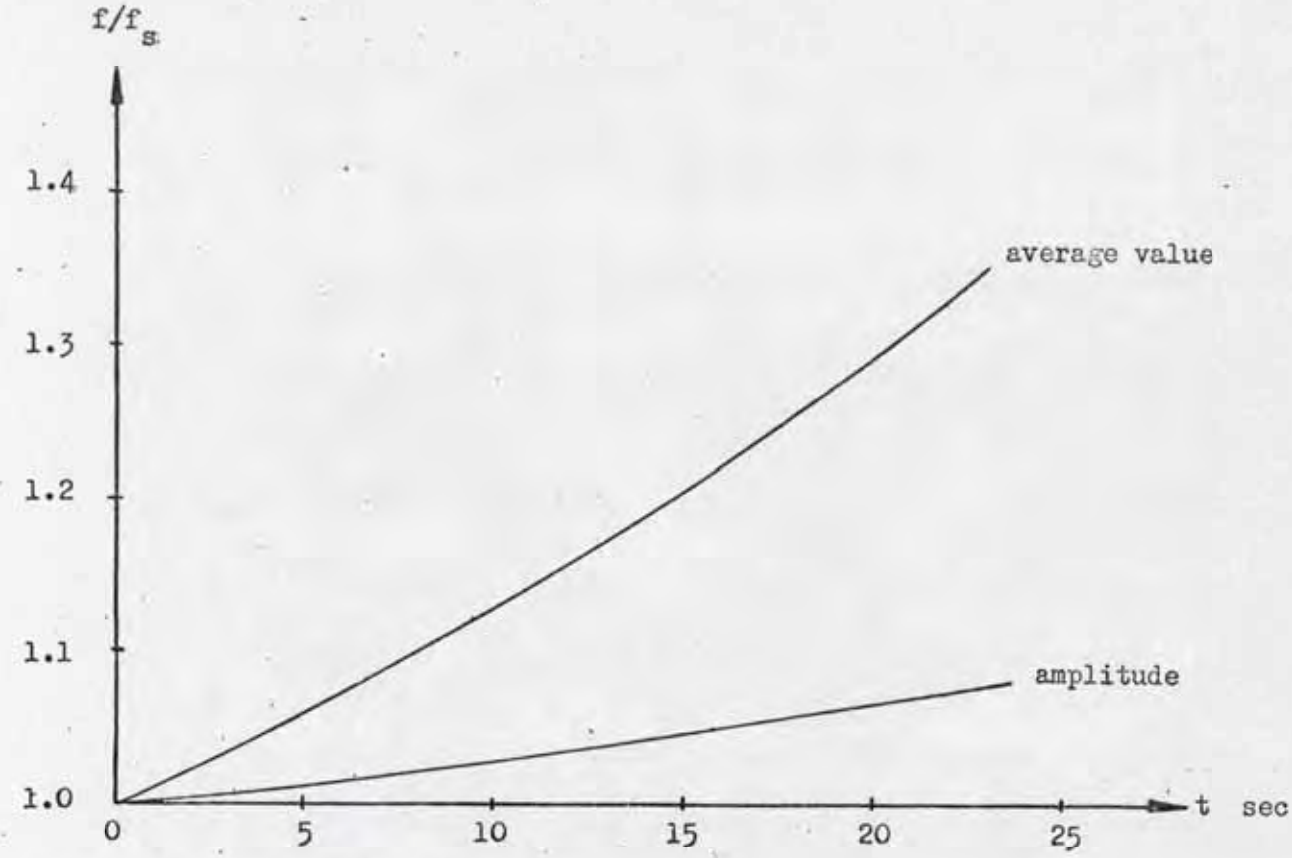

Fig. 1 Transient deflections

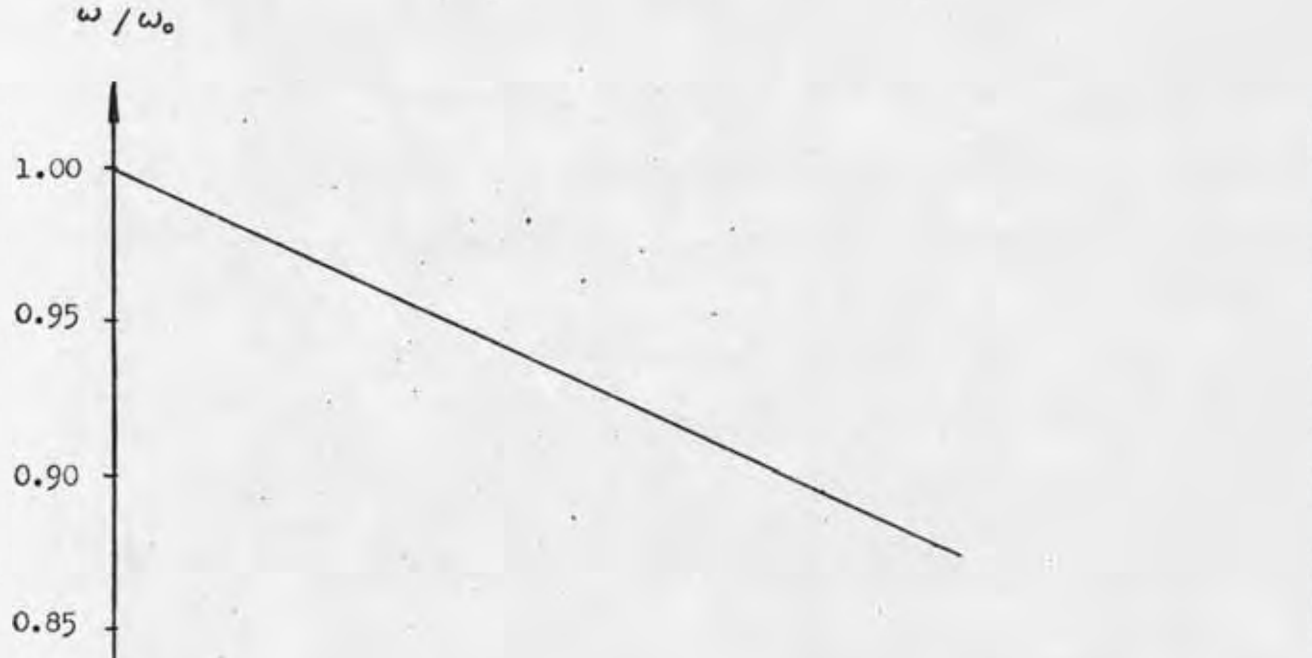

Fig. 2 Variation of angular frequency with time

NONLINEAR THERMOELASTIC EQUATIONS FOR BEAMS AND CYLINDRICAL SHELLS HAVING TEMPERATURE - DEPENDENT PROPERTIES

by Ulf Olsson

Summary

Proceeding from the hypothesis of Kirchoff - Love, the problem of finding the nonlinear deformations and stresses in a cylindrical shell, having temperature - dependent properties, is reduced to the solution of two coupled differential equations with the radial displacement and a stress function as dependent variables. Corresponding expressions for one - dimensional beams are given.

Introduction

In cases of instability, nonlinear effects have considerable importance. Although the linear theory may predict the conditions during which instability will occur, it gives no knowledge about the size of the corresponding displacements and stresses. Furthermore it does not describe correctly the motion of the system at large deformations, e.g. such effects as limit cycles are not taken care of.

The linear theory ceases to be applicable when the deformations become so large that they must be taken care of when formulating the equilibrium of the system. Also at very large deformations the material may deviate markedly from a linear elastic law, even displaying creep. In such cases Hookés law is not applicable and might even lead to lateral contractions larger than one. Many nonlinear theories have been formulated taking care of these geometrical and physical nonlinearities. The first treatment of the subject seems to be given by Synge and Chien [1] in 1941, developed further by Chien [2] in 1944. The work of Chien has later been critizised and corrected by many authors such as Donnell, Marquerre, Mushtari and Vlassov. A surrey of those earlier works may be found in [3] . Further developments are given by Sanders [4] Naghdi [5] , Naghdi and Nordgren [6] , who give general isothermal, nonlinear theories for elastic shells, based upon the Kirchoff - Love hypothesis.

Naghdi [7] develops a corresponding thermoelastic theory, containing general constitutive equations with physical and geometrical nonlinearities. Another type of nonlinear theory given by Zerna [8] and further developed by Wainwright [9] uses constitutive equations for isotropic shells, which are geometrically linear but physically nonlinear.

All those works are based upon the mathematical theory of elasticity using tensor formalism. The results are most general and are not readily applicable to any special case.

It seems justified therefore to derive special equations for a cylindrical shell. In doing this we will concentrate upon the geometrical nonlinearities, presupposing the deformations to be limited to the range where Hooke's law is applicable. The derivation will follow that leading to the well-known Donnell eguations for isotropic cylindrical shells. However we will extend the theory to take into account thermal deformations and temperature - dependence of the shell material. Equations of similar type are given by Apeland [13] , [14] who however considers the shell as consisting of a number of orthotropic layers and supposes the temperature to vary linearly through the wall. Tang, [15], gives linear equations for plates taking care of the temperature - dependence of Young's modulus and the thermal expansion coefficient but not of Poisson's number. Those equations can be achieved as a special case from the equations given here. Lastly a work by Ismail and Nowinski, [11] , may be mentioned. They derived linear equations for shells of revolution , studying the equilibrium of an element of the shell wall. Here we will proceed from the general equilibrium equations.

Deformation

Let the middle surface of the shell be defined by:

$$z = z(x, y) \tag{3.1}$$

where (x,y,z) are orthogonal Cartesian coordinates. Let (ξ, η) be orthogonal curvilinear coordinates in the middle surface obtained by projection of the (x,y) - system. Further let ζ be a coordinate normal to the middle surface. The cylindrical shell, see fig. 1, may then be described by a set of points (ξ, η, ζ) such that:

$$
\begin{aligned}
0 &\le \xi \le L \\
0 &\le \eta \le 2\pi R \\
-\frac{\delta}{2} &\le \zeta \le \frac{\delta}{2}
\end{aligned}
\tag{4.1}
$$

The components of the displacement vector for the middle surface in the (ξ, η, ζ) - system may be (u,v,w).

The Green's strain tensor, [16], expressed in tensorial displacement components, is:

$$E_{kl} = \frac{1}{2}\left[U_k|_l + U_l|_k + U_p|_k \, U^p|_l \right] \tag{4.2}$$

Proceeding from the hypothesis of Kirchoff - Love, [16], the displacements of the shell are assumed to vary linearly through the wall. Neglecting ζ with respect to R and assuming the deflections in the axial and circumferential directions to be small as compared to the radial deflections, the only nonlinear terms retained in (4,2) are the squares and products of $\frac{\partial w}{\partial \xi}$ and $\frac{\partial w}{\partial \eta}$. Then introducing physical components of the tensors, the strains in the middle surface of the shell will be:

$$\varepsilon_{\xi\xi} = \frac{\partial u}{\partial \xi} - \zeta \frac{\partial^2 w}{\partial \xi^2} + \frac{1}{2}\left(\frac{\partial w}{\partial \xi}\right)^2 \tag{4.3}$$

$$2\,\varepsilon_{\xi\eta} = \frac{\partial u}{\partial \eta} + \frac{\partial v}{\partial \xi} - 2\zeta \frac{\partial^2 w}{\partial \xi \partial \eta} + \frac{\partial w}{\partial \xi}\frac{\partial w}{\partial \eta} \tag{4.4}$$

$$\varepsilon_{\eta\eta} = \frac{\partial v}{\partial \eta} - \zeta \frac{\partial^2 w}{\partial \eta^2} + \frac{w}{R} + \frac{1}{2}\left(\frac{\partial w}{\partial \eta}\right)^2 \tag{4.5}$$

Stress - strain relations

Using Hooke's law in plane state of stress ($\sigma_\zeta = 0$) gives:

$$\varepsilon_{\xi\xi} = \frac{\sigma_{\xi\xi}}{E} - \frac{\nu\,\sigma_{\eta\eta}}{E} + \varepsilon_T \tag{5.1}$$

$$\varepsilon_{\xi\eta} = \frac{1+\nu}{E}\,\sigma_{\xi\eta} \tag{5.2}$$

$$\varepsilon_{\eta\eta} = \frac{\sigma_{\eta\eta}}{E} - \frac{\nu\,\sigma_{\xi\xi}}{E} + \varepsilon_T \tag{5.3}$$

where E and ν are functions of the temperature and where:

$$\varepsilon_T = \int_0^{\Theta} \alpha(\theta)\,d\theta \tag{5.4}$$

represents the thermal strain relative to the reference state $\Theta = 0$.

The stresses varying over the thickness of the shell are now reduced to forces and moments per unit length of the middle surface. Neglecting ζ with respect to R we introduce:

$$N_{ij} = \int_{-\delta/2}^{\delta/2} \sigma_{ij}\,d\zeta \tag{5.5}$$

$$M_{ij} = \int_{-\delta/2}^{\delta/2} \sigma_{ij}\,\zeta\,d\zeta \tag{5.6}$$

$(i, j) = (\xi, \eta)$

and obtain the following relations:

$$N_{\xi\xi} = E_1\left[\frac{\partial u}{\partial \xi} + \frac{1}{2}\left(\frac{\partial w}{\partial \xi}\right)^2\right] - E_2\,\frac{\partial^2 w}{\partial \xi^2} + E_3\left[\frac{\partial v}{\partial \eta} + \frac{w}{R} + \frac{1}{2}\left(\frac{\partial w}{\partial \eta}\right)^2\right] -$$

$$- E_4\,\frac{\partial^2 w}{\partial \eta^2} - N_T \qquad (6,1)$$

$$N_{\eta\eta} = E_1\left[\frac{\partial v}{\partial \eta} + \frac{w}{R} + \frac{1}{2}\left(\frac{\partial w}{\partial \eta}\right)^2\right] - E_2\,\frac{\partial^2 w}{\partial \eta^2} +$$

$$+ E_3\left[\frac{\partial u}{\partial \xi} + \frac{1}{2}\left(\frac{\partial w}{\partial \xi}\right)^2\right] - E_4\,\frac{\partial^2 w}{\partial \xi^2} - N_T \qquad (6,2)$$

$$N_{\xi\eta} = \frac{1}{2}E_5\left[\frac{\partial u}{\partial \eta} + \frac{\partial v}{\partial \xi} + \frac{\partial w}{\partial \xi}\,\frac{\partial w}{\partial \eta}\right] - E_6\,\frac{\partial^2 w}{\partial \xi\,\partial \eta} \qquad (6,3)$$

$$M_{\xi\xi} = E_2\left[\frac{\partial u}{\partial \xi} + \frac{1}{2}\left(\frac{\partial w}{\partial \xi}\right)^2\right] - E_7\,\frac{\partial^2 w}{\partial \xi^2} +$$

$$+ E_4\left[\frac{\partial v}{\partial \eta} + \frac{w}{R} + \frac{1}{2}\left(\frac{\partial w}{\partial \eta}\right)^2\right] - E_8\,\frac{\partial^2 w}{\partial \eta^2} - M_T \qquad (6,4)$$

$$M_{\eta\eta} = E_2\left[\frac{\partial v}{\partial \eta} + \frac{w}{R} + \frac{1}{2}\left(\frac{\partial w}{\partial \eta}\right)^2\right] - E_7\,\frac{\partial^2 w}{\partial \eta^2} +$$

$$+ E_4\left[\frac{\partial u}{\partial \xi} + \frac{1}{2}\left(\frac{\partial w}{\partial \xi}\right)^2\right] - E_8\,\frac{\partial^2 w}{\partial \xi^2} - M_T \qquad (6,5)$$

$$M_{\xi\eta} = \frac{1}{2}E_6\left[\frac{\partial u}{\partial \eta} + \frac{\partial v}{\partial \xi} + \frac{\partial w}{\partial \xi}\,\frac{\partial w}{\partial \eta}\right] - E_9\,\frac{\partial^2 w}{\partial \xi\,\partial \eta} \qquad (6,6)$$

where:

$$E_1 = \int_{-\delta/2}^{\delta/2} \frac{E}{1-\nu^2}\, d\zeta \qquad E_2 = \int_{-\delta/2}^{\delta/2} \frac{E}{1-\nu^2}\, \zeta\, d\zeta$$

$$E_3 = \int_{-\delta/2}^{\delta/2} \frac{\nu E}{1-\nu^2}\, d\zeta \qquad E_4 = \int_{-\delta/2}^{\delta/2} \frac{\nu E}{1-\nu^2}\, \zeta\, d\zeta$$

$$E_5 = \int_{-\delta/2}^{\delta/2} \frac{E}{1+\nu}\, d\zeta \qquad E_6 = \int_{-\delta/2}^{\delta/2} \frac{E}{1+\nu}\, \zeta\, d\zeta$$

$$E_7 = \int_{-\delta/2}^{\delta/2} \frac{E}{1-\nu^2}\, \zeta^2 d\zeta \qquad E_8 = \int_{-\delta/2}^{\delta/2} \frac{\nu E}{1-\nu^2}\, \zeta^2 d\zeta$$

$$E_9 = \int_{-\delta/2}^{\delta/2} \frac{E}{1+\nu}\, \zeta^2 d\zeta$$

$$N_T = \int_{-\delta/2}^{\delta/2} \frac{E}{1-\nu}\, \varepsilon_T\, d\zeta$$

$$M_T = \int_{-\delta/2}^{\delta/2} \frac{E}{1-\nu}\, \varepsilon_T\, \zeta\, d\zeta$$

Equilibrium

When body forces are absent, the equations of equilibrium using the Lagrange stress tensor are, [16] :

$$T^{ji}\big|_j = 0 \qquad (8,1)$$

During the deformation the stress vector changes its direction. To take care of this the Kirchoff stress tensor S^{jk} is introduced, related to the Lagrange stress tensor by:

$$T^{ji} = (\delta^i_k + U^i\big|_k)\, S^{jk} \qquad (8,2)$$

Introducing (8,2) into (8,1), going over to physical components and using the assumed linear variation of the deformations through the wall, give equations of equilibrium. Multiplying these equations successively by $d\zeta$ and $\zeta d\zeta$ and integrating from $-\delta/2$ to $\delta/2$ give the following equations if only first order terms are retained:

$$\frac{\partial N_{\xi\xi}}{\partial \xi} + \frac{\partial N_{\eta\xi}}{\partial \eta} + q_\xi = 0 \qquad (8,3)$$

$$\frac{\partial N_{\xi\eta}}{\partial \xi} + \frac{\partial N_{\eta\eta}}{\partial \eta} + q_\eta = 0 \qquad (8,4)$$

$$\frac{\partial^2 M_{\xi\xi}}{\partial \xi^2} + 2\frac{\partial^2 M_{\xi\eta}}{\partial \xi \partial \eta} + \frac{\partial^2 M_{\eta\eta}}{\partial \eta^2} + N_{\xi\xi}\frac{\partial^2 w}{\partial \xi^2} +$$

$$+ 2N_{\xi\eta}\frac{\partial^2 w}{\partial \xi \partial \eta} + N_{\eta\eta}\left(\frac{\partial^2 w}{\partial \eta^2} - \frac{1}{R}\right) + q_\zeta = 0 \qquad (8,5)$$

Where (q_ξ, q_η, q_ζ) are load components per unit surface in the directions (ξ, η, ζ).Taking care of dynamic forces, q_ζ can be written as:

$$q_\zeta = q - \rho\delta \frac{\partial^2 w}{\partial t^2} \tag{9,1}$$

where q is a load intensity due to external forces normal to the surface.

Differential equations

The equations (8,3) and (8,4) are satistied identically if the forces are expressed into a stress function ϕ as:

$$N_{\xi\xi} = \frac{\partial^2 \phi}{\partial \eta^2} + V_{\xi\xi} \tag{9,2}$$

$$N_{\eta\eta} = \frac{\partial^2 \phi}{\partial \xi^2} + V_{\eta\eta} \tag{9,3}$$

$$N_{\xi\eta} = - \frac{\partial^2 \phi}{\partial \xi \partial \eta} \tag{9.4}$$

where:

$$q_\xi = - \frac{\partial V_{\xi\xi}}{\partial \xi} \tag{9,5}$$

$$q_\eta = - \frac{\partial V_{\eta\eta}}{\partial \eta} \tag{9.6}$$

From (6,1) - (6,3) the derivatives of u and v may be solved and introduced into (6,4) - (6,6). With the help of (9,2) - (9,4) the moments are then expressed into ϕ and w as:

$$M_{\xi\xi} = K_3 \left(\frac{\partial^2 \phi}{\partial \xi^2} + V_{\eta\eta} + N_T \right) + K_4 \left(\frac{\partial^2 \phi}{\partial \eta^2} + V_{\xi\xi} + N_T \right) +$$

$$+ K_5 \frac{\partial^2 w}{\partial \eta^2} + K_6 \frac{\partial^2 w}{\partial \xi^2} - M_T \qquad (10.1)$$

$$M_{\eta\eta} = K_4 \left(\frac{\partial^2 \phi}{\partial \xi^2} + V_{\eta\eta} + N_T \right) + K_3 \left(\frac{\partial^2 \phi}{\partial \eta^2} + V_{\xi\xi} + N_T \right) +$$

$$+ K_6 \frac{\partial^2 w}{\partial \eta^2} + K_5 \frac{\partial^2 w}{\partial \xi^2} - M_T \qquad (10.2)$$

$$M_{\xi\eta} = - K_7 \frac{\partial^2 \phi}{\partial \xi \partial \eta} + K_8 \frac{\partial^2 w}{\partial \xi^2} \qquad (10,3)$$

where:

$$K_1 = \frac{E_1}{E_1^2 - E_3^2} \qquad K_2 = \frac{E_3}{E_1^2 - E_3^2}$$

$$K_3 = \frac{E_1 E_4 - E_2 E_3}{E_1^2 - E_3^2} \qquad K_4 = \frac{E_1 E_2 - E_3 E_4}{E_1^2 - E_3^2}$$

$$K_5 = E_2 K_3 + E_4 K_4 - E_8$$

$$K_6 = E_2 K_4 + E_4 K_3 - E_7$$

$$K_7 = \frac{E_6}{E_5}$$

$$K_8 = \frac{E_6^2}{E_5} - E_9$$

$$K_9 = \frac{2}{E_5}$$

Introducing (10,1)-(10,3) into (8,5) gives an equation in ϕ and w of the form:

$$\frac{\partial^2}{\partial\xi^2}\Big[K_3\Big(\frac{\partial^2\phi}{\partial\xi^2}+V_{\eta\eta}+N_T\Big)+K_4\Big(\frac{\partial^2\phi}{\partial\eta^2}+V_{\xi\xi}+N_T\Big)+$$

$$+K_5\frac{\partial^2 w}{\partial\eta^2}+K_6\frac{\partial^2 w}{\partial\xi^2}-M_T\Big]+$$

$$+2\frac{\partial^2}{\partial\xi\partial\eta}\Big[-K_7\frac{\partial^2\phi}{\partial\xi\partial\eta}+K_8\frac{\partial^2 w}{\partial\xi\partial\eta}\Big]+$$

$$+\frac{\partial^2}{\partial\eta^2}\Big[K_4\Big(\frac{\partial^2\phi}{\partial\xi^2}+V_{\eta\eta}+N_T\Big)+K_3\Big(\frac{\partial^2\phi}{\partial\eta^2}+V_{\xi\xi}+N_T\Big)+$$

$$+K_6\frac{\partial^2 w}{\partial\eta^2}+K_5\frac{\partial^2 w}{\partial\xi^2}-M_T\Big]+$$

$$+\Big[\frac{\partial^2\phi}{\partial\eta^2}+V_{\xi\xi}\Big]\frac{\partial^2 w}{\partial\xi^2}-2\frac{\partial^2 w}{\partial\xi\partial\eta}\frac{\partial^2\phi}{\partial\xi\partial\eta}+$$

$$+\Big(\frac{\partial^2 w}{\partial\eta^2}-\frac{1}{R}\Big)\Big(\frac{\partial^2\phi}{\partial\xi^2}+V_{\eta\eta}\Big)+q_\zeta=0 \qquad (11.1)$$

Eliminating u and v in (6,1) - (6,3) and introducing (9,2) - (9,4) give a compatibility equation, which after some rewriting becomes:

$$\frac{\partial^2}{\partial\xi^2}\Big[K_1\Big(\frac{\partial^2\phi}{\partial\xi^2}+V_{\eta\eta}+N_T\Big)-K_2\Big(\frac{\partial^2\phi}{\partial\eta^2}+V_{\xi\xi}+N_T\Big)+$$

$$+K_4\frac{\partial^2 w}{\partial\eta^2}+K_3\frac{\partial^2 w}{\partial\xi^2}\Big]+$$

$$+\frac{\partial^2}{\partial\eta^2}\Big[K_1\Big(\frac{\partial^2\phi}{\partial\eta^2}+V_{\xi\xi}+N_T\Big)-K_2\Big(\frac{\partial^2\phi}{\partial\xi^2}+V_{\eta\eta}+N_T\Big)+$$

$$+K_4\frac{\partial^2 w}{\partial\xi^2}+K_3\frac{\partial^2 w}{\partial\eta^2}\Big]+$$

$$+\frac{\partial^2}{\partial\xi\partial\eta}\Big[-2K_7\frac{\partial^2 w}{\partial\xi\partial\eta}+K_9\frac{\partial^2\phi}{\partial\xi\partial\eta}\Big]-$$

$$-\frac{1}{R}\frac{\partial^2 w}{\partial \xi^2} - \left(\frac{\partial^2 w}{\partial \xi \partial \eta}\right)^2 + \frac{\partial^2 w}{\partial \xi^2}\frac{\partial^2 w}{\partial \eta^2} = 0 \qquad (12,1)$$

The equations (11,1) and (12,1) give two relations from which the two unknown functions ϕ and w may be solved with suitable boundary conditions. For E and ν constants the usual Donnell equations are obtained. The corresponding equations for a flat plate is obtained letting $R \to \infty$. Considering only linear parts of the equations and assuming ν to be temperature - independent, the equations given by [15] are obtained.

<u>Beams</u>

Nonlinear equations for the deflection of plates may be obtained through letting R go to infinity as mentioned above.

Corresponding equations for beams may not be obtained so directly because the plane stress - state form of Hooke's law used above is not valid for beams but must be changed against a one - dimensional form:

$$\sigma_{\xi\xi} = E\,\varepsilon_{\xi\xi} - E\,\varepsilon_T \qquad (12,2)$$

Introducing the strain from (5,1):

$$\varepsilon_{\xi\xi} = \frac{\partial u}{\partial \xi} - \zeta\frac{\partial^2 w}{\partial \xi^2} + \frac{1}{2}\left(\frac{\partial w}{\partial \xi}\right)^2 \qquad (12,3)$$

into (12,2) and integrating over the surface of the beam give the axial force and moment as:

$$n_{\xi\xi} = B\int_{-H/2}^{H/2} \sigma_{\xi\xi}\, d\zeta = \left[\frac{\partial u}{\partial \xi} + \frac{1}{2}\left(\frac{\partial w}{\partial \xi}\right)^2\right] B\int_{-H/2}^{H/2} E\, d\zeta -$$

$$- \frac{\partial^2 w}{\partial \xi^2} B\int_{-H/2}^{H/2} E\,\zeta\, d\zeta - B\int_{-H/2}^{H/2} E\,\varepsilon_T\, d\zeta \qquad (13.1)$$

$$m_{\xi\xi} = B\int_{-H/2}^{H/2} \sigma_{\xi\xi}\,\zeta\, d\zeta = \left[\frac{\partial u}{\partial \xi} + \frac{1}{2}\left(\frac{\partial w}{\partial \xi}\right)^2\right] B\int_{-H/2}^{H/2} E\,\zeta\, d\zeta -$$

$$- \frac{\partial^2 w}{\partial \xi^2} B\int_{-H/2}^{H/2} E\,\zeta^2\, d\zeta - B\int_{-H/2}^{H/2} E\,\varepsilon_T\,\zeta\, d\zeta \qquad (13.2)$$

The equilibrium equations will be:

$$\frac{\partial n_{\xi\xi}}{\partial \xi} + q_{\xi} = 0 \qquad (13.3)$$

$$\frac{\partial^2 m_{\xi\xi}}{\partial \xi^2} + \frac{\partial^2 w}{\partial \xi^2} n_{\xi\xi} + q_{\zeta} = 0 \qquad (13.4)$$

Introducing (13,1) and (13,2) into (13,4) gives:

$$\frac{\partial^2}{\partial \xi^2}\left[\frac{c_2}{c_1}\left(n_{\xi\xi} + c_2\frac{\partial^2 w}{\partial \xi^2} + n_T\right) - c_3\frac{\partial^2 w}{\partial \xi^2} - m_T\right] +$$

$$+ \frac{\partial^2 w}{\partial \xi^2} n_{\xi\xi} + q_{\zeta} = 0 \qquad (13.5)$$

where:

$$e_1 = B \int_{-H/2}^{H/2} E \, d\zeta \qquad e_2 = B \int_{-H/2}^{H/2} E \zeta \, d\zeta$$

$$e_3 = B \int_{-H/2}^{H/2} E \zeta^2 \, d\zeta$$

$$n_T = B \int_{-H/2}^{H/2} E \varepsilon_T \, d\zeta$$

$$m_T = B \int_{-H/2}^{H/2} E \varepsilon_T \zeta \, d\zeta$$

Equations (13,3) and 13,5) provide two relations for the unknown $n_{\xi\xi}$ and w. The force Q_ξ of the middle surface will generally be zero so that $n_{\xi\xi}$ can be taken as a constant.

Notes on solution methods

No exact analytical solutions to the Donnell's equations are known, why one is forced to use numerical or approximate analytical solutions. The most frequently used method is that of Galerkin. The radial deflection is then assumed in a form, that satisfies the boundary conditions as well as possible. Substituting this assumed form of w into the compatibility equation (12.1), the particular solution of the stress function ϕ may be obtained. The complementary solution of ϕ is taken to be zero. Finally, the expressions for w and ϕ are introduced into the equilibrium equation (11.1) and a Galerkin procedure is used to obtain a set of ordinary equations for the assumed amplitudes of w. In the present case this method is not directly applicable because the varying coefficients of the differential equations make it difficult to obtain ϕ. However, the influence of the temperature - dependence is usually not greater than to allow ϕ to be taken as a solution to the compatibility equation with constant coefficients. The error introduced through the assumed form of w, which must be limited to a few terms due to calculation complexities, is probably greater. Introducing the ϕ so obtained together with the assumed form of w into the equilibrium equation and using Galerkin's method lead to rather complicated integrals. In nonstationary problems those integrals will contain time - dependent functions in an implicit manner making them intractable to direct calculation. In such cases the coefficients of the equilibrium equation should probably be linearized with regard to the temperature - dependence before the integrals could be calculated and a system of ordinary differential equations in the time variable obtained. Those equations should then be studied numerically or through special analytical techniques.

The solution procedure outlined above is clearly limited to problems where the temperature - dependence is rather weak. Because this is usually the case for most materials at moderate temperatures, it is nevertheless probable that some useful informations about the influence of the temperature - dependence could be obtained in this way.

References

[1] J.L. Synge, W.Z. Chien:
The intrinsic theory of elastic shells and plates. Th.v. Karman Anniv. 1941.

[2] Chien: The intrinsic theory of thin shells and plates. Quart. Appl. Math. p.297, 1944, p.43 o. 120, 1944.

[3] Naghdi: A survey of recent progress in the theory of thin elastic shells. Appl. Mech. Rev. p.365, 1956.

[4] Sanders: Nonlinear theories for thin shells. Quart. Appl. Math. p.21, 1963.

[5] Naghdi: Foundations of elastic shell theory. Progr. in Solid Mechanics 4, 1963, p.1.

[6] Naghdi, Nordgren:
On the non-linear theory of elastic shells under the Kirchhoff hypothesis. Quart. Appl. Math. 21, 1963, p.49.

[7] Naghdi: On the nonlinear thermoelastic theory of shells. Non-classical shell problems, North - Holland Publ. Comp. Amsterdam 1964. p.5.

[8] Zerna: Über eine nichtlineare allgemeine Theorie der Shalen. Proc. IUTAM Symp. on the theory of thin elastic shells. North - Holland Publ. Co. 1960 p.34.

[9] Wainwright:
A nonlinear theory of elastic shells. Int. Journ. of Eng. Sc. 1, 1963, p.339.

[10] Flügge: Large deformations theory of shells of revolution. Journ. of Appl. Mech. Ma. 1967. p.56.

[11] Ismail, Nowinski:

Thermoelastic problems for shells of revolution exhibiting temperature - dependent properties. Applied Scientific Research, 14, 3, 1964/65, p.211.

[12] Kalnins: On nonlinear analysis of elastic shells of revolution. Journ. of Appl. Mech. Ma. 1967.

[13] Apeland: Analysis of bending stresses in translational shells including anisotropic and inhomogeneous properties. Acta Polytechnica Scandinavica, Civil Eng. and Constr. Ser. no 22, Trondheim, 1963

[14] Apeland: Bending of orthogonally anisotropic and asymmetric rib-reinforced shallow shells subjected to temperature changes and surface loads. Non - classical shell problems, North - Holland Publ. Co. Amsterdam 1964, p.41.

[15] Tang S.: Thermal stresses in temperature - dependent isotropic plates. J.o. Spacecraft and Rockets, vol. 5 nr. 8, Aug. 1968 pp. 987-990.

[16] Fung: Foundations of solid mechanics. Prentice - Hall Inc. Englewood Cliffs, New Jersey, 1965.

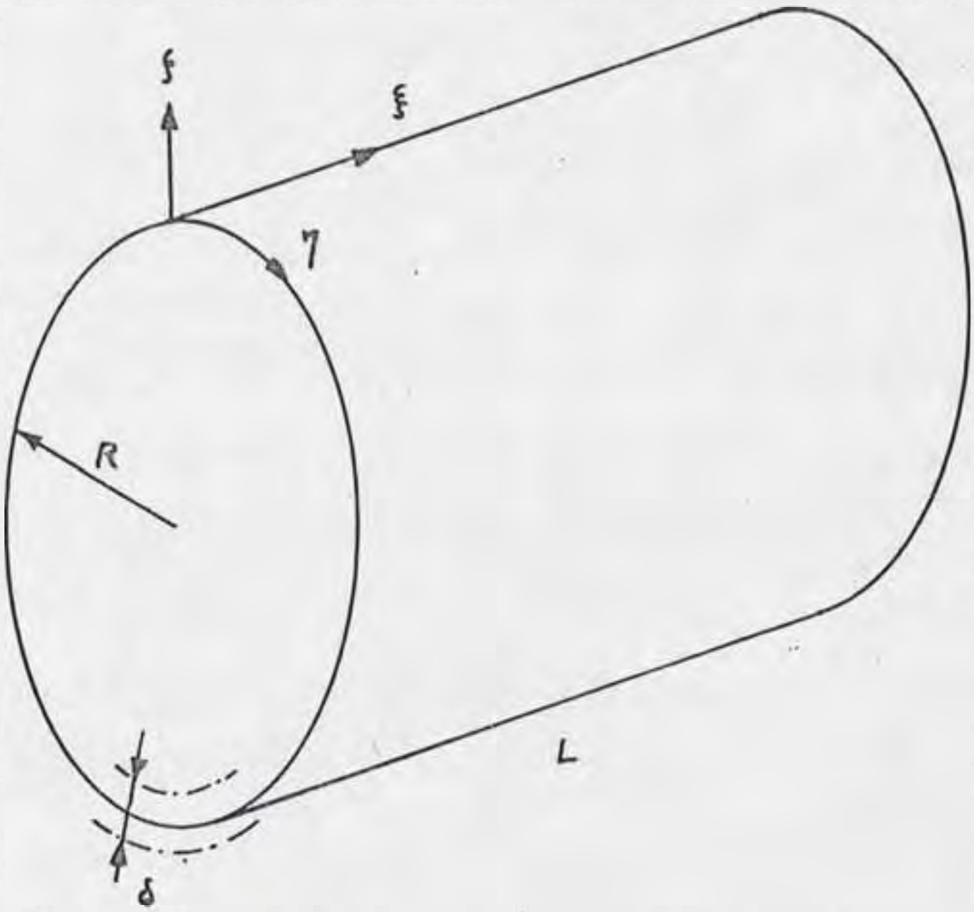

Fig. 1

REDUCTION OF THE DIFFERENTIAL EQUATIONS FOR A CYLINDRICAL SHELL OF TEMPERATURE-DEPENDENT MATERIAL PROPERTIES TO ORDINARY DIFFERENTIAL EQUATIONS

by Ulf Olsson

Summary

In order to solve the nonlinear partial shell equations derived in [1], they are reduced here to ordinary nonlinear differential equations through the application of a Galerkin procedure.

The aim of this work is to produce equations suitable for the numerical investigation of vibrations, flutter and buckling of heated cylindrical shells of the type found in e.g. the exhaust sections of jet engines.

The following cases are treated:

1. Linear thermally induced and free vibrations with temperature uniform in the plane of the shell.
2. Nonlinear flutter and buckling with neglected prestability deformations. Generally varying temperature field.
3. Nonlinear flutter and buckling with circumferentially uniform temperature field. Prestability deformations considered.

The resulting ordinary differential equations are presented in nondimensional form but not solved in this report.

T-TA (2) R RF RFF RFFU (5) CR LAA

Introduction

The following paper is one step in a work aimed at an investigation of the stability of cylindrical shells exposed to temperatures of such magnitude, that the temperature-independence of the material properties must be taken care of. This should be the case in e.g. the afterburner section of a jet engine. The cases of stability of interest here include free and forced vibrations, flutter and buckling of such cylindrical shells. In [2], such investigations have been carried out using linear shell theory and for temperature fields varying in time only. In the present work we want to include also nonlinear theory and spatially varying temperature fields. This gives rise to such effects as thermally induced vibrations, static prestability deformations and periodic oscillations, i.e. limit cycles, not considered in [2].

In a former report, [1], the nonlinear problem of finding the deformations and stresses in a cylindrical shell having temperature-dependent material properties was reduced to the solution of two coupled differential equations with the radial displacement and a stress function as dependent variables. Together with the given boundary conditions these equations pose the mathematical problem to be solved here.

This problem, belonging to a class of non-self-adjoint boundary value problems, is too complicated to be solved exactly, why it is necessary to resort to approximate methods of solution. The usual method is to express the required solution in an expansion of functions satisfying the boundary conditions and then to apply Galerkin's variational method. In this way the problem is reduced to a set of ordinary differential equations in the time variable, which may then be solved by various techniques. Direct numerical integration, [3], averaging methods, [4], and various perturbation techniques, [5], [6], have been used.

Doubts has been expressed as to the admissibility of Galerkin's method when applied to stability problems. In the linear case it leads to infinite determinants, which, as shown in [5], converge the slower the less the bending stiffness of the structure is. Thus one could expect Galerkin's method to be ineffective at very thin-walled structures, where a large number of approximating functions would be necessary to obtain convergence. Another difficulty is that it is often necessary to use approximating functions that do not satisfy all the boundary conditions. In such cases the ordinary Galerkin equations may be generalized by adding certain boundary-terms,[7]. Even if it has been shown, [8], that the so generalized Galerkin methods remain convergent in linear problems, the convergence will necessarily be slower than if all boundary conditions were satisfied. Although one does not know much theoretically about the application of Galerkin's method to nonlinear problems such as the present one, it is probable that the difficulties mentioned above remain valid. Furthermore since the volume of computations severly restrict the number of approximating functions in the nonlinear case, one must expect that the results obtained using Galerkin's method in such problems are only qualitatively correct. However, this may be considered sufficient in the present work, aimed more at a general investigation of the influence of the temperature-dependence than at exact calculations. Also, in similar cases, Galerkin's method is the most widely used, e.g. [9], [10], [11]. Thus, in spite of the limitations outlined above, we will use it here.

The shell geometry and the coordinate system are shown in Fig. 1. Internal pressure and axial loading are acting on the cylindrical shell, which is also exposed at one of its surfaces to a supersonic flow, parallell to the axial direction. As was said above it is proposed to analyze the stability of the shell, which is assumed

to be homogeneous and elastic, if it is heated to such high temperatures that the dependence of the material properties on the temperature becomes important.
To this end the nonlinear shell equations are reduced here to ordinary differential equations for the following three cases:

1. Linear thermally induced and free vibrations with temperature uniform in the plane of the shell.
   The aim here is to investigate the influence of temperature fields rapidly varying in time.
2. Nonlinear flutter and buckling with a temperature field generally varying throughout the shell.
   From this case we may obtain and compare the influences of temperature variations in the radial, circumferential and longitudinal directions respectively. Prestability deformations due to thermal expansions are neglected.
3. Nonlinear flutter and buckling with circumferentially uniform temperature field, taking care of prestability deformations. From this case we obtain the influence of the temperature-dependence on the static prestability deformations as well as the influence of these deformations on the stability of the shell.

The resulting ordinary differential equations corresponding to these three cases are given in non-dimensional form but are not solved in this report.

The shell equations

The nonlinear shallow-shell equations used here were derived in [1]. In terms of the radial deflection w and a stress function ϕ these equations are:

$$\frac{\partial^2}{\partial \xi^2}\Big[K_3\Big(\frac{\partial^2\phi}{\partial\xi^2} + V_{\eta\eta} + N_T\Big) + K_4\Big(\frac{\partial^2\phi}{\partial\eta^2} + V_{\xi\xi} + N_T\Big) +$$

$$+ K_5\frac{\partial^2 w}{\partial\eta^2} + K_6\frac{\partial^2 w}{\partial\xi^2} - M_T\Big] + 2\frac{\partial^2}{\partial\xi\partial\eta}\Big[-K_7\frac{\partial^2\phi}{\partial\xi\partial\eta} + K_8\frac{\partial^2 w}{\partial\xi\partial\eta}\Big] +$$

$$+ \frac{\partial^2}{\partial\eta^2}\Big[K_4\Big(\frac{\partial^2\phi}{\partial\xi^2} + V_{\eta\eta} + N_T\Big) + K_3\Big(\frac{\partial^2\phi}{\partial\eta^2} + V_{\xi\xi} + N_T\Big) +$$

$$+ K_6\frac{\partial^2 w}{\partial\eta^2} + K_5\frac{\partial^2 w}{\partial\xi^2} - M_T\Big] + \Big[\frac{\partial^2\phi}{\partial\eta^2} + V_{\xi\xi}\Big]\frac{\partial^2 w}{\partial\xi^2} - 2\frac{\partial^2 w}{\partial\xi\partial\eta}\frac{\partial^2\phi}{\partial\xi\partial\eta} +$$

$$+ \Big(\frac{\partial^2 w}{\partial\eta^2} - \frac{1}{R}\Big)\Big(\frac{\partial^2\phi}{\partial\xi^2} + V_{\eta\eta}\Big) + q_\xi = 0 \qquad (1)$$

$$\frac{\partial^2}{\partial\xi^2}\Big[K_1\Big(\frac{\partial^2\phi}{\partial\xi^2} + V_{\eta\eta} + N_T\Big) - K_2\Big(\frac{\partial^2\phi}{\partial\eta^2} + V_{\xi\xi} + N_T\Big) +$$

$$+ K_4\frac{\partial^2 w}{\partial\eta^2} + K_3\frac{\partial^2 w}{\partial\xi^2}\Big] +$$

$$+ \frac{\partial^2}{\partial\eta^2}\Big[K_1\Big(\frac{\partial^2\phi}{\partial\eta^2} + V_{\xi\xi} + N_T\Big) - K_2\Big(\frac{\partial^2\phi}{\partial\xi^2} + V_{\eta\eta} + N_T\Big) +$$

$$+ K_4\frac{\partial^2 w}{\partial\xi^2} + K_3\frac{\partial^2 w}{\partial\eta^2}\Big] +$$

$$+ 2\frac{\partial^2}{\partial\xi\partial\eta}\Big[-K_7\frac{\partial^2 w}{\partial\xi\partial\eta} + K_9\frac{\partial^2\phi}{\partial\xi\partial\eta}\Big] - \frac{1}{R}\frac{\partial^2 w}{\partial\xi^2} - \Big(\frac{\partial^2 w}{\partial\xi\partial\eta}\Big)^2 +$$

$$+ \frac{\partial^2 w}{}\,\frac{\partial^2 w}{} = 0 \qquad (2)$$

The functions k_n are related to the elastic properties of the material through the expressions:

$$K_1 = \frac{E_1}{E_1^2 - E_3^2} \qquad K_2 = \frac{E_3}{E_1^2 - E_3^2}$$

$$K_3 = \frac{E_1 E_4 - E_2 E_3}{E_1^2 - E_3^2} \qquad K_4 = \frac{E_1 E_2 - E_3 E_4}{E_1^2 - E_3^2} \tag{3}$$

$$K_5 = E_2 K_3 + E_4 K_4 - E_8$$

$$K_6 = E_2 K_4 + E_4 K_3 - E_7$$

$$K_7 = \frac{E_6}{E_5} \qquad K_8 = \frac{E_6^2}{E_5} - E_9 \qquad K_9 = \frac{1}{E_5}$$

where:

$$E_1 = \int_{-\delta/2}^{\delta/2} \frac{E}{1-\nu^2}\, d\zeta \qquad E_2 = \int_{-\delta/2}^{\delta/2} \frac{E}{1-\nu^2}\, \zeta\, d\zeta$$

$$E_3 = \int_{-\delta/2}^{\delta/2} \frac{\nu E}{1-\nu^2}\, d\zeta \qquad E_4 = \int_{-\delta/2}^{\delta/2} \frac{\nu E}{1-\nu^2}\, \zeta\, d\zeta \tag{4}$$

$$E_5 = \int_{-\delta/2}^{\delta/2} \frac{E}{1+\nu}\, d\zeta \qquad E_6 = \int_{-\delta/2}^{\delta/2} \frac{E}{1+\nu}\, \zeta\, d\zeta$$

$$E_7 = \int_{-\delta/2}^{\delta/2} \frac{E}{1-\nu^2} \zeta^2 d\zeta \qquad E_8 = \int_{-\delta/2}^{\delta/2} \frac{\nu E}{1-\nu^2} \zeta^2 d\zeta$$

$$E_9 = \int_{-\delta/2}^{\delta/2} \frac{E}{1+\nu} \zeta^2 d\zeta$$

Furthermore the thermal "force" and "moment" per unit length of the middle surface are represented by:

$$N_T = \int_{-\delta/2}^{\delta/2} \frac{E}{1-\nu} \varepsilon_T d\zeta$$

$$M_T = \int_{-\delta/2}^{\delta/2} \frac{E}{1-\nu} \varepsilon_T \zeta d\zeta \tag{5}$$

where the thermal strain:

$$\varepsilon_T = \int_0^\theta \alpha(\theta) d\theta \tag{6}$$

The Eqs. (1) and (2) are now to be reduced to ordinary equations with the help of Galerkin's method.

I. Linear equations with temperature uniform in the plane of the shell

We will consider here rapidly transient temperature fields, i.e. we will assume that the temperature varies significantly during a period of oscillation of the shell. Such temperature fields are usually connected with large temperature gradients through the shell wall, giving rise to thermo-shock conditions such as thermally induced vibrations. This is a special case of forced vibrations, in which the amplitude is directly determined by the temperature field. Thus the nonlinear terms are not necessary in order to obtain the magnitude of the amplitudes and may be neglected so as to facilitate the calculations.

Since the temperature is assumed to vary only in time and radially through the shell wall, the coefficients (3)-(4) will depend on time only and the following relations between them may easily be found:

$$
\begin{aligned}
K_9 - K_2 &= K_1 \\
K_4 - K_7 &= K_3 \qquad\qquad (7) \\
K_5 + K_8 &= K_6
\end{aligned}
$$

Then, if no in-plane loads are taken care of, the linearized Eqs. (1) and (2) will be:

$$K_3 \nabla^4 \phi + K_6 \nabla^4 w + (K_3 + K_4) \nabla^2 N_T - \nabla^2 M_T - \frac{1}{R} \frac{\partial^2 \phi}{\partial \xi^2} + q_\xi = 0 \qquad (8)$$

$$K_1 \nabla^4 \phi + K_3 \nabla^4 w + (K_1 - K_2) \nabla^2 N_T - \frac{1}{R} \frac{\partial^2 w}{\partial \xi^2} = 0 \qquad (9)$$

Eliminating ϕ gives:

$$\nabla^8 w + C_1 \nabla^4 \frac{\partial^2 w}{\partial \xi^2} + C_2 \frac{\partial^4 w}{\partial \xi^4} + C_3 \nabla^4 q_\xi + C_4 \nabla^6 N_T +$$

$$+ C_5 \nabla^2 \frac{\partial^2 N_T}{\partial \xi^2} + C_6 \nabla^6 M_T = 0 \tag{10}$$

where:

$$C_1 = \frac{2}{R} \frac{E_1 E_4 - E_2 E_3}{E_2^2 - E_1 E_7} \qquad C_2 = -\frac{1}{R^2} \frac{E_1^2 - E_2^2}{E_2^2 - E_1 E_7}$$

$$C_3 = \frac{E_1}{E_2^2 - E_1 E_7} \qquad C_4 = \frac{E_1 (E_2 + E_4)}{(E_1 + E_3)(E_2^2 - E_1 E_7)} \tag{11}$$

$$C_5 = \frac{1}{R} \frac{E_1 - E_3}{E_2^2 - E_1 E_7} \qquad C_6 = - \frac{E_1}{E_2^2 - E_1 E_7}$$

Concentrating upon thermally induced vibrations, the aerodynamic forces are neglected here so that:

$$q_\xi = - \delta \rho_0 \frac{\partial^2 w}{\partial t^2} \tag{12}$$

The solution of Eq. (10) is taken as the sum of one quasi-static and one dynamic solution. Since the temperature is uniform over the plane of the shell, the quasi-static deflection w_s will be independent of the circumferential coordinate η and may be obtained from the equation:

$$\frac{\partial^4 w_s}{\partial \xi^4} + C_1 \frac{\partial^2 w_s}{\partial \xi^2} + C_2 w_s + C_4 \frac{\partial^2 N_T}{\partial \xi^2} + C_5 N_T + C_6 \frac{\partial^2 M_T}{\partial \xi^2} = 0 \quad (13$$

In order to use Galerkin's method, w_s is assumed in the form:

$$w_s = \sum_{m=1}^{\infty} W_{sn} \sin \frac{n\pi\xi}{L} \quad (14)$$

Here W_{sn} are time-dependent deflection parameters of the deformed shell. The relation (14) corresponds to elastically supported shell, whose ends are neither clamped nor simply supported. Because it is unlikely that boundary conditions are of extreme importance provided the length of the shell is greater than approximately 1.5 diameters, it seems justified to use this simple relation in order to facilitate the calculations.

Introducing Eq. (14) into Eq. (13) and using Galerkin's method with the weighting functions $\frac{\partial w_s}{\partial W_{sn}}$ give the quasi-static deflection parameter W_{sn} as:

$$W_{sn} = \left[\frac{m^4\pi^4}{L^4} - C_1 \frac{n^2\pi^2}{L^2} + C_2 \right]^{-1} \Big\{ C_4 \frac{2n\pi}{L^2} \left[1-(-1)^n\right] N_T -$$

$$- C_5 \frac{2}{m\pi} \left[1-(-1)^n\right] N_T +$$

$$+ C_6 \frac{2n\pi}{L^2} \left[1-(-1)^n\right] M_T \Big\} \quad (15)$$

When the quasi-static deflection is known, the dynamic one may be obtained from the equation:

$$\nabla^8 w_d + C_1 \nabla^4 \frac{\partial^2 w_d}{\partial \xi^2} + C_2 \frac{\partial^4 w_d}{\partial \xi^4} - C_3 \delta \rho_0 \nabla^4 \frac{\partial^2 w_d}{\partial t^2} = C_3 \delta \rho_0 \frac{\partial^2 w_s}{\partial t^2} \quad (16)$$

together with homogeneous boundary conditions at $\xi = 0$ and $\xi = L$ and continuity demanded in circumferential direction.

If the dynamic solution is assumed in the form:

$$w_d = \sum_{m=0}^{\infty} \sum_{n=1}^{\infty} W_{dmn} \cos \frac{m\eta}{R} \sin \frac{n\pi\xi}{L} \tag{17}$$

Galerkin's method gives the following relation in partly nondimensionalized form:

$$\frac{\partial^2 f_{dmn}}{\partial t^2} + \omega_{mn}^2 f_{dmn} = -\delta_{om} \frac{\partial^2 f_{sn}}{\partial t^2} \tag{18}$$

$$m = 0, 1, 2 \ldots \qquad n = 1, 2 \ldots$$

where:

$$\omega_{mn}^2 = -\frac{1}{\delta \rho_0 C_3} \left[\left(\frac{m^2}{R^2} + \frac{n^2\pi^2}{L^2} \right)^2 - C_1 \frac{n^2\pi^2}{L^2} + \frac{C_2}{\left(1 + \frac{m^2}{R^2} \frac{L^2}{n^2\pi^2}\right)^2} \right] \tag{19}$$

$$f_{dmn} = \frac{W_{dmn}}{\delta} \qquad f_{sn} = \frac{W_{sn}}{\delta} \tag{20}$$

It is not convenient to nondimensionalize the time t, because each of the equations has a different time scale. We note that m=o corresponds to thermally induced vibrations, while for m≠o free vibrations are obtained. Furthermore, because of the temperature-dependence of the coefficients C_i, ω_{mn} varies in time. Thus, if the variation of ω_{mn} during a period of the oscillations is not to be neglected, f_{dmn} must be solved from a linear differential equation with variable coefficients.

II. Nonlinear equations with a generally varying temperature field

This case may be used to analyze the influence of temperature variations in the radial, circumferential and longitudinal directions as well as in time. Concentrating upon the influence of the correspondingly varying material properties we will assume the temperature fields to be such that static pre-stability deformations may be neglected. Because it is known, [12], that their influence on the stability of a cylindrical shell is important, they will be considered later on, see Case III below. Nonlinear theory will be used so as to be able to analyze the deflections after instability has occured. It may be noted that the present case is equivalent to analyzing the nonlinear stability of a cylindrical shell having generally varying elastic properties.

The mode of application of the force N is such that the rate of end elongation is constant, why inertia forces in the plane of the shell may be neglected. Furthermore, one side of the shell is exposed to a supersonic gas stream eventually giving rise to flutter instability. If the Mach number of the flow is sufficiently high, $M > 2$, then the resulting aerodynamic forces on the surface of the shell may be approximated by the linear piston theory including a curvature correction term, [13].

The load q_ζ is the sum of these aerodynamic forces and the radial inertia forces so that:

$$q_\zeta = -\rho a U \frac{\partial w}{\partial \xi} - \rho a \frac{\partial w}{\partial t} + \frac{\rho a^2}{2R} w - \delta \rho_0 \frac{\partial^2 w}{\partial t^2} \qquad (21)$$

With:

$$w = w_d \tag{22}$$

$$\phi = \phi_d + \tfrac{1}{2} N \eta^2 \tag{23}$$

the Eqs. (1) and (2) may then be rewritten as:

$$L_1[w_d, \phi_d] + \frac{\partial^2 \phi_d}{\partial \eta^2}\frac{\partial^2 w_d}{\partial \xi^2} - 2\frac{\partial^2 w_d}{\partial \xi \partial \eta}\frac{\partial^2 \phi_d}{\partial \xi \partial \eta} + \frac{\partial^2 w_d}{\partial \eta^2}\frac{\partial^2 \phi_d}{\partial \xi^2} - \frac{1}{R}\frac{\partial^2 \phi_d}{\partial \xi^2} +$$

$$+ N\frac{\partial^2 w_d}{\partial \xi^2} - \rho a U\frac{\partial w_d}{\partial \xi} - \rho a\frac{\partial w_d}{\partial t} + \frac{\rho a^2}{2R} w_d - \delta \rho_0 \frac{\partial^2 w_d}{\partial t^2} = 0 \tag{24}$$

$$L_2[w_d, \phi_d] - \frac{1}{R}\frac{\partial^2 w_d}{\partial \xi^2} - \left(\frac{\partial^2 w_d}{\partial \xi \partial \eta}\right)^2 + \frac{\partial^2 w_d}{\partial \xi^2}\frac{\partial^2 w_d}{\partial \eta^2} = 0 \tag{25}$$

where the linear parts L_1 and L_2 are the same as in Eqs. (1) and (2).

A two-mode solution is now assumed in the form:

$$w_d = \delta\left(f_d \sin\frac{\pi\xi}{L} + g_d \sin\frac{2\pi\xi}{L}\right)\cos\frac{m\eta}{R} -$$

$$- \delta^2 \frac{m^2}{4R}\left(f_d \sin\frac{\pi\xi}{L} + g_d \sin\frac{2\pi\xi}{L}\right)^2 \tag{26}$$

The last term must be included in order to satisfy the periodic continuity condition on the circumferential displacement v, [14]. In the temperature-independent case, substitution of Eq. (26) into the compatibility equation (25) allows the latter to be solved for the particular solution ϕ_d, while the complementary solution is taken to be zero, [9], [11]. If the present solution for ϕ_d is assumed to have the same form as in the temperature-independent case, it may be written as:

$$\phi_d = \cos\frac{m\eta}{R}\sum_{n=1}^{6} F_n \sin\frac{n\pi\xi}{L} + \cos\frac{2m\eta}{R}\sum_{n=0}^{4} F_{n+7}\cos\frac{n\pi\xi}{L} \tag{27}$$

where the parameters F_n are solved in the nonlinear deflection parameters f_d and g_d through substitution into Eq. (25) and using Galerkin's method with $\partial\phi_d/\partial F_m$ as weighting functions.

The assumed form for w_d and the so obtained corresponding solution for ϕ_d imply that the following boundary conditions are satisfied:

1. The displacements u, v and w and their derivatives satisfy periodic continuity conditions of the form:

   $$v(\xi,\eta,t) = v(\xi,\eta+2\pi R,t)$$

2. The deflection w goes to zero identically at the ends of the shell, i.e., at ξ=o and ξ=L, while for v, only the linear terms vanish there but not the nonlinear ones involving $f_d^{\,2}$, $f_d g_d$ and $g_d^{\,2}$.

3. The assumed w_d corresponds to an elastically supported shell and the in-plane loading conditions are satisfied in the average at the ends.

As the stress function ϕ_d has been found, it is substituted into Eq. (24) together with the assumed form of w_d and a Galerkin procedure is used to derive nonlinear ordinary differential equations for the parameters f_d and g_d. Here $\frac{\partial w_d}{\partial f_d}$ and $\frac{\partial w_d}{\partial g_d}$ are used as weighting functions.

In carrying out the calculations indicated above, it is found that the parameters F_n may be derived from the following set of equations:

$$A\,\mathbb{F} + B\,\mathbb{G} + C\,\mathbb{H} = 0 \qquad (28)$$

Here A is a 11x11 matrix emanating from those linear parts of Eq. (25), which contain ϕ_d. B is a 5x11 matrix emanating from the corresponding parts containing w_d and c is a 9x11 matrix emanating from the nonlinear parts of Eq. (25). The elements of A, B and C are given in Appendix 1. F and G are the vectors:

$$\mathbb{F}^* = (F_1, F_2, \ldots F_{11}) \tag{29}$$

$$\mathbb{G}^* = (f, g, f^2, fg, g^2) \tag{30}$$

$$\mathbb{H}^* = (f, g, f^2, fg, g^2, f^3, f^2g, fg^2, g^3) \tag{31}$$

From Eqs. (28) the parameters F_n are found in the form, φ_{ij} being constants:

$$F_n = \varphi_{n1} f + \varphi_{n2} g + \varphi_{n3} f^2 + \varphi_{n4} fg + \varphi_{n5} g^2 + \varphi_{n6} f^3 + \\ + \varphi_{n7} f^2 g + \varphi_{n8} fg^2 + \varphi_{n9} g^3 \tag{32}$$

and, in partly nondimensionalized form, the differential equations for f_d and g_d will be:

$$\ddot{f}(1 + a_1 f^2 + a_2 g^2) + \ddot{g}(a_3 fg + a_4 g^2) + \dot{f}(a_5 + a_6 f^2 + \\ + a_7 g^2 + a_8 f\dot{f} + a_9 g\dot{g}) + \dot{g}(a_{10} fg + a_{11} f\dot{g} + a_{12} g\dot{g}) + \\ + a_{13} f + a_{14} g + a_{15} f^2 + a_{16} fg + a_{17} g^2 + a_{18} f^3 + a_{19} f^2 g + \\ + a_{20} fg^2 + a_{21} g^3 + a_{22} f^4 + a_{23} f^3 g + a_{24} f^2 g^2 + a_{25} fg^3 + \\ + a_{26} g^4 + a_{27} f^5 + a_{28} f^4 g + a_{29} f^3 g^2 + a_{30} f^2 g^3 + a_{31} fg^4 + \\ + a_{32} g^5 = a_{33} \tag{33}$$

$$\ddot{g}(1 + b_1 g^2 + b_2 f^2) + \ddot{f}(b_3 g f + b_4 f^2) + \dot{g}(b_5 + b_6 g^2 + b_7 f^2 + b_8 g\dot{g} + b_9 f\dot{g}) + \dot{f}(b_{10} f g + b_{11} g\dot{f} + b_{12} f\dot{f}) + b_{13} f + b_{14} g + b_{15} f^2 + b_{16} f g + b_{17} g^2 + b_{18} f^3 + b_{19} f^2 g + b_{20} f g^2 + b_{21} g^3 + b_{22} f^4 + b_{23} f^3 g + b_{24} f^2 g^2 + b_{25} f g^3 + b_{26} g^4 + b_{27} f^5 + b_{28} f^4 g + b_{29} f^3 g^2 + b_{30} f^2 g^3 + b_{31} f g^4 + b_{32} g^5 = b_{33} \tag{34}$$

The coefficients of these equations are given in Appendix 2.

III. Nonlinear equations. Circumferentially uniform temperature field. Prestability deformations included.

The cases treated above have been of primarily theoretical interest, why we will try here to develop the equations for a more practical case, conformable e.g. to the conditions found in a jet engine afterburner. It is then first of all necessary to take care of the prestability deformations, the influence of which are known to be important. However, the inclusion of these deformations into the analysis greatly enlarge the volume of calculations, why it has been found necessary here to restrict the investigation to circumferentially uniform temperature fields and to assume that the temperature difference through the thin shell wall is so small, that the radial variation of the material properties may be neglected. These assumptions are no severe restrictions, since they conform with the conditions found in most practical cases besides perhaps at thermal shocks.

The ends of the shell are assumed to be elastically supported but will be free to move according to the increase in temperature both in the radial and axial directions, thus preventing thermal buckling to take place. The external loads acting on the shell will be restricted to aerodynamic forces, internal pressure and axial loads at the ends of the shell. Furthermore, assuming predominant radial motion, the longitudinal and circumferential inertia terms are neglected in the equations of motion. As in the previous case, the aerodynamic loads will be approximated by the linear piston theory, including a curvature correction term, so that expression for the total surface loading will be:

$$q_\zeta = p_0 - \rho a U \frac{\partial w}{\partial \xi} - \rho a \frac{\partial w}{\partial t} + \frac{\rho a^2}{2R} w - \delta \rho_0 \frac{\partial^2 w}{\partial t^2} \qquad (35)$$

The displacement w in this expression is considered to be the total radial displacement of the middle surface with respect to an initially perfect cylinder. Thus the aerodynamic pressure is the sum of the steady-state component caused by the static deformed middle surface and the unsteady component caused by the oscillations of the shell about its mean deformed position.

We want to investigate the dynamic stability of the cylindrical shell about its deformed middle surface. To achieve this w and ϕ are separated into their static and dynamic components as follows:

$$w = w_s(\xi) + w_d(\xi, \eta, t) \tag{36}$$

$$\phi = \phi_s(\xi, \eta) + \phi_d(\xi, \eta, t) \tag{37}$$

where we note that the prestability deformations are axisymmetric due to the assumed form of the temperature field and the loading conditions.

Because equilibrium and compatibility must be maintained during prestability conditions, the resulting static components form one set of equations governing the static prestability response of the shell. A second set of equations is obtained in terms of the dynamic components, which describe the dynamic stability of the shell about its statically deformed middle surface. This second system is coupled to the first through the static deformations.

Noting that the material properties were assumed to vary only longitudinally we may write the static equations as:

$$\frac{\partial^2}{\partial \xi^2}\left[\frac{E}{1-\nu^2}\frac{\delta^3}{12}\frac{\partial^2 w_s}{\partial \xi^2}\right]+\frac{1}{R}\frac{\partial^2 \phi_s}{\partial \xi^2}-P_0+\rho a U\frac{\partial w_s}{\partial \xi}-\frac{\rho a^2}{2R}w_s-$$

$$-\frac{\partial^2 w_s}{\partial \xi^2}\frac{\partial^2 \phi_s}{\partial \eta^2}+\frac{\partial^2 M_T}{\partial \xi^2}=0 \tag{38}$$

$$\frac{\partial^2}{\partial \xi^2}\left[\frac{1}{\delta E}\frac{\partial^2 \phi_s}{\partial \xi^2}-\frac{\nu}{\delta E}\frac{\partial^2 \phi_s}{\partial \eta^2}\right]+\frac{\partial^2}{\partial \eta^2}\left[\frac{1}{\delta E}\frac{\partial^2 \phi_s}{\partial \eta^2}-\frac{\nu}{\delta E}\frac{\partial^2 \phi_s}{\partial \xi^2}\right]+$$

$$+2\frac{\partial^2}{\partial \xi \partial \eta}\left[\frac{1+\nu}{\delta E}\frac{\partial^2 \phi_s}{\partial \xi \partial \eta}\right]+\frac{\partial^2}{\partial \xi^2}\left[\frac{1-\nu}{\delta E}N_T\right]-\frac{1}{R}\frac{\partial^2 w_s}{\partial \xi^2}=0 \tag{39}$$

with the associated steady state boundary conditions at ξ=o and ξ=L:

$$w_s(0)=w_0 \qquad w_s(L)=w_L \tag{40}$$

$$\frac{\delta^3}{12}\frac{E}{1-\nu^2}\frac{\partial^2 w_s}{\partial \xi^2}+M_T=\text{some prescribed moment} \tag{41}$$

$$N_{\xi\xi}=\frac{\partial^2 \phi_s}{\partial \eta^2}=N \tag{42}$$

$$N_{\xi\eta}=-\frac{\partial^2 \phi_s}{\partial \xi \partial \eta}=0 \tag{43}$$

where:

$$w_{0,L}=\frac{R}{\delta}\frac{1-\nu}{E}N_T+\frac{P_0 R^2}{\delta E} \tag{44}$$

are the radial deflection of the ends ξ=o and ξ=L due to thermal expansion and internal pressure.

In order to solve Eqs. (38) and (39) we introduce the stress function in the form:

$$\phi_s(\xi,\eta) = \frac{1}{2} N \eta^2 + \psi_s(\xi) \tag{45}$$

The first term corresponds to the applied axial stress, which is constant throughout the shell, and the last term corresponds to the stresses due to the deformation w_s. As is seen the boundary conditions on ϕ_s are satisfied. Substituting Eq. (45) into Eqs. (38) and (39), we find that these equations may be reduced to one single linear equation of motion:

$$\frac{\partial^2}{\partial\xi^2}\left[\frac{E}{1-\nu^2}\frac{d^3}{12}\frac{\partial^2 w_s}{\partial\xi^2}\right] + \frac{\nu N}{R} - \frac{1-\nu}{R}N_T + \frac{dE}{R^2}w_s -$$

$$- p_0 + \rho a U \frac{\partial w_s}{\partial\xi} - \frac{\rho a^2}{2R}w_s - N\frac{\partial^2 w_s}{\partial\xi^2} + \frac{\partial^2 M_T}{\partial\xi^2} = 0 \tag{46}$$

with the boundary conditions (40) and (41). In the case of temperature-independent material properties this equation could be solved exactly, [12], but here we must resort to approximate methods. We therefore assume the following mode of deflection:

$$w_s = w_0 + (w_L - w_0)\frac{\xi}{L} + d f_s \sin\frac{\pi\xi}{L} + d g_s \sin\frac{2\pi\xi}{L} \tag{47}$$

and using Galerkin's method obtain a system of algebraic equations for the nondimensional parameters f_s and g_s:

$$\begin{pmatrix} a_{11} & a_{12} \\ a_{21} & a_{22} \end{pmatrix} \begin{pmatrix} f_s \\ g_s \end{pmatrix} = \begin{pmatrix} b_1 \\ b_2 \end{pmatrix} \tag{48}$$

where the numbers a_{ij} and b_i are given in Appendix 3. Here the boundary conditions (41) have been taken care of in the Galerkin procedure under the assumption of vanishing prescribed moments at the ends of the shell.

Having derived the static solution we may procede to the dynamic problem. Here the governing equations will be:

$$L_1[w_d, \phi_d] + \frac{1}{R}\frac{\partial^2 \phi_d}{\partial \xi^2} + \rho a U \frac{\partial w_d}{\partial \xi} - \frac{\rho a^2}{2R} w_d + \rho a \frac{\partial w_d}{\partial t} +$$

$$+ \delta \rho_0 \frac{\partial^2 w_d}{\partial t^2} - \frac{\partial^2 w_s}{\partial \xi^2}\frac{\partial^2 \phi_d}{\partial \eta^2} - N \frac{\partial^2 w_d}{\partial \xi^2} - \frac{\partial^2 w_d}{\partial \xi^2}\frac{\partial^2 \phi_d}{\partial \eta^2} +$$

$$+ 2 \frac{\partial^2 w_d}{\partial \xi \partial \eta}\frac{\partial^2 \phi_d}{\partial \xi \partial \eta} - \frac{\partial^2 w_d}{\partial \eta^2}\frac{\partial^2 \psi_s}{\partial \xi^2} - \frac{\partial^2 w_d}{\partial \eta^2}\frac{\partial^2 \phi_d}{\partial \xi^2} = 0 \qquad (49)$$

$$L_2[w_d, \phi_d] - \frac{1}{R}\frac{\partial^2 w_d}{\partial \xi^2} - \left(\frac{\partial^2 w_d}{\partial \xi \partial \eta}\right)^2 + \frac{\partial^2 w_s}{\partial \xi^2}\frac{\partial^2 w_d}{\partial \eta^2} + \frac{\partial^2 w_d}{\partial \xi^2}\frac{\partial^2 w_d}{\partial \eta^2} = 0 \qquad (50)$$

The linear operators L_1 and L_2 are the same as in case II but here the functions K_n, due to the assumed invariance of the material properties in the radial direction, will be:

$$K_1 = \frac{1}{\delta E} \qquad K_2 = \frac{\nu}{\delta E} \qquad K_3 = 0 \qquad K_4 = 0$$

$$K_5 = -\frac{\delta^3}{12}\frac{\nu E}{1-\nu^2} \qquad K_6 = -\frac{\delta^3}{12}\frac{E}{1-\nu^2} \qquad K_7 = 0 \qquad (51)$$

$$K_8 = -\frac{\delta^3}{12}\frac{E}{1+\nu} \qquad K_9 = \frac{1+\nu}{\delta E}$$

The boundary conditions of the dynamic problem correspond to those of an elastically supported shell, why the problem is the same as that of Case II besides that some auxiliary terms due to the prestability deformations are introduced into the equations.

Now using the same assumption for w_d as above, i.e. Eq. (26), and introducing it into Eq. (50) together with w_s, we find that ϕ_d must be enlarged in order to be compatible with the particular solution of the temperature-independent problem. In fact it must be written in the following form:

$$\phi_d = \cos\frac{m\eta}{R}\sum_{n=1}^{6} F_n \sin\frac{n\pi\xi}{L} + \cos\frac{2m\eta}{R}\sum_{n=0}^{4} F_{n+7}\cos\frac{n\pi\xi}{L} + $$

$$+ \cos\frac{m\eta}{R}\sum_{n=0}^{4} F_{n+12}\cos\frac{n\pi\xi}{L} \qquad (52)$$

where the parameters F_n may be found from a set of equations of the same type as Eqs. (28). However, the matrices and vectors must be enlarged corresponding to the new form of ϕ_d. Some parts of the enlarged matrix A will vanish identically because the functions K_n now depend on ξ, t only. The result is a 16x16 matrix of the type shown in fig. 2, where the new parts and the parts remaining from the original matrix are marked. The matrix B will vanish identically because $K_3 = K_4 = K_7 = 0$, while the matrix C will be enlarged by new elements to a size of 9x16, the original elements remaining enchanged.

Thus the set of equations giving the parameters F_n will be:

$$A\,\mathbb{F} + C\,\mathbb{H} = 0 \qquad (53)$$

where the vector:

$$\mathbb{F}^* = (F_1, F_2, \ldots F_{16}) \qquad (54)$$

while the vector $\mathbb{H}$ is given by Eq. (31).

The nonvanishing elements of A as well as the new elements of C are given in Appendix 4. When the parameters F_n have been solved in the same form as before, Eq. (32), substitution of ϕ_d, w_s and w_d into Eq. (51) and using Galerkin's method with:

$$\frac{\partial w_d}{\partial f_d}, \quad \frac{\partial w_d}{\partial g_d}$$

as weighting functions give differential equations for f_d and g_d. Those equations are of exactly the same type as Eqs. (33) and (34) but their coefficients will now contain terms emanating from the static solution. These coefficients are written out in Appendix 5.

References

[1] Olsson U.: Nonlinear Thermoelastic Equations for Beams and Cylindrical Shells Having Temperature-dependent Properties. Flygmotor Research, RF 5:3014, 1969.

[2] Ambartsumian S.A. et. al.: Some Problems of Vibration and Stability of Shells and Plates. Int. J. Solids Structures, Vol. 2, pp 59-81, 1966.

[3] Nash W.A.: Nonlinear Problems in the Dynamics of Thin Shells. In "Nonlinear Partial Differential Equations" ed. by W.F.Ames, p. 291, Academic Press, New York, 1967.

[4] Bogoliubov N.N., Mitropolsky Y.A.: Asymptotic Methods in the Theory of Non-Linear Oscillations, p. 387, Hindustan Publishing Corpn., Dehli, 1961.

[5] Bolotin V.V., Nonconservative Problems of the Theory of Elastic Stability, p. 298, Pergamon Press, New York 1963.

[6] Morino L.: A Perturbation Method for Treating Nonlinear Panel Flutter Problems. AIAA Jnl, Vol. 7, No. 3, Ma. 1969, pp 405-411.

[7] Kantorovich L.V., Krylov V.I.: Approximate Methods of Higher Analysis, pp 284-304, 4th Ed., P.Noordhoff Ltd., Groningen, The Nederlands, 1964.

[8] Leipholz, H.: Über die Wahl der Ansatzfunktionen bei der Durchführung des Verfahrens von Galerkin. Acta Mech.,Vol. 3, No. 3, 1967, p 295.

[9] Olson, M.D., Fung, Y.C.: Comparing Theory and Experiment for the Supersonic Flutter of Circular Cylindrical Shells. AIAA Jnl. Vol. 5, No. 10, p. 1849, Oct. 1967.

[10] Dowell, E.H.: Modal Equations for the Nonlinear Flexural Vibrations of a Cylindrical Shell. Int. Jnl. of Solids and Structures, Vol. 4, No. 10, p 976, 1968.

[11] Evensen, D.A., Olson, M.D.: Circumferentially Travelling Wave Flutter of a Circular Cylindrical Shell. AIAA Jnl, Vol. 6, No. 8, p. 1522, Aug. 1968.

[12] Barr, G.W., Stearman, R.O.: Aeroelastic Stability Characteristics of Cylindrical Shells Considering Imperfections and Edge Constraint. AIAA Jnl, Vol. 7, No. 5, p 912, May 1969.

[13] Krumbaar, H.: The Accuracy of Applying Linear Piston Theory to Cylindrical Shells. AIAA Jnl, Vol. 1, No. 6, p 1448, June 1963.

[14] Evensen, D.A.: Some Observations on the Nonlinear Vibrations of Thin Cylindrical Shells. AIAA Jnl, Vol. 1, p. 2857, 1963.

List of notations

E = Youngs modulus
ν = Poisson's ratio
α = thermal expansion coefficient
ϑ = temperature excess
V = load potentials per unit shell surface
q_ζ = normal load component per unit shell surface
ρ_o = density of shell material
t = time variable
a = velocity of sound
U = velocity of gas stream
ρ = density of gas
m = number of modes of the deformed shell in circumferential direction

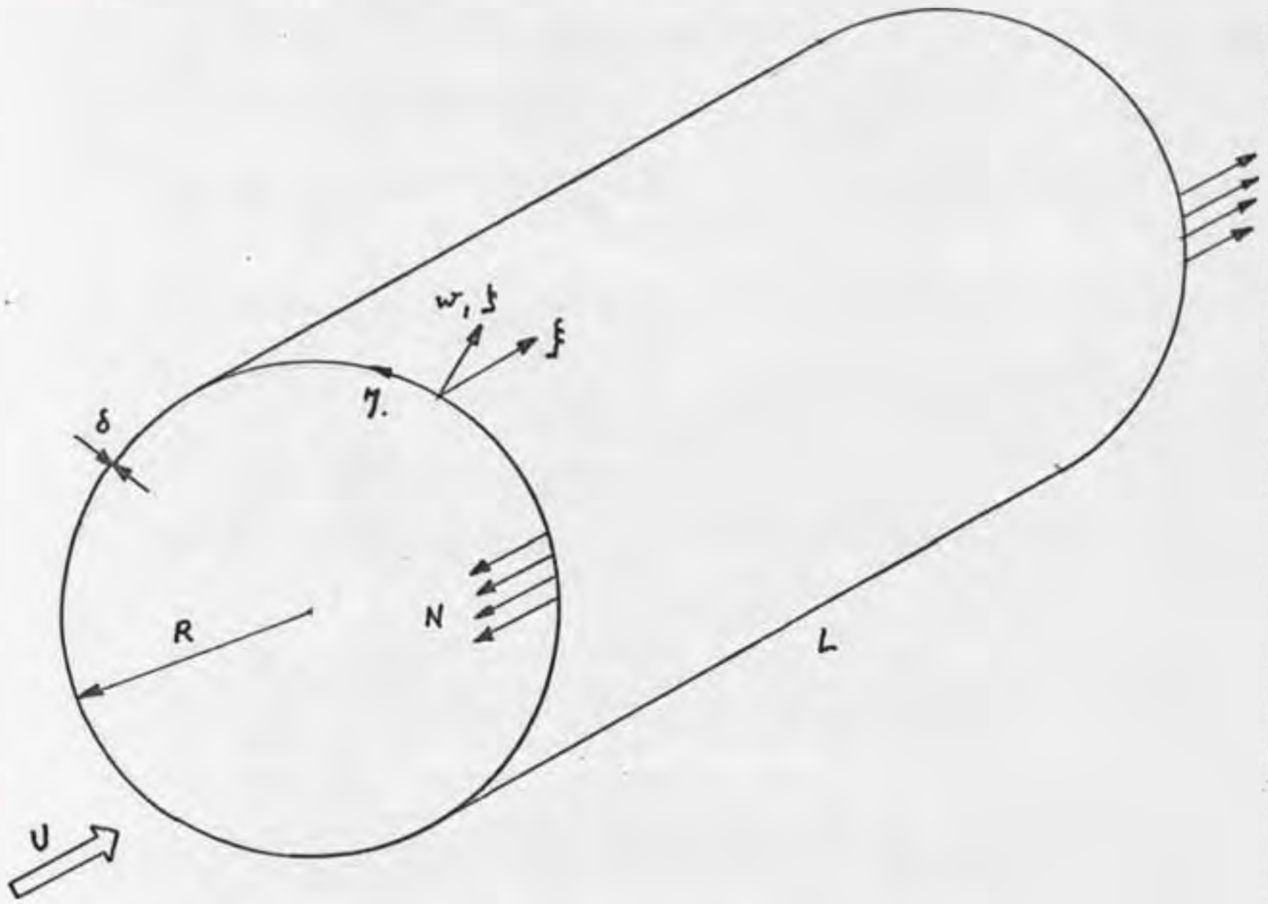

Fig. 1 Shell geometry and coordinate system

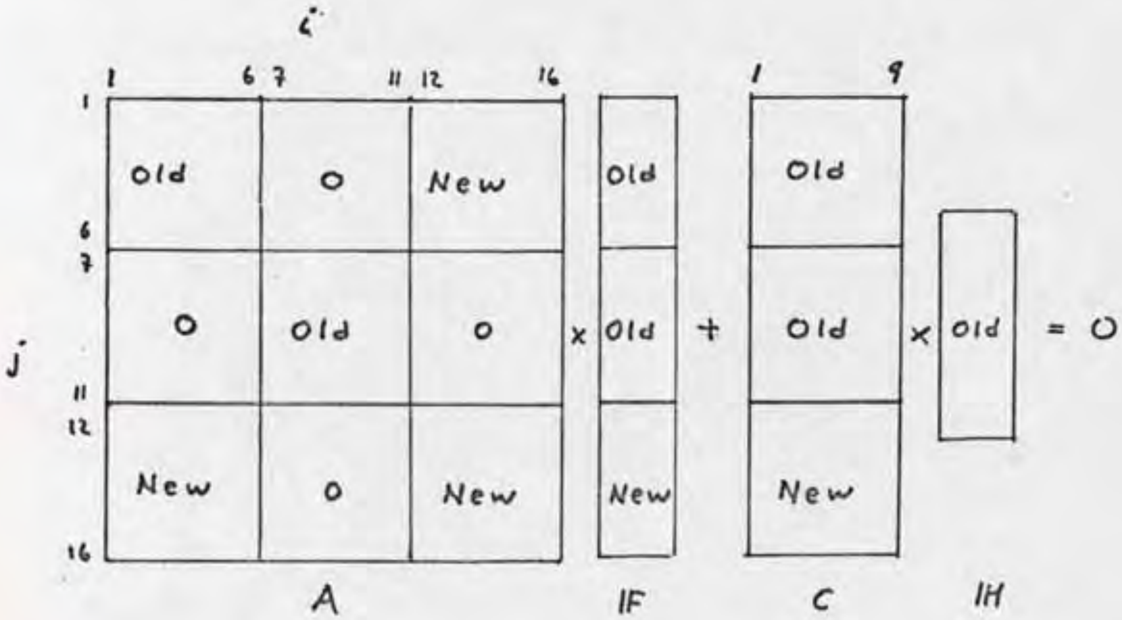

Fig. 2 Structure of Eq. (53)

Appendix 1

$$I_{p,q,r} = \int_0^{2\pi R} \int_0^{L} L_p \sin \frac{q\pi\xi}{L} \cos \frac{rm\eta}{R} \, d\xi \, d\eta$$

$$J_{p,q,r} = \int_0^{2\pi R} \int_0^{L} L_p \cos \frac{q\pi\xi}{L} \cos \frac{rm\eta}{R} \, d\xi \, d\eta$$

$$J_{p,r}(\xi) = \int_0^{2\pi R} L_p \cos \frac{rm\eta}{R} \, d\eta$$

$$L_p = L_p(\xi, \eta)$$

For $1 \le i \le 6 \quad 1 \le j \le 6$

$$\alpha_{ij}(M, L_1, L_2, L_3) =$$

$$= \frac{1}{4}\left(\frac{i^2 j^2 \pi^4}{L^4} + \frac{m^4 M^2}{R^4}\right)\left(J_{1,i-j,1+M} + J_{1,i-j,1-M} -\right.$$

$$\left. - J_{1,i+j,1+M} - J_{1,i+j,1-M}\right) +$$

$$+ \frac{m^2 \pi^2 (M^2 i^2 + j^2)}{4R^2 L^2}\left(J_{2,i-j,1+M} + J_{2,i-j,1-M} -\right.$$

$$\left. - J_{2,i+j,1+M} - J_{2,i+j,1-M}\right) +$$

$$+ \frac{m^2 M ij \pi^2}{4R^2 L^2}\left(J_{3,i+j,1-M} + J_{3,i-j,1-M} - J_{3,i+j,1+M} - J_{3,i-j,1+M}\right)$$

For $7 \le i \le 11 \quad 1 \le j \le 6$

$$\alpha_{ij}(M, L_1, L_2, L_3) =$$

$$= \frac{(i-7)^2 j \pi^3}{2L^3} \left[-(-1)^{i+j} \left(J_{1,2+M}^{(L)} + J_{1,2-M}^{(L)} \right) - \right.$$

$$\left. - \left(J_{1,2+M}^{(0)} + J_{1,2-M}^{(0)} \right] + \right.$$

$$+ \frac{2m^2 j \pi}{R^2 L} \left[-(-1)^{i+j} \left(J_{2,2+M}^{(L)} + J_{2,2-M}^{(L)} \right) - \right.$$

$$\left. - \left(J_{2,2+M}^{(0)} + J_{2,2-M}^{(0)} \right) \right] +$$

$$+ \frac{1}{4} \left[\frac{(i-7)^2 j^2 \pi^4}{L^4} + \frac{4M^2 m^4}{R^4} \right] \left[I_{1,i+j-7,2+M} + I_{1,i+j-7,2-M} - \right.$$

$$\left. - I_{1,i-j-7,2+M} - I_{1,i-j-7,2-M} \right] +$$

$$+ \frac{\pi^2 m^2}{4R^2 L^2} \left[4j^2 + M^2 (i-7)^2 \right] \left[I_{2,i+j-7,2+M} + I_{2,i+j-7,2-M} - \right.$$

$$\left. - I_{2,i-j-7,2+M} - I_{2,i-j-7,2-M} \right] -$$

$$- \frac{\pi^2 m^2 M j (i-7)}{2R^2 L^2} \left[I_{3,i+j-7,2-M} + I_{3,i-j-7,2-M} - \right.$$

$$\left. - I_{3,i+j-7,2+M} - I_{3,i-j-7,2+M} \right]$$

For $1 \leq i \leq 6 \quad 7 \leq j \leq 11$

$$\alpha_{ij}(M, L_1, L_2, L_3) =$$

$$= \frac{\pi^3 i^3}{2L^3}\left[J_{1,1+M}^{(0)} + J_{1,1-M}^{(0)} + (-1)^{i+j}\left(J_{1,1+M}^{(L)} + J_{1,1-M}^{(L)}\right)\right] +$$

$$+ \frac{\pi m^2 i}{2R^2 L}\left[J_{2,1+M}^{(0)} + J_{2,1-M}^{(0)} + (-1)^{i+j}\left(J_{2,1+M}^{(L)} + J_{2,1-M}^{(L)}\right)\right] +$$

$$+ \frac{1}{4}\left[\frac{M^2 m^4}{R^4} + \frac{i^2 (j-7)^2 \pi^4}{L^4}\right]\left[I_{1,i+j-7,1+M} + I_{1,i+j-7,1-M} -\right.$$

$$\left. - I_{1,j-i-7,1+M} - I_{1,j-i-7,1-M}\right] -$$

$$- \frac{m^2 \pi^2}{4R^2 L^2}\left[(j-7)^2 + M^2 i^2\right]\left[I_{2,i+j-7,1+M} + I_{2,i+j-7,1-M} -\right.$$

$$\left. - I_{2,j-i-7,1+M} - I_{2,j-i-7,1-M}\right] -$$

$$- \frac{\pi^2 M m^2 (j-7) i}{4R^2 L^2}\left[J_{3,i+j-7,1-M} + J_{3,j-i-7,1-M} -\right.$$

$$\left. - J_{3,i+j-7,1+M} - J_{3,j-i-7,1+M}\right] +$$

$$+ \frac{\pi M m^2 i}{2R^2 L}\left[J_{3,1-M}^{(0)} - J_{3,1+M}^{(0)} + (-1)^{i+j}\left(J_{3,1-M}^{(L)} - J_{3,1+M}^{(L)}\right)\right]$$

For $7 \le i \le 11 \quad 7 \le j \le 11$

$$\alpha_{ij}(M, L_1, L_2, L_3) =$$

$$= \frac{\pi^2 (i-7)^2}{2L^2}\left[\frac{\partial}{\partial\xi} J_{1,2+M}(0) + \frac{\partial}{\partial\xi} J_{1,2-M}(0) - (-1)^{i+j}\left(\frac{\partial}{\partial\xi} J_{1,2+M}(L) + \frac{\partial}{\partial\xi} J_{1,2-M}(L)\right)\right] +$$

$$+ \frac{2m^2}{R^2}\left[\frac{\partial}{\partial\xi} J_{2,2+M}(0) + \frac{\partial}{\partial\xi} J_{2,2-M}(0) - (-1)^{i+j}\left(\frac{\partial}{\partial\xi} J_{2,2+M}(L) + \frac{\partial}{\partial\xi} J_{2,2-M}(L)\right)\right] +$$

$$+ \frac{1}{4}\left(\frac{\pi^4 (i-7)^2 (j-7)^2}{L^4} + 4\frac{M^2 m^4}{R^4}\right]\left[J_{1,i+j-14,2+M} + J_{1,j-i,2+M} +\right.$$

$$\left. + J_{1,i+j-14,2-M} + J_{1,j-i,2-M}\right] +$$

$$+ \frac{\pi^2 m^2}{4R^2L^2}\left[4(j-7)^2 + M^2(i-7)^2\right]\left[J_{2,i+j-14,2+M} + J_{2,j-i,2+M} +\right.$$

$$\left. + J_{2,i+j-14,2-M} + J_{2,j-i,2-M}\right] +$$

$$+ \frac{M m^2 (i-7)(j-7)\pi^2}{2R^2L^2}\left[I_{3,i+j-14,2-M} - I_{3,j-i,2-M} -\right.$$

$$\left. - I_{3,i+j-14,2+M} + I_{3,j-i,2+M}\right]$$

For $1 \le j \le 6$

$$\beta_{1j}(M, L_1, L_2, L_3) =$$

$$= \frac{\pi^2 m^2 d}{4R^2L^2}(j^2+M^2)\left[J_{1,1-j,1+M} + J_{1,1-j,1-M} - J_{1,1+j,1+M} - J_{1,1+j,1-M}\right] +$$

$$+ \frac{d}{4}\left(\frac{M^2m^4}{R^4} + \frac{\pi^4 j^2}{L^4}\right)\left[J_{2,1-j,1+M} + J_{2,1-j,1-M} - J_{2,1+j,1+M} - J_{2,1+j,1-M}\right] +$$

$$+ \frac{\pi^2 M m^2 j d}{4R^2L^2}\left[J_{3,1+j,1-M} + J_{3,1-j,1-M} - J_{3,1+j,1+M} - J_{3,1-j,1+M}\right]$$

$$\beta_{2j}(M, L_1, L_2, L_3) =$$

$$= \frac{\pi^2 j^2 d}{4L^2}\left(\frac{m^2}{R^2} + \frac{4\pi^2}{L^2}\right)\left[J_{1,2-j,1+M} + J_{1,2-j,1-M} - J_{1,2+j,1+M} - J_{1,2+j,1-M}\right] +$$

$$+ \frac{M^2m^2 d}{4R^2}\left(\frac{m^2}{R^2} + \frac{4\pi^2}{L^2}\right)\left[J_{2,2-j,1+M} + J_{2,2-j,1-M} - J_{2,2+j,1+M} - J_{2,2+j,1-M}\right] +$$

$$+ \frac{\pi^2 M m^2 j d}{2L^2R^2}\left[J_{3,2+j,1-M} + J_{3,2-j,1-M} - J_{3,2+j,1+M} - J_{3,2-j,1+M}\right]$$

$$\beta_{3j}(M, L_1, L_2, L_3) =$$

$$= -2\,\frac{\pi^3 m^2 j d}{RL^3}\left[(-1)^j J_{2,M}(L) + J_{2,M}(0)\right] +$$

$$+ \frac{\pi^4 m^2 j^2 d^2}{4RL^4}\left[I_{2,2+j,M} - I_{2,2-j,M}\right] + \frac{\pi^2 M^2 m^4 d^2}{4R^3L^2}\left[I_{1,2+j,M} - I_{1,2-j,M}\right]$$

Flygmotor

$\beta_{4j}(M, L_1, L_2, L_3) =$

$$= -2\,\frac{\pi^3 m^2 j\, \delta^2}{R L^3}\left[(-1)^j\, J_{2,M}(L) + J_{2,M}(0) \right] +$$

$$+ \frac{\pi^4 m^2 j^2 \delta^2}{8\, R L^4}\left[9 I_{2,3+j,M} - 9 I_{2,3-j,M} - 4 I_{2,1+j,M} + 4 I_{2,1-j,M} \right] +$$

$$+ \frac{\pi^2 M^2 m^4 \delta^2}{8\, R^3 L^2}\left[9 I_{1,3+j,M} - 9 I_{1,3-j,M} - 4 I_{1,1+j,M} + 4 I_{1,1-j,M} \right]$$

$\beta_{5j}(M, L_1, L_2, L_3) =$

$$= 2\,\frac{\pi^3 m^2 j\, \delta^2}{R L^3}\left[(-1)^j\, J_{2,M}(L) - J_{2,M}(0) \right] +$$

$$+ \frac{\pi^4 m^2 j^2 \delta^2}{R L^4}\left[I_{2,4+j,M} - I_{2,4-j,M} \right] + \frac{\pi^2 M^2 m^4 \delta^2}{R^3 L^2}\left[I_{1,4+j,M} - I_{1,4-j,M} \right]$$

For $7 \le j \le 10$

$\beta_{1j}(M, L_1, L_2, L_2) =$

$$= \frac{\pi m^2 \delta}{2 R^2 L}\left[J_{1,1+M}(0) + J_{1,1-M}(0) - (-1)^j \left(J_{1,1+M}(L) + J_{1,1-M}(L) \right) \right] +$$

$$+ \frac{\pi^3 \delta}{2 L^3}\left[J_{2,1+M}(0) + J_{2,1-M}(0) - (-1)^j \left(J_{2,1+M}(L) + J_{2,1-M}(L) \right) \right] +$$

$$+ \frac{\pi^2 m^2 d}{4R^2L^2}(M^2+j^2)\left[I_{1,j-6,1+M} - I_{1,j-8,1+M} + I_{1,j-6,1-M} - I_{1,j-8,1-M}\right] +$$

$$+ \frac{d}{4}\left[\frac{M^2m^4}{R^4} + \frac{\pi^4(j-7)^2}{L^4}\right]\left[I_{2,j-6,1+M} - I_{2,j-8,1+M} + I_{2,j-6,1-M} - I_{2,j-8,1-M}\right] +$$

$$+ \frac{\pi M m^2 d}{2R^2L}\left[J_{3,1-M}(0) - J_{3,1+M}(0) - (-1)^j\left(J_{3,1-M}(L) - J_{3,1+M}(L)\right)\right] -$$

$$- \frac{\pi^2 M m^2 (j-7) d}{4R^2L^2}\left[J_{3,j-6,1-M} + J_{3,j-8,1-M} - J_{3,j-6,1+M} - J_{3,j-8,1+M}\right]$$

$$\beta_{2j}(M, L_1, L_2, L_3) =$$

$$= \frac{\pi m^2 d}{R^2L}\left[J_{1,1+M}(0) + J_{1,1-M}(0) + (-1)^j\left(J_{1,1+M}(L) + J_{1,1-M}(L)\right)\right] +$$

$$+ \frac{4\pi^3 d}{L^3}\left[J_{2,1+M}(0) + J_{2,1-M}(0) + (-1)^j\left(J_{2,1+M}(L) + J_{2,1-M}(L)\right)\right] +$$

$$+ \frac{\pi^2 m^2 d}{4R^2L^2}\left[4M^2 + (j-7)^2\right]\left(I_{1,j-5,1+M} - I_{1,j-9,1+M} + I_{1,j-5,1-M} - I_{1,j-9,1-M}\right] +$$

$$+ \frac{d}{4}\left[\frac{M^2m^4}{R^4} + \frac{4\pi^4(j-7)^2}{L^4}\right]\left[I_{2,j-5,1+M} - I_{2,j-9,1+M} + I_{2,j-5,1-M} - I_{2,j-9,1-M}\right] -$$

$$- \frac{\pi^2 M m^2 (j-7) d}{2R^2L^2}\left[J_{3,j-5,1-M} + J_{3,j-9,1-M} - J_{3,j-5,1+M} - J_{3,j-9,1+M}\right] +$$

$$+ \frac{\pi M m^2 d}{R^2L}\left[J_{3,1-M}(0) - J_{3,1+M}(0) + (-1)^j\left(J_{3,1-M}(L) - J_{3,1+M}(L)\right)\right]$$

Flygmotor

$$\beta_{3j}(M, L_1, L_2, L_3) =$$

$$= \frac{\pi^2 m^2 \delta^2}{2RL^2}\left[\frac{\partial}{\partial\xi} J_{2,M}^{(0)} + (-1)^j \frac{\partial}{\partial\xi} J_{2,M}^{(L)}\right] +$$

$$+ \frac{\pi^4 m^2 (j-7)^2 \delta^2}{4RL^4}\left[J_{2,j-5,M} + J_{2,j-9,M}\right] +$$

$$+ \frac{\pi^2 M^2 m^4 \delta^2}{4R^3L^2}\left[J_{1,j-5,M} + J_{1,j-9,M}\right]$$

$$\beta_{4j}(M, L_1, L_2, L_3) =$$

$$= \frac{2\pi^2 m^2 \delta^2}{RL^2}\left[\frac{\partial}{\partial\xi} J_{2,M}^{(0)} - (-1)^j \frac{\partial}{\partial\xi} J_{2,M}^{(L)}\right] +$$

$$+ \frac{\pi^4 m^2 (j-7)^2 \delta^2}{8RL^4}\left[9J_{2,j-4,M} + 9J_{2,j-10,M} - J_{2,j-6,M} - J_{2,j-8,M}\right] +$$

$$+ \frac{\pi^2 M^2 m^4 \delta^2}{8R^3L^2}\left[9J_{1,j-4,M} + 9J_{1,j-10,M} - J_{1,j-6,M} - J_{1,j-8,M}\right]$$

$$\beta_{5j}(M, L_1, L_2, L_3) =$$

$$= \frac{2\pi^2 m^2 \delta^2}{RL^2}\left[\frac{\partial}{\partial\xi} J_{2,M}^{(0)} + (-1)^j \frac{\partial}{\partial\xi} J_{2,M}^{(L)}\right] +$$

$$+ \frac{\pi^4 m^2 (j-7)^2 \delta^2}{RL^5}\left[J_{2,j-3,M} + J_{2,j-11,M}\right] +$$

$$+ \frac{\pi^2 M^2 m^4 \delta^2}{R^3L^2}\left[J_{1,j-3,M} + J_{1,j-11,M}\right]$$

Flygmotor

Now the elements A_{ij} will be:

$1 \le j \le 6 \quad 1 \le i \le 11 \qquad A_{ij} = \alpha_{ij}(1, K_1, -K_2, 2K_9)$

$7 \le j \le 11 \quad 1 \le i \le 11 \qquad A_{ij} = \alpha_{ij}(2, K_1, -K_2, 2K_9)$

and the elements B_{ij}:

$1 \le j \le 6 \quad 1 \le i \le 5 \qquad B_{ij} = \beta_{ij}(1, K_4, K_3, -2K_7)$

$7 \le j \le 11 \quad 1 \le i \le 5 \qquad B_{ij} = \beta_{ij}(2, K_4, K_3, -2K_7)$

The nonvanishing elements C_{ij} :

$$C_{11} = \frac{\pi^3 \delta}{2L} \qquad C_{16} = -\frac{\pi^3 m^4 \delta^3}{8R^2 L} \qquad C_{18} = -\frac{5\pi^3 m^4 \delta^3}{8R^2 L}$$

$$C_{22} = \frac{2\pi^3 \delta}{L} \qquad C_{27} = -\frac{5\pi^3 m^4 \delta^3}{8R^2 L} \qquad C_{29} = -\frac{\pi^3 m^4 \delta^3}{2R^2 L}$$

$$C_{36} = \frac{\pi^3 m^4 \delta^3}{8R^2 L} \qquad C_{38} = -\frac{9\pi^3 m^4 \delta^3}{16R^2 L}$$

$$C_{47} = \frac{11\pi^3 m^4 \delta^3}{16R^2 L}$$

$$C_{58} = \frac{17\pi^3 m^4 \delta^3}{16R^2 L}$$

$$C_{69} = \frac{\pi^3 m^4 \delta^3}{2R^2 L}$$

$$C_{73} = \frac{\pi^3 m^2 \delta^2}{4RL} \qquad C_{75} = \frac{\pi^3 m^2 \delta^2}{RL}$$

$$C_{84} = \frac{9\pi^3 m^2 \delta^2}{8RL}$$

$$C_{104} = -\frac{\pi^3 m^2 \delta^2}{8RL}$$

Appendix 2

With:

$$A_{ijM} = \alpha_{ij}(M, K_3, K_4, 2K_8)$$

$$B_{ijM} = \beta_{ij}(M, K_5, K_6, -2K_7)$$

the coefficients of Eqs. (33) and (34) will be:

$$a_1 = \frac{3m^4\delta^2}{8R^2} \qquad a_2 = \frac{m^4\delta^2}{4R^2} \qquad a_3 = \frac{m^4\delta^2}{2R^2}$$

$$a_4 = 0 \qquad a_5 = \frac{\rho}{\rho_0}\frac{a}{\delta} \qquad a_6 = \frac{3m^4 a\delta}{8R^2}\frac{\rho}{\rho_0}$$

$$a_7 = \frac{m^4 a\delta}{4R^2}\frac{\rho}{\rho_0} \qquad a_8 = \frac{3m^4\delta^2}{8R^2} \qquad a_9 = \frac{m^4\delta^2}{2R^2}$$

$$a_{10} = \frac{m^4 a\delta}{2R^2}\frac{\rho}{\rho_0} \qquad a_{11} = \frac{m^4\delta^2}{4R^2} \qquad a_{12} = 0$$

$$a_{13} = \frac{2}{\pi\rho_0\delta^2 RL}\sum_{i=1}^{11} A_{i11}\varphi_{i1} + \frac{2}{\pi\rho_0\delta RL}B_{111} - \frac{\pi^2}{\rho_0\delta^2 RL^2}\varphi_{11} -$$

$$-\frac{\rho}{\rho_0}\frac{a^2}{2\delta R} + \frac{\pi^2}{\rho_0\delta L^2}N$$

$$a_{14} = \frac{2}{\pi\rho_0\delta^2 RL}\sum_{i=1}^{11} A_{i11}\varphi_{i2} + \frac{2}{\pi\rho_0\delta RL}B_{211} - \frac{\pi^2}{\rho_0\delta^2 RL^2}\varphi_{12} - \frac{8aU}{3\delta L}$$

Flygmotor

$$a_{15} = \frac{2}{\pi \rho_0 \delta^2 RL} \sum_{i=1}^{11} A_{i11} \varphi_{i3} - \frac{m^2}{2\pi \rho_0 \delta R^2 L} \sum_{i=1}^{11} A_{i70} \varphi_{i1} +$$

$$+ \frac{m^2}{2\pi \rho_0 \delta R^2 L} \sum_{i=1}^{11} A_{i90} \varphi_{i1} - \frac{m^2}{2\pi \rho_0 R^2 L} B_{170} + \frac{m^2}{2\pi \rho_0 R^2 L} B_{190} +$$

$$+ \frac{2}{\pi \rho_0 RL} B_{311} - \frac{\pi^2}{\rho_0 \delta^2 RL^2} \varphi_{13} - \frac{2 m^2 \pi^2}{\rho_0 \delta R^2 L^2} \varphi_{71}$$

$$a_{16} = \frac{2}{\pi \rho_0 \delta^2 RL} \sum_{i=1}^{11} A_{i11} \varphi_{i4} - \frac{m^2}{2\pi \rho_0 \delta R^2 L} \sum_{i=1}^{11} A_{i70} \varphi_{i2} +$$

$$+ \frac{m^2}{2\pi \rho_0 \delta R^2 L} \sum_{i=1}^{11} A_{i90} \varphi_{i2} - \frac{m^2}{2\pi \rho_0 \delta R^2 L} \sum_{i=1}^{11} A_{i80} \varphi_{i1} +$$

$$+ \frac{m^2}{2\pi \rho_0 \delta R^2 L} \sum_{i=1}^{11} A_{i100} \varphi_{i1} - \frac{m^2}{2\pi \rho_0 R^2 L} B_{180} + \frac{m^2}{2\pi \rho_0 R^2 L} B_{1100} -$$

$$- \frac{m^2}{2\pi \rho_0 R^2 L} B_{270} + \frac{m^2}{2\pi \rho_0 R^2 L} B_{290} + \frac{2}{\pi \rho_0 RL} B_{411} -$$

$$- \frac{\pi^2}{\rho_0 \delta^2 RL^2} \varphi_{14} - \frac{m^2 \pi^2}{\rho_0 \delta R^2 L^2} \left(2 \varphi_{72} + \frac{1}{4} \varphi_{81} + \frac{7}{4} \varphi_{101} \right)$$

$$a_{17} = \frac{2}{\pi \rho_0 \delta^2 RL} \sum_{i=1}^{11} A_{i11} \varphi_{i5} - \frac{m^2}{2\pi \rho_0 \delta R^2 L} \sum_{i=1}^{11} A_{i80} \varphi_{i2} +$$

$$+ \frac{m^2}{2\pi \rho_0 \delta R^2 L} \sum_{i=1}^{11} A_{i100} \varphi_{i2} - \frac{m^2}{2\pi \rho_0 R^2 L} B_{280} + \frac{m^2}{2\pi \rho_0 R^2 L} B_{2100} +$$

$$+ \frac{2}{\pi \rho_0 RL} B_{511} - \frac{\pi^2}{\rho_0 \delta^2 RL^2} \varphi_{15} - \frac{m^2 \pi^2}{\rho_0 \delta R^2 L^2} \left(\frac{9}{4} \varphi_{82} - \frac{1}{4} \varphi_{102} \right)$$

Flygmotor

$$a_{18} = \frac{2}{\pi \rho_0 \delta^2 RL} \sum_{i=1}^{11} A_{i11} \varphi_{i6} - \frac{m^2}{2\pi \rho_0 \delta R^2 L} \sum_{i=1}^{11} A_{i70} \varphi_{i3} +$$

$$+ \frac{m^2}{2\pi \rho_0 \delta R^2 L} \sum_{i=1}^{11} A_{i90} \varphi_{i3} - \frac{m^2 \delta}{2\pi \rho_0 R^2 L} B_{370} + \frac{m^2 \delta}{2\pi \rho_0 R^2 L} B_{390} -$$

$$- \frac{\pi^2}{\rho_0 \delta^2 RL^2} \varphi_{16} - \frac{3 m^4 a^2 d \rho}{32 R^3 \rho_0} + \frac{m^4 \pi^2 \delta}{4 \rho_0 R^2 L^2} N +$$

$$+ \frac{3 m^4 \pi^2}{4 \rho_0 R^4 L^2} (\varphi_{11} - \varphi_{31}) - \frac{2 m^2 \pi^2}{\rho_0 \delta R^2 L^2} \varphi_{73}$$

$$a_{19} = \frac{2}{\pi \rho_0 \delta^2 RL} \sum_{i=1}^{11} A_{i11} \varphi_{i7} - \frac{m^2}{2\pi \rho_0 \delta R^2 L} \sum_{i=1}^{11} A_{i70} \varphi_{i4} +$$

$$+ \frac{m^2}{2\pi \rho_0 \delta R^2 L} \sum_{i=1}^{11} A_{i90} \varphi_{i4} - \frac{m^2}{2\pi \rho_0 \delta R^2 L} \sum_{i=1}^{11} A_{i80} \varphi_{i3} +$$

$$+ \frac{m^2}{2\pi \rho_0 \delta R^2 L} \sum_{i=1}^{11} A_{i100} \varphi_{i3} - \frac{m^2 \delta}{2\pi \rho_0 R^2 L} B_{470} + \frac{m^2 \delta}{2\pi \rho_0 R^2 L} B_{490} -$$

$$- \frac{m^2 \delta}{2\pi \rho_0 R^2 L} B_{380} + \frac{m^2 \delta}{2\pi \rho_0 R^2 L} B_{3100} - \frac{2\pi^2 \delta}{\rho_0 R L^2} \varphi_{17} -$$

$$- \frac{8}{15} \frac{m^4 a U d \rho}{R^2 L \rho_0} + \frac{m^4 \pi^2}{4 \rho_0 R^3 L^2} \left(3\varphi_{12} + \frac{15}{2} \varphi_{21} - 3\varphi_{32} - 11 \varphi_{41} \right) +$$

$$+ \frac{2 m^2 \pi^2}{\rho_0 \delta R^2 L^2} \left(- \varphi_{75} - \frac{9}{8} \varphi_{83} + \frac{1}{8} \varphi_{103} \right)$$

Flygmotor

$$a_{20} = \frac{2}{\pi \rho_0 d^2 RL} \sum_{i=1}^{11} A_{i11} \varphi_{i8} - \frac{m^2}{2\pi \rho_0 d R^2 L} \sum_{i=1}^{11} A_{i70} \varphi_{i5} +$$

$$+ \frac{m^2}{2\pi \rho_0 d R^2 L} \sum_{i=1}^{11} A_{i90} \varphi_{i5} - \frac{m^2}{2\pi \rho_0 d R^2 L} \sum_{i=1}^{11} A_{i80} \varphi_{i4} +$$

$$+ \frac{m^2}{2\pi \rho_0 d R^2 L} \sum_{i=1}^{11} A_{i100} \varphi_{i4} - \frac{m^2 d}{2\pi \rho_0 R^2 L} B_{480} + \frac{m^2 d}{2\pi \rho_0 R^2 L} B_{4100} -$$

$$- \frac{m^2 d}{2\pi \rho_0 R^2 L} B_{570} + \frac{m^2 d}{2\pi \rho_0 R^2 L} B_{590} - \frac{\pi^2}{\rho_0 d^2 RL^2} \varphi_{18} -$$

$$- \frac{3 m^4 a^2 d \rho}{16 \rho_0 R^3} + \frac{5 m^4 \pi^2 d}{4 \rho_0 R^2 L^2} N + \frac{2 m^4 \pi^2}{\rho_0 R^3 L^2} \left[2\varphi_{22} - 15 \varphi_{42} + \right.$$

$$\left. + 5\varphi_{11} + \frac{9}{2} \varphi_{31} - \frac{15}{2} \varphi_{51} \right] + \frac{2 m^2 \pi^2}{\rho_0 d R^2 L^2} \left[- \varphi_{74} - \frac{9}{8} \varphi_{85} + \frac{1}{8} \varphi_{105} \right]$$

$$a_{21} = \frac{2}{\pi \rho_0 d^2 RL} \sum_{i=1}^{11} A_{i11} \varphi_{i9} - \frac{m^2}{2\pi \rho_0 d R^2 L} \sum_{i=1}^{11} A_{i80} \varphi_{i5} +$$

$$+ \frac{m^2}{2\pi \rho_0 d R^2 L} \sum_{i=1}^{11} A_{i100} \varphi_{i5} - \frac{m^2 d}{2\pi \rho_0 R^2 L} B_{580} + \frac{m^2 d}{2\pi \rho_0 R^2 L} B_{5100} -$$

$$- \frac{\pi^2}{\rho_0 d^2 RL^2} \varphi_{19} - \frac{32 m^4 d a U \rho}{105 R^2 L \rho_0} + \frac{m^4 \pi^2}{4 \rho_0 R^3 L^2} \left[5\varphi_{12} + \frac{3}{2} \varphi_{32} - \frac{11}{2} \varphi_{52} \right] +$$

$$+ \frac{m^2 \pi}{4 \rho_0 d R^2 L^2} \left[- 9 \varphi_{85} + \varphi_{105} \right]$$

$$a_{22} = - \frac{m^2}{2\pi \rho_0 d R^2 L} \sum_{i=1}^{11} A_{i70} \varphi_{i6} + \frac{m^2}{2\pi \rho_0 d R^2 L} \sum_{i=1}^{11} A_{i90} \varphi_{i6} +$$

$$+ \frac{3 m^4 \pi^2}{4 \rho_0 R^3 L^2} \left(\varphi_{13} - \varphi_{33} \right) - \frac{2 m^2 \pi^2}{\rho_0 d R^2 L^2} \varphi_{76}$$

Flygmotor

$$a_{23} = -\frac{m^2}{2\pi\rho_0 \delta R^2 L}\sum_{i=1}^{11} A_{i70}\varphi_{i7} + \frac{m^2}{2\pi\rho_0 \delta R^2 L}\sum_{i=1}^{11} A_{i90}\varphi_{i7} -$$

$$-\frac{m^2}{2\pi\rho_0 \delta R^2 L}\sum_{i=1}^{11} A_{i80}\varphi_{i6} + \frac{m^2}{2\pi\rho_0 \delta R^2 L}\sum_{i=1}^{11} A_{i100}\varphi_{i6} +$$

$$+\frac{m^4\pi^2}{4\rho_0 R^3 L^2}\left[3\varphi_{14} + 10\varphi_{23} - 3\varphi_{34} - 11\varphi_{43}\right] +$$

$$+\frac{m^2\pi^2}{4\rho_0 \delta R^2 L^2}\left[-8\varphi_{77} - 9\varphi_{86} + \varphi_{106}\right]$$

$$a_{24} = -\frac{m^2}{2\pi\rho_0 \delta R^2 L}\sum_{i=1}^{11} A_{i70}\varphi_{i8} + \frac{m^2}{2\pi\rho_0 \delta R^2 L}\sum_{i=1}^{11} A_{i90}\varphi_{i8} -$$

$$-\frac{m^2}{2\pi\rho_0 \delta R^2 L}\sum_{i=1}^{11} A_{i80}\varphi_{i7} + \frac{m^2}{2\pi\rho_0 \delta R^2 L}\sum_{i=1}^{11} A_{i100}\varphi_{i7} +$$

$$+\frac{m^4\pi^2}{8\rho_0 R^3 L^2}\left[6\varphi_{15} + 20\varphi_{24} - 6\varphi_{35} - 6\varphi_{44} + 10\varphi_{13} + 9\varphi_{33} - 17\varphi_{53}\right.$$

$$+\frac{m^2\pi^2}{4\rho_0 \delta R^2 L^2}\left[-8\varphi_{78} - 9\varphi_{87} + \varphi_{107}\right]$$

$$a_{25} = -\frac{m^2}{2\pi\rho_0 \delta R^2 L}\sum_{i=1}^{11} A_{i70}\varphi_{i9} + \frac{m^2}{2\pi\rho_0 \delta R^2 L}\sum_{i=1}^{11} A_{i90}\varphi_{i9} -$$

$$-\frac{m^2}{2\pi\rho_0 \delta R^2 L}\sum_{i=1}^{11} A_{i80}\varphi_{i8} + \frac{m^2}{2\pi\rho_0 \delta R^2 L}\sum_{i=1}^{11} A_{i100}\varphi_{i8} +$$

$$+\frac{m^4\pi^2}{8\rho_0 R^3 L^2}\left[20\varphi_{25} - 22\varphi_{45} + 10\varphi_{14} + 9\varphi_{34} - 17\varphi_{54}\right] +$$

$$+\frac{m^2\pi^2}{4\rho_0 \delta R^2 L^2}\left[-8\varphi_{79} - 9\varphi_{88} + \varphi_{108}\right]$$

Flygmotor

$$a_{26} = -\frac{m^2}{2\pi \rho_0 \delta R^2 L} \sum_{i=1}^{11} A_{i80} \varphi_{i9} + \frac{m^2}{2\pi \rho_0 \delta R^2 L} \sum_{i=1}^{11} A_{i100} \varphi_{i9} +$$

$$+ \frac{m^4 \pi^2}{8 \rho_0 R^3 L^2} [8\varphi_{15} + 9\varphi_{35} - 17\varphi_{55}] + \frac{m^2 \pi^2}{4 \rho_0 \delta R^2 L^2} [-9\varphi_{89} + \varphi_{109}]$$

$$a_{27} = \frac{3 m^4 \pi^2}{4 \rho_0 R^3 L^2} [\varphi_{16} - \varphi_{36}]$$

$$a_{28} = \frac{m^4 \pi^2}{4 \rho_0 R^3 L^2} [3\varphi_{17} + 10\varphi_{26} - 3\varphi_{37} - 11\varphi_{46}]$$

$$a_{29} = \frac{m^4 \pi^2}{8 \rho_0 R^3 L^2} [6\varphi_{18} + 20\varphi_{27} - 6\varphi_{38} - 22\varphi_{47} + 10\varphi_{16} +$$

$$+ 9\varphi_{36} - 17\varphi_{56}]$$

$$a_{30} = \frac{m^4 \pi^2}{8 \rho_0 R^3 L^2} [6\varphi_{19} + 20\varphi_{28} - 6\varphi_{39} - 22\varphi_{48} + 10\varphi_{17} +$$

$$+ 9\varphi_{37} - 17\varphi_{57}]$$

$$a_{31} = \frac{m^4 \pi^2}{8 \rho_0 R^3 L^2} [26\varphi_{29} - 22\varphi_{49} + 10\varphi_{18} + 9\varphi_{38} - 17\varphi_{58}]$$

$$a_{32} = \frac{m^4 \pi^2}{8 \rho_0 R^3 L^2} [10\varphi_{19} + 9\varphi_{39} - 17\varphi_{59}]$$

$$a_{33} = 0$$

Flygmotor

$$b_1 = \frac{3m^4\delta^2}{8R^2} \qquad b_2 = \frac{m^4\delta^2}{4R^2} \qquad b_3 = \frac{m^4\delta^2}{2R^2}$$

$$b_4 = 0 \qquad b_5 = \frac{a}{\delta}\,\frac{\varrho}{\varrho_0} \qquad b_6 = \frac{3m^4\delta a}{8R^2}$$

$$b_7 = \frac{m^4\delta a}{4R^2}\,\frac{\varrho}{\varrho_0} \qquad b_8 = \frac{3m^4\delta^2}{8R^2} \qquad b_9 = \frac{m^4\delta^2}{2R^2}$$

$$b_{10} = \frac{m^4\delta a\varrho}{2R^2\varrho_0} \qquad b_{11} = \frac{m^4\delta^2}{4R^2} \qquad b_{12} = 0$$

$$b_{13} = \frac{2}{\pi\varrho_0\delta^2RL}\sum_{i=1}^{11} A_{i21}\varphi_{i1} + \frac{2}{\pi\varrho_0\delta RL}B_{121} - \frac{4\pi^2}{\varrho_0\delta^2RL^2}\varphi_{21} + \frac{8aU}{3\delta L}$$

$$b_{14} = \frac{2}{\pi\varrho_0\delta^2RL}\sum_{i=1}^{11} A_{i21}\varphi_{i2} + \frac{2}{\pi\varrho_0\delta RL}B_{221} - \frac{a^2\varrho}{2\delta R\varrho_0} - \frac{4\pi^2}{\varrho_0\delta^2RL^2}\varphi_{22} + $$
$$+ \frac{4\pi^2}{\varrho_0\delta L^2}N$$

$$b_{15} = \frac{2}{\pi\varrho_0\delta^2RL}\sum_{i=1}^{11} A_{i21}\varphi_{i2} - \frac{m^2}{2\pi\varrho_0\delta R^2L}\sum_{i=1}^{11} A_{i80}\varphi_{i1} + $$
$$+ \frac{m^2}{2\pi\varrho_0\delta R^2L}\sum_{i=1}^{11} A_{i100}\varphi_{i1} - \frac{m^2}{2\pi\varrho_0R^2L}B_{180} + \frac{m^2}{2\pi\varrho_0R^2L}B_{1100} + $$
$$+ \frac{2}{\pi\varrho_0RL}B_{321} - \frac{4\pi^2}{\varrho_0\delta^2RL^2}\varphi_{23} - \frac{m^2\pi^2}{4\varrho_0\delta R^2L^2}\left[9\varphi_{81} - \varphi_{101}\right]$$

$$b_{16} = \frac{2}{\pi\varrho_0\delta^2RL}\sum_{i=1}^{11} A_{i21}\varphi_{i4} - \frac{m^2}{2\pi\varrho_0\delta R^2L}\sum_{i=1}^{11} A_{i80}\varphi_{i2} + $$
$$+ \frac{m^2}{2\pi\varrho_0\delta R^2L}\sum_{i=1}^{11} A_{i100}\varphi_{i2} - \frac{m^2}{2\pi\varrho_0\delta R^2L}\sum_{i=1}^{11} A_{i70}\varphi_{i1} + $$
$$+ \frac{m^2}{2\pi\varrho_0\delta R^2L}\sum_{i=1}^{11} A_{i110}\varphi_{i1} - \frac{m^2}{2\pi\varrho_0R^2L}B_{280} + \frac{m^2}{2\pi\varrho_0R^2L}B_{110} -$$

$$- \frac{m^2}{2\pi \rho_0 R^2 L} B_{170} + \frac{m^2}{2\pi \rho_0 R^2 L} B_{2100} + \frac{2}{\rho_0 \pi R L} B_{321} -$$

$$- \frac{4\pi^2}{\rho_0 \delta^2 R L^2} \varphi_{24} - \frac{m^2 \pi^2}{\rho_0 \delta R^2 L^2} \left[\frac{9}{4} \varphi_{82} - \frac{1}{4} \varphi_{102} + 8 \varphi_{71} \right]$$

$$b_{17} = \frac{2}{\pi \rho_0 \delta^2 R L} \sum_{i=1}^{11} A_{i21} \varphi_{i5} - \frac{m^2}{2\pi \rho_0 \delta R^2 L} \sum_{i=1}^{11} A_{i70} \varphi_{i2} +$$

$$+ \frac{m^2}{2\pi \rho_0 \delta R^2 L} \sum_{i=1}^{11} A_{i110} \varphi_{i2} - \frac{m^2}{2\pi \rho_0 R^2 L} B_{280} + \frac{m^2}{2\pi \rho_0 R^2 L} B_{2100} +$$

$$+ \frac{2}{\pi \rho_0 R L} B_{521} - \frac{4\pi^2}{\rho_0 \delta^2 R L^2} \varphi_{25} - \frac{4 m^2 \pi^2}{\rho_0 \delta R^2 L^2} \left[2 \varphi_{72} - \varphi_{112} \right]$$

$$b_{18} = \frac{2}{\pi \rho_0 \delta^2 R L} \sum_{i=1}^{11} A_{i21} \varphi_{i6} - \frac{m^2}{2\pi \rho_0 \delta R^2 L} \sum_{i=1}^{11} A_{i80} \varphi_{i3} +$$

$$+ \frac{m^2}{2\pi \rho_0 \delta R^2 L} \sum_{i=1}^{11} A_{i100} \varphi_{i3} - \frac{m^2 \delta}{2\pi \rho_0 R^2 L} B_{380} + \frac{m^2 \delta}{2\pi \rho_0 R^2 L} B_{3100} -$$

$$- \frac{4\pi^2}{\rho_0 \delta^2 R L^2} \varphi_{26} + \frac{8 m^4 a U \delta \varrho}{15 R^2 L \varrho_0} + \frac{m^4 \pi^2}{8 \rho_0 R^3 L^2} \left[10 \varphi_{21} - 9 \varphi_{41} \right] -$$

$$- \frac{m^2 \pi^2}{2 \rho_0 \delta R^2 L^2} \left[9 \varphi_{73} - \varphi_{103} \right]$$

$$b_{19} = \frac{2}{\pi \rho_0 \delta^2 R L} \sum_{i=1}^{11} A_{i21} \varphi_{i7} - \frac{m^2}{2\pi \rho_0 \delta R^2 L} \sum_{i=1}^{11} A_{i80} \varphi_{i4} +$$

$$+ \frac{m^2}{2\pi \rho_0 \delta R^2 L} \sum_{i=1}^{11} A_{i100} \varphi_{i4} - \frac{m^2}{2\pi \rho_0 \delta R^2 L} \sum_{i=1}^{11} A_{i70} \varphi_{i3} +$$

$$+ \frac{m^2}{2\pi \rho_0 \delta R^2 L} \sum_{i=1}^{11} A_{i110} \varphi_{i3} - \frac{m^2 \delta}{2\pi \rho_0 R^2 L} B_{480} + \frac{m^2 \delta}{2\pi \rho_0 R^2 L} B_{4100} -$$

Flygmotor

$$- \frac{m^2 d}{2\pi \rho_0 R^2 L} B_{470} + \frac{m^2 d}{2\pi \rho_0 R^2 L} B_{4110} + \frac{5 m^4 \pi^2 d}{4 \rho_0 R^2 L^2} N +$$

$$+ \frac{m^4 \pi^2}{8 \rho_0 R^3 L^2} \left[20 \varphi_{11} + 36 \varphi_{31} - 36 \varphi_{51} + 10 \varphi_{22} - 11 \varphi_{42} \right] - \frac{4\pi^2}{\rho_0 \delta^2 R L^2} \varphi_{27} -$$

$$- \frac{3 m^4 a^2 d \rho}{16 R^3 \rho_0} + \frac{m^2 \pi^2}{4 \rho_0 d \; R^2 L^2} \left[-9 \varphi_{84} + \varphi_{104} - 32 \varphi_{73} \right]$$

$$b_{20} = \frac{2}{\pi \rho_0 d \; R L} \sum_{i=1}^{11} A_{i21} \varphi_{i8} - \frac{m^2}{2\pi \rho_0 d R^2 L} \sum_{i=1}^{11} A_{i70} \varphi_{i4} +$$

$$+ \frac{m^2}{2\pi \rho_0 d R^2 L} \sum_{i=1}^{11} A_{i110} \varphi_{i4} - \frac{m^2 d}{2\pi \rho_0 R^2 L} B_{470} + \frac{m^2 d}{2\pi \rho_0 R^2 L} B_{4110} -$$

$$- \frac{m^2 d}{2\pi \rho_0 R^2 L} B_{580} + \frac{m^2 d}{2\pi \rho_0 R^2 L} B_{5100} + \frac{m^4 \pi^2}{8 \rho_0 R^3 L^2} \left[10 \varphi_{12} + 5 \varphi_{32} - 5 \varphi_{52} \right]$$

$$- \frac{4\pi^2}{\rho_0 d^2 R L^2} \varphi_{28} + \frac{32 m^4 a U d \rho}{105 R^2 L \rho_0} + \frac{m^4 \pi^2}{8 \rho_0 R^3 L^2} \left[32 \varphi_{21} + 20 \varphi_{12} + \right.$$

$$\left. + 13 \varphi_{32} - 29 \varphi_{52} - 32 \varphi_{61} \right] + \frac{m^2 \pi^2}{4 \rho_0 d R^2 L^2} \left[-9 \varphi_{85} + \varphi_{105} - 32 \varphi_{74} \right]$$

$$b_{21} = \frac{2}{\pi \rho_0 d^2 R L} \sum_{i=1}^{11} A_{i21} \varphi_{i9} - \frac{m^2}{2\pi \rho_0 d R^2 L} \sum_{i=1}^{11} A_{i70} \varphi_{i5} +$$

$$+ \frac{m^4}{2\pi \rho_0 d R^2 L} \sum_{i=1}^{11} A_{i110} \varphi_{i5} - \frac{m^2 d}{2\pi \rho_0 R^2 L} B_{570} + \frac{m^2 d}{2\pi \rho_0 R^2 L} B_{5110} +$$

$$+ \frac{m^4 \pi^2 d}{\rho_0 R^2 L^2} N - \frac{4\pi}{\rho_0 d^2 R L^2} \varphi_{29} - \frac{3 m^4 a^2 d \rho}{32 R^3 \rho_0} +$$

$$+ \frac{3 m^4 \pi^2}{\rho_0 R^3 L^2} \left[\varphi_{22} - \varphi_{62} \right] - \frac{8 m^2 \pi^2}{\rho_0 d R^2 L^2} \varphi_{75}$$

Flygmotor

$$b_{22} = -\frac{m^2}{2\pi\rho_0 d R^2 L}\sum_{i=1}^{11} A_{i80}\varphi_{i6} + \frac{m^2}{2\pi\rho_0 d R^2 L}\sum_{i=1}^{11} A_{i100}\varphi_{i6} +$$

$$+ \frac{m^4\pi^2}{8\rho_0 R^3 L^2}\left[10\varphi_{23} - 7\varphi_{43}\right] + \frac{m^2\pi^2}{4\rho_0 d R^2 L^2}\left[-9\varphi_{86} + \varphi_{106}\right]$$

$$b_{23} = -\frac{m^2}{2\pi\rho_0 d R^2 L}\sum_{i=1}^{11} A_{i80}\varphi_{i7} + \frac{m^2}{2\pi\rho_0 d R^2 L}\sum_{i=1}^{11} A_{i100}\varphi_{i7} -$$

$$- \frac{m^2}{2\pi\rho_0 d R^2 L}\sum_{i=1}^{11} A_{i70}\varphi_{i6} + \frac{m^2}{2\pi\rho_0 d R^2 L}\sum_{i=1}^{11} A_{i110}\varphi_{i6} +$$

$$+ \frac{m^4\pi^2}{8\rho_0 R^3 L^2}\left[20\varphi_{13} + 18\varphi_{33} - 36\varphi_{53} + 10\varphi_{24} - 11\varphi_{44}\right] +$$

$$+ \frac{m^2\pi^2}{4\rho_0 d R^2 L^2}\left[-9\varphi_{87} + \varphi_{107} - 32\varphi_{76}\right]$$

$$b_{24} = -\frac{m^2}{2\pi\rho_0 d R^2 L}\sum_{i=1}^{11} A_{i80}\varphi_{i8} + \frac{m^2}{2\pi\rho_0 d R^2 L}\sum_{i=1}^{11} A_{i100}\varphi_{i8} -$$

$$- \frac{m^2}{2\pi\rho_0 d R^2 L}\sum_{i=1}^{11} A_{i70}\varphi_{i7} + \frac{m^2}{2\pi\rho_0 d R^2 L}\sum_{i=1}^{11} A_{i110}\varphi_{i7} +$$

$$+ \frac{m^4\pi^2}{8\rho_0 R^3 L^2}\left[20\varphi_{14} + 18\varphi_{34} - 36\varphi_{54} + 10\varphi_{25} - 11\varphi_{45} +\right.$$

$$\left. + 24\varphi_{23} - 24\varphi_{63}\right] + \frac{m^2\pi^2}{4\rho_0 d R^2 L^2}\left[-9\varphi_{88} + \varphi_{108} - 32\varphi_{77}\right]$$

$$b_{25} = -\frac{m^2}{2\pi\rho_0 d R^2 L}\sum_{i=1}^{11} A_{i80}\varphi_{i9} + \frac{m^2}{2\pi\rho_0 d R^2 L}\sum_{i=1}^{11} A_{i100}\varphi_{i9} -$$

$$- \frac{m^2}{2\pi\rho_0 d R^2 L}\sum_{i=1}^{11} A_{i70}\varphi_{i8} + \frac{m^2}{2\pi\rho_0 d R^2 L}\sum_{i=1}^{11} A_{i110}\varphi_{i8} +$$

$$+ \frac{m^4\pi^2}{4\rho_0 R^3 L^2}\left[10\varphi_{15} + 9\varphi_{35} - 18\varphi_{55} + 12\varphi_{24} - 12\varphi_{64}\right] +$$

$$+ \frac{m^2\pi^2}{4\rho_0 d R^2 L^2}\left[-9\varphi_{89} + \varphi_{109} - 32\varphi_{78}\right]$$

Flygmotor

$$b_{26} = -\frac{m^2}{2\pi\rho_0\delta R^2L}\sum_{i=1}^{11} A_{i70}\,\varphi_{i9} + \frac{m^2}{2\pi\rho_0\delta R^2L}\sum_{i=1}^{11} A_{i110}\,\varphi_{i9} +$$

$$+ \frac{3m^4\pi^2}{\rho_0 R^3L^2}\left[\varphi_{25} - \varphi_{65}\right] - \frac{8m^2\pi^2}{\rho_0\delta R^2L^2}\varphi_{79}$$

$$b_{27} = \frac{m^4\pi^2}{8\rho_0 R^3L^2}\left[10\varphi_{26} - 11\varphi_{46}\right]$$

$$b_{28} = \frac{m^4\pi^2}{8\rho_0 R^3L^2}\left[20\varphi_{16} + 6\varphi_{36} - 36\varphi_{56} + 10\varphi_{27} - 11\varphi_{47}\right]$$

$$b_{29} = \frac{m^4\pi^2}{8\rho_0 R^3L^2}\left[20\varphi_{17} + 18\varphi_{37} - 36\varphi_{57} + 10\varphi_{28} - 11\varphi_{48} + 24\varphi_{26} - 24\varphi_{66}\right]$$

$$b_{30} = \frac{m^4\pi^2}{8\rho_0 R^3L^2}\left[20\varphi_{18} + 18\varphi_{38} - 36\varphi_{58} + 10\varphi_{29} - 11\varphi_{49} + 24\varphi_{27} - 24\varphi_{67}\right]$$

$$b_{31} = \frac{m^4\pi^2}{4\rho_0 R^3L^2}\left[10\varphi_{19} + 9\varphi_{39} - 18\varphi_{59} + 12\varphi_{28} - 12\varphi_{68}\right]$$

$$b_{32} = \frac{3m^4\pi^2}{\rho_0 R^3L^2}\left[\varphi_{29} - \varphi_{69}\right]$$

$$b_{33} = 0$$

Appendix 3

With the functions K_n given by Eqs. (51), we introduce the following notations to be used in App. 3 - 5:

$$L_1 = \frac{1}{\delta E} \qquad L_2 = \frac{\nu}{\delta E} \qquad L_3 = -\frac{\delta^3 \nu E}{12(1-\nu^2)}$$

$$L_4 = -\frac{\delta^3 E}{12(1-\nu^2)} \qquad L_5 = -\frac{\delta^3 E}{12(1+\nu)} \qquad L_6 = \nu$$

$$L_7 = E \qquad L_8 = (1-\nu) N_T \qquad L_9 = \xi E \qquad L_{10} = M_T$$

$$I_{pq} = \int_0^L L_p \sin \frac{q\pi\xi}{L} \, d\xi$$

$$J_{pq} = \int_0^L L_p \cos \frac{q\pi\xi}{L} \, d\xi$$

Then the numbers a_{ij} and b_i will be:

$$a_{11} = \frac{\pi^4 \delta}{2L^4} (J_{42} - J_{40}) + \frac{\delta^2}{2R^2} (J_{70} - J_{72}) - \frac{\rho a^2 \delta L}{4R} + \frac{\pi^2 \delta}{2L} N$$

$$a_{12} = \frac{2\pi^4 \delta}{L^4} (J_{43} - J_{41}) + \frac{\delta^2}{2R^2} (J_{71} - J_{73}) - \frac{4}{3} \rho a U \delta$$

$$-b_1 = \frac{1}{R} I_{61} N - \frac{1}{R} I_{81} + \frac{w_0 \delta}{R^2} I_{71} - \frac{\rho a^2 w_0 L}{\pi R} +$$

$$+ \frac{\delta}{R^2 L} (w_L - w_0) I_{91} - \frac{\rho a^2 L}{2\pi R} (w_L - w_0) - \frac{\pi^2}{L^2} I_{101} -$$

$$- [p_0 + \rho a U \frac{1}{L} (w_L - w_0)] \frac{2L}{\pi}$$

Flygmotor

$$a_{21} = \frac{2\pi^4 \delta}{L^4} (J_{43} - J_{41}) + \frac{\delta^2}{2R^2} (J_{71} - J_{73}) - \frac{2}{3} \rho a U \delta$$

$$a_{22} = - \frac{8\pi^4 \delta}{3L^4} (J_{44} - J_{40}) + \frac{\delta^2}{2R^2} (J_{70} - J_{74}) - \frac{\rho a^2 L \delta}{4R} + \frac{2\pi^2 \delta}{L} N$$

$$-b_2 = \frac{1}{R} I_{62} N - \frac{1}{R} I_{82} + \frac{w_0 \delta}{R^2} I_{72} + \frac{\delta}{R^2 L} (w_L - w_0) I_{92} +$$

$$+ \frac{\rho a^2 L}{4\pi R} (w_L - w_0) - \frac{4\pi^2}{L^2} I_{10\,2}$$

Flygmotor

Appendix 4

$1 \le i \le 6 \quad 1 \le j \le 6$

$$A_{ij} = \frac{1}{2}\left(\frac{ij\pi^2}{L^2} + \frac{m^2}{R^2}\right)^2 J_{1\,i-j} - \frac{1}{2}\left(\frac{ij\pi^2}{L^2} - \frac{m^2}{R^2}\right)^2 J_{1\,i+j} -$$

$$- \frac{m^2\pi^2}{2R^2L^2}(i-j)^2 J_{2\,i-j} + \frac{m^2\pi^2}{2R^2L^2}(i+j)^2 J_{2\,i+j}$$

$0 \le i \le 4 \quad 1 \le j \le 6$

$$\frac{1}{\pi R} A_{i+12\,j} = \frac{1}{2}\left(\frac{ij\pi^2}{L^2} + \frac{m^2}{R^2}\right)^2 I_{1\,i+j} + \frac{1}{2}\left(\frac{ij\pi^2}{L^2} - \frac{m^2}{R^2}\right)^2 I_{1\,i-j} -$$

$$- \frac{m^2\pi^2}{2R^2L^2}(i+j)^2 I_{2\,i+j} - \frac{m^2\pi^2}{2L^2}(i-j)^2 I_{2\,i-j} +$$

$$+ \frac{m^2\pi i}{R^2L}\left[\frac{\nu}{E}(0) - (-1)^{i+j}\frac{\nu}{E}(L)\right] -$$

$$- \frac{2ij^2\pi^3}{L^3}\left[\frac{1}{E}(0) - (-1)^{i+j}\frac{1}{E}(L)\right]$$

$0 \le i \le 4 \quad 0 \le j \le 4$

$$\frac{1}{\pi R} A_{i+7\,j+7} = \frac{1}{2}\left(\frac{ij\pi^2}{L^2} - \frac{4m^2}{R^2}\right)^2 J_{1\,i+j} + \frac{1}{2}\left(\frac{ij\pi^2}{L^2} + \frac{4m^2}{R^2}\right)^2 J_{1\,i-j} -$$

$$- \frac{2m^2\pi^2}{R^2L^2}(i+j)^2 J_{2\,i+j} - \frac{2m^2\pi^2}{R^2L^2}(i-j)^2 J_{2\,i-j} +$$

$$+ \frac{j^2\pi^2}{2L^2}\left[\frac{\partial}{\partial\xi}\frac{1}{E}(0) - (-1)^{i+j}\frac{\partial}{\partial\xi}\frac{1}{E}(L)\right] -$$

$$- \frac{2m^2}{R^2}\left[\frac{\partial}{\partial\xi}\frac{\nu}{E}(0) - (-1)^{i+j}\frac{\partial}{\partial\xi}\frac{\nu}{E}(L)\right]$$

Flygmotor

$1 \le i \le 6 \qquad 0 \le j \le 4$

$$\frac{1}{\pi R} A_{i\,j+12} = \frac{1}{2}\left(\frac{ij\pi^2}{L^2} + \frac{m^2}{R^2}\right)^2 I_{1\,i+j} - \frac{1}{2}\left(\frac{ij\pi^2}{L^2} - \frac{m^2}{R^2}\right)^2 I_{1\,i-j} -$$

$$- \frac{m^2\pi^2}{2R^2L^2}(i+j)^2 I_{2\,i+j} + \frac{m^2\pi^2}{2R^2L^2}(i-j)^2 I_{2\,i-j} +$$

$$+ \frac{j\pi}{L}\left(\frac{j^2}{L^2} + \frac{2m^2}{R^2}\right)\left[\frac{1}{E}(0) - (-1)^{i+j}\frac{1}{E}(L)\right] +$$

$$+ \frac{m^2\pi j}{R^2 L}\left[\frac{\nu}{E}(0) - (-1)^{i+j}\frac{\nu}{E}(L)\right]$$

$0 \le i \le 4 \qquad 0 \le j \le 4$

$$\frac{1}{\pi R} A_{i+12\,j+12} = \frac{1}{2}\left(\frac{ij\pi^2}{L^2} - \frac{m^2}{R^2}\right)^2 J_{1\,i+j} + \frac{1}{2}\left(\frac{ij\pi^2}{L^2} + \frac{m^2}{R^2}\right)^2 J_{1\,i-j} -$$

$$- \frac{m^2\pi^2}{2R^2L^2}(i+j)^2 J_{2\,i+j} - \frac{m^2\pi^2}{2R^2L^2}(i-j)^2 J_{2\,i-j} +$$

$$+ \frac{j^2\pi^2}{2L^2}\left[\frac{\partial}{\partial\xi}\frac{1}{E}(0) - (-1)^{i+j}\frac{\partial}{\partial\xi}\frac{1}{E}(L)\right] -$$

$$- \frac{m^2}{2R^2}\left[\frac{\partial}{\partial\xi}\frac{\nu}{E}(0) - (-1)^{i+j}\frac{\partial}{\partial\xi}\frac{\nu}{E}(L)\right]$$

The nonvanishing elements c_{ij} will be

$$c_{11} = \frac{\pi^3 \delta}{2L} + \frac{4}{3}\,\frac{m^2\pi^2\delta^2}{RL} f_s$$

$$c_{12} = \frac{32}{15}\,\frac{m^2\pi^2\delta^2}{RL} g_s \qquad c_{16} = -\frac{\pi^3 m^4 \delta^3}{8R^2L} \qquad c_{18} = -\frac{5\pi^3 m^4 \delta^3}{8R^2L}$$

$$c_{21} = \frac{112}{15}\,\frac{m^2\pi^2\delta^2}{RL} g_s \qquad c_{22} = \frac{28}{15}\,\frac{m^2\pi^2\delta^2}{RL} f_s$$

$$c_{27} = -\frac{5\pi^3 m^4 \delta^3}{8R^2L} \qquad c_{29} = -\frac{\pi^3 m^4 \delta^3}{2R^2L}$$

$$c_{31} = -\frac{4}{5}\,\frac{m^2\pi^2\delta^2}{RL} f_s \qquad c_{32} = \frac{32}{7}\,\frac{m^2\pi^2\delta^2}{RL} g_s$$

$$c_{36} = \frac{\pi^3 m^4 \delta^3}{8R^2L} \qquad c_{38} = -\frac{9\pi^3 m^4 \delta^3}{16R^2L}$$

$$c_{41} = -\frac{304}{105}\,\frac{m^2\pi^2\delta^2}{RL} g_s \qquad c_{42} = -\frac{76}{105}\,\frac{m^2\pi^2\delta^2}{RL} f_s$$

$$c_{47} = \frac{11\pi^3 m^4 \delta^3}{16R^2L}$$

$$c_{51} = -\frac{4}{21}\,\frac{m^2\pi^2\delta^2}{RL} f_s \qquad c_{52} = -\frac{32}{9}\,\frac{m^2\pi^2\delta^2}{RL}$$

$$c_{58} = \frac{17\pi^3 m^4 \delta^3}{16R^2L}$$

Flygmotor

$$C_{61} = -\frac{208}{315}\,\frac{m^2\pi^2\delta^2}{RL}\,g_s \qquad C_{62} = -\frac{52}{315}\,\frac{m^2\pi^2\delta^2}{RL}\,f_s$$

$$C_{69} = \frac{\pi^3 m^4 \delta^3}{2R^2L}$$

$$C_{73} = \frac{\pi^3 m^2 \delta^2}{4RL} \qquad C_{75} = \frac{\pi^3 m^2 \delta^2}{RL}$$

$$C_{84} = \frac{9\pi^3 m^2 \delta^2}{8RL}$$

$$C_{104} = -\frac{\pi^3 m^2 \delta^2}{8RL}$$

$$C_{121} = \frac{m^2\pi^3\delta^2}{4RL}\,f_s \qquad C_{122} = \frac{m^2\pi^3\delta^2}{RL}\,g_s$$

$$C_{131} = \frac{m^2\pi^3\delta^2}{RL}\,g_s \qquad C_{132} = \frac{m^2\pi^3\delta^2}{4RL}\,f_s + \frac{16\pi^2\delta}{3L}$$

$$C_{137} = -\frac{13}{10}\,\frac{m^4\pi^2\delta^3}{R^2L} \qquad C_{139} = -\frac{128}{105}\,\frac{m^4\pi^2\delta^3}{R^2L}$$

$$C_{141} = -\frac{m^2\pi^3\delta^2}{4RL}\,f_s - \frac{8\pi^2\delta}{3L}$$

$$C_{146} = \frac{16}{15}\,\frac{m^4\pi^2\delta^3}{R^2L} \qquad C_{148} = \frac{82}{35}\,\frac{m^4\pi^2\delta^3}{R^2L}$$

Flygmotor

$$C_{151} = -\frac{m^2\pi^3}{RL}g_s \qquad C_{152} = -\frac{m^4\pi^3\delta^2}{4RL}f_s - \frac{48}{5}\frac{\pi^2 d}{L}$$

$$C_{157} = \frac{75}{14}\frac{m^4\pi^2\delta^3}{R^2L} \qquad C_{159} = \frac{128}{45}\frac{m^4\pi^2\delta^3}{R^2L}$$

$$C_{161} = -\frac{16}{15}\frac{\pi^2 d}{L} \qquad C_{162} = -\frac{m^2\pi^3 d^2}{RL}g_s$$

$$C_{166} = -\frac{32}{105}\frac{m^4\pi^2\delta^3}{R^2L} \qquad C_{168} = \frac{403}{63}\frac{m^4\pi^2\delta^3}{R^2L}$$

Flygmotor

Appendix 5

Including terms emanating from the static solution, the coefficients of Eqs. (33) and (34) will be:

$$a_1 = \frac{3m^4\delta^2}{8R^2} \qquad a_2 = \frac{m^4\delta^2}{4R^2} \qquad a_3 = \frac{m^4\delta^2}{2R^2}$$

$$a_4 = 0 \qquad a_5 = \frac{a}{\delta}\frac{\varrho}{\varrho_0} \qquad a_6 = \frac{3m^4\delta\, a}{8R^2}\frac{\varrho}{\varrho_0}$$

$$a_7 = \frac{m^4\delta a}{4R^2}\frac{\varrho}{\varrho_0} \qquad a_8 = \frac{3m^4\delta^2}{8R^2} \qquad a_9 = 0$$

$$a_{10} = \frac{m^4\delta a}{2R^2}\frac{\varrho}{\varrho_0} \qquad a_{11} = \frac{m^4\delta^2}{4R^2} \qquad a_{12} = 0$$

$$a_{13} = -\frac{\pi^3}{2\varrho_0\delta RL^5}(J_{400} - J_{420}) - \frac{m^2\pi}{2\varrho_0\delta R^3L^3}\Big[2J_{300} - 2J_{320} +$$

$$+ 2J_{520} + 2J_{500} + \frac{m^2L^2}{\pi^2R^2}(J_{400} - J_{420})\Big] - \frac{\pi^2}{\varrho_0\delta^2RL^2}\varphi_{11} -$$

$$- \frac{a^2}{2\delta R}\frac{\varrho}{\varrho_0} + \frac{\pi^2}{\varrho_0\delta L^2}N + \frac{16\pi}{3\varrho_0\delta^2RL^2}\varphi_{141} - \frac{m^2}{\delta R}\left(\delta\frac{\partial^2 w_0}{\partial t^2} + \frac{\varrho a}{\varrho_0}\frac{\partial w_0}{\partial t}\right) -$$

$$- \frac{8m^2}{3\pi R}\left(\frac{\varrho}{\varrho_0}a\frac{\partial f_s}{\partial t} + \delta\frac{\partial^2 f_s}{\partial t^2}\right) - \frac{m^2}{2\delta R}\Big[a\left(\frac{\partial w_L}{\partial t} - \frac{\partial w_0}{\partial t}\right)\frac{\varrho}{\varrho_0} +$$

$$+ \delta\left(\frac{\partial^2 w_L}{\partial t^2} - \frac{\partial^2 w_0}{\partial t^2}\right)\Big] + \frac{m^2\pi}{\varrho_0\delta R^2L^2}\Big[-\frac{8}{3}f_s\varphi_{11} - \frac{128}{15}g_s\varphi_{21} +$$

$$+ \frac{8}{15}f_s\varphi_{31} + \frac{256}{105}g_s\varphi_{41} + \frac{8}{105}f_s\varphi_{51} + \frac{128}{315}g_s\varphi_{61}\Big] +$$

$$+ \frac{2m^2\pi^2}{\varrho_0\delta R^2L^2}\Big[g_s\varphi_{151} - \frac{1}{2}f_s\varphi_{121} - g_s\varphi_{131} + \frac{1}{4}f_s\varphi_{141}\Big] +$$

$$+ \frac{m^2}{2\pi \rho_0 \delta R^3 L} \left[(J_{600} - J_{620}) N - (J_{800} - J_{820}) + \frac{\delta w_0}{R} (J_{700} - J_{720}) \right] +$$

$$+ \frac{m^2}{2\pi \rho_0 R^4 L^2} (w_L - w_0)(J_{900} - J_{920}) +$$

$$+ \frac{m^2 \delta}{4\pi \rho R^4 L} \left[2 f_s (3 I_{710} - I_{730}) + g_s (2 I_{720} - I_{700} - I_{740}) \right]$$

$$a_{14} = - \frac{2\pi^3}{\rho_0 \delta R L^5} (J_{410} - J_{430}) - \frac{m^2 \pi}{2 \rho_0 \delta R^3 L^3} \left[5 J_{310} - 5 J_{330} + 4 J_{530} + \right.$$

$$\left. + 4 J_{510} + \frac{m^2 L^2}{\pi^2 R^2} (J_{410} - J_{430}) \right] - \frac{\pi^2}{\rho_0 \delta^2 R L^2} \varphi_{12} + \frac{16 \pi}{3 \rho_0 \delta^2 R L^2} \varphi_{142} -$$

$$- \frac{8 a U}{3 \delta L} \frac{\rho}{\rho_0} - \frac{32 m^2}{15 \pi R} \left(\delta \frac{\partial^2 g_s}{\partial t^2} + a \frac{\rho}{\rho_0} \frac{\partial g_s}{\partial t} \right) +$$

$$+ \frac{16 m^2}{9 \pi^2 \delta R} \left[a \frac{\rho}{\rho_0} \left(\frac{\partial w_L}{\partial t} - \frac{\partial w_0}{\partial t} \right) + \delta \left(\frac{\partial^2 w_L}{\partial t^2} - \frac{\partial^2 w_0}{\partial t^2} \right) \right] +$$

$$+ \frac{m^2 \pi}{\rho_0 \delta R^2 L^2} \left[- \frac{8}{3} f_s \varphi_{12} - \frac{128}{15} g_s \varphi_{22} + \frac{8}{15} f_s \varphi_{32} + \frac{256}{105} g_s \varphi_{42} + \right.$$

$$\left. + \frac{8}{105} f_s \varphi_{52} + \frac{128}{315} g_s \varphi_{62} \right] + \frac{2 m^2 \pi^2}{\rho_0 \delta R^2 L^2} \left[g_s \varphi_{152} - \frac{1}{2} f_s \varphi_{122} - \right.$$

$$\left. - g_s \varphi_{132} + \frac{1}{4} f_s \varphi_{142} \right] + \frac{m^2}{2\pi \rho_0 \delta R^3 L} \left[(J_{610} - J_{630}) N - (J_{810} - J_{830}) + \right.$$

$$\left. + \frac{\delta w_0}{R} (J_{710} - J_{730}) \right] + \frac{m^2}{2\pi \rho_0 R^4 L^2} (w_L - w_0)(J_{910} - J_{930}) +$$

$$+ \frac{m^2 \delta}{4\pi \rho_0 R^4 L} \left[f_s (2 I_{720} - I_{700} - I_{740}) + g_s (2 I_{710} - I_{750} + I_{730}) \right]$$

Flygmotor

$$a_{15} = -\frac{\pi^2}{\rho_0 \delta^2 R L^2}\varphi_{13} + \frac{16\pi}{3\rho_0\delta^2 R L^2}\varphi_{143} + \frac{m^2\pi}{\rho_0 \delta R^2 L^2}\Big[-\frac{8}{3} f_s \varphi_{13} -$$

$$-\frac{128}{15} g_s \varphi_{23} + \frac{8}{15} f_s \varphi_{33} + \frac{256}{105} g_s \varphi_{43} + \frac{8}{105} f_s \varphi_{53} + \frac{128}{315} g_s \varphi_{63}\Big] +$$

$$+\frac{2m^2\pi^2}{\rho_0\delta R^2 L^2}\Big[-\frac{1}{2} f_s \varphi_{123} - g_s \varphi_{133} + \frac{1}{4} f_s \varphi_{143} + g_s \varphi_{153}\Big] - \frac{2m^2\pi^2}{\rho_0\delta R^2 L^2}\varphi_{71}$$

$$a_{16} = -\frac{\pi^2}{\rho_0 \delta^2 R L^2}\varphi_{14} + \frac{16\pi}{3\rho_0\delta^2 R L^2}\varphi_{144} + \frac{m^2\pi}{\rho_0 \delta R^2 L^2}\Big[-\frac{8}{3} f_s \varphi_{14} - \frac{128}{15} g_s \varphi_{24} +$$

$$+\frac{8}{15} f_s \varphi_{34} + \frac{256}{105} g_s \varphi_{44} + \frac{8}{105} f_s \varphi_{54} + \frac{128}{315} g_s \varphi_{64}\Big] +$$

$$+\frac{2m^2\pi^2}{\rho_0\delta R^2 L^2}\Big[-\frac{1}{2} f_s \varphi_{124} - g_s \varphi_{134} + \frac{1}{4} f_s \varphi_{144} + g_s \varphi_{154}\Big] -$$

$$-\frac{m^2\pi^2}{\rho_0\delta R^2 L^2}\Big[2\varphi_{72} + \frac{7}{4}\varphi_{101} + \frac{1}{4}\varphi_{81}\Big]$$

$$a_{17} = -\frac{\pi^2}{\rho_0 \delta^2 R L^2}\varphi_{15} + \frac{16\pi}{3\rho_0\delta^2 R L^2}\varphi_{145} + \frac{m^2\pi}{\rho_0 \delta R^2 L^2}\Big[-\frac{8}{3} f_s \varphi_{15} - \frac{128}{15} g_s \varphi_{25} +$$

$$+\frac{8}{15} f_s \varphi_{35} + \frac{256}{105} g_s \varphi_{45} + \frac{8}{105} f_s \varphi_{55} + \frac{128}{315} g_s \varphi_{65}\Big] +$$

$$+\frac{2m^2\pi^2}{\rho_0\delta R^2 L^2}\Big[-\frac{1}{2} f_s \varphi_{125} - g_s \varphi_{135} + \frac{1}{4} f_s \varphi_{145} + g_s \varphi_{155}\Big] -$$

$$-\frac{2m^2\pi^2}{\rho_0\delta R L^2}\left(\frac{9}{8}\varphi_{82} - \frac{1}{8}\varphi_{102}\right)$$

$$a_{18} = -\frac{\pi^2}{\rho_0 \delta^2 R L^2}\varphi_{16} + \frac{16\pi}{3\rho_0\delta^2 R L^2}\varphi_{146} - \frac{m^4\pi^3\delta}{2\rho_0 R^3 L^5}\left(J_{440} + J_{400}\right) -$$

$$-\frac{3m^4 a^2 \delta \rho}{32 R^3 \rho_0} + \frac{m^4\pi^2\delta}{4\rho_0 R^2 L^2}N + \frac{m^2\pi}{\rho_0\delta R^2 L^2}\Big[-\frac{8}{3} f_s \varphi_{16} - \frac{128}{15} g_s \varphi_{26} +$$

$$+\frac{8}{15} f_s \varphi_{36} + \frac{256}{105} g_s \varphi_{46} + \frac{8}{105} f_s \varphi_{56} + \frac{128}{315} g_s \varphi_{66}\Big] +$$

$$+ \frac{2m^2\pi^2}{\rho_0 \delta R^2 L^2}\left[-\tfrac{1}{2} f_s \varphi_{126} - g_s \varphi_{136} + \tfrac{1}{4} f_s \varphi_{146} + g_s \varphi_{156}\right] +$$

$$+ \frac{3m^4\pi^2}{4\rho_0 R^3 L^2}\left[\varphi_{11} - \varphi_{21}\right] - \frac{2m^2\pi^2}{\rho_0 \delta R^2 L^2}\varphi_{73} - \frac{2m^4\pi}{\rho_0 R^3 L^2}\left[\tfrac{7}{5}\varphi_{141} - \varphi_{121} - \tfrac{19}{35}\varphi_{161}\right]$$

$$a_{19} = -\frac{m^4\pi^3\delta}{2\rho_0 R^3 L^5}\left[-\tfrac{3}{4} J_{430} + 6 J_{410} + \tfrac{27}{4} J_{450}\right] - \frac{2\pi^2}{\rho_0 \delta^2 R L^2}\varphi_{17} -$$

$$- \frac{8}{15}\frac{m^4 a U \delta S}{R^2 L S_0} + \frac{16\pi}{3\rho_0 \delta^2 R L^2}\varphi_{147} + \frac{m^2\pi}{\rho_0 \delta R^2 L^2}\left[-\tfrac{8}{3} f_s \varphi_{17} -\right.$$

$$\left.- \tfrac{128}{15} g_s \varphi_{27} + \tfrac{8}{15} f_s \varphi_{37} + \tfrac{256}{105} g_s \varphi_{47} + \tfrac{8}{105} f_s \varphi_{57} + \tfrac{128}{315} g_s \varphi_{67}\right] +$$

$$+ \frac{2m^2\pi^2}{\rho_0 \delta R^2 L^2}\left[-\tfrac{1}{2} f_s \varphi_{127} - g_s \varphi_{137} + \tfrac{1}{4} f_s \varphi_{147} + g_s \varphi_{157}\right] +$$

$$+ \frac{2m^4\pi^2}{\rho_0 R^3 L^2}\left[\tfrac{3}{8}\varphi_{12} + \tfrac{15}{16}\varphi_{21} - \tfrac{3}{8}\varphi_{32} - \tfrac{11}{8}\varphi_{41}\right] +$$

$$+ \frac{2m^2\pi^2}{\rho_0 \delta R^2 L^2}\left[-\varphi_{74} - \tfrac{9}{8}\varphi_{83} + \tfrac{1}{8}\varphi_{103}\right] + \frac{2m^4\pi}{\rho_0 R^3 L^2}\left[-\tfrac{7}{5}\varphi_{142} +\right.$$

$$\left.+ \tfrac{19}{35}\varphi_{162} - \tfrac{36}{7}\varphi_{151} + \varphi_{122} + \tfrac{32}{15}\varphi_{131}\right]$$

$$a_{20} = -\frac{m^4\pi^3\delta}{16\rho_0 R^3 L^5}\left[15 J_{420} + 82 J_{400} - 18 J_{440} + 113 J_{460}\right] -$$

$$- \frac{\pi^2}{\rho_0 \delta^2 R L^2}\varphi_{18} + \frac{16\pi}{3\rho_0 \delta^2 R L^2}\varphi_{148} - \frac{3m^4 a^2 \delta S}{16\rho_0 R^3} +$$

$$+ \frac{m^2\pi}{\rho_0 \delta R^2 L^2}\left[-\tfrac{8}{3} f_s \varphi_{18} - \tfrac{128}{15} g_s \varphi_{28} + \tfrac{8}{15} f_s \varphi_{38} + \tfrac{256}{105} g_s \varphi_{48} +\right.$$

$$\left.+ \tfrac{8}{105} f_s \varphi_{58} + \tfrac{128}{315} g_s \varphi_{68}\right] +$$

Flygmotor

$$+ \frac{2m^2\pi^2}{\rho_0 \delta R^2 L^2}\left[-\frac{1}{2} f_s \varphi_{128} - g_s \varphi_{138} + \frac{1}{4} f_s \varphi_{148} + g_s \varphi_{158}\right] +$$

$$+ \frac{5m^4\pi^2\delta}{4\rho_0 R^2 L^2} N + \frac{m^4\pi^2}{4\rho_0 R^3 L^2}\left[10\varphi_{22} - 15\varphi_{42} + 5\varphi_{11} + \frac{9}{2}\varphi_{31} - \frac{15}{2}\varphi_{51}\right] +$$

$$+ \frac{2m^2\pi^2}{\rho_0 \delta R^2 L^2}\left[-\varphi_{75} - \frac{9}{8}\varphi_{84} + \frac{1}{8}\varphi_{104}\right] +$$

$$+ \frac{2m^4\pi\delta}{\rho_0 R^3 L^2}\left[-\frac{36}{7}\varphi_{152} + \frac{353}{105}\varphi_{132} + \frac{12}{5}\varphi_{121} - \frac{4}{27}\varphi_{141} - \frac{74}{21}\varphi_{161}\right]$$

$$a_{21} = -\frac{m^4\pi^3\delta}{2\rho_0 R^3 L^5}\left[-J_{450} - J_{430} + 9J_{470} + 9J_{410}\right] -$$

$$- \frac{\pi^2}{\rho_0 \delta^2 R L^2}\varphi_{19} + \frac{16\pi}{3\rho_0\delta^2 R L^2}\varphi_{147} - \frac{32 m^4 a U \delta g}{105 R^2 L \rho_0} +$$

$$+ \frac{m^2\pi}{\rho_0 \delta R^2 L^2}\left[-\frac{8}{3} f_s \varphi_{19} - \frac{128}{15} g_s \varphi_{29} + \frac{8}{15} f_s \varphi_{39} + \frac{256}{105} g_s \varphi_{49} +\right.$$

$$\left. + \frac{8}{105} f_s \varphi_{59} + \frac{128}{315} g_s \varphi_{69}\right] + \frac{2m^2\pi^2}{\rho_0 \delta R^2 L^2}\left[-\frac{1}{2} f_s \varphi_{129} - g_s \varphi_{139} +\right.$$

$$\left. + \frac{1}{4} f_s \varphi_{149} + g_s \varphi_{159}\right] + \frac{m^4\pi^2}{2\rho_0 R^3 L^2}\left[\frac{5}{2}\varphi_{12} + \frac{3}{4}\varphi_{32} - \frac{11}{4}\varphi_{52}\right] +$$

$$+ \frac{2m^2\pi}{\rho_0 \delta R^2 L^2}\left[-\frac{9}{8}\varphi_{85} + \frac{1}{8}\varphi_{105}\right] + \frac{2m^4\pi}{\rho_0 R^3 L^2}\left[\frac{4}{7}\varphi_{122} + \frac{53}{105}\varphi_{142} - \frac{220}{63}\varphi_{162}\right]$$

$$a_{22} = \frac{3m^4\pi^2}{4\rho_0 R^3 L^2}\left[\varphi_{13} - \varphi_{33}\right] - \frac{2m^2\pi^2}{\rho_0 \delta R^2 L^2}\varphi_{76} +$$

$$+ \frac{2m^4\pi}{\rho_0 R^3 L^2}\left[\varphi_{123} - \frac{7}{5}\varphi_{143} + \frac{121}{105}\varphi_{163} - \frac{16}{105}\varphi_{165}\right]$$

Flygmotor

$$a_{23} = \frac{2m^4\pi^2}{\rho_0 R^3 L^2}\left[\frac{3}{8}\varphi_{14} + \frac{5}{4}\varphi_{23} - \frac{3}{8}\varphi_{34} - \frac{11}{8}\varphi_{43}\right] +$$

$$+ \frac{2m^4\pi}{\rho_0 R^3 L^2}\left[\varphi_{124} + \frac{8}{3}\varphi_{133} - \frac{1}{3}\varphi_{144} - \frac{12}{7}\varphi_{153} + \frac{5}{7}\varphi_{164}\right] +$$

$$+ \frac{2m^2\pi^2}{\rho_0 \delta R^2 L^2}\left[-\varphi_{77} - \frac{9}{8}\varphi_{86} + \frac{1}{8}\varphi_{106}\right]$$

$$a_{24} = \frac{2m^4\pi^2}{\rho_0 R^3 L^2}\left[\frac{3}{8}\varphi_{15} + \frac{5}{4}\varphi_{24} - \frac{3}{8}\varphi_{35} - \frac{3}{8}\varphi_{44} + \frac{5}{8}\varphi_{13} +\right.$$

$$\left. + \frac{9}{16}\varphi_{33} - \frac{17}{16}\varphi_{53}\right] + \frac{2m^4\pi}{\rho_0 R^3 L^2}\left[\frac{9}{5}\varphi_{145} - \frac{13}{35}\varphi_{144} + \frac{19}{35}\varphi_{165} +\right.$$

$$\left. + \varphi_{125} + \frac{8}{3}\varphi_{134} + \frac{12}{5}\varphi_{123} + \frac{181}{105}\varphi_{143} - \frac{220}{63}\varphi_{163} - \frac{24}{5}\varphi_{154}\right] +$$

$$+ \frac{2m^2\pi^2}{\rho_0 \delta R^2 L^2}\left[-\varphi_{78} - \frac{9}{8}\varphi_{87} + \frac{1}{8}\varphi_{107}\right]$$

$$a_{25} = \frac{2m^4\pi^2}{\rho_0 R^3 L^2}\left[\frac{5}{4}\varphi_{25} - \frac{11}{8}\varphi_{45} + \frac{5}{8}\varphi_{14} + \frac{9}{16}\varphi_{34} - \frac{17}{16}\varphi_{54}\right] +$$

$$+ \frac{2m^4\pi}{\rho_0 R^3 L^2}\left[\frac{8}{3}\varphi_{135} - \frac{207}{70}\varphi_{155} + \frac{12}{5}\varphi_{124} + \frac{53}{105}\varphi_{144} -\right.$$

$$\left. - \frac{220}{63}\varphi_{164} - \frac{153}{70}\varphi_{154}\right] + \frac{2m^2\pi^2}{\rho_0 \delta R^2 L^2}\left[-\varphi_{79} - \frac{9}{8}\varphi_{88} + \frac{1}{8}\varphi_{108}\right]$$

$$a_{26} = \frac{2m^4\pi^2}{\rho_0 R^3 L^2}\left[\frac{1}{2}\varphi_{15} + \frac{9}{16}\varphi_{35} - \frac{17}{16}\varphi_{55}\right] +$$

$$+ \frac{2m^4\pi}{\rho_0 R^3 L^2}\left[\frac{12}{5}\varphi_{125} + \frac{53}{105}\varphi_{145} - \frac{220}{63}\varphi_{165}\right] +$$

$$+ \frac{2m^2\pi^2}{\rho_0 \delta R^2 L^2}\left[-\frac{9}{8}\varphi_{89} + \frac{1}{8}\varphi_{109}\right]$$

Flygmotor

$$a_{27} = \frac{3m^4\pi^2}{4\rho_0 R^3 L^2}\left[\varphi_{16} - \varphi_{36}\right] + \frac{2m^4\pi}{\rho_0 R^3 L^2}\left[\varphi_{126} - \frac{7}{5}\varphi_{146} + \frac{19}{35}\varphi_{166}\right]$$

$$a_{28} = \frac{2m^4\pi^2}{\rho_0 R^3 L^2}\left[\frac{3}{8}\varphi_{17} + \frac{5}{4}\varphi_{26} - \frac{3}{8}\varphi_{37} - \frac{11}{8}\varphi_{46}\right] +$$

$$+ \frac{2m^4\pi}{\rho_0 R^3 L^2}\left[-\frac{36}{7}\varphi_{156} + \frac{57}{105}\varphi_{167} + \varphi_{127} + \frac{8}{3}\varphi_{126} - \frac{7}{5}\varphi_{147}\right]$$

$$a_{29} = \frac{2m^4\pi^2}{\rho_0 R^3 L^2}\left[\frac{3}{8}\varphi_{18} + \frac{5}{4}\varphi_{27} - \frac{3}{8}\varphi_{38} - \frac{22}{16}\varphi_{47} + \frac{5}{8}\varphi_{16} + \frac{9}{16}\varphi_{36} -\right.$$

$$\left. - \frac{17}{16}\varphi_{56}\right] + \frac{2m^4\pi}{\rho_0 R^3 L^2}\left[-\frac{7}{5}\varphi_{148} - \frac{36}{7}\varphi_{157} + \frac{57}{105}\varphi_{168} +\right.$$

$$\left. + \varphi_{128} + \frac{8}{3}\varphi_{137} + \frac{12}{5}\varphi_{126} + \frac{53}{105}\varphi_{146} - \frac{220}{63}\varphi_{166}\right]$$

$$a_{30} = \frac{2m^4\pi^2}{\rho_0 R^3 L^2}\left[\frac{3}{8}\varphi_{19} + \frac{5}{4}\varphi_{28} - \frac{3}{8}\varphi_{39} - \frac{11}{8}\varphi_{48} + \frac{5}{8}\varphi_{17} +\right.$$

$$\left. + \frac{9}{16}\varphi_{37} - \frac{17}{16}\varphi_{57}\right] + \frac{2m^4\pi}{\rho_0 R^3 L^2}\left[-\frac{7}{5}\varphi_{149} - \frac{36}{7}\varphi_{158} +\right.$$

$$\left. + \frac{57}{105}\varphi_{169} + \varphi_{129} + \frac{8}{3}\varphi_{138} + \frac{12}{5}\varphi_{127} + \frac{53}{105}\varphi_{147} - \frac{220}{63}\varphi_{167}\right]$$

$$a_{31} = \frac{2m^4\pi}{\rho_0 R^3 L^2}\left[\frac{8}{3}\varphi_{139} - \frac{36}{7}\varphi_{159} + \frac{4}{3}\varphi_{128} + \frac{69}{105}\varphi_{148} - \frac{84}{45}\varphi_{168}\right] +$$

$$+ \frac{2m^4\pi^2}{\rho_0 R^3 L^2}\left[\frac{5}{4}\varphi_{29} - \frac{11}{8}\varphi_{49} + \frac{5}{8}\varphi_{18} + \frac{9}{16}\varphi_{38} - \frac{17}{16}\varphi_{58}\right]$$

$$a_{32} = \frac{2m^4\pi^2}{\rho_0 R^3 L^2}\left[\frac{5}{8}\varphi_{19} + \frac{9}{16}\varphi_{39} - \frac{17}{16}\varphi_{59}\right] +$$

$$+ \frac{2m^4\pi}{\rho_0 R^3 L^2}\left[\frac{12}{5}\varphi_{129} + \frac{53}{105}\varphi_{149} - \frac{220}{63}\varphi_{169}\right]$$

$$a_{33} = -\delta_{m0}\left[\frac{2a\delta}{\pi\delta^2\rho_0}\left(\frac{\partial w_0}{\partial t} + \frac{\partial w_L}{\partial t}\right) + \frac{2}{\pi\delta}\left(\frac{\partial^2 w_0}{\partial t^2} + \frac{\partial^2 w_L}{\partial t^2}\right) + \frac{\delta a}{\rho_0\delta}\frac{\partial f_s}{\partial t} + \frac{\partial^2 f_s}{\partial t^2}\right]$$

$$b_1 = \frac{3m^4\delta^2}{8R^2} \qquad b_2 = \frac{m^4\delta^2}{4R^2} \qquad b_3 = \frac{m^4\delta^2}{2R^2}$$

$$b_4 = 0 \qquad b_5 = \frac{a}{\delta}\frac{\rho}{\rho_0} \qquad b_6 = \frac{3m^4\delta a}{8R^2}\frac{\rho}{\rho_0}$$

$$b_7 = \frac{m^4\delta a}{4R^2}\frac{\rho}{\rho_0} \qquad b_8 = \frac{3m^4\delta^2}{8R^2} \qquad b_9 = 0$$

$$b_{10} = \frac{m^4\delta a}{2R^2}\frac{\rho}{\rho_0} \qquad b_{11} = \frac{m^4\delta^2}{4R^2} \qquad b_{12} = 0$$

$$b_{13} = -\frac{2\pi^3}{\rho_0\delta R L^5}(J_{410} - J_{430}) - \frac{m^2\pi}{2\rho_0\delta R^3L^3}(5J_{310} - 5J_{330} + 4J_{530} + 4J_{510})$$

$$- \frac{m^4}{2\pi\rho_0\delta R^5 L}(J_{410} - J_{430}) - \frac{4\pi^2}{\rho_0\delta^2 R L^2}\varphi_{21} - \frac{8\pi^2}{3\rho_0\delta^2 R L^2}\varphi_{131} +$$

$$+ \frac{8aU\rho}{3\delta L\rho_0} + \frac{16m^2}{9\pi^2\delta R}\left[a\frac{\rho}{\rho_0}\left(\frac{\partial w_L}{\partial t} - \frac{\partial w_0}{\partial t}\right) + \delta\left(\frac{\partial^2 w_L}{\partial t^2} - \frac{\partial^2 w_0}{\partial t^2}\right)\right] -$$

$$- \frac{32m^2}{15\pi R}\left(a\frac{\rho}{\rho_0}\frac{\partial g_s}{\partial t} + \delta\frac{\partial^2 g_s}{\partial t^2}\right) - \frac{2m^2\pi}{\rho_0\delta R^2L^2}\left[\frac{16}{15}f_s\varphi_{21} + \frac{64}{15}g_s\varphi_{11} +\right.$$

$$\left.+ \frac{64}{21}g_s\varphi_{31} - \frac{32}{105}f_s\varphi_{41} - \frac{64}{45}g_s\varphi_{51} - \frac{16}{315}f_s\varphi_{61}\right] +$$

$$+ \frac{m^2\pi^2}{\rho_0\delta R^2L^2}\left[-4g_s\varphi_{121} - \frac{1}{2}f_s\varphi_{131} + \frac{1}{2}f_s\varphi_{151}\right] +$$

$$+ \frac{m^2}{2\pi\rho_0\delta R^3L}\left[(J_{610} - J_{630})N - (J_{810} - J_{830}) + \frac{\delta w_0}{R}(J_{710} - J_{730})\right] +$$

$$+ \frac{m^2}{2\pi\rho_0 R^4L^2}(w_L - w_0)(J_{910} - J_{930}) + \frac{m^2}{2\pi\rho_0\delta R^4L}\left[f_s(2I_{720} - I_{740} + I_{700})\right.$$

$$\left.+ \frac{1}{2}g_s(I_{730} + 2I_{710} - I_{750})\right]$$

Flygmotor

$$b_{14} = -\frac{8\pi^3}{\rho_0 \delta R L^5}(J_{400} - J_{440}) - \frac{4m^2\pi}{\rho_0 \delta R^3 L^3}(J_{500} + J_{540} + J_{340} + J_{300}) -$$

$$-\frac{m^4}{2\pi\rho_0 \delta R^5 L}(J_{400} - J_{440}) - \frac{4\pi^2}{\rho_0 \delta^2 R L^2}\varphi_{22} - \frac{8\pi^2}{3\rho_0 \delta^2 R L^2}\varphi_{132} -$$

$$-\frac{a^2}{2\delta R}\frac{\rho}{\rho_0} - \frac{m^2}{\delta R}\left(\delta\frac{\partial^2 w_0}{\partial t^2} + a\frac{\rho}{\rho_0}\frac{\partial w_0}{\partial t}\right) -$$

$$-\frac{m^2}{2\delta R}\left[a\left(\frac{\partial w_L}{\partial t} - \frac{\partial w_0}{\partial t}\right)\frac{\rho}{\rho_0} + \delta\left(\frac{\partial^2 w_L}{\partial t^2} - \frac{\partial^2 w_0}{\partial t^2}\right)\right] -$$

$$-\frac{32 m^2}{15\pi R}\left(a\frac{\rho}{\rho_0}\frac{\partial f_s}{\partial t} + \delta\frac{\partial^2 f_s}{\partial t^2}\right) + \frac{2m^2\pi}{\rho_0 \delta R^2 L^2}\left(-\frac{16}{15}f_s\varphi_{22} - \frac{64}{15}g_s\varphi_{12} -\right.$$

$$\left.-\frac{64}{21}g_s\varphi_{32} + \frac{32}{105}f_s\varphi_{42} + \frac{64}{45}g_s\varphi_{52} + \frac{16}{315}f_s\varphi_{62}\right) +$$

$$+\frac{m^2\pi^2}{\rho_0 \delta R^2 L^2}\left(-4g_s\varphi_{122} - \frac{1}{2}f_s\varphi_{132} + \frac{1}{2}f_s\varphi_{152}\right) +$$

$$+\frac{m^2}{2\pi\rho_0 \delta R^3 L}\left[(J_{600} - J_{640})N - (J_{800} - J_{840}) + \frac{\delta w_0}{R}(J_{700} - J_{740})\right]$$

$$+\frac{m^2}{2\pi\rho_0 R^4 L^2}(w_L - w_0)(J_{900} - J_{940}) + \frac{m^2}{4\pi\rho_0 \delta R^4 L}\left[f_s(I_{730} + 2I_{710} -\right.$$

$$\left.-I_{750}) + g_s(3I_{720} - I_{760})\right] + \frac{4\pi^2}{\rho_0 \delta L^2}N$$

$$b_{15} = -\frac{4\pi^2}{\rho_0 \delta^2 R L^2}\varphi_{23} - \frac{8\pi^2}{3\rho_0 \delta^2 R L^2}\varphi_{123} + \frac{2m^2\pi}{\rho_0 \delta R^2 L^2}\left(-\frac{16}{15}f_s\varphi_{23} -\right.$$

$$\left.-\frac{64}{15}g_s\varphi_{13} - \frac{64}{21}g_s\varphi_{33} + \frac{32}{105}f_s\varphi_{43} + \frac{64}{45}g_s\varphi_{53} + \frac{16}{315}f_s\varphi_{63}\right) +$$

$$+\frac{m^2\pi^2}{\rho_0 \delta R^2 L^2}\left(-4g_s\varphi_{123} - \frac{1}{2}f_s\varphi_{133} + \frac{1}{2}f_s\varphi_{153}\right) -$$

$$-\frac{m^2\pi^2}{4\rho_0 \delta R^2 L^2}(9\varphi_{81} - \varphi_{101})$$

Flygmotor

$$b_{16} = -\frac{4\pi^2}{\rho_0\delta^2 RL^2}\varphi_{24} - \frac{8\pi^2}{3\rho_0\delta^2 RL^2}\varphi_{124} + \frac{2m^2\pi}{\rho_0\delta R^2L^2}\Big[-\frac{16}{15}f_s\varphi_{24} -$$

$$-\frac{64}{15}g_s\varphi_{14} - \frac{64}{21}g_s\varphi_{34} + \frac{32}{105}f_s\varphi_{44} + \frac{64}{45}g_s\varphi_{54} + \frac{16}{315}f_s\varphi_{64}\Big] +$$

$$+\frac{m^2\pi^2}{\rho_0\delta R^2L^2}\Big[-4g_s\varphi_{124} - \frac{1}{2}f_s\varphi_{134} + \frac{1}{2}f_s\varphi_{154}\Big] -$$

$$-\frac{m^2\pi^2}{\rho_0\delta R^2L^2}\Big(\frac{9}{4}\varphi_{82} - \frac{1}{4}\varphi_{102} + 8\varphi_{71}\Big)$$

$$b_{17} = -\frac{4\pi^2}{\rho_0\delta^2 RL^2}\varphi_{25} - \frac{8\pi^2}{3\rho_0\delta^2 RL^2}\varphi_{125} + \frac{2m^2\pi}{\rho_0\delta R^2L^2}\Big[-\frac{16}{15}f_s\varphi_{25} -$$

$$-\frac{64}{15}g_s\varphi_{15} - \frac{64}{21}g_s\varphi_{35} + \frac{32}{105}f_s\varphi_{45} + \frac{64}{45}g_s\varphi_{55} + \frac{16}{315}f_s\varphi_{65}$$

$$+\frac{m^2\pi^2}{\rho_0\delta R^2L^2}\Big[-4g_s\varphi_{125} - \frac{1}{2}f_s\varphi_{135} + \frac{1}{2}f_s\varphi_{155}\Big] -$$

$$-\frac{4m^2\pi^2}{\rho_0\delta R^2L^2}\big(2\varphi_{72} - \varphi_{112}\big)$$

$$b_{18} = \frac{m^4\pi^3\delta}{8\rho_0R^3L^5}\Big[J_{430} + J_{420} - 9J_{450} - 9J_{410}\Big] - \frac{4\pi^2}{\rho_0\delta^2 RL^2}\varphi_{26} -$$

$$-\frac{8\pi^2}{3\rho_0\delta^2 RL^2}\varphi_{136} + \frac{8m^4aU\delta\rho}{15R^2L\rho_0} + \frac{2m^2\pi}{\rho_0\delta R^2L^2}\Big[-\frac{16}{15}f_s\varphi_{26} -$$

$$-\frac{64}{15}g_s\varphi_{16} - \frac{64}{21}g_s\varphi_{36} + \frac{32}{105}f_s\varphi_{46} + \frac{64}{45}g_s\varphi_{56} + \frac{16}{315}f_s\varphi_{66}\Big] +$$

$$+\frac{m^2\pi^2}{\rho_0\delta R^2L^2}\Big[-4g_s\varphi_{126} - \frac{1}{2}f_s\varphi_{136} + \frac{1}{2}f_s\varphi_{156}\Big] +$$

$$+\frac{2m^4\pi^2}{\rho_0R^3L^2}\Big(\frac{5}{8}\varphi_{21} - \frac{9}{16}\varphi_{41}\Big) + \frac{2m^4\pi}{\rho_0R^3L^2}\Big[\frac{14}{15}\varphi_{131} - \frac{18}{7}\varphi_{151}\Big] -$$

$$-\frac{m^2\pi^2\delta}{4\rho_0R^2L^2}\big(9\varphi_{13} - \varphi_{33}\big)$$

Flygmotor

$$b_{19} = -\frac{m^4\pi^3 d}{2\rho_0 R^3 L^5}\left(\frac{15}{8} J_{420} + \frac{41}{4} J_{400} - \frac{9}{4} J_{440} + \frac{113}{8} J_{460}\right) +$$

$$+ \frac{5 m^4\pi^2 d}{4\rho_0 R^2 L^2} N + \frac{m^4\pi^2}{8\rho_0 R^3 L^2}\left[20\varphi_{11} + 36\varphi_{21} - 36\varphi_{51} + 10\varphi_{22} - 11\varphi_{42}\right]$$

$$- \frac{4\pi^2}{\rho_0 d^2 R L^2}\varphi_{27} - \frac{8\pi^2}{3\rho_0 d^2 R L^2}\varphi_{137} - \frac{3m^4 a^2 d S}{16\rho_0 R^3} +$$

$$+ \frac{2m^2\pi}{\rho_0 d R^2 L^2}\left[-\frac{16}{15} f_s\varphi_{27} - \frac{64}{15} g_s\varphi_{17} - \frac{64}{21} g_s\varphi_{37} + \frac{32}{105} f_s\varphi_{47} +\right.$$

$$\left.+ \frac{64}{45} g_s\varphi_{57} + \frac{16}{315} f_s\varphi_{67}\right] + \frac{m^2\pi^2}{\rho_0 d R^2 L^2}\left[-4 g_s\varphi_{127} - \frac{1}{2} f_s\varphi_{137} +\right.$$

$$\left.+ \frac{1}{2} f_s\varphi_{157}\right] + \frac{2m^4\pi}{\rho_0 R^3 L^2}\left[\frac{24}{5}\varphi_{121} - \frac{941}{210}\varphi_{141} - \frac{376}{63}\varphi_{161} +\right.$$

$$\left.+ \frac{14}{15}\varphi_{132} - \frac{18}{7}\varphi_{152}\right] + \frac{2m^2\pi^2}{\rho_0 d R^2 L^2}\left[-\frac{9}{8}\varphi_{84} + \frac{1}{8}\varphi_{104} - 4\varphi_{73}\right]$$

$$b_{20} = -\frac{m^4\pi^3 d}{2\rho_0 R^3 L^5}\left[-3J_{450} - 3J_{430} + 27J_{470} + 27J_{410}\right] +$$

$$+ \frac{5m^4\pi^2}{4\rho_0 R^3 L^2}\varphi_{12} - \frac{4\pi^2}{\rho_0 d^2 R L^2}\varphi_{28} - \frac{8\pi^2}{3\rho_0 d^2 R L^2}\varphi_{138} + \frac{32 m^4 a U d S}{105 R^2 L \rho_0} +$$

$$+ \frac{2m^2\pi}{\rho_0 d R^2 L^2}\left[-\frac{16}{15} f_s\varphi_{28} - \frac{64}{15} g_s\varphi_{18} - \frac{64}{21} g_s\varphi_{38} + \frac{32}{105} f_s\varphi_{48} +\right.$$

$$\left.+ \frac{64}{45} g_s\varphi_{58} + \frac{16}{315} f_s\varphi_{68}\right] + \frac{m^2\pi}{\rho_0 d R^2 L^2}\left[-4 g_s\varphi_{128} - \frac{1}{2} f_s\varphi_{138} + \frac{1}{2} f_s\varphi_{158}\right] +$$

$$+ \frac{2m^4\pi^2}{\rho_0 R^3 L^2}\left[2\varphi_{21} + \frac{5}{8}\varphi_{12} + \frac{13}{16}\varphi_{32} - \frac{29}{16}\varphi_{52} - 2\varphi_{61}\right] +$$

$$+ \frac{2m^4\pi}{\rho_0 R^3 L^2}\left[\frac{24}{5}\varphi_{122} - \frac{941}{210}\varphi_{142} - \frac{376}{63}\varphi_{162} + \frac{376}{105}\varphi_{131} + 8\varphi_{151}\right] +$$

$$+ \frac{2m^2\pi^2}{\rho_0 d R^2 L^2}\left[-\frac{9}{8}\varphi_{85} + \frac{1}{8}\varphi_{105} - 4\varphi_{74}\right]$$

Flygmotor

$$b_{21} = -\frac{8m^4\pi^3\delta}{\rho_0 R^3 L^5}\left(J_{480} + J_{400}\right) + \frac{m^4\pi^2\delta}{\rho_0 R^2 L^2} N - \frac{4\pi^2}{\rho_0 \delta^2 R L^2}\varphi_{29} -$$

$$- \frac{8\pi}{3\rho_0\delta^2 R L^2}\varphi_{139} - \frac{3m^4 a^2 \delta \rho}{32 R^3 \rho_0} + \frac{2m^2\pi}{\rho_0 \delta^2 R^2 L^2}\left[-\frac{16}{15} f_s \varphi_{29} -\right.$$

$$\left. - \frac{64}{15} g_s \varphi_{19} - \frac{64}{21} g_s \varphi_{39} + \frac{32}{105} f_s \varphi_{49} + \frac{64}{45} g_s \varphi_{59} + \frac{16}{315} f_s \varphi_{69}\right] +$$

$$+ \frac{m^2\pi^2}{\rho_0 \delta R^2 L^2}\left[-4 g_s \varphi_{129} - \frac{1}{2} f_s \varphi_{139} + \frac{1}{2} f_s \varphi_{159}\right] +$$

$$+ \frac{3m^4\pi^2}{\rho_0 R^3 L^2}\left(\varphi_{22} - \varphi_{62}\right) + \frac{2m^4\pi}{\rho_0 R^3 L^2}\left[\frac{64}{21}\varphi_{132} - \frac{64}{15}\varphi_{152} -\right.$$

$$\left. - \frac{32}{105}\varphi_{131} + \frac{32}{15}\varphi_{151}\right] - \frac{8m^2\pi^2}{\rho_0 \delta R^2 L^2}\varphi_{75}$$

$$b_{22} = \frac{2m^4\pi^2}{\rho_0 R^3 L^2}\left[\frac{5}{8}\varphi_{23} - \frac{7}{16}\varphi_{43}\right] + \frac{m^2\pi^2}{4\rho_0 \delta R^2 L^2}\left[-9\varphi_{86} + \varphi_{106}\right] +$$

$$+ \frac{2m^4\pi}{\rho_0 R^3 L^2}\left[\frac{14}{15}\varphi_{133} - \frac{18}{7}\varphi_{153}\right]$$

$$b_{23} = \frac{2m^4\pi^2}{\rho_0 R^3 L^2}\left[\frac{5}{4}\varphi_{13} + \frac{9}{8}\varphi_{33} - \frac{9}{4}\varphi_{53} + \frac{5}{8}\varphi_{24} - \frac{11}{16}\varphi_{44}\right] +$$

$$+ \frac{2m^2\pi^2}{\rho_0 \delta R^2 L^2}\left[-\frac{9}{8}\varphi_{87} + \frac{1}{8}\varphi_{107} - 4\varphi_{76}\right] +$$

$$+ \frac{2m^4\pi}{\rho_0 R^3 L^2}\left[\frac{24}{5}\varphi_{123} - \frac{941}{210}\varphi_{143} - \frac{376}{63}\varphi_{163} + \frac{14}{15}\varphi_{134} - \frac{18}{7}\varphi_{154}\right]$$

$$b_{24} = \frac{2m^4\pi^2}{\rho_0 R^3 L^2}\left[\frac{5}{4}\varphi_{14} + \frac{9}{8}\varphi_{34} - \frac{9}{4}\varphi_{54} + \frac{5}{8}\varphi_{25} - \frac{11}{16}\varphi_{45} + \frac{3}{2}\varphi_{23} -\right.$$

$$\left. - \frac{3}{2}\varphi_{63}\right] + \frac{2m^2\pi^2}{\rho_0 \delta R^2 L^2}\left[-\frac{9}{8}\varphi_{88} + \frac{1}{8}\varphi_{108} - 4\varphi_{77}\right] +$$

$$+ \frac{2m^4\pi}{\rho_0 R^3 L^2}\left[\frac{24}{5}\varphi_{124} - \frac{941}{210}\varphi_{144} - \frac{376}{63}\varphi_{164} + \frac{14}{15}\varphi_{135} -\right.$$

$$\left. - \frac{18}{7}\varphi_{155} + \frac{288}{105}\varphi_{133} - \frac{32}{15}\varphi_{153}\right]$$

Flygmotor

$$b_{25} = \frac{2m^4\pi^2}{\rho_0 R^3 L^2}\left[\frac{5}{4}\varphi_{15} + \frac{9}{8}\varphi_{35} - \frac{9}{4}\varphi_{55} + \frac{3}{2}\varphi_{24} - \frac{3}{2}\varphi_{64}\right] +$$

$$+ \frac{2m^4\pi}{\rho_0 R^3 L^2}\left[\frac{24}{5}\varphi_{125} - \frac{941}{210}\varphi_{145} - \frac{376}{63}\varphi_{165} + \frac{288}{105}\varphi_{124} -\right.$$

$$\left.- \frac{32}{15}\varphi_{154}\right] + \frac{2m^2\pi^2}{\rho_0 \delta R^2 L^2}\left[-\frac{9}{8}\varphi_{89} + \frac{1}{8}\varphi_{109} - 4\varphi_{78}\right]$$

$$b_{26} = \frac{3m^4\pi^2}{\rho_0 R^3 L^2}\left(\varphi_{25} - \varphi_{65}\right) + \frac{2m^4\pi}{\rho_0 R^3 L^2}\left[\frac{288}{105}\varphi_{135} - \frac{32}{15}\varphi_{155}\right] -$$

$$- \frac{8m^2\pi^2}{\rho_0 \delta R^2 L^2}\varphi_{79}$$

$$b_{27} = \frac{2m^4\pi^2}{\rho_0 R^3 L^2}\left[\frac{5}{8}\varphi_{26} - \frac{11}{16}\varphi_{46}\right] + \frac{2m^4\pi}{\rho_0 R^3 L^2}\left[\frac{14}{15}\varphi_{136} - \frac{18}{7}\varphi_{156}\right]$$

$$b_{28} = \frac{2m^4\pi^2}{\rho_0 R^3 L^2}\left[\frac{5}{4}\varphi_{16} + \frac{9}{8}\varphi_{36} - \frac{9}{4}\varphi_{56} + \frac{5}{8}\varphi_{27} - \frac{11}{16}\varphi_{47}\right] +$$

$$+ \frac{2m^4\pi}{\rho_0 R^3 L^2}\left[\frac{24}{5}\varphi_{126} - \frac{941}{210}\varphi_{146} - \frac{376}{63}\varphi_{166} + \frac{14}{15}\varphi_{137} - \frac{18}{7}\varphi_{157}\right]$$

$$b_{29} = \frac{2m^4\pi^2}{\rho_0 R^3 L^2}\left[\frac{5}{4}\varphi_{17} + \frac{9}{8}\varphi_{37} - \frac{9}{4}\varphi_{57} + \frac{5}{8}\varphi_{28} - \frac{11}{16}\varphi_{48} +\right.$$

$$\left.+ \frac{3}{2}\varphi_{26} - \frac{3}{2}\varphi_{66}\right] + \frac{2m^4\pi}{\rho_0 R^3 L^2}\left[\frac{24}{5}\varphi_{127} - \frac{941}{210}\varphi_{147} -\right.$$

$$\left.- \frac{376}{63}\varphi_{167} + \frac{14}{15}\varphi_{138} - \frac{18}{7}\varphi_{158} + \frac{288}{105}\varphi_{136} - \frac{32}{15}\varphi_{156}\right]$$

$$b_{30} = \frac{2m^4\pi^2}{\rho_0 R^3 L^2}\left[\frac{5}{4}\varphi_{18} + \frac{9}{8}\varphi_{38} - \frac{13}{8}\varphi_{58} + \frac{5}{8}\varphi_{29} - \frac{11}{16}\varphi_{49} +\right.$$

$$+ \frac{3}{2}\varphi_{27} - \frac{3}{2}\varphi_{67}\Big] + \frac{2m^4\pi}{\rho_0 R^3 L^2}\Big[\frac{24}{5}\varphi_{128} - \frac{941}{210}\varphi_{148} - \frac{376}{63}\varphi_{168}$$

$$\left.+ \frac{14}{15}\varphi_{139} - \frac{18}{7}\varphi_{159} + \frac{288}{105}\varphi_{137} - \frac{32}{15}\varphi_{157}\right]$$

$$b_{31} = \frac{2m^4\pi^2}{\rho_0 R^3 L^2}\left[\frac{5}{4}\varphi_{19} + \frac{9}{8}\varphi_{39} - \frac{9}{4}\varphi_{59} + \frac{3}{2}\varphi_{28} - \frac{3}{2}\varphi_{68}\right] +$$

$$+ \frac{2m^4\pi}{\rho_0 R^3 L^2}\left[\frac{24}{5}\varphi_{129} - \frac{941}{210}\varphi_{149} - \frac{376}{63}\varphi_{169} + \frac{288}{105}\varphi_{138} -\right.$$

$$\left. - \frac{32}{15}\varphi_{158}\right]$$

$$b_{32} = \frac{3m^4\pi^2}{\rho_0 R^3 L^2}\left[\varphi_{29} - \varphi_{69}\right] + \frac{2m^4\pi}{\rho_0 R^3 L^2}\left[\frac{288}{105}\varphi_{139} - \frac{32}{15}\varphi_{159}\right]$$

$$b_{33} = \delta_{m0}\left[\frac{\rho a}{\pi\rho_0\delta^2}\left(\frac{\partial w_L}{\partial t} - \frac{\partial w_0}{\partial t}\right) + \frac{1}{\pi\delta}\left(\frac{\partial^2 w_L}{\partial t^2} - \frac{\partial^2 w_0}{\partial t^2}\right) - \frac{a\rho}{\delta\rho_0}\frac{\partial g_s}{\partial t} - \frac{\partial^2 g_s}{\partial t^2}\right]$$

SUPERSONIC FLUTTER OF HEATED CIRCULAR CYLINDRICAL SHELLS WITH TEMPERATURE DEPENDENT MATERIAL PROPERTIES

Ulf Olsson*

Volvo Flygmotor AB, Trollhattan, Sweden

Abstract

This paper presents a theoretical analysis on the supersonic flutter of thin circular cylindrical shells exposed to transient temperature variations of such magnitudes, that the temperature dependence of the material properties must be taken into account.

Nonlinear shell equations of Donnell's type are developed for arbitrarily varying material properties. With the help of Galerkin's method these equations are reduced to ordinary differential equations which are then solved asymptotically according to the method of Krylov-Bogoliubov. Instationary, axially varying temperature fields are considered, corresponding to convective heating of the shell wall as in a jet engine afterburner.

---

* Scientist, Research Department

Linear analytic solutions are given for the flutter frequency and the first mode amplitude in the assumed series solution. The results are verified through comparison to nonlinear numerical solutions.

The nonlinear solutions show that initially stable states of vibration may change into instable ones during the heating of the shell wall provided that the gas velocity is within certain boundaries. This is because the curves describing the limit cycle amplitudes at various gas velocities are moved to lower velocities with increasing shell wall temperature. This tendency is found to be counteracted by axial temperature variations which also may have a considerable influence on the limit cycle amplitudes at certain gas velocities.

1. Introduction

A thin-walled circular cylindrical shell, Fig. 1, exposed at one of its sides to a super-sonic gas stream parallell to its axis, may exhibit self-excited oscillations provided that certain critical conditions are fulfilled. These conditions depend among other factors on the material properties of the shell wall, which in their turn depend on the temperature field to which the shell is exposed. Thus, one might expect that large temperature variations as in e.g. a jet engine afterburner, should have a considerable effect on the critical conditions as well as on the amplitude and frequency of the excited oscillations.

The presence of such effects has been shown by Ambartsumian et al.[1], who found that the critical gas velocity at linear flutter of an infinite circular cylindrical shell may decrease by as much as 50% when the shell is exposed to a uniformly distributed, linearly transient temperature field. Likewise, it has been found by Tang[2], that the frequency of linear free vibrations or plates may be reduced up to 10% if the plate is exposed to a nonuniformly distributed, stationary temperature field.

Taking care of the temperature dependence of the material properties at generally varying temperature fields is the same as to introduce general anisotropy into the material . Such problems are untractable to analytic solutions and hitherto only a few one-dimensional cases have been solved. The work was started in the fifties by Hilton[3] and Nowinski[4]. Further progress was made by Trostel[5,6], who used perturbation methods to solve the general stationary thermoelastic problem. Subsequent works have used the same methods in analyzing the stress states in circular plates and thickwalled cylinders and spheres[7-12]. For a review of this earlier literature, see Ref 13. More recently, extensions have been given to thin-walled shells of revolution by Ismail and Nowinski[14] and to stationary thermal stresses in rectangular plates and simply connected bodies by Tang[15,16].

It is the intention here to investigate the influence of the temperature dependence of the material properties on the supersonic flutter of a finite, circular cylindrical shell exposed to an axially non-uniform and exponentially transient temperature field. In order to use the methods developed for isothermal problems of this type, [17,18] we begin by deriving non-linear differential equations for a circular cylindrical shell taking care of the temperature dependence of the material properties. This has been done in Ref. 1 for general shells of revolution and linearly for plates in Ref. 15. This done, we will expand the radial deflection of the shell in functions satisfying the prescribed boundary conditions and use Galerkin's variational method in order to reduce the problem to a set of nonlinear ordinary differential equations in the time variable. These equations will then be solved asymptotically according to the method of Krylov-Bogoliubov[19]. With the help of these solutions, the influence of axially and transiently varying temperatures on the stability of the flutter oscillations will be studied.

2. Basic equations

Let the median surface of the cylindrical shell be described by the longitudinal coordinate ξ and the circumferential coordinate η. Let the coordinate ζ be directed along the outward normal of the median surface. Further, let (u,v,w) be the corresponding displacement vector in the (ξ,η,ζ)-system, Fig. 1.

Then, using geherally known simplifications from the thin shell theory, the strains in the median surface will be:

$$\varepsilon_{\xi\xi} = \frac{\partial u}{\partial \xi} - \zeta \frac{\partial^2 w}{\partial \xi^2} + \frac{1}{2}\left(\frac{\partial w}{\partial \xi}\right)^2 \qquad (1)$$

$$2\varepsilon_{\xi\eta} = \frac{\partial u}{\partial \eta} + \frac{\partial v}{\partial \xi} - 2\zeta \frac{\partial^2 w}{\partial \xi \partial \eta} + \frac{\partial w}{\partial \xi}\frac{\partial w}{\partial \eta} \qquad (2)$$

$$\varepsilon_{\eta\eta} = \frac{\partial v}{\partial \eta} - \zeta \frac{\partial^2 w}{\partial \eta^2} + \frac{w}{R} + \frac{1}{2}\left(\frac{\partial w}{\partial \eta}\right)^2 \qquad (3)$$

Using Hookeś law in plane state of stress, assuming $\zeta << R$ and introducing

$$\varepsilon_T = \int_0^\theta \alpha(x)\,dx \qquad (4)$$

$$N_{ij} = \int_{-\delta/2}^{\delta/2} \sigma_{ij}\,d\zeta \qquad (5)$$

$$M_{ij} = \int_{-\delta/2}^{\delta/2} \sigma_{ij}\,\zeta\,d\zeta \qquad (i,j) = (\xi,\eta) \qquad (6)$$

give

$$N_{\xi\xi} = E_1\left[\frac{\partial u}{\partial \xi} + \frac{1}{2}\left(\frac{\partial w}{\partial \xi}\right)^2\right] - E_2\frac{\partial^2 w}{\partial \xi^2}$$

$$+E_3\left[\frac{\partial v}{\partial \eta} + \frac{w}{R} + \frac{1}{2}\left(\frac{\partial w}{\partial \eta}\right)^2\right] - E_4\frac{\partial^2 w}{\partial \eta^2} - N_T \qquad (7)$$

$$N_{\eta\eta} = E_1\left[\frac{\partial v}{\partial \eta} + \frac{w}{R} + \frac{1}{2}\left(\frac{\partial w}{\partial \eta}\right)^2\right] - E_2\frac{\partial^2 w}{\partial \eta^2}$$

$$+E_3\left[\frac{\partial u}{\partial \xi} + \frac{1}{2}\left(\frac{\partial w}{\partial \xi}\right)^2\right] - E_4\frac{\partial^2 w}{\partial \xi^2} - N_T \qquad (8)$$

$$N_{\xi\eta} = \frac{1}{2}E_5\left[\frac{\partial u}{\partial \eta} + \frac{\partial v}{\partial \xi} + \frac{\partial w}{\partial \xi}\frac{\partial w}{\partial \eta}\right] - E_6\frac{\partial^2 w}{\partial \xi\,\partial \eta} \qquad (9)$$

$$M_{\xi\xi} = E_2\left[\frac{\partial u}{\partial \xi} + \frac{1}{2}\left(\frac{\partial w}{\partial \xi}\right)^2\right] - E_7\frac{\partial^2 w}{\partial \xi^2}$$

$$+E_4\left[\frac{\partial v}{\partial \eta} + \frac{w}{R} + \frac{1}{2}\left(\frac{\partial w}{\partial \eta}\right)^2\right] - E_8\frac{\partial^2 w}{\partial \eta^2} - M_T \qquad (10)$$

$$M_{\eta\eta} = E_2\left[\frac{\partial v}{\partial \eta} + \frac{w}{R} + \frac{1}{2}\left(\frac{\partial w}{\partial \eta}\right)^2\right] - E_7\frac{\partial^2 w}{\partial \eta^2}$$

$$+E_4\left[\frac{\partial u}{\partial \xi} + \frac{1}{2}\left(\frac{\partial w}{\partial \xi}\right)^2\right] - E_8\frac{\partial^2 w}{\partial \xi^2} - M_T \qquad (11)$$

$$M_{\xi\eta} = \frac{1}{2}E_6\left[\frac{\partial u}{\partial \eta} + \frac{\partial v}{\partial \xi} + \frac{\partial w}{\partial \xi}\frac{\partial w}{\partial \eta}\right] - E_9\frac{\partial^2 w}{\partial \xi\,\partial \eta} \qquad (12)$$

where

$$E_1 = \int_{-\delta/2}^{\delta/2} \frac{E}{1-\nu^2}\, d\zeta \qquad E_2 = \int_{-\delta/2}^{\delta/2} \frac{E}{1-\nu^2}\, \zeta\, d\zeta$$

$$E_3 = \int_{-\delta/2}^{\delta/2} \frac{\nu E}{1-\nu^2}\, d\zeta \qquad E_4 = \int_{-\delta/2}^{\delta/2} \frac{\nu E}{1-\nu^2}\, \zeta\, d\zeta$$

$$E_5 = \int_{-\delta/2}^{\delta/2} \frac{E}{1+\nu}\, d\zeta \qquad E_6 = \int_{-\delta/2}^{\delta/2} \frac{E}{1+\nu}\, \zeta\, d\zeta$$

$$E_7 = \int_{-\delta/2}^{\delta/2} \frac{E}{1-\nu^2}\, \zeta^2 d\zeta \quad E_8 = \int_{-\delta/2}^{\delta/2} \frac{\nu E}{1-\nu^2}\, \zeta^2 d\zeta \qquad (13)$$

$$E_9 = \int_{-\delta/2}^{\delta/2} \frac{E}{1+\nu}\, \zeta^2 d\zeta \qquad N_T = \int_{-\delta/2}^{\delta/2} \frac{E}{1-\nu}\, \epsilon_T d\zeta$$

$$M_T = \int_{-\delta/2}^{\delta/2} \frac{E}{1-\nu}\, \epsilon_T \zeta\, d\zeta$$

Lastly, the equations of equilibrium are

$$\frac{\partial N_{\xi\xi}}{\partial \xi} + \frac{\partial N_{\xi\eta}}{\partial \eta} + q_{\xi} = 0 \qquad (14)$$

$$\frac{\partial N_{\xi\eta}}{\partial \xi} + \frac{\partial N_{\eta\eta}}{\partial \eta} + q_{\eta} = 0 \qquad (15)$$

$$\frac{\partial^2 M_{\xi\xi}}{\partial \xi^2} + 2\frac{\partial^2 M_{\xi\eta}}{\partial \xi \partial \eta} + \frac{\partial^2 M_{\eta\eta}}{\partial \eta^2} + N_{\xi\xi}\frac{\partial^2 w}{\partial \xi^2} + 2N_{\xi\eta}\frac{\partial^2 w}{\partial \xi \partial \eta}$$

$$+ N_{\eta\eta}\left(\frac{\partial^2 w}{\partial \eta^2} - \frac{1}{R}\right) + q_{\zeta} = 0 \qquad (16)$$

where (q_ξ, q_η, q_ζ) are load components per unit surface in the directions (ξ, η, ζ). Taking care of inertial forces in the radial direction, one has

$$q_\zeta = q - \rho_s\, \delta\, \frac{\partial^2 w}{\partial t^2} \tag{17}$$

where q is the load intensity due to external forces normal to the surface.

Eqs. (14)-(15) are satisfied identically if the tangential forces are expressed in a stress function Φ as:

$$N_{\xi\xi} = \frac{\partial^2 \Phi}{\partial \eta^2} + V_{\xi\xi} \tag{18}$$

$$N_{\eta\eta} = \frac{\partial^2 \Phi}{\partial \xi^2} + V_{\eta\eta} \tag{19}$$

$$N_{\xi\eta} = - \frac{\partial^2 \Phi}{\partial \xi \partial \eta} \tag{20}$$

where:

$$q_\xi = - \frac{\partial V_{\xi\xi}}{\partial \xi} \tag{21}$$

$$q_\eta = - \frac{\partial V_{\eta\eta}}{\partial \eta} \tag{22}$$

From Eqs. (7)-(9), the derivatives of u and v may be solved and introduced into Eqs. (10)-(12) together with Eqs. (18)-(20). Thus the tangential moments are expressed into Φ and w and may be introduced into Eq. (16) to give a differential equation

$$\frac{\partial^2}{\partial\xi^2}\Big[K_3\Big(\frac{\partial^2\Phi}{\partial\xi^2}+V_{\eta\eta}+N_T\Big)+K_4\Big(\frac{\partial^2\Phi}{\partial\eta^2}+V_{\xi\xi}+N_T\Big)+$$

$$+K_5\frac{\partial^2 w}{\partial\eta^2}+K_6\frac{\partial^2 w}{\partial\xi^2}-M_T\Big]$$

$$+2\frac{\partial^2}{\partial\xi\partial\eta}\Big[-K_7\frac{\partial^2\Phi}{\partial\xi\partial\eta}+K_8\frac{\partial^2 w}{\partial\xi\partial\eta}\Big]$$

$$+\frac{\partial^2}{\partial\eta^2}\Big[K_4\Big(\frac{\partial^2\Phi}{\partial\xi^2}+V_{\eta\eta}+N_T\Big)+K_3\Big(\frac{\partial^2\Phi}{\partial\eta^2}+V_{\xi\xi}+N_T\Big)$$

$$+K_6\frac{\partial^2 w}{\partial\eta^2}+K_5\frac{\partial^2 w}{\partial\xi^2}-M_T\Big]$$

$$+\Big[\frac{\partial^2\Phi}{\partial\eta^2}+V_{\xi\xi}\Big]\frac{\partial^2 w}{\partial\xi^2}-2\frac{\partial^2 w}{\partial\xi\partial\eta}\frac{\partial^2\Phi}{\partial\xi\partial\eta}$$

$$+\Big(\frac{\partial^2 w}{\partial\eta^2}-\frac{1}{R}\Big)\Big(\frac{\partial^2\Phi}{\partial\xi^2}+V_{\eta\eta}\Big)+q_\zeta=0 \qquad (23)$$

Eliminating u and v in Eqs. (7)-(9) and introducing Eqs. (18)-(20) gives a compatibility equation, which after some rewriting becomes

$$\frac{\partial^2}{\partial\xi^2}\Big[K_1\Big(\frac{\partial^2\Phi}{\partial\xi^2}+V_{\eta\eta}+N_T\Big)-K_2\Big(\frac{\partial^2\Phi}{\partial\eta^2}+V_{\xi\xi}+N_T\Big)$$

$$+K_4\frac{\partial^2 w}{\partial\eta^2}+K_3\frac{\partial^2 w}{\partial\xi^2}\Big]$$

$$+\frac{\partial^2}{\partial\eta^2}\Big[K_1\Big(\frac{\partial^2\Phi}{\partial\eta^2}+V_{\xi\xi}+N_T\Big)-K_2\Big(\frac{\partial^2\Phi}{\partial\xi^2}+V_{\eta\eta}+N_T\Big)$$

$$+K_4\frac{\partial^2 w}{\partial\xi^2}+K_3\frac{\partial^2 w}{\partial\eta^2}\Big]$$

$$+\frac{\partial^2}{\partial\xi\partial\eta}\left[-2K_7\frac{\partial^2 w}{\partial\xi\partial\eta}+K_9\frac{\partial^2\Phi}{\partial\xi\partial\eta}\right]$$

$$-\frac{1}{R}\frac{\partial^2 w}{\partial\xi^2}-\left(\frac{\partial^2 w}{\partial\xi\partial\eta}\right)^2+\frac{\partial^2 w}{\partial\xi^2}\frac{\partial^2 w}{\partial\eta^2}=0 \qquad (24)$$

The coefficients K_n are

$$K_1=\frac{E_1}{E_1^{\,2}-E_3^{\,2}} \qquad K_2=\frac{E_3}{E_1^{\,2}-E_3^{\,2}}$$

$$K_3=\frac{E_1E_4-E_2E_3}{E_1^{\,2}-E_3^{\,2}} \qquad K_4=\frac{E_1E_2-E_3E_4}{E_1^{\,2}-E_3^{\,2}}$$

$$K_5=E_2K_3+E_4K_4-E_8 \qquad K_6=E_2K_4+E_4K_3-E_7 \qquad (25)$$

$$K_7=\frac{E_6}{E_5} \qquad K_8=\frac{E_6^{\,2}}{E_5}-E_9 \qquad K_9=\frac{2}{E_5}$$

Eqs. (23) and (24) give two relations, from which Φ and w may be solved using familiar boundary conditions. These equations are a special case of those given in Ref. 1 for general shells of revolution. For E and ν constants, the usual Donnell equations are obtained. With ν a constant, letting $R\to\infty$, the linear parts of Eqs. (23) and (24) correspond to the plate equations given in Ref. 15.

Eqs. (23) and (24) are valid for arbitrarily variable material properties. In what follows we will restrict the analysis to properties which, besides with time, vary only in the axial direction. This will simplify the equations considerably.

3. Ordinary differential equations

The shell geometry and the coordinate system are shown in Fig. 1. An internal pressure is acting on the cylindrical shell, which is also exposed at one of its sides to a supersonic flow parallell to the axial direction. Furthermore, an axial tensile load $2\pi RN$ is applied to the shell. Inertia forces in the plane of the shell will be neglected. If the Mach number of the flow is sufficiently high, $M>2$, then the resulting aerodynamic forces on the surface of the shell may be approximated by the linear piston theory including a curvature correction term [20]. The expression for the normal load intensity then will be

$$q_\zeta = p_m - \rho a U \frac{\partial w}{\partial \xi} - \rho a \frac{\partial w}{\partial t} + \frac{\rho a^2}{2R} w - \delta \rho_s \frac{\partial^2 w}{\partial t^2} \qquad (26)$$

The ends of the shell are assumed to be elastically supported but will be free to move both radially and axially due to the influence of internal pressure and wall temperature.

In order to investigate the dynamic stability of the shell about its deformed median surface, w and Φ are separated into quasistatic and dynamic components as follows

$$w = w_s(\xi) + w_d(\xi,\eta,t) \qquad (27)$$

$$\Phi = \Phi_s(\xi,\eta) + \Phi_d(\xi,\eta,t) \qquad (28)$$

where we note that the prestability deformations are axisymmetric due to the circumferentially uniform temperature and loading conditions.

Because equilibrium and compatibility must be maintained during prestability conditions, the static components form one set of equations governing the static prestability response of the shell. The dynamic components then form a second set of equations, coupled to the first through the nonlinearity and the static deformations.

Introducing Eq. (26) into the general shell equations (23) and (24), gives the static equations

$$\frac{\delta^3}{12} \frac{\partial^2}{\partial \xi^2} \left(\frac{E}{1-\nu^2} \frac{\partial^2 w_s}{\partial \xi^2}\right) + \frac{1}{R} \frac{\partial^2 \Phi_s}{\partial \xi^2} - p_m + \rho a U \frac{\partial w_s}{\partial \xi}$$

$$- \frac{\rho a^2}{2R} w_s - \frac{\partial^2 w_s}{\partial \xi^2} \frac{\partial^2 \Phi_s}{\partial \eta^2} + \frac{\partial^2 M_T}{\partial \xi^2} = 0 \tag{29}$$

$$\frac{\partial^2}{\partial \xi^2} \left(\frac{1}{E} \frac{\partial^2 \Phi_s}{\partial \xi^2} - \frac{\nu}{E} \frac{\partial^2 \Phi_s}{\partial \eta^2}\right) + \frac{\partial^2}{\partial \eta^2} \left(\frac{1}{E} \frac{\partial^2 \Phi_s}{\partial \eta^2} - \frac{\nu}{E} \frac{\partial^2 \Phi_s}{\partial \xi^2}\right)$$

$$+2 \frac{\partial^2}{\partial \xi \partial \eta}\left(\frac{1+\nu}{E} \frac{\partial^2 \Phi_s}{\partial \xi \partial \eta}\right) + \frac{\partial^2}{\partial \xi^2}\left(\frac{1-\nu}{E} N_T\right) - \frac{\delta}{R} \frac{\partial^2 w_s}{\partial \xi^2} = 0 \tag{30}$$

where it has been assumed that the temperature difference through the thin shell wall is so small that radial variations of the material properties may be neglected.

The associated steady state boundary conditions at $\xi=0$ and $\xi=L$ are

$$w_s = \frac{R}{\delta}\,\frac{1-\nu}{E}\,N_T + \frac{p_m R^2}{\delta E} = w_{0,L} \tag{31}$$

$$\frac{\delta^3}{12}\,\frac{E}{1-\nu^2}\,\frac{\partial^2 w_s}{\partial \xi^2} + M_T = 0 \tag{32}$$

$$N_{\xi\xi} = \frac{\partial^2 \Phi_s}{\partial \eta^2} = N \tag{33}$$

$$N_{\xi\eta} = -\frac{\partial^2 \Phi_s}{\partial \xi \partial \eta} = 0 \tag{34}$$

In order to solve Eqs. (29) and (30) we introduce

$$\Phi_s(\xi,\eta) = \frac{1}{2} N\eta^2 + \Psi_s(\xi) \tag{35}$$

which satisfies Eqs. (33) and (34).
Substituting Eq. (35) into Eqs. (29) and (30), we find that these equations may be reduced to one single linear equation

$$\frac{\partial^2}{\partial \xi^2}\left(\frac{E}{1-\nu^2}\,\frac{\delta^3}{12}\,\frac{\partial^2 w_s}{\partial \xi^2}\right) + \frac{\nu N}{R} - \frac{1-\nu}{R}\,N_T + \frac{\delta E}{R^2}\,w_s - p_m$$

$$+ \rho a U\,\frac{\partial w_s}{\partial \xi} - \frac{\rho a^2}{2R}\,w_s - N\,\frac{\partial^2 w_s}{\partial \xi^2} + \frac{\partial^2 M_T}{\partial \xi^2} = 0 \tag{36}$$

with the boundary conditions (31) and (32).

In the case of temperature independent material properties this equation could be solved exactly [21], but here we must resort to approximate methods. We therefore assume the following mode of deflection

$$w_s = w_o + (w_L - w_o)\frac{\xi}{L} + \delta f_s \sin\frac{\pi\xi}{L} + \delta g_s \sin\frac{2\pi\xi}{L} \quad (37)$$

and using Galerkin's method obtain a system of algebraic equations from which the non-dimensional deflection parameters f_s and g_s may be solved.

Having derived the static solution we obtain the differential equations for the dynamic problem through introducing Eqs. (27)-(28) into Eqs. (23)-(24), giving

$$\frac{\delta^3}{12}\frac{\partial^2}{\partial\xi^2}\left(\frac{\nu E}{1-\nu^2}\frac{\partial^2 w_d}{\partial\eta^2} + \frac{E}{1-\nu^2}\frac{\partial^2 w_d}{\partial\xi^2}\right) + \frac{\delta^3}{6}\frac{\partial^2}{\partial\xi\partial\eta}\left(\frac{E}{1+\nu}\frac{\partial^2 w_d}{\partial\xi\partial\eta}\right)$$

$$+ \frac{\delta^3}{12}\frac{\partial^2}{\partial\eta^2}\left(\frac{E}{1-\nu^2}\frac{\partial^2 w_d}{\partial\eta^2} + \frac{\nu E}{1-\nu^2}\frac{\partial^2 w_d}{\partial\xi^2}\right) + \frac{1}{R}\frac{\partial^2 \Phi_d}{\partial\xi^2} + \rho\, aU\frac{\partial w_d}{\partial\xi}$$

$$- \frac{\rho a^2}{2R} w_d + \rho a\frac{\partial w_d}{\partial t} + \delta\rho_s\frac{\partial^2 w_d}{\partial t^2} - \frac{\partial^2 w_s}{\partial\xi^2}\frac{\partial^2 \Phi_d}{\partial\eta^2} - N\frac{\partial^2 w_d}{\partial\xi^2}$$

$$- \frac{\partial^2 w_d}{\partial\xi^2}\frac{\partial^2 \Phi_d}{\partial\eta^2} + 2\frac{\partial^2 w_d}{\partial\xi\partial\eta}\frac{\partial^2 \Phi_d}{\partial\xi\partial\eta} - \frac{\partial^2 w_d}{\partial\eta^2}\frac{\partial^2 \Psi_s}{\partial\xi^2} -$$

$$- \frac{\partial^2 w_d}{\partial\eta^2}\frac{\partial^2 \Phi_d}{\partial\xi^2} = 0 \quad (38)$$

$$\frac{1}{\delta}\frac{\partial^2}{\partial\xi^2}\left(\frac{1}{E}\frac{\partial^2 \Phi_d}{\partial\xi^2} - \frac{\nu}{E}\frac{\partial^2 \Phi_d}{\partial\eta^2}\right) + \frac{1}{\delta}\frac{\partial^2}{\partial\eta^2}\left(\frac{1}{E}\frac{\partial^2 \Phi_d}{\partial\eta^2} - \frac{\nu}{E}\frac{\partial^2 \Phi_d}{\partial\xi^2}\right)$$

$$+ \frac{2}{\delta}\frac{\partial^2}{\partial\xi\partial\eta}\left(\frac{1+\nu}{E}\frac{\partial^2 \Phi_d}{\partial\xi\partial\eta}\right) - \frac{1}{R}\frac{\partial^2 w_d}{\partial\xi^2} - \left(\frac{\partial^2 w_d}{\partial\xi\partial\eta}\right)^2$$

$$+ \frac{\partial^2 w_s}{\partial\xi^2}\frac{\partial^2 w_d}{\partial\eta^2} + \frac{\partial^2 w_d}{\partial\xi^2}\frac{\partial^2 w_d}{\partial\eta^2} = 0 \quad (39)$$

To these equations a solution w_d is assumed in the form

$$w_d = \delta(f_d \sin\frac{\pi\xi}{L} + g_d \sin\frac{2\pi\xi}{L}) \cos\frac{m\eta}{R}$$

$$-\delta^2 \frac{m^2}{4R} (f_d \sin\frac{\pi\xi}{L} + g_d \sin\frac{2\pi\xi}{L})^2 \qquad (40)$$

where the last term must be included in order to satisfy the periodic continuity condition on the circumferential displacement v [22]. In the temperature independent case, substitution of Eq. (40) into the compatibility equation, Eq. (39), allows the latter to be solved for the particular solution Φ_d, while the complementary solution is assumed to vanish. [17,18] Here, the variable coefficients of Eq. (39) make the problem more complicated. It is assumed that Φ_d has the same form as in the temperature independent case, i.e.

$$\Phi_d = \cos\frac{m\eta}{R}\sum_{n=1}^{6} F_n \sin\frac{n\pi\xi}{L} + \cos\frac{2m\eta}{R}\sum_{n=0}^{4} F_{n+7} \cos\frac{n\pi\xi}{L}$$

$$+ \cos\frac{m\eta}{R}\sum_{n=0}^{4} F_{n+12} \cos\frac{n\pi\xi}{L} \qquad (41)$$

Then, the parameters F_n are solved in the nonlinear deflection parameters f_d and g_d through substituting Eq. (41) into Eq. (39) and using Galerkin's method with $\frac{\partial\Phi_d}{\partial F_n}$ as weighting functions. When the stress function Φ_d has been found, it is introduced into Eq. (38) together with the assumed form of w_d and

Galerkin's method is again used to derive nonlinear ordinary differential equations for the functions f_d and g_d. Now $\frac{\partial w_d}{\partial f_d}$ and $\frac{\partial w_d}{\partial g_d}$ are used as weighting functions.

The assumed form of w_d and the corresponding solution for ϕ_d imply that the following boundary conditions are satisfied

1. The displacements u, v, w and their derivatives satisfy periodic continuity conditions of the form

   $v(\xi,\eta,t) = v(\xi,\eta+2\pi R,\ t)$

2. The deflection w vanishes identically at $\xi=0$ and $\xi=L$, while for v only the linear parts vanish there.
3. The assumed w_d corresponds to an elastically supported shell and the in-plane loading conditions are satisfied in the average at the ends of the shell.

In carrying out the calculations indicated above, it is found that the coefficients F_n may be derived from a vector equation

$$A\,\underset{\sim}{F} + C\,\underset{\sim}{H} = 0 \tag{42}$$

where the transposed vectors are

$$\underset{\sim}{F}' = (F_1,\ F_2,\ \dots\ F_{16}) \tag{43}$$

$$\underset{\sim}{H}' = (f_d, g_d, f_d^2, f_d g_d, g_d^2, f_d^3, f_d^2 g_d, f_d g_d^2, g_d^3) \tag{44}$$

In Eq. (42), A is a 16x16 matrix emanating from those parts of Eq. (39), which include Φ_d, while C is a 9x16 matrix emanating from the other parts of this equation. The elements of these matrices are not written out here because of brevity, they may be found in Ref. 23.

From Eq. (42), the coefficients F_n are found in the form

$$F_n = \psi_{n1} f_d + \psi_{n2} g_d + \psi_{n3} f_d^2 + \psi_{n4} f_d g_d + \psi_{n5} g_d^2 + \psi_{n6} f_d^3 + \psi_{n7} f_d^2 g_d + \psi_{n8} f_d g_d^2 + \psi_{n9} g_d^3 \quad (45)$$

where ψ_{ij} are constants.

Lastly, the nonlinear ordinary differential equations for f_d and g_d will be, neglecting indices for convenience

$$\begin{aligned}
&(1+\frac{3}{8}\mu f^2+\frac{1}{4}\mu g^2)\frac{\partial^2 f}{\partial t^2}+\frac{1}{2}\mu f g\frac{\partial^2 g}{\partial t^2}+(\frac{a\rho}{\delta\rho_s}+\mu\frac{3a\rho}{8\delta\rho_s}f^2 \\
&+\mu\frac{a\rho}{4\delta\rho_s}g^2+\frac{3}{8}\mu f\frac{\partial f}{\partial t})\frac{\partial f}{\partial t}+\mu(\frac{a\rho}{2\delta\rho_s}fg \\
&+\frac{1}{4}\ f\frac{\partial g}{\partial t})\frac{\partial g}{\partial t}+a_1 f+a_2 g+a_3 f^2+a_4 f g+a_5 g^2 \\
&+a_6 f^3+a_7 f^2 g+a_8 f g^2+a_9 g^3+a_{10} f^4+a_{11} f^3 g \\
&+a_{12} f^2 g^2+a_{13} f g^3+a_{14} g^4+a_{15} f^5+a_{16} f^4 g \\
&+a_{17} f^3 g^2+a_{18} f^2 g^3+a_{19} f g^4+a_{20} g^5 = a_{21} \quad (46)
\end{aligned}$$

$$\left(1+\frac{3}{8}\mu g^2+\frac{1}{4}\mu f^2\right)\frac{\partial^2 g}{\partial t^2}+\frac{1}{2}\mu fg\frac{\partial^2 f}{\partial t^2}$$

$$+\left(\frac{a\rho}{\delta\rho_s}+\mu\frac{3a\rho}{8\delta\rho_s}g^2+\mu\frac{a\rho}{4\delta\rho_s}f^2+\frac{3}{8}\mu g\frac{\partial g}{\partial t}\right)\frac{\partial g}{\partial t}$$

$$+\mu\left(\frac{a\rho}{2\delta\rho_s}fg+\frac{1}{4}g\frac{\partial f}{\partial t}\right)\frac{\partial f}{\partial t}+b_1 f+b_2 g$$

$$+b_3 f^2+b_4 f g+b_5 g^2+b_6 f^3+b_7 f^2 g+b_8 f g^2$$

$$+b_9 g^3+b_{10} f^4+b_{11} f^3 g+b_{12} f^2 g^2+b_{13} f g^3$$

$$+b_{14} g^4+b_{15} f^5+b_{16} f^4 g+b_{17} f^3 g^2+b_{18} f^2 g^3$$

$$+b_{19} f g^4+b_{20} g^5 = b_{21} \qquad (47)$$

where the coefficients depend on the parameter μ so that μ=o linearizes the equations.

In order to solve Eqs. (46) and (47) we introduce the material properties E, ν and α in the form $E=E_o+\varepsilon E_1 \ \theta$, where ε is a small arbitrary parameter. Then for a temperature field

$$\theta = \theta_o(t) + \theta_1(t)\cos\frac{\pi\xi}{L} \qquad (48)$$

retaining only first order terms in ε and μ, the nonvanishing coefficients will be

$$a_1 = \frac{\omega_o^2\,\mu}{12(1-\nu_o^2)}\,(1+\beta^2)^2\,\left(1+\varepsilon\frac{E_1}{E_o}\,\theta_o+\varepsilon\frac{2\nu_o\nu_1}{1-\nu_o^2}\,\theta_o\right)$$

$$+\frac{\omega_o^2\,\beta^4}{(1+\beta^2)^2}\,\left(1+\varepsilon\frac{E_1}{E_o}\,\theta_o\right)+\frac{m^2}{\rho_s\delta R^2}\,N\nu_o\left(1+\varepsilon\frac{\nu_1}{\nu_o}\,\theta_o\right)$$

$$+\frac{m^2\beta^2}{\rho_s\delta R^2}\,N+\frac{m^2}{\rho_s\delta R}\,p_m-\frac{a^2\rho}{2\delta R\rho_s}$$

$$a_2 = -\frac{8a\rho}{3\delta L\rho_s}\,U+\varepsilon\left(1+\frac{1}{4\beta^4}\right)\frac{2\beta^4\mu\omega_o^2}{12(1-\nu_o^2)}\left(\frac{E_1}{E_o}+\frac{2\nu_o\nu_1}{1-\nu_o^2}\right)\theta_1$$

$$+\varepsilon\frac{\beta^2\mu\,\omega_o^2}{24(1-\nu_o^2)}\left[5\nu_o\left(\frac{E_1}{E_o}+\frac{\nu_1}{\nu_o}+\frac{2\nu_o\nu_1}{1-\nu_o^2}\right)+\right.$$

$$\left.+4(1-\nu_o)\left(\frac{E_1}{E_o}-\frac{\nu_1}{1+\nu_o}\right)\right]\theta_1+\varepsilon\left[2\,\frac{E_1}{E_o}\,(1+2\beta^2)^2\,\beta^4\omega_o^2+\right.$$

$$\left.+2\nu_o\omega_o^2\beta^6\left(\frac{\nu_1}{\nu_o}-\frac{E_1}{E_o}\right)\right](1+\beta^2)^{-2}\,(1+4\beta^2)^{-2}\,\theta_1$$

$$+\,\varepsilon\frac{m^2}{2\rho_s\delta R^2}\,N\,\nu_1\theta_1$$

$$a_3 = a_4 = a_5 = 0$$

$$a_6 = -\frac{\omega_o^2\beta^4\mu}{(1+\beta^2)^2}+\frac{\omega_o^2\mu^2\beta^4}{12(1-\nu_o^2)}+\frac{\omega_o^2\beta^4\mu}{16}-\frac{3\mu a^2\rho}{32\delta R\rho_s}+$$

$$+\frac{\mu\pi^2}{4\rho_s\delta L^2}\,N$$

$$a_7 = -\frac{8\mu a\rho}{15\delta L\rho_s} U$$

$$a_8 = \frac{41\mu^2\beta^4\omega_o^2}{48(1-\nu_o^2)} - \frac{5\mu\omega_o^2\beta^4}{2(1+\beta^2)^2} - \frac{10\mu\omega_o^2\beta^4}{(1+4\beta^2)^2} + \frac{\mu\omega_o^2\beta^4}{4}$$

$$+ \frac{81\mu\omega_o^2\beta^4}{16(4+\beta^2)^2} + \frac{\mu\omega_o^2\beta^4}{16(4+9\beta^2)^2} + \frac{5\mu\pi^2}{4\rho_s\delta L^2} N - \frac{3\mu a^2\rho}{16\rho_s\delta R}$$

$$a_9 = -\frac{32\mu a\rho U}{105\delta L\rho_s}$$

$$b_1 = a_2 + \frac{16a\rho U}{3\delta L\rho_s}$$

$$b_2 = \frac{\mu\omega_o^2}{12(1-\nu_o^2)} (1+4\beta^2)^2 \left(1+\varepsilon\frac{E_1}{E_o}\theta_o + \varepsilon\frac{2\nu_o\nu_1}{1-\nu_o^2}\theta_o\right)$$

$$+ \frac{16\omega_o^2\beta^4}{(1+4\beta^2)^2}\left(1+\varepsilon\frac{E_1}{E_o}\theta_o\right) + \frac{m^2}{\rho_s\delta R^2}\nu_o N\left(1+\varepsilon\frac{\nu_1}{\nu_o}\theta_o\right)$$

$$+ \frac{m^2}{\rho_s\delta R^2} 4\beta^2 N + \frac{m^2}{\rho_s\delta R} p_m - \frac{a^2\rho}{2\delta R\rho_s}$$

$$b_3 = b_4 = b_5 = o$$

$$b_6 = -a_7$$

$$b_7 = a_8$$

$$b_8 = -a_9$$

$$b_9 = \frac{4\omega_o^2\mu^2\beta^4}{3(1-\nu_o^2)} - \frac{16\mu\omega_o^2\beta^4}{(1+4\beta^2)^2} + \mu\omega_o^2\beta^4 + \frac{\mu\pi^2}{\rho_s\delta L^2}N - \frac{3\mu a^2\rho}{32\delta R\rho_s} \quad (49)$$

where

$$\mu = \frac{m^4\delta^2}{R^2} \qquad \omega_o^2 = \frac{E_o}{\rho_s R^2} \qquad \beta = \frac{\pi R}{mL}$$

To facilitate the calculations, the quasistatic deflections have been neglected in the derivation of these coefficients. This is motivated by the fact that the ends of the shell are free to expand with the temperature and the internal pressure. Therefore, at realistic axial temperature variations and internal pressures, the quasistatic deflections should be small compared to the dynamic ones.

4. Solutions

According to linear flutter theory in the isothermal case, disturbances of the modal amplitudes away from zero are damped out with time as long as the gas velocity U is below a certain critical value U_c. Conversely, the linear theory predicts that the amplitudes will grow exponentially with time when U is greater than U_c. However, the conditions are somewhat more complicated when nonlinear terms are taken into account. Thus, at stationary temperature fields, steady-state vibrations with finite amplitudes, so called "limit cycle oscillations", may occur.[24] Eqs. (46) and (47) describe such oscillations.

These equations are too complicated to be solved exactly. Thus, approximate methods must be resorted to and here we will use the one due to Krylov and Bogoliubov.[19] Experiments indicate,[17] that the flutter motion is nearly sinusoidal in time so that the solutions may be sought in the form

$$f = F \cos \psi \qquad (50)$$

$$g = G \cos (\psi + \phi) \qquad (51)$$

where F, G and ϕ are slowly varying functions of time for which we assume[19]

$$\frac{dF}{dt} = \mu F_1 \, (F, G, \mu t) \qquad (52)$$

$$\frac{dG}{dt} = \mu G_1 \, (F, G, \mu t) \qquad (53)$$

$$\frac{d\psi}{dt} = \Omega = \Omega_{co} + \mu\psi_1 \; (F, G, \mu t) \tag{54}$$

$$\frac{d\phi}{dt} = \mu\phi_1 \; (F, G, \mu t) \tag{55}$$

In the first order approximation, the method of Krylov and Bogoliubov reduces to that of harmonic balance. Eqs. (50)-(51) are differentiated twice taking care of Eqs. (52)-(55) and then substituted into Eqs. (46)-(47). The resulting expressions are linearized with regard to ε and μ and grouped into terms multiplying $\sin\psi$, $\cos\psi$ and higher harmonics of ψ. Then, following the method of harmonic balance, these expressions are multiplied successively by $\sin\psi$ and $\cos\psi$ and integrated in ψ from 0 to 2π. This gives four first order differential equations for the functions F, G, ϕ and Ω in the form

$$Y_i = A_{ij} \; (U, t, \phi) \; X_j \tag{56}$$

where the transposed vectors are

$$\underset{\sim}{Y}' = \left\{ \frac{dF}{dt}, F(\Omega - \Omega_{co}), \frac{dG}{dt}, G(\frac{d\phi}{dt} + \Omega - \Omega_{co}) \right\} \tag{57}$$

$$\underset{\sim}{X}' = \left\{ F, G, F^3, F^2G, FG^2, G^3 \right\} \tag{58}$$

and where A_{ij} is a 4x6 matrix which is not written out here because of brevity.

For steady-state oscillations we obtain a set of algebraic equations, whose solutions give the limit cycle amplitudes. For instationary oscillations, Eqs. (56) provide solutions for the variation of the amplitudes, the phase angle and the frequency with time.

Eqs. (56) must be solved numerically under prescribed initial conditions. This is, however, much easier than to calculate the solutions to Eqs. (46)-(47) directly. This is because there appear only slowly transient functions in Eqs. (56). Therefore, it is sufficient to calculate a relatively small number of points along comparatively smooth curves in order to obtain the solutions. In the direct integration of Eqs. (46)-(47) we have to determine not an envelope but a rapidly varying sinusoid.

In the linear case, i.e. $\mu = o$, it is possible to find analytical solutions to F and Ω at a transient, uniformly distributed temperature field. Eliminating g in the linearized equations (46) and (47) we obtain a fourth order differential equation in f. The solution to this equation is then sought as in the nonlinear case, i.e. changing μ for ε in Eqs. (50), (52) and (54) and using these expressions in a solution procedure according to the harmonic balance method. This leads to first order differential equations which may be linearized in ε and solved to give

$$\frac{F}{F_i} = \exp\left\{\left[(\lambda^2-\lambda_{co}^2)t+\varepsilon(a_1^{11}b_2^1+a_1^1b_2^{11}\right.\right.$$

$$-(a_1^{11}+b_2^{11})(\Omega_{co}^2+\frac{a^2\rho^2}{2\delta^2\rho_s^2})) \int_0^t \theta_o(x)dx$$

$$\left.\left.+\varepsilon a_1^{11}(\frac{d\theta_o}{dt}-\frac{d\theta_o}{dt}(o))\right]/\left[\frac{a\rho}{\delta\rho_s}(4\Omega_{co}^2+\frac{a^2\rho^2}{\delta^2\rho_s^2})\right]\right\} \quad (59)$$

$$\psi = \Omega_{co}t+\varepsilon\frac{a_1^{11}\delta\rho_s}{2\Omega_{co}\rho a}(\theta_o-\theta_o(o))$$

$$+\left[(\lambda^2-\lambda_{co}^2)t+\varepsilon a_1^{11}(\frac{d\theta_o}{dt}-\frac{d\theta_o}{dt}(o))+\varepsilon(\Omega_{co}^2(a_1^{11}+b_2^{11})\right.$$

$$\left.+a_1^{11}b_2^1+a_1^1b_2^{11})\int_0^t\theta_o(x)dx)\right]/\left[2\Omega_{co}(4\Omega_{co}^2+\frac{a^2\rho^2}{\delta^2\rho_s^2})\right] \quad (60)$$

where $\Omega_{co}^2 = (a_1^1+b_2^1)/2$, $\quad \lambda = \frac{8aU\rho}{3\delta\rho_s L}$ and

where $(\ )^1$ denote temperature independent and $(\ )^{11}$ temperature dependent parts of the coefficients in Eqs. (49). It is not possible to use the same method to obtain expressions for G and ϕ because we can not get rid of the nonlinear terms sin ϕ and cos ϕ in this case. However, g may be expressed into f from the linearized Eq. (46) thus providing an asymptotic solution.

Lastly, for a shell exposed to a stationary, uniformly distributed temperature field, we may assume that F, G and ϕ are constants in Eqs. (50)-(51) and that $\psi=\Omega_c t$. This gives the following solution

$$\Omega_c^{\,2} = (a_1+b_2)/2 \tag{61}$$

$$\tan \phi_c = -\frac{\rho a}{\delta \rho_s} \frac{\Omega_c}{\Omega_c^{\,2}-a_1} \tag{62}$$

$$\lambda_c^{\,2} = \frac{\rho^2 a^2}{\delta^2 \rho_s^{\,2}} \Omega_c^{\,2}-(\Omega_c^{\,2}-a_1)(\Omega_c^{\,2}-b_2) \tag{63}$$

At a given value of $\frac{\rho a}{\delta \rho_s}$, the last expression gives the critical velocity U_c for flutter according to the linear theory.

5. Results and Discussion

The shell is assumed to be initially at a reference temperature T_r=300°K. It is then momentarily exposed to a hot gas stream of 2000°K at its inner side and to a cooling gas stream of 400°K at its outer side. The temperature of the hot gas stream is assumed to vary axially as a first order cosine series increasing in the flow direction. The variation is assumed to be 100°K about the mean value.

Through convective heating, the shell wall temperature increases exponentially so that in Eq. (48)

$$\theta_o = \theta_{oo}(1-\exp(-\frac{t}{\tau})) \tag{64}$$

$$\theta_1 = \theta_{10}(1-\exp(-\frac{t}{\tau})) \tag{65}$$

$$\tau = \delta\rho_s\, c_s/2h \tag{66}$$

where in the present case θ_{oo}=900°C and θ_{10}=-50°C. The variation of θ_o/θ_{oo} with time is shown in Fig. 2.

The shell properties, flow conditions and loading have been chosen as

$p = 2b$	$p_m = 0$
$\delta = 10^{-3}$ m	$R = 0.5$ m
$\rho_s = 8150$ kg/m^3	$c_s = 432$ J/kg °C
$E_o = 2.12\cdot10^{11}$ N/m^2	$\nu_o = 0.30$
$\varepsilon E_1 = -7.4\cdot10^7$ N/m^2 °C	$\varepsilon\nu_1 = 5.8\cdot10^{-5}$ 1/°C

$N = 0 \qquad h = 190\ W/m^2\ {}^oC$

$L = 3\ m$

The calculations have been carried out for a circumferential wave number of m=8, which results in minimum critical velocity U_{co} for flutter of the unheated shell in linear theory. There may be a tendency for the circumferential wave number to change during the heating up of the shell. This question is, however, complicated enough to demand an investigation of its own. Therefore, it is not considered here.

The structural damping has been neglected also. The significance of this will be discussed later on.

Using linear theory, the variations of Ω_c, ϕ_c and U_c with temperature have been calculated from Eqs. (61)-(63) for the coefficients a_1 and b_2 as in Eqs. (49). The results are shown in Figs. 3-5. For the unheated shell it is found that Ω_{co}=369 sec^{-1}, ϕ_{co}=139.3^o and U_{co}=633 m/sec. The decrease of the frequency with increasing temperature as observed in Fig. 3 depends on the weakening of the material and is typical for the vibrations of heated structures, compare e.g. Ref. 1. As is seen from Fig. 4, the phase angle does also decrease with increasing temperature and as regards the critical velocity for flutter, Fig. 5, it decreases considerably during the heating up of the structure. As will be shown below, this may have severe consequences for the stability of the flutter oscillations.

In order to study these questions in more detail, it is necessary to solve the nonlinear problem posed by Eqs. (56).

These equations have been solved numerically on a Saab D22 computer. The results in the stationary case are shown in Figs. 6-8, those in the instationary case in Figs. 9-16.

Fig. 6 shows the limit cycle amplitudes at various gas velocities. During the heating up of the shèll, curve A will move to curve B or at a uniformly distributed temperature field to curve C. For small amplitudes the curves approach the linear flutter boundaries of Fig. 5. In the linear theory, the curves of Fig. 6 would be straight vertical lines. It is probable, that the curves would bend back to the right for larger amplitudes if higher order approximations were included in the nonlinear analysis.

It is seen from Fig. 6, that the axial temperature variation tends to move the curves for the limit cycle amplitudes to higher velocities. Although this tendency is moderate in the present case, it still has a large influence on the limit cycle amplitudes at certain gas velocities.

The flutter angular frequency Ω_c and the phase angle ϕ_c between the two modes are shown in Figs. 7 and 8. Both of them decrease with increasing limit cycle amplitudes. It is seen, that the axial temperature variations leave the flutter frequency almost uninfluenced but that they have a considerable effect on the phase angle, tending to decrease it. The observed decrease of the frequency with increasing amplitudes is typical for the present type of so called "weak nonlinearities".

Numerical stability studies [17] for the stationary case have shown that only those parts of the curves in Fig. 6 which have positive slope, represent stable limit cycle oscillations. Thus, for all initial conditions to the left of and below the curves, the oscillations will be damped out with time. For all other initial conditions they will grow, either up to the curves or to infinitely large values. Therefore and because of the movement of the curves, initially stable oscillations may change over to instable ones at transient temperatures. For initial conditions below and to the left of curve A and to the right of curve B, e.g. point p_1 in Fig. 6, the amplitudes will first be damped out along a vertical line corresponding to the prescribed gas velocity. Simultaneously, however, the curves move to the left so that after some time the point p_1 will be in the instable region to the right of the curves. The amplitudes then pass through a minimum and begin to grow towards infinitely large values. Conversely, for initial conditions corresponding to e.g. the points p_2 and p_3, the amplitudes will be monotoneously increasing and decreasing respectively.

Such courses of events are shown in Fig. 9. Although the amplitudes may disappear almost altogether, they still remain latent and suddenly rise to very large values.

In connection with this one might ask what influence the structural damping would have on this picture. From results given in Ref. 18 one may conclude that the damping would move the points of vertical tangency of the curves in Fig. 6, i.e. the domain of the points p_1, to somewhat higher velocities. This would, quite naturally, lead to an increased damping of the curves in Fig. 9, but it would not change the results qualitatively.

As is seen from Fig. 9, the amplitudes for the two modes follow each other very closely at equal initial values. For different initial values they rapidly grow together and then follow each other asymptotically, Fig. 10.

The influence of various initial values of the phase angle on the stability of the system is shown in Fig. 11. For initial values above those corresponding to a stable limit cycle, curve A of Fig. 8, the amplitudes are initially damped out. Conversely, for initial values below the limit cycle values the growth of the amplitudes, i.e. the instability of the system, is increased. In Figs. 9 and 10 an initial value of the phase angle close to that for a limit cycle was chosen in order to rule out these effects.

Typical variations of the phase angle and the angular frequency with time is presented in Figs. 12 and 13 for a case with amplitudes as in Fig. 14. The phase angle rapidly takes on values close to those of a limit cycle at the given gas velocity. It then remains relatively constant until instability occurs when it falls very steeply towards a limiting value of 90^o. The angular frequency Ω also rapidly assumes values characteristic for a limit cycle, remains relatively constant for a while and then rapidly diminishes as the amplitudes take on large values.

When the variations with time of the quantities F, G, ϕ and ψ are known, the dynamic deflections of the shell wall may be obtained from Eq. (40) together with Eqs. (50) and (51). Furthermore, the quasistatic deflections are given by Eq. (37) once f_s and g_s have been calculated. Lastly, the total deflection is obtained through adding the dynamic and quasistatic parts. Typical results of such calculations are shown in Figs. 15 and 16 for the quantities F, G, ϕ and Ω as in Figs. 12-14. Fig. 15 presents the variation of the deflections during one half of a period while Fig. 16 gives the corresponding results during several periods. In the present case, the axial temperature variation gives a quasistatic deflection $w_s \ll \delta$. This verifies that it is possible to neglect it, as was done in Sec. 3, without restricting the accuracy of the analysis severly.

In order to check the validity of Eqs. (59)-(60), calculations have been carried out with θ_o according to Eq. (64) and with θ_{oo}=900°C. The results are shown in Figs. 17 and 18. It is found, that when the gas velocity is greater than U_{co}=633 m/sec, the amplitude F will grow monotoneously. If the velocity is less than U_{co} but greater than a critical value of U_{ch}=460 m/sec, the amplitude will first be damped out, then again will rise to infinitely large values. Lastly, if the gas velocity is less than U_{ch}=460 m/sec, the amplitude will be damped out with time. It may be shown that G will follow F asymptotically as in the nonlinear case. The value U_{ch} which corresponds to the critical velocity for flutter of the stationary heated shell is about 5% lower than the corresponding value in Fig. 6. This is due to the further linearizations necessary in the derivation of Eqs. (59)-(60).

As regards the angular flutter frequency Ω, it decreases with time as the temperature increases, Fig. 18. This behavior depends on the weakening of the structure and was observed previously as regards Ω_c, see Fig. 3. In the nonlinear case, Fig. 13, this tendency is counteracted at decreasing amplitudes by the previously mentioned tendency of weakly nonlinear systems to decrease their frequency at increasing amplitudes or vice versa. Comparing Figs. 13 and 18, it is also noted that the linear theory fails to predict the rapid decrease of the frequency as instability occurs. At increasing gas velocities the linear theory gives a small general increase of Ω but this tendency is too weak to be shown in Fig. 18.

As a whole, the linear theory of Eqs. (59)-(60) seems to give a qualitatively correct picture of the variation of the amplitudes during the heating up of the shell wall, while its predictions as regards the frequency are less reliable.

6. Conclusions

The differential equations describing the nonlinear, supersonic flutter of heated, circular cylindrical shells have been formulated and solved using a two-mode approximation of the shell deflections. In linear theory, analytic solutions were given for the variation with time of the first mode amplitude and the flutter frequency. Through comparison to nonlinear numerical solutions, it was shown that this linear theory gave a qualitatively correct description of the course of events during the heating up of the shell.

In the isothermal case, possible stationary states of vibration may be described by curves in a diagram of the limit cycle amplitudes versus the gas velocity. These curves bend to the left and points below and to the left of them represent stable oscillatory conditions. The nonlinear analysis carried out here showed that the curves are moved to lower gas velocities at increasing temperature. Therefore, initially stable states of vibration may pass into the instable domain during transient heating of the shell wall provided that the gas velocity is within certain boundaries. In such cases, the amplitudes are first damped out with time, then pass through a minimum and begin to grow to infinitely large values. Other states of vibration will remain stable or instable during the heating up period. The conditions under which the various courses of events take place were described in this work.

It was found that axial temperature variations tended to move the curves for the limit cycle amplitudes to higher velocities. Although this tendency was shown to be moderate at realistic temperature variations, it might still have a large influence on the limit cycle amplitudes at certain gas velocities.

Nomenclature

θ = temperature excess over reference temperature T_r

α = coefficient of thermal expansion

σ_{ij} = stress components

E = Young's modulus

ν = Poisson's ratio

ρ_s = shell material density

t = time

N = tensile load per unit length

M = freestream Mach number

p_m = pressure difference over shell wall

ρ = freestream density

a = freestream speed of sound

U = freestream velocity

F, G = nondimensional vibrational amplitudes

Ω = angular flutter frequency

ϕ = phase angle between flutter modes

c_s = specific heat of shell material

h = heat transfer coefficient

p = freestream static pressure

Subscripts

o	refers to unheated shell
i	" " initial conditions
c	" " stationary flutter conditions

References

[1] Ambartsumian, S.A. et al., "Some Problems of Vibration and Stability of Shells and Plates", Int. J. Solids Structures, Vol. 2, 1966, pp. 59-81.

[2] Tang, S., "Natural Vibration of Isotropic Plates with Temperature-Dependent Properties", AIAA Jnl, Vol. 7, No. 4, April 1969, pp. 725-727.

[3] Hilton, M.H., "Thermal Stresses in Bodies Exhibiting Temperature-Dependent Elastic Properties", J. Appl. Mech., Vol. 19, 1952, p. 350.

[4] Nowinski, J.L., "Thermal Stresses in a Thick-walled Cylinder with Variable Elastic Properties", Arch. Mech. Stos., Vol. 5, No. 2, 1953, p. 295.

[5] Trostel, R., "Wärmespannungen in Hohlzylindern mit temperaturabhängigen Stoffwerten", Ing.-Archiv, Vol. 26, 1958, p. 134.

[6] Trostel, R., "Stationäre Wärmespannungen mit temperaturabhängigen Stoffwerten", Ing.-Archiv, Vol. 26, 1958, p. 416.

[7] Nowinski, J.L., "Thermoelastic Problem for an Isotropic Sphere with Temperature Dependent Properties", ZAMP, vol. 10, No. 6, 1959, p. 565.

[8] Nowinski. J.L., " A Betti-Rayleigh Theorem for Elastic Bodies Exhibiting Temperature Dependent Properties", Appl. Sci. Res., Vol. 9, No.6, 1960, pp. 429-436.

[9] Sokolowski, M., "One-Dimensional Thermoelastic Problems for Elastic Bodies with Material Constants Depending on Temperature", Bull. Acad. Polonaise Sci., Ser. Sci. Tech., Vol. 8, No.4, 1960, p. 153.

[10] Nowinski, J.L., "Transient Thermoelastic Problem for an Infinite Medium with a Spherical Cavity Exhibiting Temperature Dependent Properties", J. Appl. Mech., 1962, p. 399.

[11] Nowinski, J.L., Ismail, I.A., "Application of a Multiparameter Perturbation Method to Elastostatics", Proceedings of the Second Southeastern Conference on Theoretical and Applied Mechanics, 1963.

[12] Nowinski, J.L., "Axisymmetric Problem of the Steady State Thermal Stresses in Elastic Media with Temperature Dependent Properties", Appl. Sci. Res., Vol. 12, No. 4/5, 1964, p. 349.

[13] Nowacki, W., Thermoelasticity, Pergamon, London-Warsaw, 1962.

[14] Ismail, I.A., Nowinski, J.L., "Thermoelastic Problems for Shells of Revolution Exhibiting Temperature Dependent Properties", Appl. Sci. Res., Vol. 14, No. 3, 1964/1965, p. 211.

[15] Tang, S., "Thermal Stresses in Temperature Dependent Isotropic Plates", J. Spacecrafts and Rockets, Vol. 5, No. 8, Aug. 1968, pp. 987-990.

[16] Tang, S., "Some Problems in Thermoelasticity with Temperature Dependent Properties", J. Spacecrafts and Rockets, Vol. 6, No. 2, Febr. 1969, pp. 217-219.

[17] Olson, M.D., Fung, Y.C., "Comparing Theory and Experiment for the Supersonic Flutter of Circular Cylindrical Shells", AIAA Jnl., Vol. 5, No. 10, Oct. 1967, pp. 1849-1855.

[18] Evensen, D.A., Olson, M.D., "Circumferentially Traveling Wave Flutter of a Circular Cylindrical Shell", AIAA Jnl, Vol. 6, No. 8, Aug. 1968, pp. 1522-1527.

[19] Bogoliubov, N.N., Mitropolsky, Y.A., Asymptotic Methods in the Theory of Nonlinear Oscillations, Hindustan Publ. Corpn., Dehli-6, 1961.

[20] Krumhaar, H., "The Accuracy of Applying Linear Piston Theory to Cylindrical Shells", AIAA Jnl, Vol. 1, No. 6, June 1963, p. 1448-1449.

[21] Barr, G.W., Sterman, R.O., "Aeroelastic Stability Characteristics of Cylindrical Shells Considering Imperfections and Edge Constraints", AIAA Jnl, Vol. 7, No. 5, May 1969, pp. 912-919.

[22] Evensen, D.A., "Some Observations on the Nonlinear Vibrations of Thin Cylindrical Shells", AIAA Jnl, Vol. 1, 1963, pp. 2857-2858.

[23] Olsson, U., "Reduction of the Differential Equations for a Cylindrical Shell of Temperature Dependent Material Properties to Ordinary Differential Equations", Flygmotor Research, RF 5:3155, April 1970.

[24] Minorsky, N., Nonlinear Oscillations, D. Van Nostrand Co., Inc., Princeton, New Jersey, 1962.

Acknowledgement

The author wants to express his gratitude to Mr L.Mossberg, who made the numerical solutions of Sec. 5. The SAAB D22 Computer of Volvo Flygmotor was used in the calculations.

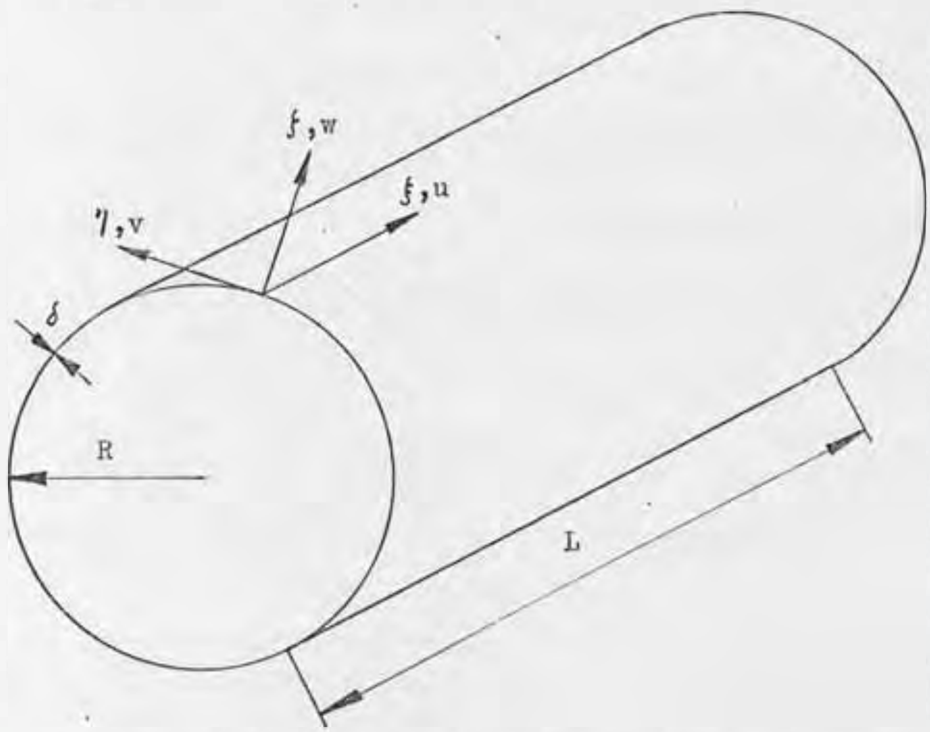

Fig. 1 Shell geometry and coordinate system.

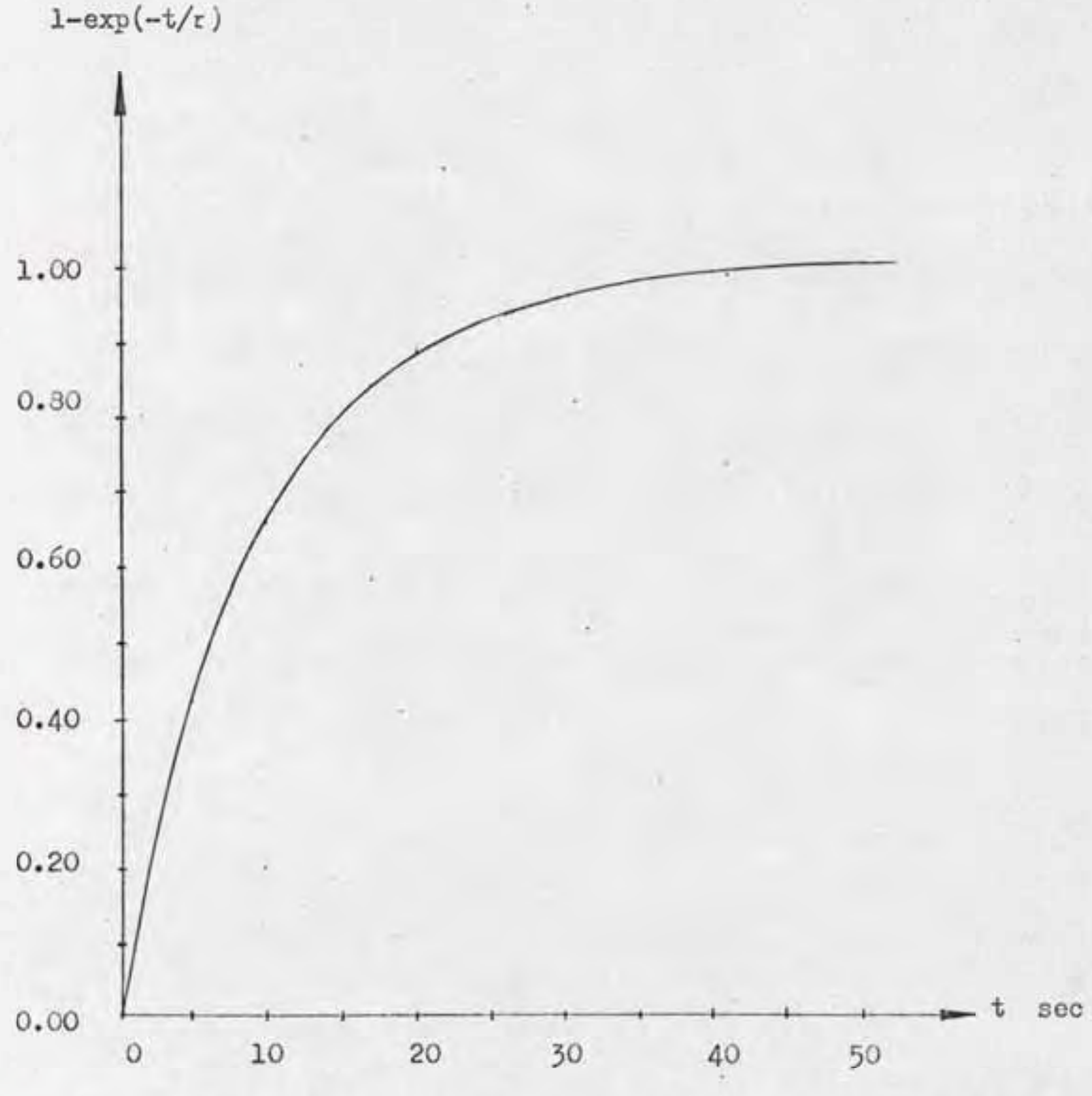

Fig. 2

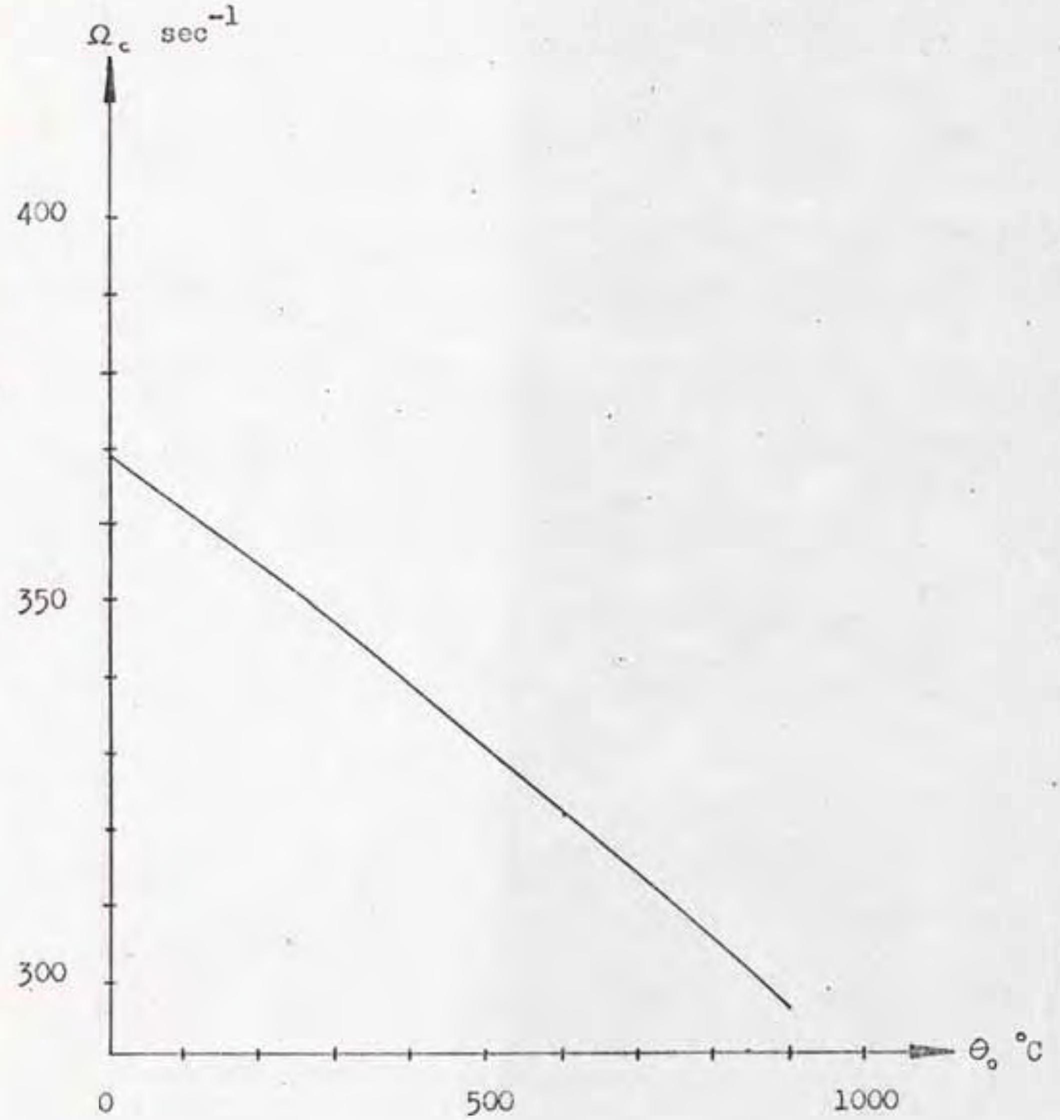

Fig. 3 Angular frequency of stationary flutter oscillations versus average shell wall temperature.

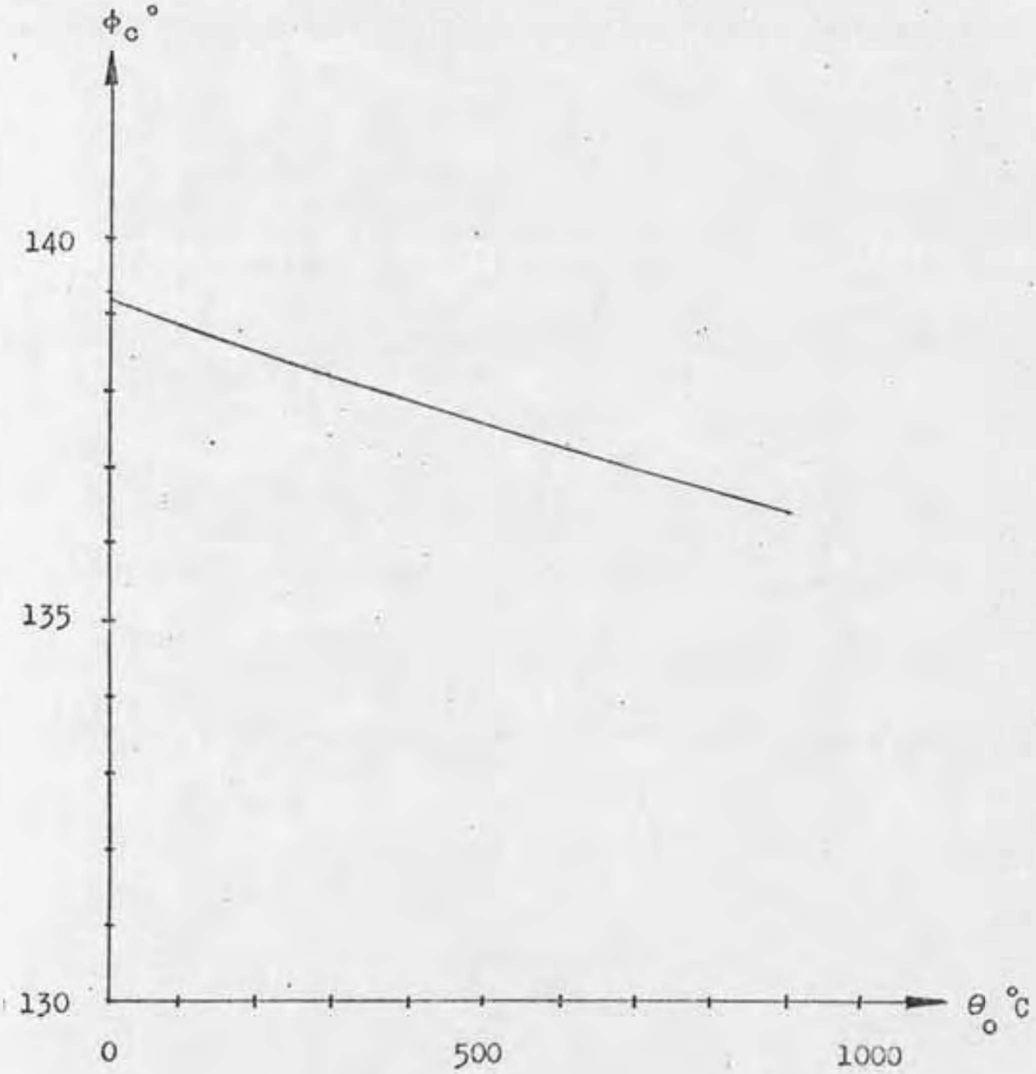

Fig. 4 Phase angle of stationary flutter oscillations versus average shell wall temperature.

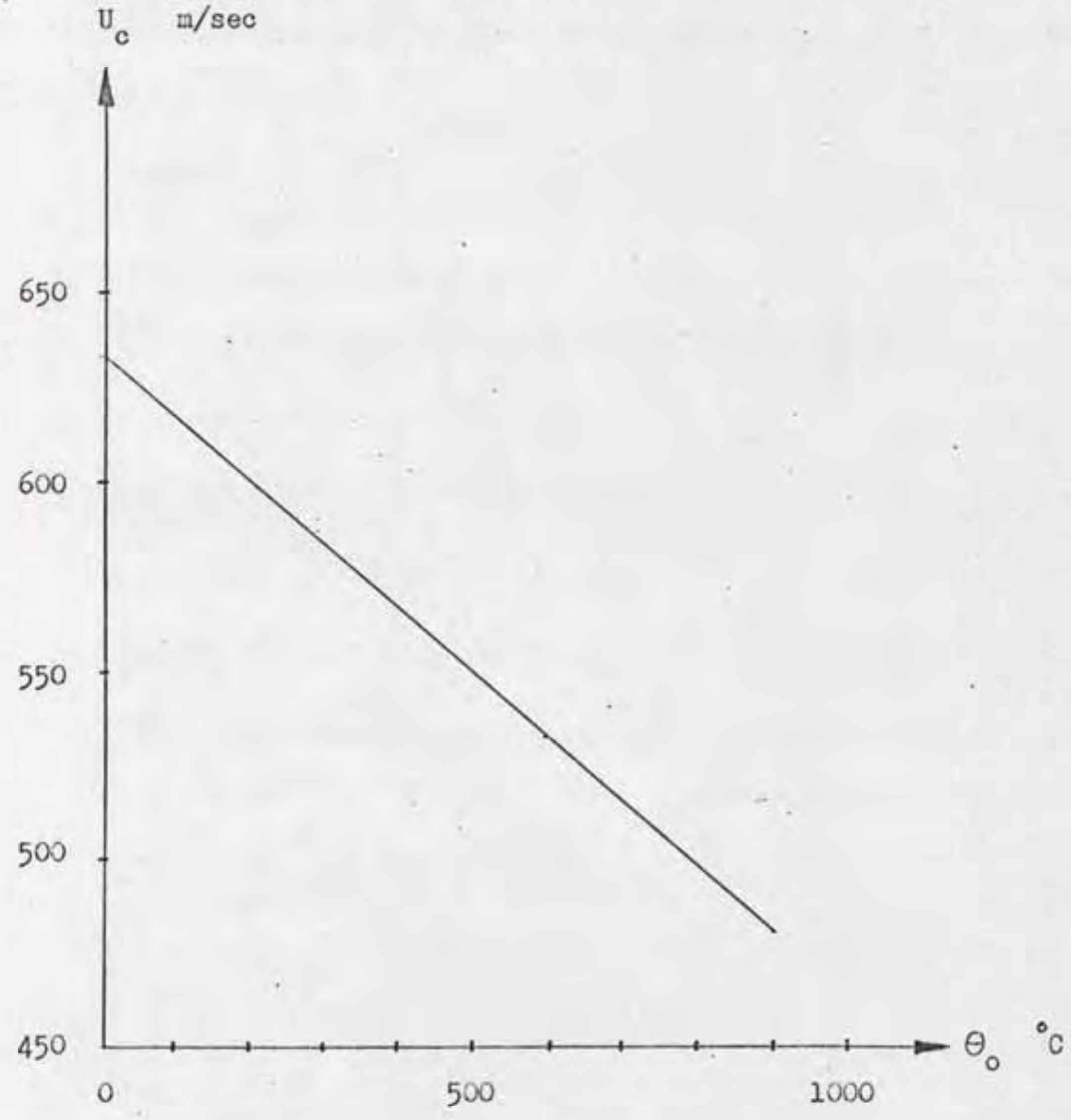

Fig. 5 Critical flutter velocity versus average shell wall temperature.

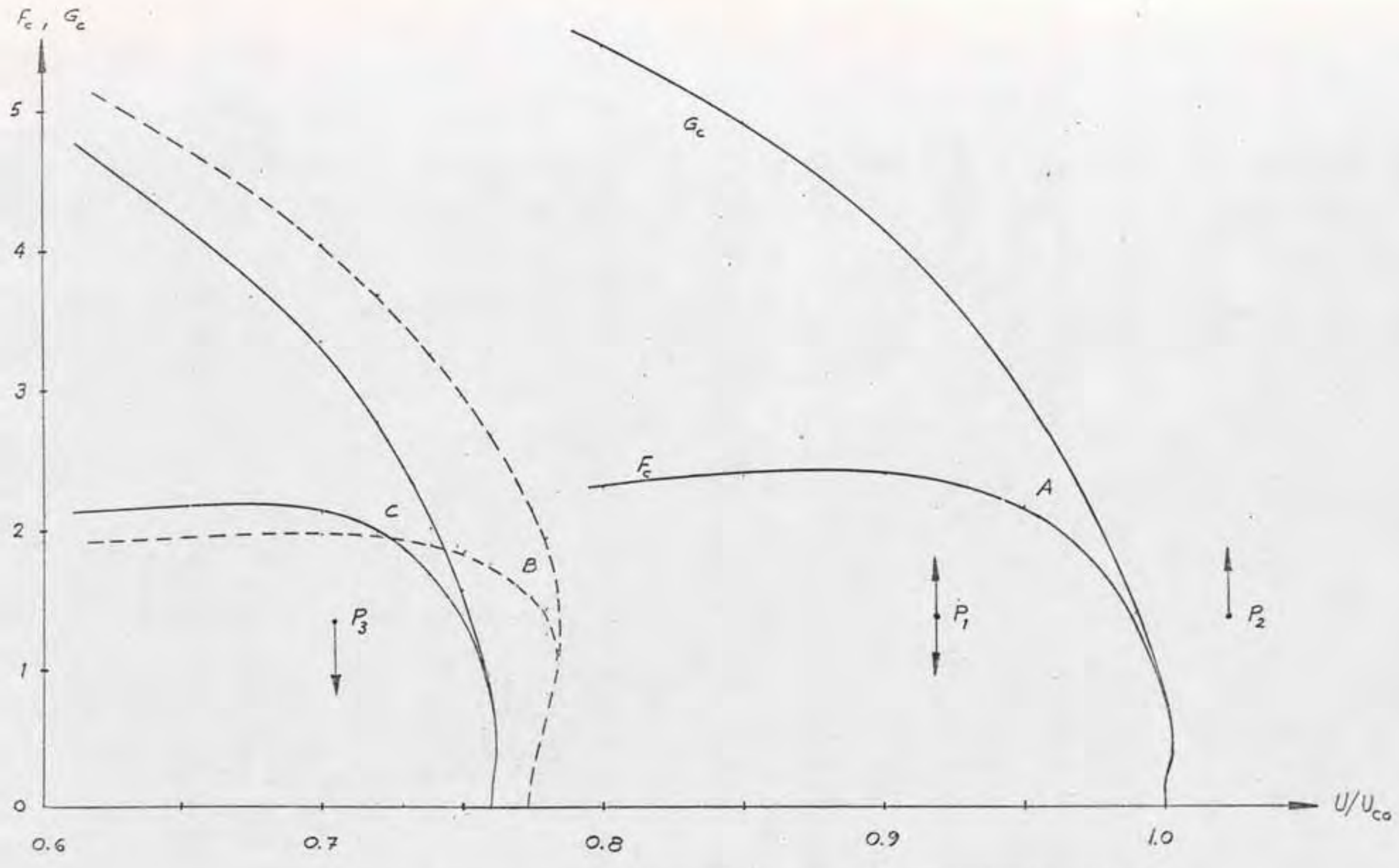

Fig. 6 Limit cycle amplitudes of stationary flutter oscillations versus gas velocity.

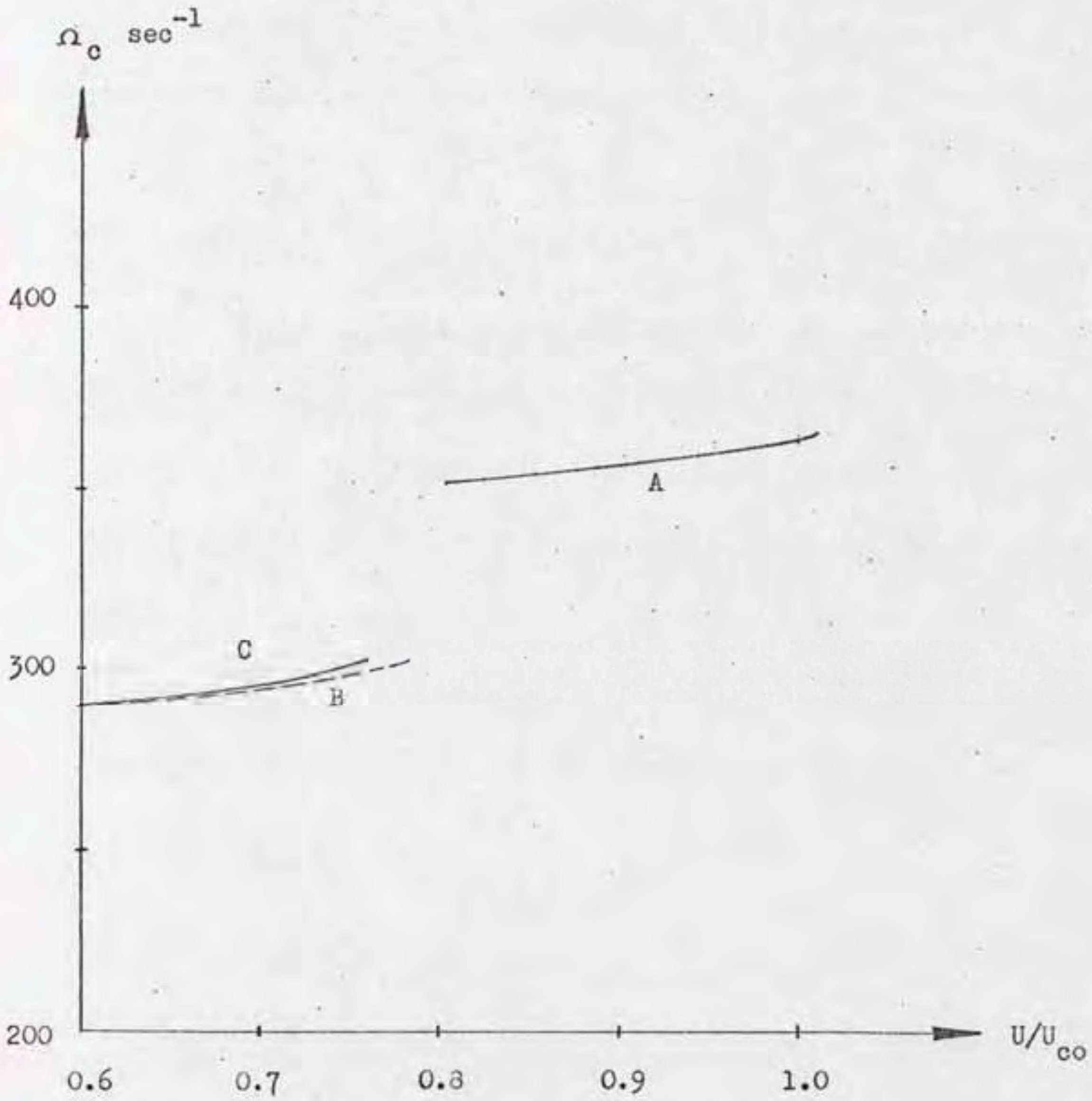

Fig. 7 Angular frequency of stationary flutter oscillations versus gas velocity.

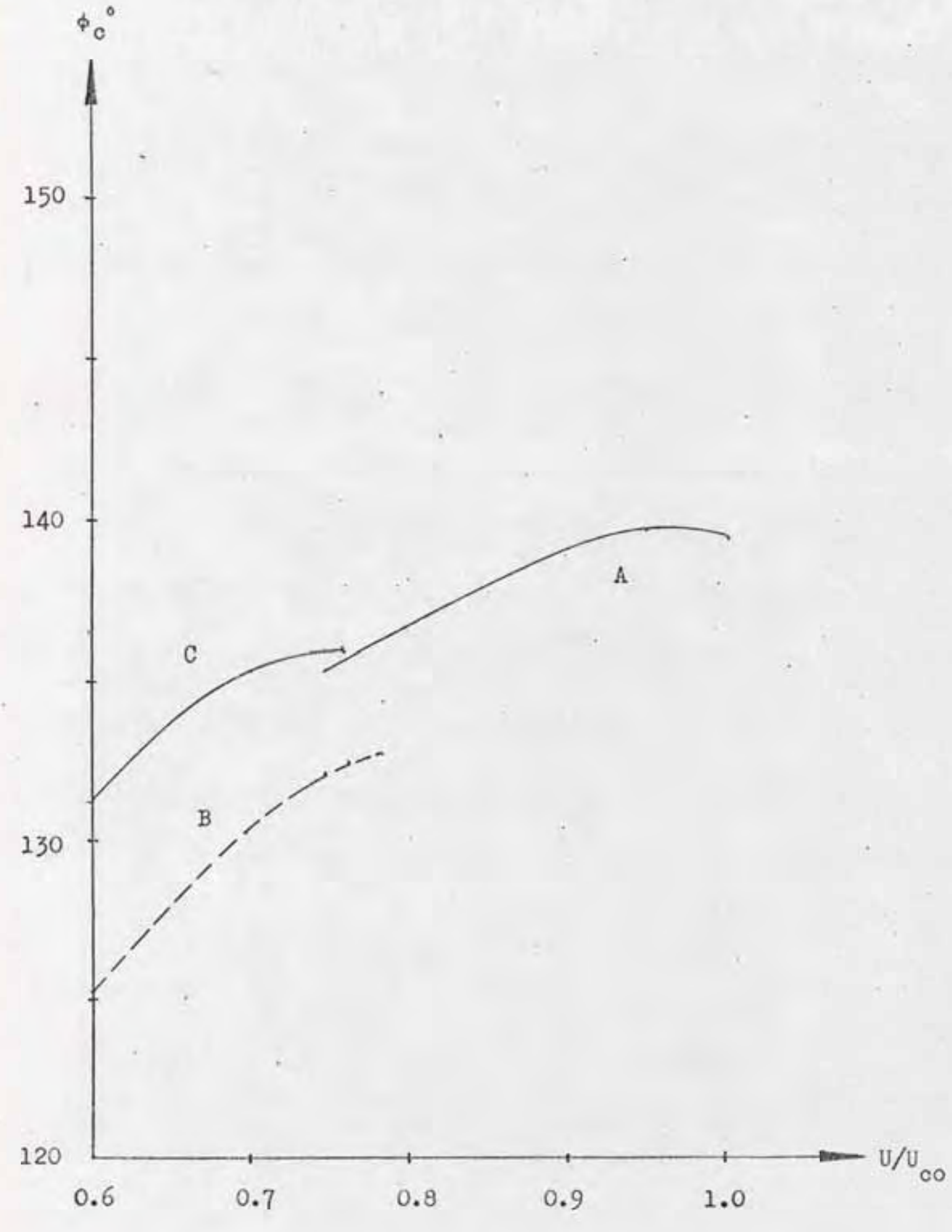

Fig. 8 Phase angle of stationary flutter oscillations versus gas velocity.

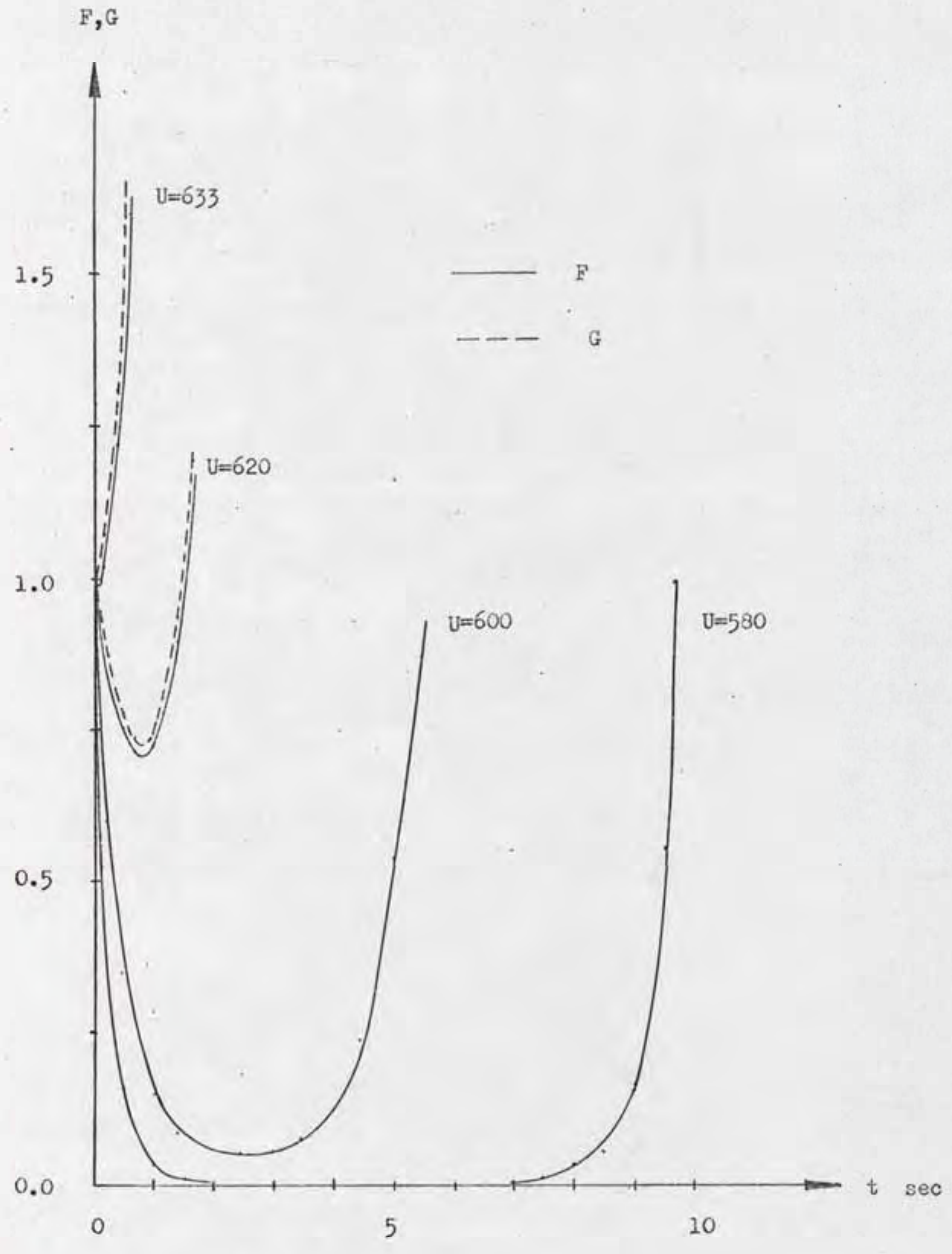

Fig. 9 Amplitudes of the flutter oscillations versus time, $\phi_i = \pi - 0.7$.

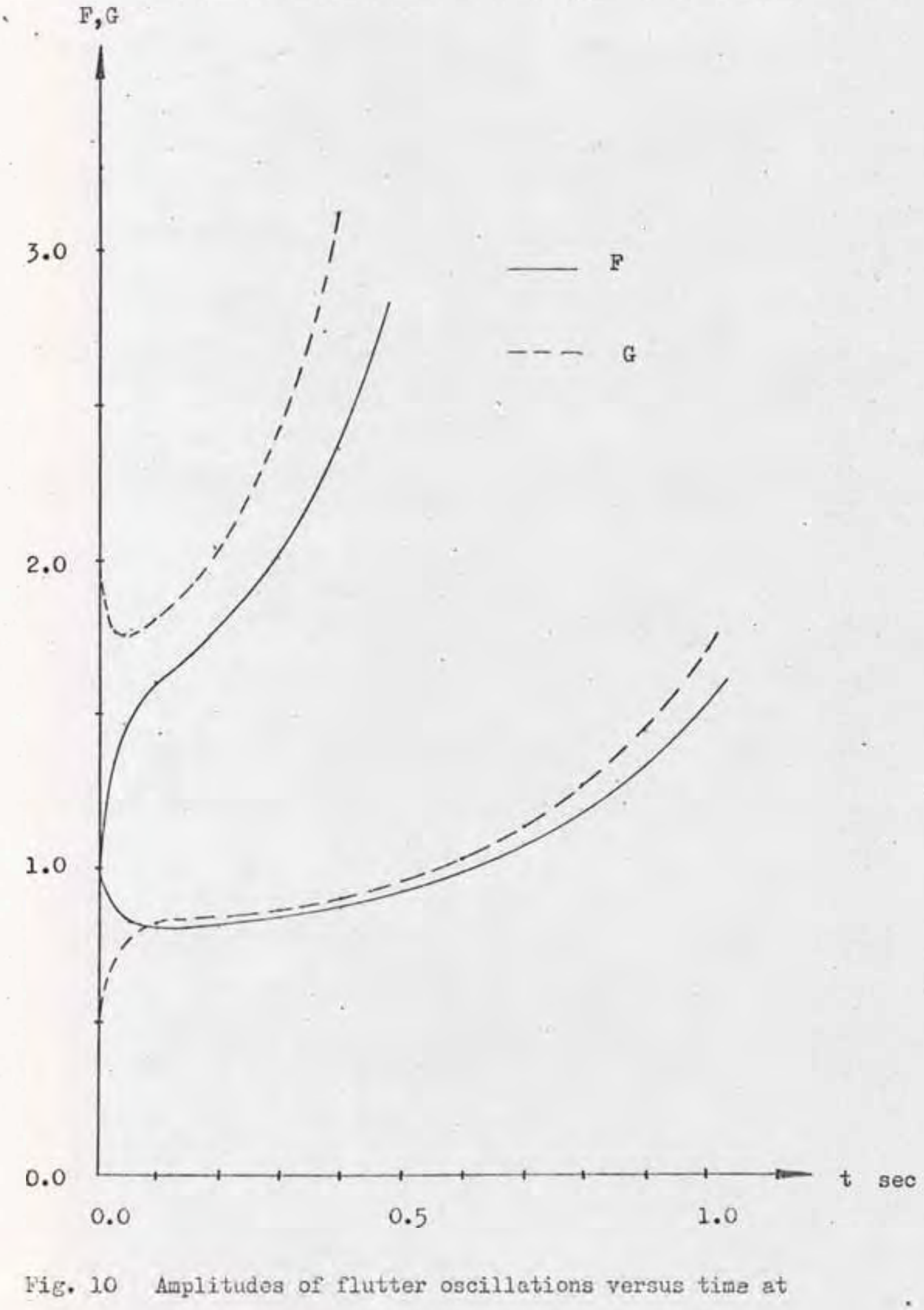

Fig. 10 Amplitudes of flutter oscillations versus time at different initial values, $\Phi_i = \pi - 0.7$, U=633 m/sec.

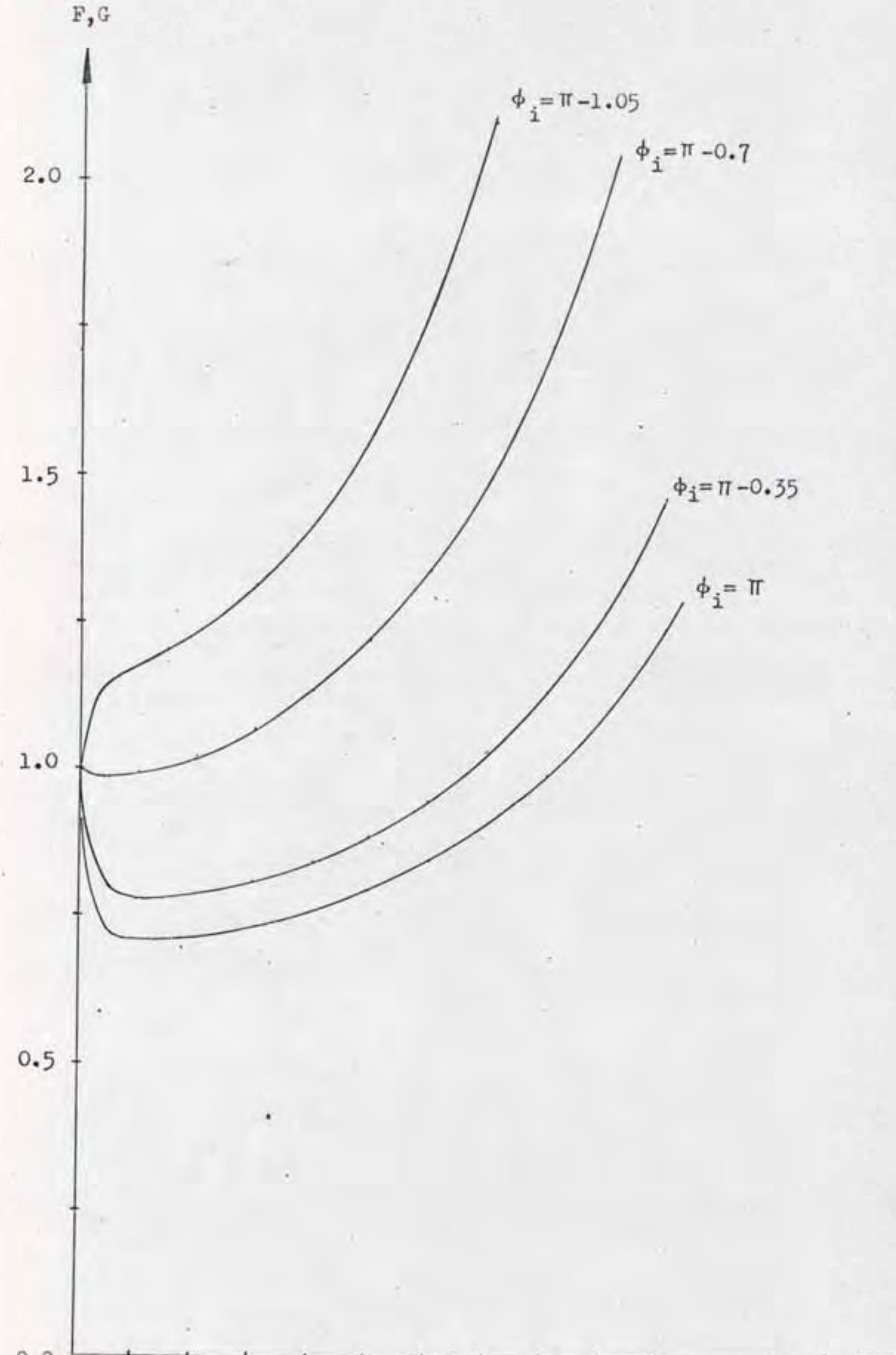

Fig. 11 Amplitudes of flutter oscillations versus time at various initial values of the phase angle, U=633 m/sec.

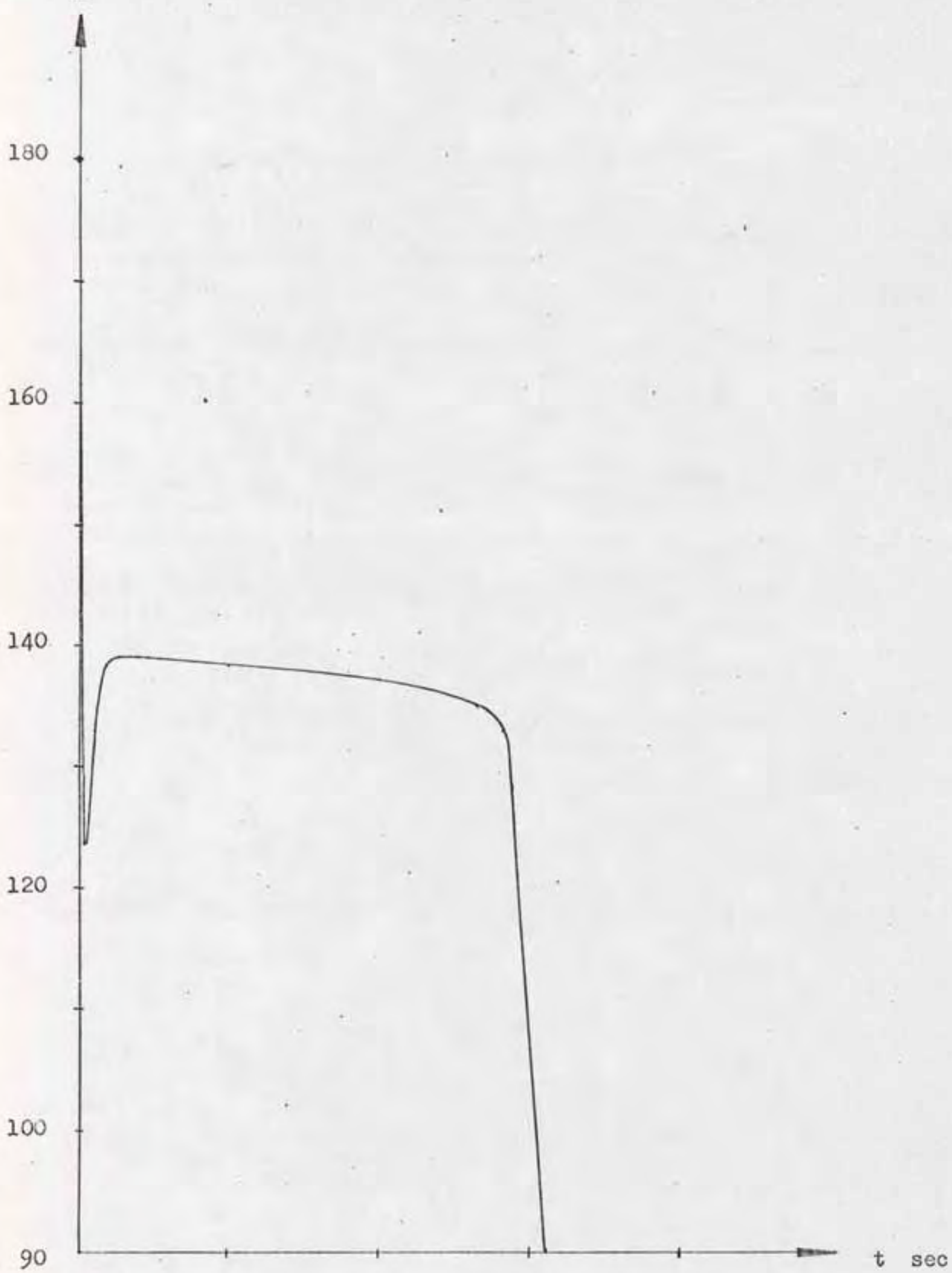

Fig. 12 Phase angle versus time, $\phi_i=180^\circ$, U=633 m/sec.

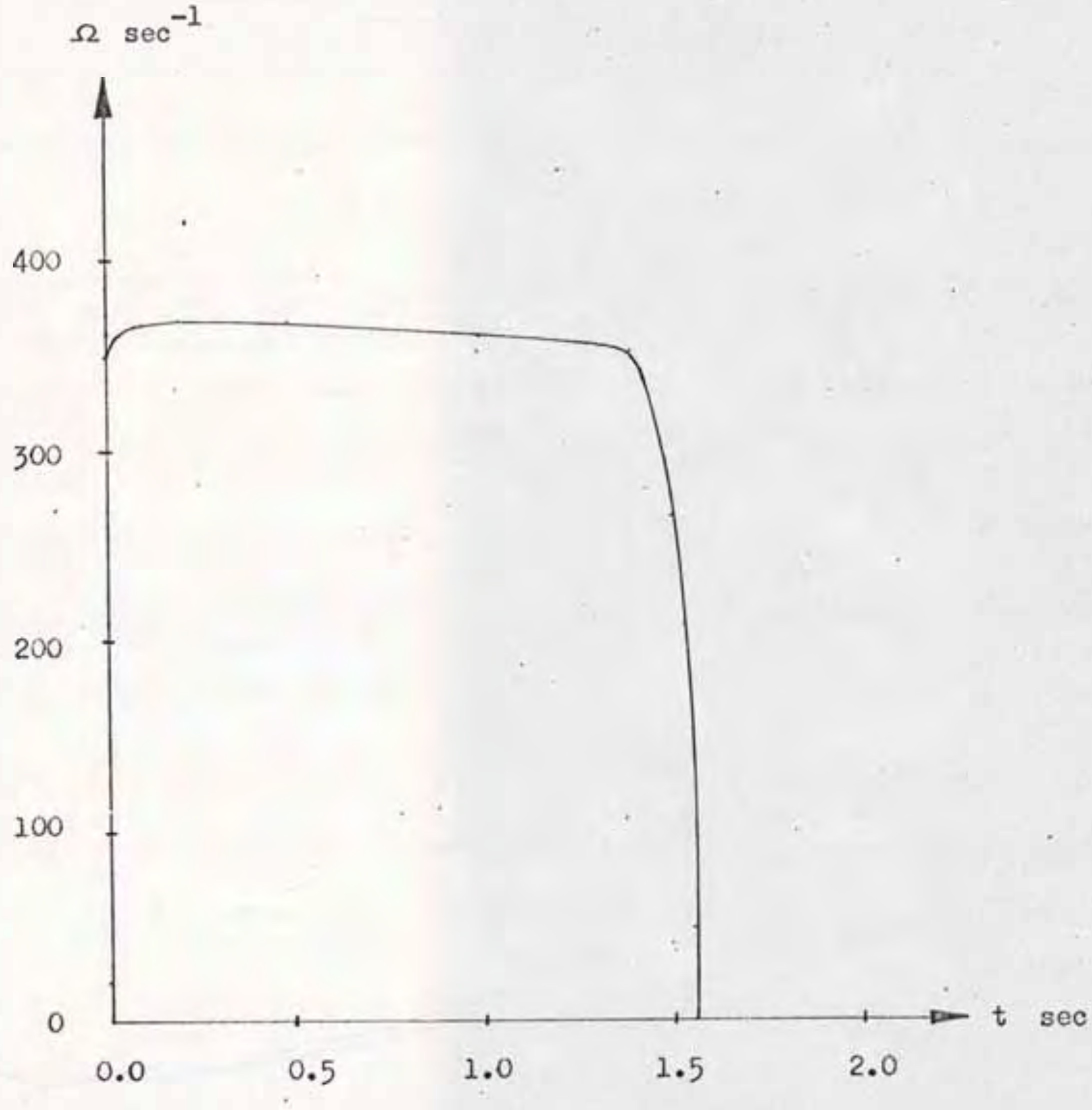

Fig. 13 Flutter frequency versus time, U=633 m/sec.

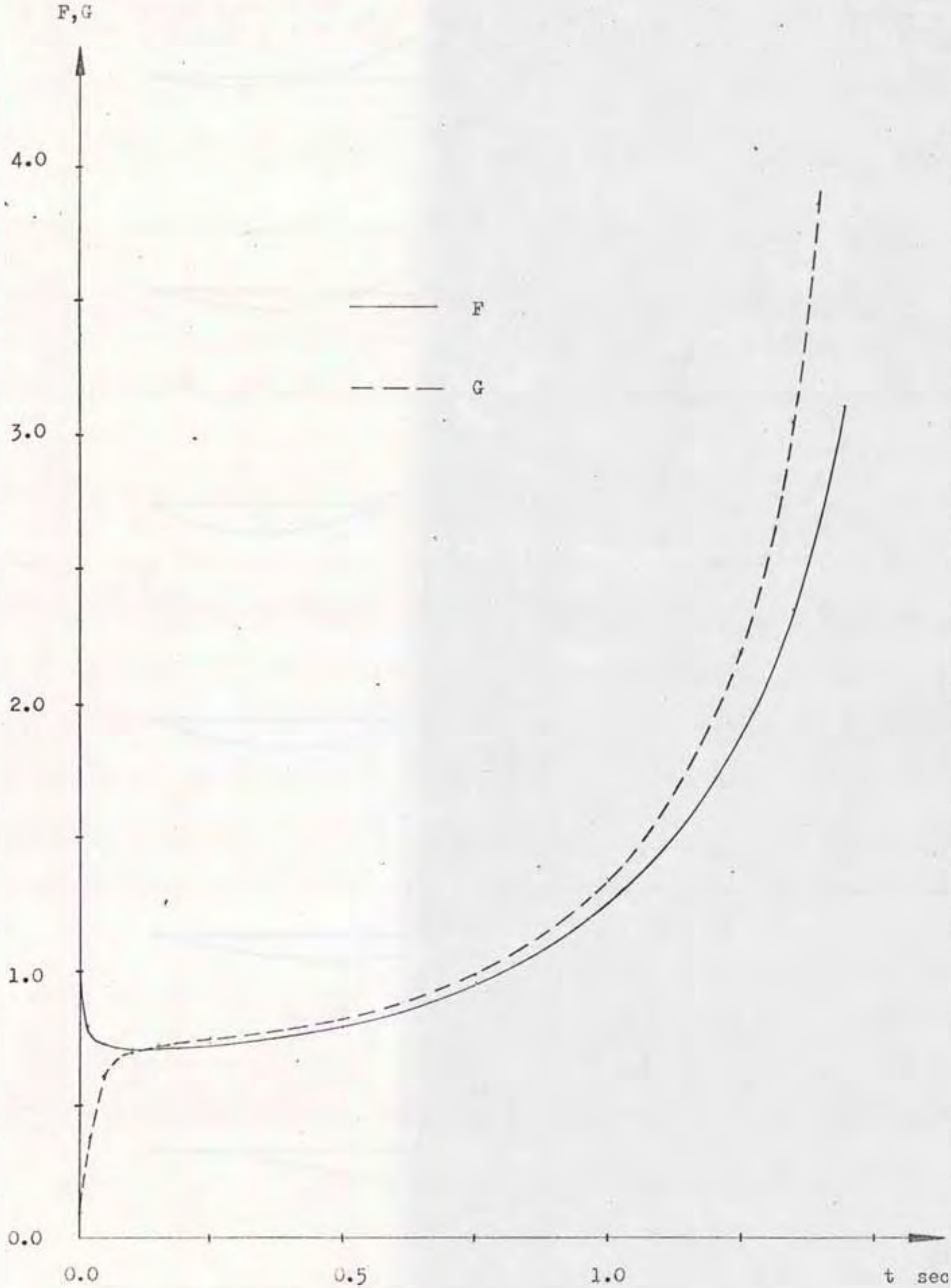

Fig. 14 Amplitudes versus time, $F_i=1.0$, $G_i=0.1$, $\phi_i=180°$, $U=633$ m/sec.

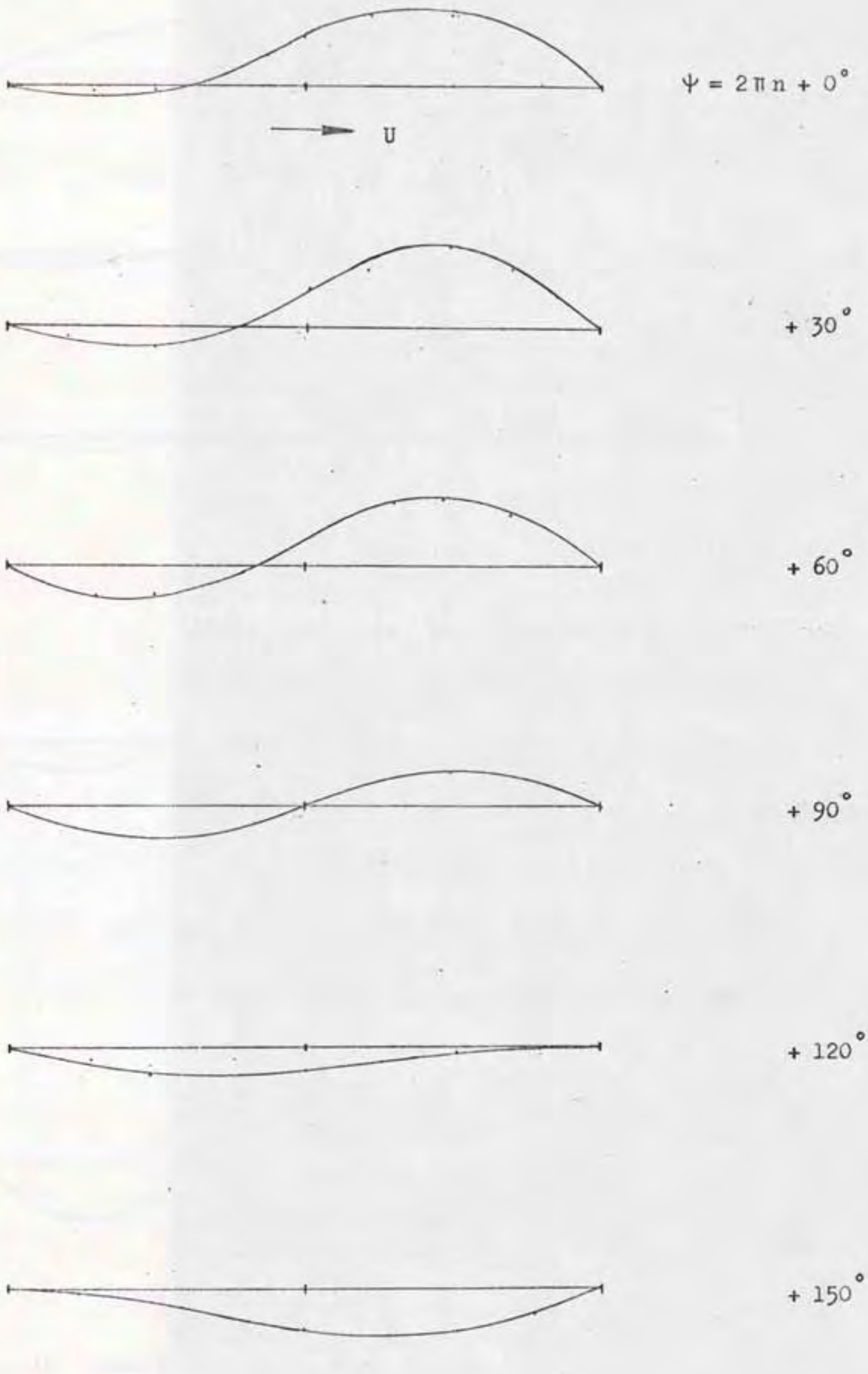

Fig. 15 Deflections during one half of a period.

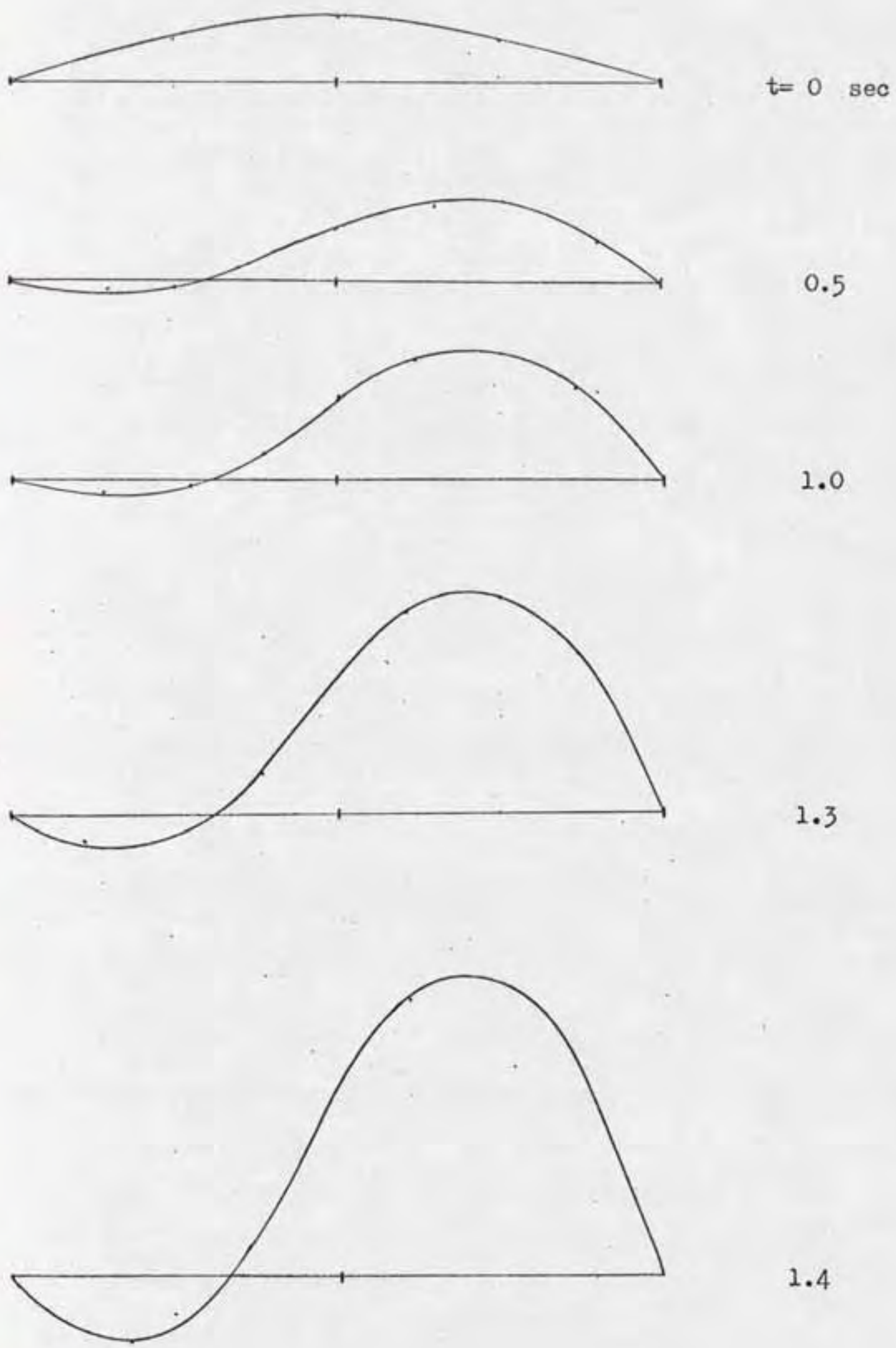

Fig. 16 Deflections at various times.

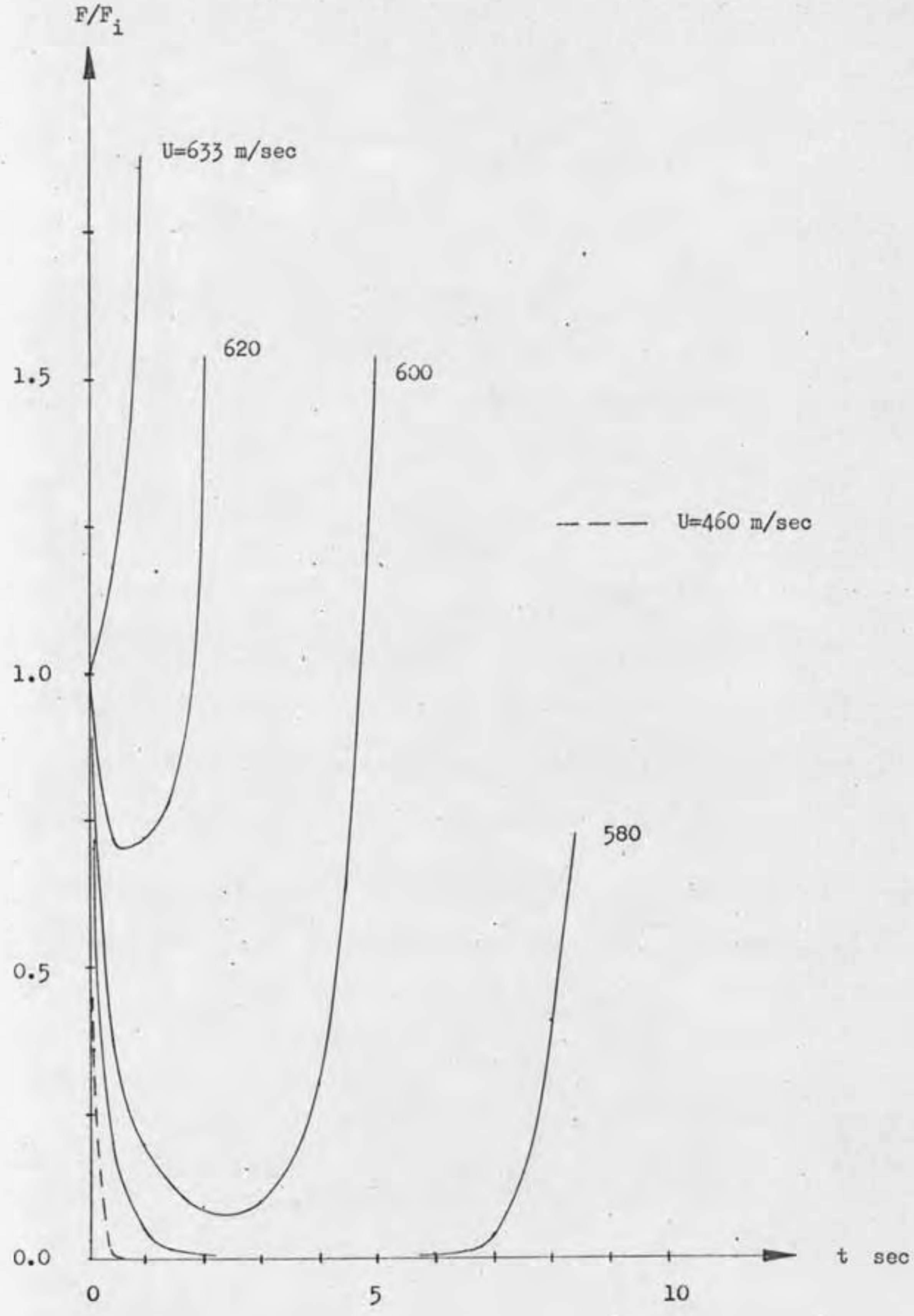

Fig. 17 Variation of amplitude F with time according to linear theory.

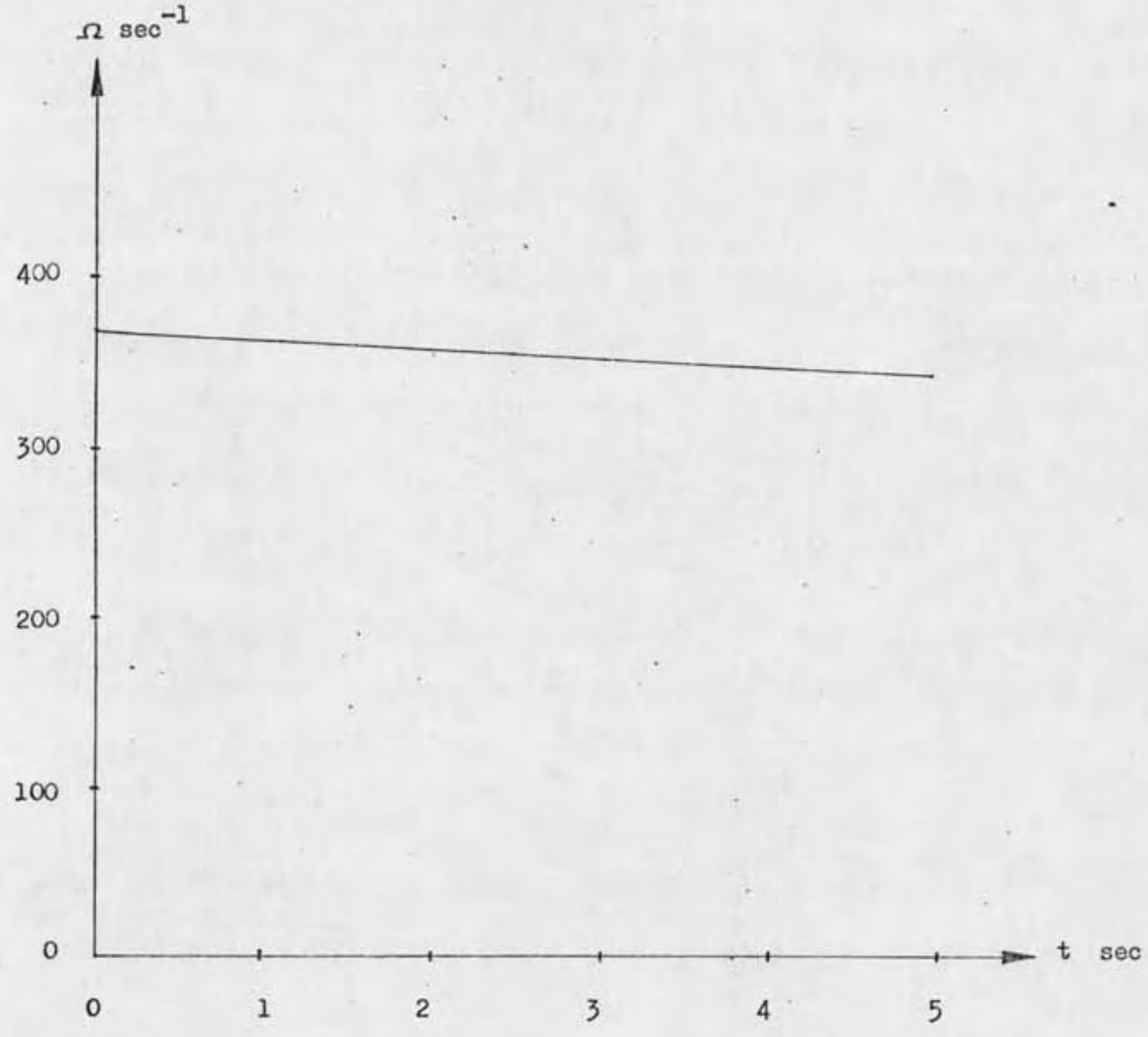

Fig. 18 Variation of flutter frequency Ω with time according to linear theory.

NEW OH RADIO EMISSION SOURCES IN CYGNUS

By
JOEL ELLDÉR, BERNT RÖNNÄNG
and
ANDERS WINNBERG

(*Reprinted from Nature, Vol. 222, No. 5188, pp. 67–69, April 5, 1969*)

(*Reprinted from Nature, Vol. 222, No. 5188, pp. 67-69, April 5, 1969*)

New OH Radio Emission Sources in Cygnus

All radio observational work on OH has so far been concentrated on previously known astronomical objects. Initially the OH microwave radiation was found absorbed in the spectra of strong continuum sources[1], but in the search for more OH absorption lines weaker and weaker continuum sources were investigated. The guide in this search was the source catalogue made by Westerhout[2], which contains sources around the galactic plane measured at the frequency 1,390 MHz. Many of these sources have a thermal spectrum and therefore are associated with H II regions. Because the first OH emission sources were found in or near some of these H II regions[3,4], the search for more OH emission was carried out chiefly on thermal radio sources. Many new OH emission sources were found in this way and theories of maser action in OH associated with H II regions were produced[5,6].

The discovery by Raimond and Eliasson[7] that the position of the OH source in the Orion Nebula coincides with an infrared point source[8] must be considered as a turning point. Mezger *et al.*[9] found evidence for an identification of certain OH emission sources with a new class of compact H II regions which they believed to be the ionized remnants around recently formed stars. The theory of these so-called "cocoon-stars" is proposed by Reddish[10].

The idea that the OH microwave emission should be associated with extremely young stellar objects inspired Wilson and Barrett[11] to look for OH emission from infrared stars and four out of twenty of these stars were found to have OH emission. One of them (NML Cygni) radiates the strongest radio emission line so far detected and, because this OH emission source is not associated with any radio continuum emission, we thought it worth while to make a survey over a limited region of the sky and try to find other OH sources not connected with continuum emission. Considering the very strong 1,612 MHz radiation from NML Cyg, we also decided that this survey should be carried out on all OH frequencies.

Our equipment consists of an 84 foot (25·6 m) radio telescope, a travelling-wave maser, a 100-channel frequency switched receiver and a small on-line computer[12]. The efficiency of the antenna system is 53 per cent at 18 cm wavelength and the half-power beamwidth is 32′ and 27′ in the E and H-plane, respectively[14]. The travelling-wave maser brings the total system noise temperature down to about 40° K. Two sets of filter-banks are used, one with a 10 kHz bandwidth and the other with a 1 kHz bandwidth. We use the 10 kHz filters for the search, because this bank covers the possible OH velocity range completely. When a source is found, however, we switch over to the 1 kHz filters for more detailed studies. The computer performs the sampling of the channels and integration of the signal as well as storing and plotting the data. The channel voltages are graphically displayed on a cathode ray tube controlled by the computer. In this way we can immediately detect a line signal during the observation.

We started the search in a narrow strip within approximately $\pm 1{\cdot}5^{b}$ from the galactic equator. As the initial longitude interval we chose the Cygnus direction because it is tangential to the local spiral arm and thus we might have a better chance to detect more nearby sources in this area of the sky than in other directions. So far we have investigated a strip between the galactic longitudes 68° and 92°. The points of observation within the area are separated by 0·5° in both right ascension and declination. We observe the difference between the spectrum in the current point and the spectrum in another arbitrary point, thus eliminating any off-set in the channels. With a difference between the signal and reference frequencies of 100 kHz a true line signal is revealed through the appearance on the cathode ray tube display of one positive-going line and one negative-going line separated by 100 kKz (ten channels). We integrate the signal for about 2 min (twelve samples) in each point, which makes it possible to detect sources with an antenna temperature of about 0·5° K (averaged over the 10 kHz filter width).

We have scanned the area at the frequencies 1,665 and 1,612 MHz, in both cases with a right circular polarized feed only. We plan to complete the survey by observing at the other OH frequencies and by using both senses of circular polarization. It is also planned to extend the survey primarily in galactic latitude and later in longitude towards the galactic centre.

We have detected four OH emission sources which, we believe, have not been observed before. Their coordinates (as measured with our antenna) are summarized in Table 1, which also gives approximate distances estimated from the differential galactic rotation model given by M. Schmidt[15].

Table 1

No.	Equatorial coord. (1950·0)	Galactic coord.	Adopted mean velocity (km/s)	Distance (kpc)	Possible identification
1	α = 20 h 08 m 03 s ± 10 s δ = 31° 22′ ± 2′	l = 69·58° b = − 0·96°	+14·5	1·8/5·2	—
2	α = 20 h 19 m 57 s ± 10 s δ = 37° 19′ ± 2′	l = 75·75° b = 0·35°	−0·5	5·7	W 64 ?
3	α = 19 h 59 m 51 s ± 15 s δ = 33° 25′ ± 3′	l = 70·37° b = 1·60°	−17·0	8·2	W 58
4	α = 20 h 26 m 54 s ± 15′ δ = 38° 56′ ± 3′	l = 77·92° b = 0·17°	−38·5	8·1	DR 9 ?

The spectra of the four sources are shown in Fig. 1*a*–*c* at 1,612, 1,665, 1,667 and 1,720 MHz with both right-hand (solid line) and left-hand (dashed line) circular polarization. Spectra of source No. 4 have been omitted because of space limitations.

Around the position of source No. 1 there is no trace of any H II region or other conspicuous object on the Palomar Sky Survey plates. Nor did we find any 1,666 MHz continuum radiation. The detection limit of these measurements was 0·2° K antenna temperature. Within a circle of radius 2′ centred on the position of source No. 1 as given in Table 1 we have found five weak stars which can only be seen on the red-sensitive Palomar plate. The whole area seems to be much obscured, however, and therefore these objects might be ordinary but highly reddened stars.

Source No. 2 is situated approximately 7′ north-east of a small galactic star cluster. The area seems to have an even higher absorption than the area around source No. 1. Consequently there are a few stars around source No. 2 which can only be seen on the red-sensitive plate. The nearest of these stars lies about 3′ from the measured OH position. There is a small maximum of continuum radiation ($T_A \simeq 3{\cdot}5°$ K) at the source position which is close to the position of W 64. Source No. 3 is unusual because it is strongest at the 1,720 MHz line. Very few of the known OH sources have this property (W 28, W 44, W 81) (ref. 16). The source is probably associated with the thermal continuum source W 58 ($T \simeq 2\cdot5°$ K) which has the coordinates[9]

$$\alpha(1950\cdot0) = 20\text{ h }00\cdot1\text{ m} \pm 1\cdot2\text{ m}$$
$$\delta(1950\cdot0) = 33° 23' \qquad \pm 12'$$

The optical counterpart of W 58 consists of two small H II regions approximately 11′ apart and connected by weakly visible ionized gas. The OH source is situated approximately 2′ north of the eastern H II region. Because of the high field density of stars in this area we have not been able to find any suspiciously red stars in the vicinity of the OH source.

Source No. 4 is of special interest because it radiates strongest in the 1,612 MHz line. It has two peaks at −49 and −28 km/s equally strong on both polarizations. This is similar to the OH spectral distribution of NML Cyg, NML Tau and CIT-3 (ref. 11). On the Palomar plate an extended weak H II region with central obscuring dust clouds can be seen. The OH source lies in the eastern part of this weak nebula about 8′ south-east of the star BD +38° 4100. Approximately 1·5′ from the position given for source No. 4 in Table 1 a weak star is seen on the red-sensitive plate with no counterpart on the blue-sensitive plate. The estimated coordinates of the star are

$$\alpha(1950\cdot0) = 20\text{ h }26\text{ m }51\cdot4\text{ s} \pm 0\cdot4\text{ s}$$
$$\delta(1950\cdot0) = 38° 55\cdot5' \qquad \pm 0\cdot1'$$

There are many other stars, however, with the same property lying farther away from the OH position. The nearest continuum radiation maximum is the source DR 9 (ref. 17) ($T_A \simeq 2\cdot0°$ K) with the position

$$\alpha(1950\cdot0) = 20\text{ h }27\text{ m }50\text{ s}$$
$$\delta(1950\cdot0) = 38° 53'$$

It is interesting to note that the discovered sources are usually strongest at the frequency and polarization used when they were found. We might therefore expect to detect a few more sources when continuing the survey at the other OH frequencies and polarizations. This also might give a hint of the statistics of OH sources. Until now, the search for OH sources has often been guided by already detected H II regions or by the Westerhout catalogue, but we think that a search of an arbitrarily chosen area of the sky would give important information about the properties of OH emitting regions. From all available observations of OH sources it is evident that most sources are strongest at the 1,665 MHz line. Is this a reality or is it an apparent effect caused by an intense search at 1,665 MHz? The strong radiation of NML Cyg at 1,612 MHz, recently discovered, motivates this question. There are reasons to believe that all anomalous OH microwave emission originates from processes connected with the formation of stars. It would therefore be inter-

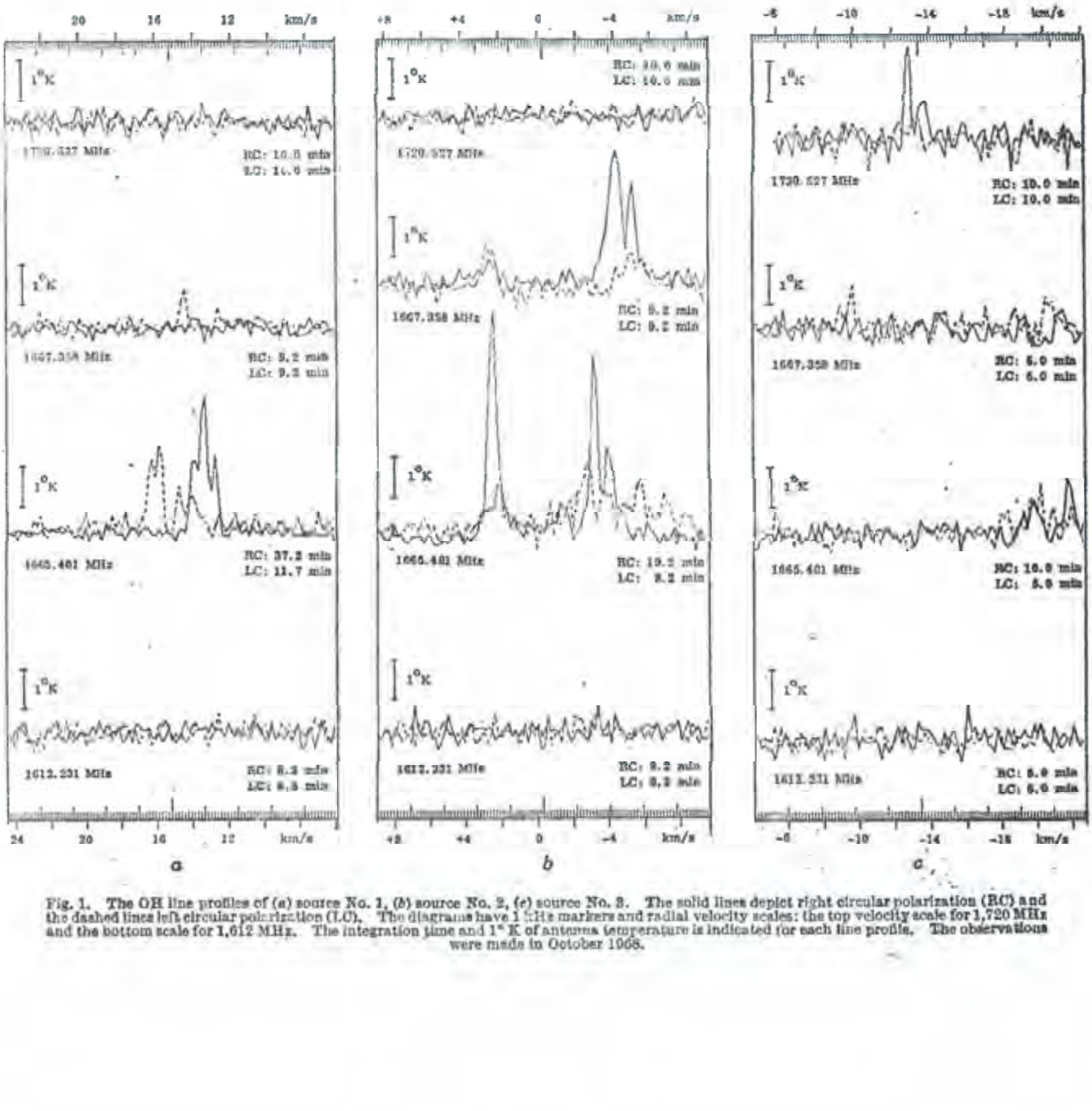

Fig. 1. The OH line profiles of (a) source No. 1, (b) source No. 2, (c) source No. 3. The solid lines depict right circular polarization (RC) and the dashed lines left circular polarization (LC). The diagrams have 1 kHz markers and radial velocity scales: the top velocity scale for 1,720 MHz and the bottom scale for 1,612 MHz. The integration time and 1° K of antenna temperature is indicated for each line profile. The observations were made in October 1968.

esting to make infrared observations of all known OH emission sources.

We thank the staff of Onsala Space Research Observatory and especially Professor O. E. H. Rydbeck and Dr E. Kollberg for discussions and cooperation. This work was supported by the Swedish Natural Science Research Council and the Swedish Board for Technical Development.

JOEL ELLDÉR
BERNT RÖNNÄNG
ANDERS WINNBERG

Onsala Space Research Observaotory,
Chalmers University of Technolgy, Gothenburg.

Received December 9, 1968.

[1] Weinreb, S., Barrett, A. H., Meeks, M. L., and Henry, J. C., *Nature*, 200, 829 (1963).
[2] Westerhout, G., *Bull. Astro. Inst. Ned.*, 14, 215 (1958).
[3] Gundermann, E., thesis, Harvard Univ. (1965).
[4] Weaver, H., Williams, D. R. W., Dieter, N. H., and Lum, W. T., *Nature*, 208, 29 (1965).
[5] Perkins, F., Gold, T., and Salpeter, E. E., *Astrophys. J.*, 145, 361 (1966).
[6] Cook, A. H., *Nature*, 210, 611 (1966).
[7] Raimond, E., and Eliasson, B., *Astrophys. J.*, 150, L171 (1967).
[8] Becklin, E. E., and Neugebauer, G., *Astrophys. J.*, 147, 799 (1967).
[9] Mezger, P. G., Altenhoff, W., Schraml, J., Burke, B. F., Reifenstein III, E. C., and Wilson, T. L., *Astrophys. J.*, 150, L157 (1967).
[10] Reddish, V. C., *Mon. Not. Roy. Astro. Soc.*, 135, 251 (1967).
[11] Wilson, W. J., and Barrett, A. H., *Science*, 161, 778 (1968).
[12] Neugebauer, G., Martz, D. E., and Leighton, R. B., *Astrophys. J.*, 142, 399 (1965).
[13] Kollberg, E., and Rydbeck, O. E. H., *IEEE Trans. Microw.*, MTT-16, 799 (1968).
[14] Elldér, J., *Res. Lab. Electronics*, Chalmers Univ. of Tech., Res. Rep. No. 87 (1968).
[15] *IAU Inform. Bull.*, No. 11 (1963).
[16] Ball, J. A., and Staelin, D. H., *Astrophys. J.*, 153, L41 (1968).
[17] Downes, D., and Rinehart, R., *Astrophys. J.*, 144, 937 (1966).

Printed in Great Britain by Fisher, Knight & Co., Ltd., St. Albans.

SEARCHES FOR MICROWAVE SPECTRAL LINE RADIATION FROM SOME MOLECULES IN THE INTERSTELLAR MEDIUM

BY

T. CATO, J. ELLDER, B. HÖGLUND, O.E.H. RYDBECK, B. RÖNNÄNG, AND A. SUME

RESEARCH REPORT NO 109

1972

RESEARCH LABORATORY OF ELECTRONICS
AND ONSALA SPACE OBSERVATORY

CHALMERS UNIVERSITY OF TECHNOLOGY

GOTHENBURG, SWEDEN

Research Laboratory of Electronics
and
Onsala Space Observatory
CHALMERS UNIVERSITY OF TECHNOLOGY
S - 402 20 Göteborg, Sweden

RESEARCH REPORT No. 109

SEARCHES FOR MICROWAVE SPECTRAL LINE RADIATION FROM SOME MOLECULES IN THE INTERSTELLAR MEDIUM

By
T. Cato, J. Elldér, B. Höglund, O. E. H. Rydbeck, B. Rönnäng, and A. Sume

Gothenburg, 1972

Searches for microwave spectral line radiation from some molecules in the interstellar medium

by

T. Cato, J. Elldér, B. Höglund, O. E. H. Rydbeck, B. Rönnäng, and A. Sume

Onsala Space Observatory, Chalmers University of Technology,

Onsala, Sweden

Abstract

The Onsala 25.6 m radio telescope equipped with travelling wave maser radiometers at the appropriate frequencies has been used in searches for absorption or emission lines from a number of different organic and inorganic molecules in the direction of several radio sources. The molecules include OH (the $v = 1$ vibrational state, $^2\pi_{3/2}$, $J = 3/2$; and the second and third harmonics of some ground state transitions), CH (the ground state $^2\pi_{1/2}$, $J = 1/2$, and the $^2\pi_{3/2}$, $J = 3/2$ excited state), SO_2, HCN, H_2CS, NH_2CHO, and CH_3CHO. All searches gave negative results, with possible exception for H_2CS. Details of the observations are tabulated.

Introduction

As of today, the existence of more than twenty different molecules (and some of their isotopic species) in interstellar space has been established. A picture of a surprisingly complex chemistry is beginning to emerge, and will, no doubt, be considerably extended during the next few years.

This paper describes some of the results obtained at Onsala Space

Observatory in a number of searches for new microwave molecular lines. All of the spectral lines looked for have reasonably well determined frequencies, obtained either from reported laboratory measurements or, in a few cases, calculated from molecular constants given in the literature. In all searches the frequency ranges covered were large enough to include the estimated errors in the laboratory or computed frequencies.

Equipment and method of observation

The observations were made with the 25.6 m Cassegrainian radio telescope and with a maser front- end at the appropriate frequency. The back-end consisted of one, or both, of two 100-channel filter receivers, with individual channel bandwidths of 1 and 10 kHz, respectively. The 100 kHz band of the narrow filter bank could be centered anywhere within the 1 MHz band of the wide filter bank. Every ten seconds the signal voltages of the filter banks were scanned and read in digital form into an on-line computer performing the signal integration. For the observations reported here the total system noise temperature (with the antenna pointed towards the zenith) ranged between 25 and 65 ^{o}K; the higher figures were obtained with an older feed system.

The spectrum was determined as the difference between the signals on and off the source. Frequency switching was used. Since the expected line width for all the spectral lines investigated was quite small, less than 100 kHz, the frequency displacement during the switching was kept in the range 200 - 300 kHz. Eventual spectral lines would therefore be observed twice within the 1 MHz band of the 10 kHz receiver, once as a positive deflection and once as a negative one. In this way the recognition of a true line signal was improved, and the number of "false alarms" caused by noise was reduced considerably.

Observations and results

a) Harmonic radiation from ground state OH

In the highly non-linear maser processes most likely responsible for the intense ground state OH emission, generation of harmonics appears feasible if the emitting objects are very small and contain free electrons in sufficient numbers. Results of searches for 2 x 1665, 2 x 1667, and 3 x 1612 MHz are given in Table I.

b) Vibrationally excited OH

The vibrationally excited OH transitions $^2\pi_{3/2}$, J = 3/2, v = 1, have been calculated from magnetic resonance experiments (Churg et al., 1970). The frequencies of the transitions F = 1-2, 1-1, 2-2, and 2-1 are 1489.05, 1536.79, 1538.96, and 1586.70 MHz, respectively. In a laboratory experiment, Potter et al. (1971) obtained a value of 0.3 sec for the radiative lifetime of the v = 1-0 transition of vibrationally excited OH. In dense regions like OH emission sources, however, radiation trapping could increase the radiative lifetime, and if one assumes a non-thermal population of the rotational and Λ -doublet states for v = 1, the vibrationally excited transitions $^2\pi_{3/2}$, J = 3/2, v = 1, could possibly be observed. Detection of radiation at any of the transition frequencies given above could supply important information on the near-infrared pumping mechanism proposed by Litvak (1969).

The OH sources W3 (OH) and NML Cyg were investigated. The latter source has an IR radiation maximum near 2.8 μ (Hyland et al., 1969), i.e., at the wavelength required to pump the first vibrationally excited state of OH from the ground state. There is no IR source in W3 (OH) proper, but one about 30'' away (Hilgeman, 1968; see Raimond et al., 1969). This IR-source is not necessarily related to the OH-emission (see for example Neugebauer et al., 1971) but is very similar to the IR-source found in the Orion nebula.

In the present investigation no radiation was detected down to a level of about 0.1 f.u. (1 f.u. $= 10^{-26}$ W. $m^{-2} Hz^{-1}$) for the three lowest transitions, see Table II. The line at 1586.70 MHz was not included in the search.

c) The $^2\Pi_{1/2}$, J = 1/2 and $^2\Pi_{3/2}$, J = 3/2 states of CH

The energy levels of the CH radical are similar to those of OH. In the case of CH, however, the $^2\Pi_{1/2}$, J = 1/2 state is the ground state. Several attempts have been made by various groups to detect ground state interstellar CH, mainly in a several hundred MHz wide band around 3000 MHz, all with negative results (including Onsala, 1968, unpublished). Recently, new spectroscopic data of CH, obtained from infrared laser magnetic resonance experiments, have been published (Evenson et al., 1971), as well as a new laboratory determination of the ground state transition at 10 cm (Baird et al., 1971).

We have searched both for the $^2\Pi_{1/2}$, J = 1/2 transition near the latest frequency determination 3374 MHz, and for the $^2\Pi_{3/2}$, J = 3/2 transition near 4771 MHz, but with negative results, see Table III.

d) SO_2

Sulphur dioxide (SO_2) is a slightly asymmetric molecule. Since the dipole moment (≈ 1.59 Debye units) is along the a-axis, the $1_{10} - 1_{11}$ transition at 1518.14 MHz is allowed (Microwave Spectral Tables, 1968).

The sources observed were W3 (OH), W3 (cont.), and W51. In the latter source, Penzias et al. (1971 b) report the presence of carbon monosulfide (CS). Our negative results on SO_2 are given in Table IV (see also the following Section f on H_2CS).

e) HCN

Hydrogen cyanide, HCN, is a linear molecule with dipole moment of approximately 2.99 D (Microwave Spectral Tables, 1968). The transition is caused by l-splitting, and quadrupole interaction due to the nitrogen atom splits the levels further. The frequencies of the transitions J = 4, F = 4-4, 3-3, and 5-5 are 4488.381 $\pm$ .020 MHz, 4488.522 $\pm$ .020 MHz, and 4488.522 $\pm$ .020 MHz (i.e., the two latter are equal), respectively (Microwave Spectral Tables, 1968). The transitions J = 1-0, F = 1-1, 2-1, and 0-1 around 88.6 GHz have been observed in emission by Snyder et al. (1971) in a number of sources.

The present observations in several sources are summarized in Table V. Three of the sources, W3 (OH), W51, and DR 21, are among those showing emission at 88.6 GHz.

f) H_2CS

Thioformaldehyde, H_2CS, is a slightly asymmetric molecule. The transition $1_{10} - 1_{11}$ at 1046.48 $\pm$ .02 MHz (Johnson et al., 1970), is allowed, since the dipole moment (about 1.6 D) is along the a-axis. Previously reported searches by Evans et al. (1970) and Davies et al. (1971) in several radio sources have given negative results. The limits reported by the Berkeley and Jodrell Bank teams have been considerably improved on in the present observations. Somewhat to our surprise, integration times as long as 50 hours appear to be feasible with the filter receivers used. Table VI shows the results. Evans et al. (1970) predict antenna temperatures under various hypotheses. Since their antenna beam size is the same as ours, a direct comparison can be made with our results. From their Table I it can be seen that their lowest expected antenna temperatures are higher by a factor 5 to 10 than our observed values. This lends support to their suspicion that either the ratio H_2CS/H_2CO is less than the cosmic abundance ratio S/O (1/40), or that the lower H_2CS abundance is due to the chemical and excitation processes involved.

Recently the $2_{11} - 2_{12}$ transition at 3139.38 MHz has been observed in Sgr B 2 (Sinclair et al., 1971), with an intensity corresponding to an abuncance ratio S/O of about 1/15 in this somewhat peculiar source. If this ratio is the same in other sources as well, this would indicate that at 1046 MHz the 1_{11} level is underpopulated. We have searched for the $2_{11} - 2_{12}$ transition in a few other sources, with negative results, however, see Table VI.

Although we tentatively consider the present results on H_2CS to be negative, there is some indication of an absorption feature in W51 at about + 52 km/sec. Figure 1 shows the combined results of two series of observations centered at + 52 and + 65 km/s (weighed with respect to integration time as well as system noise temperature, see Table IV). In the figure we have for comparison also plotted the emission profiles of the 140.8 GHz ortho - H_2CO line, $2_{12} \rightarrow 1_{11}$, (Thaddeus, et al., 1971), and the 147.0 GHz, $J = 3 \rightarrow 2$ transition in CS (Penzias, et al., 1971 b). Both emissions have their maxima, at + 55 km/s, and + 57 km/s respectively, in the velocity region between the H_2CO - and the (possible) H_2CS -absorptions, whose maxima lie about 14 km/s apart (with H_2CO at 66 km/s). In this context it is also interesting to notice that the $J = 1 \rightarrow 0$ transition at 88.6 GHz of HCN has an emission maximum at + 53 km/s (Snyder, et al., 1971), and the $J = 1 \rightarrow 0$, 115.3 GHz transition of $^{12}C^{16}O$ one at + 57 km/s (the $^{13}C^{16}O$ spectrum, the 110.2 GHz line, is comparable in intensity, with a peak at about + 56 km/s, which seems to indicate that $^{12}C^{16}O$ is highly saturated; Penzias et al., 1971 a).

Since molecular emission lines at millimeter wavelengths are generally signs of ultradense regions, where H_2CS may be more abundant, the velocity difference between the H_2CO and the H_2CS ground state absorptions does not seem to be unnatural. It should be mentioned in this context that a distinct velocity difference between the 140.8 GHz and the 4.83 GHz lines of formaldehyde exists also in the Sgr A source (it has the same sign and amounts to about 15 km/s).

Our main reason for questioning the reality of the H_2CS absorption feature shown in Figure 1 is due first of all to the long integration time required (about 52 hours), during which the highly sensitive low-noise system could have picked up some interfering signals (for example down-scattered pulse transmissions), and, second, to the presence of the adjacent H 184 α - line, at 1047.095 MHz (see Fig. 1). We urge observers with access to a bigger telescope to confirm or reject this feature.

g) $\underline{NH_2CHO}$

Formamide, NH_2CHO, is also a slightly asymmetric molecule, with the dipole moment along the a-axis ($\approx$ 3.61 D, Landolt-Börnstein, 1967) allowing the $1_{10} - 1_{11}$ transition at 1539.53 MHz. A further splitting of the levels occurs by quadrupole interaction due to the nuclear spin of the nitrogen atom. The frequencies of the transitions F = 2-2 and F = 1-1 are 1539.82 and 1538.08 MHz, respectively. Formamide emission has been detected at 4617.14 and 4620.03 MHz (corresponding to the transitions $2_{12} - 2_{11}$, F = 2-2 and 1-1) in Sgr A and Sgr B 2 by Rubin et al. (1971).

When the present observations around 1540 MHz were made, the molecular constants were not known with sufficient accuracy to permit an exact calculation of the $1_{10} - 1_{11}$ frequencies, and thus the line at 1538.08 MHz was not included in the search. By chance, however, the frequency range covered in NML Cyg and W3 (OH) in the observations of vibrationally excited OH was large enough to include the 1538.08 MHz line (see Table II). A fair amount of integration time was obtained on W3 (cont.) and W51, see Table VII.

Litvak (private communication) has recently informed us that the ground state line at 1539.82 MHz has been found in Sgr A and Sgr B 2. No numerical values are available at the moment.

h) $\underline{CH_3CHO}$

Acetaldehyde, CH_3CHO, is a molecule with internal rotation. The asymmetric rigid rotor levels are split into an A-level (non-degenerate) and an E-level (degenerate). The dipole moment along the a-axis is 2.55 D (Microwave Spectral Tables, 1968), and the allowed $1_{..} - 1_{..}$ ...

of the pseudo-rigid rotor is 1065.1 $\pm$.8 MHz for the A-level.

Observations were made on W3 (cont.), W51, and DR 21. The results are listed in Table VIII.

* * *

We wish to thank the entire staff at Onsala Space Observatory for contributing in various ways to the observations.

These observations have in part been supported by the Swedish Natural Science Research Council, and the Swedish Board for Technical Development.

References

Baird, K.M., and Bredohl, H. 1971, Ap.J. (Letters), 169, L83.

Cato, T. 1970 (unpublished).

Churg, A., and Levy, D.H. 1970, Ap.J. (Letters), 162, L161.

Davies, R.D., Booth, R.S., and Pedlar, A. 1971, Mon.Not.R.astr. Soc., 152, 7p.

Evans, N.J., Townes, C.H., Weaver, H.F., and Williams, D.R.W. 1970, Science, 169, 681.

Evenson, K.M., Radford, H.E., and Moran, M.M. 1971, Appl.Phys. Letters, 18, 426.

Hyland, A.R., Becklin, E.E., Neugebauer, G., and Wallerstein, G. 1969, Ap.J., 158, 619.

Johnson, D.R., and Powell, F.X.1970, Science, 169, 679.

Landolt-Börnstein, New Series, Group II, Vol. 4, 1967.

Litvak, M.M. 1969, Ap.J., 156, 471.

Litvak, M.M. 1971 (private communication).

Microwave Spectral Tables. 1968, N.B.S. Monog. 70 (Washington: Superintendent of Documents).

Neugebauer, G., Becklin, E., and Hyland, A.R. 1971, Ann.Rev.Astron. Ap., 9, 67.

Penzias, A.A., Jefferts, K.B., Wilson, R.W. 1971 a, Ap.J., 165, 229.

Penzias, A.A., Solomon, P.M., Wilson, R.W., and Jefferts, K.B. 1971 b, Ap.J. (Letters), 168, L53.

Potter, A.E., Coltharp, R.N., and Worley, S.D. 1971, J.Chem. Phys., 54, 992.

Raimond, E., and Eliasson, B. 1969, Ap.J., 155, 817.

Rubin, R.H., Swenson, G.W., Benson, R.C., Tigelaar, H.L., Flygare, W.H. 1971, Ap.J. (Letters), 169, L39.

Sinclair, M.W., Ribes, J.-C., Fourikis, N., Brown, R.D., and Godfrey, P.D. 1971, IAU Circular No. 2362.

Snyder, L.E., and Buhl, D. 1971, Ap.J. (Letters), 163, L47.

Thaddeus, P., Wilson, R.W., Kutner, M., Penzias, A.A., Jefferts, K.B. 1971, Ap.J. (Letters), 168, L59.

Comments to the tables

The radial velocities are given with respect to the local standard of rest.

If not otherwise indicated in the tables the filterbanks have been centered on the rest frequency of the line at the given radial velocity.

The source antenna temperatures given are approximate.

The rms-sensitivities have been calculated according to the following formulas with usual meaning of symbols:

$$\Delta T_{rms} = \frac{2 \cdot T_{syst}}{\sqrt{B \cdot \tau}} ; \qquad \Delta S_{rms} = \frac{2 k \Delta T_{rms}}{A_{eff}}$$

The polarization has been linear if not otherwise stated.

TABLE I

Harmonics of OH ground state $^2\Pi_{3/2}$, $J = 3/2$

a) Rest frequency: 2 x 1665.401 = 3330.802 MHz
Time of observation: August 1968
Filter bandwidth: 10 kHz
System temperature off source: 75°K

Source	Radial velocity km/s	Integration time	Source antenna temperature °K	Sensitivity ΔT_{rms} °K	Sensitivity ΔS_{rms} f.u.
W3	−44.5	2^h45^m	≈ 0	0.015	0.19
W49	+10	1^h	4	0.026	0.34
W75	+ 5	3^h30^m	5	0.014	0.18

b) Rest frequency: 2 x 1667.358 = 3334.716 MHz
Time of observation: August 1968
Filter bandwidth: 10 kHz
System temperature off source: 75°K

Source	Radial velocity km/s	Integration time	Source antenna temperature °K	Sensitivity ΔT_{rms} °K	Sensitivity ΔS_{rms} f.u.
W3	−44.5	1^h40^m	≈ 0	0.019	0.25
W49	+10	1^h20^m	4	0.023	0.29
W75	+ 5	55^m	5	0.028	0.36

c) Rest frequency: 3 x 1612.231 = 4836.693 MHz
Time of observation: April 1969
Filter bandwidth: 10 kHz
System temperature off source: 55°K

Source	Radial velocity km/s	Integration time	Source antenna temperature °K	Sensitivity ΔT_{rms} °K	Sensitivity ΔS_{rms} f.u.
NML Cyg	−20	1^h	0	0.018	0.32

TABLE II

Vibrationally excited OH, $^2\Pi_{3/2}$, J = 3/2, v = 1

Rest frequencies: 1489.05 MHz (F = 1 – 2)
1536.79 MHz (F = 1 – 1)
1538.96 MHz (F = 2 – 2)
1586.70 MHz (F = 2 – 1)

Time of observation: March 1971
Filter bandwidth: 10 kHz
System temperature off source: 25 °K

Source	Radial velocity km/s	Center frequency MHz	Integration time	Source antenna temperature °K	Polarization	Sensitivity ΔT_{rms} °K	ΔS_{rms} f.u.
NML Cyg	–23.9	1488.40	40^m	≈ 0	Linear *	0.008	0.08
		1489.10	1^h50^m		"	0.005	0.05
		1489.80	40^m		"	0.008	0.08
		1536.20	2^h05^m		"	0.005	0.05
		1536.90	1^h50^m		Left circ.	0.005	0.05
		1536.90	2^h20^m		Right circ.	0.005	0.05
		1537.60	1^h50^m		Linear	0.005	0.05
		1538.30	1^h40^m		"	0.005	0.05
		1539.00	3^h20^m		Left circ.	0.004	0.04
		1539.00	2^h00^m		Right circ.	0.005	0.05
		1539.70	2^h00^m		Linear	0.005	0.05
W3 (OH)	–45	1489.10	45^m	7.5	Linear	0.011	0.11
		1536.20	2^h30^m		"	0.006	0.06
		1536.90	1^h30^m		Left circ.	0.008	0.08
		1536.90	2^h25^m		Right circ.	0.006	0.06
		1537.60	2^h00^m		Linear	0.007	0.07
		1538.30	2^h20^m		"	0.006	0.06
		1539.00	2^h30^m		Left circ.	0.006	0.06
		1539.00	1^h55^m		Right circ.	0.007	0.07
		1539.70	2^h00^m		Linear	0.007	0.07

* E-plane in the N – S direction

TABLE III

$CH, {}^2\Pi_{1/2}, J = 1/2$

Time of observation: October, November 1971
Filter bandwidth: 10 kHz
System temperature off source: 37°K

Source	Radial velocity km/s	Frequency range MHz	Integration time	Source antenna temperature °K	Sensitivity ΔT_{rms} °K	ΔS_{rms} f.u.
Cas A	-25	3366.78-3383.38	30^m	84	0.057	0.78
DR 21	0	3361.98-3385.06	40^m	3	0.016	0.22
Orion A	0	3365.82-3385.06	40^m	29	0.027	0.37
Sgr B2	+50	3365.82-3384.10	30^m	≈0	0.034	0.47
W51	+60	3361.98-3385.06	40^m	13	0.020	0.28

Excited $CH, {}^2\Pi_{3/2}, J = 3/2$

Time of observation: June 1971
Filter bandwidth: 10 kHz
System temperature off source: 45°K

W3 (cont)	-40	4765.5-4771.5	20^m	6	0.028	0.47
"	-40	4771.5-4773.5	40^m	6	0.020	0.34

TABLE IV

SO_2

Rest frequency: 1518.14 MHz
Time of observation: May 1971
Filter bandwidth: 1 and 10 kHz
System temperature off source: 25°K

Source	Radial velocity km/s	Integration time	Source antenna temperature °K	Sensitivity ΔT_{rms} °K	ΔS_{rms} f.u.
W3 (cont.)	−40	2^h20^m	15	0.009	0.09
W3 (OH)	−40	3^h50^m	8	0.006	0.06
W51	+60	5^h30^m	30	0.008	0.08

TABLE V

HCN

Adopted center frequency: 4488.4 MHz
Time of observation: March 1970
Filter bandwidth: 10 kHz
System temperature off source: 60°K

Source	Radial velocity km/s	Integration time	Source antenna temperature °K	Sensitivity ΔT_{rms} °K	Sensitivity ΔS_{rms} f.u.
Cyg A	+3.7	30^m	24	0.04	0.6
DR 21	-3	30^m	2	0.03	0.5
NGC 2024	+8.5	1^h25^m	≈ 0	0.02	0.3
ON 3 (K3-50)	-14	30^m	≈ 0	0.03	0.5
Sgr B2	+60	40^m	8	0.03	0.5
W3 (cont.)	-40	1^h15^m	6	0.02	0.3
W3 (OH)	-45	1^h15^m	≈0	0.02	0.3
W43	+80	30^m	6	0.03	0.5
W51	+65	45^m	8	0.03	0.4

TABLE VI

$\underline{H_2CS}$ $1_{10} - 1_{11}$

Rest frequency: 1046.48 MHz
Time of observation: September 1970 - April 1971
Filter bandwidth: 1 and 10 kHz

Source	Radial velocity km/s	Integration time	System temperature off source ^oK	Source antenna temperature ^oK	Sensitivity ΔT_{rms} ^oK	ΔS_{rms} f.u.
Cyg A	0	5^h25^m	45	210	0.037	0.36
DR 21	-24	23^h30^m	40	10	0.003	0.034
"	- 4	20^h40^m	40	10	0.004	0.036
M 8	0	35^m	45	10	0.024	0.24
ON 4	- 4	3^h	40	10	0.010	0.096
Orion A	+ 9	35^h50^m	45	6	0.003	0.028
Sgr A	0	7^h10^m	45	60	0.013	0.13
W3 (cont.)	-40	12^h20^m	40	15	0.005	0.052
W4	-40	12^h20^m	40	6	0.004	0.043
W5	-100	7^h35^m	25	12	0.005	0.047
W12	-91	8^h35^m	25	6	0.004	0.035
"	+ 9	35^h50^m	45	6	0.003	0.028
W44	-20	3^h50^m	25	10	0.006	0.059
"	+65	44^h25^m	40	10	0.003	0.025
W51	-20	11^h20^m	25	30	0.006	0.054
"	+52	8^h05^m	25	30	0.007	0.064
"	+65	44^h25^m	40	30	0.004	0.035
W67	-24	23^h30^m	40	10	0.004	0.034
"	- 4	17^h40^m	40	10	0.004	0.039

$\underline{H_2CS}$ $2_{12} - 2_{11}$

Rest frequency: 3139.38 MHz
Time of observation: October 1971
Filter bandwidth: 10 kHz

DR 21	0	3^h20^m	35	3	0.007	0.085
Orion A	0	4^h	35	29	0.011	0.14
W3 (cont)	-40	1^h35^m	35	7	0.011	0.14
W51	+60	3^h30^m	35	13	0.009	0.10

TABLE VII

NH_2CHO

Rest frequencies: 1539.82 MHz (Transition $1_{10} - 1_{11}$, F = 2 - 2)
1538.08 MHz (Transition $1_{10} - 1_{11}$, F = 1 - 1)

Time of observation: April - May 1971
Filter bandwidth: 1 and 10 kHz
System temperature off source: 25 °K

Source	Radial velocity km/s	Center frequency MHz	Integration time	Source antenna temperature °K	Sensitivity ΔT_{rms} °K	ΔS_{rms} f.u.
W3 (cont)	-40	1539.35	4^h50^m	15	0.006	0.062
"	"	1540.25	1^h40^m	"	0.010	0.10
"	"	1540.35	3^h55^m	"	0.007	0.068
W51	+60	1539.35	6^h25^m	30	0.007	0.073
"	"	1540.25	6^h	"	0.008	0.076
"	"	1540.35	10^h	"	0.006	0.059

TABLE VIII

CH_3CHO

Rest frequencies: 1065.1 ± 0.8 MHz (Transition $(1_{11} - 1_{10})_A$)

Time of observation: February 1971
Filter bandwidth: 1 and 10 kHz

Source	Radial velocity km/s	Center frequency MHz	Integration time	System temperature off source °K	Source antenna temperature °K	Sensitivity ΔT_{rms} °K	ΔS_{rms} f.u.
DR 21	− 4	1066.0	2^h55^m	45	10	0.011	0.11
W3	−40	1061.7	2^h	65	15	0.019	0.19
"	−40	1062.1	3^h20^m	65	15	0.015	0.15
"	−40	1063.1	4^h	65	15	0.013	0.13
"	−40	1064.1	4^h50^m	65	15	0.012	0.12
"	−40	1065.1	8^h30^m	65	15	0.009	0.09
"	−40	1066.1	7^h50^m	65	15	0.010	0.10
W51	+60	1062.1	50^m	65	30	0.035	0.34
"	+60	1064.1	1^h50^m	65	30	0.023	0.23
"	+60	1065.1	2^h40^m	65	30	0.019	0.19
"	+60	1066.1	3^h40^m	65	30	0.017	0.16

Figure caption

Figure 1. The observed H_2CS spectrum after 52^h30^m integration (solid line), showing possible absorption at + 52 km/sec. As comparison the emission lines of ortho-H_2CO at 140.8 GHz (Thaddeus et al., 1971) and of CS at 147.0 GHz (Penzias et al., 1971 b) are plotted, as well as the H_2CO absorption at 4.83 GHz. The asymmetric CS profile indicates a possible component near + 52 km/sec.

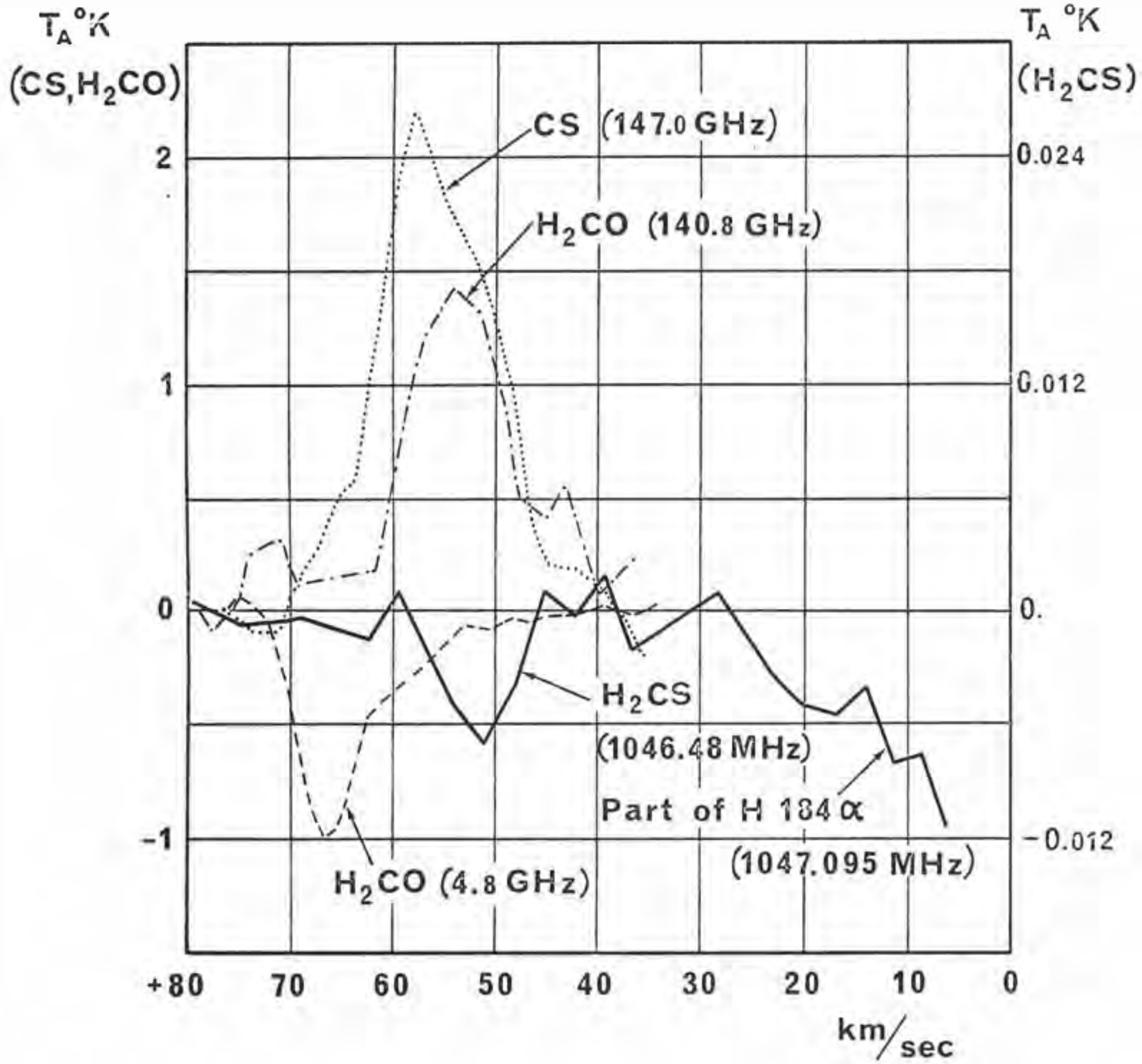

T_A °K
(CS, H_2CO)
T_A °K
(H_2CS)
CS (147.0 GHz)
H_2CO (140.8 GHz)
H_2CS
(1046.48 MHz)
Part of H 184 α
(1047.095 MHz)
H_2CO (4.8 GHz)
2
1
0
-1
0.024
0.012
0.
-0.012
+80
70
60
50
40
30
20
10
0
km/sec

Research Reports from the Research Laboratory of Electronics:

1. O.E.H. Rydbeck and K.H.B. Wilhelmsson: The influence of the electron velocity distribution on space charge waves. 1959.

2. K.H.B. Wilhelmsson: Oscillatory properties of gyromagnetic electronic cold plasmas with drift motion. 1959.

3. H.B.Hvatum: Solar radio noise measurements during the 1954 solar eclipse. 1959.

4. T.Aa. Orhaug: Ionospheric observations during the solar eclipse June 30, 1954. 1959.

5. K.H.B. Wilhelmsson: The electromagnetic coupling between an electron beam and incident plane waves for an axially finite interaction domain. 1960.

6. Research notes communicated at the radio scientific conference in Stockholm, February 29 - March 2, 1960. 1960.

7. O.E.H. Rydbeck: The propagation and coupling of waves in inhomogeneous media with applications to electromagnetic and space charge waves. (On the propagation of waves in an inhomogeneous medium II).

8. O.E.H. Rydbeck: Electromagnetic and space charge waves in inhomogeneous structures with applications to ionized media and microwave tubes. 1960.

9. K.H.B. Wilhelmsson: On the geometrical theory of diffraction with application to the electron beam. 1960.

10. O.E.H. Rydbeck: The Doppler effect in dispersive, inhomogeneous media with applications to electromagnetic waves in ionized media. 1960.

11. S. Olving and A. Ots: An experimental investigation of the propagation of space charge waves along radially inhomogeneous electron beams. 1960.

12. A.V.Stomberg: The rotatron-an electron tube for shift and multiplication of frequencies. 1960.

13. O.E.H. Rydbeck and M.R.Fischer: Space charge waves in an electron beam of Gaussian cross section. 1960.

14. O.E.H. Rydbeck: The integral equation of traveling wave tubes with electron beams of arbitrary cross section. 1960.

15. O.E.H. Rydbeck and A.R. Thomasson: Low frequency waves in inhomogeneous magneto ionic media. 1960.

16. T.Aa.Orhaug: Observations of radio star scintillations at high latitudes. 1960.

17. T.Aa. Orhaug: Observations of solar radio noise at 150 Mc/s. 1960.

18. O.E.H. Rydbeck and J. Askne: Whistler mode - ionized stream interactions. Part I, 1963.

19. K.H.B. Wilhelmsson: On the problem of overtaking in a velocity distributed electron stream. 1960.

20. O.E.H. Rydbeck: On the coupling between waves in inhomogeneous systems. 1960.

21. O.E.H. Rydbeck: Research in the field of propagation and interaction of electromagnetic waves and space charge type waves in homogeneous and inhomogeneous media. 1960.

22. D.T. Farley, J.P. Dougherty and D.W. Barron: A theory of incoherent scattering of radio waves by a plasma in a uniform magnetic field. 1961.

23. L.F. Eastman: Coherent non-linearities in a magneto-ionic medium. 1961.

24. D.T. Farley: Artificial heating of the electrons in the F-region of the ionosphere. 1961.

25. K.H.B. Wilhelmsson: Scattering of electromagnetic waves by an anisotropic medium. 1961.

26. K.H.B. Wilhelmsson: The interaction between an obliquely incident plane electromagnetic wave and an electron beam in the presence of a static magnetic field of arbitrary strength. 1961.

27. O.E.H. Rydbeck: Dynamic non-linear wave propagation in ionized media. 1. The isotropic medium. 1961.

28. O.E.H. Rydbeck: Dynamic non-linear wave propagation in ionized media. 2. The magneto-ionic medium. 1962.

HIGH RESOLUTION SPECTRA OF SOME STRONG GALACTIC OH EMISSION SOURCES

BY

B.O. RÖNNÄNG

RESEARCH REPORT NO 101

1972

RESEARCH LABORATORY OF ELECTRONICS AND ONSALA SPACE OBSERVATORY

CHALMERS UNIVERSITY OF TECHNOLOGY

GOTHENBURG, SWEDEN

CHALMERS TEKNISKA HÖGSKOLA GÖTEBORG

Research Laboratory of Electronics
CHALMERS UNIVERSITY OF TECHNOLOGY
Gothenburg, Sweden

RESEARCH REPORT No. 101

HIGH RESOLUTION SPECTRA OF SOME STRONG GALACTIC OH EMISSION SOURCES

By

B. O. Rönnäng

Gothenburg, 1972

HIGH RESOLUTION SPECTRA OF SOME STRONG GALACTIC OH EMISSION SOURCES

Abstract: The 84-foot (25. 6 m) radio telescope of the Onsala Space Observatory has been used for detailed examinations with 250 Hz resolution of the 18 - cm spectral line emission from eight well-known strong OH sources. Models obtained by incoherent superposition of circularly polarized Gaussian features have been fitted to the spectra. No significant deviations from Gaussian shape of the individual features, for example caused by the OH maser amplification, could be seen. The observations were compared with earlier measurements made since 1969 with the same receiver system for evidence of variabilities and of possible correlation between changes in intensity and line-width. An intensity change by a factor of seven over a week was observed in one component of the right circularly polarized emission of W75B at 1665 MHz.

I. Introduction

Although spectra of a great number of strong ground state OH emission sources have been published in recent years only a few spectra have been measured with rms noise low enough and velocity resolution high enough to reveal and analyse weak and narrow components [Meeks et al (1966), Ball and Meeks (1968), Palmer and Zuckerman (1967), Coles and Rumsey (1970)] . As many spectral components have been reported to vary in strength,observations with high velocity resolution and high signal to noise ratio would offer an improved ability todetect variations in all three parameters — intensity , half-power width and center velocity — defining an individual feature.

Rotating, contracting as well as expanding geometric models have been suggested for the masering OH cloud. One observational test of the models would be to observe the possible changes in the radial velocities of the features as a function of time. It has been pointed out by Wilson et al (1970) that the rotational model proposed for the OH/IR sources could result in a velocity change observable over a few years. Furthermore, if the masering OH cloud is unsaturated variations in intensity should be correlated with changes in the spectral linewidth. An assumed amplification factor of 10 and a 3 dB decrease in intensity should result in line-broadening of 3. 5 % , which might be observable if appropriate filter bandwidth and high signal to noise ratio are used.

The study reported here was undertaken to investigate the number of velocity components, their center velocities, velocity broadenings, and flux densities of a few of the strongest OH line emitters of various classes. The results are compared with the same parameters of spectra measured earlier with the same system and with spectra published from other observatories. A particular goal of the measurements was to get good data for planned very long baseline interferometer measurements. Some of the sources measured with 250 Hz resolution were, in fact, included in the July 1969 Onsala to Haystack VLBI experiment [Rönnäng et al (1970)] . The high-resolution interferometer observations done so far reveal the bright Doppler features in the spectra to be separate emission sources. Single antenna high resolution spectra combined with a decomposition of the spectra into Gaussian components are therefore a useful guide for these observations.

II Equipment and Observations

The observations were made with the 25. 6 m radio telescope of the Onsala Space Observatory. The receiver system consisted of a traveling-wave maser, a multichannel spectrograph and a real time computer. At the wavelength of 18 cm the half power beamwidth of the antenna was 32' x 27' and the aperture efficiency was 53 % making 1 f. u. (10^{-26} Wm^{-2} Hz^{-1}) correspond to 0.1 ^{o}K antenna temperature . Various parts of the receiver system have been described by Elldér (1968), Rydbeck and Kollberg (1968) and Winnberg (1971).

Circular polarization was achieved by a dielectric quarter wavelength plate inserted in the circular part of the waveguide after the feed horn. The measured isolation between left and right circular polarization was greater than 20 dB and the differences in system gain at each polarization were less than a few per cent.

Out of the available bandwidths of the spectrograph 60 channels with 10 kHz bandwidth (to check gain stability), 100 channels with 1 kHz bandwidth and 40 channels with 250 Hz bandwidth were used. By means of the second local oscillator the center frequency of the 250 Hz filter bank could be moved to give the total spectrum with 250 Hz resolution. Some of the 250 Hz resolution spectra are composed of seven filter banks with different center frequencies. The first local oscillator, controlled by a rubidium frequency standard, was set to compensate for the

Doppler shift due to the motions of the earth. The local oscillator frequency was kept constant during a 10 minutes integration interval, thus resulting in a line broadening of at most about 20 Hz. All calculations of radial velocities were carried out relative to the local standard of rest assuming a solar motion of 20 km/s towards the direction $\alpha = 18^h01^m54^s.97$, $\delta=30^o\ 00'\ 03''.96$, epoch 1950.0.

The receiver was frequency switched over an interval of 240 kHz and the system noise temperature varied between 30^oK and 40^oK. The increased system temperature was probably due to attenuation in front of the maser.

The observations were carried out in the following way:

1. A calibration level was measured with the aid of a noise tube giving a 22.5^oK calibration signal with an integration time of 10 minutes.

2. A zero line was measured 2^o off the source followed by a ten minutes on source integration. As the total observed bandwidth for the 250 Hz filter bank was 10 kHz and the maser bandwidth was about 6 MHz (Kollberg, 1970) a straight line could be fitted (least-square fit) to the zero line and the observing time off source could be minimized. Three on-off source observations were taken using the same calibration. As the calibration signal is comparable with the strongest OH features the spectrum was moved in the filter banks, thus reducing calibration errors of the individual channels and also errors due to the individual filter characteristics. The above routine was done automatically by means of the on-line Linc-8 computer and the resulting spectra were stored on magnetic tapes for further integration and analysis.

The rest frequencies of the OH emission used were 1612.231 MHz, 1665.401 MHz, 1667.358 MHz and 1720.528 MHz. Notice that the 1720 MHz frequency generally employed for astronomical observations is 1720.527 MHz. The 1720.528 MHz used in these measurements implies that the velocities given in figure 16 and table VII have been increased by 0.174 km/s.

III Gaussian analysis of measured spectra

The extremely high brightness temperatures (greater than 10^{13} ^{o}K in some cases) of the emission regions, the narrowness of the emission lines, and the anomalous intensity ratios of the different lines can all be explained by the maser mechanism. The problem is to get enough evidence to find the right maser model for the various OH classes. One of the question is if the maser is saturated or not. The analysis of the statistical properties of the OH radiation by Evans et al (1972) gave no answer.

It is well-known that in an unsaturated maser the received flux is proportional to exp ($\int$ Gdl), where G is the gain per unit length in the masering cloud. The intensity will grow exponentially with amplification path length. If the velocity distribution of the OH molecules is Gaussian the final line shape will be exponential Gaussian and the line will be narrowed by a factor $(\int \mathrm{Gdl})^{-1/2}$.
In the fully saturated maser, on the other hand, where the output is limited by the number of OH molecules, the line shape will exactly reflect the molecular velocity distribution. There will be no line narrowing and the line shape will be Gaussian.

The model used here represents the emission spectrum as an incoherent superposition of left and right circularly polarized features each with a Gaussian profile. Such a representation is of course not unique when two or more components overlap in Doppler frequency. However, we restrict the model to comprise a minimum number of components and include only those features that are clearly evident above noise in the data. The method reported by Kaper et al. (1966) has been used in the Gaussian analysis program written for the IBM 360/65 computer of the Gothenburg Universities' Computing Centre.

The rms error in the Gaussian parameters has been estimated by Gaussian fits to an estimated mean profile with a half-power-width of 0.3 km/s. If the components in the total spectrum are well separated, an integration time of 1 hour results in an rms error of 0.05 ^{o}K of the spectrum (if the source emission $<<$ 30^{o}K) and approximate rms errors in the Gaussian parameters of 0.03 ^{o}K and 0.005 km/s for the amplitude and half-power-width, respectively. Normally several components overlap and the errors are much larger. Also, the systematic errors due to calibration errors and other instrumental effects may be of the same order.

In the following paragraph the measured spectra are denoted, for example, "right circularly polarized emission from", which in this case means spectra measured with right circular polarization. The emission in itself may be linearly or elliptically polarized,or unpolarized as in the case of the OH/IR sources NML Cygnus and R Aql.

IV Observations

ON 2 [$RA_{1950.0} = 20^h19^m 51^s.9$; $\delta_{1950.0} = 37^o17'02''$]

The ON2 source, discovered by Elldér et al (1969) is a Type I OH source (Turner, 1969) and is the strongest of the ON 1- ON4 sources. It has been observed and discussed in detail by Winnberg (1970). The right circularly polarized spectrum at 1665 MHz has been reexamined in December 1971 and April 1972. Winnberg noticed an intensity variation in the -3. 95 km/s feature. However, figure 1 indicates that the -3. 05 km/s feature has the strongest variation. Its amplitude has changed from 3. 8 ^{o}K in Dec. 1968 and April 1970 to 0. 7^{o}K in Dec. 1971 and April. 1972. No detectable changes have taken place between Dec. 1971 and April 1972. Figure 1 shows 1 kHz spectra observed 1968.8 , 1970. 3, 1971. 9 and 1972. 3.

The 250 Hz-resolution spectrum and the 1971. 9 1 kHz-resolution spectrum have been decomposed into Gaussian components. Table I gives the parameters of the 9 dominating components in the velocity range from - 4. 6 km/s to + 2. 5 km/s. Notice that the components obtained from the 1 kHz spectra agree very well with those obtained from the high-resolution spectrum. Figure 2 shows the 250 Hz-resolution spectrum, the fitted Gaussian components, and the residuals between measured spectrum and the sum of the Gaussian components. Due to space limitation the spectrum has been divided into two overlapping parts. Notice the different antenna temperature scales of the two parts.

It was suggested by Gehrz et al (1970) that ON2 was associated with the red star BC Cygni. However, interferometer position measurements made by Hardebeck and Wilson (1971) show that ON2 lies 5' south of the position of BC Cygni. ON 2 is probably associated with the HII region catalogued by Reifenstein et al (1970) at a position of $RA_{1950.0} = 20^h19^m47^s$ and $\delta_{1950.0} =$ $= 37^o19'53''$.

TABLE I A

PARAMETERS OF OH EMISSION COMPONENTS IN ON2 RC 1665 MHZ

COMP.	CENTER VELOCITY (KM/S)	AMPLITUDE (K)	HALF POWER WIDTH* (KM/S)	INTEGRATED FLUX (WM^{-2} *10^{-22})	EQUIVALENT KINETIC TEMPERATURE** (K)
1	2.46	4.19	0.485	6.0	87.
2	1.99	0.68	0.229	0.5	19.
3	1.66	0.42	1.279	1.6	607.
4	0.47	0.53	0.443	0.7	73.
5	-1.32	0.79	0.774	1.8	223.
6	-2.42	0.33	0.562	0.6	117.
7	-3.05	0.84	0.430	1.1	69.
8	-3.95	1.99	0.409	2.4	62.
9	-4.58	0.55	0.315	0.5	37.

* INSTRUMENTAL BROADENING REMOVED
** THE EQUIVALENT KINETIC TEMPERATURES HAVE NOT BEEN CORRECTED FOR ANY TURBULENT BROADENING

TABLE I B

PARAMETERS OF OH EMISSION COMPONENTS IN ON2 RC 1665 MHZ

COMP.	CENTER VELOCITY (KM/S)	AMPLITUDE (K)	HALF POWER WIDTH* (KM/S)	INTEGRATED FLUX (WM^{-2} *10^{-22})	EQUIVALENT KINETIC TEMPERATURE** (K)
1	-4.53	0.45	0.407	0.5	62.
2	-3.92	1.91	0.322	1.8	38.
3	-3.07	0.66	0.579	1.1	124.
4	-1.36	0.58	0.820	1.4	249.
5	-2.39	0.27	0.407	0.3	62.
6	0.51	0.50	0.356	0.5	47.
7	1.43	0.30	0.702	0.6	183.
8	2.47	4.25	0.471	5.9	82.
9	1.98	0.70	0.346	0.7	44.

* INSTRUMENTAL BROADENING REMOVED
** THE EQUIVALENT KINETIC TEMPERATURES HAVE NOT BEEN CORRECTED FOR ANY TURBULENT BROADENING

The parameters in table I A are obtained from the 250 Hz resolution spectrum and the parameters in table I B are obtained from the 1 kHz resolution spectrum.

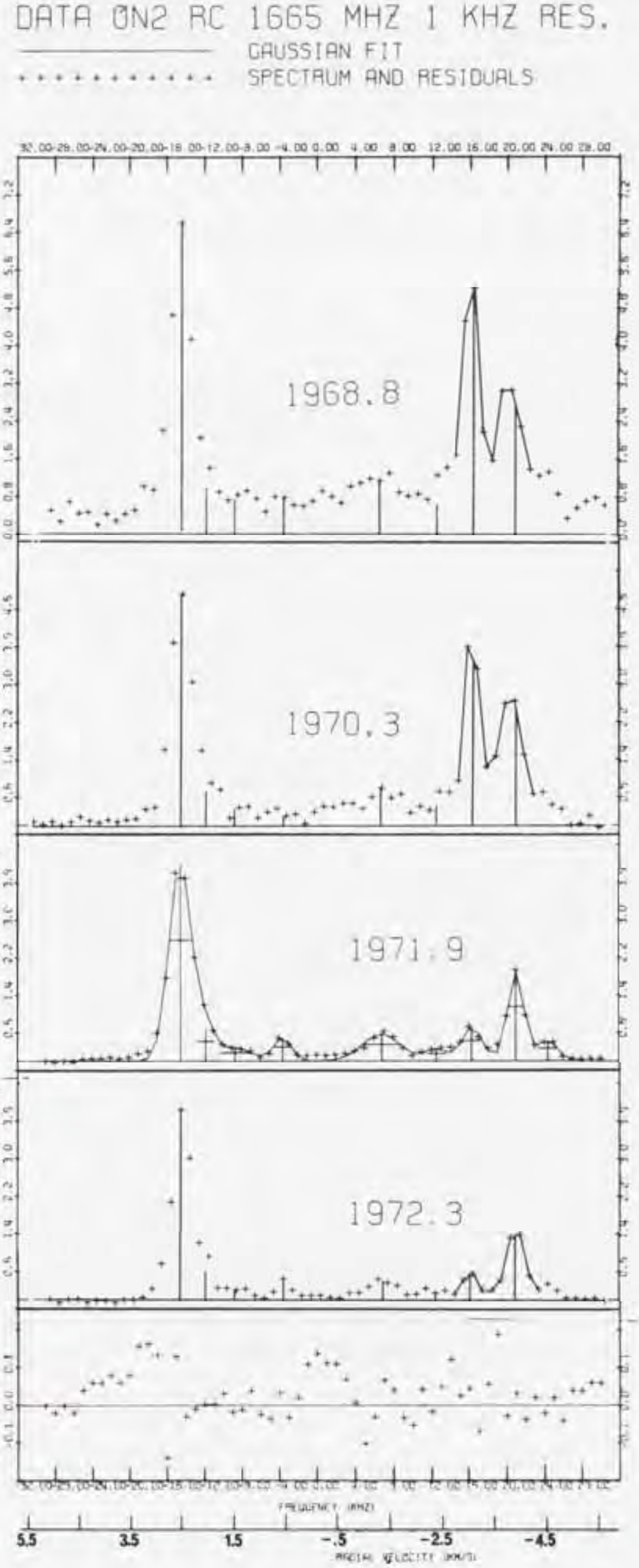

Fig. 1 Spectra of the right circularly polarized OH emission from ON2 at 1665 MHz measured 1968.8, 1970.3, 1971.9 and 1972.3. Radial velocity is relative LSR. Notice the strong amplitude change in the -3.1 km/s component. The residuals plotted are the 1971.9 spectrum minus the sum of the Gaussian components listed in table I B. Frequency resolution is 1 kHz.

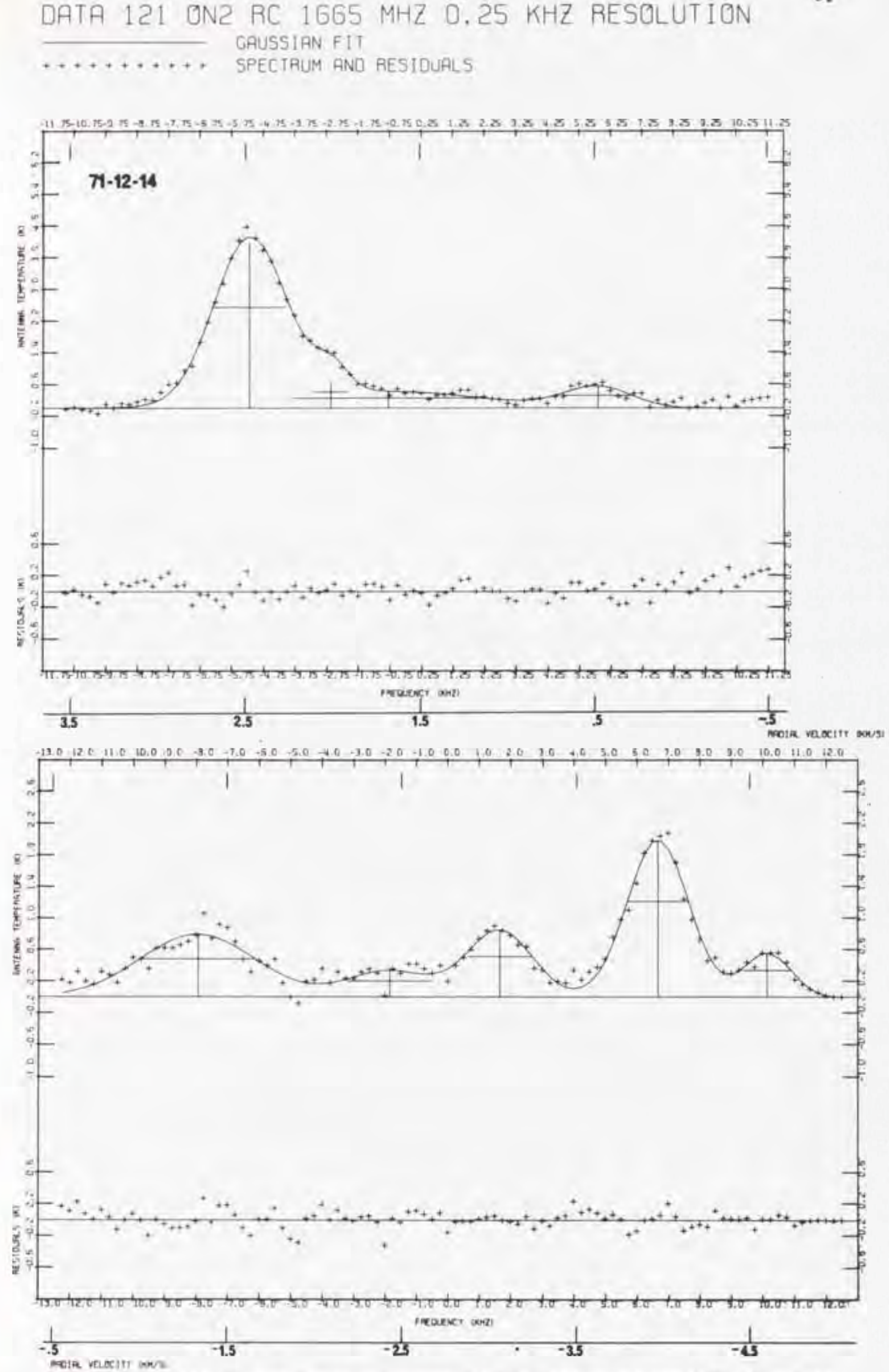

Figure 2. 250 Hz-resolution spectrum of OH emission source ON2. Gaussian components have been fitted to the spectrum and the residuals (measured spectrum minus the sum of the Gaussian components) are plotted. Notice the different amplitude scales.

NML Cygnus [$RA_{1950.0} = 20^h44^m34^s$; $\delta_{1950.0} = 39^o55'56''$]

The 1612 MHz OH emission from NML Cygnus* is the strongest that has been found, so far. Both emission regions, centered at -22 km/s and + 20 km/s, are complex and at least twenty components can be seen in the 250 Hz resolution spectrum shown in figure 3. No attempt has been made to fit Gaussian components to the spectrum.

The unpolarized OH emission from NML Cygnus was first detected by Wilson and Barret (1968) and detailed single antenna and VLBI studies have been performed by Wilson et al (1970). They measured a total integrated flux of 1250 $Wm^{-2} \cdot 10^{-22}$ for the lower velocity emission and 410 $Wm^{-2} \cdot 10^{-22}$ for the higher velocity emission, in good agreement with the 1140 $Wm^{-2} \cdot 10^{-22}$ and 420 $Wm^{-2} \cdot 10^{-22}$ obtained from figure 3.

No time variations have been seen in the 1612 MHz emission observed with 1 kHz resolution at Onsala on different occations from July 1968 to Dec. 1971.

Davies et al (1972) measured the relative positions of the principal features or groups of features in NML Cygnus. All the components are distributed in an elongated region 3.3 arc sec x 2.3 arc sec at a position angle of 150^o.

---

* The IR star NML Cygni, discovered by Neugebauer et al (1965), is one of the brightest IR star at 10 μ with an I-K magnitude of 8.2.

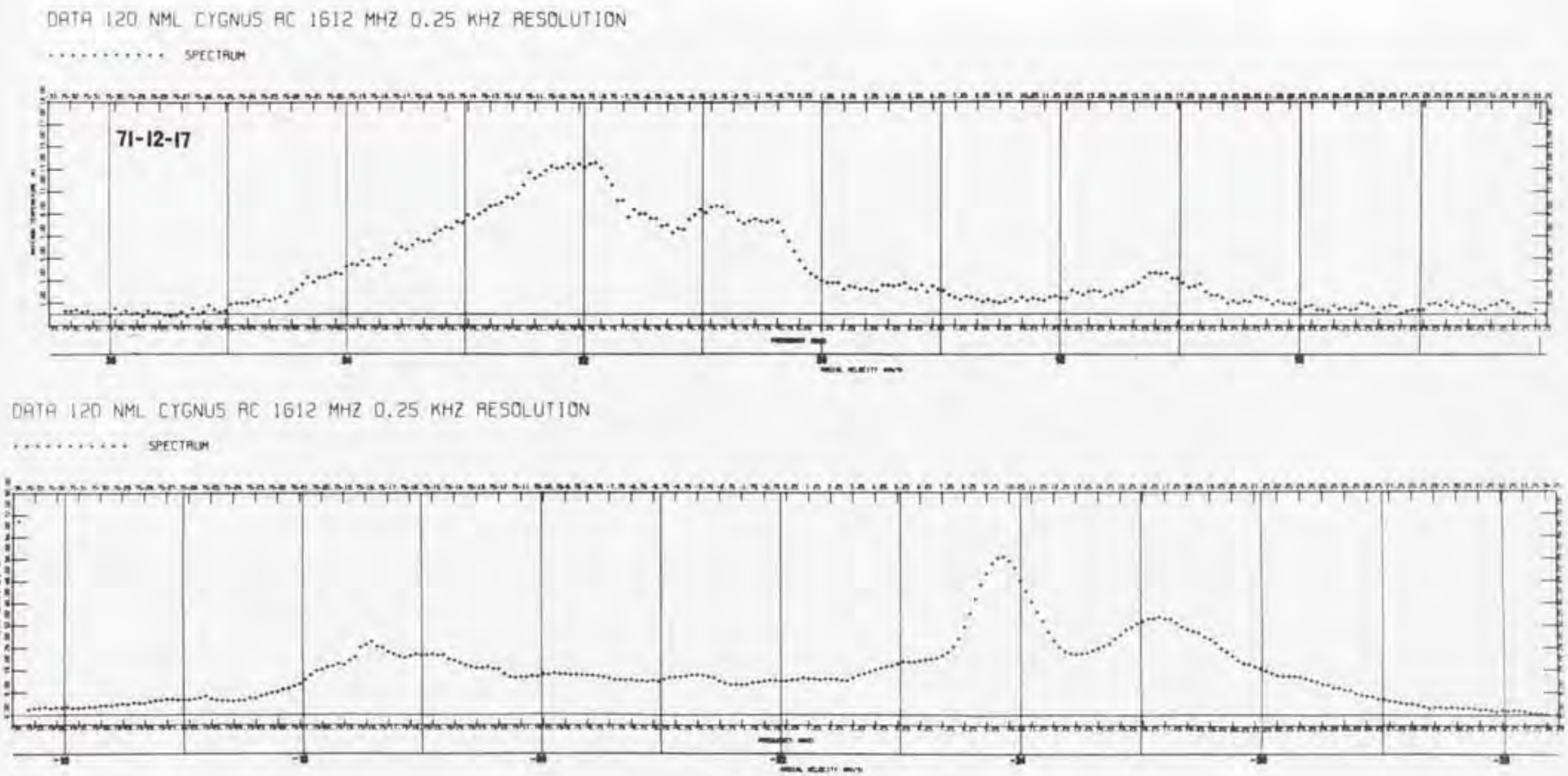

Fig. 3 High velocity-resolution spectrum of the OH emission from NML Cygnus at 1612 MHz.

IRC + 10406 (R Aquila) [$RA_{1950.0} = 19^h 03^m 58.0^s$; $\delta_{1950.0} = 08^o 09.'1$]

IRC + 10406, identified with the Mira variable R. Aql, is one of the strongest of the Type II OH/IR sources so far detected [Wilson et al, 1970]. The 1612 MHz high-velocity spectrum is shown in figure 4. (The low-velocity component is very weak with a peak flux of a few f. u. at a velocity of 43 km/s.) The component at 53.96 km/s has an equivalent half-width of 0.83 km/s, corresponding to a kinetic temperature of 257 ^oK if the width is due entirely to thermal broadening. In December 1968 Wilson et al. (1970) observed a half-width of 1 km/s for the same feature and a total integrated flux of 5.6 $Wm^{-2} \cdot 10^{-22}$ for the low-velocity emission and 38.4 $Wm^{-2} \cdot 10^{-22}$ for the high-velocity emission. In Sept. 1970 the total integrated flux of the high-velocity feature had increased to 46.1 $Wm^{-2} \cdot 10^{-22}$ [Wilson et al, 1972]. The integrated flux of the spectrum in figure 4 is 43.8 $Wm^{-2} \cdot 10^{-22}$. Table II lists the parameters of the four emission components. Like other OH/IR sources IRC +10406 is unpolarized.

IRC +10406 was included in the Dec. 1971 Haystack - Green Bank - Onsala VLBI experiment.

TABLE II

PARAMETERS OF OH EMISSION COMPONENTS IN R AQL AC 1612 MHZ

COMP.	CENTER VELOCITY (KM/S)	AMPLITUDE (K)	HALF POWER WIDTH* (KM/S)	INTEGRATED FLUX (WM^{-2} $*10^{-22}$)	EQUIVALENT KINETIC TEMPERATURE** (K)
1	54.69	0.55	0.200	0.3	15.
2	54.32	0.63	0.232	0.4	20.
3	53.96	8.28	0.831	19.7	256.
4	52.83	0.82	0.655	1.5	159.

* INSTRUMENTAL BROADENING REMOVED
** THE EQUIVALENT KINETIC TEMPERATURES HAVE NOT BEEN CORRECTED FOR ANY TURBULENT BROADENING

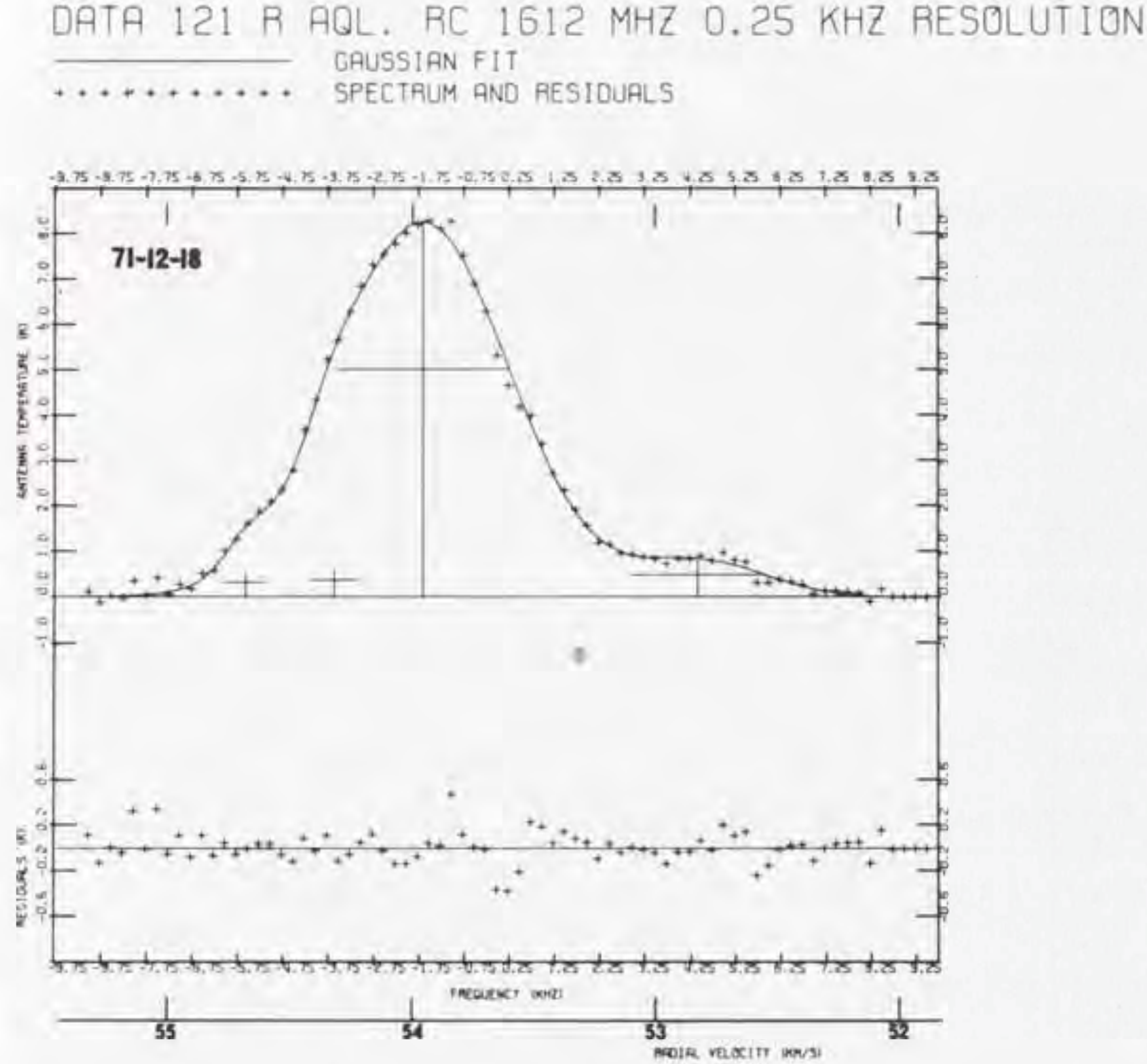

Fig. 4 High-resolution 1612 MHz spectrum of IRC + 10406 centered at 54 km/s.

W3 OH [$RA_{1950.0} = 2^h 23^m 16.^s 8$; $\delta_{1950.0} = 61^o 38' 54''$]

The class I OH emission source near W3 was used as a calibration source because of its great strength and because it has been thoroughly observed. Single antenna observations of the Stokes parameters have been reported by Meeks et al (1966) and by Coles et al (1968). Interferometer position measurements have been made by Rogers (1967) and Raimond and Eliasson (1969) and radio maps of the individual RC and LC polarized components have been obtained by Moran et al (1968) and Cooper et al (1970). The W3 OH source is associated with a compact HII region at a distance of 2. 6 kpc mapped by Wynn-Williams (1971).

Figures 5 and 6 show the right and left circularly polarized emission from W3 OH at 1665 MHz measured with 250 Hz frequency resolution. As seen from the figures Gaussian components fit the profile very well. The rms deviation between the measured profile and the sum of Gaussian components is equal to $0.2^o K$. in agreement with the theoretical value. Notice that the rms fluctuation is 2. 5 times higher at the top of the -45. 1 km/s component than in velocity intervals with no emission.

The deviation from Gaussian shape mentioned by Meeks et al. (1966), especially for the LC polarized 1665 MHz feature at a velocity of -45 km/s, is probably due to th fact that this feature is composed of at least two Gaussian components.

The Gaussian components are listed in table III for the RC and LC polarized emission. Also included are the components of the 1667 MHz emission, the spectra of which are shown in figures 7 and 8.

The component with a radial velocity of -41.7 km/s in the right circularly polarized emission at 1665 MHz has been reported to be variable by Wilson et al. (1972). They studied the relative intensities of several features as a function of time. In 1971.3 they measured relative amplitudes of 100/18/22/25/30/26 for the features with radial velocities and polarizations -46.5,LC/-47.4,RC+LC/ -41.3,RC/-43.0,RC/-49.1,RC+LC/-41.7,RC km/s, respectively. Our spectra measured in December 1971 with 250 Hz resolution, give the following relative intensities 100/18/25/24/38/25.

The right circularly polarized emission at 1667 MHz contains the narrowest feature detected. The -43.1 km/s component has a half-power-width of 0.14 km/s corresponding to an equivalent kinetic temperature of 7 ^{o}K, if the width is due entirely to thermal broadening and the maser amplification is fully saturated.

TABLE III A

PARAMETERS OF OH EMISSION COMPONENTS IN W3 RC 1665 MHZ

COMP.	CENTER VELOCITY (KM/S)	AMPLITUDE (K)	HALF POWER WIDTH* (KM/S)	INTEGRATED FLUX $(WM^{-2} *10^{-22})$	EQUIVALENT KINETIC TEMPERATURE** (K)
1	-39.46	0.81	0.220	0.5	18.
2	-40.76	1.33	0.198	0.8	15.
3	-41.25	6.38	0.511	9.6	97.
4	-41.72	5.51	0.357	5.8	47.
5	-42.24	2.24	0.558	3.7	115.
6	-42.70	2.85	0.268	2.3	27.
7	-43.03	6.07	0.259	4.6	25.
8	-43.77	22.24	0.289	19.0	31.
9	-44.31	5.72	0.502	8.5	94.
10	-45.05	54.70	0.332	53.7	41.
11	-45.30	19.93	0.263	15.5	26.
12	-45.57	0.39	0.953	1.1	337.
13	-47.40	1.52	0.207	0.9	16.
14	-48.48	1.74	0.185	1.0	13.
15	-49.05	1.72	0.242	1.2	22.

* INSTRUMENTAL BROADENING REMOVED
** THE EQUIVALENT KINETIC TEMPERATURES HAVE NOT BEEN CORRECTED FOR ANY TURBULENT BROADENING

TABLE III B

PARAMETERS OF OH EMISSION COMPONENTS IN W3 LC 1665 MHZ

COMP.	CENTER VELOCITY (KM/S)	AMPLITUDE (K)	HALF POWER WIDTH* (KM/S)	INTEGRATED FLUX $(WM^{-2} *10^{-22})$	EQUIVALENT KINETIC TEMPERATURE** (K)
1	-43.73	1.00	0.268	0.8	27.
2	-44.47	6.96	0.562	11.6	117.
3	-44.54	2.47	0.150	1.1	8.
4	-45.02	14.82	0.323	14.2	39.
5	-45.31	11.42	0.224	7.6	19.
6	-45.54	18.74	0.409	22.6	62.
7	-46.31	25.29	0.592	44.2	130.
8	-46.62	11.57	0.246	8.4	22.
9	-47.40	2.70	0.289	2.3	31.
10	-47.67	0.30	1.610	1.4	962.
11	-48.66	1.35	0.494	2.0	91.
12	-49.09	8.11	0.263	6.3	26.

* INSTRUMENTAL BROADENING REMOVED
** THE EQUIVALENT KINETIC TEMPERATURES HAVE NOT BEEN CORRECTED FOR ANY TURBULENT BROADENING

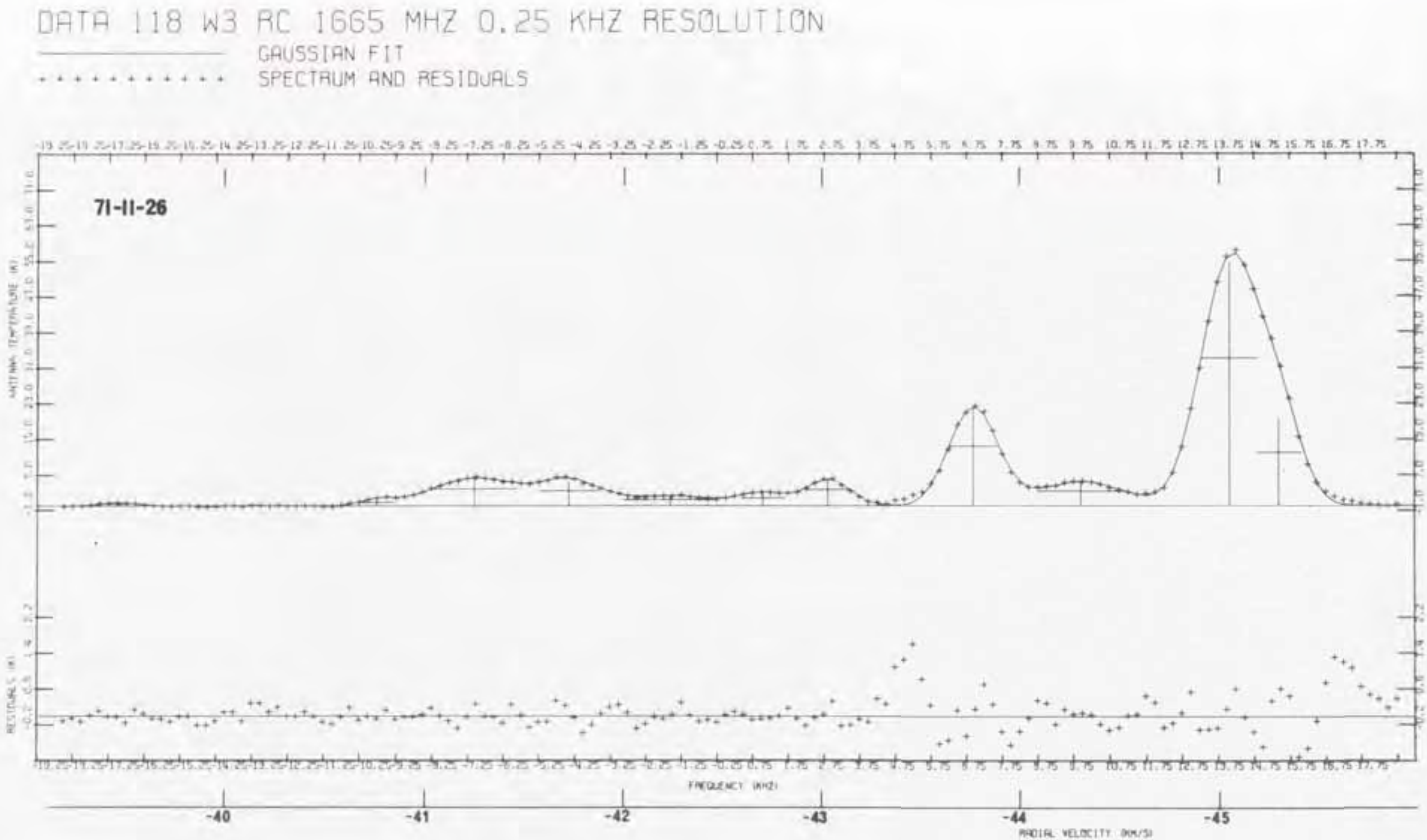

Figure 5. Right circularly polarized emission from W3 at 1665 MHz. The spectrum in the velocity interval -44 to -50 km/s is shown on next page. Frequency resolution is 250 Hz.

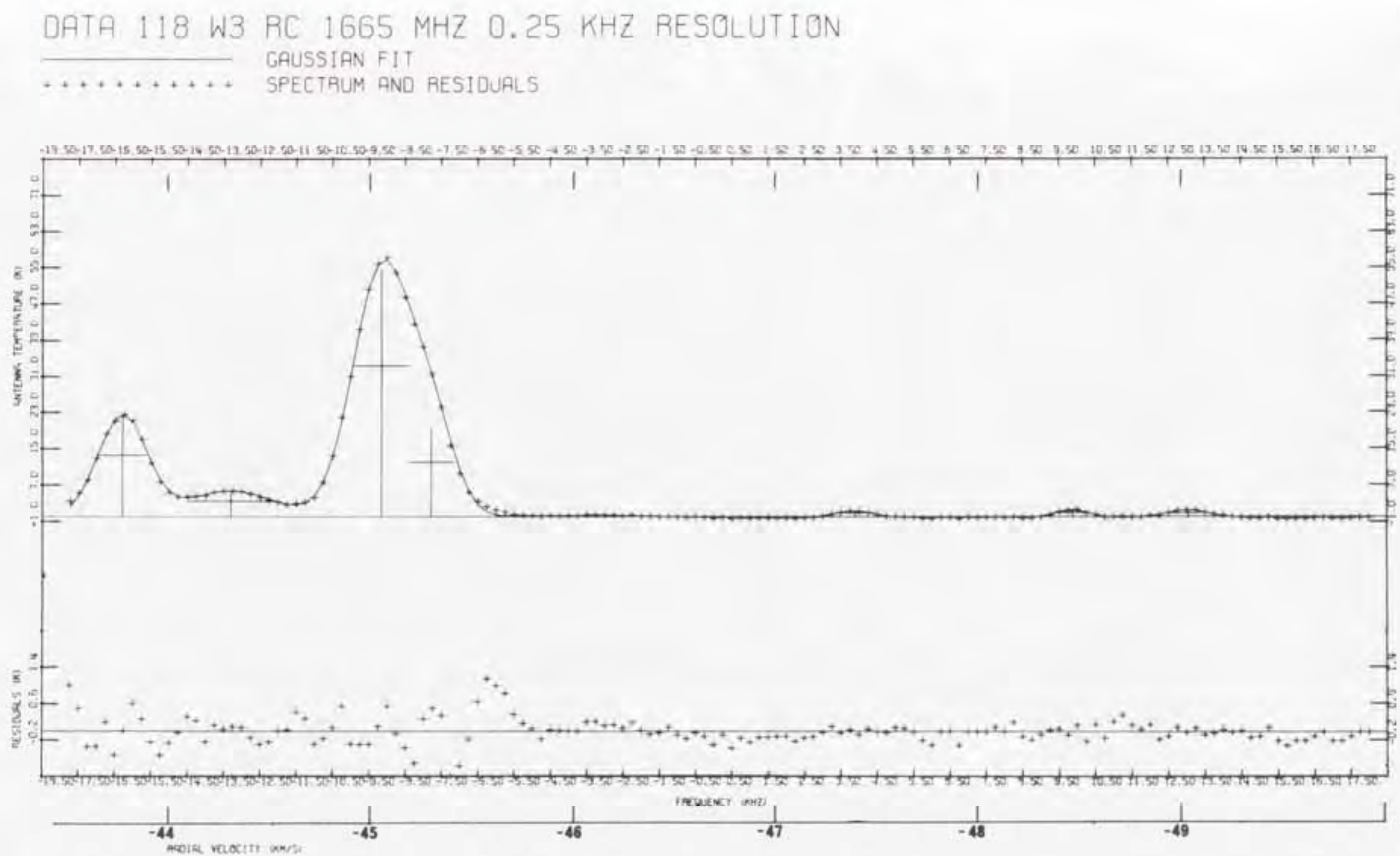

Figure 5 (cont.) Right circularly polarized emission from W3 at 1665 MHz. The spectrum in the velocity interval -39 to -46 km/s is shown on previous page. Frequency resolution is 250 Hz.

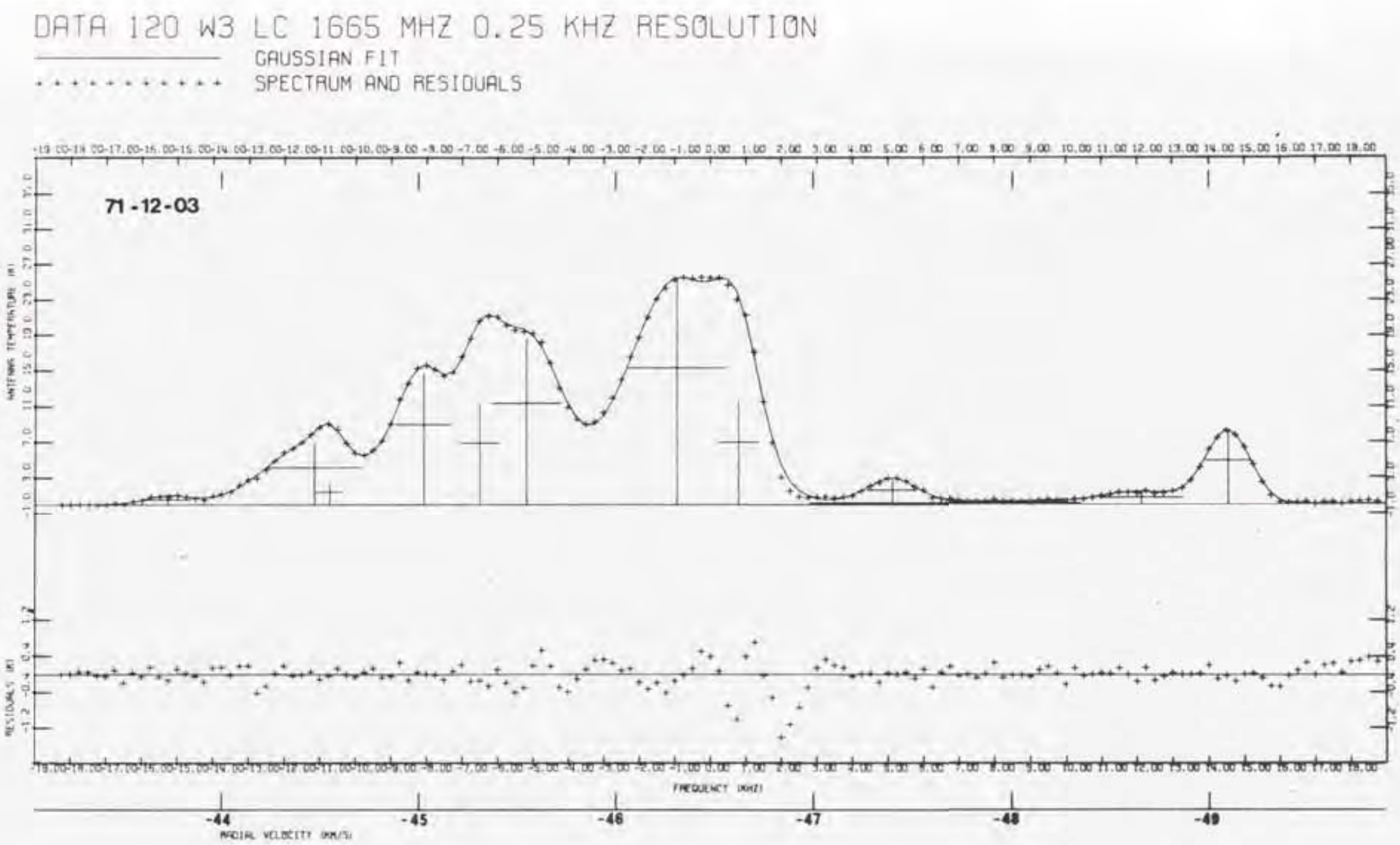

Figure 6 Left circularly polarized emission from W3 at 1665 MHz. Frequency resolution is 250 Hz.

TABLE **IV A**

PARAMETERS OF OH EMISSION COMPONENTS IN W3 RC 1667 MHZ

COMP.	CENTER VELOCITY (KM/S)	AMPLITUDE (K)	HALF POWER WIDTH* (KM/S)	INTEGRATED FLUX ($WM^{-2}*10^{-22}$)	EQUIVALENT KINETIC TEMPERATURE** (K)
1	-41.78	0.30	0.181	0.2	12.
2	-42.32	2.22	0.220	1.4	18.
3	-42.64	0.93	0.267	0.7	26.
4	-42.73	-0.27	2.464	-2.0	****
5	-43.11	1.85	0.141	0.8	7.

* INSTRUMENTAL BROADENING REMOVED
** THE EQUIVALENT KINETIC TEMPERATURES HAVE NOT BEEN CORRECTED FOR ANY TURBULENT BROADENING

TABLE **IV B**

PARAMETERS OF OH EMISSION COMPONENTS IN W3 LC 1667 MHZ

COMP.	CENTER VELOCITY (KM/S)	AMPLITUDE (K)	HALF POWER WIDTH* (KM/S)	INTEGRATED FLUX ($WM^{-2}*10^{-22}$)	EQUIVALENT KINETIC TEMPERATURE** (K)
1	-43.25	0.47	0.408	0.6	62.
2	-43.94	0.96	0.150	0.4	8.
3	-44.29	0.94	0.198	0.6	15.
4	-44.70	3.86	0.387	4.4	56.
5	-45.05	3.12	0.211	2.0	17.

* INSTRUMENTAL BROADENING REMOVED
** THE EQUIVALENT KINETIC TEMPERATURES HAVE NOT BEEN CORRECTED FOR ANY TURBULENT BROADENING

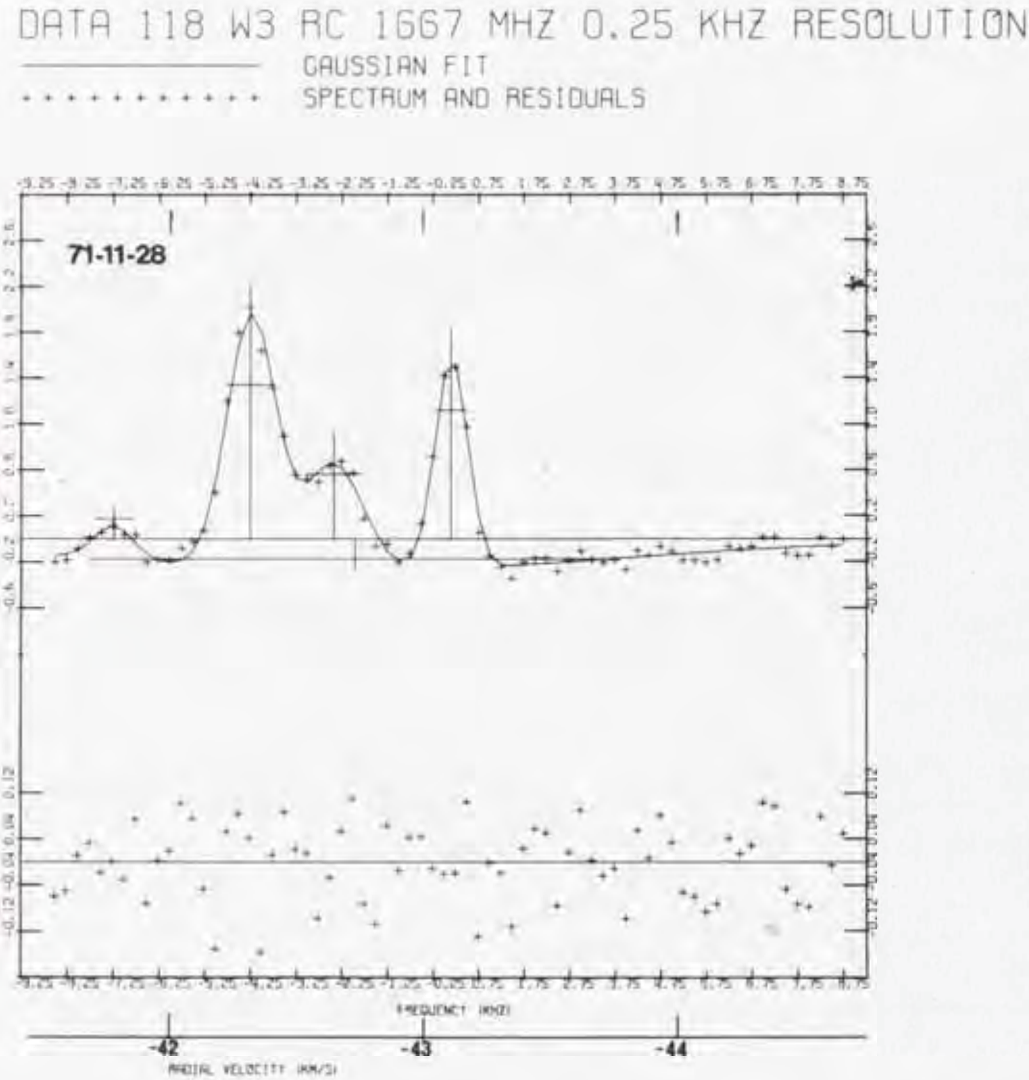

Figure 7 Right circularly polarized emission from W3 at 1667 MHz. Frequency resolution is 250 Hz.

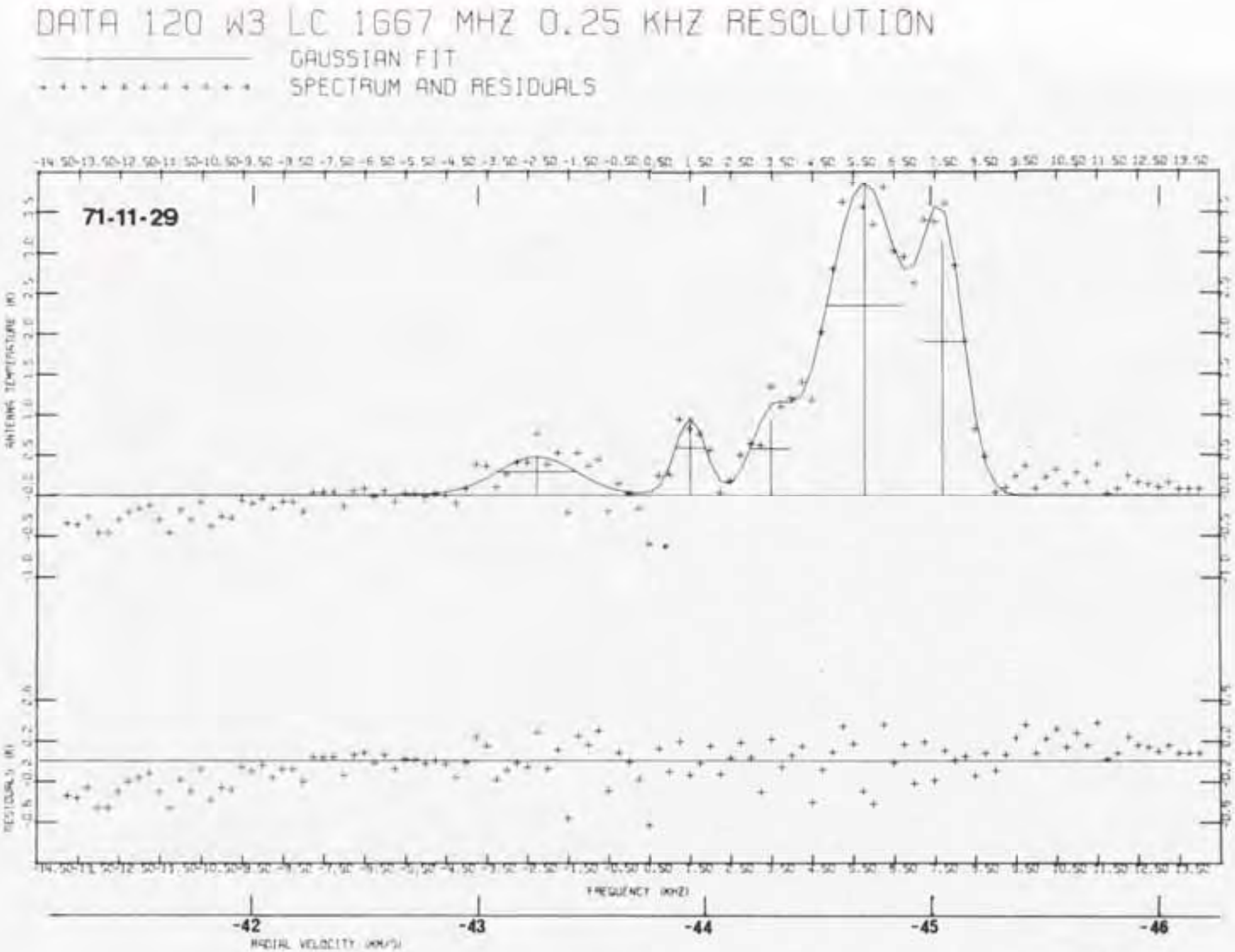

Figure 8 Left circularly polarized emission from W3 at 1667 MHz. Frequency resolution is 250 Hz.

W 75 A (S) [$RA_{1950.0} = 20\ 37^m\ 15^s$; $\delta_{1950.0} = 42^o 12' 09''$]

W 75 B (N) [$RA_{1950.0} = 20^h 36^m 50^s$; $\delta_{1950.0} = 42^o 26' 58''$]

The position of the W75A OH source, determined by Raimond and Eliasson, is 3 arc min north of the compact HII region DR21 in the diffuse HII region W75. The northern source W75B was detected by Rydbeck et al. (1969) and Zuckerman et al (1969) and is situated 25^s west and 15' north of W75A. This is fairly close to a weak continuum source in the 1407 MHz map published by Wynn-Williams (1971).

Ryle and Downes (1967) give a probable location of the continuum source DR21 in the Perseus arm at a distance of 6 kpc, while Mezger et al (1971) give a distance to DR 21 of 1.5 -3 kpc. Peculiar motions and deviations from circular motions in the direction of CygnusX introduce these uncertainties in the kinematic distance determination.

Rydbeck et al. (1970) have detected strong intensity variations in the emission from the F = 3 → 3 transition of the $^2\Pi_{3/2}$, J = 5/2 state of OH in W75B and have correlated the time variations of the excited OH emission with variations of the 1667 MHz emission. They also reported weak temporal variations in the 1665 MHz emission of W75A but no variations in the 1665 MHz emission of W75B. Figure 9 shows the RC polarized spectrum of W75B measured with 1 kHz resolution on the 13th and 20th Dec. 1971. Notice the low intensity of the 9.3 km/s feature in the upper spectrum. This component normally shows up with an intensity of about 3.5^oK. The fast intensity variation can hardly be an instrumental effect as four independent spectra were taken with the lower intensity and the change can be seen in the spectra measured with 1 kHz as well as 10 kHz resolution. It is also hard to explain the variations on the basis of two separate sources and an antenna pointing error as W75A (in velocity interval 0 to 4 km/s), half a beam-width away, has the expected intensity. The 9.3 km/s component may be of the same type as the transient source found by Elldér at 1667 MHz at the position $20^h 36^m 58^s$; $+42^o 50'$ (Elldér,1971).

The Gaussian components obtained from the measurements with 250 Hz resolution are summarized in tables V- VI and Figures 10 - 13 show the high resolution spectra.

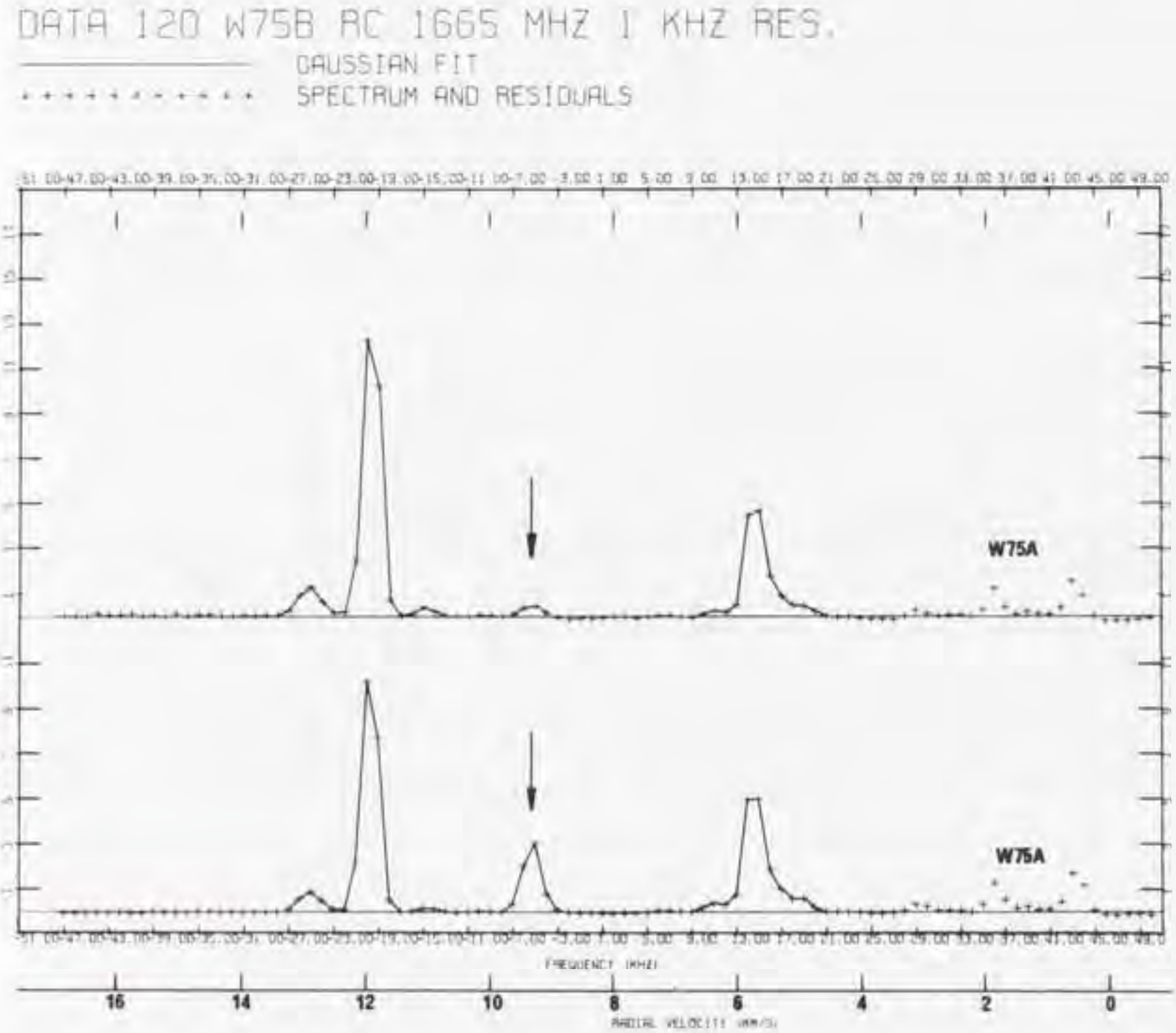

Fig. 9 Right circularly polarized 1665 MHz emission from W75B observed Dec. 13 and Dec. 20, 1971 with 1 kHz frequency resolution. The 9.3 km/s component has increased in intensity by a factor of 7.

TABLE **V A**

PARAMETERS OF OH EMISSION COMPONENTS IN W75A RC 1665 MHZ

COMP.	CENTER VELOCITY (KM/S)	AMPLITUDE (K)	HALF POWER WIDTH* (KM/S)	INTEGRATED FLUX $(WM^{-2} * 10^{-22})$	EQUIVALENT KINETIC TEMPERATURE** (K)
1	2.44	0.53	1.284	2.0	611.
2	1.78	3.03	0.224	2.0	19.
3	1.31	0.72	0.728	1.6	196.
4	0.71	0.99	0.259	0.8	25.
5	0.45	5.27	0.211	3.3	17.

* INSTRUMENTAL BROADENING REMOVED
** THE EQUIVALENT KINETIC TEMPERATURES HAVE NOT BEEN CORRECTED FOR ANY TURBULENT BROADENING

TABLE **V B**

PARAMETERS OF OH EMISSION COMPONENTS IN W75A LC 1665 MHZ

COMP.	CENTER VELOCITY (KM/S)	AMPLITUDE (K)	HALF POWER WIDTH* (KM/S)	INTEGRATED FLUX $(WM^{-2} * 10^{-22})$	EQUIVALENT KINETIC TEMPERATURE** (K)
1	-1.42	0.49	0.137	0.2	7.
2	-0.60	0.89	0.211	0.6	17.
3	-0.37	1.54	0.507	2.3	95.
4	0.57	10.96	0.349	11.3	45.
5	1.07	4.75	0.558	7.8	115.
6	1.34	1.07	0.146	0.5	8.

* INSTRUMENTAL BROADENING REMOVED
** THE EQUIVALENT KINETIC TEMPERATURES HAVE NOT BEEN CORRECTED FOR ANY TURBULENT BROADENING

TABLE VI A

PARAMETERS OF OH EMISSION COMPONENTS IN W75B RC 1665 MHZ

COMP.	CENTER VELOCITY (KM/S)	AMPLITUDE (K)	HALF POWER WIDTH* (KM/S)	INTEGRATED FLUX (WM^{-2} $*10^{-22}$)	EQUIVALENT KINETIC TEMPERATURE** (K)
1	12.89	1.66	0.417	2.1	65.
2	11.97	8.41	0.211	5.3	17.
3	11.83	11.79	0.177	6.2	12.
4	10.98	0.55	0.357	0.6	47.
5	9.31	3.78	0.302	3.4	34.
6	6.37	0.53	0.519	0.8	100.
7	5.75	6.60	0.207	4.0	16.
8	5.47	2.11	0.549	3.4	112.
9	4.91	0.86	0.375	1.0	52.
10	4.37	0.45	0.340	0.5	43.

* INSTRUMENTAL BROADENING REMOVED
** THE EQUIVALENT KINETIC TEMPERATURES HAVE NOT BEEN CORRECTED FOR ANY TURBULENT BROADENING

TABLE VI B

PARAMETERS OF OH EMISSION COMPONENTS IN W75B LC 1665 MHZ

COMP.	CENTER VELOCITY (KM/S)	AMPLITUDE (K)	HALF POWER WIDTH* (KM/S)	INTEGRATED FLUX (WM^{-2} $*10^{-22}$)	EQUIVALENT KINETIC TEMPERATURE** (K)
1	3.06	4.97	0.198	2.9	15.
2	3.23	1.47	0.101	0.4	4.
3	3.43	1.65	0.272	1.3	27.
4	3.92	0.99	0.306	0.9	35.
5	4.40	1.34	0.323	1.3	39.
6	4.91	3.45	0.323	3.3	39.
7	5.55	0.87	0.881	2.3	288.
8	5.96	0.99	0.237	0.7	21.

* INSTRUMENTAL BROADENING REMOVED
** THE EQUIVALENT KINETIC TEMPERATURES HAVE NOT BEEN CORRECTED FOR ANY TURBULENT BROADENING

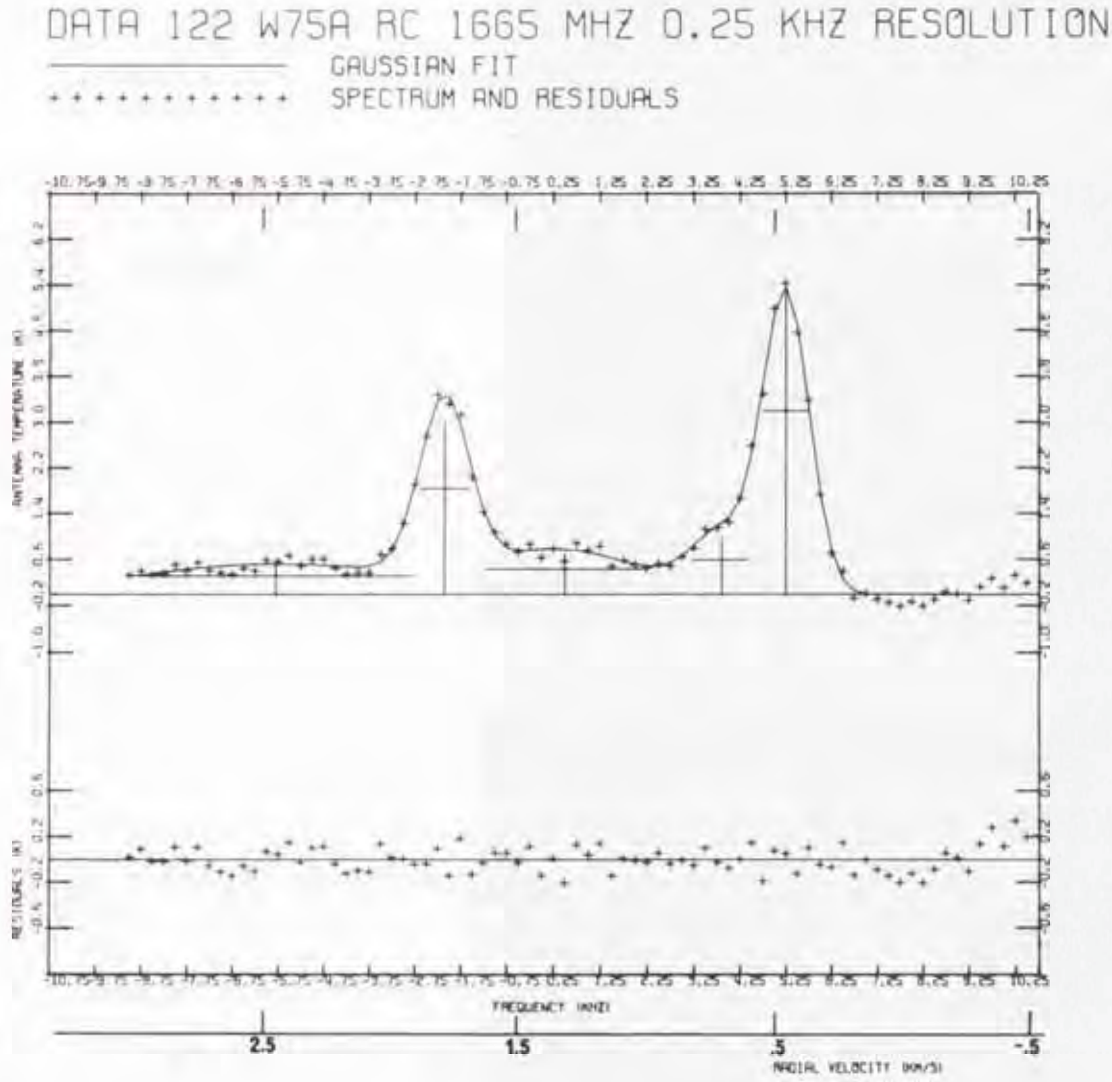

Fig. 10 Right circularly polarized emission from W75A. Frequency resolution is 250 Hz.

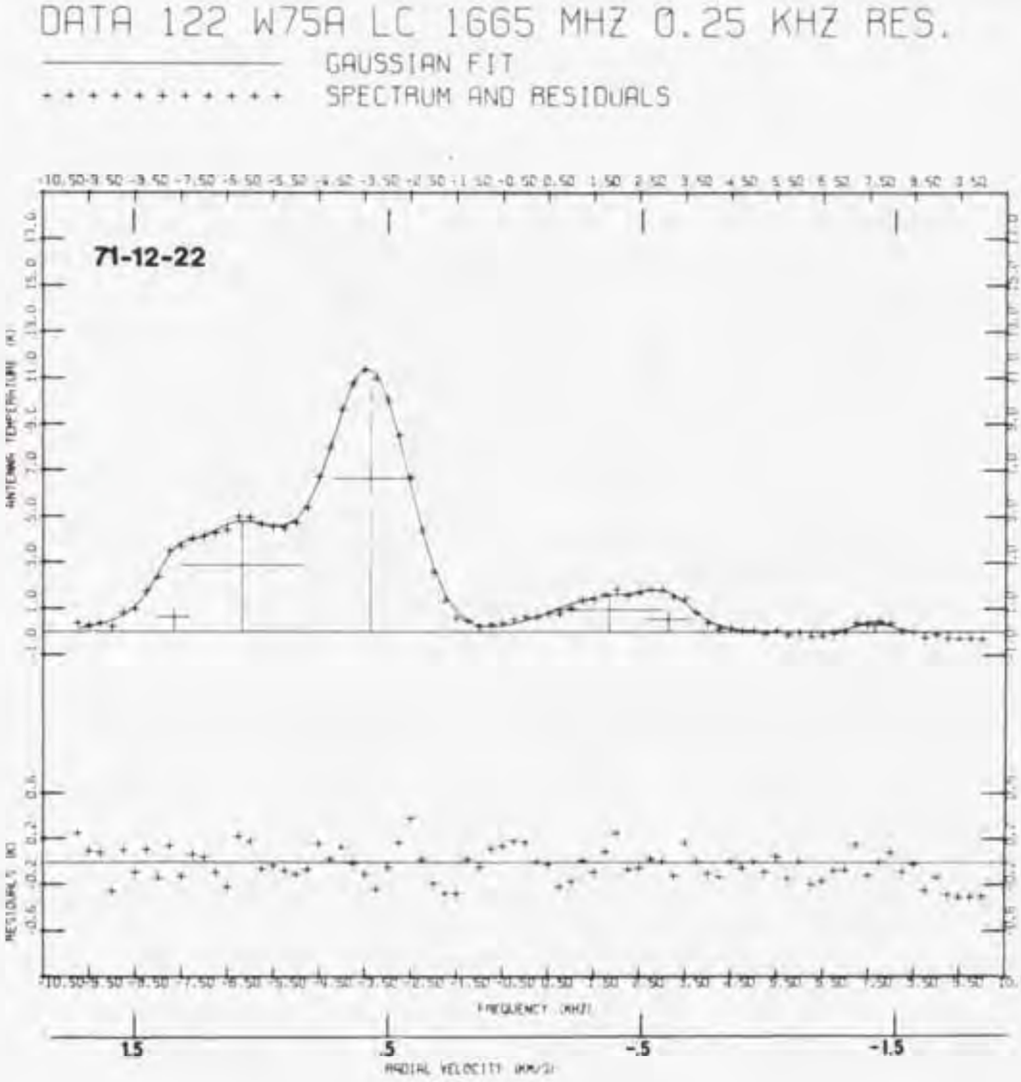

Fig. 11 Left circularly polarized 1665 MHz emission from W75A. Frequency resolution is 250 Hz.

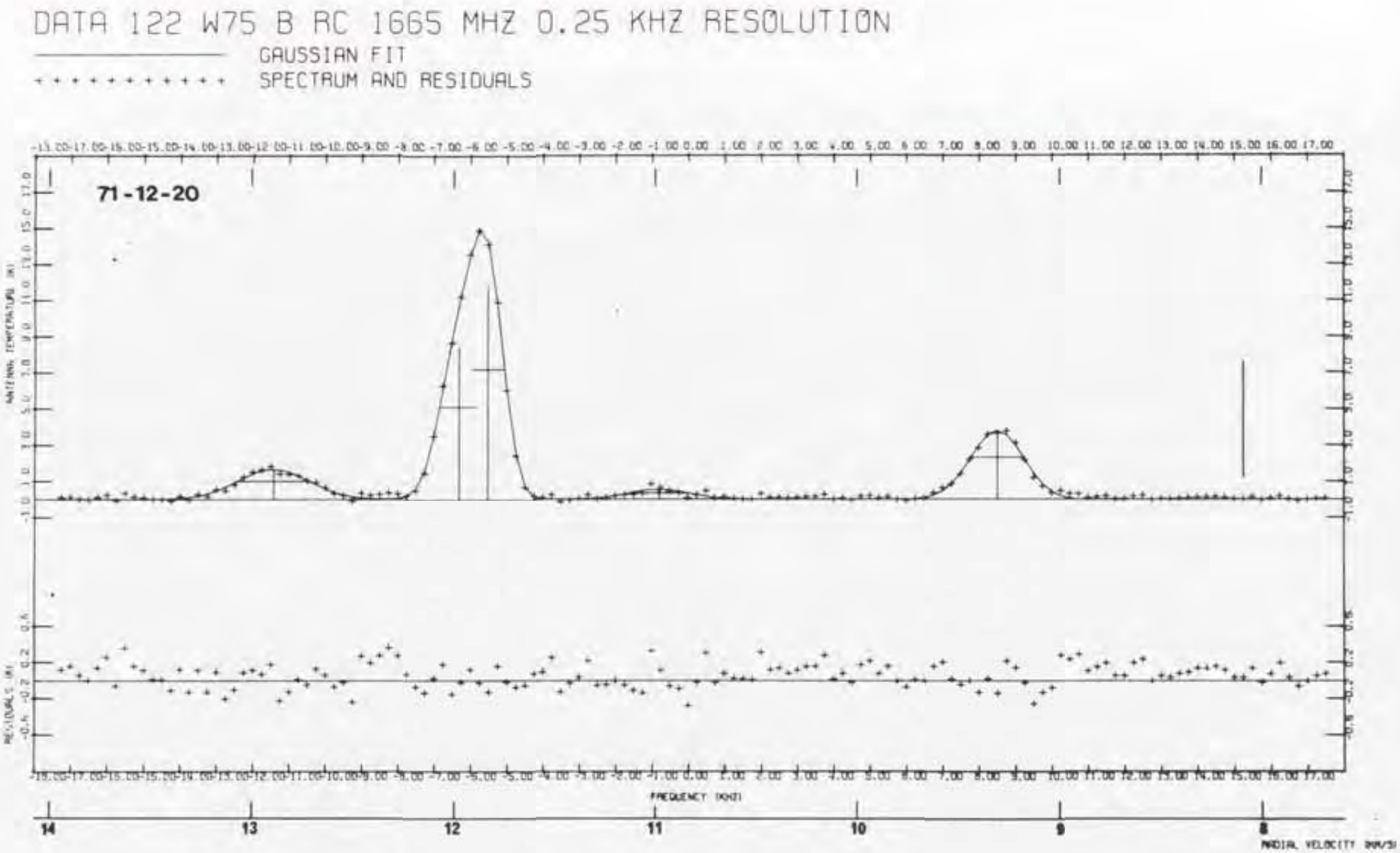

Fig. 12 Right circularly polarized 1665 MHz emission from W75B. The emission in the velocity interval from 8 to 4 km/s is shown on next page. Notice the different intensity scales. Frequency resolution is 250 Hz.

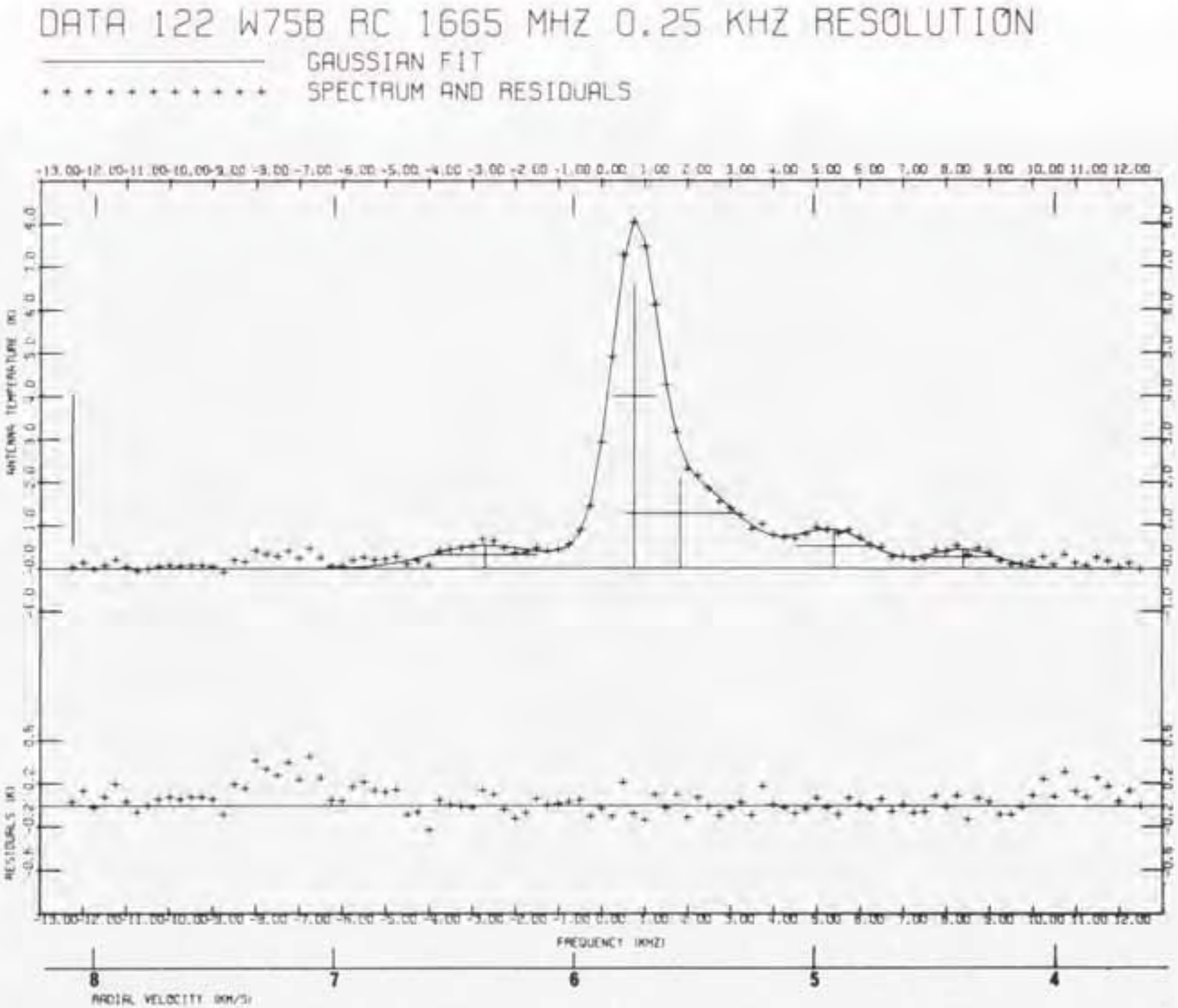

Fig. 12 (cont.) Right circularly polarized 1665 MHz emission from W75B in the velocity interval 8 to 4 km/s. The emission in the interval 14 to 8 km/s is shown on the previous page.

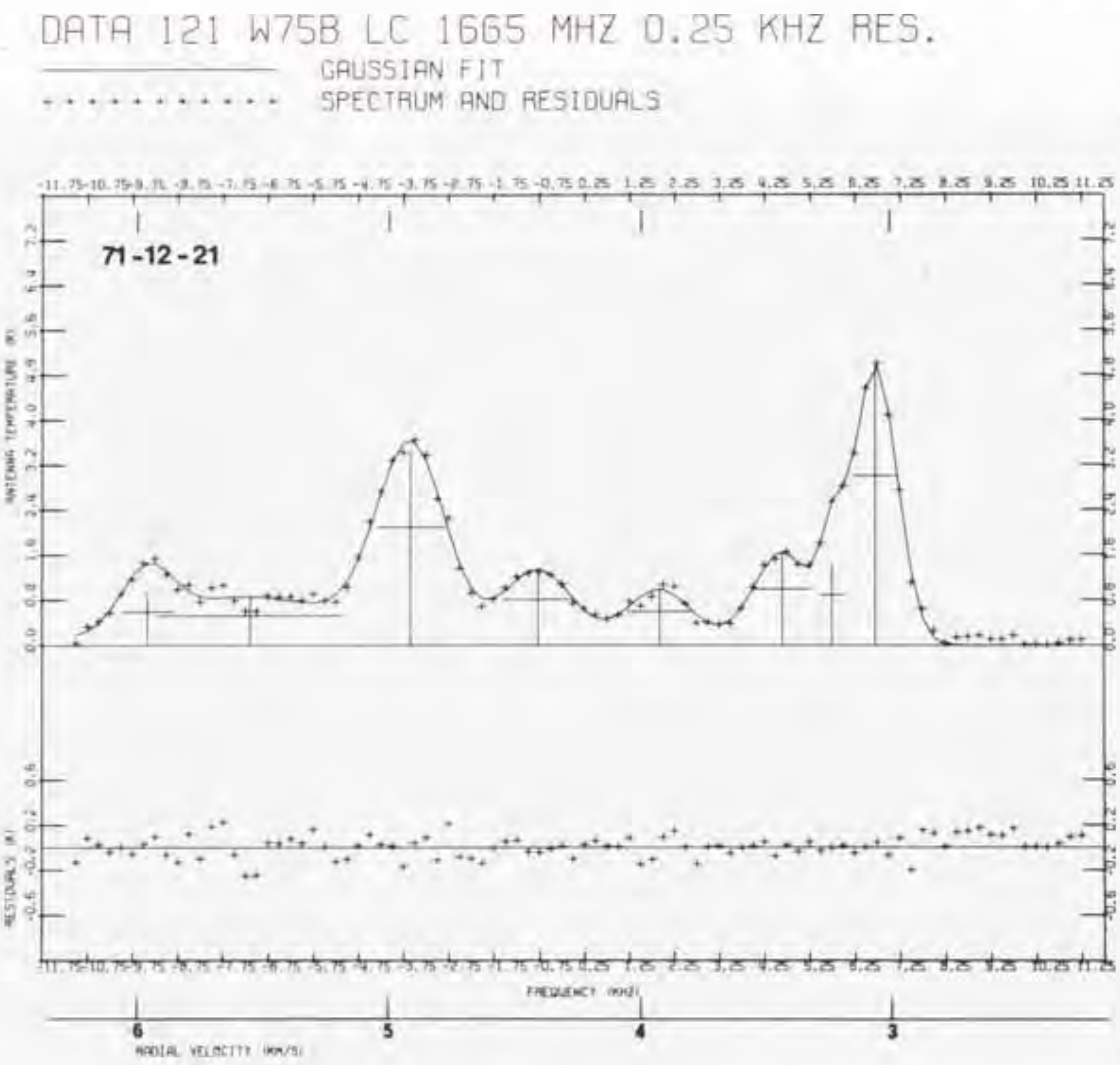

Fig. 13 Left circularly polarized 1665 MHz emission from W75B.

W 49 Position 1 [$RA_{1950.0} = 19^h07^m50^s$; $\delta_{1950.0} = 09^o01'24''$]

Position 2 [$RA_{1950.0} = 19^h07^m58^s$; $\delta_{1950.0} = 08^o59'58''$]

The ground state emission lines in W49 have been observed and discussed in detail by Palmer and Zuckerman (1967) and by Ball and Meeks (1968). Figure 14 and 15 show the circularly polarized emission at 1665 MHz observed with the Onsala 1 kHz filter receiver. The total spectrum is composed of emission coming from two sources at a distance of about 14 kpc separated about 8^s in right ascension and 1'26" in declination [Rogers et al, 1967; Raimond and Eliasson, 1969] . The W49 OH positions coincide with compact HII regions mapped by Wynn-Williams (1971).

The 1665 and 1667 MHz spectra in the velocity range -2 km/s to +24 km/s show about twenty more or less overlapping features. Ball and Meeks (1968) decomposed the 1665 MHz spectra into seventeen components. In order to compare the spectra taken in 1971 at Onsala with those observed in 1966 with the Haystack antenna the feature parameters given by Ball and Meeks were used as input Gaussian parameters. No converging solutions could be obtained, which means that the spectra measured by Ball and Meeks in 1966 deviate too much from those shown in figures 14 and 15 .

The 1720 MHz emission from W49 is located at the main line position generally referred to as position 2 [Hardebeck, 1971] . This line is 100 % circularly polarized and was reported to vary in intensity by Zuckerman et al (1969) and by Robinson et al (1970). Figure 16 shows the high velocity resolution, left circularly polarized 1720 MHz emission decomposed into Gaussian components. Robinson et al.reported an almost linear increase in the integrated flux from 7 $Wm^{-2}\cdot 10^{-22}$ in Dec. 1966 to 25 $Wm^{-2}\cdot 10^{-22}$ in Aug. 1969. The spectrum in Figure 16, measured in Dec. 1971, has an integrated flux of 36.4 $Wm^{-2}\cdot 10^{-22}$, which is in agreement with the data of Robinson et al. extrapolated to Dec. 1971.

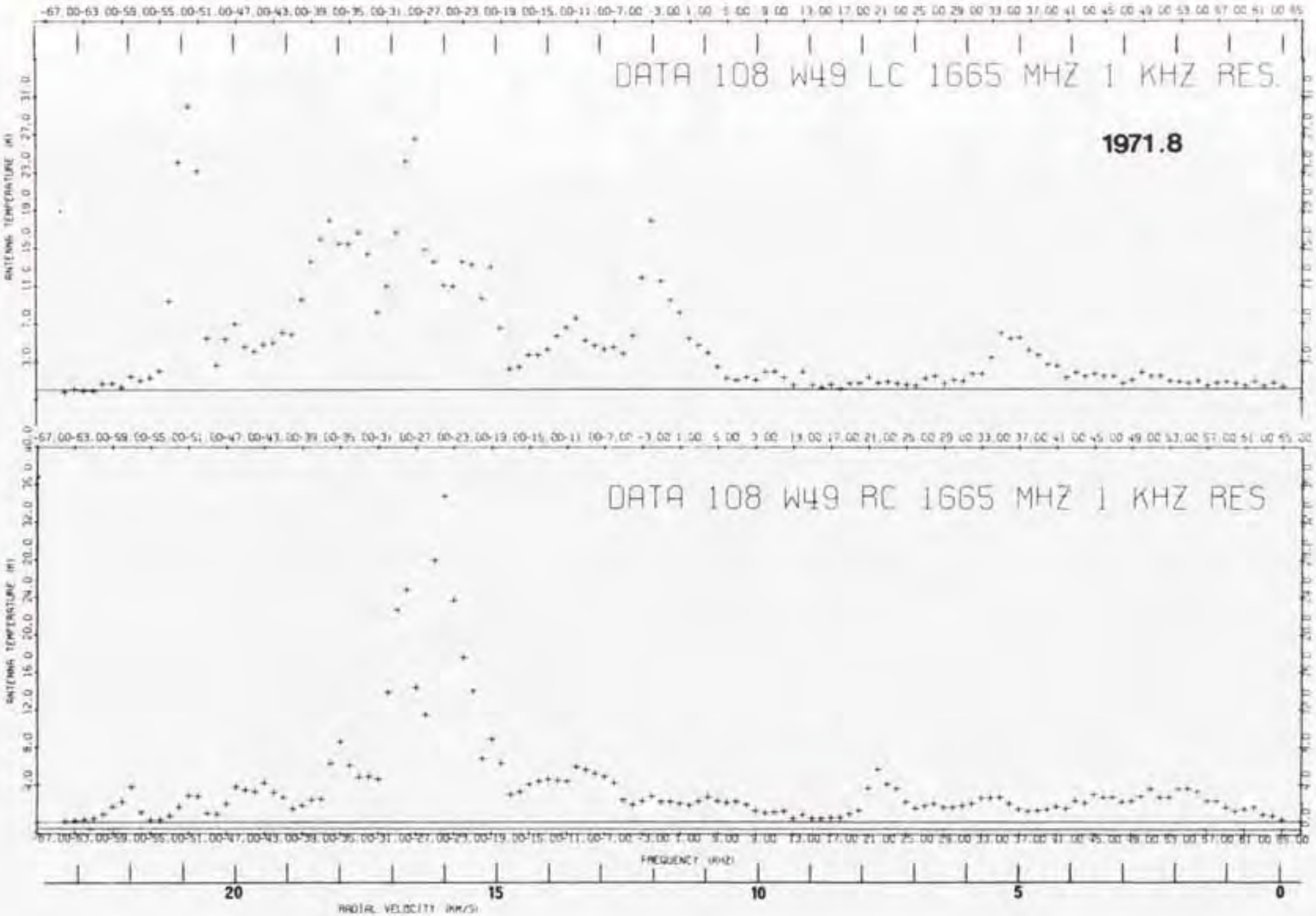

Fig. 14 Left and right circularly polarized 1665 MHz emission from W49. Frequency resolution is 1 kHz. Integration time is 30 min.

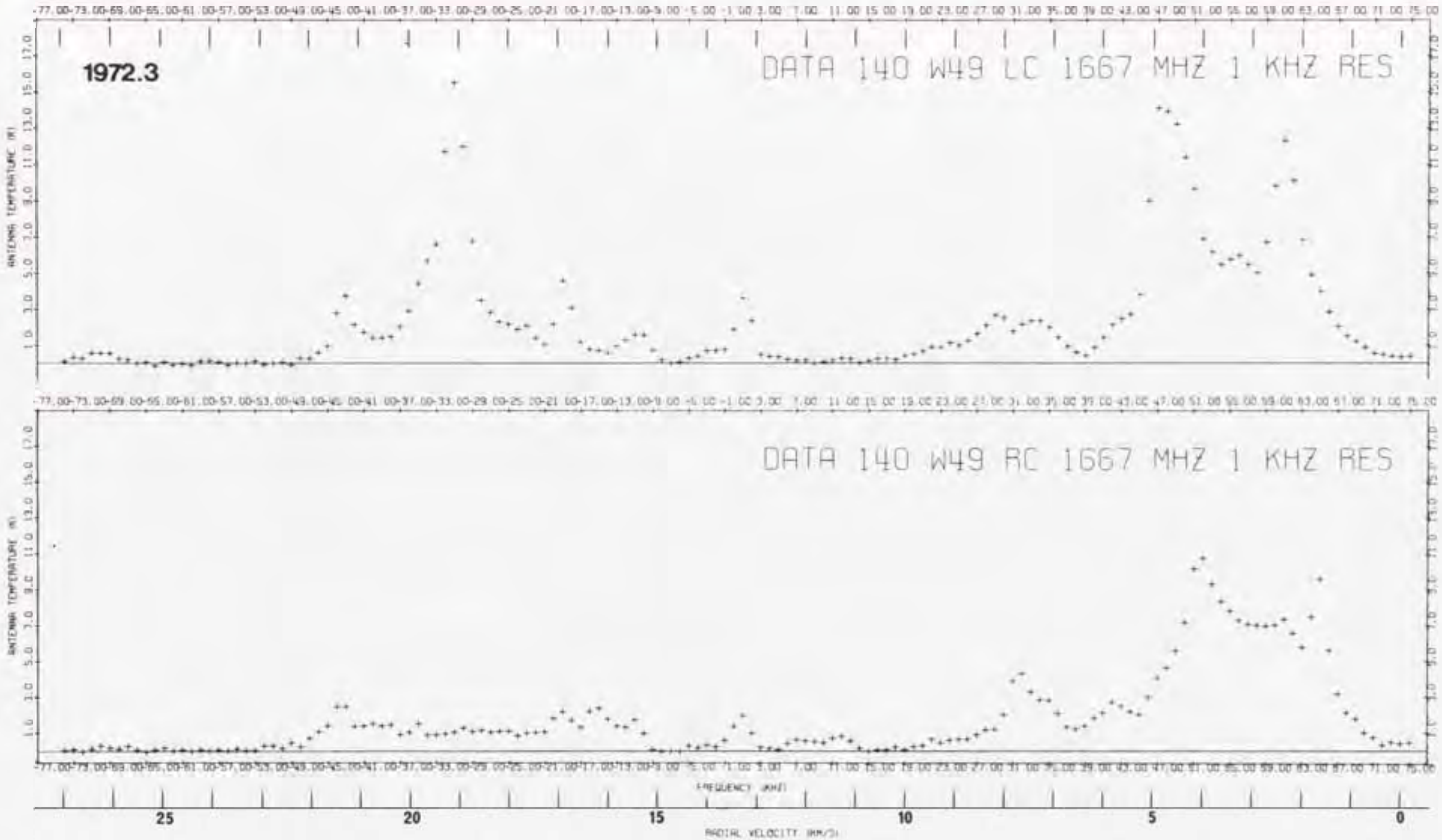

Fig. 15 Left and right circularly polarized 1667 MHz emission from W49. Frequency resolution is 1 kHz. Integration time is 30 min.

Tables VII A and VII B list the parameters of the three emission features obtained from the 250 Hz resolution and the 1 kHz resolution spectrum, respectively. It is evident from the integrated flux of the two strong components that an intensity variation must be present in both components.

TABLE **VII A**

PARAMETERS OF OH EMISSION COMPONENTS IN W49 LC 1720 MHZ

COMP.	CENTER VELOCITY (KM/S)	AMPLITUDE (K)	HALF POWER WIDTH* (KM/S)	INTEGRATED FLUX $(WM^{-2} *10^{-22})$	EQUIVALENT KINETIC TEMPERATURE** (K)
1	16.72	-0.47	2.285	-3.3	****
2	14.79	9.67	0.569	16.8	120.
3	14.29	14.41	0.425	18.7	67.
4	13.28	0.75	0.317	0.7	37.

* INSTRUMENTAL BROADENING REMOVED
** THE EQUIVALENT KINETIC TEMPERATURES HAVE NOT BEEN CORRECTED FOR ANY TURBULENT BROADENING

TABLE **VII B**

PARAMETERS OF OH EMISSION COMPONENTS IN W49 LC 1720 MHZ

COMP.	CENTER VELOCITY (KM/S)	AMPLITUDE (K)	HALF POWER WIDTH* (KM/S)	INTEGRATED FLUX $(WM^{-2} *10^{-22})$	EQUIVALENT KINETIC TEMPERATURE** (K)
1	16.79	-0.25	2.386	-1.8	****
2	14.76	8.56	0.578	15.1	124.
3	14.26	11.93	0.421	15.3	66.
4	13.27	0.82	0.408	1.0	62.

* INSTRUMENTAL BROADENING REMOVED
** THE EQUIVALENT KINETIC TEMPERATURES HAVE NOT BEEN CORRECTED FOR ANY TURBULENT BROADENING

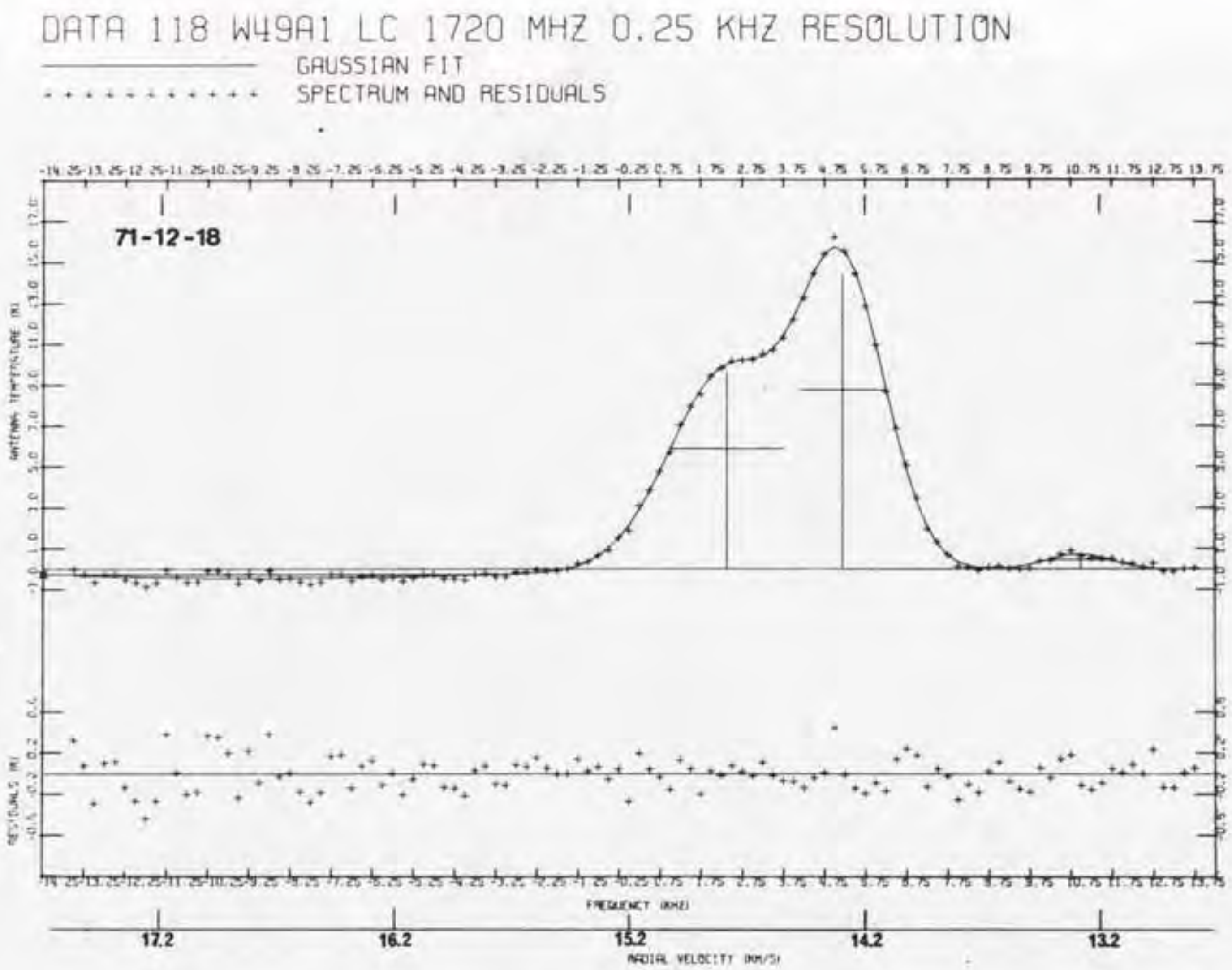

Fig. 16 250 Hz resolution spectrum of W49 observed at 1720 MHz with left circular polarization.

W 51 $RA_{1950.0} = 19^h 21^m 26^s$; $\delta_{1950.0} = 14^o 24' 39'']$

The OH source in W51 has been studied by Ball and Meeks (1968) at 1665 MHz and by Coles and Rumsey (1970) at 1612 and 1720 MHz. It has been shown by Hardebeck (1971) that the 1720 MHz emission around +60 km/s originates from the same position as the 1665 MHz emission at a distance of about 6.3 kpc obtained from hydrogen recombination line measurements (Me zger and Höglund 1967).

Most features in the 1665 MHz emission have a low degree of polarization. Figures 17 and 18 show the spectra measured with right and left circular polarization and 250 Hz wide filters. The decomposition into Gaussian components is indicated in the figures, and the parameters and the features are tabulated in Table VIII.

Ball and Meeks observed the sources in Sept. and Oct. 1966 and gave the parameters of the six components from 56.8 km/s to 61.4 km/s. However, W51 is a strongly variable source and no comparision between their result and the parameters in Table VIII is possible.

TABLE **VIII A**

PARAMETERS OF OH EMISSION COMPONENTS IN W51 RC 1665 MHZ

COMP.	CENTER VELOCITY (KM/S)	AMPLITUDE (K)	HALF POWER WIDTH* (KM/S)	INTEGRATED FLUX ($WM^{-2} * 10^{-22}$)	EQUIVALENT KINETIC TEMPERATURE** (K)
1	56.92	0.84	0.323	0.8	39.
2	57.25	0.92	0.072	0.2	2.
3	57.73	3.33	0.485	4.8	87.
4	58.32	5.10	0.545	8.2	110.
5	58.82	9.73	0.387	11.1	56.
6	59.20	5.54	0.268	4.4	27.
7	59.46	4.41	0.519	6.8	100.
8	60.21	1.35	0.524	2.1	102.

* INSTRUMENTAL BROADENING REMOVED
** THE EQUIVALENT KINETIC TEMPERATURES HAVE NOT BEEN CORRECTED FOR ANY TURBULENT BROADENING

TABLE **VIII B**

PARAMETERS OF OH EMISSION COMPONENTS IN W51 LC 1665 MHZ

COMP.	CENTER VELOCITY (KM/S)	AMPLITUDE (K)	HALF POWER WIDTH* (KM/S)	INTEGRATED FLUX ($WM^{-2} * 10^{-22}$)	EQUIVALENT KINETIC TEMPERATURE** (K)
1	56.86	2.51	0.310	2.3	36.
2	57.24	0.74	0.203	0.4	15.
3	57.70	6.18	0.280	5.1	29.
4	58.56	2.29	1.212	8.2	545.
5	58.75	4.59	0.319	4.3	38.
6	59.22	18.69	0.422	23.3	66.
7	59.71	2.06	0.332	2.0	41.
8	60.03	1.16	0.298	1.0	33.
9	60.43	3.99	0.426	5.0	67.
10	61.38	3.22	0.315	3.0	37.

* INSTRUMENTAL BROADENING REMOVED
** THE EQUIVALENT KINETIC TEMPERATURES HAVE NOT BEEN CORRECTED FOR ANY TURBULENT BROADENING

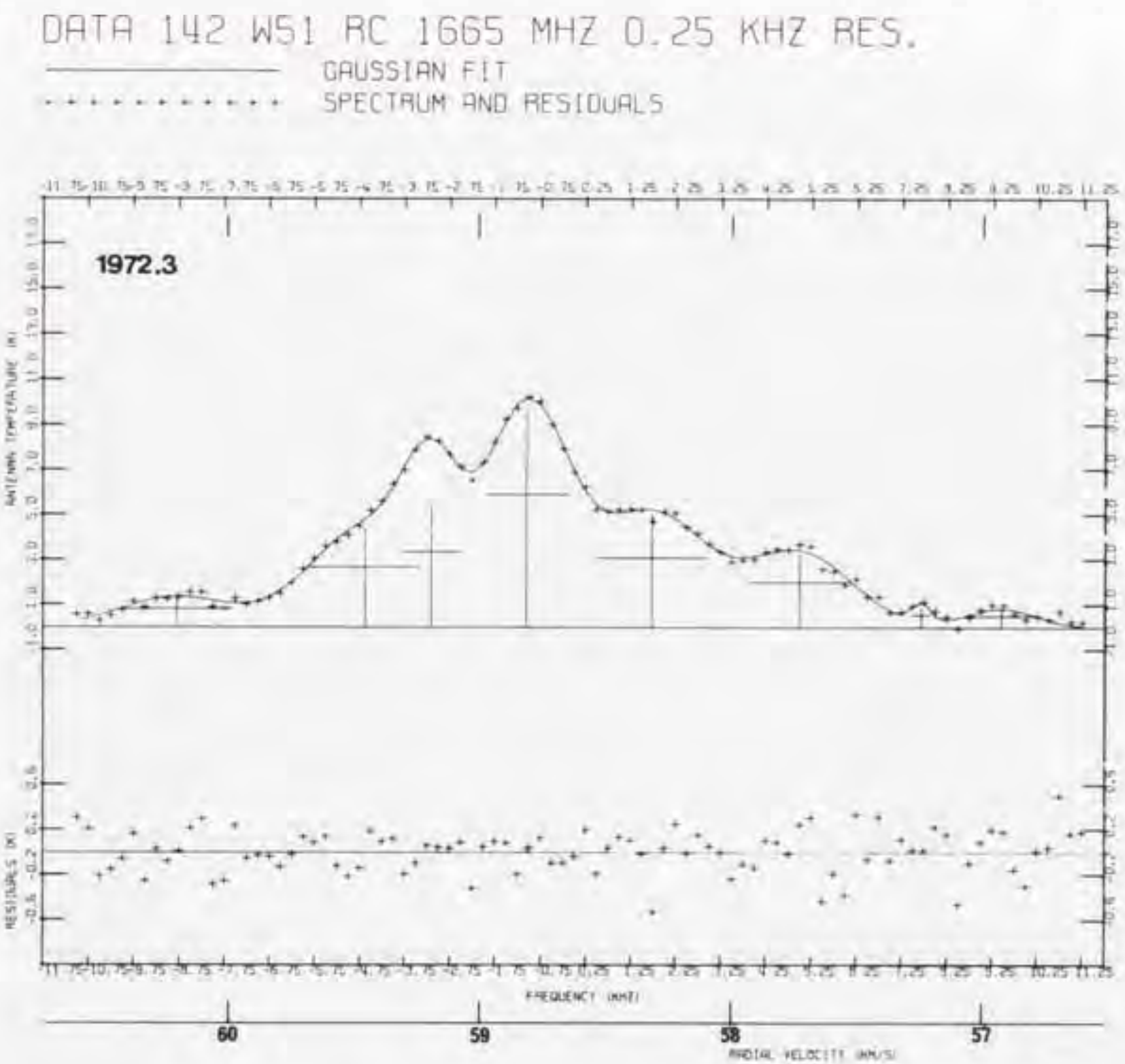

Fig. 17 250 Hz resolution spectrum of W51 observed at 1665 MHz with right circular polarization.

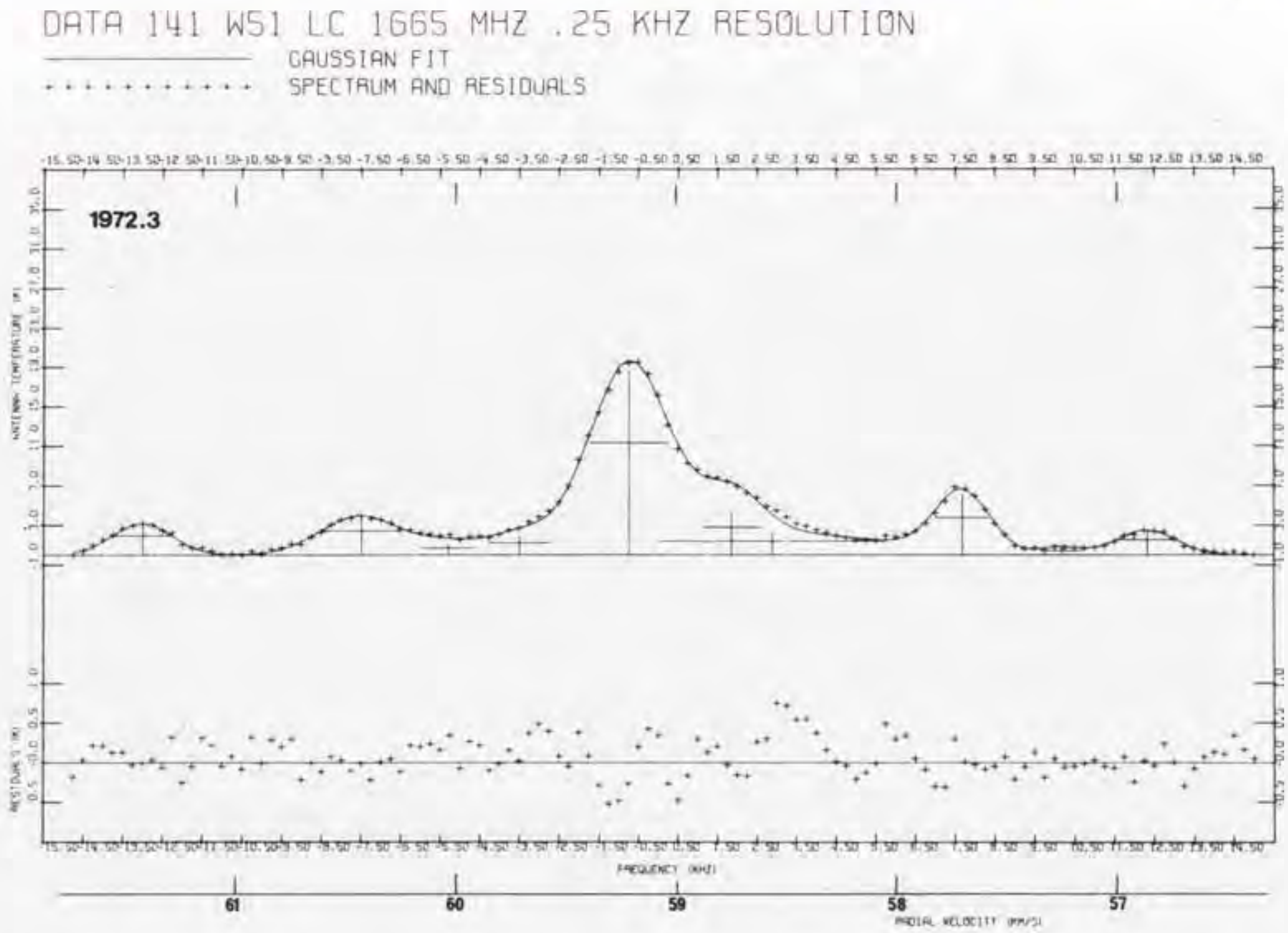

Fig. 18 250 Hz resolution spectrum of W51 observed at 1665 MHz with left circular polarization.

V. Conclusion

With future very long baseline interferometer measurements of OH emission sources in view eight strong OH emission sources have been observed with 250 Hz resolution and a peak-to-peak noise fluctuation of about 0.5 $^{\circ}$K (5 f.u.). A decomposition of the individual features of the spectra into Gaussian components shows that there is no significant deviation from Gaussian form of the components, thus indicating that the maser mechanism is at least partially saturated.

Typical half power widths of the stronger components (>1 $^{\circ}$K) vary from 0.2 km/s to 0.4 km/s corresponding to kinetic temperatures of 15 $^{\circ}$K to 60 $^{\circ}$K if the widths are due entirely to thermal broadening. No correlation between intensity and half power width of the components could be seen.

The spectra of NML Cygnus and R Aql. indicate that OH/IR sources normally have wider components than Class I sources.

The narrowest component found was the -43.1 km/s, right circularly polarized feature in the 1667 MHz spectrum of W3 OH which has a half power width of 0.14 km/s corresponding to an equivalent kinetic temperature of 7 $^{\circ}$K. The total integrated flux of this component is 0.8 $Wm^{-2} \cdot 10^{-22}$.

Most of the observed emission sources show intensity variations on time scale of a few years. Variability on a shorter time scale, sometimes as short as a few months, has also been reported. We found one component in the 1665 MHz emission of W75 B which changed its intensity by a factor of seven on a time scale of a week or shorter. The observations reported here may therefore be a useful guide not only for VLBI measurements but also for future accurate observations of possible variations in intensity as well as line width and radial velocity of OH emission sources.

Acknowledgement

I am indebted to Professor O. E. H. Rydbeck and Professor B. Höglund for helpful discussions. I am also indebted to Dr. J. Elldér, Mr. L. Lundahl, and Mr. J. Hirschberg for technical assistance and to the rest of the staff at the Onsala Space Observatory for assistance with the observations. This work was supported financially by the Swedish Board for Technical Development, the Swedish Natural Science Research Council, and the W. and M. Lundgren Foundation.

References

Ball, J.A., Meeks, M.L., 1968, Ap.J. 153, 577.

Coles, W.A., Rumsey, V.H., 1970, Ap.J. 159, 247.

Cooper, A.J., Davies, R.D., Booth, R.S., 1971, M.N.R.A.S., 152, 383.

Elldér, J., 1971, I.A.U. Circular No. 2364.

Elldér, J. Rönnäng, B.O., Winnberg, A., 1969, Nature, 222, 67-69.

Evans, N.J., Hills, R.E., Rydbeck, O.E.H., Kollberg, E., to be published.

Gehrz, R.D., Ney, E.P., Stecker, D.W., 1970, Ap.J. Letters, 161, L219.

Hardebeck, E.G., 1971, Ap.J., 170, 281.

Hardebeck, E.G., Wilson, W.J., 1971, Ap.J., 16?, L123.

Hardebeck, E.G., 1972, Ap.J., 172, 583.

Kaper, H.G., Smits, D.W., Schwarz, U., Takakubo, K., Woerden, H. van., 1966, B.A.N., 18, 465.

Meeks, M.L., Ball, J.A., Carter, J.C., Ingalls, R.P., 1966, Science, 153, 978.

Mezger, P.G., Höglund, B., 1967, Ap.J., 147, 490.

Mezger, P.G., Altenhoff, W.J., Schrank, J., Burke, B.F., Reifenstein, E.C. III, Wilson, T.L., 1967, Ap.J. Letters, 150, L157.

Moran, J.M., Burke, B.F., Barret, A.H., Rogers, A.E.E., Ball, J.A., Carter, J.C., Cudaback, D.D., 1968, Ap.J. Letters, 152, L97.

Palmer, P., Zuckerman, B., 1967, Ap.J. 148, 727.

Raimond, E., Eliasson, B., 1969, Ap.J., 155, 817.

Reifenstein III, E.C., Wilson, T.L., Burke, B.F., Mezger, P.G., Altenhoff, W.J., 1970, Astron. & Astrophys., 4, 357.

Robinson, B.J., Goss, W.M., and Manchester, R.N., 1970, Aust.J.Phys., 23, 363.

Rogers A.E.E., Moran, J.M. Crowther, P.P., Burke, B.F., Meeks, M.L., Ball, J A., and Hyde, G.M., 1967, Ap.J., 147, 369.

Rydbeck, O.E.H., Kollberg, E., 1968, IEEE Trans. Microw. MTT-16, 799.

Rydbeck, O.E.H., Elldér, J., Kollberg, E., 1969, Ap.J., 156, L141.

Rydbeck, O. E. H., Kollberg, E., Elldér, J., 1970, Ap. J. Letters, 161, L25.

Ryle, M., Downes, D., 1967, Ap. J. Letters, 148, L17.

Rönnäng, B. O., Rydbeck, O. E. H., Moran, J. M., 1970, Radio Science, 5, 1227.

Turner, B. E., 1969, Ap. J., 157, 103.

Wilson, W. J., Barret, A. H., Moran, J. M., 1970, Ap. J. 160, 545.

Wilson, W. J., Barret, A. W., 1972, Astron. & Astrophys., 17, 385.

Wilson, A. J., Davies, R. D., Elldér, J., 1972, M. N. R. A. S., 157, 21P.

Winnberg, A., 1971, Sky and Telescope, 42, No. 5.

Winnberg, A., 1970, Astron. & Astrophys., 9, 259.

118 Bil. 4

Tp

Radio Science, Volume 5, Number 10, pages 1227–1231, October 1970

Very long baseline interferometry of galactic OH sources

B. O. Ronnang and O. E. H. Rydbeck

Onsala Space Observatory, Research Laboratory of Electronics, Chalmers University of Technology, Gothenburg, Sweden

J. M. Moran

Massachusetts Institute of Technology, Lincoln Laboratory, Lexington, Massachusetts 02173

Radio Science, Volume 5, Number 10, pages 1227–1231, October 1970

Very long baseline interferometry of galactic OH sources

B. O. Ronnang and O. E. H. Rydbeck

Onsala Space Observatory, Research Laboratory of Electronics, Chalmers University of Technology, Gothenburg, Sweden

J. M. Moran

Massachusetts Institute of Technology, Lincoln Laboratory, Lexington, Massachusetts 02173

(Received June 2, 1970.)

Several hydroxyl radical (OH) microwave emission sources were studied in July 1969 with very long baseline interferometry (VLBI). The elements of the interferometer were the 84-foot telescope of the Onsala Space Observatory at Chalmers University of Technology, Sweden, and the 120-foot telescope of the Haystack Microwave Research Facility at Lincoln Laboratory, MIT; a baseline of 31.1×10^6 wavelengths, or a fringe spacing of 0.0066 sec of arc at a frequency of 1665 MHz, resulted. Earlier spectral line interferometric observations have given detailed information on the angular sizes and spatial separations of the 1665-MHz OH sources in the W3 source. The measurements reported here confirm these results and give additional information on the complex structure of the various features. Four other galactic OH emission sources with unknown angular sizes were also investigated. Only one (the 5-km/sec component in the 1667-MHz spectrum of W49) gave reliable fringes.

INTRODUCTION

In the past few years, application of VLBI has yielded accurate values of the angular sizes and spatial separations of the different emission components of several galactic OH radio sources. For example, in January 1968 three radio observatories in the United States and the Onsala Space Observatory in Sweden cooperated to form an interferometer with six different baselines. This experiment showed that the main features in the 1665-MHz-spectrum of W3 were resolved with a fringe space of 0.003″. The smallest feature was the one at −43.7 km/s, which has a size of 0.005″ [*Moran*, 1968].

This paper presents the result of a spectral line VLBI observation using the Onsala Space Observatory and the MIT Haystack Mircowave Facility telescopes. The measurements were performed (on July 17 and 18, 1969) for the following major reasons: to confirm the angular sizes and spatial separations previously determined for some of the strongest and smallest W3 components, to look for possible temporal variations in sizes and relative positions, to obtain more information about the complex structure of the compound components, and to search for fringes from a few weaker OH sources.

EQUIPMENT AND OBSERVATIONS

The baseline parameters of the Onsala-Haystack interferometer are given in Table 1. This baseline gives a minimum interferometer fringe spacing of about 0.0066 sec of arc. The Onsala telescope was equipped with a rutile traveling wave maser radiometer system (giving a zenith system noise temperature of less than 40°K [*Rydbeck and Kollberg*, 1968]), a rubidium frequency standard, and the digital data recording system developed by the National Radio Astronomy Observatory group [*Bare et al.*, 1967]. The Haystack station used a parametric amplifier, which gave a system noise temperature of about 200°K, and a hydrogen maser frequency standard. The data were recorded on magnetic tape through a Univac 490 computer [*Moran*, 1968]. Although relative time of the two stations is not as critical as in the wide-band VLBI measurements because of the narrow line width the time and frequency of the rubidium clock at Onsala were compared with the cesium standard of the Swedish National Defense Research Establishment and continuously compared with the slave Loran-C station at Sylt in Germany. Haystack time is routinely kept to within a microsecond of UTC.

The observations were planned by use of a Fortran

TABLE 1. The Onsala-Haystack radio interferometer parameters
(Baseline length, 5599.79 km.)*

	Onsala	Haystack
Antennas	84-ft	120-ft
Aperture efficiency at 1665 MHz	≈50%	≈25%
System noise temperature	≈40°K	≈200°K
Longitude	−11° 55′ 12.8″	71° 29′ 19.2″
Geodetic latitude	57° 23′ 36.1″	42° 37′ 23.5″
Geocentric latitude	57° 13′ 3″	42° 25′ 50″
Heights	14 m	145 m

* Baseline hour angle, 8h 7m 34.6s; baseline declination, −10.835°.

program, which provides the local hour angles and elevations, as well as the local oscillator settings of the two stations, the projected baseline, geometrical delay, and fringe rate for the actual sources and time intervals. 120-kHz bandwidth was used for observing the spatial separation among strong features; 6-kHz bandwidth was used for studying the complex fine structure of the individual compound components. The sample rate of the clipped video signal was fixed by the seven-track tape drive at Onsala to be 720 kbit/sec. For the bandwidths used in this experiment, either every sixtieth or every third sample was extracted; the remainder were discarded. The fringe amplitude and fringe phase were obtained by a Fortran and a machine-language program written for the IBM 360/65 computer of the Chalmers University of Technology. This program computes the geometrical delay and fringe rate for each data block of 0.2-sec duration. The digitized signals from the two stations are then cross correlated over a time period that must be short compared with the apparent fringe period.

The local oscillator settings must be fixed during the recording. The cross-correlation function that is obtained is time dependent, since there can be an unknown difference between the two frequency standards or an error in the baseline coordinates or in source position. The cross-correlation function is therefore multiplied by sine and cosine of the calculated fringe phase for a number of fringe frequency offsets and accumulated for the total desired integration time of up to 180 sec. The fringe amplitude and fringe phase are derived as a function of frequency from the complex Fourier transform. The best fitted fringe frequency gives the maximum fringe visibility.

Forty pairs of tape were recorded during this one-day experiment. Fifteen of these have been completely reduced so far. Table 2 lists the sources and their parameters.

RESULTS

The most extensive observations were made on the OH source in W3 at 1665 MHz. Measurements were made with the wide bandwidth of 120 kHz and with

TABLE 2. Observed sources in the July 1969 VLBI measurements

Source	Frequency, MHz	Velocity, km/sec	Polarization	Bandwidth, kHz	Position (1950.0) α	Position (1950.0) δ, deg	Antenna temp at Onsala, °K	Projected baseline, cycles/second of arc S_x	Projected baseline, cycles/second of arc S_y
W3	1665.401	−43.5	RC	120	2h23m16.8s	61.648		134.96	40.41
								−74.18	−126.39
								74.35	−126.30
								146.07	−35.51
		−46.0	LC	120				56.93	−133.20
		−43.7	RC	6			25	−140.08	29.08
								146.98	−29.87
		−45.1	RC	6			53	−142.94	20.90
		−46.5	LC	6			24	−129.75	59.64
W49	1667.358	5.0	LC	6	19h 7m49.6s	9.020	12	−142.53	−34.48
W49*	1665.401	14.0	RC/LC	120					
W51†	1720.528	58.5	RC	6	19h21m26.5s	14.411		−148.67	−19.33
NML Cyg†	1612.231	−23.9	RC	6	20h44m38.9s	39.931	60	59.97	−104.77
W75A†	1665.401	0.35	LC	6	20h37m11.9s	42.20	9	−99.79	−94.62
W75B†	1665.401	11.7	RC	6	20h36m58.0s	42.43	8	−48.50	72.22

* No tapes processed.
† No detectable fringes.

the narrow bandwidth of 6 kHz. Figure 1 shows the amplitude of the interference spectra and the total power spectra for both right and left circular polarization obtained with the wide-bandwidth system. The spectra were computed from 100-point correlation functions; this procedure resulted in a resolution of 4.8 kHz, or 0.9 km/sec, since Hanning weighting was used. The fringe amplitude at any velocity is the ratio of the two spectra at that velocity. The observed fringe amplitudes are much less than unity. This is caused by the fact that most of the features consist of several components that interfere with one another. The components themselves, however, appear to be partially resolved on this baseline.

An example of the high resolution spectra obtained on the right circularly polarized -45.1-km/sec feature is shown in Figure 2. The total power spectrum

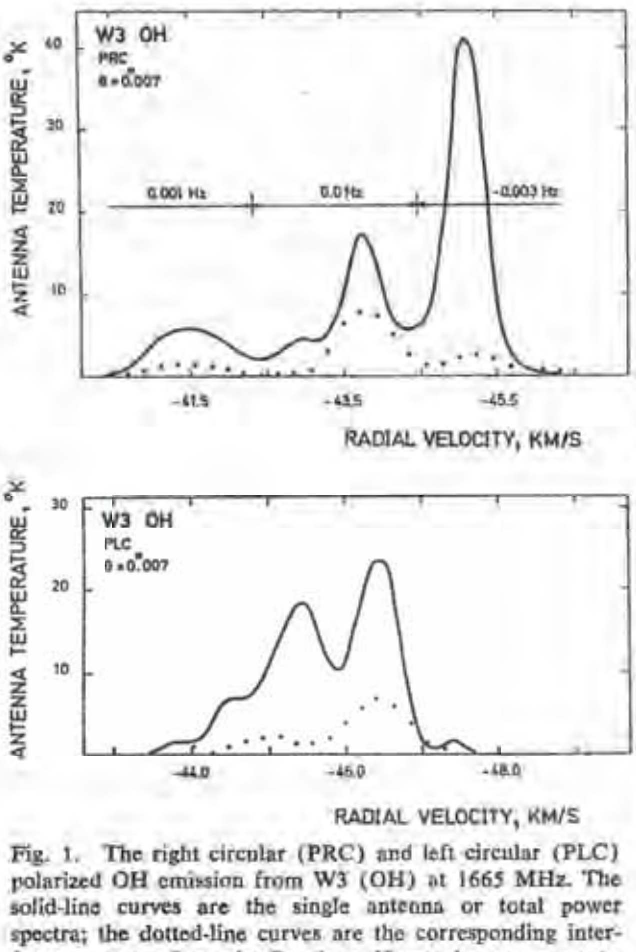

Fig. 1. The right circular (PRC) and left circular (PLC) polarized OH emission from W3 (OH) at 1665 MHz. The solid-line curves are the single antenna or total power spectra; the dotted-line curves are the corresponding interference spectra from the Onsala to Haystack measurements. The integration time is 120 seconds; the frequency resolution is 4.8 kHz (0.9 km/sec). The antenna temperature are normalized to the Onsala single antenna temperature.

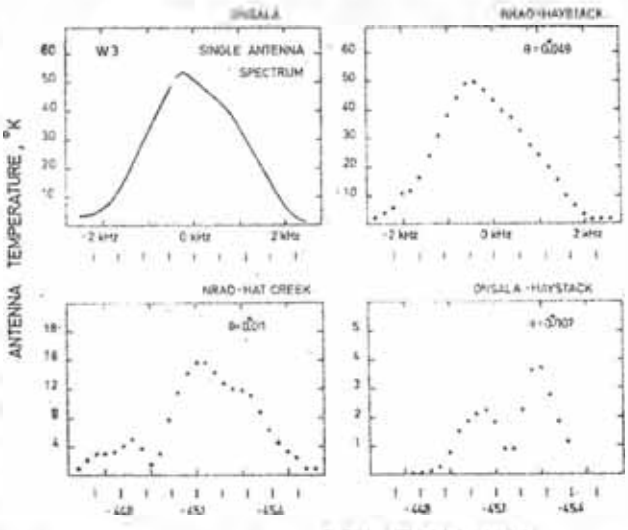

Fig. 2. An example of the high resolution spectra obtained on the -45.1-km/sec PRC feature of W3(OH) at 1665 MHz for different baselines, from zero baseline (solid-line curve) to a baseline length of 31×10^6 wavelengths (fringe spacing 0.007″). The integration time is 160 seconds (1800 seconds for the total power spectrum); the frequency resolution is 480 Hz (250 Hz for the total power spectrum).

was obtained with the multichannel receiver at the Onsala Observatory; it has a resolution of 250 Hz, or 0.05 km/sec. This feature can be decomposed into two components with Gaussian profiles centered at -45.0 and -45.3 km/sec with a relative intensity ratio of 2:1. The interference spectra shown were taken with fringe spacings of 0.049″, 0.011″, and 0.007″. All the projected baselines had approximately the same position angles. The data on the larger fringe spacings ($\theta = 0.049''$ and $0.011''$) are from another experiment [*Moran*, 1968]. These spectra clearly show the presence of three spatially distinct components centered at -44.8, -45.0, and -45.3, km/sec. The component at -45.3 km/sec appears to have the smallest angular size of the three, since it has the highest fringe amplitude on all baselines. Its size is about 0.005″. The separation between the -45.0- and -45.3-km/sec features is about 0.02″, which agrees with the value reported by *Moran et al.* [1968].

The -43.7-km/sec feature in W3 was also examined with high frequency resolution. Its fringe amplitude was found earlier to decrease monotonically with increasing baseline length and to have little dependence on the direction of the baseline [*Moran et al.*, 1968]. A size of 0.005″ was finally assigned to this feature by VLBI measurements between the United States and Sweden.

Figure 3 shows the total power spectrum and two interference spectra from the July 1969 measurements taken at different local hour angles. The total power spectrum measured on the Onsala multichannel receiver has a notch in the center of the profile when observed at 250-Hz resolution. The profile is almost symmetrical about its center but does not decompose into two Gaussian components. Furthermore, the phase shift across the profile of the interference spectra is different for the two local hour angles. This may, for example, indicate a small spatial separation between two frequency components rather than some kind of maser saturation effect. It is interesting to notice in this context that *Rydbeck et al.* [1970] suggest that the main 6-GHz OH excited state emissions from W3 could be generated by a ring source of angular diameter 0.005″ and a center velocity of about −43.7 km/sec. Finally, it should be mentioned that the average visibility of the feature in question is the same in July 1969 as in January 1968.

The difference in fringe rate has been measured as a function of local hour angle between the feature groups at −43.7 and −45.1 km/sec. The spatial separation in right ascension $\Delta\alpha$ and declination $\Delta\delta$ between two sources is given by the equation

$$\Delta f_R = (D f_1/c)\omega_E \cos \delta_B [\sin \delta_B \sin (H_S - H_B)\,\Delta\delta + \cos \delta_B \cos (H_S - H_B)\,\Delta\alpha] \qquad (1)$$

where D is the baseline length, c is the velocity of light, ω_E is the rotation frequency of the earth, and f_1 is the net local oscillator frequency; δ_B and δ_S are the declinations of the baseline and source, respectively, and H_B and H_S are the hour angles of the base line and source, respectively. On W3 the equation becomes

$$\Delta f_R = 5.3 \sin (H_S - H_B)\,\Delta\delta + 11.1 \cos (H_S - H_B)(\cos \delta_S\,\Delta\alpha) \qquad (2)$$

where f_R is in millihertz and $\Delta\delta$ and $\Delta\alpha$ are in seconds of arc. From the measurement at three different local hour angles the −45.1-km/sec feature is located 0.8″ ± 0.2 west and 0.2″ ± 0.2 north of the −43.7-km/sec feature. The errors depend on the signal-to-noise ratio of the interferometer system, or, in practice, on the available integration time (which for the present equipment is less than three minutes). Future VLBI terminals will allow longer integration times and hence smaller positional errors. Within the limits of error the present spatial separation agrees with the separation measured in July 1967 [*Moran et al.*, 1968].

Fringes were detected on W49 at 1667 MHz. This is the first reported measurement on any OH source at 1667 MHz with a very long baseline interferometer. The interference spectrum is shown in Figure 4. The integration time is 160 sec and the velocity resolution is 0.1 km/sec. The spectrum shows two spatial components with fringe amplitudes of about 0.1. It would be meaningless to assign a size to this feature, because only one measurement is available which shows very low fringe amplitude. The source can, however, be said to have structure on the scale of the fringe spacing, which is 0.007″. Fringe amplitudes on W49 at 1665 MHz were found to be reduced

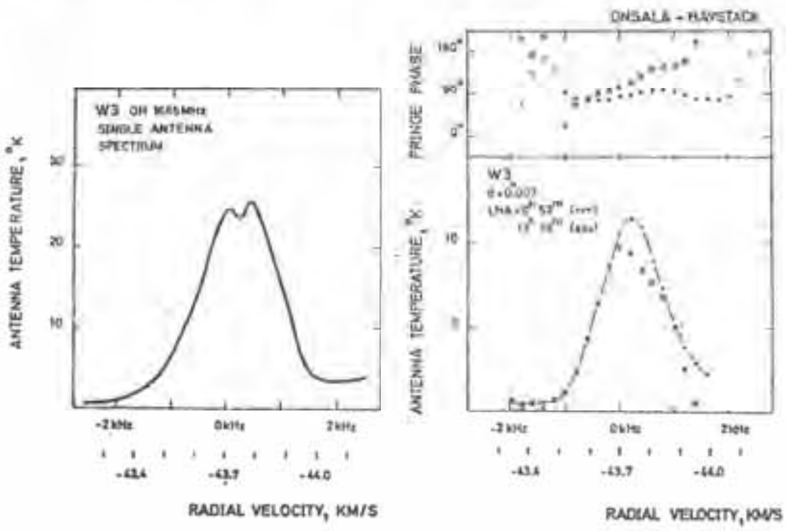

Fig. 3. High resolution total power and interference spectra of the −43.7-km/sec feature of W3 (OH) at two local hour angles. The total power spectrum has a frequency resolution of 250 Hz and was obtained with an integration time of 1800 seconds. The resolution of the interference spectra is 480 Hz; the integration time is 160 seconds.

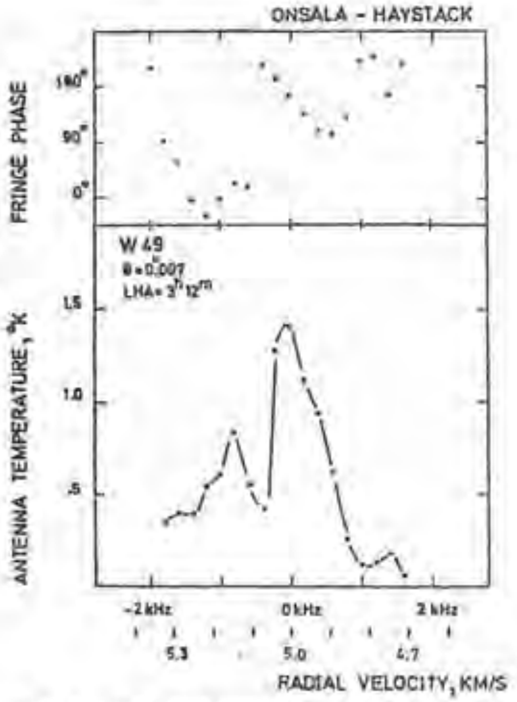

Fig. 4. The interference spectrum of the 5-km/sec feature in the 1667-MHz OH emission from W49. The fringe visibility is about 0.1.

from unity on the Haystack- NRAO baseline; the amplitudes result in a characteristic size of 0.05″ [*Moran*, 1968]. However, the 1665 features at 1665 MHz may have fine structures of the size observed at 1667 MHz.

Negative results were obtained on W75A and W75B at 1665 MHz and on W51 at 1720 MHz. The signal-to-noise ratio was sufficient for the detection of these sources if the fringe amplitudes were greater than 0.2. The data were also processed at a large range of fringe rates; therefore, the inaccuracy of the source positions could not account for the lack of correlation. These sources have not been observed before on any shorter baseline. NML Cygnus was also observed at 1612 MHz with negative results. This source was reported to have a characteristic size of 0.08″ [*Wilson et al.*, 1970].

The results in this paper have clearly shown the need for extended VLBI measurements of OH sources with different frequency resolutions. The most serious limitation of the measurements has been the short available integration time, which makes it extremely difficult to study (for example) the weaker OH emission from W3 at 1667 MHz and the excited OH emission. The Mark 2 VLBI terminals now being developed at NRAO will therefore be of great future importance to the spectral line VLBI.

Acknowledgments. We thank J. C. Carter, B. F. Burke, M. L. Meeks, P. Landgren, and the staffs of the Haystack facility and the Onsala Space Observatory for their assistance.

The Lincoln Laboratory, at MIT, is supported in part by the Department of the Air Force and by the National Science Foundation; the Onsala Observatory is supported in part by the Swedish Foundation for the Natural Sciences.

REFERENCES

Bare, C., B. G. Clark, K. I. Kellerman, M. H. Cohen, and D. L. Jauncey (1967), Interferometer experiment with independent local oscillators, *Science, 157*, 189–191.

Moran, J. M., (1968), Interferometric observations of galactic OH emission, Ph.D. thesis, Massachusetts Institute of Technology, Cambridge, Massachusetts.

Moran, J. M., B. F. Burke, A. H. Barrett, A. E. E. Rogers, J. A. Ball, J. C. Carter, and D. D. Cudaback (1968), The structure of the OH source in W3, *Astrophys. J., 152*, L97–L101.

Rydbeck, O. E. H., and E. Kollberg (1968), Rutile traveling-wave maser system for the Onsala 84-foot radio telescope, *IEEE, Trans. Microwave Theory Tech., MTT-16*, 799–803.

Rydbeck, O. E. H., E. Kollberg, and J. Elldér (1970), OH excited state emissions from W75B and W3, OH *Astrophys. J. Lett., 16*, L25–L35.

Wilson, W. J., A. H. Barrett, and J. M. Moran (1970), OH radio emission associated with infrared stars, *Astrophys. J., 159*, 545–571.

1:45

Tp

ON THE THEORY, TECHNIQUES, AND DATA PROCESSING OF VERY LONG BASELINE INTERFEROMETRY

BY
B. O. RÖNNÄNG

RESEARCH REPORT NO 105
1971

RESEARCH LABORATORY OF ELECTRONICS

CHALMERS UNIVERSITY OF TECHNOLOGY

GIBRALTARGATAN 5 G

GOTHENBURG S, SWEDEN

CHALMERS TEKNISKA HÖGSKOLA GÖTEBORG

Research Laboratory of Electronics
CHALMERS UNIVERSITY OF TECHNOLOGY
Gothenburg, Sweden

RESEARCH REPORT No. 105

ON THE THEORY, TECHNIQUES, AND DATA PROCESSING OF VERY LONG BASELINE INTERFEROMETRY

By

Bernt Rönnäng

Gothenburg, 1970/71

TABLE OF CONTENTS

GLOSSARY

Symbols	Definition
	<u>Time functions</u>
$s(t)$	A stationary, ergodic, random signal having Gaussian statistics.
$x(t)$	The function formed by infinite clipping of $s(t)$.
$v(t)$	A complex analytic signal, the real part of which is $s(t)$. The imaginary part is obtained by changing the phase of each spectral component of $s(t)$ by $\pi/2$.
$e(t)$	The signal into the correlator.
$V(f)$	The Fourier transform of $v(t)$.
$n(t)$	Receiver noise signal.
	<u>Power spectra</u>
$P(f)$	The power spectrum. The total average power is $P_T = \int_{-\infty}^{\infty} P(f)\, df$
$\hat{P}(f)$	A statistical estimate of $P(f)$.
$S(f)$	The normalized power spectrum.
	<u>Temperature</u>
$T_A(f)$	The antenna temperature expressed in degrees Kelvin.
T_S	The system noise temperature.
$T_B(\xi)$	The brightness distribution of the radio source.

Coherence functions

Γ	Mutual coherence function defined on page 13
γ	Lateral coherence function defined on page 13

Time and frequency

Δt	The sampling interval of the time function s(t).
Δf	The frequency resolution of a spectral measurement.
f_o	Local oscillator frequency
τ	Time delay.
τ_i	Instrumental time delay at station number two.
τ_g	Geometrical time delay (positive if there is an excess delay at station number two).
$\Delta\tau_g$	$= \tau_g + \tau_i$
f_f	Fringe frequency
$\Delta\omega$	Local oscillator frequency offset; positive if the LO-frequency is higher at station no. 2 and the upper sidebands are used.
Ω	Angular velocity of the earth.
B	Bandwidth of a rectangular filter.
b(f)	Bandwidth of lowpass filter.
B_N	Equivalent noise bandwidth.
T_i	Integration time
$\Delta\tau$	Time delay offset

Correlation function

$R_{v_1, v_2}(\tau)$	Cross-correlation function of $v_1(t)$ and $v_2(t)$.
$\hat{R}_{v_1, v_2}(\tau)$	A statistical estimate of $R_{v_1, v_2}(\tau)$
$\rho(\tau)$	Normalized correlation function
$w(\tau)$	Weighting function.

Interferometer geometry and source position

H_s, h_b	Hour angles of radio source and interferometer baseline.
δ_s , δ_b	Declination of radio source and interferometer baseline.
Az, El	Azimuth and elevation, respectively.
D	Baseline length.
θ, θ_o	Angle of incidence measured from the plane normal to the interferometer baseline.
ξ	$= \sin\theta$
u , v	Spatial spectral components in east-west and north-south direction, equal to the projected baseline components in the direction of the source (measured in wavelengths).
w	$= \sqrt{u^2+v^2}$
ϕ	Geodetic latitude
ϕ'	Geocentric latitude
$\mathbf{f}$	Fringe rate vector.

Miscellaneous

$F(\xi, f)$	Antenna radiation pattern.
$H(f)$	Complex transfer function of the receiver.

ACKNOWLEDGEMENT

Research in very long baseline interferometry must be a team work. Therefore, many people have contributed in various ways to the observations as well as to the receiver and data reduction system described in this report.

I am especially grateful to Professor Olof Rydbeck, director of the Research Laboratory of Electronics, and the Onsala Space Observatory, for his encouraging interest in this work. I also thank Prof. B. Höglund, Mr. P. Landgren, Dr. A Winnberg, Mr. B. Hansson, Dr. J. Elldér and others at the Onsala Space Observatory; and Dr. J. Moran at MIT-Lincoln Laboratory; and Dr. B. Clark at the National Radio Astronomy Observatory for valuable discussions and technical assistance.

I am also grateful to the National Radio Astronomy Observatory for the loan of their Mark I VLB I recording system.

This work was supported by the Swedish Natural Science Research Council and the Swedish Board for Technical Development.

CHAPTER I

INTRODUCTION

Interferometers have played a more prominent part in radio astronomy than in optical astronomy due to the poor resolving power of single radio telescopes. The largest radio reflectors give a resolution of 2 to 3 arcminutes (close to that of the unaided human eye), and the most powerful conventional radio interferometer has a resolution of about 0.2 arcseconds, compared to the theoretical resolving power of about 0.03 arcseconds for the 200 - inch Palomar telescope. With this in mind the recent very long baseline interferometer (VLBI) observations between the Onsala Space Observatory and various radio observatories in the United States, which gave an angular resolution of about 0.001 arcseconds at the highest frequency used, were a great step forward. Using the VLBI techniques the resolution power is in fact unlimited.

Interferometry at radio wavelengths began in 1946, twenty-six years after the optical, stellar interferometer was used by Michelson, when Mc Cready, Pawsey, and Payne-Scott [1947] started observing with the cliff interferometer at Sidney. The same year Ryle and Vonberg [1947] used a two-element interferometer to study the radiation from the sun. Both these interferometers worked at a wavelength near 1.5 m and had a resolution of about ten arcminutes. Twenty years later the interferometer techniques had been improved so that a group at the Jodrell Bank Observatory [Adgie et al (1965)] could make observations with a baseline $6 \cdot 10^5$ wavelengths [≈ 130 km] long, giving a resolution of about 0.2 arcseconds.

A number of extragalactic sources remained unresolved with the Jodrell Bank interferometer. The time variations of a few compact sources pointed towards a diameter as small as 0.001 arcseconds. Such a high resolution could not be realized by the use of cables or microwave links connecting the antennas. A very long baseline interferometer had to be built without real time connection between the stations, but still with the ability of syncronizing the receivers. Such a system was realized by means of high speed magnetic tape recorders, high-stable oscillators (atomic frequency standards), and a general purpose computer.

Two different groups, one associated with the National Radio Astronomy Observatory and Cornell University in the United States, and the other with the National Research Council of Canada, began developing such systems based on highly stable atomic frequency standards. Both systems were brought into operation in the spring of 1967 [Broten et al (1967), Bare et al (1967)] , and successful observations of both quasars and hydroxyl OH-line emission sources over transcontinental distances were made.

A year later radio astronomers at Lincoln Laboratory-MIT, National Radio Astronomy Observatory, University of California,and the Onsala Space Observatory were able to operate a four antennas VLBI system to study the OH spectral line source W3. The maximum antenna separation was 7719 km giving a resolution of 0. 0015 seconds at the observing wavelength of 18 cm. [Moran et al (1968)] . At the same time a number of compact extragalactic radio sources were studied using the Onsala Space Observatory to National Radio Astronomy Observatory (Green Bank) baseline [Kellermann et al (1968)] .

Along with the measurements,a complete data reduction system for very long baseline interferometry was developed at the Onsala Observatory. Such a system consists of a set of computer programs to organize an observation period, to lead the observations,and to analyze the recorded signals to get the interferometer fringe visibility.

The following report gives the basic theoretical background for interferometric observations at radio wavelengths, and describes the receiver system for very long baseline interferometry and the computer programs which process the recorded data to get the fringe amplitude and fringe phase versus frequency. In chapter II we derive the formulae giving the baseline parameters, the geometrical time delay and fringe rate for given station coordinates and radio source coordinates. The positions of some of the VLBI stations are tabulated and parameters for nine important interferometer baselines are listed.

Chapter III gives a brief review of the theory of the two-element radio interferometer. A VLBI observation normally gives the fringe amplitude at one or a few spacings. All one can do with it alone is to calculate a diameter (or limit) based on a model, typically a circularly symmetric source with a uniform or Gaussian brightness distribution. Table 3. 1 in chapter III gives examples of simple brightness distributions and their visibility functions.

The receiver system at each station consists of a superheterodyne receiver with its local oscillator signal controlled by an atomic frequency standard. In chapter IV the relation between the cross-correlation function and the cross-power spectrum for such a system is given. The obtained formulae are then used in the computer program which processes the recorded data.

In chapter V the sensitivity formulae for an interferometric observation are derived and in chapter VI we discuss the one-bit correlation method of cross-spectral analysis, which is the method used in the data reduction.

As mentioned above only one or a few points on the visibility versus projected baseline curve are obtained from a VLBI observation. However, if the radiation from different nearby objects can be separated in one way or another, it is possible to draw a map showing the position of the different objects by means of the fringe rate offset and/or the geometrical time delay offset. Chapter VII describes the method.

In the last two chapters we describe the receiver and recorder used at the Onsala Space Observatory and the data program developed for the IBM 360/65 computer to compute fringe amplitude, fringe phase, accurate time delay and fringe rate from a VLBI observation.

CHAPTER II

GEOMETRY OF THE INTERFEROMETER

Consider two antennas a distance D apart receiving radiation from a point source making an angle θ with the plane normal to the baseline (figure 2.1). The radiation reaching antenna no. 2 travels an extra distance of $-D\sin\theta$ relative to radiation reaching antenna no. 1.

On the celestial sphere in figure 2.2 P is the north pole, S is the source being observed, and B is the point representing the baseline direction $\theta = \pi/2$. Let H_s, δ_s and h_b, δ_b be the hour angles and declinations of the source and baseline as seen from station no. 1. Then

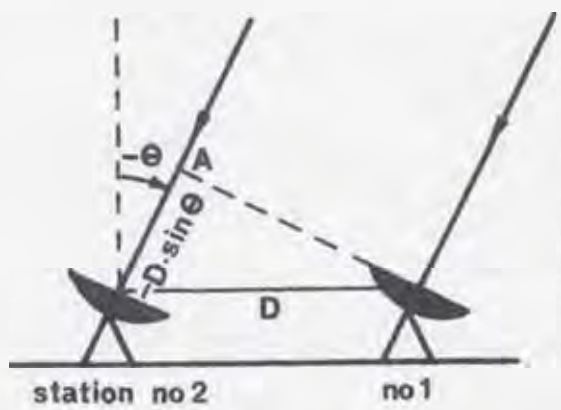

Figure 2.1. The two element interferometer.

$$\cos\left(\frac{\pi}{2} - \theta\right) = \cos\left(\frac{\pi}{2} - \delta_b\right)\cos\left(\frac{\pi}{2} - \delta_s\right) +$$

$$+ \sin\left(\frac{\pi}{2} - \delta_b\right)\sin\left(\frac{\pi}{2} - \delta_s\right)\cos(h_b - H_s) \qquad (2.1)$$

which simplifies to give the geometrical time delay τ_g

$$\tau_g = -\frac{D}{c}\sin\theta = -\frac{D}{c}\left[\sin\delta_b \sin\delta_s + \cos\delta_b \cos(h_b - H_s)\right] \qquad (2.2)$$

where c is the velocity of light. τ_g is negative if there is an excess delay at station no. 1. Notice that expression (2.2) is derived on the assumption that station no. 2 does not move while the wave propagates from point A to antenna no. 2. A first order correction to equation (2.2) will be given below.

From equation (2.2) we see that τ_g varies with time due to the rotation of the earth or the motion of the source on the celestial sphere. Let us assume that the radiation is monochromatic. Then, if the two signals, which are received at station no. 1

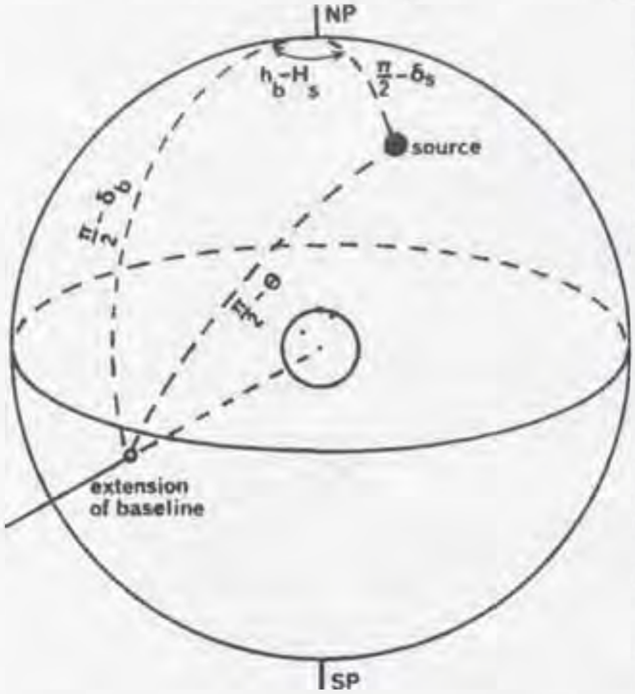

Figure 2. 2 The geometry of the interferometer.

and no. 2, are multiplied there will be a sinusoidally varying beat signal due to the different Doppler frequency shift. One period of the beat signal is called an interferometer fringe.

The total fringe phase is $\omega \tau_g$, where ω is the angular frequency of the signals. $\omega_f = \omega \dfrac{\partial \tau_g}{\partial t}$ is called the angular fringe frequency. From equation (2. 2) we obtain

$$f_f = \frac{D}{\lambda} \, \Omega \cos \delta_b \cos \delta_s \, \sin (H_s - h_b) \qquad (2.3)$$

where λ is the wavelength and

$$\Omega = \frac{2\pi}{86164.09} = 7.292116 \cdot 10^{-5} \text{ radians per second}$$

is the angular velocity of the earth. 86164. 09 is the number of UT seconds per sidereal day.

The expressions (2.2) and (2.3), giving the geometrical time delay and fringe rate, do not take into account the effect of the diurnal rotation of the earth, while the wave propagates the extra distance $c \cdot \tau_g$ to station number 2. Let $\tau_{g,1}$ denote the corrected value of τ_g. It is easy to see that $\tau_{g,1}$ can be obtained by changing the true longitude of station no. 2 by $\Omega \tau_{g,1}$ radians. Ω is the angular velocity of the earth. This gives a new virtual baseline, which is also a function of the position of the source.

If $\bar{\rho}_2$ is the radius vector to station no. 2 then the first order approximation of $\tau_{g,1}$ is obtained by using instead the radius vector

$$\bar{\rho}_{2,1} = \bar{\rho}_2 + \Omega\tau_g \cos \phi_2' \; \bar{\Omega} \times \bar{\rho}_2 \tag{2.4}$$

where ϕ_2' is the geocentric latitude of station no. 2 and $\bar{\Omega}$ is the unit spin vector of the earth. The geometrical time delay is then

$$\tau_{g,1} \approx \tau_g (1 + \varepsilon) \simeq \tau_g (1 - \frac{\Omega}{c} \cos \phi_2' \; \rho_2 \cos \delta_s \sin H_{s,2}) \tag{2.5}$$

where $H_{s,2}$ is the local hour angle of the source as seen from station no. 2.

From equation (2.5) the corrected fringe rate $f_{f,1}$ is given by

$$f_{f,1} = f \cdot \frac{\partial \tau_{g,1}}{\partial t} = f_f + f_f \cdot \varepsilon + \tau_g \cdot f \cdot \frac{\partial \varepsilon}{\partial t} \tag{2.6}$$

where

$$\frac{\partial \varepsilon}{\partial t} = - \frac{\Omega^2}{c} \cos \phi_2 \rho_2 \cos H_{s,2} \cos \delta_s \tag{2.7}$$

The correction in fringe rate can be several millihertz and must be taken into account if the fringe rate data are used to measure the position of a radio source.

As both observatories move with different velocities due to the earth rotation there will also be a small correction in fringe rate due to the relativistic effect. This effect has not been taken into account in the equation above — the time scales are measured in different moving systems. If the velocities of the stations are v_1 and v_2 the fringe rate correction will be of the order

$$\frac{1}{2} \; f\left(\frac{v_2 - v_1}{c}\right)^2$$

Assuming the extreme situation with one station at the equator and one at the north or south pole the relativistic effect contributes with about 10 millihertz to the fringe rate at a frequency of 10 GHz.

The interferometer baseline parameters D, h_b, and δ_b used in equation (2. 1), (2. 2), and (2. 3) are defined in figure 2. 3. They can be calculated from the coordinates of the stations and an adopted equatorial radius and flattening factor of the earth using simple trigonometric formulae.

The altitudes of the stations are normally assumed to be constant. This is an approximation, of course, as one has to count not with the physical antenna position but with the phase centre of the antenna. The geometrical position of the phase centre varies with the local hour angle and the declination of the observed source. This effect must be taken into account when a VLBI observation deals with accurate measurement of source position and baseline parameters.

In order to determine the positions of the observing stations one has, a priori, to determine a fixed coordinate system in the earth. Normally one adopts a system with its z-axis through the mean pole of 1900-1905 and the x-z plane given by the adopted longitudes of the observing stations of the Bureau International de l'Heure, BIH. The VLBI station coordinates can then be obtained by conventional methods with an uncertainty of about 100 m and by laser satellite tracking technique with an uncertainty of between 5 and 10 m. One also has to adopt a rotational model of the earth. The pole position of the earth is obtained from formulae for astronomical precession and nutation and data provided by Bureau International de l'Heure and Internation Polar Motion Service. The angular rotation about this axis is obtained from tables of UT1 provided by BIH.

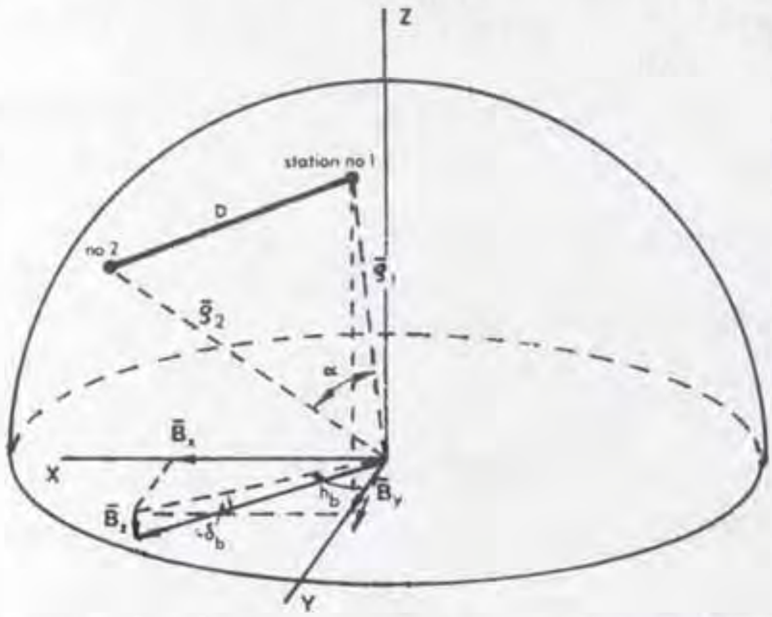

Figure 2. 3 The baseline parameters of a two-element interferometer.

Four different very long baselines with Onsala Space Observatory as one of the stations have so far (Jan. 1971) been used, viz.

Onsala Space Observatory - Haystack Microwave Facility, Lincoln Lab. MIT

Onsala Space Observatory - Green Bank, National Radio Astronomy Obs. , W. Va.

Onsala Space Observatory - Owens Valley Radio Obs. , Caltech.

Onsala Space Observatory - Hat Creek Observatory Univ. of California

Table 2. 1 lists the positions of these observatories as given by the Astronomical Ephemeris, 1970. Also included are two observatories in Europe which will co-operate with the Onsala Space Observatory in a near future. The geocentric latitude and radius vector are obtained by assuming an equatorial earth radius of 6378160 m and a flattening factor f = 1/298. 25. These values are the ones adopted by IAU in 1964. More accurate values are available, the 1969 Smithsonian Standard Earth (II) for example, but are not necessary as long as the VLBI measurements are used for studying the angular size and structure of radio sources.

Using the IAU earth the reduction from geodetic latitudes ϕ to geocentric latitude ϕ' is given by

$$\phi' = \phi - 11'32.''7430 \sin 2\phi + 1''.1633 \sin 4\phi - 0.''0026 \sin 6\phi \qquad (2.8)$$

and the radius vector ρ of the station (in meters) is

$$\rho = 6378160\,(0.998327073 + 0.001676438 \cos 2\phi - 0.000003519 \cos 4\phi + 0.000000008 \cos 6\phi) + \text{the altitude of the station} \qquad (2.9)$$

Table 2.1 includes seven (N) stations which can give an interferometer system with twenty-one [$\frac{N(N-1)}{2}$] baselines. The parameters of nine of them are listed in table 2.2.

OBSERVATORY	ANTENNA	GEODETIC LATITUDE DEGREES		LONGITUDE DEGREES		ALTITUDE M	GEOCENTRIC LATITUDE DEGREES	
Onsala Space Observatory, Chalmers Univ. of Technology, Sweden	84 -ft	57.3934	$57^{\circ}23'36.1''$	-11.9202	$-11^{\circ}55'12.8''$	14	57.2184	$57^{\circ}13'06.3''$
Max-Planck-Institut für Radio-astronomie, Germany	100 m	50.5250	$50^{\circ}31'30''$	-6.8842	$-6^{\circ}53'03''$	319	50.3360	$50^{\circ}20'09.7''$
Nuffield Radio Astronomy Laboratories, England	250-ft Mark I Jodrell Bank	53.2364	$53^{\circ}14'11.0''$	1.6396	$1^{\circ}38'22.5''$	70	53.0517	$53^{\circ}03'06.1''$
Haystack Microwave Facilities Lincoln Lab., MIT, USA	120-ft	42.6232	$42^{\circ}37'23.5''$	71.4887	$71^{\circ}29'19.1''$	145	42.4315	$42^{\circ}25'53.4''$
National Radio Astronomy Observatory, USA	140-ft Green Bank	38.4376	$38^{\circ}26'15.4''$	79.8367	$79^{\circ}50'12.1''$	823	38.2504	$38^{\circ}15'01.3''$
Owens Valley Radio Observatory California Institute of Technology USA	120-ft	37.2317	$37^{\circ}13'54.0''$	118.2942	$118^{\circ}17'39.0''$	1216	37.0464	$37^{\circ}02'47.2''$
Hat Creek Radio Observatory Univ. of California, USA	84-ft	40.8179	$40^{\circ}49'04.4''$	121.4733	$121^{\circ}28'23.9''$	1050	40.6276	$40^{\circ}37'39.4''$

Table 2.1. The coordinates of some VLBI stations.

Interferometer baseline	α degrees	B_x M	B_y M	B_z M	Length M	Local hour angle*		Decl.* Degrees	Azimuth* Degrees	Elevation* Degrees
Ons-Jodrell Bank	8.7788	821064	453229	-2632571	974098	4.8681	$4^h52^m5.1^s$	-15.6796	-112.5680	-4.3008
Ons-Max Planck	7.4933	224580	662984	-449279	831767	2.0422	$2^h02^m32.1^s$	-32.6939	-154.5549	-3.5580
Ons-Haystack	52.1842	5168925	-1878517	-1052755	5599545	8.1262	$8^h07^m34.2^s$	-10.8365	-68.1445	-26.0415
Ons-Green Bank	59.5049	5636141	-2488089	-1405532	6319192	8.3826	$8^h22^m57.5^s$	-12.8514	-65.6376	-29.6916
Ons-Owens Valley	76.8501	5189487	-5781402	-1511022	7914454	10.0006	$10^h00^m02.1^s$	-11.0064	-38.7486	-38.3766
Ons-Hat Creek	74.6253	4834994	-5895074	-1201825	7718384	10.1708	$10^h10^m15.0^s$	-8.9579	-34.8875	-37.2709
Green-Bank-Haystack	7.6080	-467216	609572	352777	845175	16.1796	$16^h10^m46.7^s$	24.6706	54.0366	-3.9540
Owens Valley-Green Bank	30.2531	446654	3293313	105489	3325137	4.6286	$4^h37^m43.1^s$	1.8180	-101.2570	17.4222
Haystack-Hat Creek	36.9159	-333930	-4016557	-149069	4033170	7.5509	$7^h33^m03.3^s$	-2.1182	-75.4066	-18.4367

*) measured from station no. 1 to station no. 2.

Table 2.2. The parameters of someVLB interferometer baselines.

CHAPTER III

COHERENCE FUNCTION AND FRINGE VISIBILITY

The radiation in point P_1 and P_2 (figure 3.1) from a point source S has complete coherence since P_1 and P_2 are at the same distance from the source. However, when the source is an incoherent extended source we have to deal with the simultaneous effect of many point sources. The fields are no longer completely coherent as the distance from the different point sources are no longer the same. It is evident that the degree of coherence between the radiation in point P_1 and P_2 is a function of the extension of the radiating source. We will in this chapter give the relations between the mutual coherence function as defined by Born and Wolf [1959] , the observed complex fringe visibility of a two-element interferometer, and the brightness distribution of the source.

Figure 3.1.

Normally all radio sources are incoherent radiators. The theoretical treatment will, however, also include the case of partially coherent extended sources. The maser mechanism, generally accepted as the explanation of the strong galactic hydroxyl line and water vapor line emission sources, can give rise to such coherent radiation. In that case it is clear that the measured visibility versus projected baseline does not give information about the angular size of the object.

Interferometer theory assuming partially coherent, extended sources has been studied earlier by several authors [Drane and Parrent, 1962] , [Mac Phie, 1964] , [Swenson and Mathur, 1968] .

The incident radiation is a function of the direction of arrival and of time. In the one dimensional case the electric field of this radiation can be represented by $s(\xi, t) = \text{Re}\left\{v(\xi, t)\right\}$, where Re denotes "the real part of" , $\xi = \sin\theta$ and t is the time variable. The complex part of $v(\xi, t)$ is obtained by changing the phase of each spectral component of $s(\xi, t)$ by $\pi/2$.

Following the notation of Born and Wolf [1959] , we define the mutual coherence function

$$\Gamma(\xi_1, \xi_2, \tau) = \lim_{T\to\infty} \frac{1}{2T} \int_{-T}^{T} v(\xi_1, t)\, v^*(\xi_2, t-\tau)\, dt \tag{3.1}$$

which is the cross-correlation of the signals received from the directions ξ_1 and ξ_2 at different times. When $\xi_1 = \xi_2$ and $\tau = 0$ $\Gamma(\xi_1, \xi_2, \tau) = \Gamma(\xi)$ is proportional to the average power from the source in the ξ - direction , i. e. the brightness distribution of the source is measured.

$$T_B(\theta) \sim \lim_{T\to\infty} \frac{1}{2T} \int_{-T}^{T} |\, v(\xi_1\, t)\,|^2\, dt = \Gamma(\xi) \tag{3.2}$$

The normalized mutual coherence function

$$\frac{\Gamma(\xi_1, \xi_2, \tau)}{\left[\Gamma(\xi_1, 0)\, \Gamma(\xi_2, 0)\right]^{1/2}} \tag{3.3}$$

is called the complex degree of coherence.

Let us now define the lateral coherence function

$$\gamma(u_1, u_2, \tau) = \lim_{T\to\infty} \int_{-T}^{T} V(u_1, t)\, V^*(u_2, t-\tau)\, dt \tag{3.4}$$

where

$$V(u, t) = \int_{-\infty}^{\infty} v(\xi, t)\, e^{-j2\pi\xi u}\, d\xi \tag{3.5}$$

is the spatial Fourier transform of $v(\xi, t)$. We thus get the complex Fourier transform pair

$$\gamma(u_1, u_2, \tau) = \int_{-\infty}^{\infty}\int_{-\infty}^{\infty} \Gamma(\xi_1, \xi_2, \tau)\, e^{-j2\pi(\xi_1 u_1 - \xi_2 u_2)}\, d\xi_1\, d\xi_2 \quad (3.6)$$

$$\Gamma(\xi_1, \xi_2, \tau) = \int_{-\infty}^{\infty}\int_{-\infty}^{\infty} \gamma(u_1, u_2, \tau)\, e^{j2\pi(\xi_1 u_1 - \xi_2 u_2)}\, du_1\, du_2 \quad (3.7)$$

If the source is assumed to be completely incoherent, i.e. $\Gamma(\xi_1, \xi_2, \tau) = 0$ if $\xi_1 \neq \xi_2$ for all values of τ one obtains

$$\Gamma(\xi, \tau) = \int_{-\infty}^{\infty} \gamma(u, \tau)\, e^{j2\pi u \xi}\, du \quad (3.8)$$

$$\gamma(u, \tau) = \int_{-\infty}^{\infty} \Gamma(\xi, \tau)\, e^{-j2\pi u \xi}\, d\xi \quad (3.9)$$

where $u = u_1 - u_2$,

which for $\tau = 0$ gives

$$\gamma(u) = \lim_{T \to \infty} \int_{-T}^{T} V(u_1, t)\, V^*(u_1 - u, t)\, dt = \int_{-\infty}^{\infty} \overline{|v(\xi)|^2}\, e^{-j2\pi u \xi}\, d\xi \quad (3.10)$$

where $\overline{}$ denotes the time average. $\gamma(u)$ is the quantity measurable by interferometry. Notice that the equation (3.10) is valid only for completely incoherent sources.

Up to this point we have not taken into account the influence of the antennas and receivers of the interferometer system. Let us assume that the two antennas have radiation patterns $F_1(\xi, f)$ and $F_2(\xi, f)$ and that the complex transfer functions of the receivers are $H_1(f)$ and $H_2(f)$. The output voltages are then

$$E_1(\xi_1, f) = \int_{-\infty}^{\infty} V_1(\xi_1', f) H_1(f) \cdot F_1(\xi_1 - \xi_1', f) \, d\xi_1' \tag{3.11}$$

and

$$E_2(\xi_2, f) = \int_{-\infty}^{\infty} V_2(\xi_2', f) H_2(f) \cdot F_2(\xi_2 - \xi_2', f) \, d\xi_2' \tag{3.12}$$

where

$$V(\xi, f) = \int_{-\infty}^{\infty} v(\xi, t) \, e^{-j2\pi f t} \, dt \tag{3.13}$$

When the output voltages are cross-correlated we obtain

$$R(\xi_1, \xi_2, \tau) = \lim_{T \to \infty} \frac{1}{2T} \int_{-T}^{T} e_1(\xi_1, t) \, e_2^*(\xi_2, t-\tau) \, dt =$$

$$= \int_{-\infty}^{\infty} E_1(\xi_1, f) \, E_2^*(\xi_2, f) \cdot e^{j2\pi f \tau} \, df \tag{3.14}$$

using the convolution theorem. From equation (3 . 1),(3 . 11),and (3 . 12)

$$R(\xi_1, \xi_2, \tau) = \int_{-\infty}^{\infty} \int_{-\infty}^{\infty} \int_{-\infty}^{\infty} \Gamma(\xi_1', \xi_2', f) \cdot F_1(\xi_1 - \xi_1', f) \, F_2^*(\xi_2 - \xi_2', f) \cdot$$

$$\cdot H_1(f) \cdot H_2^*(f) \, e^{j2\pi f \tau} \, d\xi_1' \, d\xi_2' \, df \tag{3.15}$$

Let us now assume that the source is completely incoherent, i. e.

$$\Gamma(\xi_1, \xi_2, f) = 0 \quad \text{if } \xi_1 \neq \xi_2$$

With both antennas pointing in the direction ξ, we obtain

$$R(\tau, \xi) = \int_{-\infty}^{\infty} \int_{f_o - \frac{\Delta f}{2}}^{f_o + \frac{\Delta f}{2}} \Gamma(\xi', f_o)\; F_1(\xi - \xi', f_o)\, F_2^*(\xi - \xi', f_o)$$

$$H_1(f) \cdot H_2^*(f) \cdot e^{\,j2\pi f \tau}\, d\,\xi'\, df \qquad (3.16)$$

In equation (3.16) we assume that $\Gamma(\xi', f)$, $F_1(\xi - \xi', f)$ and $F_2(\xi - \xi', f)$ do not vary significantly over the passband from $f_o - \frac{\Delta f}{2}$ to $f_o + \frac{\Delta f}{2}$.

If we now ajust the instrumental delay τ_i to compensate for the geometrical delay $\tau_g = -D\,\xi_o/c$ in the direction ξ_o and instead refer the ξ direction to the ξ_o direction so that

$\xi' - \xi_o \approx \xi \cos\theta_o \qquad \xi \ll 1$

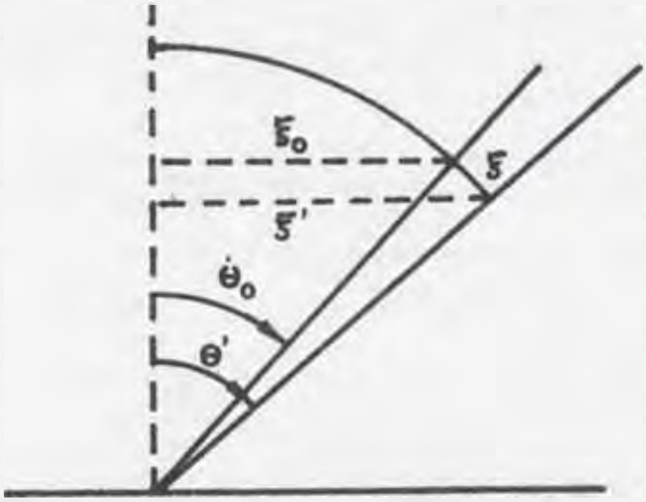

Figure 3.2. Showing the relation between ξ', ξ_o and ξ.

$$R\left(\frac{D}{\lambda_o}\cos\theta_o\right) = \int_{-\infty}^{\infty} \Gamma(\xi, f_o) \cdot F_1(\xi, f_o) \cdot F_2^*(\xi, f_o)$$

$$\cdot \left[\int_{-\Delta f/2}^{\Delta f/2} H_1(f+f_o)\, H_2^*(f+f_o)\, e^{-j2\pi\,\xi\,\frac{D\cos\theta_o}{c} f} df\right] e^{-j2\pi\,\xi\,\frac{D\cos\theta_o}{\lambda_o}}\, d\,\xi$$

(3.17)

In very long baseline interferometry the width of the interferometer fringes can be 100000 times smaller than the individual antenna beams (with antennas of ordinary sizes). Normally one can therefore put $|F_1(\xi, f_o)| = |F_2(\xi, f_o)| = 1$ in the ξ - range of interest. However, there can be cases where this assumption is not correct. For example, in accurate measurements of the angular separation of different point sources.

With $F_1(\xi, f_o) \cdot F_2^*(\xi, f_o) = 1$ where $\Gamma(\xi, f_o) \neq 0$ and with the bandwidth pattern

$$\int_{-\Delta f/2}^{\Delta f/2} H_1(f+f_o)\, H_2^*(f+f_o)\, e^{-j2\pi\xi \frac{D\cos\theta}{c} f}\, df = 1$$ over the ξ - range of interest

we obtain

$$R(u) = \int_{-\infty}^{\infty} \Gamma(\xi, f_o)\, e^{-j2\pi\xi u}\, d\xi \tag{3.18}$$

where $u = \dfrac{D\cos\theta_o}{\lambda_o}$ is the projected baseline measured in wavelengths. The crosscorrelation function is thus the Fourier transform of the brightness distribution $\Gamma(\xi, f_o) = \overline{|V(\xi)|^2}$ with the spatial frequency $u = \dfrac{D\cos\theta_o}{\lambda_o}$. Compare equation (3.10).

The amplitude of the normalized crosscorrelation function

$$\rho(u) = \frac{\int T_B(\xi)\, e^{-j2\pi\xi u}\, d\xi}{\int T_B(\xi)\, d\xi} \tag{3.19}$$

is called the fringe visibility or fringe amplitude and the phase is accordingly called the fringe phase.

The visibility can be understood in the following way:

It is possible to compensate for the geometrical delay only for a precalculated direction ξ_o by inserting an instrumental delay. The radiation from all other directions will be phase-shifted and will interfere with the wave from the direction ξ_o. The fringe visibility will go down more or less depending on the total phase delay. The case with an incoherent source is particularly simple to treat as the different elements of the source can be seen as individual point sources.

For simplicity only the one-dimensional case has been considered above. The generalization to the two-dimensional case is straight forward. Using polar coordinates one obtains

$$R(w, \Phi) = \int_0^{2\pi} \int_0^{\infty} T_B(r, \varphi)\, e^{j2\pi w r \cos(\varphi - \Phi)}\, r\,dr\,d\varphi \qquad (3.20)$$

$$T_B(r, \varphi) = \int_0^{2\pi} \int_0^{\infty} R(w, \Phi)\, e^{-j2\pi w r \cos(\varphi - \Phi)}\, w\,dw\,d\Phi \qquad (3.21)$$

$$u = w \cos\Phi$$

$$v = w \sin\Phi$$

$$x = r \cos\varphi$$

$$y = r \sin\varphi$$

which in the circularly symmetric case gives the Hankel transform pairs

$$R(w) = 2\pi \int_0^{\infty} T_B(r)\, J_o(2\pi w r)\, r\,dr \qquad (3.22)$$

$$T_B(r) = 2\pi \int_0^{\infty} R(w)\, J_o(2\pi w r)\, w\,dw \qquad (3.23)$$

In principle the true brightness distribution $T_B(r, \varphi)$ of a source may be obtained from the observed complex visibility function using equation (3.21) or (3.23). In practice the result depends upon the available spacing interval, the maximum baseline length, and the signal-to-noise ratio. The highest spatial frequency component determines the resolution and the necessary spacing interval is given by (the full source extent)$^{-1}$ The radio link controlled interferometers with baseline lengths up to several hundred miles, and the VLB interferometers using independent local oscillators give very high resolution but little information about the fine structure of the observed sources. They are therefore not competing with the full aperature synthesis antennas but necessary complements, as the maximum baseline lengths of the later system must be limited at least for economical reasons. The limited number of available baselines and the difficulty of having control over the absolute phase of VLB interferometers mean that a simplified technique of restoring the brightness distribution has to be used. On the longest baselines the requirement of common visibility at reasonable elevation ($>10^{\circ}$) requires that the observations are near the interferometer meridian and only a few points on the visibility versus projected baseline curve are obtained. This means that one has to assume the simplest and most feasible source distribution and adapt its parameters to the observed visibility. Such distributions and the corresponding fringe visibilities are shown in table 3.1.

SOURCE DESCRIPTION	BRIGHTNESS DISTRIBUTION	VISIBILITY FUNCTION
	$T_B(x,y)$; $T_B(r)$	$\gamma(u,v)$
A point source	$\frac{1}{\pi r}\ \delta(r)$	1
Two point sources	$\delta(x-x_o,\ y-y_o)+\delta(x+x_o,\ y+y_o)$	$\cos[2\pi(ux_o+vy_o)]$
Uniform brightness distribution	$1/\pi a^2 \quad r < a$ $0 \quad r > a$	$\frac{J_1(2\pi a w)}{\pi a w}$
Gaussian brightness distribution	$\frac{1}{\pi a^2}\ e^{-r^2/a^2}$	$e^{-\pi^2 a^2 w^2}$
Two Gaussian components at $(x_o,\ y_o)$ and $(-x_o,-y_o)$		$e^{-\pi^2 a^2 w^2}\ \cos 2\pi(ux_o+vy_o)$
A ring source	$\frac{1}{2\pi a}\ \delta(r-a)$	$J_o(2\pi a w)$
A Gaussian ring source with radius b		$e^{-\pi^2 a^2 w^2}\ J_0(2\pi bw)$

Table 3.1 Some simple source brightness distributions and the corresponding visibility functions. $w = \sqrt{u^2+v^2}$

CHAPTER IV

MEASUREMENT OF THE COMPLEX CROSS SPECTRAL FUNCTION

The signals $s_1(t)$ and $s_2(t)$, whose cross power spectrum we wish to measure, are stationary and ergodic, which means that statistical averages such as $\bar{s}_1$, $\overline{s_1^2}$, $\bar{s}_2$, $\overline{s_2^2}$ and $\overline{s_1 \cdot s_2}$ exist and are independent of time. The statistical averages are equal to the infinite time averages. The cross power spectrum of the signals can be defined as the Fourier transform of the complex cross-correlation function

$$S(f) = \int_{-\infty}^{\infty} \rho(\tau)\, e^{-j2\pi f \tau}\, d\tau \tag{4.1}$$

where

$$\rho(\tau) = \lim_{T \to \infty} \frac{1}{2T} \int_{-T}^{T} v_1(t)\, v_2^*(t-\tau)\, dt \tag{4.2}$$

and $v_1(t)$ and $v_2(t)$ are the complex signals the real parts of which are $s_1(t)$ and $s_2(t)$.

Consequently $\lim_{T \to \infty} \frac{1}{2T} \int_{-T}^{T} s_1(t)\, s_2(t+\tau)\, dt = \frac{1}{2}\, \mathrm{Re} \left\{ \rho(\tau) \right\}$

In practice the signal $s_1(t)$ and $s_2(t-\tau_g)$, where τ_g is the geometrical delay in the direction of the source $\tau_g = -D\, \xi_o / c$, are converted to video before crosscorrelation. After mixing with local oscillator signals $\cos\left[(\omega_o + \Delta\omega)t + \varphi_1\right]$ and $\cos(\omega_o t + \varphi_2)$ the video signals [see figure 4.1] are

$$s_1(t) \cos\left[(\omega_o + \Delta\omega)t + \varphi_1\right] \tag{4.3}$$

and

$$s_2(t-\tau_g) \cos(\omega_o t + \varphi_2) \tag{4.4}$$

Insertion of a time delay τ_i at station number 2 gives the cross-correlation function

$$\rho(\tau) = \frac{1}{2T}\int_{-T}^{T} v_1(t)\, e^{-j[(\omega_o + \Delta\omega)t + \varphi_1]}\, v_2^*(t - \tau_g - \tau_i - \tau)\cdot$$

$$\cdot\, e^{j[\omega_o(t - \tau_i - \tau) + \varphi_2]}\, dt \qquad (f > 0) \tag{4.5}$$

Using the upper sideband and assuming that $(\omega_o \cdot \frac{\partial \tau_g}{\partial t} - \Delta\omega)\, T \ll 1$ $\rho(\tau)$ can be written

$$\rho(\tau) = \int_0^{\infty} e^{j(\omega_o \tau_g - \Delta\omega t - \varphi_1 + \varphi_2)}\, S(f+f_o)\, e^{j2\pi f(\tau_g + \tau_i + \tau)}\, df +$$

$$+ \int_{-\infty}^{0} e^{-j(\omega_o \tau_g - \Delta\omega t - \varphi_1 + \varphi_2)}\, S(f-f_o)\, e^{j2\pi f(\tau_g + \tau_i + \tau)}\, df \tag{4.6}$$

where S(f) is defined by equation (4. 1).

From equation (4. 6) the cross-correlation function becomes

$$\rho(\tau) = 2\cos(\omega_o \tau_g - \Delta\omega t - \varphi_1 + \varphi_2) \int_0^{\infty} S(f+f_o)\cos 2\pi f(\tau_g + \tau_i + \tau)\, df -$$

$$- 2\sin(\omega_o \tau_g - \Delta\omega t - \varphi_1 + \varphi_2) \int_0^{\infty} S(f+f_o)\sin 2\pi f(\tau_g + \tau_i + \tau)\, df \tag{4.7}$$

which is a real function as $s_1(t)$ and $s_2(t)$ are real functions of time.

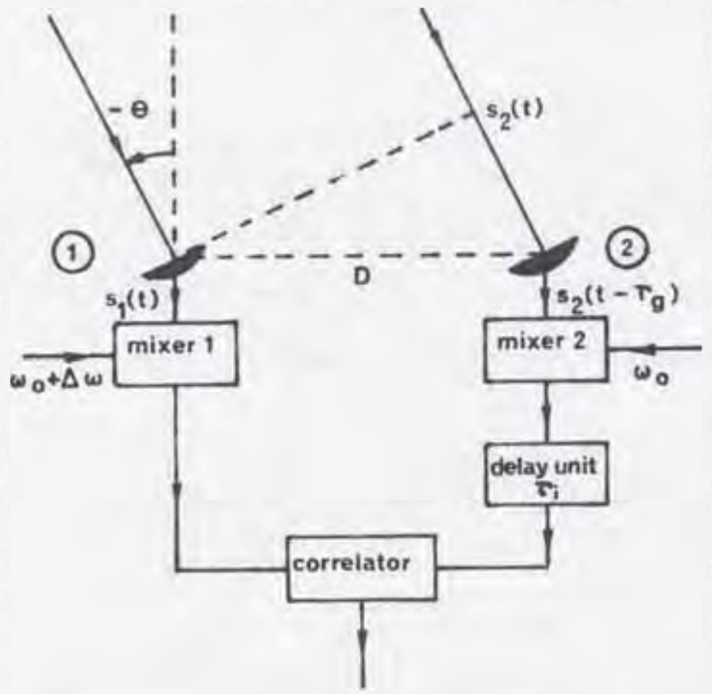

Figure 4.1. The crosscorrelator interferometer.

From equation (4.7) we see that the fringe rotation rate is

$$f_f = f_o \cdot \frac{\partial \tau_g}{\partial t} - \Delta\omega/2\pi \tag{4.8}$$

if τ_i is ajusted to be equal to $-\tau_g$. It is consequently possible to offset the local oscillator at one of the stations to take out the linear portion of the fringe rotation.

Assuming a white noise signal and a rectangular bandpass filter of width B the cross-correlation function becomes

$$p(\tau) = 2\cos(\omega_o \tau_g - \Delta\omega t - \varphi_1 + \varphi_2) \frac{\sin[2\pi B(\tau_g + \tau_i + \tau)]}{2\pi B(\tau_g + \tau_i + \tau)} +$$

$$+ 2\sin(\omega_o \tau_g - \Delta\omega t - \varphi_1 + \varphi_2) \frac{\cos[2\pi B(\tau_g + \tau_i + \tau)] - 1}{2\pi B(\tau_g + \tau_i + \tau)}$$

$$= 2 \cos \left[\omega_o \tau_g - \Delta \omega t - \varphi_1 + \varphi_2 + \pi B (\tau_g + \tau_i + \tau) \right] \; \frac{\sin \pi B(\tau_g + \tau_i + \tau)}{\pi B (\tau_g + \tau_i + \tau)} \qquad (4.9)$$

where the factor 2 is due to the definition of the complex cross-correlation function. See equation (4.2). It is clear that in the single sideband case the fringe amplitude cannot be estimated merely by taking the peak value of the cross correlation function. If $\rho(\tau)$ in equation (4.6) is multiplied by exp $j[\omega_o \tau_i(t) + \Delta\omega t)]$, where $\tau_i(t) = -\tau_g(t)$ is the computed time delay using the best known interferometer parameters and source position, and integrated over a time period the complex cross-correlation function $\rho_c(\tau)$ becomes

$$\rho_c(\tau) = \frac{1}{T_i} \int_0^{T_i} \rho(\tau)\, e^{j(\omega_o \tau_i + \Delta\omega t)} \, dt =$$

$$= \int_0^{\infty} S(f + f_o)\, e^{j 2 \pi (f+f_o) \Delta \tau_g}\, e^{-j(\varphi_1 - \varphi_2)}\, e^{j2\pi f \tau} \, df \,,$$

$$= \int_0^{\infty} S_c(f+f_o)\, e^{j2 \pi f \tau} \, df \qquad (4.10)$$

where $2\pi (f+f_o) \Delta \tau_g$ is the fringe phase offset due to source position offset and errors in the baseline parameters. If τ_g is independent of frequency and $\Delta \tau_g = 0$ the fringe phase is constant over the frequency band. A small error in time delay $\Delta \tau_g = \tau_g + \tau_i \neq 0$ will make the fringe phase vary like $2\pi f \Delta \tau_g$. This effect has to be taken into account when correlating digitized signals as the time delay τ_i has to be truncated to an integer number of sample periods. The residual time delay offset after integration will, of course, be a small number, but it has to be evaluated to correct the obtained fringe phase versus frequency. The truncation of the time delay will also have an unfavourable effect on the measured cross power spectrum.

There will be a decrease in amplitude according to

$$\sin(\pi f \Delta t)/\pi f \Delta t\,, \qquad 0 < f < 1/2\Delta t$$

as the time error will be uniformly spread over $\pm \Delta t/2$.

The maximum change in fringe rate is equal to

$$\frac{D}{\lambda}\ \Omega^2 \ \cos\delta_b \cos\delta_s \qquad \text{Hz/sec}$$

and occurs when $H_s - h_b = n\pi$. Assuming a wavelength of 18 cm and the Onsala to Owens Valley baseline the maximum change is equal to 0.2 Hz/second for a source circumpolar at Onsala. The integration time before the phase detection described above is therefore restricted to a number much less than 1/0.2 seconds, if $\Delta\omega$ is constant during the observation. This is true if the fringe rate compensation is perfect. Normally the uncertainty in actual fringe rate and the frequency increment in the local oscillator chains used can result in a fringe rate offset of several Hz.

If low-pass filters with frequency transfer functions $H_1(f)$ and $H_2(f)$ are used the measured cross-power spectrum is

$$H_1(f)\, H_2^*(f)\, S_c(f+f_o)$$

and $S_c(f+f_o)$ can easily be obtained if $H_1(f) \cdot H_2^*(f)$ is known. Normally $H_1(f) \cdot H_2^*(f)$ is determined by measuring the complex cross-power spectrum of a strong unresolved continuum source.

CHAPTER V

THE SENSITIVITY OF AN INTERFEROMETER SYSTEM

The radiating point source is assumed to give input signals $\sqrt{T_{A1}}\ s_1(t)$ and $\sqrt{T_{A2}}\ s_2(t)$, where T_{A1} and T_{A2} are the equivalent antenna temperatures of the two interferometer systems. If the system noise temperatures are T_{S1} and T_{S2} there will also be input noise voltages $\sqrt{T_{S1}}\ n_1(t)$ and $\sqrt{T_{S2}}\ n_2(t)$. In spectral line work T_{A1} and T_{A2} are functions of the frequency. We assume, however, that T_{A1} and T_{A2} are constant over the actual filter bandwidth. $n_1(t)$ and $n_2(t)$ are ergodic, independent, Gaussian noise signals, while $s_1(t)$ and $s_2(t)$ are correlated, Gaussian signals. $s_1(t)$, $s_2(t)$ and $n_1(t)$, $n_2(t)$ are normalized with $\overline{[s_1(t)]^2}$, $\overline{[s_2(t)]^2}$, $\overline{[n_1(t)]^2}$ and $\overline{[n_2(t)]^2}$ equal to 1. Furthermore we assume that $s_{\frac{1}{2}}(t)$ and $n_{\frac{1}{2}}(t)$ have the power spectrum $B_{\frac{1}{2}}(f) = |H_{\frac{1}{2}}(f)|^2$, where $H_{\frac{1}{2}}(f)$ is the transfer frequency characteristic of the hf-filter.

Let us before we study the interferometer system determine the well-known sensitivity formulae of the total power receiver and the correlator receiver.

The total power receiver

The power spectrum after the square law detector in a total power receiver is

$$\left\{T_{A1} + T_{S1}\right\}^2 \left\{2 \cdot \int_{-\infty}^{\infty} B_1(f_1)\, B_1(f_1 - f)\, df_1 + \left[\int_{-\infty}^{\infty} B_1(f_1) \cdot df_1\right]^2 \delta(f)\right\} \qquad (5.1)$$

which after integration with a low pass filter b(f) becomes

$$\left\{T_{A1} + T_{S1}\right\}^2 \int_{-\infty}^{\infty} b(f) \left\{2 \int_{-\infty}^{\infty} B_1(f_1)\, B_1(f_1 - f)\, df_1 + \left[\int_{-\infty}^{\infty} B_1(f_1)\, df_1\right]^2 \delta(f)\right\} df$$

(5.2)

If the bandwidth of the rf-filter is much larger than the bandwidth of the low pass filter the mean value of the output is

$$\left\{T_{A1} + T_{S1}\right\} \sqrt{b(0)} \int_{-\infty}^{\infty} B_1(f_1)\ df_1 \tag{5. 3}$$

and the root mean square deviation is

$$\left\{T_{A1} + T_{S1}\right\} \cdot \left\{2 \int_{-\infty}^{\infty} [\,B_1(f_1)\,]^2\ df_1 \int_{-\infty}^{\infty} b(f)\ df\right\}^{1/2} \tag{5. 4}$$

Inserting the equivalent noise bandwidth

$$B_N = [\int_0^{\infty} [\,B_1(f)\ df]^2 \Big/ \int_0^{\infty} [\,B_1(f]^2\ df \tag{5. 5}$$

and the integration time T_i

$$T_i = b\ (0) \Big/ 2 \cdot \int_0^{\infty} b(f)\ df \tag{5. 6}$$

we obtain the wellknown sensitivity formula of the total power receiver

$$\Delta T_{A1} = \frac{T_{A1} + T_{S1}}{\sqrt{B_N\ T_i}} \tag{5. 7}$$

where the minimum observed change in antenna temperature ΔT_{A1} is defined to be equal to the mean square fluctuation of the observed temperature $T_{A1} + T_{S1}$.

The correlation receiver

The sensitivity of the correlator receiver can be determined in the same way. The signals into the correlator are

$$\sqrt{T_{A1}}\ s_1(t) + \sqrt{T_{S1}}\ n_1(t) \tag{5. 8}$$

and

$$\sqrt{T_{A2}}\ s_2(t) + \sqrt{T_{S2}}\ n_2(t) \tag{5. 9}$$

Here $s_1(t)$ and $s_2(t)$ are correlated and will give a mean value

$$\sqrt{T_{A1}\ T_{A2}}\ \sqrt{b(0)} \int_{-\infty}^{\infty} H_1(f)\ H_2^*\ (f)\ df \tag{5. 10}$$

The rms value is

$$\left\{(2\ T_{A1}\ T_{A2} + T_{A2}\ T_{S1} + T_{A1}\ T_{S2} + T_{S1}\ T_{S2}) \int_{-\infty}^{\infty} B_1\ (f)\ B_2(f)\ df \cdot \int_{-\infty}^{\infty} b(f)\ df\right\}^{1/2} \tag{5. 11}$$

as $n_1(t)$ and $n_2(t)$ are uncorrelated and the low-pass filter is much narrower than the hf-filter.

With

$$B_N = \frac{\left[\int_{-\infty}^{\infty} B_{12}\ (f)\ df\right]^2}{\int_{-\infty}^{\infty} B_{12}^{\ 2}\ (f)\ df} \tag{5. 12}$$

where $B_{12}(f) = H_1(f)\ H_2^*\ (f) = |H_1\ (f)\ |^2$ if the two receivers are identical, the sensitivity formula is

$$\sqrt{\Delta T_{A1} \cdot \Delta T_{A2}} = \frac{[\ 2T_{A1}\ T_{A2} + T_{A2}\ T_{S1} + T_{A1}\ T_{S2} + T_{S1}\ T_{S2}\ ]^{1/2}}{\sqrt{2\ B_N\ T_i}} \tag{5. 13}$$

where T_i is defined by equation (5. 6).

If $T_{A1}\ T_{A2} \ll T_{S1}\ T_{S2}$ we see that the sensitivity of the total power receiver is $\sqrt{2}$ times better than that of the correlator receiver assuming the same antenna aperture. Notice that the signal in this case is spitted into two channels with half the power in each. However, there is no need of receiver zero line subtraction when the correlator receiver is used.

The crosscorrelator interferometer

In the correlator receiver the input signal is splitted into the two channels, which means that $s_1(t) = s_2(t)$. However in the interferometer case there is an unknown phase shift - the fringe phase - between $s_1(t)$ and $s_2(t)$. By phaseshifting one of the signals either 0^o or 90^o two ortogonal components Re R and Im R are obtained (R is the complex correlation function, i. e. the visibility function). The fringe amplitude is $|R| = \sqrt{T_{A1} T_{A2}}$ (as we assumed the radio source to be unresolved) and the fringe phase φ is given by

$$\operatorname{tg} \varphi = \frac{\operatorname{Im} R}{\operatorname{Re} R}$$

The noise fluctuation n_x and n_y of the ortogonal components have Gaussian distributions

$$p(n_x) = \frac{1}{\sqrt{2\pi}\,\sigma}\ e^{-\frac{n_x^2}{2\sigma^2}} \tag{5.14}$$

$$\text{where} \quad \sigma = \frac{[(T_{A1} + T_{S1})(T_{A2} + T_{S2}) + T_{A1}\ T_{A2}]^{1/2}}{\sqrt{2\, B_N T_i}}$$

according to eq. (5.13)

Using a vector representation for the complex visibility function

$$\mathbb{R} = |R| \cos\varphi\, \hat{x} + |R| \sin\varphi\, \hat{y}$$

the total noise vector $\mathbf{n} = n_x\, \hat{x} + n_y\, \hat{y}$ (see figure 5.1) is made up of two vectors, one in the direction of the signal vector $\mathbb{R}$ with approximately Gaussian distribution (zero mean value and rms fluctuation $\sqrt{T_{A1} T_{A2}}/\sqrt{B_N T_i}$) and the other Rayleigh distributed with a completely random phase. The root mean square of the

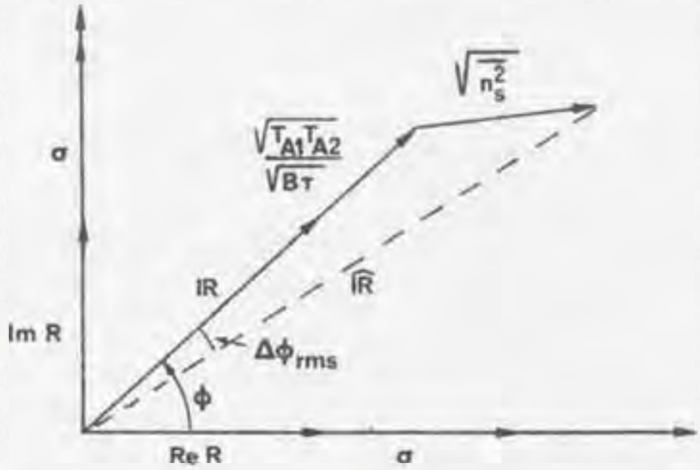

Fig. 5.1 Cross-correlation vector and noise vectors. IR is the estimated cross correlation vector.

amplitude of this vector is

$$\sqrt{\overline{|n_s|^2}} = \frac{[\,T_{S1}\,T_{S2} + T_{A1}T_{S2} + T_{A2}\,T_{S1}\,]^{1/2}}{\sqrt{B_N T_i}} \tag{5.15}$$

For the large signal - to - noise case the rms deviation of the fringe phase is thus

$$\Delta\varphi_{rms} = \frac{[\,T_{S1}\,T_{S2} + T_{A1}\,T_{S2} + T_{A2}\,T_{S1}\,]^{1/2}}{\sqrt{B_N T_i}\cdot\sqrt{T_{A1}\,T_{A2}}} \cdot [\overline{\sin^2\theta}]^{1/2} =$$

$$= \frac{[\,T_{S1}\,T_{S2} + T_{A1}\,T_{S2} + T_{A2}\,T_{S1}\,]^{1/2}}{\sqrt{2\,B_N\,T_i.T_{A1}\,T_{A2}}} \tag{5.16}$$

The rms error in the fringe amplitude $\Delta |R|_{rms}$ is obtained directly from eq. (5.15)

$$\Delta |R|_{rms} = \frac{[(T_{A1} + T_{S1})(T_{A2} + T_{S2})]^{1/2}}{\sqrt{B_N T_i}} \qquad (5.17)$$

For the weak signal case ($T_{A1} T_{A2} \ll T_{S1} T_{S2}$) the rms fluctuation goes up by a factor $\sqrt{2}$ due to the unknown fringe phase. If the one-bit correlation method is used to obtain the fringe amplitude and fringe phase, another factor is added to expressions (5.16) and (5.17) due to the clipping losses. This factor is a function of the filter characteristics and the sampling rate. Compare equation (6.17).

CHAPTER VI

THE ONE-BIT CORRELATION METHOD OF CROSS-SPECTRAL ANALYSIS

The total signals into the correlator is the sum of the antenna signals, $\sqrt{T_{A\frac{1}{2}}}\ s_{\frac{1}{2}}(t)$ plus system noise $\sqrt{T_{S1}}\ n_{\frac{1}{2}}(t)$. We assume that $s_{\frac{1}{2}}(t)$ as well as $n_{\frac{1}{2}}(t)$ are normalized with $\overline{|s_1(t)|^2}$, $\overline{|s_2(t)|^2}$, $\overline{|n_1(t)|^2}$ and $\overline{|n_2(t)|^2}$ equal to 1 and with zero mean values.

The normalized <u>auto-correlation function</u> of the total signal is

$$\rho(\tau) = \frac{T_A}{T_A+T_S}\ \rho_s(\tau) + \frac{T_S}{T_A+T_S}\ \rho_n(\tau) \tag{6.1}$$

as s (t) and n(t) are uncorrelated.

The power spectrum of each signal is therefore the sum of the signal spectrum plus the receiver noise spectrum. In order to determine the desired signal spectrum $T_A(\omega)$ an on-off source measurement must be done to give

$$T_A(\omega) = \frac{(T_A+T_S)\, S_{ON}(\omega) - T_S\, S_{OFF}(\omega)}{S_{OFF}(\omega)} \tag{6.2}$$

In interferometry the correlation method of spectral analysis implies measurement of the cross-correlation function of the total signals from the two receivers

$$\begin{aligned} &\sqrt{T_{A1}}\, s_1(t) + \sqrt{T_{S1}}\, n_1(t) \\ &\sqrt{T_{A2}}\, s_2(t) + \sqrt{T_{S2}}\, n_2(t) \end{aligned} \tag{6.3}$$

As $\overline{n_1 n_2}$, $\overline{s_1 n_1}$, $\overline{s_2 n_2}$, $\overline{s_1 n_2}$ and $\overline{s_2 n_1}$ are equal to zero the cross-correlation function of the total signals is

$$R(\tau) = \frac{\sqrt{T_{A1}\ T_{A2}}}{\sqrt{(T_{A1}+T_{S1})(T_{A2}+T_{S2})}}\ \rho_{12}(\tau) \tag{6.4}$$

where $\rho_{12}(\tau) = \lim\limits_{T\to\infty} \frac{1}{2T} \int\limits_{-T}^{T} v_1(t)\, v_2^*(t-\tau)\, dt$,

and the normalized cross-power spectrum is

$$S(f) = \int\limits_{-\infty}^{\infty} \rho_{12}(\tau)\ e^{-j2\pi f\tau}\ d\tau =$$

$$= \frac{\sqrt{(T_{A1}+T_{S1})(T_{A2}+T_{S2})}}{\sqrt{T_{A1}\ T_{A2}}} \int\limits_{-\infty}^{\infty} R(\tau)\ e^{-j2\pi f\tau}\ d\tau \tag{6.5}$$

It is evident that the spectral function S(f) cannot be measured exactly. The measured quantity is dependent on the time interval of the random signal which is used. It is a sample function of a random process and its statistical average approximates S(f). The root mean square fluctuations are dependent of the necessarily limited integration time [see equation (5.17)] . Furthermore the integration interval in equation (6.5) from minus infinity to plus infinity must be made finite, which means that we get a spectral function with limited frequency resolution Δf.

In practice the correlation function must be sampled, i. e. it can be measured only for $\tau = \pm n \Delta\tau$, where n is an integer between 0 and N-1, and $\Delta\tau = \Delta t$ is the sampling period of the signals. From the Nyquist sampling theorem it follows that Δt should be equal to 1/2 B, where B is the bandwidth of the video signals.

Let us therefore define the cross power spectrum and cross-correlation function

$$S'(f) = \Delta\tau \sum_{n=-\infty}^{\infty} R'(n\Delta\tau)\, w(n\Delta\tau)\, e^{-j2\pi f n \Delta\tau} \tag{6.6}$$

$$R'(n\Delta\tau) = \frac{1}{K} \sum_{k=1}^{K} s_1(k\Delta t)\, s_2(k\Delta t + n\Delta\tau) \tag{6.7}$$

where the integration time $T_1 = K \cdot \Delta t$ and $\Delta t = \Delta\tau$. The function $w(n\Delta\tau)$ in equation (6.6) is samples of a weighting function, $w(\tau)$. The weighting function must be even and have $w(\tau) = 0$ for $\tau \geqslant N\Delta\tau$. It is included in the definition as a convenient method of handling the truncation of the cross-correlation function. $w(\tau)$ determines the frequency resolution. The true power spectrum S(f) obtained from a correlation function defined in an infinite number of points from $\tau = -\infty$ to $\tau = \infty$ will be convoluted by the Fourier transform of $w(\tau)$, $[= W(f)]$, the smoothing function

$$S'(f) = \int_{-\infty}^{\infty} S(x)\, W(x-f)\, dx \tag{6.8}$$

The choice of $w(n\Delta\tau)$ is usually a compromise between obtaining individual equivalent filter bandpass with narrow main lobe and high spurious lobes or broadened main lobe and low spurious lobes.

The equivalent noise bandwidth B_N is given by the relation

$$B_N = \frac{\left[\int_{-\infty}^{\infty} W(f)\, df\right]^2}{\int_{-\infty}^{\infty} W^2(f) df} = \frac{w(0)^2}{\int_{-\infty}^{\infty} w^2(\tau)\, d\tau} = \frac{1}{\int_{-\infty}^{\infty} w^2(\tau)\, d\tau} \tag{6.9}$$

The problem of choosing the optimum weighting function is well known in antenna theory and optics. It is beyond the scope of this report to discuss it. In radio astronomy the uniform weighting function

$$\begin{aligned} w(n\Delta\tau) &= 1 \qquad |n| < N \\ w(n\Delta\tau) &= 0 \qquad |n| \geqslant N \end{aligned} \tag{6.10}$$

or the cosine weighting function (Hanning weighting function)

$$w(n\Delta\tau) = 0.5 + 0.5 \cos \frac{\pi n}{N} \quad |n| < N$$

$$w(n\Delta\tau) = 0 \quad |n| \geq N \qquad (6.11)$$

are commonly used [Weinreb, 1963].

The uniform weighting function [equation (6.10)] gives a corresponding filter transfer function, the smoothing function,

$$W_{uniform}(f) = \left| \frac{\sin 2\pi f \frac{N}{f_s}}{2\pi f \frac{N}{f_s}} \right|, \qquad (6.12)$$

where $f_s = \frac{1}{\Delta t}$ is the sampling rate and N is half the number of points in the cross-correlation function. The 3 dB-bandwidth is $0.604 \frac{f_s}{N}$ and the equivalent noise bandwidth is $B_N = f_s/2N$. The highest spurious sidelobe is 0.22 times the main lobe.

The cosine weighting function [equation (5.28)] has an equivalent filter bandpass equal to

$$W_{cosine}(f) = \frac{1}{2} W_{uniform}(f) + \frac{1}{4} \left[W_{uniform}\left(f + \frac{f_s}{2N}\right) + W_{uniform}\left(f - \frac{f_s}{2N}\right) \right] \qquad (6.13)$$

The half power bandwidth is f_s/N and the equivalent noise bandwidth is $4 f_s/3N$. The highest spurious sidelobe is 0.025 times the main lobe. The cosine weighting will give about the same frequency resolution if $N_{cosine} = 1.65 N_{uniform}$. The signal noise ratio is then 1.27 times higher with the cosine weighting. On the other hand, with a limited and constant number of delay channels $N_{uniform} = N_{cosine} = N$, the spectrum can be unresolved with the cosine weighting. Then the uniform weighting will be preferable. Figure 6.1 shows the equivalent filter curve for uniform and cosine weighting functions.

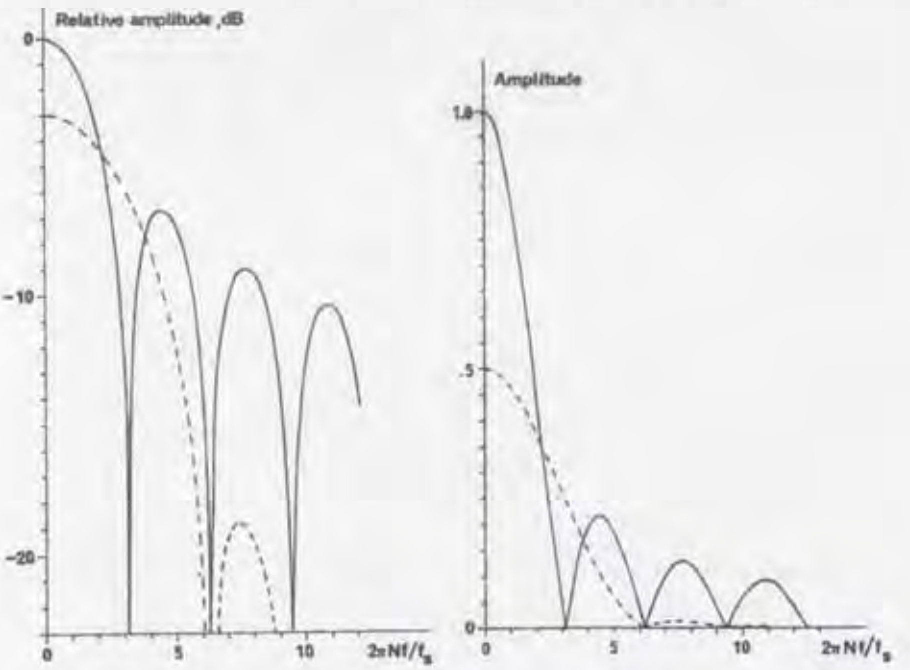

Fig. 6.1 The equivalent filter curves for uniform (solid lines) and cosine (dashed lines) weighting of the correlation function drawn with logarithmic and linear amplitude scale.

The one-bit correlation method of spectral analysis.

The one-bit correlation method to obtain the spectrum of a Gaussian signal has become a common technique in astrophysical work. It was first used in 1961 by Goldstein [1961] to study radar echoes from Venus, and in 1963 by Weinreb [1963] in searching for new spectral lines. The technique is built upon the well-known theorem by Van Vleck [1966], which says that the true normalized correlation function of a Gaussian signal can be obtain from the correlation function of the corresponding infinitely clipped signal, the amplitude of which is defined by one bit. It is accordingly possible to obtain the true frequency spectrum from the correlation function of the digitized signal. An excellent description of the method has been given by Weinreb [1963].

The data processing of "very long baseline" interferometry between the United States and Sweden uses the one-bit correlation method to obtain the cross-spectral function. The method is consequently not new as the Van Vleck theorem easily can be generalized to the cross-correlation case. However, in VLBI all data reduction is performed by a general purpose computer, which implies that a very flexible system is obtained without any hard-ware constructions. It should be mentioned, however, that a hard-ware correlator is much faster than normal general purpose computers (for example the IBM 360/65).

Figure 6.2 illustrates the signal recording at one of the stations and the data processing. The signal s_1 (t) and s_2(t) are infinitely amplified, clipped, sampled

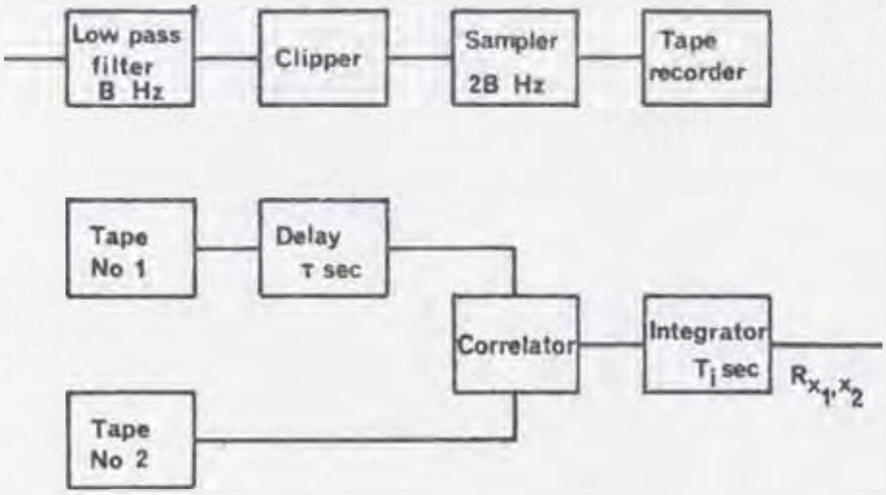

Figure 6.2 The signal recording and data processing in very long baseline interferometry.

(sampling period Δt) and recorded digitally on tapes. These digital signals are then read and one of the signals x_1 (t) and x_2 (t) is delayed τ seconds. A product is formed followed by a finite time integration of length T_i seconds. The output can be written as follows

$$R_{x_1,x_2}(n\,\Delta\tau) = \frac{1}{N}\sum_{k=1}^{N} x_1(k\Delta t)\cdot x_2(k\Delta t + n\Delta\tau) \tag{6.14}$$

where

$$x_{\frac{1}{2}} = \begin{cases} +1 \text{ if } s_{\frac{1}{2}}(t) > 0 \\ -1 \text{ if } s_{\frac{1}{2}}(t) < 0 \end{cases}$$

Δt = sampling period

$\Delta\tau$ = correlation interval variable

Equation (6.14) is the cross correlation function of the infinite clipped signals. Using the theorem by Van Vleck [1966], this function is related to the normalized cross correlation function of the unclipped signals s_1(t) and s_2(t)

$$\rho_{s_1,s_2}(n\,\Delta\tau) = \sin\left[\frac{\pi}{2}\,\rho_{x_1,x_2}(n\,\Delta\tau)\right] \tag{6.15}$$

This is true only for certain classes of functions of which the Gaussian random process is the one of interest here.

The real cross-correlation function ρ_{s_1, s_2} $(n \Delta \tau)$ is a function of time according to equation (4.9). After phase detection and integration we can form a complex correlation function ρ_c $(n \Delta \tau)$ [compare equation (4.10)]. As the signals are sampled the complex correlation function ρ_c $(n \Delta \tau)$ can be seen as a continuous function ρ_c (τ) multiplied by a train of delta functions to characterize the sampling process. The complex power spectrum S_c (f) is then the Fourier transform

$$S_c(f) = \int_{-\infty}^{\infty} \sum_{n=-\infty}^{\infty} \delta(\tau - n\Delta\tau)\, \rho_c(\tau)\, e^{-j2\pi f\tau} d\tau =$$

$$= \sum_{n=-N}^{N} \rho_c(n\Delta\tau) \cos(2\pi f n \Delta\tau) -$$

$$-j \sum_{n=-N}^{N} \rho_c(n\Delta\tau) \sin(2\pi f n \Delta\tau) \qquad (6.16)$$

where 2 N is the number of points in the cross-correlation function. The power spectrum is accordingly periodic with the period equal to the sampling rate. It is therefore essential that the filters have as sharp sides as possible in order to get the total spectrum from 0 to $1/2 \Delta\tau$ usable.

Clipping losses assuming a rectangular power spectrum

It is well-known that in the non-clipped case a higher sampling rate than the Nyqvist sampling rate of 2 B, where B is the signal bandwidth, cannot improve the spectral estimate. However, in the clipped (one-bit) case a higher sampling rate does decrease the spectral variance. This is evident as the power spectrum of the signal — originally with bandwidth equal to B — will be spread out due to the clipping.

The spectrum after clipping can be written

$$S(f) = \int_{-\infty}^{\infty} \frac{2}{\pi} \sin^{-1} \left[\frac{\sin 2\pi B\tau}{2\pi B\tau} \right] e^{-j2\pi f\tau} \, d\tau \qquad (6.17)$$

if a rectangular input spectrum is assumed. S(f) has been tabulated by Van Vleck and Middleton (1966).

Assuming a rectangular spectrum sampled at the Nyquist rate and using equation (5.17) the rms error in the measured fringe amplitude will be

$$\Delta R_{rms} = \frac{\pi}{2} \frac{[(T_{A1} + T_{S1})(T_{A2} + T_{S2})]^{1/2}}{\sqrt{B_N T_i}} \qquad (f_s = 2B) \tag{6.18}$$

where the factor $\pi/2$ is due to the clipping losses. This factor has been calculated by Goldstein [1962] and others.

Generally the factor due to clipping losses can be written [Rodemich (1966)]

$$\frac{\pi}{2} \left[B \int_{-B}^{B} S_s^{\,2}(f)\, df\right]^{1/2} \tag{6.19}$$

where $S_s(f)$ is the spectrum of the clipped and sampled signal. With $f_s = 2B$ equation (6.19) equals $\pi/2$, which is the factor in equation (6.18). With $f_s = \infty$ we obtain

$$\frac{\pi}{2} \left[B \int_{-B}^{B} S_s^{\,2}(f)\, df\right]^{1/2} = \frac{\pi}{2} \left[B \int_{-B}^{B} S^2(f)\, df\right]^{1/2} \approx 1.25 \tag{6.20}$$

as

$S_s(f) = S(f)$ if $f_s = \infty$

Figure 6.2 shows the decrease in clipping losses [equation (6.19)] as a function of the sampling rate for a rectangular spectrum. From figure 6.2 we notice that very little improvement is obtained by increasing the sampling rate above 4B. Moreover the spectral resolution will go down by the same factor if the sampling rate is increased,as the correlator normally gives a limited number of points in the correlation function.

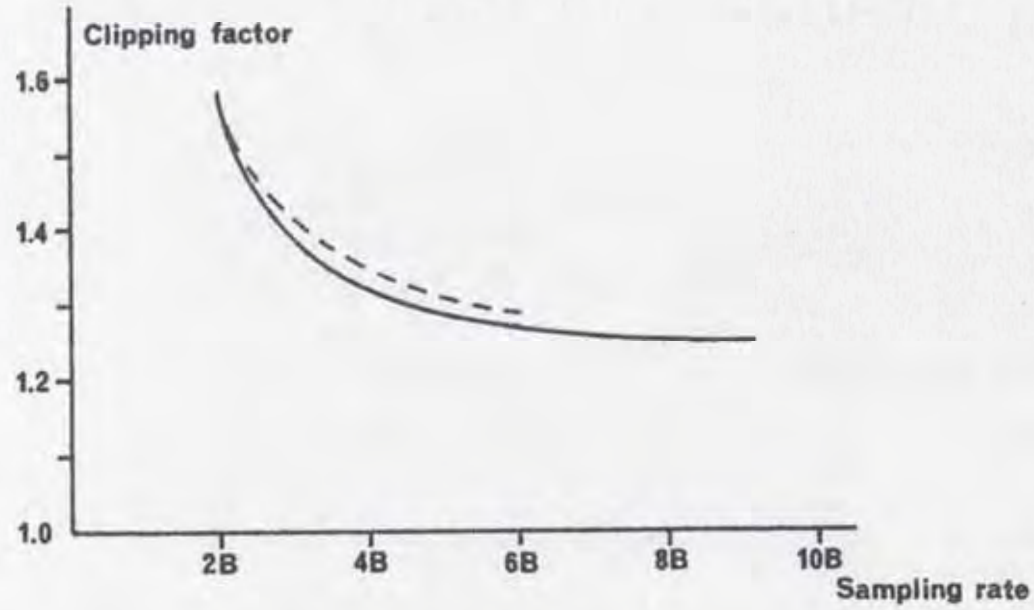

Figure 6.2. Showing the decrease in rms fluctuations with increasing sampling rate. The input signal has a rectangular power spectrum and is spectrum analysed by means of the one-bit correlation techniques. The solid curve is computed from equation (6.19) and the dashed curve is from Burns and Yao [1969].

CHAPTER VII

THE ANGULAR RESOLUTION OF LONG BASELINE INTERFEROMETERS

The angular resolution of a two element interferometer is normally defined from the interferometer fringe pattern

$$F(\theta) = \cos\left[2\pi \frac{D}{\lambda} (\xi - \xi_o)\right] = \cos\left[2\pi \frac{D}{\lambda} (\sin\theta - \sin\theta_o)\right] \tag{7.1}$$

The fringe pattern is zero along small circles on the celestial sphere where the path difference of the signal is an odd number of half-wavelengths, i. e. where

$$(\sin\theta - \sin\theta_o)\, D = n \cdot \frac{\lambda}{2} \qquad n = 1,\ 3,\ 5,\ \ldots \tag{7.2}$$

Referring the ξ-direction to the ξ_o - direction we can write

$$\xi - \xi_o = \sin\theta' - \sin\theta_o \approx \Delta\theta \cos\theta_o \tag{7.3}$$

if $\xi - \xi_o \ll 1$.

The fringe spacing is accordingly $\lambda/D\cos\theta_o$ radians and the minimum fringe spacing is λ/D radian. This is also the first zero of the visibility versus angular size of a source with a onedimensional uniform brightness distribution.

The relations between $\sin\theta_o$ and the hour angle and declination of the baseline and the source are given by equation (2. 2)

$$\sin\theta_o = \sin\delta_b \sin\delta_s + \cos\delta_b \cos\delta_s \cos(h_b - H_s) \tag{7.4}$$

A source with position $\alpha_s + \Delta\alpha_s$, $\delta_s + \Delta\delta_s$ will give a fringe phase (referred to the direction ξ_o)

$$2\pi\,\Delta\xi\,\frac{D}{\lambda} = \frac{2\pi D}{\lambda}\left[-\frac{\partial(\sin\theta)}{\partial H_s}\,\Delta\alpha_s + \frac{\partial(\sin\theta)}{\partial\delta_s}\,\Delta\delta_s\right] =$$

$$= 2\pi\left[u\,x + v\,y\right] \tag{7.5}$$

where from equation (7.4)

$$u = \frac{D}{\lambda}\left[\cos\delta_b\ \sin(H_s - h_b)\right] \tag{7.6}$$

$$v = \frac{D}{\lambda}\left[\sin\delta_b\ \cos\delta_s - \cos\delta_b\sin\delta_s\ \cos(h_b - H_s)\right] \tag{7.7}$$

$$x = \cos\delta_s\ \Delta\alpha_s \tag{7.8}$$

$$y = \Delta\delta_s \tag{7.9}$$

u and v are the spatial frequency components of the system or the components of the projected baseline on the celestial sphere in the direction of the source. Compare equation (3.18).

The projected baseline vector $u\hat{x} + v\hat{y}$ describes an ellipse as the earth rotates. The center of the ellipse is at $(0, \frac{D}{\lambda}\sin\delta_b\cos\delta_s)$, and the ellipticity is equal to $1/\sin\delta_s$. Figure 7.1 shows the projected baseline ellipse for the OH-sources W49 ($RA_{1950.0} = 19^h7^m49.6^s$, $\delta_{1950.0} = 9^o.020$) and W3 ($RA_{1950.0} = 2^h23^m16.8^s$, $\delta_{1950.0} = 61^o.648$) and the Onsala Space Observatory to Haystack Microwave Facility baseline.

As the fringe visibility only defines the brightness distribution if it is known over the whole spatial frequency plane, it is clear that one observation needs an assumption of the source shape to give the source width. By expanding the one-dimensional fringe visibility $\gamma(u)$ in a Taylor series about the origin

$$\gamma(u) = \gamma(o) + \left(\frac{\partial\gamma}{\partial u}\right)_o u + \left(\frac{\partial^2\gamma}{\partial u^2}\right)_o u^2 + \dots$$

$$= \frac{1}{\int T_B(\xi)\,d\xi}\left[\int T_B(\xi)\,d\xi + u\int\xi\,T_B(\xi)\,d\xi + u^2\int\xi^2\,T_B(\xi)\,d\xi + \dots\right] \tag{7.10}$$

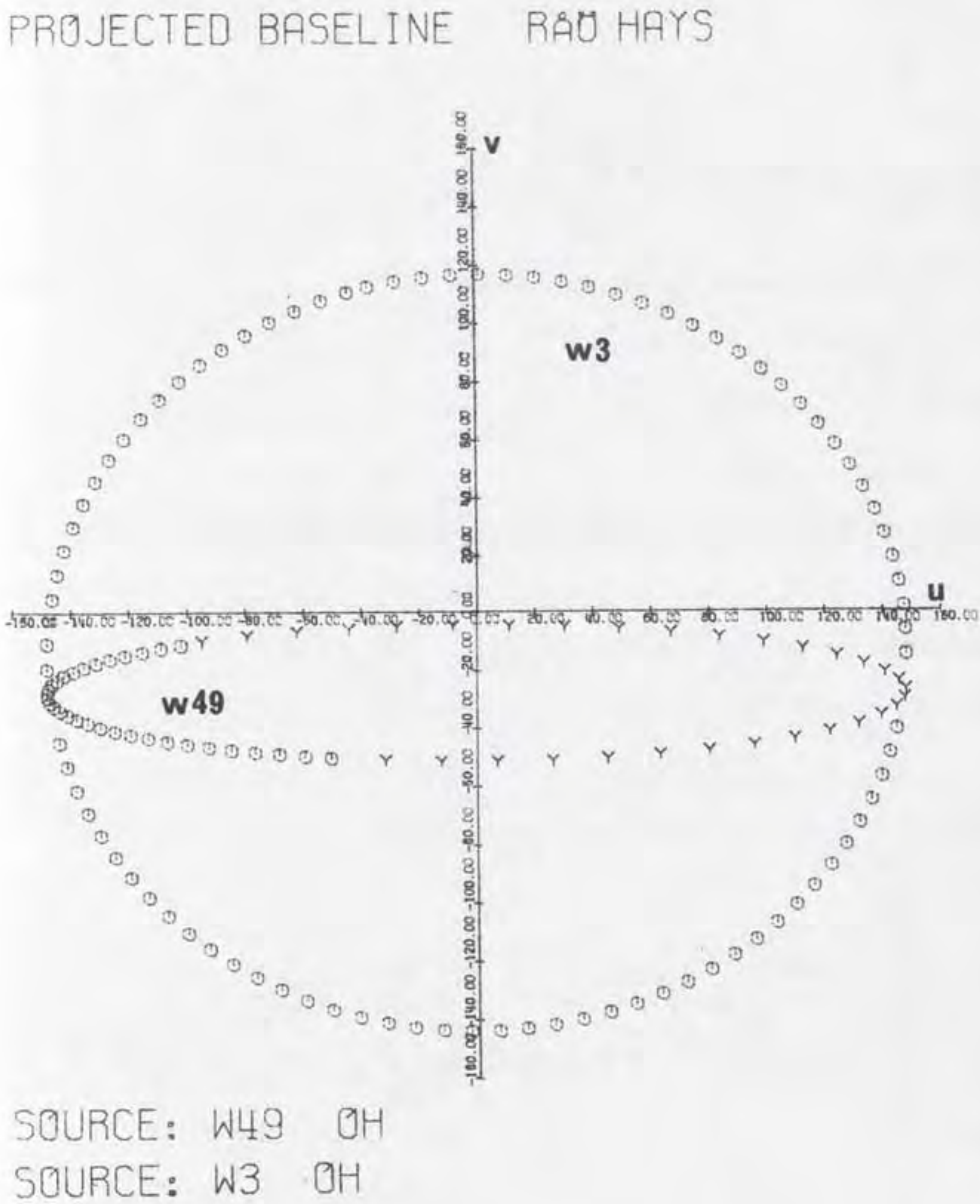

Fig. 7.1 The projected baseline ellipses for the OH radio sources W 3 and W 49 and the Onsala to Haystack baseline. u and v are in cycles/arc. sec.

we notice that only the first two series coefficients can be determined from one measurement of a radio source.

In the case of two fixed antennas the interferometer response $\gamma(u, v)$ can be determined along the ellipse given by equations (7. 6) and (7. 7) on the assumption that the source is circumpolar at both stations. Bracewell's "principal solution" [Bracewell (1958] of the brightness distribution $T_B(x, y)$ is obtained by putting $\gamma(u, v) = 0$ for all values of u and v except where we know $\gamma(u, v)$, i. e.

$$\Gamma_B(x, y) = \frac{T_B(x, y)}{\int_{-\infty}^{\infty}\int_{\infty}^{\infty} T_B(x,y)\, dx\, dy} =$$

$$= \int_{-\infty}^{\infty}\int_{-\infty}^{\infty} \gamma(u, v)\, e^{j 2\pi (xu + yv)}\, du\, dv =$$

$$= \mathrm{Re}\left\{ \int_0^{2\pi} \frac{\gamma(\Phi)\, e^{j2\pi (a x \sin\Phi + by - cy \cos\Phi}\, w(\Phi)\, d\Phi +}{\int_0^{2\pi} \gamma(\Phi)\, w(\Phi)\, d\Phi} \right\} \tag{7.11}$$

as $\gamma(u, v) = \gamma(-u, -v)$

Here we have introduced

$$w^2(\Phi) = u^2 + v^2$$

and

$$a = \frac{D}{\lambda} \cos\delta_b$$

$$b = \frac{D}{\lambda} \sin\delta_b \sin\delta_s$$

$$c = \frac{D}{\lambda} \cos\delta_b \sin\delta_s$$

With elliptical coordinates (r,φ), where

$$ax = r\cos\varphi$$

$$cy = r\sin\varphi$$

$$\Gamma_B(r, \varphi) = 2 \operatorname{Re} \left\{ e^{j2\pi by} \frac{\int_0^{2\pi} \gamma(\Phi)\, e^{j2\pi r \sin(\varphi - \Phi)}\, w(\Phi)\, d\Phi}{\int_0^{2\pi} \gamma(\Phi)\; w(\Phi)\, d\Phi} \right\} \tag{7.12}$$

With $\gamma(\Phi) \cdot w(\Phi) = 1$ we obtain

$$\Gamma_B(r) = 2 \cos(2\pi by)\, J_o(2\pi r)$$

$\Gamma_B(r)$ has a width of $1.52/2\pi$ in the east-west direction.

The most common models used to fit a visibility curve with only a few known points are the one-dimensional uniform source, the uniform disk model or the two-dimensional Gaussian source. If the spatial frequency component u_{3dB} or w_{3dB} has a visibility equal to 0.5, the widths of the different sources are

$$\frac{1.9}{\pi u_{3dB}}, \qquad \frac{2.2}{\pi w_{3dB}} \quad \text{and} \quad \frac{2 \ln 2}{\pi w_{3dB}} \quad \text{respectively.}$$

These values can easily be obtained from table 3.1.

Time delay and fringe rate mapping.

It is often convenient in very long baseline interferometry to define the resolution from the measurement of the time delay offset $\Delta\tau_g$ and fringe rate offset Δf_f between two radio sources.

Let us define the delay resolution function as the magnitude of the complex cross-correlation function

$$|\rho(\tau)| = \left| \int_0^{\infty} S(f+f_o)\, e^{j2\pi f(\tau + \Delta\tau_g)}\, df \right|$$

where $\Delta\tau_g = \frac{D}{c} \cos\theta_o \;\; \Delta\theta$

Assuming a rectangular frequency spectrum

$$S(f+f_o) = \begin{cases} 1/B & 0 < f < B \\ 0 & f > B \end{cases}$$

the delay resolution function becomes

$$|\rho(\tau)| = \left| \frac{\sin[\pi B(\tau + \Delta\tau_g)]}{\pi B(\tau + \Delta\tau_g)} \right| \qquad (7.13)$$

according to equation (4.9) with $\Delta\tau_g = \tau_g + \tau_i$. If the two sources can be separated in the frequency plane, i.e. if they are spectral line sources emitting at different not overlapping frequencies, or separated by the single antenna beam the delay resolution function can be used to define the resolution on the sky.

Then the resolution in the direction of the projected baseline on the sky (the maximum resolution) is equal to

$$\Delta\theta_T = C_T \; \frac{c}{B \cdot D \cos\theta_o} \tag{7.14}$$

i.e. inversely proportional to the relative bandwidth B/f_o and the projected baseline measured in wavelengths.

$$\Delta\theta_T = C_T \; \frac{1}{\frac{B}{f_o}\sqrt{u^2+v^2}} \tag{7.15}$$

where u and v are given by equations (7.6) and (7.7). C_T is a constant, the value of which is a function of the S/N ratio.

The projected baseline direction is given by the vector

$$w = u\,\hat{x} + v\hat{y} = \frac{D}{\lambda}\Big\{\cos\delta_b \;\sin(H_s - h_b)\,\hat{x} + [\sin\delta_b \cos\delta_s - \cos\delta_b \;\sin\delta_s \;\cos(h_b - H_s)]\;\hat{y}\Big\} \tag{7.16}$$

Perpendicular to this direction we get no information about the angular separation. In most cases it is , however, possible to use the fringe frequency for this measurement. The fringe frequency f_f is given by equation (2. 3). Two sources separated ΔH_s and $\Delta\delta_s$ in hour angle and declination give rise to a fringe frequency offset Δf_f equal to

$$\Delta f_f = \frac{D}{\lambda_o}\;\Omega\cos\delta_b\,[\sin\delta_s \sin(H_s - h_b)\,\Delta\delta_s - \cos\delta_s \;\cos(H_s - h_b)\;\Delta H_s] \tag{7.17}$$

A fringe frequency offset will cause a time variation in the complex cross-correlation function

$$\rho(t) = \rho_o \, e^{j\Delta \omega_f t} \tag{7.18}$$

according to equation (4. 6)

If we integrate over T_i seconds the fringe visibility will decrease by a factor

$$\left| \frac{\sin \left(\Delta \omega_f \cdot \frac{T_i}{2}\right)}{\Delta \omega_f \cdot \frac{T_i}{2}} \right| \tag{7.19}$$

The resolution in fringe frequency is then given by

$$\Delta f_f = C_f \cdot \frac{1}{T_i} \tag{7.20}$$

The maximum angular resolution is obtained in a direction perpendicular to the constant fringe frequency lines on the sky, i. e. in the direction of the vector

$$\mathrm{f} = \frac{D}{\lambda} \left\{ \cos \delta_b \cos(H_s - h_b)\, \hat{x} + \cos \delta_b \sin \delta_s \sin (H_s - h_b)\, \hat{y} \right\} \tag{7.21}$$

We see from eq. (7. 16) that

$$\mathrm{w} (H_s + 6^h) = \mathrm{f} (H_s) + \frac{D}{\lambda} \sin \delta_b \cos \delta_s \, \hat{y}$$

which means that for an east-west baseline the time delay mapping and fringe rate mapping give the angular separation in two ortogonal directions. If we define

$$f_x = \frac{D}{\lambda} \cos \delta_b \cos (H_s - h_b) \tag{7.22}$$

$$f_y = \frac{D}{\lambda} \cos \delta_b \sin \delta_s \sin (H_s - h_b) \tag{7.23}$$

the angular resolution on the sky becomes

$$\Delta\theta_{f_f} = C_f \frac{1}{\Omega T_i \sqrt{f_x^2 + f_y^2}} \tag{7.24}$$

It is interesting to compare the two methods. They give the same accuracy if

$$\Omega T_i = B/f_o \tag{7.25}$$

The Mark I VLBI terminal allows a total integration time of about 180 seconds (the limitation is due both to the tape recorder and the phase stability of the rubidium standard) and a recordable bandwidth of maximum 360 kHz, which means that the fringe rate mapping is a factor of about ten better than the time delay mapping at 6 cm wavelength. In spectral line interferometry of OH-sources the line width is as small as a few kHz, which in this case means that the time delay mapping is unusable (Rönnäng, Rydbeck and Moran, 1970).

The technical improvement of the VLBI systems, which is now under way, will make the two methods more comparable as long as the two sources radiate over a frequency band broader than 2 MHz. The fringe rate resolution can be improved by improving the phase stability of the LO-systems. By using a hydrogen maser frequency standard the integration time T_i can be as long as about 1 hour at a wavelength of 6 cm. This gives a maximum angular resolution

$$\Delta\theta_{f\,min} = C_f \frac{2\pi}{\Omega T_i \frac{D}{\lambda}} \approx C_f \frac{\lambda}{D} \cdot 3.8 \quad \text{radians} \tag{7.26}$$

However, a larger effective bandwidth can be synthesized by recording short time sequences with different local oscillator frequencies. The Onsala traveling wave maser receiver system at 6 cm wavelength is tunable over a frequency range of about 650 MHz (Kollberg, 1970). If a bandwidth of let us say a few hundred MHz can be synthesized, the time delay and fringe rate mapping will again be comparable.

Synthesizing of large bandwidth to get high time delay resolution.

The optimum method to synthesize a large frequency band is equivalent to the problem of spacing the antennas in an interferometer system to get the best antenna pattern. The number of frequency windows and the spacing between them determines the delay resolution function. The acceptable sidelobe level is due to the signal to noise ratio as it must be possible to separate the sidelobes from the narrow main lobe.

The cross-correlation function is given by equation (4.10)

$$\rho_c(\tau) = \int_0^\infty S_o(f + f_o)\, e^{j 2\pi (f + f_o) \Delta \tau_g}\, e^{-j(\varphi_1 - \varphi_2)}\, e^{j 2\pi f \tau}\, df \tag{4.10}$$

from which we see that the fringe phase will vary linearly with frequency over the actual frequency band, if the time delay offset $\Delta\tau_g$ differs from zero. If one measures the fringe phase versus frequency the time delay offset can be determined. With a rectangular frequency band of width B the rms error of the measured fringe phase is given by equa‿‿n (5.16)

$$\Delta\varphi_{rms} = \frac{1}{\sqrt{2}\ S/N} \tag{7.27}$$

where

$$S = \sqrt{T_{A1} \cdot T_{A2}} \tag{7.28}$$

and

$$N = \frac{\pi}{2}\ \frac{[T_{S1}T_{S2} + T_{A1}T_{S2} + T_{A2}T_{S1}]^{1/2}}{\sqrt{B\,T_i}} \tag{7.29}$$

If the fringe phase is determined at two independent points on the frequency band the equivalent noise bandwidth is $B_N = \frac{B}{2}$ and the time uelay offset can be determined to within

$$\Delta\tau_1 = \pm\ \frac{2\ \Delta\varphi_{rms}}{\pi B} = \pm\ \frac{2\sqrt{2}}{\omega_B \cdot S/N} \tag{7.30}$$

where $\omega_B = 2\pi B$

The delay resolution function is then

$$|\rho_c(\tau)| = \left| \frac{\sin(\omega_B \Delta\tau/2)}{\omega_B \Delta\tau/2} \right| \qquad (7.31)$$

with the first zeros at $\Delta\tau_1 = \pm 1/B$. Let us now add another frequency window covering the frequency band from $\omega_0 + \omega_2$ to $\omega_0 + \omega_2 + \omega_B$ and try to determine the maximum value of ω_2. The maximum value is given by (say)

$$\omega_2 \, \Delta\tau_1 = 1 < \pi \qquad (7.32)$$

in order to eliminate the 2π ambiguity in the measured fringe phase in frequency window number 2.

The accuracy of the measured time delay offset is then

$$\Delta\tau_2 = \pm \frac{1}{\omega_2 \cdot S/N} = \pm \frac{2\sqrt{2}}{\omega_B \, (S/N)^2}$$

with

$$\omega_2 = \frac{\omega_B \, (S/N)}{2\sqrt{2}}$$

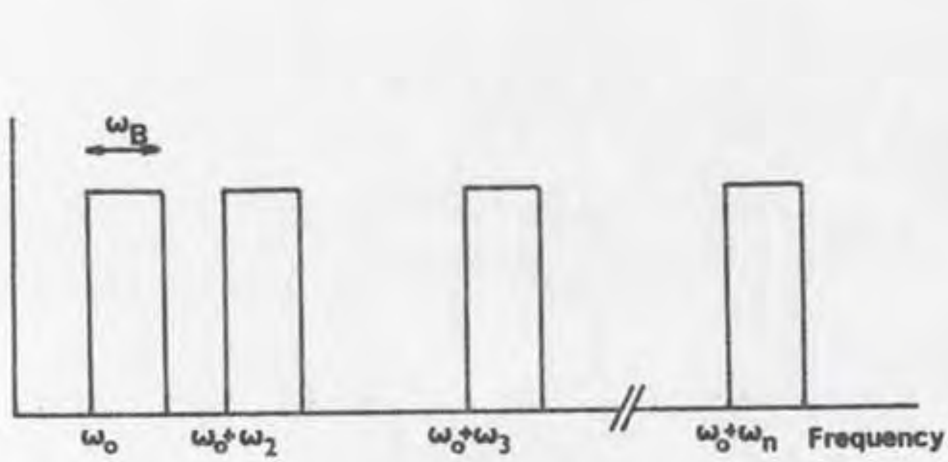

Fig. 7.2 Frequency windows to synthesize a large frequency band.

In the same way the local oscillator frequency of the next window (compare figure 7.2) will be at $\omega_o + \omega_3$ where

$$\omega_3 = \omega_B \, (S/N)^2 / 2\sqrt{2} \tag{7.33}$$

and generally for the n:th window

$$\omega_n = \omega_B \; 2^{-3/2} \; (S/N)^{n-1} \tag{7.34}$$

and

$$\Delta\tau_n = \pm \frac{2\sqrt{2}}{\omega_B \; (S/N)^n} = \pm \frac{1}{2\pi B_E S/N} \approx \pm \frac{1}{2\pi B_E} \left[\frac{T_{S1} \, T_{S2}}{T_{A1} \, T_{A2} B T_i} \right]^{1/2} \tag{7.35}$$

where $B_E = \frac{\omega_n}{2\pi}$

The delay resolution function is then

$$|\rho_c(\Delta\tau)| = \left| \frac{\sin(\pi B \Delta\tau)}{\pi B \Delta\tau} \right| \; \left| 1 + e^{-j \, \omega_2 \Delta\tau} + e^{-j \, \omega_3 \Delta\tau} + \ldots \right| \tag{7.36}$$

It ought to be pointed out that the above derivation of the optimum spacing of the frequency windows is approximative and not mathematically stringent. Rogers (1970) proposes that the frequency windows should be spaced in a sequence that is like a geometric progression and that contains as many different spacings as possible.

Figure 7.3 shows the delay resolution function for five windows spaced at 0, 1, $2\sqrt{2}$, 8 and $16\sqrt{2}$ times the video bandwidth B.

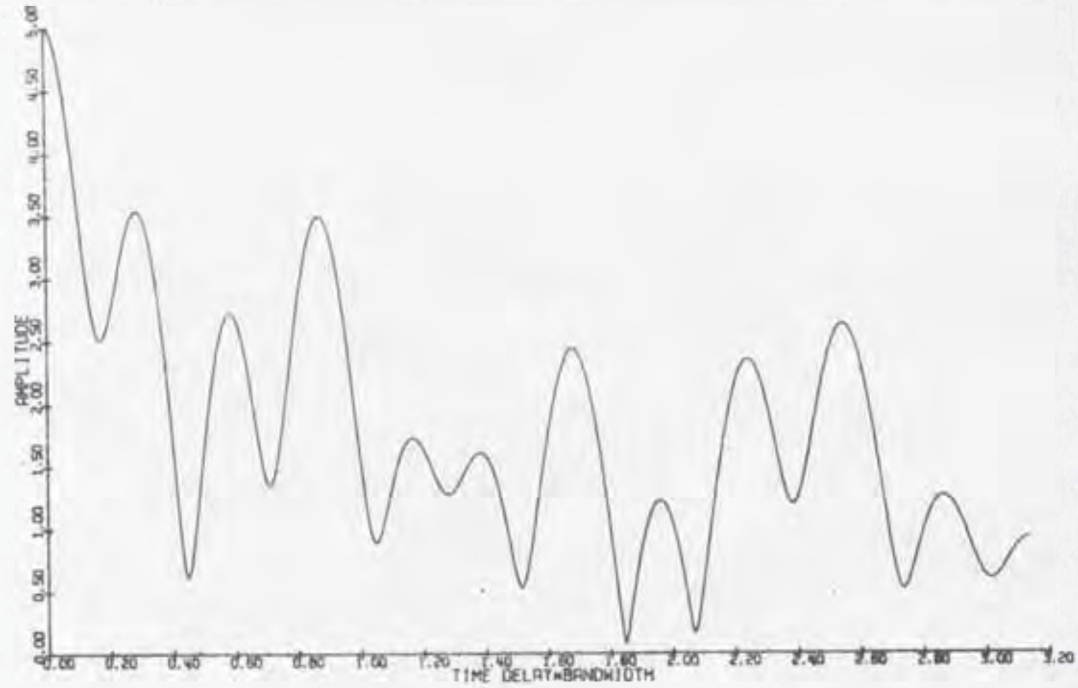

Figure 7.3 The delay resolution function obtained by frequency switching the local oscillator between f_o, $f_o + B$, $f_o + 2\sqrt{2}\,B$, $f_o + 8\,B$, and $f_o + 16\sqrt{2}\,B$ to get an equivalent total bandwidth of $16\sqrt{2}\,B$.

CHAPTER VIII

THE VLBI RECEIVER SYSTEM

The very long baseline interferometry experiments between Onsala Space Observatory and observatories in the United States have so far been carried out at the wavelengths 18 cm, 6 cm, and 5 cm. The Onsala Observatory is equipped with traveling wave masers covering these wavelengths. The masers have a net gain of typically 30 dB and gave a system noise temperature of about 40 ^{o}K* at the longest wavelength and about 55 ^{o}K at the two shorter wavelengths [Rydbeck et al (196
The masers are tunable over about 15 % of their center frequencies.

The polarized feed consists of a horn with a quarter wave section, which produces either right or left circular polarization. The observed polarization can be changed manually within a few seconds.

The upper or lower sidebands of the amplified signal are converted to 30 MHz I F and then to the video range in a single sideband video converter (compare fig. 8.1)

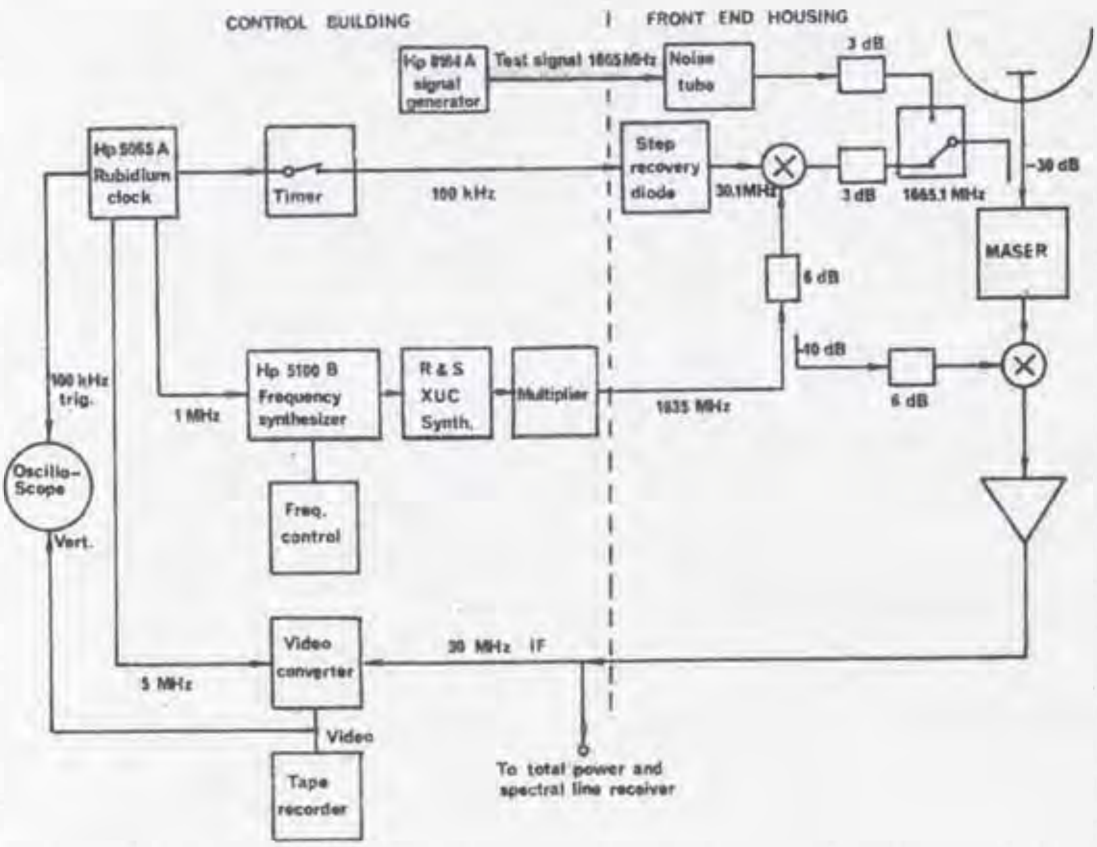

Figure 8.1 The VLBI receiver system at the Onsala Space Observatory.

---

*) This noise temperature is now (1971) lowered to about 27 ^{o}K.

Care must be taken that the same sideband is recorded at both observatories during a run. If a spectral line is recorded the spectrum is displayed at the same time by means of a multichannel receiver. The signal is then split at the 30 MHz level, and the system is frequency switched by means of a second local oscillator at 24$\pm$ B/2 MHz, $\pm$ depending on the used sideband. The total power is also monitored by means of an analog recorder. In order to test the phase stability of the receiver and to measure the relative phase of the LO signals at different frequencies a reference signal of frequency $f_{lo} \pm 30 \pm$ B/2 MHz can be injected in the receiver horn. The front end also contains a noise tube for calibration purposes.

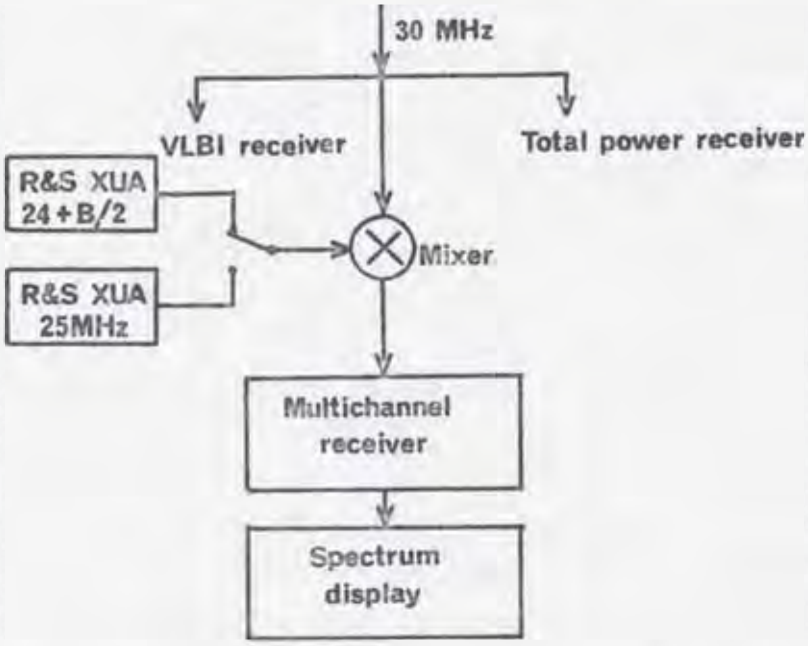

Figure 8.2 The Onsala multichannel receiver used to monitor the recorded spectral line during a VLBI run.

Local oscillator chain

As mentioned earlier the success of a VLBI experiment depends on the ability to maintain phase coherence between the local oscillator at each site. The root mean square of the relative phase fluctuation must be much less than π.

The local oscillator system at Onsala is shown in figure 8.3. The phase stable reference signal is derived from a Hp 5065 A rubidium standard, the frequency of which was ajusted to the UTC time scale before each experiment.

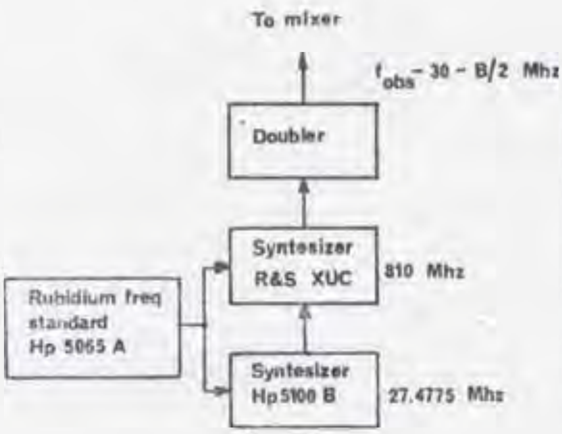

Fig. 8.3 The local oscillator chain. The numbers are to get the frequency 1665 MHz at the center of the recorded video band.

The 1 MHz signal from the standard is used as input reference to a Hp 5100 B frequency synthesizer. The output signal from this unit, in the frequency range 0 - 49.9999999 MHz is then synthesized by a Rodhe & Schwartz XUC, which gives an output signal

$$f_{XUC} + (f_{Hp\ 5100\ B} - 20)\ \text{MHz}$$

where $f_{Hp\ 5100\ B}$ must be in the frequency range from 20 MHz to 30 MHz and f_{XUC} can be varied from 470 MHz to 1000 MHz.

The output signal from the XUC is then multiplied by commersial multipliers up to the actual local oscillator frequency f_o. This system was tested before the experiment by comparing it's phase stability with another system of comparable quality.

The local oscillator frequency can be changed very rapidly to precalculated frequencie by means of a remote control unit to the Hp 5100 B synthesizer. The LO signal phase will not change if one steps in frequency as long as the 10 kHz to 0.01 Hz decades are not changed. The phase φ at a given local oscillator frequency must be reproducable for example when a large bandwidth is synthesized by switching the LO frequency (compare chapter VII).

The LO frequency can be referred to either of the two time scale: Universal time C or Atomic time. The UTC time scale, which approximate UT_2, gives a slightly longer time interval — second — than the atomic time. The frequency offset $1\ Hz_{UTC} - 1\ Hz_{A1}$ is fixed each year by the Bureau International de l'Heur. The offset is now $- 300 \times 10^{-10}$ Hz. Normally all radio observatories have their frequency standards referred to UTC. However, if the reference frequency at one of the stations is adjusted to the atomic time scale this can easily be taken into account by offsetting one of the LO frequencies. At 1665 MHz this offset is about 50 Hz.

Timing

Before a VLBI experiment the rubidium clock at Onsala is set to UTC by comparison with the cesium standards at "Sektionen för mätteknik och normaler, FOA 3" in Stockholm. After the eight hours' transport back to the observatory the time is continously compared with the pulses from the Loran-C station at Sylt, which is one of the slave stations in the Norwegian chain. To get UTC time from the received Loran-C pulses four different quantities have to be known: 1) the time offset between the pulses from the master station in the chain and UTC, 2) the emission delay of the transmitted pulses from the slave station (compared to the master), 3) the propagation delay between the slave station and the receiver, which can be calculated to within a few μ sec over distances less than 1000 miles (the propagation delay from Sylt to Onsala is 1219.2 μsec), and 4) the instrumental delay of the receiver.

The timing accuracy of the Loran-C system has been discussed by Pakos [1969] and Shapiro and Fisher [1970].

The recording system

The recording system at Onsala consists of on AMPEX TM-10 seven track tape tmnsport, which records at 800 bpi. With the fixed speed of 150 inches/second the sampling rate is 720 kbits/second. This tape transport and the interface have been borrowed from the National Radio Astronomy Observatory, where a similar system is used. The data on the tape is blocked in data blocks of 0.2 second duration with (720 x 0.2 - 3.6) kbits in each. The last 0.005 seconds form the intergap between each block. As the sampling rate is fixed a series of computer programs have been written which discard the redundant bits if narrower video filters are used and block the remaining bits on nine track tapes.

As the sampler and interface to the recorder are controlled by the rubidium frequency standard the time information is obtained by counting data blocks and bits from the beginning of the recording. A start puls every ten UTC-second starts the tape transport if the switch "READY TO GO" is on. A preset time for this switch to be turned on can be dialed in on thumb- wheel switches on the station sidereal clock. The data recording starts 0.3 seconds after the start time and lasts about 3 minutes.

CHAPTER IX

THE OBSERVATIONAL PROGRAMS

The Onsala Space Observatory joined the VLBI group in 1968 without any practical experience in interferometric observations. Therefore, a large variety of computer programs had to be written before the observatory could be the head station in a joint VLBI experiment. General computer programs among others for very accurate precession, nutation and aberration of astronomical coordinates and to determine the sidereal time versus UTC and special programs necessary to organize an interferometer observation have been written. [Landgren and Rönnäng (1971)]. One of the programs, called BASE, computes the baseline parameters listed in table 2.2. from the geodetic coordinates of the stations and the adopted ellipsoid model for the shape of the earth. Another program — PREVLB — draws the projected baseline ellipses shown in figure 7.1 and lists the important observational parameters versus GMT for a given baseline and a selected radio source. Table 9.1 gives an example of such a line printer list, which besides precessed source coordinates to point the antenna gives the local sidereal time and local hour angle of the source at station number 1, the local oscillator settings at both station (based on given local oscillator chains), the elevation of the source at both stations, the projected base lines in east-west and south-north direction (u = SX and v= SY in cycles/arc.sec.), the geometrical delay and the fringe rate. The mathematical formulae used to compute the geometrical delay τ_g, the baseline parameters, the fringe rate and projected baselines are given in chapter II and VII.

The local oscillator settings will place the actual velocity component in the center of the frequency band and make the apparent fringe rate equal to zero. The local oscillator setting at station no 2, FREQ (2), is obtained from the identity

(FREQ (1) · MULT. FACTOR + MF at station 1) –
– (FREQ (2) · MULT. FACTOR + MF at station 2)=
= FRINGE RATE

An observational session is organized by means of lists like the one shown in table 8.1. The same lists are also used during the observations for local oscillator settings. Notice that the source W 49 with the declination of 9.053 degrees is available only about seven hours per day.

1970.07.30 THURSDAY

FREQUENCY: 1665.401 MHZ
VELOCITY: 4.000 KM/S

SOURCE: W49 OH
RA: 19.130 HOURS 19 H 7 M 49.5 S DEC: 9.020 DEGREES EPOCH: 1950.0
RA: 19.147 HOURS 19 H 8 M 50.3 S DEC: 9.053 DEGREES EPOCH: 1970.6

BASELINE: 5599.545 KILOMETERS
AZIMUTH: -68.145 DEG ELEVATION: -26.041 DEG
HA: 8.126 HOURS 8 H 7 M 34.2 S DEC:-10.837 DEGREES
LC-FORMULA ONS TO HAYS
HF 30. 30. MHZ
MULT.FACTOR 60. 60.

THE OBSERVED FREQUENCY IS THE LINE FREQUENCY
PLUS OR MINUS 3.0 KHZ DEPENING ON THE LO.
IT IS MINUS IF THE LO IS BELOW THE LINE.

GMT	LST(1)	LHA(1)	VELOCITY	FREQ(1)	FREQ(2)	ELEV(1)	ELEV(2)	U	V	DELAY	FR RATE
H M	H M S	H M S	KM/S	MHZ	MHZ	DEG	DEG	CYCLES PER	SEC ARC	MICROSEC	HZ
0 0	21 16 33	2 7 42	-10.5875	27.25724325	27.25727992	35.86	34.06	-148.12	-28.01	542.0	-2200.17
0 10	21 26 34	2 17 44	-10.5756	27.25724215	27.25727878	34.98	35.77	-147.98	-29.03	-250.4	-2198.00
0 20	21 36 36	2 27 46	-10.5639	27.25724107	27.25727760	34.03	37.46	-147.55	-30.05	-1041.2	-2191.64
0 30	21 46 37	2 37 47	-10.5526	27.25724002	27.25727637	33.04	39.11	-146.84	-31.06	-1829.0	-2181.07
0 40	21 56 39	2 47 49	-10.5415	27.25723899	27.25727510	32.00	40.73	-145.94	-32.07	-2612.2	-2168.33
0 50	22 6 41	2 57 50	-10.5307	27.25723800	27.25727379	30.93	42.30	-144.57	-33.07	-3389.4	-2147.45
1 0	22 16 42	3 7 52	-10.5203	27.25723703	27.25727244	29.81	43.83	-143.03	-34.06	-4159.1	-2124.45
1 10	22 26 44	3 17 54	-10.5102	27.25723610	27.25727105	28.67	45.31	-141.20	-35.04	-4919.7	-2097.39
1 20	22 36 46	3 27 55	-10.5005	27.25723520	27.25726964	27.49	46.73	-139.11	-36.01	-5669.8	-2066.32
1 30	22 46 47	3 37 57	-10.4912	27.25723433	27.25726819	26.29	48.09	-136.75	-36.96	-6408.0	-2031.29
1 40	22 56 49	3 47 59	-10.4822	27.25723350	27.25726671	25.06	49.37	-134.13	-37.89	-7132.9	-1992.37
1 50	23 6 51	3 58 0	-10.4737	27.25723271	27.25726521	23.81	50.58	-131.26	-38.80	-7843.1	-1949.64
2 0	23 16 52	4 8 2	-10.4655	27.25723196	27.25726368	22.54	51.70	-128.13	-39.69	-8537.3	-1903.18
2 10	23 26 54	4 18 4	-10.4578	27.25723124	27.25726213	21.25	52.73	-124.75	-40.57	-9214.0	-1855.07
2 20	23 36 56	4 28 5	-10.4505	27.25723057	27.25726056	19.94	53.65	-121.14	-41.41	-9872.0	-1799.42
2 30	23 46 57	4 38 7	-10.4436	27.25722993	27.25725897	18.62	54.47	-117.30	-42.23	-10510.1	-1742.32
2 40	23 56 59	4 48 9	-10.4372	27.25722934	27.25725737	17.29	55.16	-113.23	-43.03	-11127.0	-1681.89
2 50	0 7 0	4 58 10	-10.4313	27.25722879	27.25725576	15.95	55.73	-108.95	-43.79	-11721.6	-1618.24
3 0	0 17 2	5 8 12	-10.4258	27.25722828	27.25725414	14.60	56.16	-104.45	-44.53	-12292.7	-1551.49
3 10	0 27 4	5 18 13	-10.4207	27.25722781	27.25725251	13.25	56.45	-99.76	-45.23	-12839.1	-1481.78
3 20	0 37 5	5 28 15	-10.4161	27.25722739	27.25725087	11.90	56.60	-94.87	-45.90	-13360.0	-1409.22
3 30	0 47 7	5 38 17	-10.4120	27.25722701	27.25724924	10.54	56.61	-89.81	-46.54	-13854.2	-1333.97
3 40	0 57 9	5 48 18	-10.4084	27.25722667	27.25724761	9.18	56.47	-84.57	-47.14	-14320.9	-1256.17
3 50	1 7 10	5 58 20	-10.4052	27.25722638	27.25724598	7.83	56.18	-79.17	-47.70	-14759.0	-1175.96
4 0	1 17 12	6 8 22	-10.4026	27.25722613	27.25724435	6.48	55.76	-73.62	-48.23	-15167.9	-1093.50
4 10	1 27 14	6 18 23	-10.4004	27.25722592	27.25724274	5.13	55.21	-67.93	-48.71	-15546.7	-1008.95
4 20	1 37 15	6 28 25	-10.3986	27.25722576	27.25724114	3.79	54.52	-62.10	-49.16	-15894.7	-922.47
4 30	1 47 17	6 38 27	-10.3974	27.25722565	27.25723955	2.47	53.72	-56.16	-49.57	-16211.1	-834.22
4 40	1 57 19	6 48 28	-10.3966	27.25722557	27.25723798	1.15	52.80	-50.11	-49.93	-16495.6	-744.38
21 0	18 20 0	23 11 9	-10.4136	27.25722715	27.25725349	40.91	1.99	-106.36	-11.78	13161.0	-1579.88

1970.07.30 THURSDAY PAGE 2
SOURCE: W49 OH
FREQUENCY: 1665.401 MHZ VELOCITY: 4.000 KM/S

GMT	LST(1)	LHA(1)	VELOCITY	FREQ(1)	FREQ(2)	ELEV(1)	ELEV(2)	U	V	DELAY	FR RATE
H M	H M S	H M S	KM/S	MHZ	MHZ	DEG	DEG	CYCLES PER	SEC ARC	MICROSEC	HZ
21 10	18 30 1	23 21 11	-10.4001	27.25722591	27.25725333	41.25	3.82	-110.77	-12.53	12579.9	-1645.34
21 20	18 40 3	23 31 12	-10.3866	27.25722465	27.25725311	41.51	5.65	-114.97	-13.30	11975.9	-1707.66
21 30	18 50 4	23 41 14	-10.3729	27.25722339	27.25725283	41.70	7.49	-118.94	-14.11	11349.9	-1766.70
21 40	19 0 6	23 51 16	-10.3593	27.25722212	27.25725249	41.80	9.33	-122.69	-14.94	10703.5	-1822.37
21 50	19 10 8	0 1 17	-10.3456	27.25722085	27.25725210	41.83	11.18	-126.20	-15.80	10037.3	-1874.54
22 0	19 20 9	0 11 19	-10.3319	27.25721959	27.25725164	41.78	13.03	-129.47	-16.68	9353.1	-1923.13
22 10	19 30 11	0 21 21	-10.3183	27.25721832	27.25725112	41.66	14.88	-132.49	-17.58	8652.0	-1968.04
22 20	19 40 13	0 31 22	-10.3046	27.25721706	27.25725055	41.45	16.73	-135.26	-18.50	7935.5	-2009.18
22 30	19 50 14	0 41 24	-10.2911	27.25721581	27.25724992	41.17	18.58	-137.78	-19.44	7204.8	-2046.47
22 40	20 0 16	0 51 26	-10.2776	27.25721456	27.25724923	40.81	20.42	-140.02	-20.40	6461.4	-2079.85
22 50	20 10 18	1 1 27	-10.2643	27.25721333	27.25724848	40.38	22.25	-142.00	-21.37	5706.7	-2109.24
23 0	20 20 19	1 11 29	-10.2510	27.25721210	27.25724768	39.88	24.08	-143.71	-22.35	4942.1	-2134.60
23 10	20 30 21	1 21 31	-10.2380	27.25721089	27.25724682	39.31	25.89	-145.14	-23.35	4169.1	-2155.88
23 20	20 40 23	1 31 32	-10.2250	27.25720969	27.25724591	38.67	27.70	-146.30	-24.35	3389.2	-2173.02
23 30	20 50 24	1 41 34	-10.2123	27.25720851	27.25724495	37.98	29.49	-147.17	-25.36	2603.9	-2186.01
23 40	21 0 26	1 51 35	-10.1998	27.25720735	27.25724393	37.22	31.26	-147.76	-26.38	1814.7	-2194.82
23 50	21 10 27	2 1 37	-10.1875	27.25720621	27.25724287	36.40	33.01	-148.07	-27.40	1023.0	-2199.42
24 0	21 20 29	2 11 39	-10.1754	27.25720510	27.25724176	35.53	34.74	-148.10	-28.41	230.4	-2199.81

Table 8.1 An example of a line printer output used to schedule a VLBI experiment.

CHAPTER X

VLBI DATA PROCESSING USING THE IBM 360/65 COMPUTER.

The theoretical formulae used to determine the power spectrum of the individual signals and to obtain the cross power spectrum are given in chapter IV and VI. In the following chapter X we will briefly describe the computer programs to get the cross power spectrum (the interferometer fringe amplitude and fringe phase) and discuss some of the problems due to the fact that one has to work with digitized data and with unknown geometrical delay and fringe rate.

The AUTOCORR program

Figure 10.1 shows the principle construction of the AUTOCORR program which is a spectrum analyser using the one-bit correlation technique. It is used to test the system and the recorded signals. The program is run on the individual tapes before the time-consuming search for correlation between the two recorded signals. It computes the power spectrum in degrees Kelvin antenna temperature according to equations (6.2), (6.6) and (6.7) using either cosine weighting [equation (6.11)] or uniform weighting [equation (6.10)] of the autocorrelation function. The total integration time and the frequency resolution can be chosen via input cards. The off source spectrum $S_{OFF}(\omega)$ can either be computed from the signals on an input tape recorded with the antenna pointing towards a continuum radio source or from a

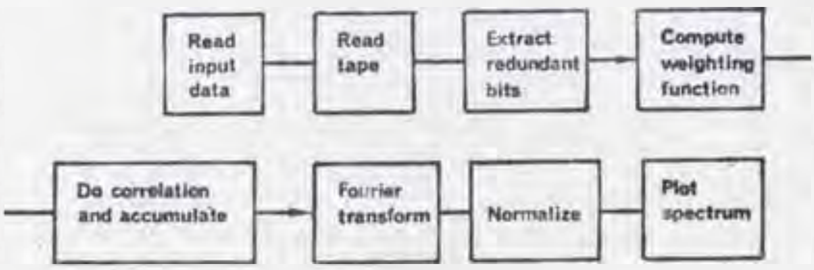

Figure 10.1 A block diagram showing the construction of the AUTOCORR program.

precalculated zero line spectrum stored on tape or cards. Figure 10.2 gives an example of the output spectra obtained by means of the AUTOCORR program.

OBSERVATORY: ONSALA OBS.
FREQUENCY: 1665.401 MHZ
SAMPLE RATE: 12 KHZ
DELAY CHANNELS (POSITIVE+NEGATIVE DELAY): 50

HANNING WEIGHTING FUNCTION HAS BEEN USED
FREQUENCY RESOLUTION: 0.60 KHZ

W3OH,-43.7 KM/S,RRC,TAPE NO 551.1. UNNORMALIZED SPECTRUM

NO OF INTEGRATED RECORDS: 400
FIRST RECORD TO BE USED: 1

1	0.3234
2	0.4172
3	0.6932
4	0.9229
5	1.1374
6	1.2650
7	1.3284
8	1.3639
9	1.3930
10	1.4197
11	1.4460
12	1.4688
13	1.4964
14	1.5250
15	1.5453
16	1.5474
17	1.5246
18	1.4757
19	1.3958
20	1.2918
21	1.1833
22	1.0139
23	0.8487
24	0.6784
25	0.5142
26	0.3683
27	0.2502
28	0.1664
29	0.1094
30	0.0799

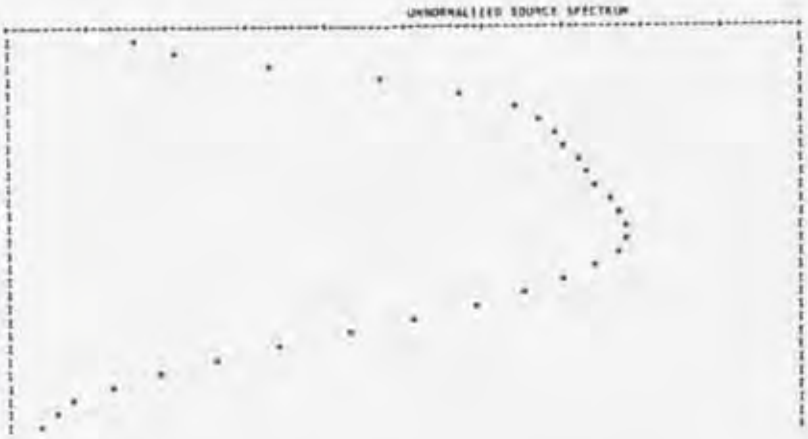

3C273,0.0 KM/S,RRC,TAPE NO 551.2. ZERO LINE SPECTRUM

NO OF INTEGRATED RECORDS: 400
FIRST RECORD TO BE USED: 1

1	0.3709
2	0.4785
3	0.7458
4	1.0480
5	1.2783
6	1.4039
7	1.4563
8	1.4817
9	1.5040
10	1.5225
11	1.5291
12	1.5200
13	1.4972
14	1.4639
15	1.4229
16	1.3764
17	1.3263
18	1.2733
19	1.2159
20	1.1492
21	1.0661
22	0.9603
23	0.8301
24	0.6814
25	0.5269
26	0.3827
27	0.2624
28	0.1733
29	0.1157
30	0.0847

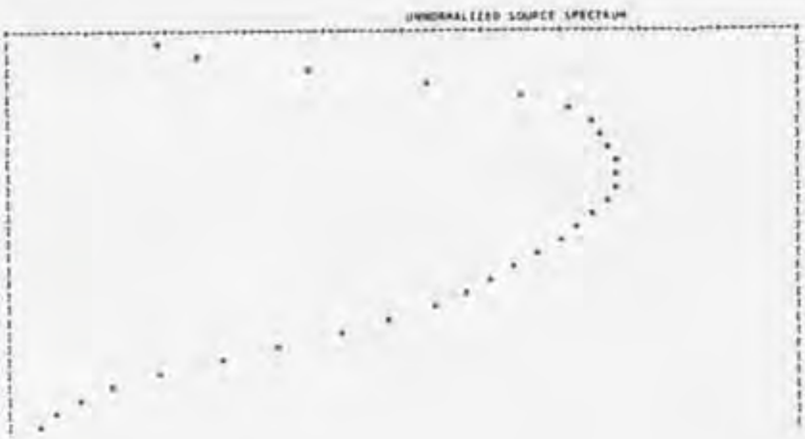

W3OH,-43.7 KM/S,RRC,TAPE NO 551.4. NORMALIZED SPECTRUM, TOTAL WIDTH 6 KHZ

CH.NO.	DEGREE K
1	0.6767
2	0.6852
3	0.8040
4	1.0833
5	1.5154
6	2.0424
7	2.5576
8	2.9485
9	3.2127
10	3.5056
11	4.0625
12	5.0847
13	6.6401
14	8.6028
15	10.6684
16	12.4535
17	13.6262
18	14.0000
19	13.5603
20	12.4671
21	10.9105
22	9.2437
23	7.7050
24	6.4526
25	5.5326
26	4.9005
27	4.5017
28	4.2500
29	4.0968
30	3.9932

END OF SPECTRUM PLOT

Figure 10.2 Showing an example of the power spectrum of an OH signal obtained by means of the AUTOCORR program. Total bandwidth 6 kHz.
Spectrum 1. Zero line + W3 OH radiation
Spectrum 2. Zero line + 3C273 radiation
Spectrum 3. Normalized spectrum of the -43.7 km/s, right circular polarized W3 OH radiation.

The OHVLBI program

The OHVLBI program, which is used to compute the fringe amplitude and fringe phase, is constructed as a main program to control the processing with subroutines for the mathematical computation. The main program is listed in appendix 1. It uses the following subroutines:

Fortran subroutines

BASE, which computes the interferometer baseline parameters from the latitudes and longitudes of the stations.

FRINGE, which computes the fringe rate given by equation (2.3).

HOURAN, which computes the hour angle of the source using the 1950.0 coordinates.

DATE, which gives the name of the day at an arbitrary date.

CPXFOU, which performs complex Fourier transform on the complex correlation function.

PLOT 2 V, which draws the complex cross-power spectrum (the fringe phase and fringe amplitude) on line printer.

SID, which gives the local sidereal time

NUTABE and

PRECES, which convert the source coordinates given at an arbitrary epoch to the actual epoch.

HOURS, which is called when converting from hours in decimal form to hours, minutes and seconds.

CHANGE, which converts between different astronomical coordinate systems.

JULIAN, which computes the Julian day number.

Assembler subroutines

READT, which reads the input signals. One block at a time.

CONV 3, CONV 4 and CONV 60, which extract the redundant bits on the original tape. Conv 3 keeps every third bit and is used for the 120 kHz total bandwidth. Conv 4 keeps every fourth bit and conv. 60 every sixtieth bit.

CORREL, which computes

$$R_t(J) = \sum_{I=1}^{32 \times \mathrm{IWORDS}} X\left(I - \underset{\substack{\text{geometrical and instrumental}\\ \text{delay}}}{I(t)} - J\right) \cdot Y(I)$$

where X (I) is the bit string from tape number 1 and Y (I) is the bit string from tape number 2. The bit multiplication is performed by means of an "exclusive or" instruction with the arithmetic

$1 \times 1 = 0 \times 0 = 1$

$0 \times 1 = 1 \times 0 = 0$

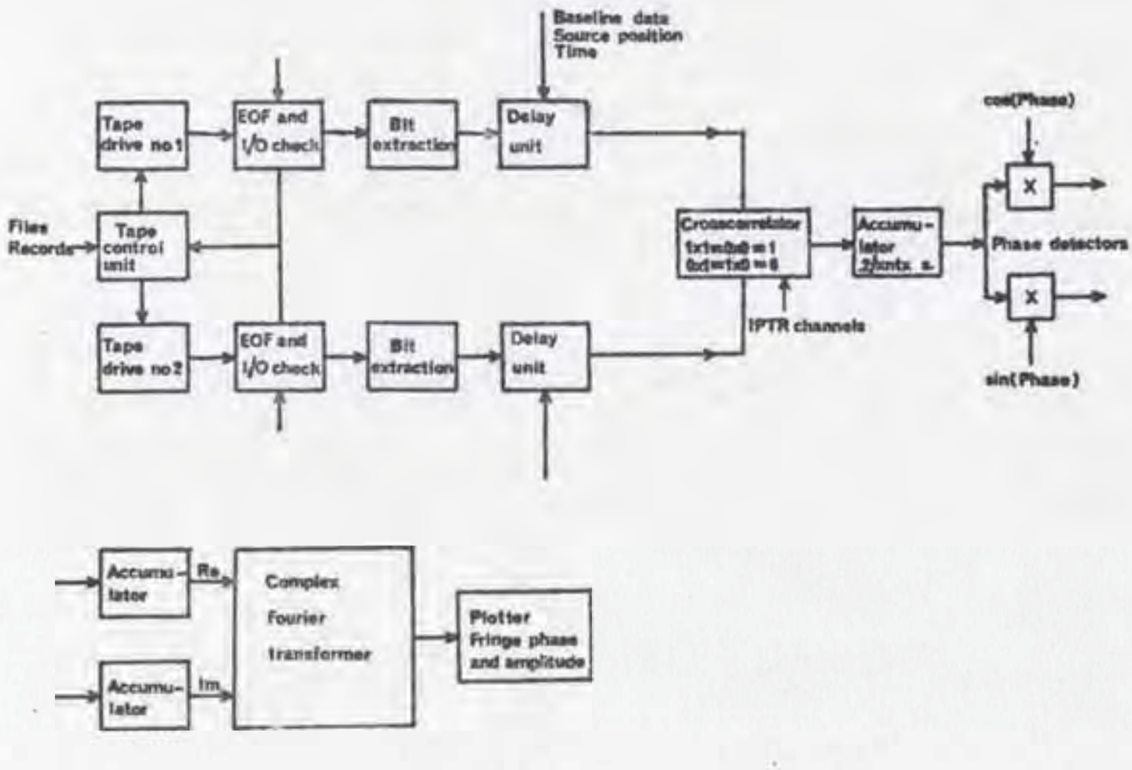

Figure 10.3 Block diagram of the VLBI data processing.

Figure 10.3 shows a block diagram of the data processing. There are two important parameters in the data reduction both of which are functions of the position of the recording stations and the radio source, viz. the geometrical delay and the fringe rate. The total delay is normally known to within about $\pm$ ten microseconds and before the real data reduction a test run has to be made to determine a more accurate value of the time delay. At the cross correlation of the bit strings the delay has to be truncated to an integral bit, which will produce an error both in the measured fringe phase and fringe amplitude versus frequency. The delay error is roughly uniformly spread between $\pm$ 1/2 bit, i.e. $\pm\ \tau/2 = 1/2\ f_s$. Hence the spectrum is phase shifted between $\pm\ 2\pi\ f/2f_s$ according to equation(4.10)and the fringe amplitude will decrease with a factor

$$f_s \int_{-\frac{1}{2f_s}}^{\frac{1}{2f_s}} e^{j\,2\pi f\tau}\ d\tau = \frac{\sin \pi f/f_s}{\pi f/f_s} \qquad f < B = \frac{f_s}{2} \tag{10.1}$$

which is a function of the frequency.

The total resulting delay error after integration over several hundreds of block segments will be much less than $1/2\ f_s$. However, it has to be taken into account, as a time error of $\Delta\tau$ will make the fringe phase vary like $2\pi f \cdot \Delta\tau$ over the frequency spectrum.

The cross correlation function is a function of time. Even if one of the local oscillators is offset to compensate for the phase change — the fringe rate — there will be a resulting time variation due to uncertainty in τ_g and in the local oscillator frequencies, and due to the nonlinear terms in τ_g. It is therefore impossible to integrate the correlation function over longer time intervals. Normally the integration time is equal to 0.02 seconds, but it can be chosen longer or chorter due to the expected fringe rate.

The obtained $R_t(\tau)$ for each 0.02 second segment is multiplied by sine and cosine of the fringe phase $\omega_o\tau_g$, plus the instrumental phase $\Delta\omega t$ due to the offset of the local oscillator frequencies, plus the phase of a series of offset fringe frequencies $\Delta\omega_{offset}$ to compensate for errors in the computed time delay and in the local oscillator frequency offset. An error $\Delta\omega_f$ in the fringe rate will degrade the fringe amplitude like

$$\left| \frac{\sin \left(\Delta\omega_f \frac{T_i}{2}\right)}{\Delta\omega_f \frac{T_i}{2}} \right| \tag{10.2}$$

according to equation (7.18) , which means that the right $\Delta\omega_f$ can be obtained by a least square fit of the computed fringe amplitude. Figure 10.4 shows the fringe amplitude versus fringe frequency offset. The difference between the measured curve and the theoretical curve is due mainly to phase noise in the local oscillator signals. This phase noise will degrade the fringe amplitude. The possibility to compensate for this degradation using the curve shown in figure 10.4 has been discussed by Kellerman et al [1968]

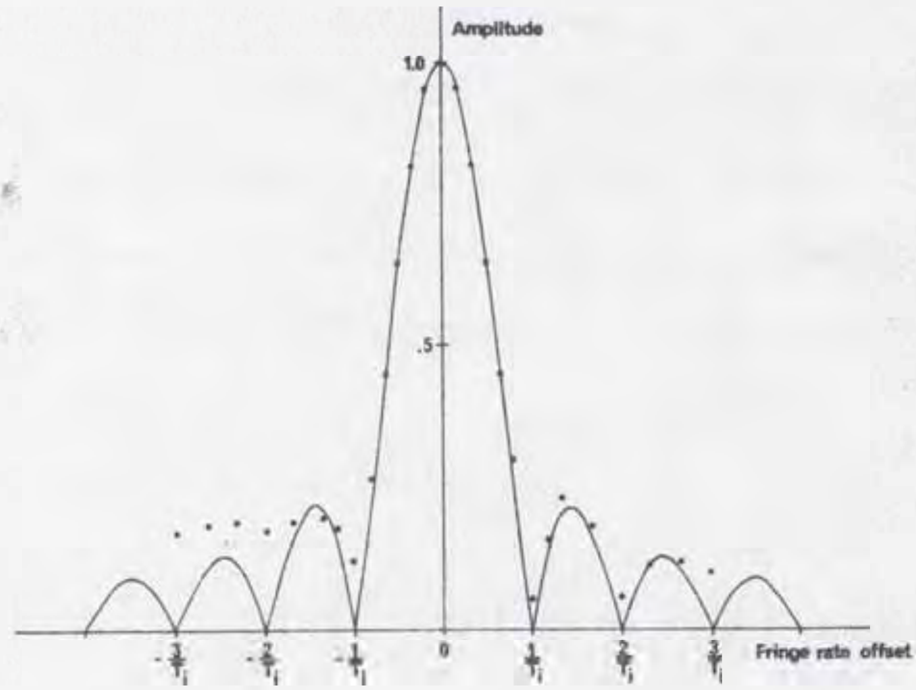

Figure 10.4 The fringe amplitude versus fringe rate offset. The dots are measured values with an integration time of 150 seconds. The solid line curve is the theoretical curve without any phase noise.

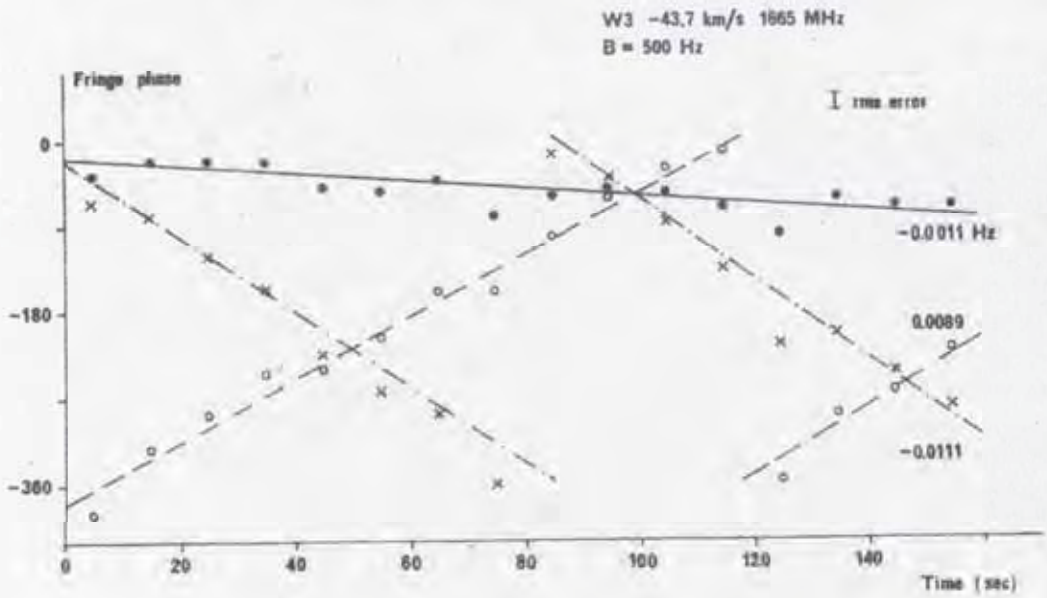

Figure 10. 5. Showing the fringe phase variation versus time due to a fringe rate offset. The numbers to the right in the figure are the fringe rate offset obtained by fitting a straight line to the measured values. In this case the true fringe rate is 0. 000 Hz.

The right fringe frequency can also be obtained by plotting the fringe phase versus time. The phase will vary like $\Delta\omega_f\, t$. Figure 10. 5 shows an example of the measured fringe phase for three different $\Delta\omega_f$. The real fringe rate is obtained by fitting a straight line to the measured values.

The OHVLB program can be run in two different modes, viz.

1. Computation of the complex cross correlation function over short intervals (typical length of 0. 02 seconds), which is stored on magnetic tapes for later processing.

2. crosscorrelation directly followed by synchronous detection and Fourier transformation. The fringe visibility can be determined and displayed for short time sequences and then accumulated to give the desired integration time

Figure 10. 6 shows the output from a OHVLBI run. The input signals are from the OH spectral line source W3 recorded with the Onsala to Haystack interferometer at a wavelength of 18 cm. The recorded signal to noise ratio of the strongest correlated signal is about - 10 dB. The frequency resolution of the spectra is 400 Hz and the total bandwidth is 6 kHz. The spectrum is shown for two different $\Delta\omega_{offset}$. This feature has a visibility of about 0. 5 which gives an angular size of about 0. 005". The result from this measurement and several other interferometric observations of galactic OH sources have been published by Rönnäng et al. [1970] . The results of VLBI observations of continuum radio sources are summarized in a paper by Kellerman et al [1971] .

FREQUENCY: 1665.401 MHZ
VELOCITY: -43.700 KM/S

W3 OH
RA: 2.388 HOURS 2 H 23 M 16.8 S DEC: 61.648 DEGREES EPOCH: 1950.0
RA: 2.413 HOURS 2 H 24 M 45.4 S DEC: 61.736 DEGREES EPOCH: 1969.5

BASELINE: 5999.848 KILOMETERS
BASE LHA: 8.126 HOURS 8 H 7 M 33.6 S DEC: -10.835 DEG
ONS TC HAYS

1	0.0053	49.7908
2	0.0035	84.6185
3	0.0088	149.5222
4	0.0104	145.9237
5	0.0042	88.6880
6	0.0075	9.6853
7	0.0059	25.4826
8	0.0083	87.1615
9	0.0124	81.5968
10	0.0141	54.0049
11	0.0162	35.9052
12	0.0196	33.4200
13	0.0279	34.0467
14	0.0424	34.5095
15	0.0597	38.3160
16	0.0726	42.6521
17	0.0733	46.4603
18	0.0614	51.1304
19	0.0462	58.5366
20	0.0353	63.9431
21	0.0258	58.6920
22	0.0156	42.5843
23	0.0070	24.3883
24	0.0030	36.0495
25	0.0035	38.2548
26	0.0035	0.2059
27	0.0018	-65.1420
28	0.0030	177.7901
29	0.0037	147.7737
30	0.0007	140.4478

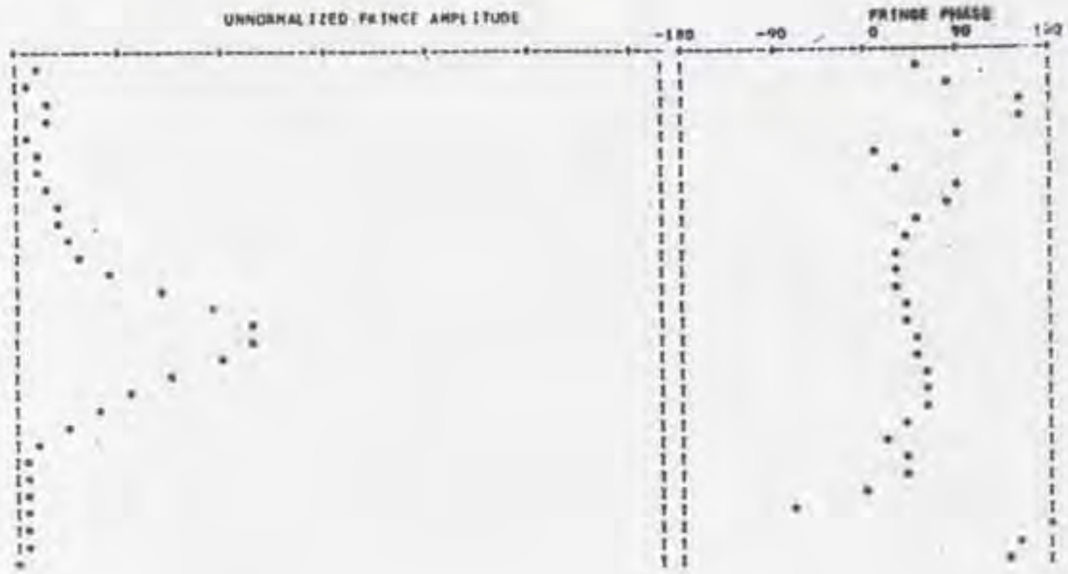

CCNT= 0.0238

0.008 3 7200

1	0.0045	-45.8035
2	0.0033	-23.2778
3	0.0086	39.0614
4	0.0112	53.2268
5	0.0075	-20.6415
6	0.0109	-74.7836
7	0.0090	-67.2004
8	0.0065	-2.5007
9	0.0119	13.0313
10	0.0110	-12.6373
11	0.0161	-47.9435
12	0.0287	-56.5349
13	0.0460	-58.2354
14	0.0654	-58.8255
15	0.0842	-56.9175
16	0.0974	-52.7746
17	0.0993	-47.9857
18	0.0873	-43.2054
19	0.0665	-38.5166
20	0.0475	-36.6094
21	0.0327	-41.4348
22	0.0221	-51.5551
23	0.0132	-58.6435
24	0.0065	-56.9409
25	0.0045	-57.1349
26	0.0036	-64.4511
27	0.0014	-31.1136
28	0.0028	62.8142
29	0.0035	76.6693
30	0.0020	86.2356

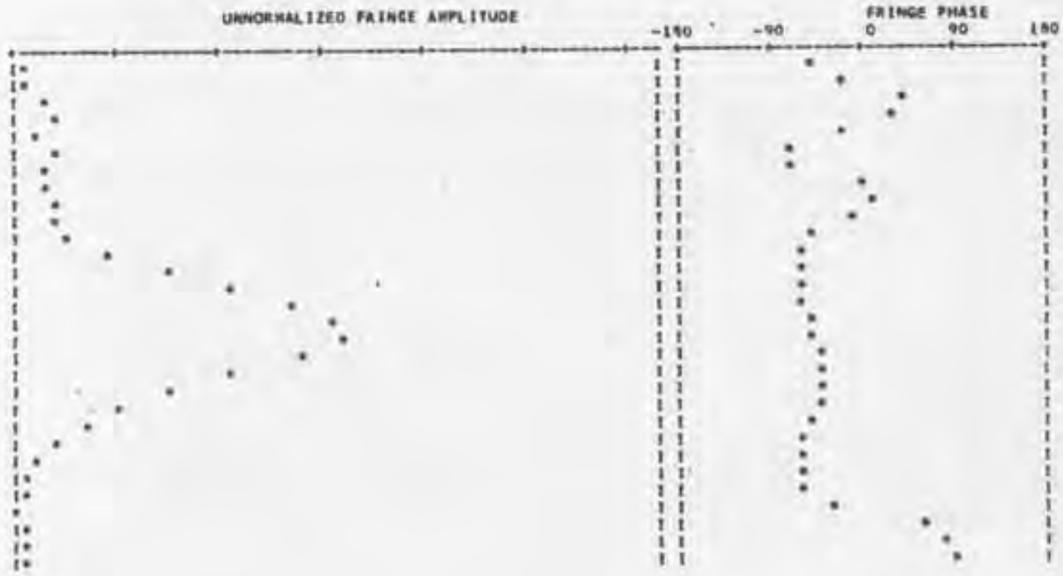

CCNT= 0.0331

0.010 5 7200

Radio source: W3 OH

Figure 10.6 The amplitude and phase of complex cross power spectrum of one component in the OH spectral line radiation. Two different fringe rate offsets have been used, 0.008 Hz and 0.010 Hz. The maximum fringe amplitude is obtained at 0.010 Hz. The total integration time is 130 seconds and the frequency resolution is 800 Hz.

APPENDIX I

The following ten pages give a line printer listing of the main OHVLBI program, which reads the recorded signals, cross-correlates the data and computes the fringe amplitude and fringe phase versus frequency and fringe rate. Beside the main program there are fifteen subroutines which are not listed, viz.

READT, CPXFOU, HOURAN, SID, NUTABE, PRECES, PLOT 2 V, CORREL, FRINGE, CONV 4, HOURS, DATE, BASE, CHANGE and JULIAN

Some of these subroutines are described in a report by Landgren and Rönnäng [1971]. The others are explained in the main program.

```
C     PROGRAM OHVLB
C     RONNANG 6.6.69
C     THIS PROGRAM TAKES DATA TAPES RECORDED ON TWO TELESCOPES AND
C     CROSSCORRELATES THE DATA BIT STRINGS
C     A FOURIER TRANSFORM IS TAKEN ON THE CORRELATION FUNCTIONS GIVING
C     THE FRINGE VISIBILITY WHICH IS DISPLAYED AS A FUNCTION OF
C     FREQUENCY AND FRINGE RATE
      DIMENSION JSWTCH(12),TMAX(6),IBAND(3),COSPH(10,21),SINPH(10,21)
     F,IOBS1(1100),IOBS2(1100),ICORR(181),RSIN(180,21),RCOS(180,21),
     FTREAL(180),TIMAG(180),FAMP(180),FASE(180),WT(181),ISOUR(20),
     FISITE(2),I1ARR(4380),I2ARR(4380),CORR(181)
      DOUBLE PRECISION PH,TIME,PHASE,DELAY,DANG,SLHA,DOPFQ(21),
     FTIMEST,FREQ1,FREQ2,FRLO1,FRLO2,FROT,FOFF2,
     FFRATE ,IMF1,IMF2,SEC,SECS,PHD,PHI,PRD,PRH,DEC,
     FLATGC(2),WLONG(2),ELEV(2),BL,BAZ,BEL,BLHA,BDEC,RV(2),
     FSLHA1,STHR,RAH,RAHP,DECL,DECP,
     FSX,SY
C          C A R D  N O  1 ,
C          WHICH IS A PROGRAM CONTROL CARD
      READ (1,46) (JSWTCH(I),I=1,9)
   46 FORMAT (9I1)
C          JSWTCH (1)   SPARE SWITCH
C          JSWTCH(2)=I FRAMP---FRINGE AMPLITUDE PLOT SCALE CODE
C          JSWTCH(3)  CLEARS ARRAYS AND CONTINUES TO INTEGRATE FROM
C                PRESENT TAPE POSITION
C          JSWTCH(4) NUMBER OF INTEG. INTERVALS
C          JSWTCH(5)   INCLUDE DEBUGGING PRINTOUT FOR JSWITCH(5)
C                RECORDS
C          JSWTCH(6)=1 SPECTRUM WILL BE PLOTTED
C          JSWTCH(7) SPARE SWITCH
C          JSWTCH(8)=1 IF CORRELATION FUNCTION IS TO BE STORED ON
C               TAPE, ELSE EQUAL TO 0
C          JSWTCH(9)=1 IF CORRELATION FUNCTION WILL BE STORED AND NO
C               FOURIER TRANSFORMATION
      PHI=3.14159265358979 32
      PRD=PHI/180.
      PRH=PHI/12.
      DO 12 I=1,181
   12 ICORR(I)=0
C     ----------
C          THE COMPLEX CROSS POWER SPECTRUM CAN BE PLOTTED.
C          TMAX IS THE FULL SCALE AMPLITUDE ---TMAX(JSWTCH(2))
      TMAX(1)=1.0
      TMAX(2)=0.5
      TMAX(3)=0.2
      TMAX(4)=0.1
      TMAX(5)=0.05
      TMAX(6)=0.02
C     ----------
C          THREE DIFFERENT VIDEO BANDWIDTHS CAN BE HANDLED
C          BY CHOOSING DIFFERENT BANDWIDTH  CODES IBW.
C          BANDWIDTH CODE IBAND(IBW) IBW=1,2,3 --- 6,90,120 KHZ
C          OTHER BANDWIDTHS ARE ACCEPTABLE IF IBAND AND
C          DATA ARRAYS IOBS1 AND IOBS2 ARE CHANGED
      IBAND(1)=1
      IBAND(2)=15
      IBAND(3)=20
C     ----------
   10 CONTINUE
C     IBPW, NO OF BITS PER WORD=32
      IBPW=32
C     IREC1,IREC2= ST.1, ST.2 RECORD COUNT RESPECTIVELY
      IREC1=0
```

```
      IREC2=0
      IACUM=0
C     DSHIFT=FRACTIONAL BIT SHIFT
      DSHIFT=0.
C     IWRITE=CROSSCORRELATED RECORD SEGMENT COUNT
      IWRITE=0
C     CLEAR CORRELATION FUNCTION ARRAYS
C     I,J,DELAY AND DOPPLER INDICES
      DO 40 I=1,180
      DO 40 J=1,21
      RCOS(I,J)=0.
   40 RSIN(I,J)=0.
C
C     INPUT PARAMETER CARDS
C         C A R D  N O  2
C     ITAPE1, ITAPE2, TAPE NO OF ST.1 AND ST.2
C     IFILE1, IFILE2, FILE ON INPUT TAPES NO.1 AND NO.2
C     ICV1, ICV2, =1, 2, 3, ... FOR SELECTION OF EVERY, EVERY SECOND,
C         EVERY THIRD, ... BIT ON INPUT TAPES
C     IBW, 1=6KHZ, 2=90 KHZ 3=120KHZ
C     INTEG, INTEGRATION PERIOD IN RECORDS
C     IPTR, NUMBER OF POINTS IN CORRELATION FUNCTION MAX 181
C     IPTS, NUMBER OF POINTS IN VISIBILITY SPECTRUM  MAX 180
C     IWT, WEIGHTING FUNCTION, 1 FOR  UNIFORM, 2 FOR COSINE
      READ (1,85) ITAPE1,ITAPE2,IFILE1,IFILE2,ICV1,ICV2,
     FIBW,INTEG,IPTR,IPTS,IWT
   85 FORMAT(11I4)
C         C A R D  N O  3
C     DOP, EXPECTED FRINGE FREQUENCY IN HZ
C     DOPD, FRINGE FREQUENCY SEARCH INTERVAL IN HZ. SHOULD BE SET
C         PROPORTIONAL TO RECIPROCAL OF INTEGRATION TIME. DOPD SHOULD BE
C         LESS THAN (4/INTEG)
C     NDOP, NUMBER OF FRINGE FREQUENCY SEARCH MAX 21
C     ADELAY, INSTRUMENTAL DELAY ST.2 REL TO ST.1 IN MICROSEC
      READ (1,105) DOP,DOPD,NDOP,ADELAY
  105 FORMAT (2(F6.3),I2,F8.2)
C         C A R D  N O  4
C     HRS, MIN, SECS, TIME AT START OF FIRST RECORD TO BE INTEGRATED
C     I1ST, FIRST RECORD TO BE USED FROM 1TAPE, CORRESPONDING TO TIME
C     I2ST, FIRST RECORD TO BE USED FROM 2TAPE
      READ (1,115) IHRS,IMINS,SECS,I1ST,I2ST
  115 FORMAT(2(I2,1X),F4.1,1X,2(I3,1X))
C         C A R D  N O  5
C         INPUT DATA TO COMPUTE LO-FREQUENCIES
C     FRLO1,FRLO2, SYNTHESIZER SETTINGS
C     ILOM1,ILOM2, MULTIPLICATION FACTORS
C     IMF1,IMF2, MF-FREQUENCIES
C     INTX, EACH RECORD IS BROKEN INTO INTX
C           RECORD SEGMENTS. MAX 10, IF MORE ONLY ARRAY LENGTH HAS TO
C     BE CHANGED
      READ (1,125) FRLO1,FRLO2,ILOM1,ILOM2,IMF1,IMF2,INTX
  125 FORMAT(2F13.8,2I3,2F9.3,I3)
C         C A R D  N O  6
C         C A R D  N O  7
C     LATD,LATM,LATS, LATITUDES OF STATION 1 AND 2
C     LONGD,LONGM,LONGS, LONGITUDES OF STATION 1 AND 2
C     EL, ALTITUDE IN METERS
C     INPUT CARDS 8 AND 9 NOT USED
C         C A R D  N O  8
C         C A R D  N O  9
C     INPUT CARD 10 TO 13 ARE IN SUBROUTINE HOURAN
      CALL BASE(LATGC,WLONG,ELEV,BL,BAZ,BEL,BLHA,BDEC,ISITE,RV)
C     BASE COMPUTES BASELINE COORDINATES BL=BASELINE
```

```
C         LENGTH IN KM, BLHA=HOUR ANGLE STATION 1 TO
C         STATION 2 , BDEC = DECLINATION
C     -----------
C     -----------
C     SLHA1, SOURCE LHA (HOURS) AT 0 HOURS UT AT ST.1 ON SAME DAY
C     DEC, SOURCE DEC IN DEGREES
C
C     -----------
C     HOURAN COMPUTES SOURCE LOCAL HOUR ANGLE (HOURS)
C         AT 0 HOURS UT AT STATION NO 1 ON SAME DAY (SLHA1)
      CALL HOURAN(SLHA1,STHR,RAH,RAHP,DECL,DECP,NYEAR,MONTH,NDAY,ISOUR,
     FNDAYOB,VEL,BCO,FREK,WLONG(1))
      DEC=DECP
      TIME=IHRS*3600+IMINS*60
      TIMEST=TIME+SECS
C     -----------
C     COMPUTE WEIGHTING FUNCTION
      GO TO (160,140), IWT
C     HANNING WEIGHTING FUNCTION
  140 DO 150 I=1,IPTR
      A=PHI*(2.*(I-1)/IPTR-1.)
  150 WT(I)=.5+.5*COS(A)
      GO TO 180
C     UNIFORM WEIGHTING FUNCTION
  160 DO 170 I=1,IPTR
  170 WT(I)=1.
  180 CONTINUE
C     -----------
C     FREQUENCY FORMULA FOR ST.NO 1 AND NO.2
      FREQ1=FREQ1*ILOM1+IMF1
      FREQ2=FREQ2*ILOM2+IMF2
      FOFF2=(FREQ1-FREQ2)*1000000.
C     -----------
C
  [illegible]0 PRINT 370,ITAPE1,ITAPE2,IFILE1,IFILE2
     F,ICV1,ICV2,IBW,INTEG,IPTR,IPTS,
     FIWT,DOP,DOPD,NDOP
  370 FORMAT('1',1X,24HDATA REDUCTION CONSTANTS,///,2X,6HITAPE1,I6,/,2X,
     F6HITAPE2,I6,/,2X,6HIFILE1,I6,/,2X,6HIFILE2,I6,/,
     F/,2X,
     F'BIT SELECTION ON TAPE1',I6,/,2X,'BIT SELECTION ON TAPE2'I6,/,
     F2X,3HIBW,I9,/,2X,5HINTEG,I7,/,2X,4HIPTR,I8,/,2X,4HIPTS,I8,/,2X,
     F3HIWT,I9,/,2X,3HDOP,F12.4,/,2X,4HDOPD,F12.4,/,2X,4HNDOP,I8)
C
      PRINT 372,ADELAY,IHRS,IMINS,SECS,I1ST,I2ST,SLHA1,DEC,FREQ1,FREQ2,
     FILOM1,ILOM2,IMF1,IMF2
  372 FORMAT(/,2X,6HADELAY,F9.2,/,2X,6HTIMEST,I6,I4,F7.2,/,2X,4HI1ST,I8,
     F/,2X,4HI2ST,I8,/,2X,5HSLHA1,F13.5,/,2X,3HDEC,F15.5,/,2X,5HFREQ1,
     FF15.7,/,2X,5HFREQ2,F15.7,/,2X,5HILOM1,I7,/,2X,5HILOM2,I7,/,2X,
     F'IMF1',F14.5/2X,'IMF2',F14.5)
      EPOCH=1950.0
C
      CALL DATE(NYEAR,NDAYOB,MONTH,NDAY,0)
      CALL HOURS(RAH,IRAH,IRAM,RAS,IRAS)
      CALL HOURS(RAHP,IRAHP,IRAMP,RASP,IRASP)
      CALL HOURS(BLHA,IBLHA,IBLHM,BLHS,IBLHS)
      CALL HOURS(STHR,ISTHR,ISTHM,STS)
C        PRINT THE MAIN PART OF THE HEADLINES.
      EPOCH1=NYEAR+NDAYOB/365.
      WRITE(3,900)    FREK,VEL,ISOUR,RAH,IRAH,IRAM,RAS,DECL,EPOCH,
     1                RAHP,IRAHP,IRAMP,RASP,DEC,EPOCH1,
     2                BL,BAZ,BEL,BLHA,IBLHA,IBLHM,BLHS,BDEC
  900 FORMAT('0',9X,'FREQUENCY:',F12.3,' MHZ'/10X,'VELOCITY:   ',F10.3,
```

```
    1' KM/S'//10X,20A4/10X,'RA:',F7.3,' HOURS ',I3,' H  ',I2,' M ',F5.1
    2,' S     DEC:',F7.3,' DEGREES    EPOCH:',F8.1/10X,'RA:',F7.3,' HOU
    3RS ',I3,' H  ',I2,' M ',F5.1,' S     DEC:',F7.3,' DEGREES    EPOCH
    4: ',F7.1///10X,'BASELINE:',F10.3,' KILOMETERS'/10X,'AZIMUTH: ',F10
    5.3,' DEG      ELEVATION:',F10.3,' DEG'/10X,'HA:',F7.3,' HOURS ',I3,
    6' H  ',I2,' M ',F5.1,' S',5X,'DEC:',F7.3,' DEGREES')
     WRITE(3,901) ISITE(1),ISITE(2),IMF1,IMF2,ILOM1,ILOM2
 901 FORMAT(10X,'LO-FORMULA ',A4,' TO ',A4/
    1       10X,'MF          ',2F8.3,'      MHZ'/
    2       10X,'MULT.FACTOR',2I3,/)
     WRITE(3,9011)  BCO
9011 FORMAT('0',9X,'THE OBSERVED FREQUENCY IS THE LINE FREQUENCY'/
    1           10X,'PLUS OR MINUS',F6.1,' KHZ DEPENING ON THE LO.'/
    2           10X,'IT IS MINUS IF THE LO IS BELOW THE LINE.'//)
     WRITE(3,9014) ISITE(1),ISTHR,ISTHM,STS
9014 FORMAT('0',9X,'SIDEREAL TIME AT ',A4,' IS:',I4,' H ',I4,' M ',F5.1
    F,' S'/10X,'AT UT: 00 H  00 M  00.0 S')
C
C     INPUT PARAMETERS ENTERED AND SETUP COMPLETED
C
C
C     ----------
C
C          IT IS POSSIBLE TO CHOOSE THE FIRST RECORD
C          TO BE PROCESSED BY FORWARDING THE TAPES
C          I1ST AND I2ST RECORDS
C        READT(ITAPE,IARR,INO1,INO2) IS AN ASSEMBLER
C        SUBROUTINE WHICH READS THE DATA FROM A TAPE.
C        ITAPE (1 OR 2) IS NUMBER OF TAPE TO READ  TAPE1 OR TAPE2 DD
C        IARR IS AN ARRAY TO WHICH DATA IS READ.
C        INO1 IS NUMBER OF BYTES THAT ARE TO BE READ FROM TAPE
C        INO2 IS NUMBER OF BYTES THAT ACTUALLY WERE READ.
C        IF PERMANENT I/O-ERROR OCCURS DURING READ INO2 CONTAINS TWO:S
C        COMPLEMENT OF READ NUMBER. INO2 = 0 INDICATES END OF FILE.
C        THE FOLLOWING ABENDS MAY OCCUR
C        U0001   OPEN FAILED FOR TAPE1 (POSSIBLY NO DD-CARD)
C        U0002   SAME FOR TAPE2
C        U0003   READT WAS CALLED WITH ITAPE NEITHER 1 NOR 2
C        U0004   READT WAS CALLED WITH INO1 NEGATIVE
C        U0005   READT WAS CALLED WITH INO1 > 32767
C        U0011   READ WAS ATTEMPTED AFTER EOF ON TAPE1
C        U0012   READ WAS ATTEMPTED AFTER EOF ON TAPE2
C     SRATE, SAMPLING RATE IN BITS PER SECOND
     SRATE=12000.*IBAND(IBW)
C    ILEN1, ILEN2  RECORD LENGTH ON INPUT TAPES
     ILEN1=ICV1*0.195*SRATE/8-1
     ILEN2=ICV2*0.195*SRATE/8-1
     IST=I1ST-1
     IF(IST.EQ.0) GO TO 4200
     DO 420 I=1,IST
     IREC1=IREC1+1
 420 CALL READT(1,I1ARR,ILEN1,IOUT1)
4200 IST=I2ST-1
     IF(IST.EQ.0) GO TO 4300
     DO 430 I=1,IST
     IREC2=IREC2+1
 430 CALL READT(2,I2ARR,ILEN2,IOUT2)
C
4300 CALL READT(1,I1ARR,ILEN1,IOUT1)
     IREC1=IREC1+1
 406 CALL READT(2,I2ARR,ILEN2,IOUT2)
     IREC2=IREC2+1
     IF (IOUT1) 4311,4321,4331
```

```
 4311 PRINT 4310,IREC1
 4310 FORMAT(1X,' I/O ERROR ON TAPE NO 1, ON RECORD NO ',I6)
      GO TO 790
 4321 PRINT 4320,IREC1
 4320 FORMAT(1X,' END OF FILE ON TAPE NO.1',I6,' RECORDS OUT')
      IF((IREC1-I1ST).EQ.0) GO TO 1232
      GO TO 830
C          CHECK IF THE RECORD IS SHORTER THAN ILEN1
 4331 IF (ILEN1.EQ.IOUT1) GO TO 4312
      PRINT 401,IREC1,IOUT1
  401 FORMAT (1X,23HERROR ON ST.NO.1,RECORD,I6,17H  NO OF BYTES OUT,I6)
      GO TO 790
 4312 IF (IOUT2) 4011,4021,4031
 4011 PRINT 4010,IREC2
 4010 FORMAT(1X,' I/O ERROR ON TAPE NO 2, ON RECORD NO ',I6)
      GO TO 790
 4021 PRINT 4020,IREC2
 4020 FORMAT(1X,' END OF FILE ON TAPE NO.2',I6,' RECORDS OUT')
      IF((IREC2-I2ST).EQ.0) GO TO 1232
      GO TO 830
C          CHECK IF THE RECORD IS SHORTER THAN ILEN2
 4031 IF (ILEN2.EQ.IOUT2) GO TO 405
      PRINT 402, IREC2,IOUT2
  402 FORMAT(1X,23HERROR ON ST.NO.2,RECORD,I6,17H  NO OF BYTES OUT,I6)
      GO TO 790
  405 GO TO (403,403,403,404),ICV1
  404 CALL CONV4(IOBS1,I1ARR,ILEN1)
      IN1=ILEN1/4
      GO TO 407
  403 IN1=ILEN1
  407 GO TO (408,408,408,409),ICV2
  409 CALL CONV4(IOBS2,I2ARR,ILEN2)
      IN2=ILEN2/4
      GO TO 421
  408 IN2=ILEN2
C     IACUM, ACCUMULATED RECORD COUNT
  421 IACUM=IACUM+1
C     THE FIRST RECORD TO BE USED ARE READ AND REDUNDANT BITS EXTRACTED
C     ------------------------
C     ------------------------
  440 CONTINUE
C
      XNTX=INTX
      NWDOU=IN1/4
C     IWORDS, WORDS PER RECORD SEGMENT
      IWORDS=NWDOU/XNTX
      IWORD1=IWORDS
      IWORD2=IWORDS
      IF(IN1-IN2)4401,4402,4401
 4401 PRINT 4403
 4403 FORMAT(1X,'RECORDLENGTH NOT EQUAL ON BOTH TAPES')
      GO TO 830
 4402 CONTINUE
C     USE SIDERIAL SECONDS IN COMPUTING LOCAL HOUR ANGLE AT ST.1
C     86164.09=UTC SECONDS PER SIDERIAL DAY
      TIME=TIMEST+(IREC1-I1ST)*.2
      SLHA=SLHA1/24.+TIME/86164.09
C
C     DEBUG PRINTOUT IS INCLUDED FOR JSWTCH(5) RECORDS
      IF (IREC1.GT.(I1ST+JSWTCH(5)-1)) GO TO 480
      PRINT 460,TIME
  460 FORMAT (1H1,16HSTATION 1 RECORD,F10.3,10H   SECONDS,///)
      PRINT 470, (IOBS1(I),I=1,NWDOU)
```

```
  470 FORMAT (2X,10Z12)
  480  CONTINUE
      IF (IREC2.GT.(I2ST+JSWTCH(5)-1)) GO TO 510
  490 PRINT 500, IREC2
  500 FORMAT (1H1,23HSTATION 2 RECORD NUMBER,I8,///)
      PRINT 470, (IOBS2(I),I=1,NWDOU)
      PRINT 571
  571 FORMAT('1')
  510 CONTINUE
C
C           COMPUTE GEOMETRICAL DELAY, FRINGE RATE, TOTAL DELAY
C           INCLUDING THE INSTRUMENTAL DELAY, ISHIFT= INTEGRAL
C           BIT SHIFT CORRESPONDING TO TOTAL DELAY, AND APFRAT=
C           THE APPARENT FRINGE RATE (FOFF2 IS THE LO-OFFSET AT
C           ST.NO 1 TO SLOW DOWN THE FRINGE RATE)
      CALL FRINGE (SLHA*2.*PHI,DEC*PRD,BL,BLHA*PRH,BDEC*PRD,
     FFREQ1,FRATE,DELAY,SX,SY)
C      GEOMETRIC PHASE OF SIGNAL AT ST.2 W/R TO ST.1
      PHASE=2.*3.1415926535*DELAY*FREQ1
C      ISHIFT, INTEGRAL BIT SHIFT CORRESPONDING TO TOTAL DELAY
C
      ASHIFT=-(DELAY+ADELAY)*(SRATE/1000000.)
  540 ISHIFT=ASHIFT+SIGN(0.5,ASHIFT)
C
      APFRAT=FRATE-FOFF2
      IF (ABS(APFRAT)-XNTX) 570,550,550
  550 PRINT 560, APFRAT
  560 FORMAT (1X,29HAPPARENT FRINGE RATE TOO HIGH,F10.2)
      GO TO 1241
C      EACH RECORD IS BROKEN INTO INTX SEGMENTS OF .2/INTX SECONDS
C      HENCE APPARENT FRINGE RATES UP TO ABOUT XNTX CAN BE HANDLED.
C
C
  570 CONTINUE
       IF (JSWTCH(9).EQ.1) GO TO 630
C      ----------
C      THE COSINE AND SINE SIGNALS FOR THE PHASE DETECTION OF
C      THE CORR.FUNCTION ARE COMPUTED
C      THE PHASE FORMULA IS
C           2*PHI*(FREQ1*DELAY -(FOFF2 + DOPFQ(L))*TIME))
      LR=0
      DO 630 L=1,NDOP
      LR=LR+1
      DOPFQ(L)=(L-NDOP/2-1)*DOPD+DOP
C      FROT, TOTAL CONSTANT OFFSET FREQUENCY
      FROT=-FOFF2+DOPFQ(L)
C      PH, TOTAL PHASE, ASSUMING PHASE OF FROT IS ZERO AT TIME=ZERO
      PH=PHASE+2.*3.1415926535*FROT*TIME
C      DELPH, TOTAL PHASE INCREMENT IN RAD. PER RECORD SEGMENT
      DELPH=(FRATE+FROT)*PHI*2.*IWORDS*IBPW/SRATE
      PHD=PH/(2.*PHI)
      IHEL=PHD
      PHD=PH-IHEL*(2.*PHI)
      PHE=PHD
      CX=COS(DELPH)
      SX=SIN(DELPH)
      C=COS(PHE)
      S=SIN(PHE)
      DO 580 I=1,INTX
      COSPH(I,L)=C
      SINPH(I,L)=S
      ST=S
      S=S*CX+C*SX
```

```
  580 C=C*CX-ST*SX
C
C     ----------
C     ----------
      IF (IREC1.GT.(I1ST+JSWTCH(5)-1)) GO TO 630
C
C     PRINTOUT OF TABLES FOR EACH DOPPLER INCREMENT AND RECORD
C     SEGMENT
  590 PRINT 586,DOPFQ(L)
  586 FORMAT(//,' COSPH(I) I=1,INTX   DOPFQ=',F7.3)
C
      PRINT 600,  (COSPH(I,L),I=1,INTX)
  600  FORMAT (1X,10F10.4)
C
      PRINT 587,DOPFQ(L)
  587 FORMAT('0','SINPH(I) I=1,INTX    DOPFQ=',F7.3)
C
      PRINT 600, ((SINPH(I,L),I=1,INTX))
C
       PRINT 588
  588 FORMAT('0',12X,5HDELPH,9X,5HPHASE,14X,2HPH,17X,4HFROT,13X,5HDOPFQ,
     F10X,5HFRATE,17X,5HFOFF2)
C
      PRINT 610,DELPH,PHASE,PH,FROT,DOPFQ(L),FRATE,FOFF2
  610 FORMAT (1X,7F17.4,///)
  620 CONTINUE
      IF(LR.EQ.5) PRINT 635
  635 FORMAT('1')
      IF(LR.EQ.5) LR=1
C     ----------
  630 CONTINUE
      SLHOUR=SLHA*24.
      IHOURS=TIME/3600.
      IMIN=(TIME-IHOURS*3600.)/60.
      SEC=(TIME-IHOURS*3600.-IMIN*60.)
C
C     ----------
C     ----------
C     COMPUTE ABSOLUTE DELAY AND DO CROSSCORRELATION
C     CORREL IS THE SUBROUTINE WHICH TAKES THE BIT STRINGS FROM EACH
C     TAPE AND CROSSCORRELATE THEM. IT MUST BE GIVEN A POSITIVE BIT
C     SHIFT HENCE IT IS SOMETIMES NECESSARY TO SHIFT ONE WORD STRING.
C     THE CORREL. FUNCTION IS STORED IN ICORR, ISTART IS THE BIT NUMBER
C     IN IST1 WHICH IS MULTIPLIED WITH THE FIRST BIT OF IST2. ISTOP-
C     ISTART IS THE NUMBER OF DELAYS. LAST ARGUMENT IS THE NUMBER OF
C     WORDS CORRELATED.
C     CORRL ARITHMETIC IS  1X1=0X0=1, 1X0=0X1=0
C
C
C     MSHIFT, NUMBER OF WORDS THAT ST.1 RECORD IS SHIFTED FORWARD
      MSHIFT=0
C     ISTART. THE NUMBER OF THE BIT IN A ST.1 RECORD WITH RESPECT TO THE
C     L'TH WORD IN IT WHICH GETS MULTIPLIED WITH THE FIRST BIT OF L'TH
C     OR LL'TH WORD OF THE ST.2 RECORD DEPENDING ON WHETHER OR NOT
C     MSHIFT=0
      ISTART=ISHIFT-IPTR/2
      ISTOP=ISHIFT+IPTR/2
C
C     IF ISTART IS NEGATIVE I.E. IF SIGNAL ARRIVES AT ST.1 LATER THAN AT
C     ST.2 THEN ST.1 RECORD IS EFFECTIVELY SHIFTED FORWARD BY MSHIFT
C     WORDS
      IF (ISTART) 650,660,660
  650 MSHIFT=-ISTART/IBPW+1
```

```
      ISTART=ISTART+MSHIFT*IBPW
      ISTOP=ISTOP+MSHIFT*IBPW
  660 CONTINUE
      DO 770 I=1,INTX
C
C     FRACTIONAL BIT SHIFT ACCUMULATED FOR EACH RECORD SEGMENT
      DSHIFT=DSHIFT+(ASHIFT-ISHIFT)
C
C     WORD INDEX RELATED TO RECORD SEGMENT INDEX
      L=(I-1)*IWORDS+1
      LL=L+MSHIFT
      IF((LL-1+IWORDS)*IBPW-(IN1/4)*IBPW) 661,661,7700
 7700 IWORD2=IN2/4-LL
  661 IF((L-1+IWORDS)*IBPW+ISTOP -(IN1/4)*IBPW) 680,680,7701
 7701 IWORD1=IN1/4-L-ISTOP/IBPW
      IWORDS=MIN0(IWORD1,IWORD2)
      IF(IWORDS.LE.0) GO TO 770
C
  680 CALL CORREL (ICORR,ISTART,ISTOP,IOBS2(LL),IOBS1(L),IWORDS)
C
C     NBITS, NUMBER OF BITS IN A RECORD SEGMENT, EQUALS TWICE STATISTICAL
C     AVARAGE OF ICORR(J) FOR UNCORRELATED DATA
C
      NBITS=IWORDS*IBPW
C
C     IWRITE, NUMBER OF RECORD SEGMENT PROCESSED
      IWRITE=IWRITE+1
C
C
      IXT=NBITS/2
      XT=IXT
      DO 7101 J=1,IPTR
 7101 CORR(J)=(ICORR(J)-IXT)/XT
      IF (JSWTCH(8).NE.1) GO TO 7103
      WRITE(6,7104) IWRITE,DSHIFT
 7104 FORMAT(I4,F11.7)
      WRITE (6,7102) (CORR(J),J=1,IPTR)
 7102 FORMAT(8F9.6)
C     CORRELATION FUNCTION STORED ON TAPE
 7103 CONTINUE
      DO 710 J=1,IPTR
      DO 710 JJ=1,NDOP
      RSIN(J,JJ)=RSIN(J,JJ)+CORR(J)*SINPH(I,JJ)
  710 RCOS(J,JJ)=RCOS(J,JJ)+CORR(J)*COSPH(I,JJ)
C     ----------
C
      IF (IREC1.GT.(I1ST+JSWTCH(5)-1)) GO TO 770
C
C
      PRINT 730,L
  730 FORMAT ('1',28HCROSSCORRELATION FUNCTION,L=,I6/)
      PRINT 740, (ICORR(KJ),KJ=1,IPTR)
  740 FORMAT (2X,10I12)
C
      PRINT 741
  741 FORMAT(//,' RSIN(IPTR,NDOP) ',/)
      WRITE(3,760) ((RSIN(K,M), M=1,NDOP),K=1,IPTR)
  760 FORMAT(9F14.5)
      PRINT 742
  742 FORMAT(//,' RCOS(IPTR,NDOP) ',/)
      WRITE(3,761) ((RCOS(K,M), M=1,NDOP),K=1,IPTR)
  761 FORMAT(9F14.5)
  770 CONTINUE
```

```
      IF (IACUM.GT.1) GO  TO 771
      PRINT 772
  772 FORMAT(1H1)
      PRINT 725,MSHIFT,ISTART,ISTOP,IPTR,ISHIFT
  725 FORMAT(//,'    MSHIFT    ISTART     ISTOP     IPTR    ISHIFT'/1X
     F,5I10/)
      PRINT 612
  612 FORMAT (1X,   ' IACUM IREC1     TIME          PHASE      FRINGE RATE
     F      DELAY    LHA     OBS1(1)  OBS2(1)   RECORDLENGTH   SHIFT
     F    APF',/)
  771 CONTINUE
C
C     IMPORTANT PARAMETERS FOR EACH RECORD ARE PRINTED OUT.
      PRINT 640,IACUM,IREC1,TIME           ,PHASE,FRATE,DELAY,SLHOUR ,
     FIOBS1(1),IOBS2(1),NWDOU,ISHIFT,APFRAT
  640 FORMAT(3X,2I4,4X,F8.2,2X,F13.2, F10.2,F14.2,F10.4,2X,Z8,Z10,
     F3X,I8,3X,I8,F13.6)
C
C     ----------
  780 IF (INTEG.EQ.IACUM) GO TO 830
  790 CONTINUE
C     READ MORE DATA AND SELECT BITS
      GO TO 4300
C
  830 CONTINUE
      IF (JSWTCH(9).EQ.1) GO TO  1232
C     ENTER TRANSFORM PART OF PROGRAM
C     COMPLEX FOURIER TRANSFORM FOR SPECTRAL DATA
C     SHIFT, AVERAGE FRACTIONAL BIT SHIFT
C
 8310 SHIFT=DSHIFT/IWRITE
C     IP, CENTER OF CORRELATION FUNCTION
      IP=IPTR/2+1
C     COHERENT AVERAGING
C     SPECTRA ARE NORMALIZED INSTEAD OF CORRELATION FUNCTIONS SO THAT
C     THE LATTER CAN BE ACCUMULATED
C     NORMALIZATION FACTOR IS IWRITE, THE NUMBER OF RECORD SEGMENT
C     ACCUMULATED. PHI/2 IS DUE TO ONE-BIT CORRELATION
      ANORM=PHI/(2.*IWRITE)
      DO 1120 I=1,NOOP
  832 PRINT 954
  954 FORMAT(1H1)
C     SPECTRUM PLOT HEADING
      PRINT 956, DOPFQ(I),I,IWRITE
  956 FORMAT(/,F10.3,2I8)
      PRINT 970
  970 FORMAT(///,20X,25HSINE CORRELATION FUNCTION,// )
      PRINT 980,(RSIN(K,I),K=1,IPTR)
  980 FORMAT(5X,10F10.5)
      PRINT 990
  990 FORMAT  (///,20X,27HCOSINE CORRELATION FUNCTION,//)
      PRINT 980,(RCOS(K,I),K=1,IPTR)
C
      DO 991 K=1,IPTR
  991 TREAL(K)=SQRT(RSIN(K,I)**2+RCOS(K,I)**2)
      PRINT 992
  992 FORMAT(///,20X,'CORRELATION FUNCTION',//)
      PRINT 980,(TREAL(K),K=1,IPTR)
      PRINT 1000
 1000 FORMAT (///,20X,18HWEIGHTING FUNCTION,//)
      PRINT 980, (WT(K),K=1,IPTR)
C
C     DO COMPLEX FOURIER TRANSFORM ON COMPLEX CORRELATION FUNCTIONS
```

```
1001 CALL CPXFOU (RCOS(1,I),RSIN(1,I),IPTR,TREAL,TIMAG,IPTS,-1,IP,
    F1,WT)
     DO 1040 K=1,IPTS
     TREAL(K)=TREAL(K)*ANORM
     TIMAG(K)=TIMAG(K)*ANORM
     FAMP(K)=SQRT(TREAL(K)**2+TIMAG(K)**2)
     IF (TREAL(K).EQ.0.) TREAL(K)=1.
     ANG=ATAN2(TIMAG(K),TREAL(K))
C
C    KEEP FRINGE PHASE BETWEEN 180 AND -180 DEGREES AND COMPENSATE FOR
C    FRACTIONAL BIT SHIFT
     FASE(K)=ANG/PRD-180.*(K-1)*SHIFT/IPTS
C
     IF (FASE(K)-180.) 1020,1020,1010
1010 FASE(K)=FASE(K)-360.
     GO TO 1040
1020 IF (FASE(K)+180.) 1030,1040,1040
1030 FASE(K)=FASE(K)+360.
1040 CONTINUE
C    ------------------------
C    ------------------------
C    SPECTRUM PRESENTATION
     IF(JSWTCH(6)) 1141,1141,1142
1141 PRINT 1050
1050 FORMAT(///,20X,'FRINGE AMPLITUDE',//)
     PRINT 980,(FAMP(K),K=1,IPTS)
     PRINT 1060
1060 FORMAT(///,20X,'FRINGE PHASE',//)
     PRINT 980,(FASE(K),K=1,IPTS)
     GO TO 1120
1142 CALL PLOT2V(FAMP,FASE,IPTS,TMAX(JSWTCH(2)))
1120 CONTINUE
C    ------------------------
C    ------------------------
     IACUM=0
     JSWTCH(4)=JSWTCH(4)-1
     IF (JSWTCH(4).LE.0) GO TO 1191
     PRINT 1180
1180 FORMAT (1H1,10HACCUMULATE,//)
     GO TO 790
C
1191 JSWTCH(3)=JSWTCH(3)-1
     IF (JSWTCH(3).EQ.0) GO TO 1232
     PRINT 1250
1250 FORMAT(1H1,18HCLEAR AND CONTINUE)
     DO 1231 I=1,180
     DO 1231 J=1,21
     RSIN(I,J)=0.
1231 RCOS(I,J)=0.
     IACUM=0
     IWRITE=0
     SSHIFT=0.
     GO TO 790
1232 PRINT 1240
1240 FORMAT('1',' T H E      E N D      ')
     STOP
     END
```

REFERENCES

Adgie, R.L., Gent, H., Slee, O.B., Frost, A.D., Palmer, H.P., Rowson, B., New Limits to the Angular Sizes of Some Quasars, Nature, 208, 275, (1965).

Bare, C., Clark, B.G., Kellermann, K.I., Cohen, M.H., Jauncey, D.L., Science, 157, 189 (1967).

Born, M., Wolf, E., Principles of Optics, Pergamon Press, New York, N.Y. 1959.

Bracewell, R.N., Radio Interferometry of Discrete Sources, Proc. IRE, 47, 97 (1958).

Broten, N.W., Legg, T.H., Locke, J.L., Mc Leish, C.W., Richards, R.S., Chisholm, R.M., Gush, H.P., Yen, J.L., Galt, J.A., Science, 156, 189 (1967).

Burns, W.R., Yao, S.S., Clipping loss in the one-bit autocorrelation spectral line receiver, Radio Science, 4, 431 (1969).

Drane, C.J., Parrent G.B., On the Mapping of Extended Sources with Nonlinear Correlation Antennas, IRE Trans. AP-10, 126 (1962).

Goldstein, B.M., A Technique for the Measurement of the Power Spectra of Very Weak Signals, IRE Trans. SET-8, 170, (1962).

Kellerman, K.I., Clark, B.G., Bare, C.C., Rydbeck, O., Ellder, J., Hansson, B., Kollberg, E., Höglund, B., Cohen, M.H., Jauncey, D.L., High-resolution Interferometry of Small Radio Sources Using Intercontinental Base Line, Ap.J. (letters), 153, L209 (1968).

Kellermann, K.I., Jauncey, D.L., Cohen, M.H., Shaffer, D.B., Clark, B.G., Broderick, J., Rönnäng, B.O., Rydbeck, O.E.H., Matveyenko, L., Moiseyev, I., Vitkevitch, V.V., Cooper, B.F.C., Batchelor, R., High Resolution Observation of Compact Radio Sources at 6 and 18 cm, Ap.J., in press, (1971).

Kollberg, E.L., Rutile Traveling-Wave Maser System for the Frequency Range 1.3 - 6.2 GHz and Radio Astronomy Applications, Dr. Thesis, Chalmers University of Technology, Gothenburg, Sweden, (1970).

Landgren, P.G., Rönnäng, B.O., An Astronomical Computer Program Package for the Onsala Space Observatory, Research Report 102, Research Lab. of Electronics, Chalmers Univ. of Technology, Gothenburg, Sweden (1971).

Mac Phie, R.H., On the Mapping by a Cross-Correlation Antenna System of Partially Coherent Radio Sources, IEEE Trans. AP-12, 118 (1964).

Mc Cready, L.L., Pawsey, J.L., Payne-Scott, R., Solar radio radiation and its relation to sunspots, Proc. Roy. Soc. A., 190, 357, (1947).

Moran, J.M., Burke, B.F., Barret, A.H., Rydbeck, O.E.H., Hansson, B., Rogers, A.E.E., Ball, J.A., Cudaback, D.D., Long Baseline OH Interferometry, Ap. J., (Supplement), No.5, Part II, 73, (1968).

Moran, J.M., Burke, B.F., Barret, A.H., Rogers, A.E.E., Ball, J.A., Carter, J.C., Cudaback, D.D., The structure of the OH source in W 3, Ap. J. Letters, 152, L 97, (1968).

Moran, J.M., Interferometric Observations of Galactic OH Emission, Dr Thesis, MIT, (1968)

Pakos, P.E., Use of the Loran-C system for time and frequency dissemination, Freq. Tech., 7, 12, (1969).

Rodemich, E.R., Spectral Estimates Using Nonlinear Functions, Ann. Math. Statist., 37 (5), (1962).

Rönnäng, B.O., Rydbeck, O.E.H., Moran, J.M., Very long baseline interferometry of galactic OH sources, Radio Science, 5, 1227, (1970).

Rydbeck, O.E.H., Kollberg, E., Rutile Traveling Wave Maser System for the Onsala 84 foot Radio Telescope, IEEE Trans. MTT-16, 799, (1968).

Shapiro, L.D., Fisher, D.O., Using Loran-C transmissions for long baseline synchronization, Radio Science, 5, 1233, (1970).

Swenson, G.W., Mathur, N.C., The Interferometer in Radio Astronomy, Proc. IEEE, 56, 2114 (1968).

The Astronomical Ephemeris, Her Majesty's Stationery Office, London (1970).

Van Vleck, J.H., Middleton, D., The Spectrum of Clipped Noise, Proc. IEEE, 54, 2, (1966).

Weinreb, S., A Digital Spectral Analysis Technique and its Application to Radio Astronomy, MIT Research Lab. of Electronics, Cambridge, Mass., Tech.Report 412, (1963).

Research Reports from the Research Laboratory of Electronics:

1. O.E.H. Rydbeck and K.H.B. Wilhelmsson: The influence of the electron velocity distribution on space charge waves. 1959.

2. K.H.B. Wilhelmsson: Oscillatory properties of gyromagnetic electronic cold plasmas with drift motion. 1959.

3. H.B.Hvatum: Solar radio noise measurements during the 1954 solar eclipse. 1959.

4. T.Aa. Orhaug: Ionospheric observations during the solar eclipse June 30, 1954. 1959.

5. K.H.B. Wilhelmsson: The electromagnetic coupling between an electron beam and incident plane waves for an axially finite interaction domain. 1960.

6. Research notes communicated at the radio scientific conference in Stockholm, February 29 - March 2, 1960. 1960.

7. O.E.H. Rydbeck: The propagation and coupling of waves in inhomogeneous media with applications to electromagnetic and space charge waves. (On the propagation of waves in an inhomogeneous medium II).

8. O.E.H. Rydbeck: Electromagnetic and space charge waves in inhomogeneous structures with applica - tions to ionized media and microwave tubes. 1960.

9. K.H.B. Wilhelmsson: On the geometrical theory of diffraction with application to the electron beam. 1960.

10. O.E.H. Rydbeck: The Doppler effect in dispersive, inhomogeneous media with applications to electromagnetic waves in ionized media. 1960.

11. S. Olving and A. Ots: An experimental investigation of the propagation of space charge waves along radially inhomogeneous electron beams. 1960.

12. A.V.Stomberg: The rotatron-an electron tube for shift and multiplication of frequencies. 1960.

13. O.E.H. Rydbeck and M.R.Fischer: Space charge waves in an electron beam of Gaussian cross section. 1960.

14. O.E.H. Rydbeck: The integral equation of traveling wave tubes with electron beams of arbitrary cross section. 1960.

15. O.E.H. Rydbeck and A.R. Thomasson: Low frequency waves in inhomogeneous magneto ionic media. 1960.

16. T.Aa.Orhaug: Observations of radio star scintillations at high latitudes. 1960.

17. T.Aa. Orhaug: Observations of solar radio noise at 150 Mc/s. 1960.

18. O.E.H. Rydbeck and J. Askne: Whistler mode - ionized stream interactions. Part I, 1963.

19. K.H.B. Wilhelmsson: On the problem of overtaking in a velocity distributed electron stream. 1960.

20. O.E.H. Rydbeck: On the coupling between waves in inhomogeneous systems. 1960.

21. O.E.H. Rydbeck: Research in the field of propagation and interaction of electromagnetic waves and space charge type waves in homogeneous and inhomogeneous media. 1960.

22. D.T. Farley, J.P. Dougherty and D.W. Barron: A theory of incoherent scattering of radio waves by a plasma in a uniform magnetic field. 1961.

23. L.F. Eastman: Coherent non-linearities in a magneto-ionic medium. 1961.

24. D.T. Farley: Artificial heating of the electrons in the F-region of the ionosphere. 1961.

25. K.H.B. Wilhelmsson: Scattering of electromagnetic waves by an anisotropic medium. 1961.

26. K.H.B. Wilhelmsson: The interaction between an obliquely incident plane electromagnetic wave and an electron beam in the presence of a static magnetic field of arbitrary strength. 1961.

27. O.E.H. Rydbeck: Dynamic non-linear wave propagation in ionized media. 1. The isotropic medium. 1961.

28. O.E.H. Rydbeck: Dynamic non-linear wave propagation in ionized media. 2. The magneto-ionic medium. 1962.

29. O.E.H.Rydbeck: Dynamic non-linear wave propagation in ionized media. 3. Electromagnetic non-linear wave interaction and reflection from a plane ionized medium. 1963.

30. O.E.H.Rydbeck: Dynamic non-linear wave propagation in ionized media. 4. Non-linear electromagnetic wave propagation and harmonic radiation in magneto-ionic media. 1963.

31. K.H.B.Wilhelmsson: Dynamic non-linear wave propagation in ionized media. 5.Reflection of electromagnetic waves from an ionized stream in the presence of a high power primary wave. 1962.

32. K.H.B.Wilhelmsson: Dynamic non-linear wave propagation in ionized media. 6. Scattering of electromagnetic waves by an anisotropic medium with an harmonically time-varying dielectric tensor. 1962.

33. O.E.H.Rydbeck: Dynamic non-linear wave propagation in ionized media. 7. Non-linear plasma waves in a streaming homogeneous, cold ionized medium. 1962.

34. A.R.Thomasson: Dynamic non-linear wave propagation in ionized media. 8. Reflection of electromagnetic waves from a dielectric plane layer varying periodically in space and time. 1962.

35. K.H.B.Wilhelmsson: Dynamic non-linear wave propagation in ionized media. 9. A non-linear coupling mechanism for generation of very low frequency waves. 1963.

36. K.H.B.Wilhelmsson: Dynamic non-linear wave propagation in ionized media. 10. Non-linear interaction between an obliquely incident plane electromagnetic wave and an electron beam. 1963.

37. S.Olving: On the non-linear theory of the plane travelling wave tube. 1963.

38. K-O.Yngvesson: Observations of the Venus probe Mariner R-2 at the Onsala Space Observatory. 1963.

39. K.H.B.Wilhelmsson: Dynamic non-linear wave propagation in ionized media. 11. Non-linear excitation of hydromagnetic waves and hybrid resonances by two interacting high power primary waves. 1963.

40. S.Olving and O.Nilsson: Propagation of non-linear Hahn-Ramo waves along an annular electron current-sheath. 1963.

41. S.Olving and M.Fischer: Small-signal nonlinear klystron waves. 1964.

42. S.Olving and S.Wallander: Non-linear space charge wave theory of the hydrodynamic disc-electron beam. 1964.

43. O.E.H.Rydbeck: Dynamic non-linear wave propagation in ionized media. 12. Electromagnetic wave reflection from an oscillating, collision free magneto-ionic medium. 1964.

44. A.R.Thomasson: Dynamic non-linear wave propagation in ionized media. 13. Microscopic treatment of the interaction between a plane electromagnetic wave and an oscillating medium. 1964.

45. K.H.B.Wilhelmsson: Dynamic non-linear wave propagation in ionized media. 14. Generation of longitudinal plasma waves by non-linear coupling of two high-power circularly polarized transverse waves. 1964.

46. K.H.B.Wilhelmsson and A.R.Thomasson: Dynamic non-linear wave propagation in ionized media. 15. Čerenkov effect in a pre-oscillating medium. 1964.

47. K.H.B.Wilhelmsson: The magneto-ionic theory for mass-anisotropic electrons. 1964.

48. O.E.H.Rydbeck: Research in the field of propagation of high power waves in ionized media. 1964.

49. R.Tengblad: Concentration effects in a maser material. 1964.

50. O.Nilsson: Some frequency and power conversion proper ties of cyclotron waves. 1965.

51. O.Nilsson: Anomalous noise peak in Adler tubes. 1965.

52. B.Geidne: Non-linear analysis of a microwave beamplasma amplifier. 1965.

53. J.Askne: Stimulated scattering from a semi-infinite dispersive medium periodic in time and space. 1965.

54. S. Yngvesson: Chromium-doped rutile: Maser properties at 1420 Mc/s and application to a traveling-wave maser, 1965.

55. T.M.Srinivasan: Measurements on nonlinear space charge waves. 1965.

56. O.E.H. Rydbeck: Wave coupling in multi-mode, inhomogeneous, ionized media, with applications to electron stream-whistler mode interactions. 1966.

57. P.McIsaac: Wave propagation in a dispersive medium. 1966.

58. S.Wallander: Nonlinear theory of the planar microwave vacuum diode. 1966.

59. S.Wallander: Nonlinear traveling wave tube analysis with two signal frequencies. 1966.

60. O.Nilsson: Approximate theory of the wire helix slow wave structure. 1966.

61. O.E.H.Rydbeck:and Å.Hjalmarson: Coupled wave equations for multi-mode inhomogeneous media. 1966.

62. O.E.H.Rydbeck: and Å.Hjalmarson: Coupled waves in magneto-ionic media. Part I. 1966.

63. J,Askne: Reflection and amplification of electromagnetic waves in an oscillating ionized medium. Part. I. 1966.

64. J.Askne: Instability properties of an ionized medium periodic in time and space. B.Rönnäng: Transient wave propagation in symmetric, ionized Epstein layers. 1966.

65. J.I.Lindström: Measurements of nonlinearities in a traveling wave tube. 1966.

66. J.Jäderblom: Cyclotron wave amplification using self generated pump power.1966.

67. O.Nilsson: Nonlinear distortion in traveling wave tubes 1965.

68. S.Kronlund: Measurements on a beam-plasma microwave amplifier. 1966.

69. P.R.McIsaac: Boundary conditions for ferromagnetic media. 1966.

70. B.O.Rönnäng: Transient wave propagation in inhomogeneous ionized media. 1966.

71. S.Olving: Nonlinear microwave tube studies. 1966.

72. E.L.Kollberg: A dielectrically loaded slow-wave structure for traveling-wave maser applications. 1966.

73. B.O.Rönnäng: Signal distortion in anisotropic homogeneous ionized media. 1967.

74. A.Winnberg: The structure of galactic neutral hydrogen in a region of Cygnus. 1967.

75. Å.Hjalmarson: Coupled Wave Equations for Multi-Mode Inhomogeneous Media. II. 1967.

76. D. Barkley: Elastic Analysis of the Cornea. 1967.

77. S.Wallander: Large Signal Analytical Theory of Klystron Waves. 1967.

78. S.Wallander: Large Signal Computer Analysis of Klystron Waves. 1967.

79. O.E.H. Rydbeck: Energy Flow in Multi-Mode Systems, 1967.

80. J.Askne: Reflection and Amplification of Electromagnetic Waves in an Oscillating Ionized Medium. Part II. 1967.

81. L.Hansson: Measurements of the Pointing Error for the Automatic Steering System of the Chalmers 84 Foot Radio Telescope. 1967.

82. E.A.Harris & K.S.Yngvesson: Spin-Lattice Relaxation in Some Iridium Salts, Part I, 1:25, 1968.

83. E.A.Harris & K.S.Yngvesson: Spin-Lattice Relaxation in Some Iridium Salts, Part II, 1:26,1968.

84. K.S.Yngvesson: Maser Properties of Cr - TiO_2 at L-and S-Band and Their Interpretation in Terms of Crystal Field and Exchange-Coupled Cluster Relaxation Processes, 1968.

85. I.Ewaldz: Observations of the 189 (966 MHz) Excited Hydrogen Line in Orion A and M 17 . 1968.

86. J.I.Lindström & O.Nilsson: Crossmodulation in Traveling Wave Tubes, 1968.

87. J.Elldér : OH Spectral Line Measurements of Radiation from the Galactic H II Regions W 3 and W 49 at 1665 MHz, 1968.

88. O.E.H.Rydbeck: Multi-Mode Wave Coupling in Inhomogeneous, Anisotropic Media - with Some Magneto-Ionic Applications, 1968.

89. O.E.H.Rydbeck and E.L.Kollberg: Rutile Traveling Wave Masers for the Frequency Range 1300 - 3400 MHz and their Application to the Onsala 84 foot Radio Telescope to Galactic Spectral Line Emission Studies, 1968.

90. Jumpol Prompitaks: The performance of a $LiNbO_3$ light modulator at 1.6 GHz, 1968.

91. J.Askne: Energy Considerations and Coupled Mode Analysis. 1969.

92. S.Wallander: Large Signal Computer Analysis of distortion in Traveling Wave Tubes, 1969.

93. S.Wallander: Nonlinear Multi-Signal Traveling Wave Tube Theory, 1969.

94. J.Askne: Reflection and amplification of electromagnetic Waves in an Oscillating Ionized Medium. Part III. Wave Propagation in a bounded time-space periodic plasma medium. 1969.

95. E.L.Kollberg: Measurments at noise in maser systems, theory and experiments. 1969.

96. J.Elldér: Some OH and Formaldehyde Properties of W 3 and W 51 Regions. 1970.

97. O.E.H.Rydbeck et al: Exited State OH Emissions From W 75 B and W 3, OH. 1970.

98. E.L.Kollberg: Rutile Traveling Wave Maser Systems for the Micro wave range 1.3-6.2 GHz. 1970.

99. P.Ingvarson: The Diffraction of an Electromagnetic Wave by Sound. 1970.

100. O.E.H.Rydbeck, B.Rönnäng and J.M.Moran: Very Long Interferometry of Galactic OH Sources. 1970

101.

102. P.G.Landgren and B.O.Rönnang: An astronomical computer program package for Onsala Space Observatory. 1971.

103. E.Kollberg , C.O.Lindström: A Traveling-Wave Maser for the Frequency Range 960 - 1170 MHz. 1971

104. G.P.R. Metzler: A System for Automatic time synchronization based on the timing capability of the Loran-C navigational network. 1971

118

THE ASTROPHYSICAL JOURNAL, 169:1–24, 1971 October 1

Tp

HIGH-RESOLUTION OBSERVATIONS OF COMPACT RADIO SOURCES AT 6 AND 18 CENTIMETERS

K. I. KELLERMANN
National Radio Astronomy Observatory,* Green Bank, West Virginia, and Owens Valley Radio Observatory,† California Institute of Technology, Pasadena, California

D. L. JAUNCEY‡
Cornell-Sydney University Astronomy Center,§ Cornell University, Ithaca, New York

M. H. COHEN AND B. B. SHAFFER
Owens Valley Radio Observatory,† California Institute of Technology, Pasadena, California

B. G. CLARK AND J. BRODERICK
National Radio Astronomy Observatory,* Green Bank, West Virginia

B. RÖNNÄNG AND O. E. H. RYDBECK
Onsala Space Observatory,# Chalmers Institute of Technology, Gothenburg, Sweden

L. MATVEYENKO
Institute for Space Research, Moscow, U.S.S.R.

I. MOISEYEV
Crimean Astrophysical Observatory, Crimea, U.S.S.R.

V. V. VITKEVITCH
Lebedev Physical Institute, Moscow, U.S.S.R.

AND

B. F. C. COOPER AND R. BATCHELOR
CSIRO Radiophysics Laboratory, Epping, N.S.W., Australia
Received 1971 April 26

ABSTRACT

The small-scale structure of extragalactic radio sources has been studied at 18 and 6 cm wavelengths by using a tape-recording interferometer. At the longest antenna spacing, 10536 km, the baseline at 6 cm was 176 million wavelengths and the resolution was about 0".0004 for the stronger sources.

Many sources, including optically identified galaxies and QSOs, are found to have several distinct components of widely differing size in the range from a few hundredths of a second of arc to the limit of our resolution. In general, the smallest components are strongest at the shortest wavelengths, and the dimensions are in good agreement with those expected if the low-frequency cutoffs are due to synchrotron self-absorption. The magnetic field strengths deduced from our observations and the self-absorption cutoff frequency are typically of the order of 10^{-4} gauss. The maximum brightness temperatures observed are 10^{11}°–10^{12}° K.

Many sources, including 0106+01, 3C 273, 3C 279, 1555+00, 2145+06, 3C 446, 3C 454.3, and 2345−16 all contain components which are unresolved on the longest baseline and are less than 0".0004

* Operated by Associated Universities, Inc., under contract with the National Science Foundation.

† Supported by ONR contract N 00014-67-A-0094-0008.

‡ Supported by NSF grant GP 13950.

§ Supported by NSF grant GP 4262.

‖ Supported by AFOSR grant AFOSR-69-1684.

Supported jointly by the Swedish National Science Research Council and the Swedish Council for Applied Research.

in diameter. Observations at shorter wavelengths are required to resolve these sources. Because the maximum brightness temperature is limited to 10^{12} °K by inverse Compton scattering, baselines no greater than the diameter of the Earth are probably adequate to resolve all of the stronger extragalactic sources.

One source, 3C 84, has shown an apparent increase in angular size of about 35 percent in one year.

I. INTRODUCTION

We have previously reported long-baseline interferometer measurements of compact extragalactic radio sources made near 50, 18, 13, 6, and 3 cm wavelengths with resolutions up to about 0".001 (Clark *et al.* 1968*a*, *b*; Kellermann *et al.* 1968, 1970; Jauncey *et al.* 1970; Broderick *et al.* 1970*a*, *b*). These experiments have shown that angular structure exists in many QSOs and radio galaxies on scales of one thousandth to a few hundredths of an arc second.

This paper presents data obtained in two series of observations made in 1967 April at 18 cm between Lincoln Laboratory in Massachusetts and Green Bank, West Virginia, and during 1969 at 18 and 6 cm using stations in Green Bank and California in the United States, and in Sweden, Australia, and the U.S.S.R. The highest resolution obtained was between Owens Valley, California, and Parkes, Australia, at 6 cm where the baseline was 10536 km or 176 million wavelengths long. Sources larger than 4×10^{-4} arc seconds were resolved on this baseline, which is greater than 80 percent of the Earth's diameter.

The new data have been combined with the previously published material to determine in more detail the small-scale radio structure over a wide range of wavelength, and also to estimate, where possible, the spectra of the individual components within the compact sources. The sources studied include identified QSOs and radio galaxies as well as some unidentified sources.

The observational details are described in § II of this paper. The observed fringe visibilities are tabulated in § III, and the structure of the individual sources is given in § IV. The observations of variable sources are described in § V, and all the results are discussed further in § VI.

II. OBSERVATIONS

All of the observations were made by using the digital tape-recording system developed at the National Radio Astronomy Observatory (Bare *et al.* 1967). Three of these units are in operation. One of the units was used in Green Bank while a second one has been used in Sweden, the Soviet Union, and Australia. The third unit was used at the Lincoln Laboratory and at the Owens Valley Radio Observatory.

A description of the instrumentation, and of the observing and reduction procedures, has been given previously (Clark *et al.* 1968*a*). Standard computer-tape drives were used at each station to record digitally with one-bit samples the signal in a 330-kHz band. Atomic frequency standards were used to synchronize the data recording and to provide a coherent local oscillator signal at each station. Hydrogen masers were used at Green Bank and Lincoln Laboratory as time and frequency standards, while portable rubidium vapor standards were used at all of the other locations (and on a few occasions at Green Bank).

Initial clock synchronization was achieved by receiving the time signals from one or more Loran C navigational stations or by direct comparison with a clock which had previously been compared with the master clock at the U.S. Naval Observatory. In the latter case, the Loran signals or WWVL were still used whenever possible to monitor the time.

The local oscillator frequency at each antenna was derived by using the atomic frequency standard to control a frequency synthesizer. The output of the synthesizer was then amplified and multiplied to 18 cm. For operation at 6 cm, the 18-cm signal was further multiplied in the front end box. Two different arrangements were used. At Green Bank, a Hewlett Packard Model 5105A synthesizer was operated near 272 MHz, multiplied by 6, and amplified. This is the standard local oscillator system commonly in use at NRAO for spectral-line observations, except that the frequency synthesizer was controlled by an atomic standard. At the other stations a Rhode and Schwartz XUC synthesizer was operated at 820 MHz, amplified, and multiplied by 2. For operation at 18 cm (1670 MHz) the local oscillator frequency was 1640 MHz, and a 30-MHz intermediate frequency was used. For operation at 6 cm (5010 MHz), a multiplier was used to obtain a local oscillator signal at 4860 or 4980 MHz, and the intermediate frequency was either 150 or 30 MHz. In the former case a second local oscillator at 120 MHz, also locked to the atomic standard, was then used to convert to 30 MHz. The 30-MHz intermediate-frequency signal in both cases was then converted in two stages to the range 20–350 kHz, clipped, and sampled at a 720-kHz rate.

Observations were made by using various combinations of stations as shown in Table 1. Where possible, the data were obtained over a range of hour angles to vary the length and direction of the projected baseline. On the longer baselines, however, the requirement of common visibility at reasonable elevations required the observations at the lower declinations to be made only near the interferometer meridian. Most of the observations were made by using only two stations simultaneously, although a three-station experiment was carried out between Green Bank, Owens Valley, and Onsala at 6 cm (1969 January-February).

On each of the baselines we generally observed for from one to three days. Typically we ran from 75 to 100 tape pairs each day at intervals of about 15 minutes, often recording two tapes in succession on each source. Each tape is sufficient to record about 3 minutes of data. For each series of observations, the starting time of each tape was scheduled in advance, although from time to time technical difficulties required minor last-minute modifications to the schedule. Communication between observing sites was usually done by telephone or by teletype machines. Commercial telegraph facilities were also used between the U.S.S.R. and Green Bank.

The observations are summarized in Table 1, which lists all of the baselines which

TABLE 1

INTERFEROMETER BASELINES

Baseline* (1)	λ (cm) (2)	Separation (km) (3)	Separation ($10^6\lambda$) (4)	Dates (5)
GB–HSK, GB–MS	18	845	4.7	1967 July and August, 1968 April
GB–HC	18	3500	19.4	1967 August
GB–ONS	18	6319	35.1	1968 January I, 1969 April II
GB–ONS	6	6319	105	1968 February I, 1969 January II
GB–OVRO	6	3324	55.5	1969 January, March, April, May
OVRO–ONS	6	7914	132	1969 February
OVRO–PKS	6	10536	176	1969 April
GB–CAO	6	8035	134	1969 October

* GB = Green Bank; HSK = Haystack; MS = Millstone; HC = Hat Creek; ONS = Onsala; OVRO = Owens Valley Radio Observatory; PKS = Parkes; CAO = Crimean Astrophysical Observatory.

gave results. Not listed are attempted observations made between Green Bank and Parkes at 6 and 18 cm, and between Parkes and OVRO at 18 cm. Column (1) identifies the two stations, column (2) gives the wavelength, column (3) the antenna separation in kilometers, column (4) the baseline length in wavelengths, and column (5) the dates of the observations. For completeness Table 1 includes the earlier measurements at 6 and 18 cm which have already been published.

a) Instrumentation

The instrumentation used at each station is described below.

i) *Green Bank (GB)*

The observations at Green Bank were made by using the 140-foot (42 m) antenna. The 18-cm receiver used a room-temperature nondegenerate parametric amplifier as the first stage with an overall system noise temperature near 200° K. At 6 cm a two-stage nondegenerate cooled parametric amplifier was used, giving a system temperature of about 110° K.

As a local oscillator reference and time standard, we used either a Varian H-10 hydrogen maser on loan from the NASA Goddard Space Flight Center or a Hewlett Packard HP 5065 rubidium vapor standard.

Time at Green Bank was established by receiving the Loran C transmissions from the station at Cape Fear in North Carolina, which was monitored throughout each observing period.

ii) *Lincoln Laboratory, Haystack (HSK) and Millstone (MS)*

The early 18-cm observations from Lincoln Laboratory were made by using the 120-foot (37 m) Haystack antenna (Clark *et al.* 1968*a*). The new observations were made in 1967 April using the 84-foot (25.6 m) Millstone Hill reflector. A room-temperature nondegenerate parametric amplifier was used, to give an overall system noise temperature of 200° K. As a time and frequency standard, we used the Lincoln Laboratory hydrogen maser which is kept in continuous operation. In addition, the time was checked by monitoring the Loran transmission from Cape Fear, North Carolina.

iii) *Owens Valley Radio Observatory (OVRO)*

The observations at OVRO used the 130-foot (40 m) antenna. Nondegenerate room-temperature parametric amplifiers were used as the first stage at both 6 and 18 cm with overall system noise of 150° and 250° K, respectively. Time was established by comparing a portable rubidium-controlled clock with clocks at the Timing Center at Point Mugu, California, or at the NASA Deep Space Network Station at Goldstone, California, both of which had been directly compared with the U.S. Naval Observatory clock.

iv) *Parkes, Australia (PKS)*

The observations from Australia were made by using the 210-foot (65 m) antenna at the Australian National Radio Astronomy Observatory near Parkes. The 6-cm receiver was a portable unit constructed at the NRAO especially for used at remote sites and gave a system temperature of 130° K. This receiver, including parametric amplifier, mixer, radiofrequency amplifier, power supplies, and multiplier for the local oscillator chain, was housed in a small temperature-controlled box that was mounted directly at the focus.

Time in Australia was synchronized with the time in Owens Valley via the NASA tracking stations at Tidbinbilla, Australia, and Goldstone, California. The tracking stations themselves were synchronized to an accuracy of a few microseconds by the transmission of a radar signal from Goldstone to Tidbinbilla via the Moon.

v) *Onsala Space Observatory, Sweden (ONS)*

The observations from Sweden were made by using the 84-foot (25.6 m) telescope at the Onsala Space Observatory near Gothenburg. Both the 6 and 18 cm receivers used a rutile traveling-wave maser as a low-noise preamplifier, and the total system noise temperature was less than 50° K at both wavelengths. Maser amplifiers are particularly suitable for long-baseline interferometry where the bandwidths and integration times are restricted by available recording facilities so that the lowest-noise receivers are important. The use of the maser preamplifier at 6 cm during the 1969 observations improved the sensitivity by a factor of about 2.5 over that obtained in the earlier observations (Kellermann *et al.* 1968).

Time in Sweden was obtained from a cesium clock located at the Research Institute for National Defense in Stockholm. The cesium clock in Stockholm had been previously compared with the U.S. Naval Observatory master clock via a flying clock experiment conducted by the USNO. The time at Onsala was further checked by monitoring the Loran C transmission from the Ejde station of the Norwegian Sea chain.

vi) *Crimean Astrophysical Observatory, U.S.S.R. (CAO)*

The observations from the U.S.S.R. were made by using the 22-m precision radio telescope of the Crimean Astrophysical Observatory located near Simeis. The 6-cm portable receiver used at Parkes was also used on the Crimean telescope.

Synchronization of time between Green Bank and Crimea was achieved by flying the Onsala rubidium clock from Stockholm, Sweden, to Crimea via Leningrad. The time in Crimea was monitored by receiving the Loran C transmission from the Mediterranean Sea chain station in Turkey, which had been synchronized to the U.S. Naval Observatory master clock in Washington immediately prior to our experiment. A preliminary account of this experiment has already been published (Broderick *et al.* 1970*a*, *b*).

b) Data Analysis

The natural interference-fringe rate varied from several hundred hertz to several kilohertz on the longer baselines. Since the fringe-reduction program averaged the data for a period of 0.4 ms, only fringe rates less than a few hundred hertz could be analyzed. During the first few series of observations, the frequency of the local oscillator at one station was offset by a small amount to reduce the fringe frequency to a few hertz. This procedure proved inconvenient for two reasons. First, it was necessary to calculate in advance the local oscillator settings, so that it was difficult to make last-minute modifications to the program. Second, it was necessary to change the synthesizer frequency often, and this provided many opportunities for operator error.

For some of the later observations, therefore, we kept the local oscillator frequencies fixed at both ends of the baseline, so that the interference fringes were at their natural rate, and the fringe-reduction program was modified to multiply the data by a square wave of the expected fringe frequency, before multiplying the two data sets together.

The analysis of the tape pairs was done with the NRAO IBM 360/50, the Caltech 360/75, or the 360/91 at the Goddard Space Flight Center. Typically, a range of fringe frequency of ± 0.3 Hz and a delay range of ± 5 μs were searched. The reduction took about 70, 10, and 5 minutes, respectively, in the three machines for a single 3-minute tape pair.

In general, somewhat less than one-half of the tape pairs showed fringes. In some cases the absence of fringes is no doubt due to the resolution of the source. Sometimes, however, when several pairs of tapes were run on the same source at similar hour angles, one or more pairs did not show fringes. Usually, but not always, when fringes were seen, the amplitudes of separate pairs agreed within the limits of error expected from the interferometer sensitivity. The reasons for the absence of fringes on some tape pairs, or discrepancies between pairs, are not fully understood, although some cases may be explained by possible operator error in setting the synthesizer frequency, in pointing the antenna, errors in the data sampling, or by instabilities in the atomic frequency standard.

We have therefore rejected all tape pairs which did not show fringes. This procedure, however, results in a systematic overestimate of fringe amplitude for those sources near the limit of detection.

c) Calibration of Fringe Amplitudes

One of the major uncertainties in interpreting the data is the difficulty in calibrating the interferometer sensitivity, particularly at the longer baselines where there are no sources which *a priori* are known to be unresolved. Furthermore, the different baselines give little or no overlap in the (u, v)-plane, and the flux density of the sources may vary between the observing periods, so that even the calibration of the relative fringe amplitudes among the different baselines is often difficult.

The calibration of the Millstone–Green Bank baseline at 18 cm is straightforward and is based on the sources CTA 102 and CTD 93, which previous measurements (Kellermann *et al.* 1968) indicated should be unresolved on this baseline. The Green Bank–Owens Valley baseline at 18 cm was calibrated by using 3C 279, which had been previously observed over a similar baseline (Clark *et al.* 1968*b*).

At 6 cm the calibration is less direct. The sensitivity of the different baselines was roughly estimated from knowledge of the gain and system temperature of the individual antenna systems which, unfortunately, were not always accurately measured. In this way four sources, 0106+01, 4C 39.25, 1555+00, and 2145+06 were found to have components which were essentially unresolved out to the longest spacing at which they were observed. The strongest of these, 4C 39.25, is not visible from Parkes and thus could be observed only out to 135 million wavelengths. At least two of these four sources were observed on each baseline at 6 cm and were used to tie together the data from different baselines. Moreover, there were a number of other sources common to the three sets of Green Bank–OVRO observations that could be used to normalize these observations. Fortunately, these sources showed little variation in total flux density during the time of the observations.

The scale of fringe amplitude was determined by estimating the unresolved flux density of the above four sources from consideration of their spectra and from previous observations at 13 cm made with comparable resolution.

Since the fringe visibility cannot exceed unity, we estimate that the results in Tables 2 and 3 are not systematically low by more than 15 percent, and we believe that they are not too high by more than 20 percent.

In addition to the calibration uncertainty described above, other errors in the quoted fringe visibilities are due to receiver noise; and to uncertainties in the determination of the total system temperature and in the antenna temperature of each source. Errors in the latter were introduced by uncertainties in the pointing of the individual antennas and to uncertainties in the gain changes caused by structural deformations at the extreme hour angles where many of the observations were made. Since unswitched total power receivers were used for most of these observations, it was difficult to measure accurately the antenna temperature of each source or to check the pointing.

III. FRINGE AMPLITUDES

The results of all the observations are shown in Table 2 for the 18-cm data and in Table 3 for the 6-cm data.

In both tables, column (1) gives the source name; column (2) the total flux density at the time of observation, column (3) the observed fringe amplitude, and columns (4) and

TABLE 2

18-CENTIMETER VISIBILITIES

Source (1)	S_t (2)	S_c (3)	d (4)	θ (5)	γ (6)	Baseline (7)
0019−00	2.6	2.2±1.0	3.1	62	0.85±0.39	GB-MS
		2.1±1.0	4.2	51	0.81±0.39	GB-MS
NRAO 91	3.3	2.4±1.0	3.5	74	0.73±0.30	GB-MS
		2.1±0.8	4.0	48	0.64±0.23	GB-HSK
		1.8±1.0	4.7	63	0.55±0.30	GB-MS
CTA 21	7.0	6.2±1.1	3.4	29	0.89±0.16	GB-HSK
		5.7±1.1	3.5	33	0.82±0.16	GB-MS
		5.7±0.9	4.0	71	0.82±0.12	GB-HSK
		5.9±0.9	4.6	61	0.84±0.12	GB-HSK
		4.9±0.9	4.7	62	0.70±0.12	GB-HSK
		2.6±1.0	15.2	81	0.37±0.14	GB-HC
		1.6±0.4	34.0	77	0.23±0.06	GB-ONS I
3C 84	11.0	5.9±1.1	1.5	146	0.54±0.10	GB-MS
		5.8±1.1	2.0	124	0.53±0.10	GB-MS
		6.2±1.1	2.4	66	0.56±0.10	GB-MS
		5.4±1.1	4.0	84	0.49±0.10	GB-MS
		3.1±1.0	4.3	171	0.28±0.09	GB-HSK
		4.8±1.1	4.7	55	0.44±0.09	GB-MS
		4.1±1.0	4.7	58	0.37±0.09	GB-HSK
		1.8±0.4	33.2	128	0.16±0.04	GB-ONS II
		2.0±0.4	34.3	142	0.18±0.04	GB-ONS II
NRAO 140	3.2	3.5±0.9	4.3	75	1.10±0.28	GB-HSK
		2.9±0.9	4.1	160	0.91±0.28	GB-HSK
NRAO 150	4.0	3.7±0.9	4.5	176	0.93±0.22	GB-HSK
3C 119	7.5	2.1±1.0	1.4	139	0.28±0.13	GB-MS
		2.9±1.0	2.0	125	0.39±0.13	GB-MS
		2.9±1.0	2.5	110	0.39±0.13	GB-MS
		4.1±1.0	4.1	81	0.55±0.13	GB-MS
		3.4±0.9	4.3	3	0.45±0.12	GB-HSK
		1.4±0.9	17.4	79	0.19±0.12	GB-OVRO
0420−01	2.1	1.0±0.9	9.1	89	0.76±0.45	GB-OVRO
0428+20	3.0	2.8±1.1	4.6	58	0.93±0.37	GB-MS
3C 120	4.0	2.6±0.8	2.4	165	0.65±0.20	GB-HSK
	4.0	3.7±1.0	3.9	55	0.92±0.25	GB-HSK
	7.0	3.0±0.9	7.6	76	0.42±0.13	GB-OVRO
	7.0	2.8±0.9	10.8	78	0.40±0.13	GB-OVRO
	6.0	1.9±0.4	34.0	74	0.31±0.06	GB-ONS I
3C 138	8.5	1.6±1.0	2.0	68	0.19±0.12	GB-MS
NRAO 190	4.0	4.2±1.0	4.2	62	1.05±0.24	GB-MS
		4.2±1.0	4.2	62	1.05±0.24	GB-MS
		3.4±1.0	4.6	65	0.81±0.24	GB-MS
		2.3±0.9	9.2	88	0.55±0.22	GB-OVRO
		2.2±0.9	14.7	88	0.53±0.22	GB-OVRO
3C 147	20	5.1±1.1	2.1	152	0.25±0.05	GB-MS
		4.0±0.8	2.6	128	0.20±0.04	GB-HSK
		3.2±0.8	3.2	106	0.16±0.04	GB-HSK
		3.7±1.0	4.0	88	0.18±0.05	GB-MS
		1.8±1.0	4.1	85	0.09±0.05	GB-MS
		2.4±1.0	4.2	83	0.12±0.05	GB-MS
		2.5±1.0	4.2	82	0.13±0.05	GB-MS
		4.2±0.9	4.5	178	0.21±0.04	GB-HSK
0607−15	2.2	1.3±1.0	4.7	26	0.60±0.45	GB-MS
0742+10	3.7	4.3±1.0	4.0	50	1.16±0.27	GB-MS
		2.5±0.9	7.2	60	0.67±0.24	GB-OVRO
		2.2±0.9	14.3	78	0.59±0.24	GB-OVRO
0834−20	3.3	3.9±1.0	1.5	73	1.18±0.30	GB-MS
		3.0±1.0	1.5	73	0.91±0.30	GB-MS
		2.9±1.0	3.0	75	0.88±0.30	GB-MS
		1.4±0.9	13.2	70	0.42±0.27	GB-OVRO

TABLE 2—*Continued*

Source (1)	S_t (2)	S_c (3)	d (4)	θ (5)	γ (6)	Baseline (7)
4C 39.25	3.0	1.8±0.9	15.3	52	0.60±0.30	GB-OVRO
		1.2±0.9	17.2	69	0.40±0.30	GB-OVRO
		1.1±0.9	16.1	60	0.37±0.30	GB-OVRO
1055+01	3.2	2.4±0.8	3.1	47	0.75±0.25	GB-HSK
		1.7±1.0	3.7	59	0.53±0.31	GB-MS
		1.1±1.0	4.5	65	0.34±0.31	GB-MS
		1.5±0.9	8.3	83	0.47±0.28	GB-OVRO
1127−14	6.4	7.3±1.2	4.2	69	1.14±0.19	GB-HSK
		4.2±1.0	12.1	104	0.66±0.16	GB-OVRO
		4.0±1.0	13.5	73	0.63±0.16	GB-OVRO
		3.7±0.8	19.5	94	0.58±0.13	GB-HC
		2.4±0.5	35.0	73	0.38±0.08	GB-ONS
1148−00	3.2	3.3±0.8	3.4	55	1.03±0.25	GB-HSK
		3.4±0.8	4.6	65	1.06±0.25	GB-HSK
		1.5±0.9	8.3	83	0.47±0.27	G3-OVRO
		1.7±0.9	13.5	86	0.53±0.27	GB-OVRO
(3C 273)	29	29.0±3.3	2.2	19	1.00±0.10	GB-MS
		24.5±2.6	2.6	36	0.85±0.09	GB-HSK
		22.7±2.5	3.9	58	0.78±0.09	GB-HSK
		20.0±2.2	4.2	61	0.69±0.08	GB-HSK
		18.8±2.1	4.2	63	0.65±0.07	GB-HSK
		18.5±2.1	4.3	62	0.64±0.07	GB-HSK
		20.5±2.2	4.5	64	0.71±0.08	GB-HSK
		21.4±2.3	4.5	65	0.74±0.08	GB-MS
		16.8±1.9	4.6	65	0.58±0.07	GB-HSK
		18.8±2.1	4.7	65	0.65±0.07	GB-HSK
		15.6±1.8	8.3	103	0.54±0.06	GB-HC
		8.6±1.4	10.3	83	0.30±0.05	GB-OVRO
		13.0±1.6	13.4	92	0.45±0.06	GB-HC
		13.9±1.7	19.3	94	0.48±0.06	GB-HC
		14.5±1.8	19.3	94	0.50±0.06	GB-HC
		10.0±2.0	27.0	74	0.35±0.07	GB-ONS I
		8.4±1.7	34.0	77	0.29±0.06	GB-ONS I
3C 279	11	9.0±1.1	3.8	64	0.82±0.10	GB-HSK
		7.6±1.1	4.3	65	0.69±0.10	GB-HSK
		8.9±1.1	4.5	66	0.81±0.10	GB-HSK
		6.6±1.1	4.7	65	0.60±0.10	GB-HSK
		5.0±1.0	9.7	87	0.45±0.09	GB-HC
		5.5±1.0	14.3	100	0.50±0.09	GB-HC
		5.5±1.1	17.5	90	0.50±0.10	GB-OVRO
		3.6±1.0	19.4	93	0.33±0.09	GB-HC
		5.7±1.0	19.5	93	0.52±0.09	GB-HC
		5.7±1.2	28.2	74	0.52±0.11	GB-ONS I
		6.3±1.3	34.4	77	0.57±0.12	GB-ONS I
1245−19	4.4	4.3±1.0	1.4	71	0.98±0.23	GB-MS II
3C 287	6.2	3.6±1.0	1.7	86	0.58±0.16	GB-MS II
		1.9±1.0	3.0	81	0.31±0.16	GB-MS II
		2.4±0.8	4.5	50	0.39±0.13	GB-HSK
		2.7±0.8	4.6	53	0.44±0.13	GB-HSK
		2.7±0.8	4.7	65	0.44±0.13	GB-HSK
3C 286	13.5	10.2±1.3	1.8	170	0.75±0.10	GB-HSK
		4.3±0.8	3.7	9	0.32±0.06	GB-HSK
		5.4±0.9	4.2	141	0.40±0.07	GB-HSK
		3.4±0.8	4.6	53	0.25±0.06	GB-HSK
		3.8±0.8	4.7	64	0.28±0.06	GB-HSK
3C 309.1	7.5	7.0±1.3	4.3	60	0.93±0.17	GB-HSK
		1.2±0.9	18.5	79	0.19±0.12	GB-OVRO
DA 406	3.2	1.6±0.9	16.6	66	0.50±0.28	GB-OVRO
1510−08	3.3	3.1±0.8	4.5	63	0.94±0.24	GB-HSK
		3.0±1.0	16.0	93	0.91±0.30	GB-OVRO

TABLE 2—*Continued*

Source (1)	S_T (2)	S_c (3)	d (4)	θ (5)	γ (6)	Baseline (7)
4C 05.64	2.5	1.3±0.9	15.8	85	0.52±0.36	GB-OVRO
		1.8±0.9	16.8	86	0.72±0.36	GB-OVRO
1555+00	1.6	1.2±0.9	15.0	86	0.75±0.56	GB-OVRO
		1.7±0.9	16.6	66	1.06±0.56	GB-OVRO
CTD 93	4.2	3.4±1.1	2.1	74	0.81±0.26	GB-MS
		3.9±1.1	4.0	30	0.93±0.26	GB-MS
		3.5±1.1	4.7	51	0.83±0.26	GB-MS
		1.6±0.4	35.0	69	0.38±0.09	GB-ONS I
3C 345	6.1	4.9±1.1	2.5	107	0.80±0.18	GB-MS
	6.1	3.9±1.1	4.5	70	0.64±0.18	GB-MS
	6.5	5.3±0.9	4.7	63	0.81±0.14	GB-HSK
	6.5	1.6±0.4	34.3	80	0.25±0.06	GB-ONS I
NRAO 530	5.2	4.7±0.9	4.7	64	0.91±0.17	GB-HSK
		1.9±0.9	18.0	87	0.37±0.17	GB-OVRO
3C 380	13.0	4.7±1.1	2.1	147	0.36±0.09	GB-MS
		3.0±0.8	4.0	86	0.23±0.06	GB-HSK
		3.9±0.9	14.7	21	0.22±0.07	GB-OVRO
3C 418	5.2	3.7±0.8	3.1	115	0.71±0.15	GB-HSK
		3.7±0.8	4.6	20	0.71±0.15	GB-HSK
2127+04	3.7	4.8±0.9	4.7	65	1.29±0.24	GB-HSK
		1.3±0.9	15.0	82	0.35±0.24	GB-OVRO
2145+06	3.0	1.7±0.9	14.4	82	0.57±0.30	GB-OVRO
VRO 42.22.01	6.4	4.7±1.0	3.6	78	0.75±0.16	GB-MS
2203−18	6.1	3.5±1.0	1.2	64	0.57±0.16	GB-MS
		2.5±0.8	2.1	72	0.41±0.13	GB-HSK
		2.2±1.0	2.7	74	0.36±0.16	GB-MS
CTA 102	6.4	6.1±1.0	2.9	18	0.96±0.16	GB-HSK
		6.1±1.0	3.2	33	0.96±0.16	GB-HSK
		6.6±1.2	4.7	66	1.03±0.19	GB-MS
		5.5±1.0	10.7	78	0.86±0.16	GB-HSK
		3.9±0.9	17.7	88	0.61±0.14	GB-HSK
		3.5±0.8	18.6	90	0.55±0.13	GB-HSK
		4.5±0.9	18.0	89	0.71±0.14	GB-OVRO
		3.5±0.7	34.8	74	0.55±0.13	GB-ONS I
3C 446	5.6	4.1±1.1	1.7	19	0.73±0.20	GB-MS
		1.9±1.0	2.0	64	0.34±0.18	GB-MS
		2.1±1.0	4.6	35	0.37±0.18	GB-MS
3C 454.3	12.8	9.4±1.4	2.6	69	0.73±0.11	GB-MS
		11.0±1.4	3.2	20	0.86±0.11	GB-HSK
		10.2±1.4	3.4	28	0.80±0.11	GB-HSK
		10.0±1.4	4.0	84	0.78±0.11	GB-HSK
		8.4±1.1	10.5	70	0.66±0.09	GB-HC
		2.6±0.8	17.8	86	0.20±0.06	GB-HC
		2.2±0.8	19.5	94	0.17±0.06	GB-HC
		4.0±0.8	34.6	73	0.31±0.06	GB-ONS I

(5) the spacing in millions of wavelengths and orientation of the projected baseline. Column (6) gives the fringe visibility γ, and column (7) the location of the ends of the baseline using the abbreviations shown in Table 1.

The errors in fringe amplitudes quoted in Tables 2 and 3 do not include the possible uncertainty in overall calibration. They do include the uncertainty due to noise fluctuations and an estimate of the errors introduced by changes in antenna gain, system temperature, and pointing. Because of the one-bit sampling, the fringe amplitudes are insensitive to changes in receiver gain.

Some of the fringe amplitudes do not greatly exceed the quoted errors, and it might

TABLE 3

6-CENTIMETER VISIBILITIES

Source (1)	S_t (2)	S_c (3)	d (4)	θ (5)	γ (6)	Baseline (7)
0106+01	2.4	2.7±1.0	23	83	1.12±0.42	GB-OVRO
	2.5	2.6±1.3	26	83	1.04±0.52	GB-OVRO
	2.5	2.3±1.3	55	89	0.92±0.52	GB-OVRO
	2.7	3.0±0.6	83	72	1.11±0.22	GB-ONS II
	2.7	3.2±0.6	105	77	1.18±0.22	GB-ONS II
	2.4	2.5±0.9	134	87	1.08±0.37	GB-CAO
	2.6	2.3±0.7	169	43	0.88±0.27	OVRO-PKS
	2.6	3.1±0.7	170	43	1.19±0.27	OVRO-PKS
CTA 21	3.1	1.4±1.0	58	31	0.45±0.32	GB-OVRO I
3C 84	22.0	14.2±1.6	37	157	0.65±0.07	GB-OVRO I
	22.0	12.2±1.7	38	6	0.56±0.08	GB-OVRO
	22.0	10.8±1.7	46	44	0.49±0.08	GB-OVRO
	22.0	8.6±1.6	51	65	0.39±0.07	GB-OVRO
	22.0	2.1±0.5	82	110	0.09±0.02	GB-ONS II
	19.7	6.4±2.2	84	0	0.32±0.11	GB-ONS I
	22.0	1.7±0.5	92	32	0.08±0.02	GB-ONS II
	22.0	2.0±0.5	97	93	0.09±0.02	OVRO-ONS
	22.0	4.0±0.7	127	90	0.18±0.03	OVRO-ONS
	22.0	5.9±0.7	135	85	0.27±0.03	GB-CAO
NRAO 140	2.5	2.1±1.2	41	50	0.84±0.48	GB-OVRO
CTA 26	2.3	2.1±0.5	83	75	0.91±0.21	GB-ONS II
	2.3	2.3±0.7	173	45	1.00±0.30	OVRO-PKS
NRAO 150	7.3	4.8±1.2	45	14	0.66±0.16	GB-OVRO
	7.3	2.0±0.5	99	35	0.27±0.07	GB-ONS II
	7.3	2.3±0.5	104	33	0.31±0.07	GB-ONS II
3C 120	8.5	4.4±1.2	28	78	0.52±0.14	GB-OVRO
	8.5	2.5±1.2	40	82	0.29±0.14	GB-OVRO
	9.0	6.2±2.1	67	74	0.68±0.23	GB-ONS I
	9.0	4.7±2.0	99	75	0.52±0.22	GB-ONS I
	10.0	1.7±0.5	104	76	0.17±0.05	GB-ONS II
0420−01	3.5	1.5±0.7	173	45	0.43±0.20	OVRO-PKS
NRAO 190	3.7	3.0±1.0	38	87	0.81±0.27	GB-OVRO
	3.2	1.7±0.7	168	44	0.53±0.21	OVRO-PKS
	3.2	1.9±0.7	170	44	0.59±0.21	OVRO-PKS
0605−08	2.7	2.5±0.5	96	79	0.92±0.18	GB-ONS II
	2.7	2.0±0.5	100	79	0.74±0.18	GB-ONS II
0607−15	3.0	1.6±1.0	36	106	0.53±0.33	GB-OVRO
0742+10	3.5	3.7±1.0	20	57	1.05±0.28	GB-OVRO
	3.5	2.4±0.7	68	55	0.68±0.20	GB-ONS
4C 39.25	8.2	8.8±1.4	42	43	1.07±0.17	GB-OVRO
	8.2	7.6±1.1	44	36	0.93±0.13	GB-OVRO
	8.2	5.1±1.4	45	66	0.62±0.17	GB-OVRO
	8.2	5.4±1.4	55	87	0.65±0.17	GB-OVRO
	8.1	7.2±0.9	83	175	0.88±0.12	GB-ONS II
	8.1	6.2±0.9	87	80	0.76±0.12	GB-ONS II
	7.6	6.5±1.5	95	72	0.80±0.18	GB-ONS I
	8.1	5.2±0.7	99	51	0.64±0.09	GB-ONS II
	8.1	7.0±0.7	102	79	0.86±0.09	GB-ONS II
	8.1	6.6±0.7	105	74	0.81±0.09	GB-ONS II
	8.2	6.0±0.8	119	95	0.73±0.10	OVRO-ONS
	8.2	6.8±0.8	119	97	0.83±0.10	OVRO-ONS
	8.6	7.0±0.8	134	89	0.81±0.09	GB-CAO
1055+01	2.5	1.6±0.5	89	74	0.64±0.20	GB-ONS II
	4.0	3.3±0.8	133	86	0.82±0.20	GB-CAO
	2.8	2.3±0.7	173	45	0.82±0.25	OVRO-PKS
	2.8	1.5±0.7	173	45	0.54±0.25	OVRO-PKS
1127−14	8.2	1.3±0.7	172	48	0.16±0.0	OVRO-PKS
	8.2	1.2±0.7	173	48	0.14±0.08	OVRO-PKS

TABLE 3—*Continued*

Source (1)	S_T (2)	S_c (3)	d (4)	θ (5)	γ (6)	Baseline (7)
3C 273*	32.0	25.5±2.5	24	81	0.80±0.08	GB-OVRO
	32.0	25.8±2.4	24	82	0.81±0.08	GB-OVRO
	32.0	24.6±2.5	30	83	0.77±0.08	GB-OVRO
	32.0	5.3±1.1	33	84	0.17±0.03	GB-OVRO
	32.0	15.3±2.0	43	86	0.48±0.06	GB-OVRO
	32.0	15.1±1.7	48	86	0.49±0.05	GB-OVRO
	32.0	14.8±2.0	49	86	0.46±0.06	GB-OVRO
	32.0	16.0±1.7	49	86	0.50±0.05	GB-OVRO
	32.0	17.0±1.7	51	87	0.53±0.05	GB-OVRO
	32.0	12.4±1.6	55	88	0.38±0.05	GB-OVRO
	30.0	9.8±2.2	74	68	0.33±0.07	GB-ONS I
	31.0	10.7±1.1	81	71	0.35±0.04	GB-ONS II
	31.0	8.3±1.1	85	71	0.27±0.04	GB-ONS II
	30.0	7.0±1.7	104	75	0.23±0.06	GB-ONS I
	34.0	7.0±1.0	124	87	0.21±0.03	GB-CAO
	34.0	9.2±1.1	128	86	0.27±0.03	GB-CAO
	31.0	6.0±1.0	132	79	0.19±0.03	OVRO-ONS
	34.0	10.9±1.2	133	86	0.32±0.03	GB-CAO
	34.0	8.7±1.1	133	86	0.29±0.03	GB-CAO
	32.0	7.4±0.9	172	43	0.23±0.03	OVRO-PKS
	32.0	6.9±0.9	172	43	0.22±0.03	OVRO-PKS
	32.0	6.2±0.9	172	45	0.19±0.03	OVRO-PKS
	32.0	3.3±0.8	175	45	0.10±0.03	OVRO-PKS
3C 279	16.5	15.1±1.7	27	84	0.92±0.10	GB-OVRO
	16.5	4.8±1.1	40	83	0.29±0.07	GB-OVRO
	16.5	16.8±1.8	45	92	1.02±0.11	GB-OVRO
	16.5	14.0±1.7	50	89	0.84±0.10	GB-OVRO
	16.5	13.4±1.8	51	90	0.81±0.11	GB-OVRO
	16.5	8.3±1.3	55	89	0.50±0.08	GB-OVRO
	15.4	5.9±1.6	102	75	0.38±0.10	GB-ONS I
	16.5	7.7±0.9	102	78	0.47±0.05	GB-ONS II
	16.5	4.6±1.0	129	80	0.28±0.06	OVRO-ONS
	16.5	4.2±1.0	130	80	0.25±0.06	OVRO-ONS
	16.5	6.3±1.0	133	86	0.38±0.06	GB-CAO
	16.5	7.1±1.0	134	87	0.43±0.06	GB-CAO
	16.5	5.4±1.0	134	86	0.32±0.06	GB-CAO
	16.5	4.2±0.8	164	45	0.25±0.05	OVRO-PKS
	16.5	4.8±0.8	164	45	0.29±0.05	OVRO-PKS
	16.5	4.9±0.8	168	46	0.30±0.05	OVRO-PKS
	16.5	4.7±0.8	170	46	0.28±0.05	OVRO-PKS
1510−08	2.4	2.0±1.2	55	89	0.83±0.50	GB-OVRO
	2.3	2.3±0.5	92	80	1.00±0.21	GB-ONS II
	2.7	3.2±0.8	134	86	1.18±0.30	GB-CAO
	2.7	3.4±0.8	134	86	1.25±0.29	GB-CAO
	2.3	1.5±0.7	173	57	0.65±0.30	OVRO-PKS
4C 05.64	2.6	1.6±0.5	104	76	0.62±0.19	GB-ONS II
1555+00	2.2	1.9±1.0	47	88	0.86±0.45	GB-OVRO
	2.2	2.8±1.0	51	88	1.27±0.45	GB-OVRO
	2.2	2.1±0.5	81	73	0.95±0.23	GB-ONS II
	2.2	2.5±0.5	104	77	1.13±0.23	GB-ONS II
	2.8	3.5±0.8	134	87	1.25±0.29	GB-CAO
	2.2	2.4±0.7	172	45	1.09±0.32	OVRO-PKS
	2.2	2.1±0.7	173	45	0.95±0.32	OVRO-PKS
	2.2	2.3±0.7	174	45	1.05±0.32	OVRO-PKS
DA 406	2.8	3.2±0.5	101	85	1.14±0.15	GB-ONS II
3C 345	7.9	8.3±1.4	37	13	1.1 ±0.2	GB-OVRO
	7.9	8.5±1.4	39	26	1.1 ±0.2	GB-OVRO
	7.9	5.5±1.3	47	55	0.70±0.16	GB-OVRO
	6.5	3.8±1.5	90	135	0.58±0.23	GB-ONS I
	7.9	6.1±0.7	95	45	0.77±0.08	GB-ONS II

* Exclusive of Component A.

TABLE 3—*Continued*

Source (1)	S_t (2)	S_c (3)	d (4)	θ (5)	γ (6)	Baseline (7)
3C 345 (*cont.*)	7.9	6.6±0.7	101	86	0.84±0.09	GB-ONS II
	7.9	5.2±0.6	105	68	0.66±0.09	GB-ONS II
	8.5	6.4±1.0	116	56	0.75±0.12	GB-CAO
	7.9	5.5±0.8	117	99	0.70±0.10	OVRO-ONS
	8.5	3.2±0.9	131	85	0.38±0.11	GB-CAO
	8.5	4.3±0.9	132	76	0.51±0.11	GB-CAO
NRAO 530	4.2	2.0±1.2	53	92	0.48±0.29	GB-OVRO
3C 380	7.2	2.9±1.2	46	36	0.39±0.17	GB-OVRO
	7.2	2.5±1.2	48	77	0.35±0.17	GB-OVRO
	7.2	2.7±1.2	53	69	0.38±0.17	GB-OVRO
2134+00	12.1	3.1±1.0	43	87	0.26±0.08	GB-OVRO
	12.1	3.3±1.0	52	88	0.27±0.08	GB-OVRO
	12.1	8.5±1.2	54	88	0.70±0.10	GB-OVRO
	12.1	4.5±2.2	95	86	0.37±0.18	GB-ONS I
	12.1	10.2±1.0	105	77	0.84±0.08	GB-ONS II
	12.1	6.6±0.9	131	79	0.55±0.07	OVRO-ONS
	12.1	8.7±1.3	134	87	0.72±0.11	GB-CAO
	12.1	3.4±1.1	134	87	0.28±0.10	GB-CAO
	12.1	2.9±0.7	174	45	0.24±0.06	OVRO-PKS
	12.1	2.8±0.7	175	46	0.23±0.06	OVRO-PKS
	12.1	2.7±0.7	175	46	0.22±0.06	OVRO-PKS
2145+06	4.6	3.5±1.1	37	85	0.76±0.24	GB-OVRO
	4.6	4.0±1.3	47	82	0.86±0.28	GB-OVRO
	4.6	6.7±1.4	53	90	1.46±0.30	GB-OVRO
	4.6	4.0±1.3	54	85	0.86±0.28	GB-OVRO
	4.6	3.1±0.5	97	73	0.67±0.11	GB-ONS II
	4.6	3.5±0.5	100	74	0.76±0.11	GB-ONS II
	4.6	3.5±0.7	169	41	0.76±0.15	OVRO-PKS
	4.6	3.6±0.7	171	43	0.78±0.15	OVRO-PKS
VRO 42.22.01	6.5	4.1±1.3	49	58	0.63±0.20	GB-OVRO
	6.5	4.7±1.0	127	89	0.72±0.15	OVRO-ONS
	6.5	6.7±1.1	132	77	1.03±0.17	GB-CAO
3C 446	4.5	2.1±1.3	49	58	0.47±0.29	GB-OVRO
	4.5	1.4±0.7	171	46	0.31±0.16	OVRO-PKS
	4.5	1.6±0.7	173	46	0.36±0.16	OVRO-PKS
3C 454.3	18.0	17.0±1.8	20	37	0.94±0.10	GB-OVRO
	18.0	14.1±1.7	27	55	0.78±0.09	GB-OVRO
	18.0	12.9±1.5	35	109	0.72±0.08	GB-OVRO
	18.0	10.4±1.5	51	81	0.58±0.08	GB-OVRO
	18.0	13.9±1.8	54	86	0.76±0.10	GB-OVRO
	18.0	15.5±1.1	55	85	0.86±0.06	GB-OVRO
	18.0	14.2±1.8	55	85	0.79±0.12	GB-OVRO
	22.0	18.8±2.7	70	88	0.85±0.12	GB-ONS I
	22.0	17.8±2.3	100	76	0.81±0.10	GB-ONS I
	22.0	17.7±1.7	105	78	0.80±0.08	GB-ONS II
	15.0	5.5±1.0	121	24	0.37±0.07	GB-CAO
	15.0	6.8±1.0	131	90	0.45±0.07	GB-CAO
	15.0	5.3±1.0	132	89	0.35±0.07	GB-CAO
	18.0	6.5±0.9	168	33	0.36±0.05	OVRO-PKS
	18.0	6.6±0.9	169	34	0.37±0.05	OVRO-PKS
	18.0	5.4±0.9	171	35	0.30±0.05	OVRO-PKS
	18.0	5.7±0.9	175	40	0.32±0.05	OVRO-PKS
2345−16	3.1	2.5±0.7	169	48	0.81±0.22	OVRO-PKS
	3.1	2.5±0.7	170	48	0.81±0.22	OVRO-PKS

be thought that the detection of fringes in these cases is not significant. This is not the case since the quoted fringe amplitudes are based on the integration of the power spectrum over the maximum frequency spread expected from local oscillator instability (Clark *et al.* 1968*a*). Sometimes, during periods of unusually good oscillator stability, the peak of the power spectrum clearly stands out above the noise, even though the integrated value appears to be barely significant. All of the sources listed in Tables 2 and 3 were selected with the requirement that the peak amplitude exceed the noise at the 95 percent confidence level.

It is important to note that an uncertainty in fringe visibility is equivalent to a reduction in resolving power. For example, on the Owens Valley–Parkes baseline, a measured fringe visibility of unity with a 5 percent error implies a Gaussian half-power width less than 0".00015. If the error is 20 percent, the size limit becomes 0".0003; and for 50 percent error, 0".0005. Thus, an increase in precision from 20 percent to 5 percent gives an improved resolution equivalent to doubling the length of the baseline.

IV. SOURCE STRUCTURE

A brief description of the small-scale structure of each source is given below. It is based not only on the data given in Tables 2 and 3 but also on previously published interferometer observations (shown in Table 4), as well as observations of interplanetary scintillations at 70 cm (Harris and Hardebeck 1969).

PKS 0019−00. The source is unresolved at 18 cm ($\lesssim$0".025). The 50-cm[b] observations[1] give $\theta = 0".015 \pm 0".005$. At 13 cm, $\gamma < 0.14$ so that there is no fine structure less than $\sim$0".002 in diameter containing more than 15 percent of the total flux.

PKS 0106+01. QSS. Most ($\gtrsim$85 percent) of the flux density at 6 cm comes from a component which has a spectral maximum near 8 GHz and is unresolved at all spacings at 6 cm, so $\theta \lesssim 0".0004$. About 80 percent of the flux density comes from this small component at 13 cm.

NRAO 91. The data at 18 and 50 cm are in good agreement and indicate a relatively simple source with $\theta \sim 0".019 \pm 0".002$. One observation at 75 cm[a] does not differ significantly from the data at shorter wavelengths.

CTA 21. The 18-cm observations suggest a core-halo structure with $\sim$75 percent in a halo 0".01 in diameter, and 25 percent in a core $\lesssim$0".002. The 6-cm observations show the core to be $\sim$0".002. A single measurement at $5 \times 10^6\ \lambda$ at 50 cm[b] is somewhat lower than expected from our model and may reflect the presence of another, more extended component at longer wavelengths, which is also suggested by a minimum in the spectrum near 75 cm. Neither our data at 6 and 18 cm nor the Jodrell Bank data at 11 and 21 cm show evidence of the double structure reported at 75 cm[a].

3C 84. Seyfert galaxy. The 18-cm data show about 40 percent of the total flux density

TABLE 4

PREVIOUSLY PUBLISHED INTERFEROMETER OBSERVATIONS

Authors	Wavelength (cm)
a) Broten *et al.* 1969; Clarke *et al.* 1969	75
b) Jauncey *et al.* 1969	50
c) Jauncey *et al.* (unpublished)	50
d) Donaldson *et al.* 1969	21, 11, 6
e) Donaldson and Miley 1971 . . .	21, 11, 6
f) Kellermann *et al.* 1970	13

[1] For an explanation of the superior Latin indices, see Table 4.

to be completely resolved at the shortest spacings. This is presumably the 5′ halo (e.g., Ryle and Wyndram 1968). Another 45 percent of the source has an angular size of 0″02 at 18 cm, and 15 percent is in a core which is not significantly resolved at $35 \times 10^6\ \lambda$. At 6 cm the Jodrell Bank data gave an unresolved flux of 16.6 flux units (f.u.) at $2 \times 10^6\ \lambda$ in 1967. The total flux density has increased by 4 f.u. during the period 1967.0–1969.0 (Kellermann and Pauliny-Toth, unpublished) so that the small core contains about 20.5 f.u. in 1969.0. Our 6-cm data indicate a minimum in the visibility function near $80 \times 10^6\ \lambda$. The data between 37 and $51 \times 10^6\ \lambda$ which range over 77° of position angle suggest that the core is nearly circularly symmetric. The simplest interpretation of our data is that the core is a circular disk or ring with a diameter 0″0025, corresponding to 2 lt-yr with $z = 0.018$ and $H = 100$ km s^{-1} Mpc^{-1}. The Jodrell Bank observations[d] do not show any evidence of the double structure reported at 75 cm[n]. The simplest interpretation of the 75-cm data suggests a component $\lesssim$0″02 which is 15 percent of the total flux density, although the scatter in the data is large. We tentatively associate this component with the one we find at 18 cm with $\theta \sim$ 0″02. Scintillation data at 178 MHz require that not more than 10 percent of the total flux be in the smaller two components at this frequency.

Figure 1 shows the spectrum of 3C 84 at the epoch 1969.0 divided into the three components based on the data described above.

NRAO 140. QSS. The source is not significantly resolved at any spacing at 6, 18, or 50 cm[b] (the 50-cm total flux density given in Jauncey *et al.* 1970 is too high by 30 percent). At 13 cm[f], $\gamma = 0.47$ at $80 \times 10^6\ \lambda$. The complex spectrum, with a minimum near 5 cm, suggests that there is a component $\lesssim$0″002 in diameter which contributes about one-half of the flux density at 13 cm, and is relatively stronger at shorter wavelengths. The other component is $\lesssim$0″03.

CTA 26. QSS. A significant fraction of the flux density at 6 and 13 cm[f] comes from a component $\lesssim$0″001.

NRAO 150. Most of the flux density (>70 percent) at 18 cm comes from <0″015. At 6 cm most of the flux comes from a region ~0″0013.

3C 119. QSS. There appears to be structure on a scale of about 0″15 with one or more components of the order of 0″01 or less.

3C 120. Seyfert galaxy. This source is highly variable, so it is difficult to compare the observations made over a period of time at different baselines. There is certainly fine

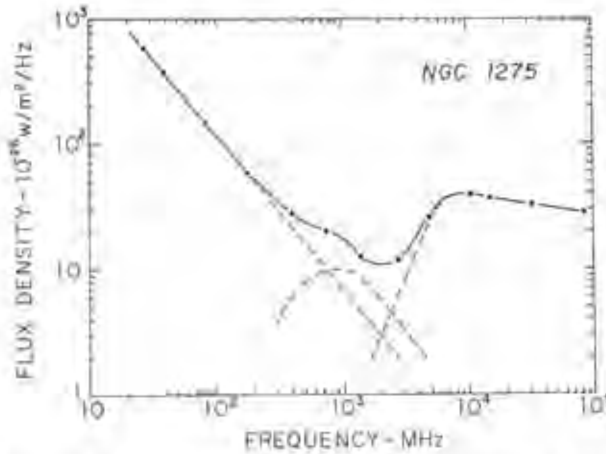

Fig. 1.—Radio spectrum of NGC 1275 (3C 84) showing the separation into separate spectral components.

structure at all wavelengths between 6 and 75 cm. At the time of the 1969 January 6-cm observations between Green Bank and Sweden, the flux density was near a maximum at 6 cm. The total amplitude of this particular outburst appears to have been at least 5 flux units, whereas the fringe amplitude was only 1.7 flux units, so that it is significantly resolved at $104 \times 10^6\ \lambda$, and the size of the variable component may be estimated to have been $\gtrsim 0''.001$.

PKS 0420−01. QSS. The observations indicate that most of the radiation at 6 cm originates in a component which is $\lesssim 0''.0007$.

3C 138. QSS. Donaldson and Miley (1971) find 3C 138 to be double at 11 cm with a component separation near $0''.4^{e}$. Our single detection requires that at least one component have structure on a scale $0''.07$ or less; similar conclusions are reached from a single measurement at 75 cm[a].

NRAO 190. The data suggest an overall size of about $0''.01$, but with one-half or more of the flux density at 6 and 13[f] cm coming from a component $\lesssim 0''.001$.

3C 147. This source does not appear to possess symmetry about either the position angle of 55° suggested by Anderson and Donaldson (1967) or the angle of 85° suggested by the 75-cm data[a]. It is clear that in both position angles there is structure at least as large as $0''.07$ as well as appreciable structure smaller than $0''.02$.

PKS 0605−08. The source is unresolved at 6 cm at $100 \times 10^6\ \lambda$. At 13 cm[f], $\gamma \sim 0.6$ at $80 \times 10^6\ \lambda$. This suggests that most of the flux density at 6 cm comes from $\lesssim 0''.0007$, and that at 13 cm this component contributes only about 60 percent to the total flux density.

PKS 0607−15. At least 30 percent of the flux density at 6 and 13 cm[f] comes from a region $\lesssim 0''.002$.

DW 0742+10. The source may be partially resolved at 18 and 6 cm. The complex spectrum suggests two components, with the smaller one being $\lesssim 0''.001$ and at least 2.4 f.u. at 6 cm and only 0.8 f.u. at 13 cm[f]. The overall size appears to be about $0''.01$.

PKS 0834−20. The limited data suggest that most of the emission at 18 cm comes from a region $\sim 0''.01$.

4C 39.25. QSS. There is an unresolved component at 6 cm which is $\lesssim 0''.0004$. Its flux density is about 6.5, 2.5, and 1.5 f.u. at 6, 13[f], and 18 cm, respectively. In addition, there is a more extended component at 18 cm which is $\gtrsim 0''.02$. The spectrum has a rather deep minimum near 30 cm.

PKS 1055+01. QSS. There appear to be at least two small components, one which contributes 60–70 percent of the total flux density at 50[g] and 75 cm[a] and is in the range $0''.001$–$0''.01$, and a second which is unresolved at 6 and 13 cm[f] and is $\lesssim 0''.0005$ and contributes about 50 percent of the total flux density at these wavelengths.

PKS 1121−14. QSS. The data indicate at least two or three distinct components. One, which is stronger at long wavelengths, is $\sim 0''.003$. The second is $\lesssim 0''.001$ and is 15 percent of the total at 13 cm[f]. It appears to be well resolved at 6 cm at $170 \times 10^6\ \lambda$, where it contributes most of the observed flux density.

PKS 1148−00. QSS. The data at 18 and 13 cm[f] are in only fair agreement. The simplest model is a source $\sim 0''.002$, but the 18-cm points are somewhat low on this model; alternatively, there may be an unresolved core $\lesssim 0''.002$.

3C 273. QSS. Both the 6- and 18-cm visibility curves suggest classical core-halo structure (Figs. 2*a* and 2*b*). The 18-cm data show that there is a halo (component B) of $0''.022$ which contributes ~ 50 percent (15 f.u.) of the total flux density at this wavelength, exclusive of component A. The second component (C), also 15 f.u., is barely resolved at 18 cm. At 6 cm this component contributes about 60 percent of the total flux (20 f.u.); it is completely resolved and is $\sim 0''.002$. A third component (D) has about 20 percent of the total flux (6 f.u.) and appears to be unresolved at $175 \times 10^6\ \lambda$, so it is $\lesssim 0''.0004$.

The absence of a significant minimum in the visibility function at 6 cm suggests that

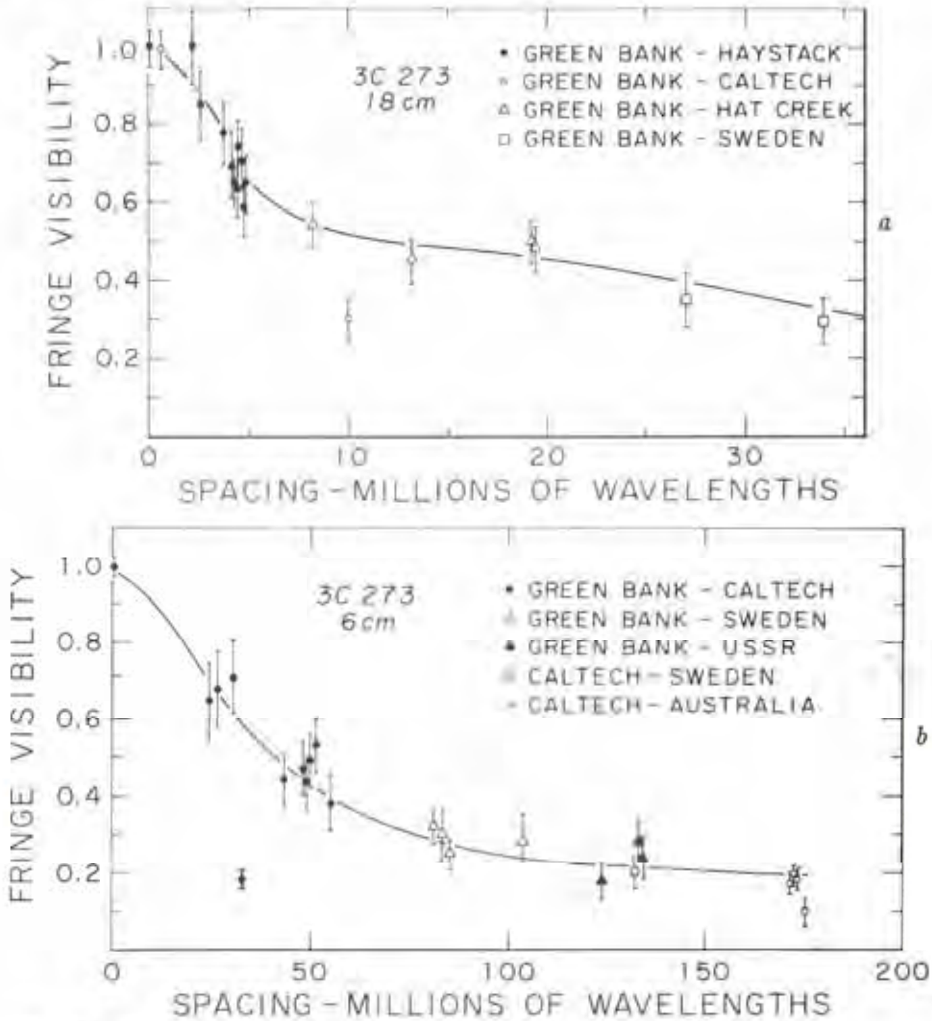

FIG. 2*a*.—Visibility function of the compact source in 3C 273 at 18 cm.
FIG. 2*b*.—Visibility function of the compact source in 3C 273 at 6 cm.

components C and D are not separated by more than the size of component C (~0″002). The absence of a clear minimum near $5 \times 10^6\ \lambda$ at 18 cm similarly suggests that components B and C are not separated by more than 0″02. There is one very low point at $10 \times 10^6\ \lambda$ at 18 cm. This may be due to component separation of about 0″01, but it may also be due to observational error. Clearly, more extensive measurements are necessary to determine the extent to which components B, C, and D are coincident.[2]

The single measurement at 2.8 cm at 280×10^6 wavelengths suggests that component D is partially resolved and is about 0″0004 in diameter (Broderick *et al.* 1970*a*, *b*);

[2] *Note added 1971 July 29.*—More recent measurements at 3.8 cm indicate that component C is double with a separation of 0″00155 (Cohen *et al.* 1971, *Ap. J.* [in press]).

but this result is very uncertain, and further high-resolution measurements are needed.

At 13 cm^f at $80 \times 10^6\ \lambda$, components B and C are nearly fully resolved and the single measurement gives the flux density of component D as 1.9 f.u. At 50 cm^e at $4.6 \times 10^6\ \lambda$, component A is completely resolved, and the main contribution to the fringe amplitude comes from component B which is partially resolved at this spacing. The estimated total flux density of component B at 50 cm based on the angular size measured at 18 cm is about 25 f.u., which is consistent with the spectrum shown in Figure 3. It is not clear how the complex model proposed by the Canadian observers from their 75-cm observations[e] relates to our model.

3C 279. QSS. It is well known that 3C 279 contains two major components, one of which is small and predominates at short wavelengths. Our data suggest that this compact component contains three subcomponents. The 18-cm and 6-cm visibility curves suggest core-halo structure at both wavelengths. At 18 cm ~20 percent (2 f.u.) of the total flux is in an extended component (A), 30 percent (3.5 f.u.) in a component B ~0".022, and 50 percent (5.5 f.u.) in an unresolved component (C). At 6 cm component C is about 60 percent of the total (10 f.u.), is resolved, and is ~0".001. Component D, which contributes about 15 percent of the total (4.5 f.u.), is unresolved and is $\lesssim$0".0004. At 13 cm^f component B must be completely resolved at $80 \times 10^6\ \lambda$. If component C is ~0".001, then its visibility at 13 cm is about 0.6. The measured fringe amplitude is 3.2 f.u., and so component D must be about 2 f.u. at 13 cm. At 75 cm, component A is completely resolved and C and D contribute negligible flux density, so the observations at 75 cm^e must refer to component B which contributes 35 percent (4.5 f.u.) at this frequency. Interplanetary scintillation (IPS) observations made close to the Sun at 11 cm (Cohen and Gundermann 1969) have shown a component $\lesssim$0".002; this must be components C and D. The size quoted by the Canadian observers (0".010 ± 0".003) at P.A. 90° does not agree too well with our size of 0".022 at P.A. 65°, so component B may be elongated.

PKS 1245−19. The source is unresolved at 18 cm at $1.4 \times 10^6\ \lambda$ and completely resolved at 13 cm^f at 80×10^6, so $0".002 \lesssim \theta \lesssim 0".04$.

3C 287. QSS. At 18 cm one-half of the source is unresolved at $4.7 \times 10^6\ \lambda$. The source is completely resolved at 13 cm at $80 \times 10^6\ \lambda$, so there must be a component $0".002 \lesssim \theta \lesssim 0".01$. At 50 cm^e this component appears to contribute only about 15 percent of the

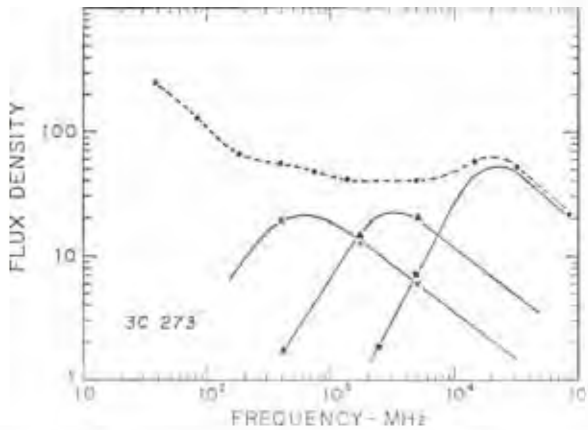

FIG. 3.—Radio spectrum of the compact source in 3C 273 showing the separation into separate components. ×, Component B; ▲, Component C; ■, Component D.

total flux density. At 70 cm the IPS index $m = 0.8$, so that the larger component is also rather compact, probably with a diameter near 0".03. The 75-cm interferometer data[d], however, indicate double structure on a scale of 0".1–0".2.

3C 286. QSS. Our data at 18 cm are consistent with a circularly symmetric source of diameter ~0".03. A single measurement at 50 cm[c] is also consistent with this. The more extensive data at 75 cm[a] imply considerably more complex structure on a scale greater than ~0".1, although this may refer to another component which contributes at longer wavelengths. The presence of this low-frequency component is suggested also from the spectrum which does not show the low-frequency cutoff expected of the 0".03 component. At 70 cm, the IPS index $m = 0.6$, which suggests that the low-frequency component contains about 40 percent of the flux at this wavelength. No fringes were seen at 13 cm[f], so there is no fine structure less than ~0".002.

3C 309.1. QSS. There is no evidence of self-absorption in a small component in the overall spectrum, which is close to a power law. The 18-cm data show that the source is unresolved at 4.3×10^6 λ and is ≲0".015. At 75 cm[a] there are at least two components.

DA 406. QSS. The source is unresolved at 6 cm at 100×10^6 λ and is less than 0".0008. About 50 percent of the flux density is in this small component at 13 cm[f] (1.6 f.u.) and at 18 cm (1.6 f.u.).

PKS 1510−08. QSS. Most of the source at 6 cm is ≲0".0004. At 13 cm[f] only 40 percent of the source is in this unresolved component. A comparable fraction is in a component ≲0".01 at 75 cm[a].

4C 05.64. At 6, 13, and 18 cm at least 40 percent of the flux comes from a component less than ~0".001. The source is unresolved at 50 cm[c] at 5×10^6 λ, so all of the source is less than ~0".015 at this wavelength.

DW 1555+00. The source is not resolved by any of our measurements. Most of the source is ≲0".01 at 50 cm[c], ≲0".0006 at 13 cm[f], and ≲0".0004 at 6 cm.

CTD 93. Galaxy. The major component is approximately 0".0025, but the high visibility observed at 13 cm[f] at 80×10^6 compared with that observed at 35×10^6 λ at 18 cm suggests possible structure ≲0".002.

3C 345. QSS. About 60 percent (4 f.u.) of the total flux density is in an unresolved component ≲0".0007 at 6 cm. At 13 cm[f] the flux density of this component is 2.5 f.u., and at 18 cm it is 1.6 f.u. In addition, there is a larger component ~0".005 which is nearly completely resolved at 35×10^6 λ at 18 cm and contributes half of the total flux density at 75 cm[a]. The remainder of the source at 75 cm[a] is in a more extended component ≳0".05, which does not contribute more than 20 percent of the total at 18 cm.

NRAO 530. There is a component which contains about 50 percent (2.0 f.u.) of the flux density at 6 cm and is less than ~0".002. At 13 cm[f] this component is much weaker and is only ~0.4 f.u. At 18 cm this component has a negligible contribution and most of the flux density comes from a region ~0".005. A considerably larger size of about 0".03 is found at 75 cm[a].

3C 380. QSS. There is a component which is ≲0".002 and contributes about 30 percent of the total flux density at 6 or 18 cm (2.5 and 3.5 f.u., respectively). The 75-cm[a] data apparently refer to a more extended component.

3C 418. At least 70 percent of the flux density at 18 cm is in an unresolved component less than ~0".015.

PKS 2127+04. The source is unresolved at 50 cm[b] and is less than ~0".015. The 13-cm[f] data give $\theta \sim$ 0".002, but the fringe amplitude observed at 18 cm at 15×10^6 is too low for a source this small, and may indicate more complex structure. Most of the flux comes from a component which has a sharp cutoff below 1 GHz.

PKS 2134+004. QSS. The 6-cm data indicate a diameter of 0".0008, but the large scatter suggests possible complex structure. The 13-cm[f] point fits better to a source about twice this size, but at this wavelength there may be more extended structure as suggested by a slight positive curvature of the spectrum. Most of the flux at centimeter wavelengths comes from a component which has a sharp cutoff near 6 cm.

PKS 2145+06. QSS. The source is essentially unresolved at 6 cm, so most of the flux is from a component of about 4 f.u. and less than $\sim 0''.0004$. This component contributes about 2 f.u. at 13 cm[f] and at 18 cm. At 50 cm[b] the source is probably unresolved at $5 \times 10^6\ \lambda$, so the entire source is less than $\sim 0''.015$.

VRO 42.22.01 (BL Lac). QSS? The source is unresolved at 6 cm and is less than $\sim 0''.0004$. At 13 cm[f] this small component is only 22 percent (1.3 f.u.) of the total flux.

PKS 2203−18. QSS. $\theta \sim 0''.05$.

CTA 102. QSS. The interferometer data indicate more complex structure than suggested by the relatively simple spectrum. At 18 cm about 50 percent of the flux comes from a halo $\sim 0''.007$, and 50 percent is unresolved and is less than $\sim 0''.003$. The 13-cm[f] measurement requires that at least 20 percent of the flux at 13 cm be in a component $\lesssim 0''.001$. The 75-cm[e] data suggest the presence of a larger component containing 15 percent of the flux, and having a size greater than $\sim 0''.2$. There is no evidence of this larger component in our 50-cm data[b] nor in the IPS data at 70 cm, which give an index $m = 1$. However, the uncertainties in the 50-cm interferometer data and the IPS data are sufficiently large that there is no real inconsistency.

3C 446. QSS. There is a component of about 2 f.u. which is unresolved at 6 cm between 50 and $170 \times 10^6\ \lambda$. It is less than $\sim 0''.0004$, and is 1 f.u. at 13 cm[f]. At 18 cm there is a second small component which has structure at 18 cm on a scale $\sim 0''.02$.

3C 454.3. QSS. The interpretation of the 6-cm data is difficult due to the large decrease in total flux density which occurred in 1969. There is a component of about 5 f.u. at 6 cm which is unresolved at $175 \times 10^6\ \lambda$ and is less than $\sim 0''.0004$. Most of the rest of the flux at 6 cm comes from a component which is resolved by $100 \times 10^6\ \lambda$ and is $\sim 0''.002$. This component is also resolved at 18 cm where it contributes most of the flux, and the 13-cm[f] data suggest possible complex structure. The entire source is unresolved by us at 50 cm[b] and is less than $\sim 0''.15$. The 75-cm interferometer data[e] suggest structure on a scale of $1''$ or greater, but the observed scintillation index of unity suggests that nearly the entire source be contained within $0''.2$ at 70 cm.

PKS 2345−16. Complex spectrum; QSS. The source is essentially unresolved at 13[f] and 6 cm, so $\theta < 0''.0004$.

The models used to describe the sources are only a first approximation to the true structure in the sense that we have always taken the simplest model which is consistent with our data. In particular, we have not forced our models to include every data point, but believing that our estimated errors are true standard deviations, we have allowed up to 30 percent of our points to differ from the model by more than the quoted error. For example, when the fringe visibility at only one out of four or five measured spacings is low, we have not interpreted this as evidence of double structure. Rather, we consider it more likely to be due to a statistical fluctuation, or to loss of coherence for some other reason. This means, however, that our analysis is biased against finding any double or other multiple structure which may exist.

Often when there is only a small range of spacings covered by the data, it is difficult to choose between a model consisting of a partially resolved simple Gaussian source and one consisting of a completely resolved component plus a completely unresolved component. To choose between these two cases we have considered the spectrum of the source. If the spectrum is simple and contains only a single maximum, we consider it likely that the structure is also simple; but if the spectrum is complex and shows one or more maxima or minima in the frequency range discussed, then we have assumed that this is due to several components which become opaque at different wavelengths. In a number of cases, however, such as 3C 84, 3C 273, and 3C 279, where there are reasonably extensive interferometer data at several wavelengths, it is clear from the fringe visibilities alone that there must be up to three or more distinct components.

V. VARIABLE SOURCES

The unambiguous resolution of variable source components would permit a direct test of the expanding source model (Shklovskii 1965) and allow the rate of expansion to be determined. It would also be possible to calculate the rate of change of the magnetic field strength and, in the case of identified sources whose distance is known, the total energy content. Also, for the identified variable sources it would be possible to test the hypothesis that the apparent expansion velocity is greater than that given by the usual light-travel-time arguments (e.g., Rees 1968). Most of the variable sources are, however, too small to be resolved with the baselines used in the measurements reported here.

One exception is the relatively nearby radio galaxy NGC 1275 (3C 84). 3C 84 was resolved on the Green Bank–Onsala baseline in both the 1968 and 1969 measurements. The fringe visibility appears to have significantly decreased during the one year between the two sets of observations, indicating an increase in angular size during this time. It is, however, difficult to be quantitative since the uncertainty in the visibility in 1968 is large and because the low values of γ cause the calculations to be strongly model dependent. If we interpret our 1969 observations as indicating a circular disk structure (see § V), then the diameter was $0''.0025 \pm 0''.0002$ in 1969.0 and $0''.0017 \pm 0''.0002$ in 1968.0. The later value is greater than the value of $0''.001$ given by Kellermann *et al.* (1969), because the results in that paper were based on a circular Gaussian model rather than the circular disk required by the new data. If we assume that $z = 0.018$ and $H = 100$ km s^{-1} Mpc^{-1}, then the distance to NGC 1275 is 78 Mpc and the corresponding diameters are 2.1 ± 0.2 and 1.4 ± 0.2 lt-yr in 1969.0 and 1968.0, respectively, so the diameter has increased by 0.7 ± 0.3 lt-yr in one year, giving an expansion velocity $v/c = 0.35 \pm 0.15$. This is greater than estimated previously (Kellermann *et al.* 1968), implying that the variable component is much younger than the ten years which was previously assumed from an analysis of the radio intensity variations. Further measurements are clearly required to confirm the observed size variation and to determine more accurately the expansion rate.

The direct resolution of a variable component has also been reported for 3C 273 (Gubbay *et al.* 1969) and for 3C 279 (Moffet *et al.* 1971). In the case of 3C 279, their 13-cm observations, which are spaced over a two-year period, suggest that the expansion is relativistic with $\gamma = (1 - v^2/c^2)^{-1/2} \gtrsim 2$. Similar data for 3C 273 show the existence of an unresolved component which does not vary in intensity, while the flux of a larger resolved component was decreasing. This is an interesting and surprising result, since it means that the observed variations in flux density do not necessarily occur in the smallest component, as might have been expected.

This suggests to us a small, well contained, but highly energetic core, which occasionally releases a cloud of relativistic particles which then expands and rapidly becomes bigger than the core.

The only other variable source for which there is a relevant observation is 3C 454.3, which showed a decrease in total flux density from 22 to 15 f.u. between the time of the Green Bank–Onsala observations in 1969 January and the Green Bank–Crimea observations in 1969 October. This is reflected by a comparable drop in fringe amplitude expected if the variable component is unresolved at $100 \times 10^6\ \lambda$.

VI. DISCUSSION

Since our observations cover only very limited regions of the (u, v)-plane, it has been difficult to determine in detail the structure of individual sources, particularly for the weaker sources where the uncertainties in fringe visibilities are large. Moreover, many of the sources are variable, a condition which further limits the interpretation of the data. We believe, however, that our data determine (1) the overall size of the compact radio sources, (2) the approximate scale of individual components, and (3) the general dependence of the structure on wavelength.

It is apparent from the present data, and from previously published work at lower resolution, that there is a continuous range of scale in extragalactic sources down to angular dimensions of 0".0004 or less. If the quasi-stellar sources are assumed to be at cosmological distances, then the typical linear dimensions of the smallest components are of the order of a few parsecs or less. The unresolved component in 3C 273 is smaller than 1 pc.

The observed peak brightness temperatures range up to a value of about $10^{12\pm}$ K, which is the limiting brightness temperature that can occur in an opaque incoherent synchrotron source (Kellermann and Pauliny-Toth 1969). We note in passing that such high measured brightness temperatures preclude any possibility that the observed radio emission in sources with peaked or complex spectra is due to any thermal process. Using the synchrotron model to interpret the measured angular size and cutoff frequency we estimate the magnetic field strengths, in the usual way, to be in the vicinity of 10^{-4} gauss in most of the resolved opaque components.

In general, when a source has been observed at several wavelengths at comparable spacings, the fringe visibility is greater at the shorter wavelengths. Figure 4 shows a plot of the fringe visibility at 6 cm measured near 80 million λ, or interpolated from data

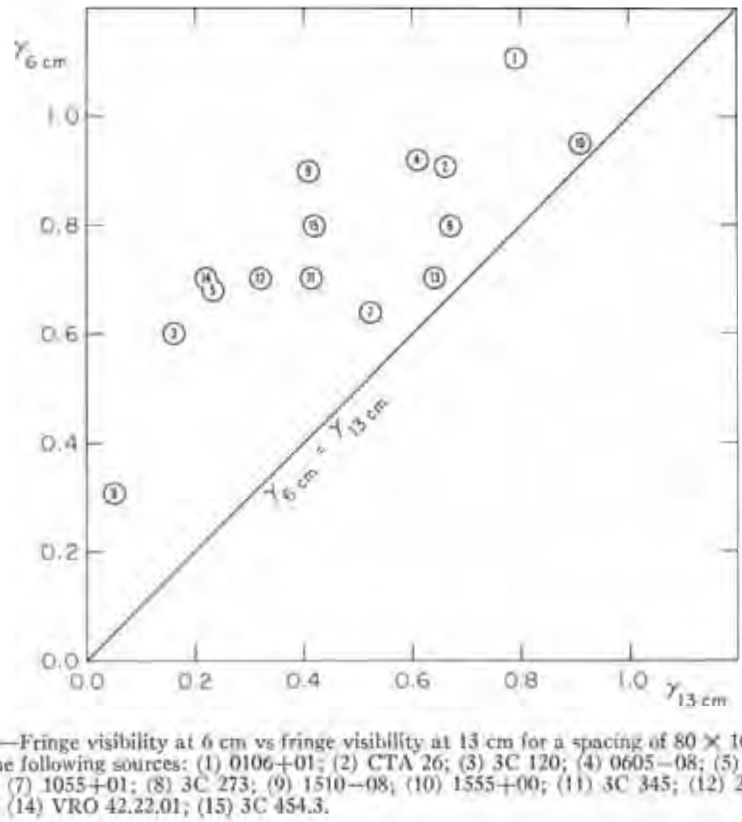

FIG. 4.—Fringe visibility at 6 cm vs fringe visibility at 13 cm for a spacing of 80×10^6 λ. Numbers refer to the following sources: (1) 0106+01; (2) CTA 26; (3) 3C 120; (4) 0605−08; (5) 0742+10; (6) 4C 39.25; (7) 1055+01; (8) 3C 273; (9) 1510−08; (10) 1555+00; (11) 3C 345; (12) 2134+00; (13) 2145+06; (14) VRO 42.22.01; (15) 3C 454.3.

near 50 and 100 million λ, versus the fringe visibility at 80 million λ measured at 13 cm (Kellermann *et al.* 1970). The visibility measured at 6 cm is in every case greater than that measured at 13 cm. This shows directly that the apparent angular dimensions are smaller at the shorter wavelengths, so the compact sources in general do not contain a single opaque component whose size is independent of wavelength.

The apparent variation of size with wavelength could be due to the presence of several components which become optically thick at different wavelengths, as suggested by the shape of the radio spectra (e.g., Kellermann and Pauliny-Toth 1969; Jauncey *et al.* 1970) or to the effect of interstellar scattering (e.g., Harris, Zeissig, and Lovelace 1970). For the following reasons, we believe that our data are not significantly affected by interstellar scattering and that the results are most simply interpreted as due to the higher self-absorption cutoff frequency in the smaller components.

1. The expected scattering size at 13 cm ($\sim 10^{-4}$ arc sec) is an order of magnitude less than the smallest source capable of being resolved on a baseline of 80×10^6 λ ($\sim 10^{-3}$ arc seconds).

2. The measured angular dimensions are generally close to what is expected from self-absorption with magnetic fields of the order of 10^{-4} gauss.

3. The measured peak brightness temperatures are of the order of 10^{12} °K at all wavelengths, as expected from self-absorption and inverse Compton cooling.

4. Sources with complex radio spectra tend to show frequency-dependent angular structure, while the size of sources with relatively simple spectra (a single maximum and sharp low-frequency cutoff) generally are independent of wavelength.

5. In several sources (e.g., 3C 273) where there is sufficient interferometer data, the fringe-visibility diagrams show directly the presence of several components, with the larger components being stronger at the longer wavelengths.

In the range of angular dimensions from 0".0005 to 0".05 where our results are most sensitive, there is no clear evidence in our data that the components are spatially separated. However, because we have considered only those observations which gave fringes and because we place little weight on the few cases where there are isolated low fringe visibilities, we have systematically discriminated against detecting multiple structure. There is, however, evidence from the observations made at 75 cm (Clarke *et al.* 1969) of component separations in the range 0".01–0".1. Clearly measurements with more coverage of the (u, v)-plane are required before more detailed models of source structure can be pursued.

A total of twelve sources gave fringes on the longest baseline, 176×10^6 λ, between California and Australia. These sources all contain significant structure on a scale of 0".0005. Several sources including 0106+01, 3C 273, 3C 279, 1555+00, 2145+06, 3C 345, 3C 454.3, and 2345−16 have unresolved components which are 0".0004 or less in extent, and observations at higher resolution are necessary to study them.

Longer baselines are impractical due to restricted common sky coverage from locations near diametrical positions on the Earth, so that the observations must be extended to shorter wavelengths.

We have reported observations at 2.8 cm made between Green Bank and the Crimea, a baseline separation of 280×10^6 λ (Broderick *et al.* 1970*a*, *b*). However, the lower sensitivity of the receivers, together with decreased local oscillator stability, allowed only weak fringes to be seen on two sources, 4C 39.25 and 3C 273. Little or no increase in the effective resolution was achieved because of the large uncertainty in fringe visibility.

It is interesting to note that all of the stronger sources should be resolved by using baselines restricted to the surface of the Earth, because a source with 1 f.u. or more of unresolved flux at this baseline (irrespective of the frequency of observation) would have a brightness temperature in excess of the limit set by inverse Compton cooling of 10^{12} °K (Kellermann and Pauliny-Toth 1969). This follows from the fact that for a constant peak brightness temperature, $T_p = \frac{1}{2}\lambda^2 S/k\theta^2$, and peak flux density S, the angular size θ of an opaque synchrotron source is directly proportional to the wavelength of maximum flux density. Thus, if on a given physical baseline D the effective resolution is given by $\theta \simeq \lambda/3D$, and if $T_p \lesssim 10^{12}$ ° K, then for all sources with $S_p \gtrsim$ 3 f.u. the maximum required baseline D is 10000 km if the observations are made at the wavelength of maximum flux density. At shorter wavelengths, sources well under 1 f.u. may be resolved with terrestrial baselines, so that there seems to be little need to use baselines in space or between the Earth and the Moon.

This conclusion does not apply to sources such as molecular masers or pulsars, which do not radiate by an incoherent synchrotron mechanism, and are not therefore limited to 10^{12} ° K. In the case of the known pulsars, however, they radiate most strongly at wavelengths where interstellar "seeing" is likely to limit the maximum usable baselines to less than one Earth diameter (e.g., Harris *et al.* 1970).

We are grateful to the many people who have contributed in various ways to the success of these observations. These include S. Weinreb, W. Vrable, M. Balister, and J. Payne at NRAO; A. Moffet and G. Seielstad at OVRO; L. Kogan and V. Kostenko, of the Institute for Space Research; V. Efanov and others at the Crimean Astrophysical Observatory; and B. Höglund, B. Hansson, E. Kollberg, and others at Onsala.

We are thankful to P. O. Lundbom and C. Åbom of the Swedish Research Institute for National Defense whose aid and cooperation allowed us to synchronize our clock in Stockholm for the observations in Sweden and the U.S.S.R. Similar assistance was given to us by the staffs of the Jet Propulsion Laboratory, the Timing Section at Point Mugu, and the NASA DSN Tidbinbilla Tracking Station. We also wish to thank Y. Pariskii and others at the Pulkova Observatory for their generous assistance in transferring the time between Stockholm and Crimea.

Many of the tapes were processed by T. Clark at the Goddard Space Flight Center, and we are grateful to him and his staff for their generous help. We are also grateful to the Goddard Space Flight Center for the loan of their hydrogen maser and to Dr. H. Peters for his continued interest and aid in the operation of the maser.

The recording system used in these experiments was developed by C. Bare before his unfortunate death, and we wish to acknowledge his extensive contribution.

These experiments would not have been possible without the effort and cooperation of J. G. Bolton, D. S. Heeschen, W. E. Howard III, A. Severny, I. Shklovskii, and G. Stanley.

Part of this work was done while one of us (K. I. K.) was on leave of absence from NRAO at the California Institute of Technology. One of us (D. B. S.) was supported by a NSF predoctoral fellowship.

REFERENCES

Anderson, B., and Donaldson, W. 1967, *M.N.R.A.S.*, **137**, 81.
Bare, C., Clark, B. G., Kellermann, K. I., Cohen, M. H., and Jauncey, D. L. 1967, *Science*, **157**, 19.
Broderick, J. J., Vitkevitch, V. V., Jauncey, J. L., Efanov, V. A., Kellermann, K. I., Clark, B. G., Kogan, L. R., Kostenko, V. I., Cohen, M. H., Matveyenko, L. I., Moiseyev, I. G., Payne, J. G., and Hansson, B. 1970*a*, *Astr. Zh.*, **47**, 784.
———. 1970*b*, *Radio Science*, **5**, 1281.
Broten, N. W., Clarke, R. W., Legg, T. H., Locke, J. L., Galt, J. A., Yen, J. L., and Chisholm, R. M. 1969, *M.N.R.A.S.*, **146**, 313.
Clark, B. G., Kellermann, K. I., Bare, C. C., Cohen, M. H., and Jauncey, D. L. 1968*a*, *Ap. J.* (*Letters*), **153**, L67.
———. 1968*b*, *Ap. J.*, **153**, 705.
Clarke, R. W., Broten, N. W., Legg, T. H., Locke, J. L., and Yen, J. L. 1969, *M.N.R.A.S.*, **146**, 381.
Cohen, M. H., and Gundermann, E. J. 1969, *Ap. J.*, **155**, 645.
Donaldson, W., and Miley, G. K. 1971 (in preparation).

Donaldson, W., Miley, G. K., Palmer, H. P., and Smith, H. 1969, *M.N.R.A.S.*, **146**, 213.
Gubbay, J., Legg, A. J., Robertson, D. S., Moffet, A. T., Ekers, R. D., and Seidel, B. 1969, *Nature*, **224**, 1094.
Harris, D. E., and Hardebeck, E. G. 1969, *Ap. J. Suppl.*, **19**, 115.
Harris, D. E., Zeissig, G. A., and Lovelace, R. V. 1970, *Astr. and Ap.*, **8**, 104.
Jauncey, D. L., Bare, C. C., Clark, B. G., Kellermann, K. I., and Cohen, M. H. 1970, *Ap. J.*, **160**, 337.
Kellermann, K. I., Clark, B. G., Bare, C. C., Rydbeck, O., Ellder, J., Hansson, B., Kollberg, E., Höglund, B., Cohen, M. H., and Jauncey, D. L. 1968, *Ap. J. (Letters)*, **153**, L209.
Kellermann, K. I., Clark, B. G., Jauncey, D. L., Cohen, M. H., Shaffer, D. B., Moffet, A. T., and Gulkis, S. 1970, *Ap. J.*, **161**, 803.
Kellermann, K. I., and Pauliny-Toth, I. I. K. 1969, *Ap. J. (Letters)*, **155**, L71.
Moffet, A. T., Gubbay, J., Robertson, D. S., and Legg, T. H. 1971, *Proc. IAU Symp. No. 44* (in press).
Rees, M. J. 1968, *Nature*, **211**, 468.
Rees, M. J., and Simon, M. 1968, *Ap. J. (Letters)*, **152**, L145.
Ryle, M., and Windram, M. D. 1968, *M.N.R.A.S.*, **125**, 1.
Shklovskii, J. 1965, *Astr. Zh.*, **42**, 30 (English transl. in *Soviet Astr.—AJ*, **9**, 22).

1:17

Tp

TRANSIENT WAVE PROPAGATION IN INHOMOGENEOUS IONIZED MEDIA

BY
B. O. RÖNNÄNG

RESEARCH REPORT NO 70
1966

RESEARCH LABORATORY OF ELECTRONICS

CHALMERS UNIVERSITY OF TECHNOLOGY

GIBRALTARGATAN 5 G

GOTHENBURG S, SWEDEN

CHALMERS TEKNISKA HÖGSKOLA GÖTEBORG

Research Laboratory of Electronics
CHALMERS UNIVERSITY OF TECHNOLOGY
Gothenburg, Sweden

RESEARCH REPORT No. 70

TRANSIENT WAVE PROPAGATION IN INHOMOGENEOUS IONIZED MEDIA

By

B. O. RÖNNÄNG

Gothenburg, August 1966

TABLE OF CONTENTS

ABSTRACT

Transient wave responses of two different inhomogeneous ionized media —the exponential medium and the symmetrical Epstein layer — are studied. By means of the linearized wave equations exact expressions for the unit step wave responses are derived. In both cases they can be written in closed mathematical forms, namely as a Bessel function and a Legendre function respectively. The unit step modulated carrier responses, written as convolution integrals, are computed at different heights in the media and at different carrier frequencies, i.e. the variations of the electric field, the magnetic field and the energy flow are determined. This makes it possible to compare the exact signal envelopes with the earlier obtained approximate results. Futhermore the strong signal distortion at tunnel transmission through a thin symmetrical Epstein layer is studied in detail.

I. INTRODUCTION

There are essentially two different methods for solving steady-state wave propagation problems in stratified, ionized media. One can express the waves by means of a multiple phase integral principle [Rydbeck, 1948] or by wave coupling techniques [Rydbeck and Hjalmarson, 1966] without simplifying the variation of the refractive index. On the other hand, one can replace the true electron density variation with some known function, such as a linear, an exponential or a parabolic one, in order to obtain an exact solution of the wave equation, known as the full wave solution. This method is advantageous as it can be used at all signal frequencies. However, the solution is often a complicated mathematical function which in many cases makes the physical insight difficult.

There exist a great deal of theory on steady-state electromagnetic wave propagation in inhomogeneous ionized media using these methods. However, for all dispersive transmission channels a deeper insight into the propagation properties requires a transient wave solution. One should determine the variation of the electromagnetic fields when a transient wave is incident upon the medium. This theory is also of practical importance when one remembers that the majority of experimental efforts in ionospherical physics is restricted to "sounding" techniques. Besides, it will be shown in this work that the transient wave responses are often remarkably simple expressions. Little work has been done in this field until now, although Sommerfeld and Brillouin as early as 1914 treated the problem of signal distortion and signal velocity in infinite, homogenous, dispersive media.

In most cases, the approximate transient wave response can be obtained by a stationary phase method from the shape of the phase versus frequency characteristics of the medium [Rydbeck, 1942]. Since a transient signal contains all frequencies, it is more realistic to assume a simple electron density profile which makes it possible to obtain a full wave solution of the Laplace-transformed wave equation. This method has been used earlier to determine the unit step wave response and the unit step modulated carrier response of a homogeneous, ionized medium (See Chapter II). The purpose of the present work is to consider the transient wave responses of two different stratified, ionized media, namely the exponential medium and the symmetrical Epstein layer.

The time variations of the electric field and the magnetic field at different heights, caused by an incident unit step wave, are especially interesting to study. These wave responses can be found by writing down the linearized wave equation, setting up the boundary conditions far below and high up in the media and then introducing suitable Laplace-transforms. Throughout this work we use bilateral Laplace transformation, defined by the transform pair [van der Pol and Bremmer, 1955]

$$\tilde{f}(p) = p \int_{-\infty}^{+\infty} e^{-pt} f(t)\, dt \qquad \alpha < \mathrm{Re}\, p < \beta$$

$$f(t) = \frac{1}{2\pi j} \int_{c-j\infty}^{c+j\infty} \frac{1}{p} e^{pt} \tilde{f}(p)\, dp \qquad \alpha < c < \beta$$

It should already be pointed out here that the unit step wave responses obtained in both cases are remarkably simple mathematical expressions. Consequently, we can easily study the propagation properties of the two media and determine the unit step modulated carrier responses by means of a digital computer. This makes it possible to study, for instance, the interesting problems of signal distortion and signal time delay at tunnel transmission through an ionized barrier. This has been demonstrated in a series of figures, depicting the electric field, the magnetic field and the energy flow at different levels at tunnel transmission through a thin symmetrical Epstein layer.

The present investigation deals with transient electromagnetic wave propagation in inhomogeneous, ionized media. As a matter of fact, the results are more general, and they can be used to study all transient wave propagation prescribed by the same wave equations.

Acknowledgement.

The author is indepted to Professor O.E.H. Rydbeck for suggesting this investigation and for his encouragement and also to L. Ladell, M.Sc., for many stimulating discussions.

Index of symbols

$\bar{B}$	$=\mu_o \bar{H}$
c_o	velocity of electromagnetic waves in free space
$\bar{D}$	electric displacement vector
e	charge on the electron
$\bar{E}$	electric field
f	frequency
f_1	carrier frequency
f_p	plasma frequency
$f_{p,m}$	maximum plasma frequency
F	hypergeometric function
h_v	virtual height of reflection
$\bar{H}$	magnetic field
H	height scale factor
$H_\nu^{(1),(2)}$	Hankel functions
j	$\sqrt{-1}$
J_ν	Bessel function of the first kind
k	propagation constant in free space
m	mass of electron
n	refractive index
N	electron density
p	complex variable in Laplace transforms
P_ν	Legendre function

$\bar{S}$ $= \bar{E} \times \bar{H}$; energy flow

t time

T $= \frac{c_o}{2H} \left(t - \frac{z}{c_o}\right)$; normalized time

T_k Tschebyscheff polynomial of degree k

T_1 $= \frac{c_o}{2H} \left(t + \frac{z}{c_o}\right)$; normalized time

U unit step function

$U_\nu(w, u)$ Lommel function of two variables

v velocity

x, y, z Cartesian coordinates

Y_o $= 1/Z_o$

Z_o characteristic impedance of free space

γ $= \left[\frac{1}{4} - \frac{4H^2}{c_o^2} \omega_{p,m}^2\right]^{1/2}$; (eq. 5.11)

Γ gamma function

δ impulse function

ε_o electric permittivity of free space

ζ $= \frac{2H}{c_o} e^{j\pi/2} \omega_p$, (eq. 4.6); $-e^{z/H}$, (eq. 5.7)

ζ_o $= \zeta(z = 0)$

η $= -j\gamma$

λ wavelength

μ_o magnetic permittivity of free space

ν $\frac{2H}{c_o} p$; (eq. 4.7)

ξ $\operatorname{arccosh}\left[1 + \frac{2}{1+e^{-z/H}} (e^T - 1)\right]$; (eq. 5.43)

τ z/c_o

χ $\frac{2H}{c_o} (\omega_1 - \omega_{p,m})$ $(\omega_1 = 2\pi f_1)$, $(\omega_{p,m} = 2\pi f_{p,m})$

ω $= 2\pi f$; angular frequency

II. SIGNAL DISTORTION IN HOMOGENEOUS IONIZED MEDIA

As an introduction to the study of the more complicated case of transient wave propagation in inhomogeneous, ionized media we will here give a short summary of signal distortion after propagation a certain distance in an infinite homogeneous plasma or after reflection from and transmission through the boundary of a semi-infinite plasma.

Approximative methods for calculating the distortion of a signal, after it has propagated through a dispersive medium, were developed many years ago by Sommerfeld [1914] and Brillouin [1914]. They used stationary phase and saddle point principles in order to determine the signal distortion and discuss the difference between group and signal velocities. They also gave an expression for the "forerunner", i.e. an expression for the initial oscillations of the wave front. A similar method may also be used to obtain the transient response of an inhomogenous medium if we know the phase versus frequency of the actual wave. By means of Fourier transform technique and Taylor expansion of the phase about the signal frequency Rydbeck [1942] determined the shape of a square pulse and a sinusoidal modulated wave-train after reflection in the ionosphere. Unfortunately this method can not be used at a carrier frequency near or at the penetration frequency of an ionospherical layer.

The wide availibility of digital computers has caused an increasing interest in transient wave propagation during the last few years. A lot of papers (Chen [1963], Knop [1964], Case [1965]) have been published presenting numerical solutions of the initial arrival and build up of waves in homogeneous plasmas or wave guides. These transient waves have been experimentally observed by Schmitt [1964] (even for anisotropic plasmas).

In order to get the theoretical insight into the problem of transient wave propagation in inhomogeneous plasmas it is instructive to start with the basic homogeneous case.

We suppose that the ionized medium is semi-infinite, isotropic and loss less. The electron density profile is given by

$$\left.\begin{aligned} \omega_p^2 &= \omega_o^2 \qquad (z > 0) \\ \omega_p^2 &= 0 \qquad (z < 0)\ , \end{aligned}\right\} \qquad (2.1)$$

where ω_p is the plasma angular frequency and z is the height coordinate. Compare figure 2.1. An upgoing, horizontally polarized unit step wave (electric field E_I)

$$E_I = U(t - \frac{z}{c_o}) , \tag{2.2}$$

strikes the medium at a time $t = 0$ and gives rise to a transmitted and a reflected wave, E_T and E_R respectively. If we omit the nonlinear effects, these waves are given by the linearized wave equation

$$\frac{\partial^2 E}{\partial z^2} - \frac{1}{c_o^2} (\frac{\partial^2}{\partial t^2} + \omega_p^2) E = 0 \quad , \tag{2.3}$$

and the boundary conditions

$$\left.\begin{aligned} E_I + E_R &= E_T \\ \frac{\partial E_I}{\partial z} + \frac{\partial E_R}{\partial z} &= \frac{\partial E_T}{\partial z} \end{aligned}\right\} \tag{2.4}$$

at $z = 0$.

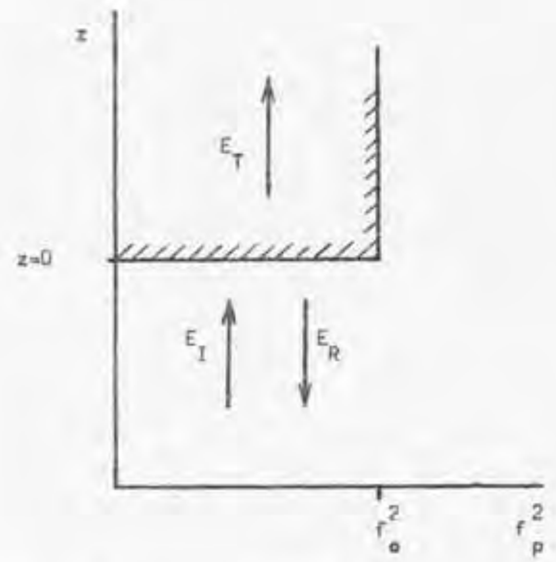

FIGURE 2.1. The semi-infinite ionized medium.

As mentioned in Chapter I we use two-sided Laplace transforms. By (2.3) and (2.4) the Laplace-transformed reflected and transmitted waves can be written

$$\tilde{E}_R = -\frac{1}{\omega_o^2}\left(\sqrt{p^2+\omega_o^2}-p\right)^2 e^{p\frac{z}{c_o}},$$

$$\tilde{E}_T = \frac{2p}{\omega_o^2}\left(\sqrt{p^2+\omega_o^2}-p\right) e^{-\sqrt{p^2+\omega_o^2}\,\frac{z}{c_o}} \qquad (2.5)$$

Using simple transform rules we obtain the time dependent electric fields as

$$E_I(t,z) = U(t-\tau)$$

$$E_R(t,z) = \left\{-1+J_o\left[\omega_o(t+\tau)\right]+J_2\left[\omega_o(t+\tau)\right]\right\}U(t+\tau) \qquad (2.6)$$

$$E_T(t,z) = \left\{J_o\left[\omega_o\sqrt{t^2-\tau^2}\right]+\frac{t-\tau}{t+\tau}J_2\left[\omega_o\sqrt{t^2-\tau^2}\right]\right\}U(t-\tau),$$

where $\tau = \frac{z}{c_o}$.

By means of relations (2.6) and Maxwell's equations the corresponding magnetic fields can be written as

$$H_I(t,z) = Y_o E_I(t,z) = Y_o U(t-\tau)$$

$$H_R(t,z) = -Y_o E_R(t,z) \qquad (2.7)$$

$$H_T(t,z) = -Y_o E_T(t,z) +$$

$$+ 2Y_o\left[1-\omega_o^2\tau\int_\tau^t \frac{J_1\left[\omega_o\sqrt{t^2-\tau^2}\right]}{\omega_o\sqrt{t^2-\tau^2}}\,dt\right]U(t-\tau).$$

where $Y_o = \frac{1}{Z_o} = \sqrt{\frac{\varepsilon_o}{\mu_o}}$ is the characteristic admittance of free space.

From eq.s (2.6) and (2.7) we notice that the reflected wave propagates without dispersion while the transmitted wave is distorted when it propagates in the ionized medium. The wavefront moves with vacuum velocity. Figure 2.2 shows the transmitted wave.

The momentary angular frequency ω_m of the transmitted electric field for large values of t can be obtained from

$$\omega_m = \frac{\partial}{\partial t}\left\{\omega_o \sqrt{t^2 - \tau^2}\right\} = \frac{\omega_o t}{\sqrt{t^2 - \tau^2}} \tag{2.8}$$

From (2.8) we can determine the veloctity of the frequency component ω_m as

$$v(\omega_m) = \frac{z}{t} = c_o\sqrt{1 - \frac{\omega_o^2}{\omega_m^2}} = c_o\, n(\omega_m) \qquad (\omega_m > \omega_o) \tag{2.9}$$

This is the well-known group velocity.

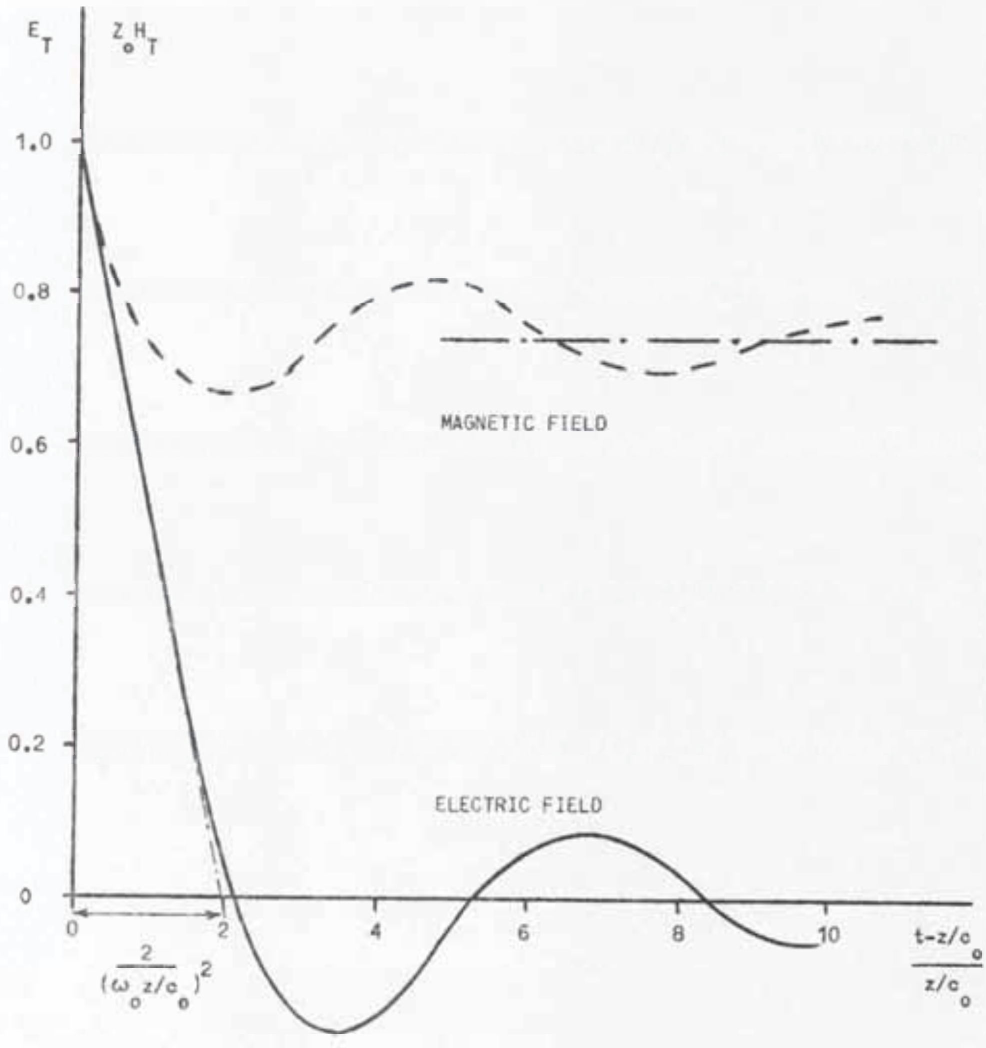

FIGURE 2.2. The unit step wave response at $\omega_o z/c_o = 1$ in a semi-infinite, homogeneous plasma.

The step modulated carrier response, i.e. the reflected and transmitted waves assuming an incident wave

$$E_{I,\sin} = \sin\left[\omega_1\left(t - \frac{z}{c_o}\right)\right] U\left(t - \frac{z}{c_o}\right), \tag{2.10}$$

is more difficult to obtain. Of course we can use the unit step wave response and write them as convolution integrals. Here we present another method.

The Laplace-transformed expressions for the reflected and the transmitted waves involve branch points at $p = \pm j\omega_o$ and poles at $p = \pm j\omega_1$. Accordingly, we have four single singularities, a fact which gives a complicated inversion. Fortunately, the poles can be eliminated by the following expansion in Bessel functions [Ladell, 1965]

$$\sin\left[\omega_1(t-\tau)\right] = 2\sum_{k=1}^{\infty}(-1)^{k-1} T_{2k-1}\left(\frac{\omega_1}{\omega_o}\right) J_{2k-1}\left[\omega_o(t-\tau)\right], \tag{2.11}$$

where $T_k\left(\frac{\omega_1}{\omega_o}\right)$ is a Tschebyscheff polynomial of degree k, defined as

$$T_k(x) = \begin{array}{ll} \cos(k \arccos x) & (|x| \leqslant 1) \\ \cosh(k \operatorname{arccosh} x) & (|x| \geqslant 1) \end{array} \tag{2.12}$$

We obtain

$$T_1(x) = x; \quad T_2(x) = 2x^2 - 1; \quad T_3(x) = 4x^3 - 3x;$$

$$T_{2k}(0) = (-1)^k; \quad T_{2k+1}(0) = 0; \quad T_k(1) = 1;$$

For large values of x

$$T_k(x) \sim 2^{k-1}(x)^k.$$

Using the expansion (2.11) we easily obtain the unit step modulated carrier response, i.e. the reflected and transmitted electric fields, as

$$E_{R,\sin}(t,z) = -2\sum_{k=o}^{\infty}\left\{(-1)^k T_{2k+1}(\omega_1/\omega_o)\ J_{2k+3}[\omega_o(t+\tau)]\right\}\cdot U(t+\tau) \qquad (2.13)$$

$$E_{T,\sin}(t,z) = 2\sum_{k=o}^{\infty}\left\{(-1)^k T_{2k+1}(\omega_1/\omega_o)\left[\left(\frac{t-\tau}{t+\tau}\right)^{(2k+1)/2} J_{2k+1}\left(\omega_o\sqrt{t^2-\tau^2}\right) -\right.\right.$$

$$\left.\left. - \left(\frac{t-\tau}{t+\tau}\right)^{(2k+3)/2} J_{2k+3}\left(\omega_o\sqrt{t^2-\tau^2}\right)\right]\right\}\cdot U(t-\tau)\,. \qquad (2.14)$$

These relations can be written in simple forms by means of Lommel functions [Case and Haskell, 1966 ; Ladell, 1966].
The Lommel function of the first kind is defined by [Dekanosidze, 1956]

$$U_\nu(w,u) = \sum_{k=o}^{\infty}(-1)^k\ (w/u)^{2k+\nu} J_{2k+\nu}(u)\ . \qquad (2.15)$$

By means of the Tschebyscheff polynomials, eq. (2.10), we easily obtain the following beautiful relations

$$E_{I,\sin}(t,z) = [\ U_1(aT^+,\ T^+) + U_1(\frac{T^+}{a},\ T^+)\ ]\cdot U(t-\tau) \qquad (2.16)$$

$$E_{R,\sin}(t,z) = -[\ a^{-2}\, U_3(aT^-,\ T^-) + a^2\, U_3(\frac{T^-}{a},\ T^-)\ ]\cdot U(t+\tau) \quad (2.17)$$

$$E_{T,\sin}(t,z) = [\ U_1(aT^+,\ u) + U_1(\frac{T^+}{a},\ u) +$$

$$+ a^{-2}\, U_3(aT^+,\ u) + a^2\, U_3(\frac{T^+}{a},\ u)\ ]\cdot U(t-\tau), \qquad (2.18)$$

where

$$u = \omega_o\sqrt{t^2-\tau^2}\ ; \quad T^+ = \omega_o(t-\tau)\ ; \quad T^- = \omega_o(t+\tau)\ ;$$

$$a = \frac{\omega_1}{\omega_o} + \sqrt{\left(\frac{\omega_1}{\omega_o}\right)^2 - 1}\ .$$

The first two functions in relation (2.18) represent the distortion of $\sin[\omega_1(t - z/c_o)]\, U(t - z/c_o)$ after propagation a certain distance z in an unbounded plasma. The same expression has been obtained by Case and Haskell [1966].

Let us study the interesting case $\omega_1 = \omega_o$. Using the relation

$$U_\nu(w,u) + U_{\nu+2}(w,u) = \left(\frac{w}{u}\right)^\nu J_\nu(u), \qquad (2.19)$$

we obtain the electric field just inside the semi-infinite ionized medium as

$$\left\{E_{T,\sin}(t,z)\right\}_{\substack{z=+0\\ \omega_1=\omega_o}} = [\,2\sin\omega_o t - 2J_1(\omega_o t)]\,U(t) \qquad (2.20)$$

Here the first term represents the steady-state field and the second term the transient distortion. The Lommel functions of two variables have been tabulated by Dekanosidze [1956] for real values of the two variables. Accordingly, $E_{R,\sin}(t,z)$ and $E_{T,\sin}(t,z)$ can be readily evaluated when $\omega_1 \gg \omega_o$. Figure 2.3 shows the transmitted electric field at different distances from the boundary. We have only consider the case $\omega_1 = \omega_o$.

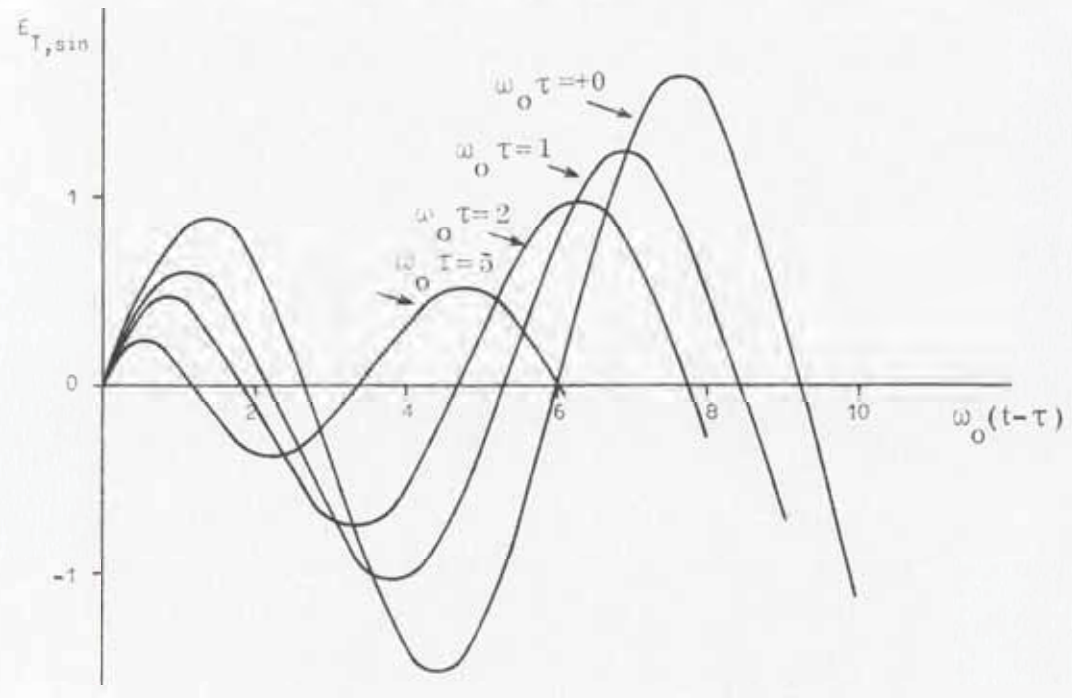

FIGURE 2.3. The initial oscillations of the transmitted electric field at four different distances in a semi-infinite ionized medium. Signal frequency f_1 = plasma frequency f_o.

III. THE WAVE EQUATION OF AN INHOMOGENEOUS IONIZED MEDIUM.

Assume that a plane, horizontally polarized electromagnetic wave is incident perpendicularly upon a medium, which is inhomogeneously ionized in one direction, isotropic and loss less. We try to find the resulting time variation of the electric field at any arbitrary height z in the medium. This will be given by Maxwell's equations

$$\operatorname{div} \bar{D} = 0 \tag{3.1}$$

$$\operatorname{div} \bar{B} = 0 \tag{3.2}$$

$$\operatorname{curl} \bar{E} = -\frac{\partial \bar{B}}{\partial t} = -\mu_o \frac{\partial \bar{H}}{\partial t} \tag{3.3}$$

$$\operatorname{curl} \bar{H} = \frac{\partial \bar{D}}{\partial t} \tag{3.4}$$

and the equation of motion

$$\frac{\partial \bar{v}}{\partial t} = -\frac{e}{m}\bar{E} \underbrace{- (\bar{v} \cdot \nabla)\bar{v} + \frac{e}{m}\mu_o(\bar{H} \times \bar{v})}_{\bar{P}} . \tag{3.5}$$

where $\bar{P}$ is a nonlinear vector when $\bar{H}$ has no static component.

With a coordinate system where the incident $\bar{E}$-vector is in the x-direction, we obtain the following coupled wave equations

$$\frac{\partial^2 E_x}{\partial z^2} - \mu_o \varepsilon_o \frac{\partial^2 E_x}{\partial t^2} = \frac{\partial^2 E_z}{\partial z \partial x} - \mu_o \frac{\partial}{\partial t}(Ne\, v_x) , \tag{3.6}$$

$$\frac{\partial^2 E_z}{\partial x^2} - \mu_o \varepsilon_o \frac{\partial^2 E_z}{\partial t^2} = \frac{\partial^2 E_x}{\partial z \partial x} - \mu_o \frac{\partial}{\partial t}(Ne\, v_z) . \tag{3.7}$$

Here N is the electron density which to first order is independent of time.

Because we have assumed vertical incidence

$$\frac{\partial}{\partial x} \equiv 0 ,$$

which by eq.s (3.5), (3.6) and (3.7) gives the linearized wave equation

$$\frac{\partial^2 E_x}{\partial z^2} - \frac{1}{c_o^2} \left(\frac{\partial^2}{\partial t^2} + \omega_p^2 \right) E_x = 0 , \tag{3.8}$$

where

$$\omega_p (z) = \left[\frac{N_o(z)\, e^2}{m\, \varepsilon_o} \right]^{1/2}$$

is the plasma angular frequency. Here we use the notation $N = N_o(z) + N_\sim$.

If we assume that the second order terms are much smaller than the first order terms, we get the following second order wave equation, given by Rydbeck [1961] ,

$$\varepsilon_o \left(\frac{\partial^2}{\partial t^2} + \omega_p^2 \right) E_z^{(2)} = - \frac{N_o e}{2} \frac{\partial}{\partial z} \left(| v_x^{(1)} |^2 \right) , \tag{3.9}$$

$$\overline{H}^{(2)} = 0 , \tag{3.10}$$

where superscripts (1) and (2) denote first and second order terms.

Furthermore from the equation of motion and

$$e N_\sim = - \varepsilon \operatorname{div} E , \tag{3.11}$$

we obtain

$$\left(\frac{\partial^2}{\partial t^2} + \omega_p^2\right) N_{\sim} = -\frac{\partial N_o}{\partial z} \cdot \frac{\partial v_z^{(2)}}{\partial t} - \frac{N_o}{2} \frac{\partial^2}{\partial z^2} \left(|v_x^{(1)}|^2\right). \qquad (3.12)$$

From eq. (3.12) we notice that the nonlinear effects are dependent on the frequency and amplitude of the actual wave as well as on the electron density profile. This is expecially serious, as we are going to determine the transient unit step wave response. In order to obtain the unit step modulated carrier responses and to analyse the propagation properties of the media we can of course use the linearized wave equations. However, we must keep in mind throughout this work that the simple expressions for the unit step wave responses are obtained by means of the linearized theory. A further analysis of the nonlinear effects, as well as the influence of the collision-losses, would lead to far and be out of the scope of this report.

IV. TRANSIENT WAVE PROPAGATION IN IONIZED MEDIA WITH EXPONENTIAL ELECTRON DENSITY PROFILES.

1. Laplace-transformed wave solutions in exponential media

Suppose that the electron density increases exponentially with height. In order to get an incident unit step wave to propagate upwards without dispersion we assume that the electron density is equal to zero in the region $z < 0$. The actual electron density profile is then given by

$$\left.\begin{aligned} \omega_p^2 &= \omega_o^2\, e^{z/H} \qquad && z > 0 \\ \omega_p^2 &= 0 && z < 0 \end{aligned}\right\} \qquad (4.1)$$

where H is a height scale factor, and ω_o is the plasma angular frequency at $z = 0$. Later we assume that ω_o is a very small quantity. The linearized wave equations for the electric field E can be written

$$\frac{\partial^2 E}{\partial z^2} - \frac{1}{c_o^2}\frac{\partial^2 E}{\partial t^2} = 0 \qquad z < 0 \qquad (4.2)$$

and

$$\frac{\partial^2 E}{\partial z^2} - \frac{1}{c_o^2}\left(\frac{\partial^2}{\partial t^2} + \omega_p^2\right) E = 0 \,. \qquad z > 0 \qquad (4.3)$$

Following the notations of van der Pol and Bremmer [1955] we now Laplacetransform these equations. Then we obtain

$$\frac{\partial^2 \tilde{E}}{\partial z^2} - \frac{1}{c_o^2}\, p^2\, \tilde{E} = 0 \qquad z < 0 \qquad (4.4)$$

and

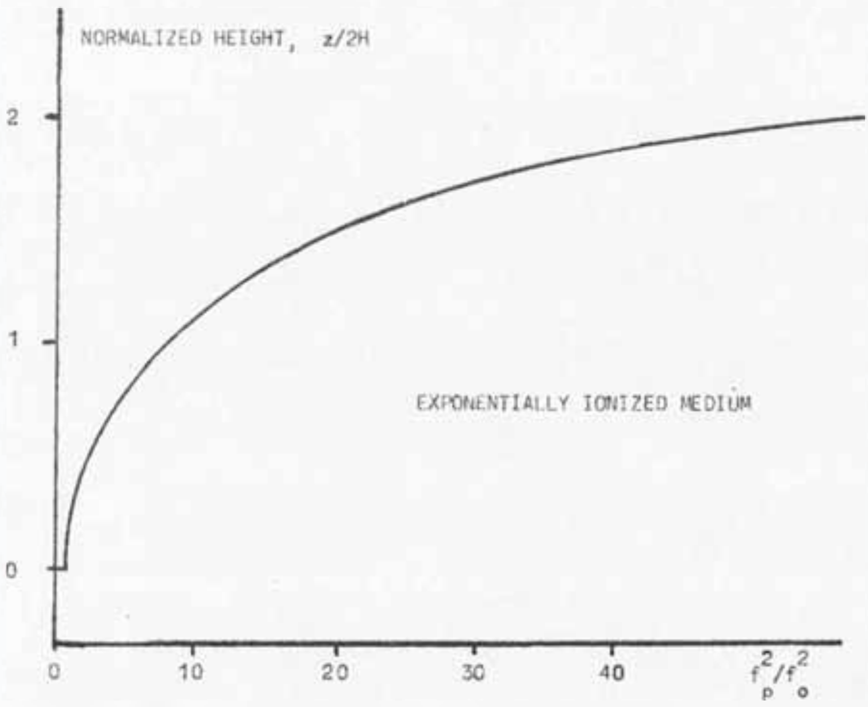

FIGURE 4.1. The exponential electron density profile.

$$\frac{\partial^2 \tilde{E}}{\partial z^2} - \frac{1}{c_o^2} \left(p^2 + \omega_p^2 \right) \tilde{E} = 0 \; , \qquad z > 0 \tag{4.5}$$

where $\tilde{E}$ denotes the Laplace-transform of E . Equation (4 .5) can be transformed into a Bessel differential equation.

Let

$$\zeta = \frac{2H}{c_o} e^{j \frac{\pi}{2}} \omega_o e^{z/2H} \tag{4.6}$$

and

$$\nu = \frac{2H}{c_o} p \; . \tag{4.7}$$

Then equation (4. 5) becomes

$$\frac{\partial^2 \tilde{E}}{\partial \zeta^2} + \frac{1}{\zeta} \frac{\partial \tilde{E}}{\partial \zeta} + \left(1 - \frac{\nu^2}{\zeta^2}\right) \tilde{E} = 0 , \qquad z > 0 \tag{4. 8}$$

which is Bessels equation of order ν. A solution must now be found which represents an upgoing wave only, at great height. Two independent solutions of (4. 8) are $H_\nu^{(1)}(\zeta)$ and $H_\nu^{(2)}(\zeta)$, where Watson's [1944] notation is used for Bessel functions of the third kind, sometimes called Hankel functions.

Now (4. 6) shows that $\arg \zeta = \frac{\pi}{2}$ and then the asymptotic approximations given by Watson [1944, p. 201] are as follows:

$$\begin{aligned} H_\nu^{(1)}(\zeta) &\sim (2/\pi\zeta)^{1/2} \exp\ j\left(\zeta - \frac{1}{2}\nu\pi - \frac{1}{4}\pi\right) \\ H_\nu^{(2)}(\zeta) &\sim (2/\pi\zeta)^{1/2} \exp\ -j\left(\zeta - \frac{1}{2}\nu\pi - \frac{1}{4}\pi\right) \end{aligned} \tag{4. 9}$$

At great heights the upgoing WKB-solution contains the factor

$$\exp\ -jk \int_o^z n dz \ = \exp\ (j\zeta).$$

Hence the required solution is $H_\nu^{(1)}(\zeta)$.

2. The unit step wave response.

In this paragraph we determine the reflected and transmitted waves when a unit step wave strikes the medium from below. An incident unit step wave,

$$\tilde{E}_I = e^{-p \frac{z}{c_o}} \qquad (z < 0) , \tag{4 .10}$$

gives rise to a reflected wave,

$$\tilde{E}_R = R(p)\, e^{p \frac{z}{c_o}} \qquad (z < 0) , \tag{4.11}$$

and a transmitted wave ,

$$\tilde{E}_T = T(p) \cdot H_\nu^{(1)}(\zeta) \qquad (z > 0) , \tag{4.12}$$

according to eq. (4 .9).

The boundary conditions

$$\tilde{E}(-0) = \tilde{E}(+0)$$

and (4 .13)

$$\frac{\partial E(-0)}{\partial z} = \frac{\partial E(+0)}{\partial z}$$

now require that

$$1 + R(p) = T(p)\, H_\nu^{(1)}(\zeta_o) \tag{4.14}$$

$$-\frac{p}{c_o} + \frac{p}{c_o} R(p) = T(p) \left\{ \frac{\partial}{\partial z} H_\nu^{(1)}(\zeta) \right\}_{\zeta = \zeta_o} , \tag{4.15}$$

where

$$\zeta_o = \zeta(z = 0) = \frac{2H}{c_o}\, \omega_o\, e^{j \frac{\pi}{2}} , \tag{4.16}$$

From eq.s (4,14) and (4 . 15) we obtain

$$T(p) = \frac{2\nu}{\zeta_o} \frac{1}{H_{\nu+1}^{(1)}(\zeta_o)} \tag{4.17}$$

and

$$R(p) = \frac{2\nu}{\zeta_o} \frac{H_\nu^{(1)}(\zeta_o)}{H_{\nu+1}^{(1)}(\zeta_o)} - 1 , \tag{4.18}$$

where we have used the linear relations

$$\left.\begin{aligned} 2\frac{\partial}{\partial\zeta} H_\nu^{(1)}(\zeta) &= H_{\nu-1}^{(1)}(\zeta) - H_{\nu+1}^{(1)}(\zeta) \\ \frac{2\nu}{\zeta} H_\nu^{(1)}(\zeta) &= H_{\nu-1}^{(1)}(\zeta) + H_{\nu+1}^{(1)}(\zeta) . \end{aligned}\right\} \tag{4.19}$$

The transmitted field $\tilde{E}_T$ at a height $z > 0$ (in the exponential medium) can now be written as

$$\boxed{\tilde{E}_T = \frac{2\nu}{\zeta_o} \frac{H_\nu^{(1)}(\zeta)}{H_{\nu+1}^{(1)}(\zeta_o)} ; \qquad (z > 0)} \tag{4.20}$$

In the same way the reflected field becomes

$$\boxed{\tilde{E}_R = \frac{2\nu}{\zeta_o} \frac{H_\nu^{(1)}(\zeta_o)}{H_{\nu+1}^{(1)}(\zeta_o)} e^{p\frac{z}{c_o}} - e^{p\frac{z}{c_o}} ; \quad (z < 0)} \tag{4.21}$$

In order to transform these step function responses into the time region we assume that $|\zeta_o| = \frac{2H}{c_o} \omega_o$ is a very small quantity and omit the boundary reflection and transmission at $z = 0$. Using the relations

$$H_\nu^{(1)}(\zeta) = \frac{J_{-\nu}(\zeta) - e^{-j\nu\pi} J_\nu(\zeta)}{j\sin\nu\pi} \tag{4.22}$$

$$J_\nu(\zeta) = \left(\frac{1}{2}\zeta\right)^\nu \sum_{k=0}^{\infty} \frac{\left(-\frac{1}{4}\zeta^2\right)^k}{k!\ \Gamma(\nu+k+1)}, \tag{4.23}$$

we obtain

$$\tilde{E}_T = \left(\frac{1}{2}\zeta_o\right)^\nu \Gamma(-\nu+1) \left[J_{-\nu}(\zeta) - e^{-j\nu\pi} J_\nu(\zeta)\right] \tag{4.24}$$

$$(\zeta_o \ll 1)$$

in the interval $-1 < \operatorname{Re}\nu < 0$.

This expression has a simple form, and it can easily be transformed into time region by means of the following Laplace transforms (Van der Pol & Bremmer [1955]):

$$(1-e^{-t})^{\frac{1}{2}\mu} J_\mu\left(a\sqrt{1-e^{-t}}\right) U(t) \fallingdotseq \left(\frac{2}{a}\right)^p \Gamma(p+1)\, J_{\mu+p}(a). \tag{4.25}$$

where $\operatorname{Re} p > 0$ and $\operatorname{Re}\mu > -1$

and

$$\frac{J_\mu\left(\sqrt{a^2+2a\,e^{-t}}\right)}{\left(1+\frac{2}{a}e^{-t}\right)^{\mu/2}} = \Gamma(p+1)\, J_{\mu-p}(a) \tag{4.26}$$

if $0 < \operatorname{Re} p < \frac{1}{2}\operatorname{Re}\mu + \frac{3}{4}$.

From relations (4.24) , (4.25) and (4.26) we obtain

$$\boxed{E_T(t,z) = J_o\left[\frac{2H}{c_o}\,\omega_p(z)\sqrt{e^{\frac{c_o}{2H}(t-z/c_o)}-1}\,\right] U\left(t-\frac{z}{c_o}\right), \quad \left(\frac{2H}{c_o}\,\omega_o \ll 1\right)} \tag{4.27}$$

which is the unit step wave (electric field) response at any arbitrary height in the exponential medium.

By means of (4 . 27) and Maxwell's equations we futhermore obtain the corresponding magnetic field as

$$H_T(t,z) = Y_o \left\{ E_T(t,z) + 2 \left[(e^{-T} - 1) E_T(t,z) + \int_o^T e^{-X} E_T(X)\, dX \right] \right\} . \tag{4 . 28}$$

where $E_T(X) = E_T(T=X)$

and $E_T(t,z)$ is given by relation (4 . 27). This relation between the magnetic and the electric fields may be compared with the same expression for the symmetrical Epstein layer which is derived in Chapter V (eq. (5.31)).

It is interesting to notice that the transmitted electric field (4 .27) has a very closed mathematical form compared to the corresponding stationary solution. Assuming an incident stationary wave

$$E_{I,\text{stationary}} = \text{Im}\left\{ e^{j\omega_1 (t - z/c_o)} \right\} , \tag{4 . 29}$$

the stationary standing wave in the medium is given by

$$E_{T,\text{stationary}} = \text{Im}\left\{ e^{j\omega_1 t} \left(\frac{2H}{c_o}\omega_o\right)^{j\frac{2H}{c_o}\omega_1} \Gamma\left(-j\frac{2H}{c_o}\omega_1 + 1\right) e^{-\frac{H}{c_o}\omega_1 \pi} \cdot \right.$$

$$\left. \cdot \left[J_{-j\frac{2H}{c_o}\omega_1}\left(j\frac{2H}{c_o}\omega_p\right) - J_{j\frac{2H}{c_o}\omega_1}\left(-j\frac{2H}{c_o}\omega_p\right) \right] \right\} . \tag{4. 30}$$

where $\frac{2H}{c_o}\omega_1$ usually is a large quantity. This simplification by means of transient wave propagation is perhaps still more obvious in the case of a symmetric Epstein layer (Chapter V).

From relation (4.27) we notice, as expected, that the wave front propagates with vacuum velocity c_o through the medium. The front amplitude is equal to 1. At large values of

$$\frac{c_o}{2H}\left(t - \frac{z}{c_o}\right)$$

we can write

$$E_T(t,z) \approx J_o\left\{\frac{2H}{c_o}\omega_o\, e^{\frac{c_o}{4H}\left(t + \frac{z}{c_o}\right)}\right\}, \qquad (4.31)$$

$$\left|\frac{c_o}{2H}\left(t - \frac{z}{c_o}\right)\text{ large}\right|$$

which represents a fast oscillating wave, propagating in negative z-direction without dispersion. This is the reflected wave which is built up by the high frequency components of the incident wave, returning after reflection at different heights high up in the inhomogeneous layer. Figure 4.2 shows the transmitted electric field versus the normalized time $\frac{c_o}{2H}\left(t - \frac{z}{c_o}\right)$ at a height where $\frac{2H}{c_o}\omega_p(z) = 0.25$. At this weak ionization the upgoing unit step wave has been very little dispersed. After a long time, however, the reflected high frequency components cause faster and faster oscillations while the amplitude is decreasing.

As a comparision we show (figure 4.3) the same transmitted electric field higher up in the layer where $\frac{2H}{c_o}\omega_p(z) = 2.5\pi$. It is interesting to compare these field variations with the corresponding results at corresponding heights in a symmetrical Epstein layer. See figures 5.2 and 5.3. The electron density variation is here approximately exponential. Consequently the transient fields are very alike. For this reason we have not computed the corresponding magnetic field for the exponential medium.

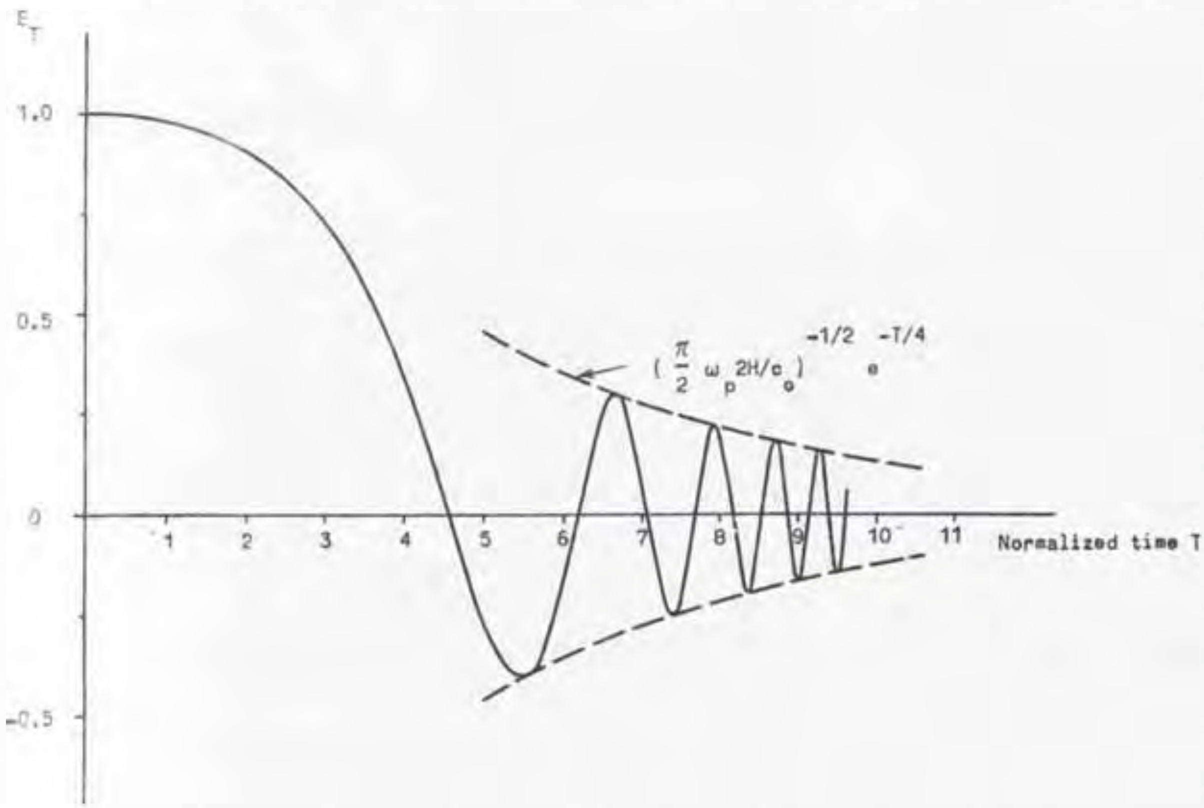

FIGURE 4.2. The unit step wave response (electric field) at a height in the exponentially ionized medium where $\omega_p(z) = 0.25\ c_o/2H$.

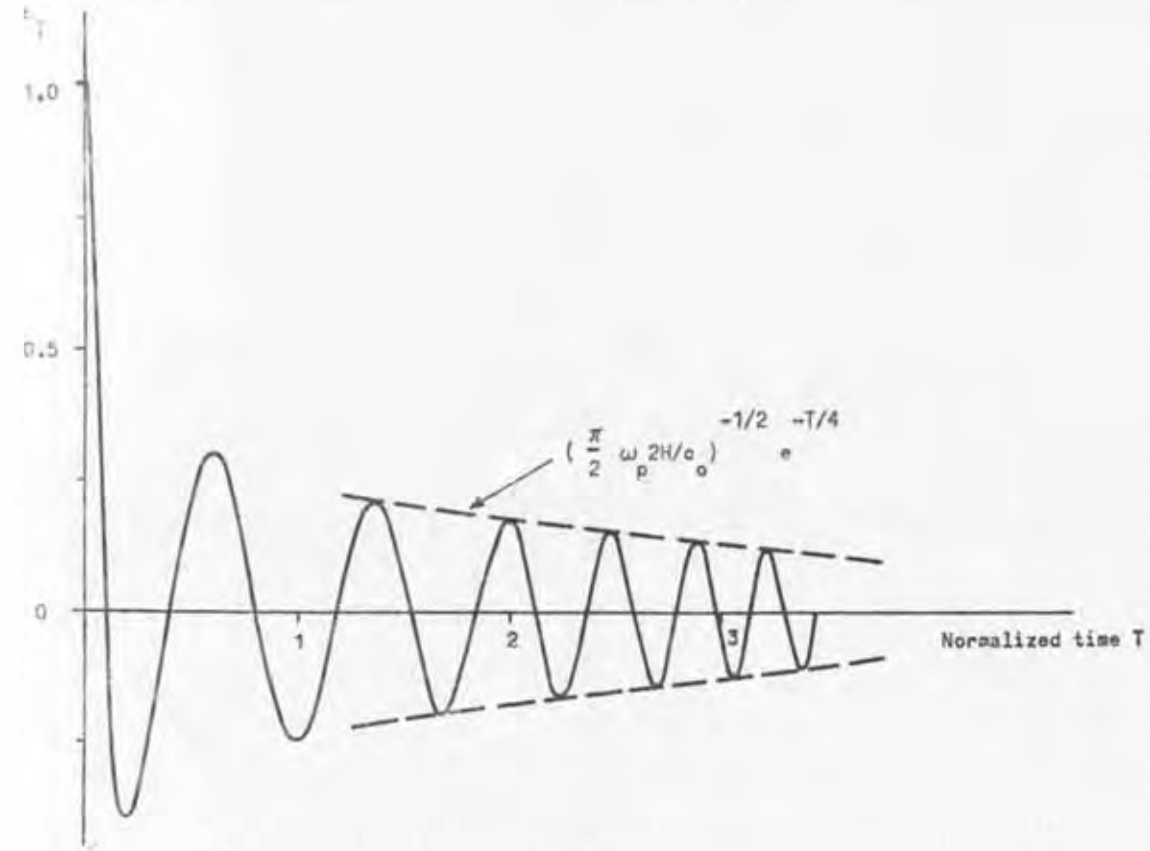

FIGURE 4.3. The unit step wave response (electric field) at a height in the exponentially ionized medium where $\omega_p(z) = 2.5\ \pi\ c_o/2H$.

The static electric field is equal to zero contrary to the magnetic field which has a finite static value, $H_{T,static}$, given by

$$H_{T,static}(z) \quad 2\,Y_o\ \frac{2H}{c_o}\ \omega_p(z)\ K_1\ \left[\frac{2H}{c_o}\ \omega_p(z)\right], \tag{4,32}$$

a relation which can be obtained from eq:s (3.3) and (4.24). When the ionization is weak we obtain

$$H_{T,static}(z) \sim 2Y_o. \tag{4,33}$$

$$\left(\frac{2H}{c_o}\ \omega_p(z) \to 0\right)$$

while at strong ionization

$$H_{T,static}(z) \sim 2Y_o \sqrt{\frac{\pi}{2}\ \frac{2H}{c_o}\ \omega_p(z)}\ e^{-\frac{2H}{c_o}\omega_p(z)} \tag{4,34}$$

$$\left(\frac{2H}{c_o}\ \omega_p(z) \gg 1\right)$$

i.e. the static magnetic field decreases very rapidly with height. Figure 4.4 shows the variation of the final, static magnetic field with the ionization.

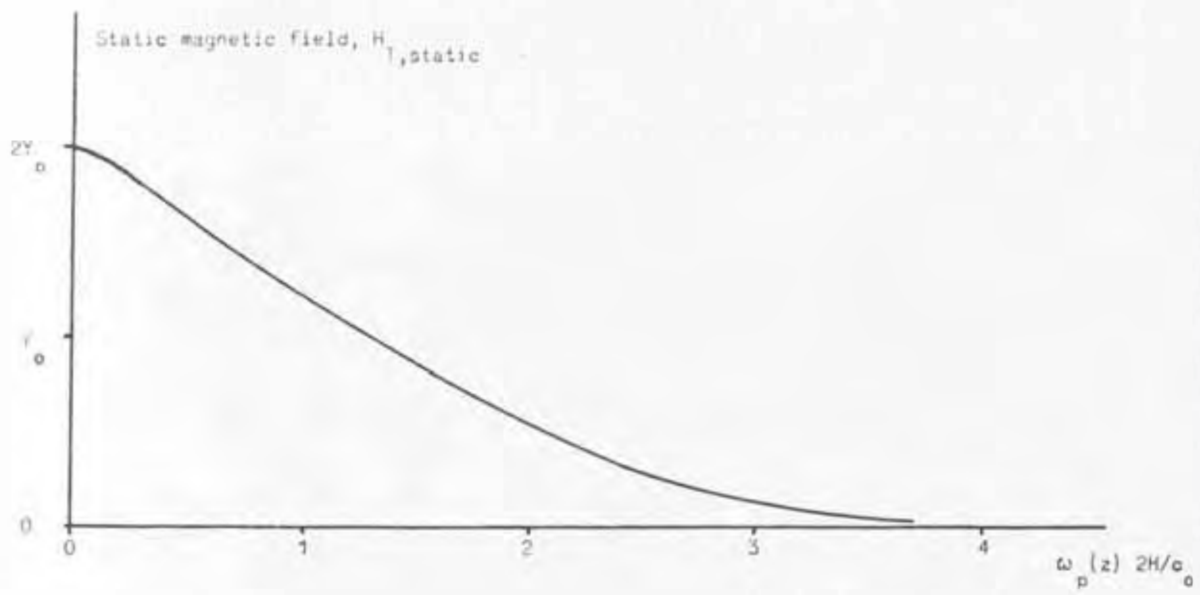

FIGURE 4.4. The final, static magnetic field versus the ionization in the exponentially ionized medium. Incident magnetic field $Y_o U(t-z/c_o)$.

3. Wave propagation properties obtained from the unit step wave response.

The frequency characteristics of the reflected wave can easily be found by means of the impulse wave response $E_{T,\delta}$ which is obtained by derivation of the unit step wave response, eq. (4.27).

$$E_{T,\delta}(t,z) = -\frac{1}{2}\,\omega_p\,\frac{e^{T}}{\sqrt{e^{T}-1}}\,J_1\left[\frac{2H}{c_o}\,\omega_p(z)\sqrt{e^{T}-1}\right]U\left(t-\frac{z}{c_o}\right)+\delta\left(t-\frac{z}{c_o}\right), \tag{4.35}$$

where as before

$$T = \frac{c_o}{2H}\left(t-\frac{z}{c_o}\right).$$

Omitting the impulse function Bowhill [1955] has obtained the same expression by means of a complicated scatter technique

For large values of T we obtain

$$E_{T,\delta}(t,z) \sim -\frac{1}{2}\,\omega_o\,e^{\frac{1}{2}T_1}\,J_1\left(\frac{2H}{c_o}\,\omega_o\,e^{\frac{1}{2}T_1}\right), \tag{4.36}$$

$$(T \gg 1)$$

where

$$T_1 = \frac{c_o}{2H}\left(t+\frac{z}{c_o}\right),$$

This is the reflected electric field.

The Fourier spectrum of the reflected wave, which we denote $S_R(f)$, can be obtained by integration of eq. (4.36) or directly from the second term in eq. (4.24), assuming ζ to be small. At $z = 0$ we obtain

$$S_R(f) = \left(\frac{\omega_o H}{c_o}\right)^{j\frac{4H}{c_o}\omega} \frac{\Gamma\left(-j\frac{2H}{c_o}\omega\right)}{\Gamma\left(j\frac{2H}{c_o}\omega\right)} \tag{4.37}$$

The incident impulse wave has a constant frequency spectrum equal to 1. Consequently, the amplitude of the reflected stationary unit wave (propagation constant $k = \frac{\omega}{c_o}$) is equal to 1, and the phase shift is

$$-4kH \ln \frac{c_o}{\omega_o H} - 2 \arg \left\{ \Gamma(j\, 2kH) \right\} \tag{4.38}$$

o o o

The unit step wave response (4.27) has a momentary angular frequency, ω_m, equal to

$$\omega_m = \frac{d}{dt}\left\{\frac{2H}{c_o}\,\omega_p \sqrt{e^T - 1}\right\}, \tag{4.39}$$

i.e.,

$$\omega_m^2 = \frac{1}{4}\,\omega_p^2\,\frac{e^{2T}}{e^T - 1} \quad . \tag{4.40}$$

This is the momentary angular frequency versus time at a height z in the exponential medium. Relation (4.40) can also be written in an alternative form

$$\left[e^T\right]_{\substack{1\\2}} = \frac{2\,\omega_m^2}{\omega_p^2} \pm \frac{2\omega_m}{\omega_p}\sqrt{\frac{\omega_m^2}{\omega_p^2} - 1} \tag{4.41}$$

At once we notice, as expected, that relation (4.41) has two different solutions (subscripted 1 and 2) when $\omega_m > \omega_p$. Higher up in the medium, where $\omega_m = \omega_p$, these two solutions coincide which means that this is the reflection level at a wave frequency equal to ω_m.

Directly from the solutions (4.41) we obtain the virtual height, $h_v(\omega_m)$, at a height z as

$$h_v(\omega_m) = \frac{c_o}{2}(t_1 - t_2) = 2H \ln\left\{\frac{\omega_m}{\omega_p} + \left(\frac{\omega_m^2}{\omega_p^2} - 1\right)^{1/2}\right\}. \qquad (4.42)$$

The virtual height can also be found from

$$h_v(\omega_m) = \int_z^{\text{reflection height}} \frac{dz}{n} = \int_z^{2H \ln \frac{\omega}{\omega_o}} \left\{1 - \frac{\omega_o^2}{\omega^2} e^{z/H}\right\}^{-1/2} dz, \qquad (4.43)$$

where n is the refractive index,
which gives

$$h_v(\omega_m) = 2H \ln\left[\frac{\omega}{\omega_p} + \left(\frac{\omega^2}{\omega_p^2} - 1\right)^{1/2}\right], \qquad (4.44)$$

i.e. the same result as eq. (4.42).

This is a good example of the deeper understanding of wave propagation phenomena which one obtains from the transient wave solutions.

4. The unit step modulated carrier response.

The unit step wave response is very interesting in itself since it yields the entire propagation properties of the medium and besides a method of analysing or probing the medium, using impulse or step formed test waves. At the same time it leads through convolution integrals to the medium responses for other types of incident waves. In this paragraph we examine the response of an incident step modulated carrier from which for instanee the distortion of a square pulse easily can be found.

Assume an incident wave

$$E_{I,sin}(t,z) = \sin\left[\omega_1\left(t - \frac{z}{c_o}\right)\right] U\left(t - \frac{z}{c_o}\right) \tag{4.45}$$

or

$$E_{I,cos}(t,z) = \cos\left[\omega_1\left(t - \frac{z}{c_o}\right)\right] U\left(t - \frac{z}{c_o}\right). \tag{4.46}$$

Using the unit step wave response, eq. (4.27), and the convolution theorem, we immediately obtain the resulting waves in the medium as

$$E_{T,sin}(t,z) = \omega_1 \frac{2H}{c_o} \int_o^T \cos\left[\omega_1 \frac{2H}{c_o}(T - x)\right] E_T(x)\, dx \tag{4.47}$$

and

$$E_{T,cos}(t,z) = E_T(t,z) - \omega_1 \frac{2H}{c_o} \int_o^T \sin\left[\omega_1 \frac{2H}{c_o}(T - x)\right] E_T(x)\, dx, \tag{4.48}$$

where

$$T = \frac{c_o}{2H}\left(t - \frac{z}{c_o}\right)$$

and

$$E_T(x) = J_0\left(\frac{2H}{c_0}\omega_p\sqrt{e^x - 1}\right) U(x) \tag{4.49}$$

(eq. 4.27)

The corresponding magnetic field is obtained if we instead use the unit step magnetic field response (ref. 4.28). In the following we concentrate our investigation on the transient response of a sinusoidial wave, i.e. on eq. (4.47).

Unfortunately, the convolution integral can not be solved analytically. As a consequence, we have used a digital computer (SAAB - D 21) in order to determine the time variation at different heights. The stationary wave in the medium consists of a standing wave which is monotonically decreasing in the evanescent region. Figure 4.5 shows the build-up of that standing wave at the classical reflection level and at two different heights in the evanescent region. The strong remarkable and interesting deformation of the wave in figure (4.5) is due to interference between up-going, time-delayed waves and reflected higher frequency components. A more detailed discussion will appear in Chapter V where we have determined the same carrier response and besides the magnetic field and energy flow at corresponding points in a symmetric Epstein layer.

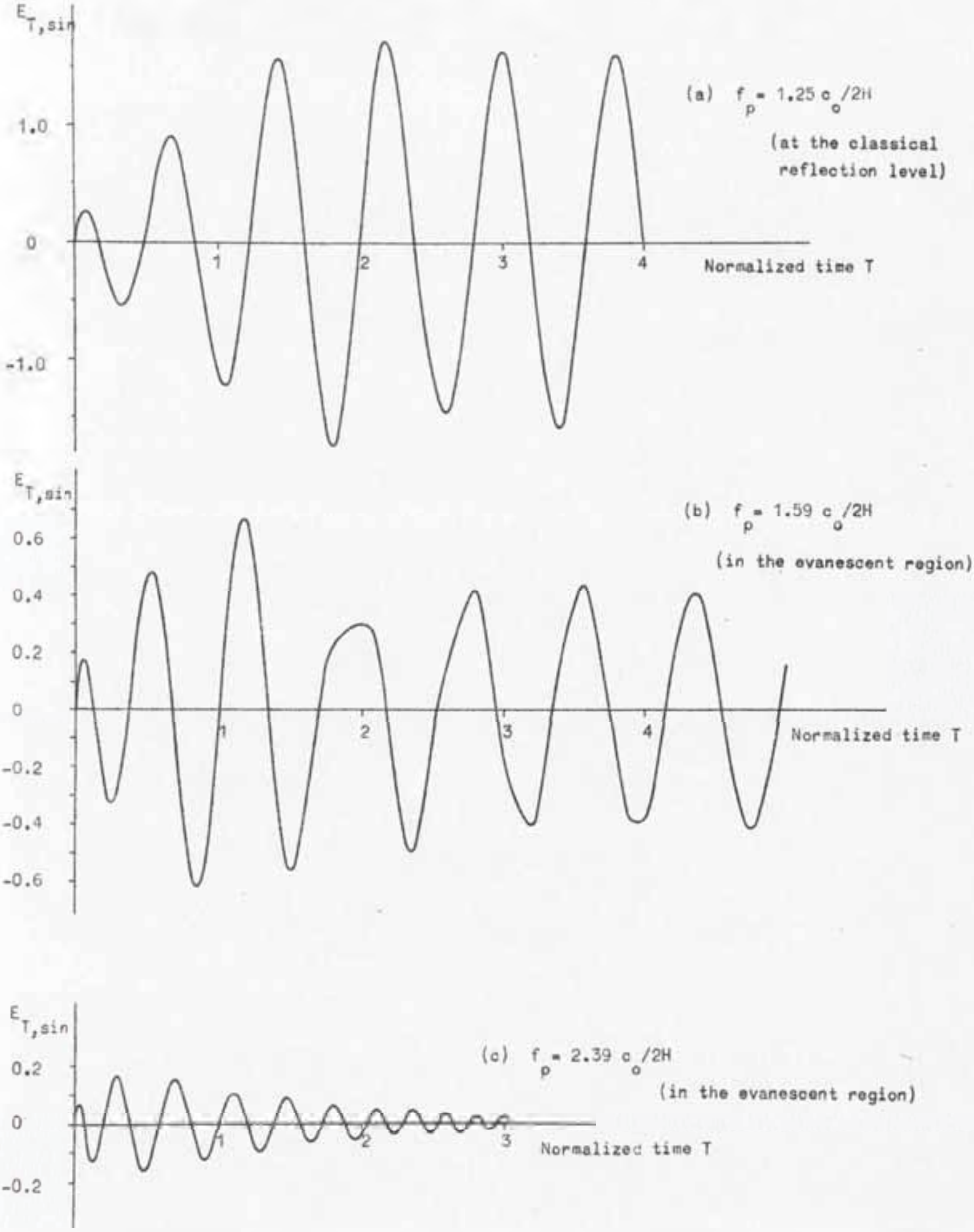

FIGURE 4.5. The unit step modulated carrier response (electric field) of the exponentially ionized medium at three different heights given by the corresponding plasma frequencies f_p. Carrier frequency $f_1 = 1.25\ c_o/2H$.

V TRANSIENT WAVE PROPAGATION IN AN IONIZED, SYMMETRICAL EPSTEIN LAYER.

1. Laplace-transformed solutions of the linearized wave equation.

In this paragraph we are going to study wave propagation in an inhomogeneous ionized medium of a type often called a symmetrical Epstein layer [Epstein, 1930]. Sometimes it is also called a sech^2- profile. The electron density variation is then given by

$$N(z) = N_m \frac{1}{\cosh^2 \frac{z}{2H}} , \tag{5.1}$$

where H is a height scale factor.

This medium is more complicated but also more interesting than the exponential layer. dealt with in Chapter IV. It is more interesting since it is an ionized barrier (see figure 5.1) which makes it possible to analyse transient wave propagation and signal distortion at or near the penetration frequency of the layer. Besides we can now study the interesting case of tunnel transmission through the barrier, a field where little has been done.

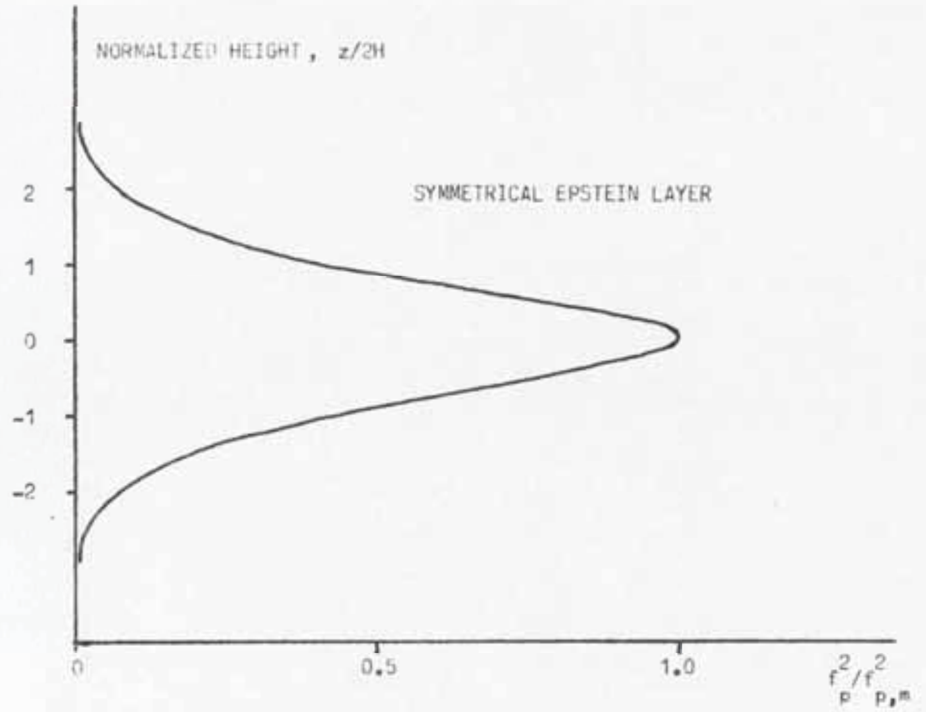

FIGURE 5.1. The symmetrical Epstein layer.

We suppose that the plasma angular frequency varies according to

$$\left.\begin{aligned} \omega_p^2 &= \omega_{p,m}^2 \; \frac{1}{\cosh^2 \frac{z}{2H}} && z > z_1 \\ \omega_p^2 &= 0 && z < z_1 \end{aligned}\right\} \tag{5.2}$$

The linearized wave equations for the electric field E at propagation in z-direction are

$$\frac{\partial^2 E}{\partial z^2} - \frac{1}{c_o^2} \frac{\partial^2 E}{\partial t^2} = 0 \quad , \qquad z < z_1 \tag{5.3}$$

$$\frac{\partial^2 E}{\partial z^2} - \frac{1}{c_o^2} \left(\frac{\partial^2}{\partial t^2} + \omega_p^2\right) E = 0 \, . \qquad z > z_1 \tag{5.4}$$

The corresponding Laplace-transformed equations then become

$$\frac{\partial^2 \tilde{E}}{\partial z^2} - \frac{1}{c_o^2} p^2 \tilde{E} = 0 \; , \qquad z < z_1 \tag{5.5}$$

$$\frac{\partial^2 \tilde{E}}{\partial z^2} - \frac{1}{c_o^2} (p^2 + \omega_p^2) \; \tilde{E} = 0 \qquad z > z_1 \tag{5.6}$$

Equation (5.6) can be transformed into a hypergeometric differential equation if we introduce a new variable

$$-\zeta = e^{z/2H} . \tag{5.7}$$

Then equation (5.6) can be written

$$\zeta\,(1-\zeta)\,\frac{\partial^2\Pi}{\partial\zeta^2} + [\,c - (a+b+1)\,\zeta\,]\,\frac{\partial\Pi}{\partial\zeta} + ab\Pi = 0 , \tag{5.8}$$

where

$$\tilde{E} = \Pi\, e^{-(1-c)\,z/2H}\,(1+e^{z/2H})^{-(c-1-a-b)/2} , \tag{5.9}$$

and

$$a - b = c - 1 = -\frac{2H}{c_o}\,p , \tag{5.10}$$

$$\frac{(a+b-c)^2}{4} = \frac{1}{4} - \frac{4H^2}{c_o^2}\,\omega_{p,m}^2 = \gamma^2 . \tag{5.11}$$

From equation (5.8) we obtain among others the following linearly dependent solutions

$$\Pi_1 = F(a,b;\,c;\,\zeta) , \tag{5.12 a}$$

$$\Pi_2 = (-\zeta)^{1-c}\,F(a-c+1\,,\,b-c+1;\,2-c;\,\zeta) , \tag{5.12 b}$$

$$\Pi_3 = (-\zeta)^{-a}\,F(a,a-c+1;\,a-b+1;\zeta^{-1}) , \tag{5.12 c}$$

$$\Pi_4 = (-\zeta)^{-b}\,F(b,b-c+1;\,b-a+1;\zeta^{-1}) . \tag{5.12 d}$$

When $\zeta \to 0$, i.e. $\frac{z}{H} \to -\infty$, equations (5.9), (5.12 a) and (5.12 b) give

$$\tilde{E}_1 \to e^{-p\frac{z}{c_o}}, \qquad \left(\frac{z}{H} \to -\infty\right) \tag{5.13 a}$$

$$\tilde{E}_2 \to e^{p\frac{z}{c_o}}, \qquad \left(\frac{z}{H} \to -\infty\right) \tag{5.13 b}$$

which represent up- and downgoing unit step waves.

When $\zeta^{-1} \to 0$, i.e. $\frac{z}{H} \to +\infty$, equations (5.9), (5.12 c) and (5.12 d) give

$$\tilde{E}_3 \to e^{p\frac{z}{c_o}}, \qquad \left(\frac{z}{H} \to +\infty\right) \tag{5.13 c}$$

$$\tilde{E}_4 \to e^{-p\frac{z}{c_o}}, \qquad \left(\frac{z}{H} \to +\infty\right) \tag{5.13 d}$$

which in the same way represent down- and upgoing unit step waves above the layer. By physical reasons we now see that a wave, incident from below, creates a Laplace-transformed wave in the ionized medium with a z-dependence according to

$$e^{-p\frac{z}{c_o}} \left(1 + e^{-z/H}\right)^{\gamma + \frac{1}{2}} F\left(\frac{1}{2} + \gamma + \frac{2H}{c_o}p,\ \frac{1}{2} + \gamma;\ 1 + \frac{2H}{c_o}p;\ -e^{-z/H}\right). \tag{5.14}$$

Futhermore we have the following circuit relation between this solution and the solutions (5.12 a) and (5.12 b)

$$\frac{\Gamma(\frac{2H}{c_o}p-\gamma+\frac{1}{2})\ \Gamma(\frac{2H}{c_o}p+\gamma+\frac{1}{2})}{\Gamma(\frac{2H}{c_o}p)\quad\Gamma(1+\frac{2H}{c_o}p)}\ e^{-p\frac{z}{c_o}}\ (1+e^{-z/H})^{\gamma+\frac{1}{2}}\ .$$

$$\cdot\ F(\tfrac{1}{2}+\gamma+\tfrac{2H}{c_o}p\ ,\ \tfrac{1}{2}+\gamma\ ;\ 1+\tfrac{2H}{c_o}p;\ -e^{-z/H}) =$$

$$= (1+e^{z/H})^{\gamma+\frac{1}{2}}\ e^{-p\frac{z}{c_o}}\ F(\tfrac{1}{2}+\gamma-\tfrac{2H}{c_o}p,\ \tfrac{1}{2}+\gamma\ ;\ 1-\tfrac{2H}{c_o}p;-e^{z/H})\ +$$

$$+\ (1+e^{z/H})^{\gamma+\frac{1}{2}}\ e^{p\frac{z}{c_o}}\ \frac{\Gamma(-\frac{2H}{c_o}p)\ \Gamma(\frac{2H}{c_o}p-\gamma+\frac{1}{2})\ \Gamma(\frac{2H}{c_o}p+\gamma+\frac{1}{2})}{\Gamma(\frac{2H}{c_o}p)\ \Gamma(-\gamma+\frac{1}{2})\ \ \Gamma(\gamma+\frac{1}{2})}$$

$$\cdot\ F(\tfrac{1}{2}+\gamma+\tfrac{2H}{c_o}p\ ,\ \tfrac{1}{2}+\gamma\ ;1+\tfrac{2H}{c_o}p\ ;\ -e^{z/H})\ , \qquad (5.15)$$

which we are going to use in next paragraph.

2. The unit step wave response

Assume that an up-going unit step wave strikes the ionized medium at the height $z = z_1$ at a time $t = \frac{z_1}{c_o}$. We try to find the time variation of the resulting wave in the layer $(z > z_1)$.

Below the medium we accordingly have the following Laplace-transformed electric field

$$\tilde{E}_{I+R} = e^{-p\frac{z}{c_o}} + R(p)\ e^{p\frac{z}{c_o}}\ , \qquad (z < z_1) \qquad (5.16)$$

and in the medium ($z > z_1$) from eq (5.14)

$$\tilde{E}_T = T(p) \cdot \tilde{E} , \tag{5.17}$$

where $\tilde{E}$ is given by the solution (5.14).

R(p) and T(p) are determined by the boundary conditions

$$e^{-p\frac{z_1}{c_o}} + R(p)\, e^{p\frac{z_1}{c_o}} = T(p) \left\{ \tilde{E} \right\}_{z=z_1} , \tag{5.18}$$

$$-\frac{p}{c_o}\, e^{-p\frac{z_1}{c_o}} + \frac{p}{c_o} R(p)\, e^{p\frac{z_1}{c_o}} = T(p) \left\{ \frac{\partial}{\partial z} \tilde{E} \right\}_{z=z_1} \tag{5.19}$$

Let us, as we did for the exponential medium, suppose that the discontinuity at $z = z_1$ is so small that no boundary reflection occurs. This means that $\frac{z_1}{H} \to -\infty$. Using the circuit relation (5.15) we then obtain

$$T(p) = \frac{\Gamma\left(\frac{2H}{c_o} p - \gamma + \frac{1}{2}\right) \Gamma\left(\frac{2H}{c_o} p + \gamma + \frac{1}{2}\right)}{\Gamma\left(\frac{2H}{c_o} p\right) \Gamma\left(1 + \frac{2H}{c_o} p\right)} , \tag{5.20}$$

and the Laplace-transformed unit step wave response (the electric field) in the ionized medium becomes

$$\boxed{\begin{aligned} \tilde{E}_T = {} & \frac{\Gamma\left(\frac{2H}{c_o} p - \gamma + \frac{1}{2}\right) \Gamma\left(\frac{2H}{c_o} p + \gamma + \frac{1}{2}\right)}{\Gamma\left(\frac{2H}{c_o} p\right) \Gamma\left(1 + \frac{2H}{c_o} p\right)} \, e^{-p\frac{z}{c_o}} \cdot \\ & \cdot \left(1 + e^{-z/H}\right)^{\gamma + \frac{1}{2}} F\left(\frac{1}{2} + \gamma + \frac{2H}{c_o} p, \frac{1}{2} + \gamma ; 1 + \frac{2H}{c_o} p ; -e^{-z/H}\right) \end{aligned}} \tag{5.21}$$

In order to transform this expression to a time varying function we use a new circuit relation and obtain

$$\tilde{E}_T = e^{-p\frac{z}{c_o}} F\left(\frac{1}{2}+\gamma,\ \frac{1}{2}-\gamma;\ 1-\frac{2H}{c_o}p;\ \frac{1}{1+e^{-z/H}}\right) +$$

$$+ e^{-p\frac{z}{c_o}} \frac{\Gamma\left(-\frac{2H}{c_o}p\right)\Gamma\left(\frac{2H}{c_o}p-\gamma+\frac{1}{2}\right)\Gamma\left(\frac{2H}{c_o}p+\gamma+\frac{1}{2}\right)}{\Gamma\left(\frac{2H}{c_o}p\right)\Gamma\left(-\gamma+\frac{1}{2}\right)\Gamma\left(\gamma+\frac{1}{2}\right)} \cdot$$

$$\cdot (1+e^{-z/H})^{-\frac{2H}{c_o}p} F\left(\frac{1}{2}+\gamma+\frac{2H}{c_o}p,\ \frac{1}{2}-\gamma-\frac{2H}{c_o}p;\ 1+\frac{2H}{c_o}p;\ \frac{1}{1+e^{-z/H}}\right).$$

(5.22)

We start looking at the first term

$$e^{-p\frac{z}{c_o}} F\left(\frac{1}{2}+\gamma,\ \frac{1}{2}-\gamma;\ 1-\frac{2H}{c_o}p;\ \frac{1}{1+e^{-z/H}}\right). \tag{5.23}$$

The hypergeometric function has singular points only in the interval Re p >0, and obviously the corresponding time function is $\equiv 0$, when $t-\frac{z}{c_o}>0$. From Appendix I (eq. A I. 4) we obtain the time function

$$-F\left[\frac{1}{2}+\gamma,\ \frac{1}{2}-\gamma;\ 1;\ \frac{1}{1+e^{-z/H}}(1-e^{T})\right] U\left[-\left(t-\frac{z}{c_o}\right)\right] =$$

$$= -P_{\gamma-\frac{1}{2}}\left[1+\frac{2}{1+e^{-z/H}}(e^{T}-1)\right] U\left[-\left(t-\frac{z}{c_o}\right)\right] \tag{5.24}$$

where

$$T = \frac{c_o}{2H} \left(t - \frac{z}{c_o}\right) \tag{5.25}$$

From Appendix I (eq. AI. 7) we also obtain the corresponding time function of the complicated second term in eq. (5.22) as

$$F\left[\frac{1}{2} + \gamma, \frac{1}{2} - \gamma; 1; \frac{1}{1 + e^{-z/H}} (1 - e^{T})\right] =$$

$$= P_{\gamma - \frac{1}{2}} \left[1 + \frac{1}{1 + e^{-z/H}} (e^{T} - 1)\right] . \tag{5.26}$$

The solutions (5.25) and (5.26) are both valid in the region $\frac{1}{2} < \mathrm{Re}\left\{\frac{2H}{c_o} p\right\} < 0$ (see Appendix 1) and consequently we obtain the resulting electric field (the unit step wave response) as

$$E_T(t,z) = F\left[\frac{1}{2} + \gamma, \frac{1}{2} - \gamma; 1; \frac{1}{1 + e^{-z/H}} (1 - e^{T})\right] U\left(t - \frac{z}{c_o}\right) =$$

$$= P_{\gamma - \frac{1}{2}} \left[1 + \frac{2}{1 + e^{-z/H}} (e^{T} - 1)\right] U\left(t - \frac{z}{c_o}\right) , \tag{5.27}$$

where

$$\gamma^2 = \frac{1}{4} - \frac{4H^2}{c_o^2} \omega_{p,m}^2 \tag{5.28}$$

and

$$T = \frac{c_o}{2H} \left(t - \frac{z}{c_o}\right) \tag{5.29}$$

The transformation to the time region has been done in the interval $\frac{1}{2} < \text{Re}\left\{\frac{2H}{c_o} p\right\} < 0$. As a matter of fact this means that eq. (5.27) is the response of an incident wave

$$E_I = -1 + U\left(t - \frac{z}{c_o}\right),$$

which is the transform of $e^{-p\frac{z}{c_o}}$ in the actual p-interval. However, -1 has a wave response equal to 0 and therefore eq. (5.27) is the unit step wave response of the layer. The same argument holds for the exponential profile, treated in Chapter IV.

Using Maxwell's equation

$$\frac{\partial H_y}{\partial t} = -\frac{1}{\mu_o} \frac{\partial E_x}{\partial z} \qquad (H_y = H_T;\ E_x = E_T) \tag{5.30}$$

and relation (5.27) we obtain the corresponding magnetic field as

$$H_T(t,z) = Y_o\left\{E_T(t,z) + \frac{2}{1+e^{z/H}}\left[(e^{-T}-1)\,E_T(t,z) + \int_o^T e^{-X} E_T(X)\,dX\right]\right\}, \tag{5.31}$$

where E_T (t,z) is given by relation (5,27) and

$$E_T(X) = P_{\gamma - \frac{1}{2}} \left[1 + \frac{2}{1 + e^{-z/H}} (e^X - 1) \right] . \tag{5,32}$$

Far below the layer where the ionization increases exponentially, relation (5,31) agrees with the corresponding expression for the exponential medium (eq. 4,28).

The static electric field is equal to zero in contrast to the magnetic field which has a finite static value. $H_{T,\text{static}}$ equal to

$$H_{T,\text{static}} = 2\, Y_o \frac{\Gamma(\frac{3}{2} - \gamma)\, \Gamma(\frac{3}{2} + \gamma)}{1 + e^{z/H}} F\left(\frac{1}{2} + \gamma, \frac{1}{2} - \gamma ; 2; \frac{1}{1 + e^{z/H}} \right) , \tag{5,33}$$

a result which can be obtained from eq:s (3,3) and (5,21)

In figure 5.2 we show the unit step wave response (the time variations of the electric field and the magnetic field) at $z/2H = -2.36$, i.e. far below the apex of the layer. At this height the electron density is so low that we still have a high static magnetic field. (In this case $Z_o H_{T,\text{ static}} = 0.525$). It is also worth noting that the electric field and the magnetic field are 180^o out of phase for $T > 3.0$. This means that there is a net energy flow in the negative z-direction.

Near the apex of the ionized layer both the electric field and the magnetic field oscillate much faster (see figure 5.3), but still the instantaneous frequency at large value of T is equal to the apex plasma frequency $f_{p,m} = 1.75\, c_o/2H$. Due to the high electron density the magnetic field $Z_o H_T$ is much weaker, and the static magnetic field can be neglected.

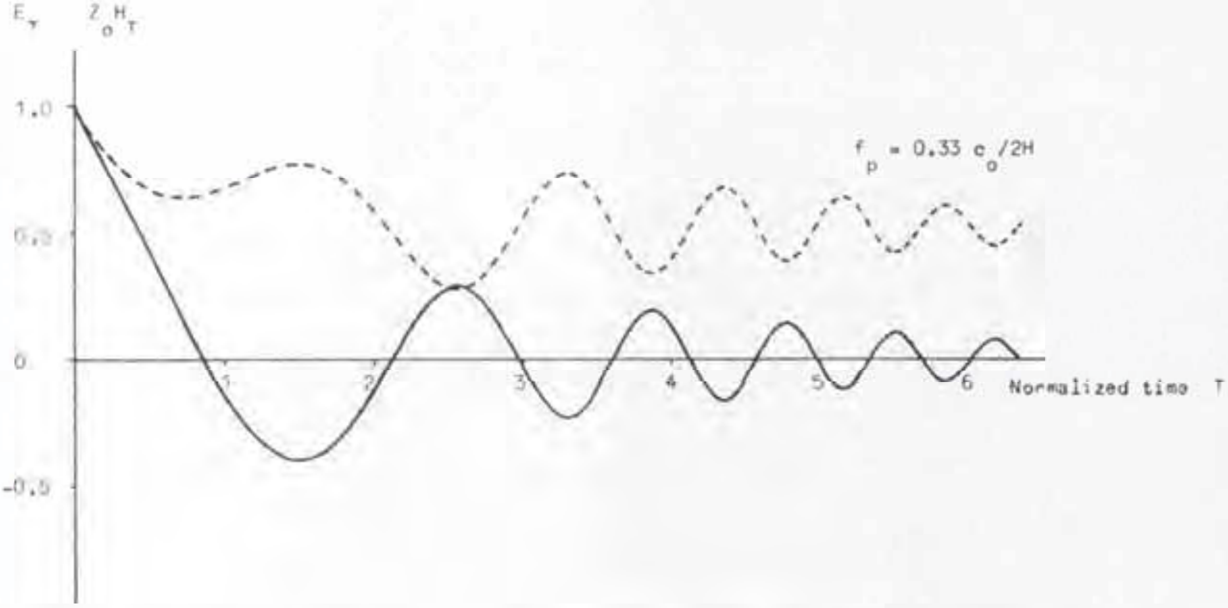

FIGURE 5.2. The unit step wave response, electric field (——) and magnetic field (- - - -), at $z/2H = -2.36$ in a symmetrical Epstein layer. Penetration frequency $f_{p,m} = 1.75\ c_o/2H$.

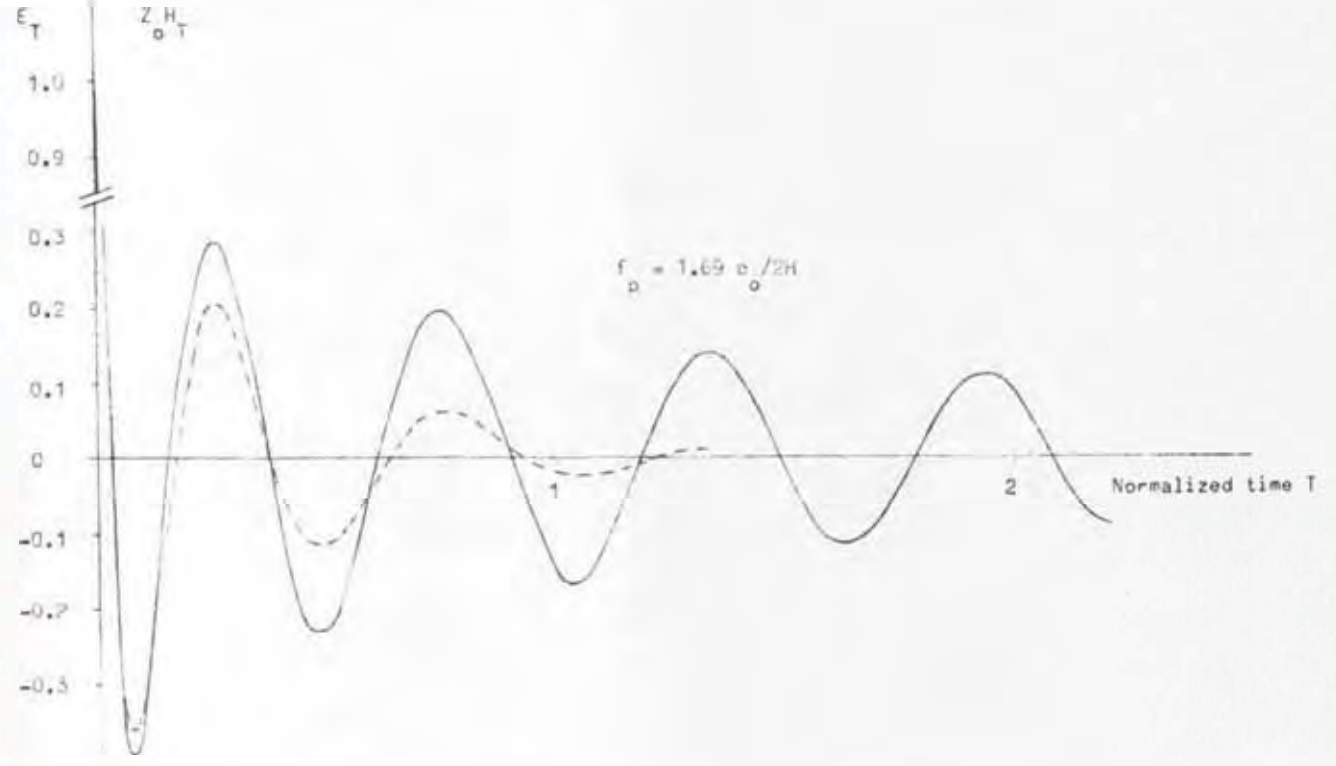

FIGURE 5.3. The unit step wave response, electric field (——) and magnetic field (- - - -), at $z/2H = -0.285$ in a symmetrical Epstein layer. Penetration frequency $f_{p,m} = 1.75\ c_o/2H$.

3. Properties of the unit step wave response

By means of eq. (5,27) we obtain the following properties of the unit step wave response

1. $z/H >> 1$, i.e. far above the layer.

Then

$$E_T(t,z) \sim P_{\gamma-\frac{1}{2}}(2e^T)\,U(t-\frac{z}{c_o}), \qquad (z/H>>1) \tag{5,34}$$

which is the wave response on the other side of the layer. This is a wave propagating upwords without dispersion.

2. $z/H << -1$, i.e. far below the layer.

Then

$$E_T(t,z) \sim P_{\gamma-\frac{1}{2}}\left[1+2e^{z/H}(e^T-1)\right]U(t-\frac{z}{c_o}), \qquad (\frac{z}{H} << -1) \tag{5,35}$$

which for large values of T becomes

$$E_T(t,z) \sim P_{\gamma-\frac{1}{2}}\left(2e^{\frac{c_o}{2H}(t+\frac{z}{c_o})}\right), \qquad (\frac{z}{H} << -1, T>> 1) \tag{5,36}$$

This represents the reflected wave far belowthe layer.

3. $\omega_{p,m}^2 = 0$. i.e. there is no ionized media.

Then $\gamma^2 = \frac{1}{4}$ and, as expected,

$$E_T(t,z) = P_o \left[1 + \frac{2}{1 + e^{-z/H}} (e^T - 1) \right] U(t - \frac{z}{c_o}) =$$

$$= U(t - \frac{z}{c_o}) \qquad (\omega_{p,m}^2 = 0) \tag{5.37}$$

4. Small value of T

$$E_T(t,z) = F\left(\frac{1}{2} + \gamma , \frac{1}{2} - \gamma ; 1 ; -x \right) =$$

$$= 1 + \frac{\frac{1}{4} - \gamma^2}{1 \cdot 1} (-x) + \frac{(\frac{1}{4} - \gamma^2)(\frac{9}{4} - \gamma^2)}{2!\,2!} (-x)^2 + \ldots =$$

$$= 1 + \sum_{m=1}^{\infty} (-1)^m x^m \prod_{n=0}^{m-1} \frac{n(n+1) + \frac{4H^2}{c_o^2} \omega_{p,m}^2}{(n+1)^2} , \tag{5.38}$$

where

$$x = \frac{1}{1 + e^{-z/H}} (e^T - 1) \tag{5.39}$$

At once we notice that

$$E_T(T = +0) = 1 . \tag{5.40}$$

i.e. the wavefront moves with vacuum velocity and the front amplitude is equal to 1.

5. Large values of $|\gamma|$ and $T > 0$.

Normally

$$\frac{2H}{c_o}\,\omega_{p,m} \gg 1$$

(for the F-layer in the ionosphere this quantity is of the order 1000), i.e. γ is imaginary and $|\gamma| \gg 1$ (eq. 5.28). We try to find an asymptotic expression for $E_T(t,z)$ for large value of $|\gamma|$.

Let us look at the following relation

$$P_\nu(\cosh\xi) = \frac{1}{\sqrt{\pi}}\Big[\frac{\Gamma(-\nu-\frac{1}{2})}{\Gamma(-\nu)}\,\frac{e^{-\nu\xi}}{(e^{2\xi}-1)^{1/2}}\,F(\tfrac{1}{2},\tfrac{1}{2};\nu+\tfrac{3}{2};\frac{1}{1-e^{2\xi}}) +$$

$$+\frac{\Gamma(\nu+\frac{1}{2})}{\Gamma(\nu+1)}\,\frac{e^{(\nu+1)\xi}}{(e^{2\xi}-1)^{1/2}}\,F(\tfrac{1}{2},\tfrac{1}{2};-\nu+\tfrac{1}{2};\frac{1}{1-e^{2\xi}})\Big]. \qquad (5.41)$$

If we put $\nu = \gamma - \frac{1}{2} = j\eta - \frac{1}{2}$ the two terms in eq. (5.41) are complex conjugate. By series expansion of the hypergeometric function we obtain

$$P_{j\eta-\frac{1}{2}}(\cosh\xi) = \frac{2}{\sqrt{\pi}}\,\mathrm{Re}\Big\{\frac{\Gamma(j\eta)}{\Gamma(j\eta+\frac{1}{2})}\,\frac{e^{j\eta\xi}}{(2\sinh\xi)^{1/2}}\,\big[1+o(\frac{1}{\eta})\big]\Big\}.$$

(5.42)

Putting

$$\cosh\xi = 1 + \frac{2}{1 + e^{-z/H}} (e^{T} - 1) , \qquad (5.43)$$

we obtain

$$E_T(t,z) \sim A(t,z) \cos(\eta\xi + \varphi) , \qquad (|\gamma| \gg 1) \qquad (5.44)$$

where

$$\xi = \operatorname{arccosh}\left[1 + \frac{2}{1 + e^{-z/H}} (e^{T} - 1)\right] , \qquad (5.45)$$

$$A(t,z) = \left[\frac{2}{\pi\eta \sinh\xi} \right]^{1/2} \qquad (5.46)$$

and

$$\varphi = \arg\left\{ \frac{\Gamma(j\eta)}{\Gamma(j\eta + \frac{1}{2})} \right\} \sim -\frac{\pi}{4} \qquad (5.47)$$

The momentary angular frequency, ω_m, of the electric field, eq. (5.44), becomes

$$\omega_m = \frac{\partial}{\partial t}\left\{ \eta \operatorname{arccosh}\left[1 + \frac{2}{1 + e^{-z/H}} (e^{T} - 1)\right] + \varphi \right\} =$$

$$= \omega_{p,m} \frac{e^{T}}{(e^{T} - 1)^{1/2} (e^{T} + e^{-z/H})^{1/2}} \qquad (5.48)$$

Equation (5.48) can also be written

$$e^{2T} + 2\,ae^{T} + b = 0\ , \tag{5.49}$$

where

$$a = -\frac{1}{2}\ \frac{e^{-z/H} - 1}{\dfrac{\omega_{p,m}^{2}}{\omega_{m}^{2}} - 1}\ , \tag{5.50}$$

$$b = \frac{e^{-z/H}}{\dfrac{\omega_{p,m}^{2}}{\omega_{m}^{2}} - 1}\ . \tag{5.51}$$

This equation has no solutions when $z > 0$ and $\omega_m < \omega_{p,m}$, one solution when $z > 0$ and $\omega_m > \omega_{p,m}$, no solutions when $z < 0$ and $\omega_m < \omega_{p,m} \dfrac{1}{\cosh \frac{z}{2H}}$ and two solutions when $z < 0$ and $\omega_m > \omega_{p,m} \dfrac{1}{\cosh \frac{z}{2H}}$.

From eq. (5.45) we easily obtain the virtual height $h_v(f)$ as

$$h_v(f) = H \ln\left\{ \frac{-a + \sqrt{a^2 - b}}{-a - \sqrt{a^2 - b}} \right\} =$$

$$= 2H \ln \left\{ \left(\frac{\omega_{p,m}^{2}}{\omega_{m}^{2}} - 1\right)^{-1/2} \cdot \sinh\left(-\frac{z}{2H}\right) + \left[\left(\frac{\omega_{p,m}^{2}}{\omega_{m}^{2}} - 1\right)^{-1} \cdot \sinh^2\left(-\frac{z}{2H}\right) - 1\right]^{1/2} \right\} . \tag{5.52}$$

All these results agree with the geometrical optics.

6. Small values of $|\gamma|$.

When $\gamma - \frac{1}{2}$ is real $E_T(t,z)$ does not oscillate. Since

$$\gamma^2 = \frac{1}{4} - \frac{4H^2}{c_o^2}\,\omega_{p,m}^2$$

this happens when

$$\frac{H}{\lambda_{p,m}} \leqslant \frac{1}{8\pi} \quad ,$$

i.e. for extremely thin layers.

4. The unit step modulated carrier response.

Assume that a unit step modulated carrier

$$E_{1,\sin}(t,z) = \sin[\omega_1 (t - \frac{z}{c_o})]\, U(t - \frac{z}{c_o}) \qquad (5.53)$$

is incident upon the layer from below. By means of the unit step wave response, eq. (5.27), and the convolution theorem, we immediately obtain the resulting electric field in the ionized layer as

$$E_{T,\sin}(t,z) = \omega_1 \frac{2H}{c_o} \int_0^T \cos\left[\omega_1 \frac{2H}{c_o}(T - x)\right] E_T(x)\, dx\,, \qquad (5.54)$$

where

$$T = \frac{c_o}{2H}\left(t - \frac{z}{c_o}\right)$$

and

$$E_T(x) = P_{\gamma - \frac{1}{2}}\left[1 + \frac{2}{1 + e^{-z/H}}(e^x - 1)\right] U(x)\ . \qquad (5.55)$$

The corresponding magnetic field can be obtained if we instead use the unit step magnetic field response, i.e.

$$H_{T,\sin}(t,z) = \omega_1 \frac{2H}{c_o} \int_0^T \cos\left[\omega_1 \frac{2H}{c_o}(T - x)\right] H_T(x)\, dx\,, \qquad (5.56)$$

where

$$H_T(x) = Y_o \cdot E_T(x,z) = \frac{2}{1+e^{z/H}} \Big[(e^{-X} - 1)\; E_T(x,z) +$$

$$+ \int_0^T e^{-X} E_T(X)\, dX \Big] , \qquad (5.57)$$

[eq. (5.31)]

$E_T(x,z)$, $H_T(x,z)$ and the convolution integrals, giving $E_{T,\sin}(t,z)$ and $H_{T,\sin}(t,z)$, have been solved by means of a digital computer, SAAB-D 21. We have used the series expansion [eq. (5.38)] and the asymptotic expansion [eq. (5.44)] for the hypergeometric function. It is especially difficult to compute the convolution integrals giving $E_{T,\sin}$ and $H_{T,\sin}$ for large values of T as the unit step wave responses vary rapidly. Fortunately the integrands contain a periodic function which makes it possible to use the relation

$$E_{T,\sin}(T) = E_{T,\sin}(T_2) + \omega_1 \frac{2H}{c_o} \int_{T_2}^{T} \cos\Big[\omega_1 \frac{2H}{c_o} (T - x) \Big] E_T(x)\, dx , \qquad (5.58)$$

where

$$T_2 = T - 2\pi \frac{c_o}{2H\,\omega_1} .$$

Three different problems are analysed;

4 a. The time variations of the electric field, the magnetic field and the energy flow (the Poynting vector) at total reflection in the layer (signal frequency $f_1 \ll$ penetration frequency $f_{p.m}$).

4 b. Signal distortion when the carrier frequency is equal to or nearly equal to the penetration frequency of the layer.

4 c. The transient response at tunnel transmission through a thin barrier ($f_1 \approx f_{p,m}$ but $f_1 < f_{p,m}$).

<u>4 a. The time variations of the electric field, the magnetic field and the energy flow at total reflection in the layer ($f_1 << f_{p,m}$).</u>

When the carrier frequency is much lower than the penetration frequency, the stationary tunnel transmission through the barrier can be neglected. Consequently, there is no net energy flow, and the steady-state wave consists of a standing wave which is monotonically decreasing in the evanescent region. The transient build-up of such a standing wave will be shown here.

For this purpose, we have chosen an Epstein layer with an apex plasma frequency $f_{p,m} = 5\ c_o/2H$ (the penetration frequency) and a unit step modulated carrier of

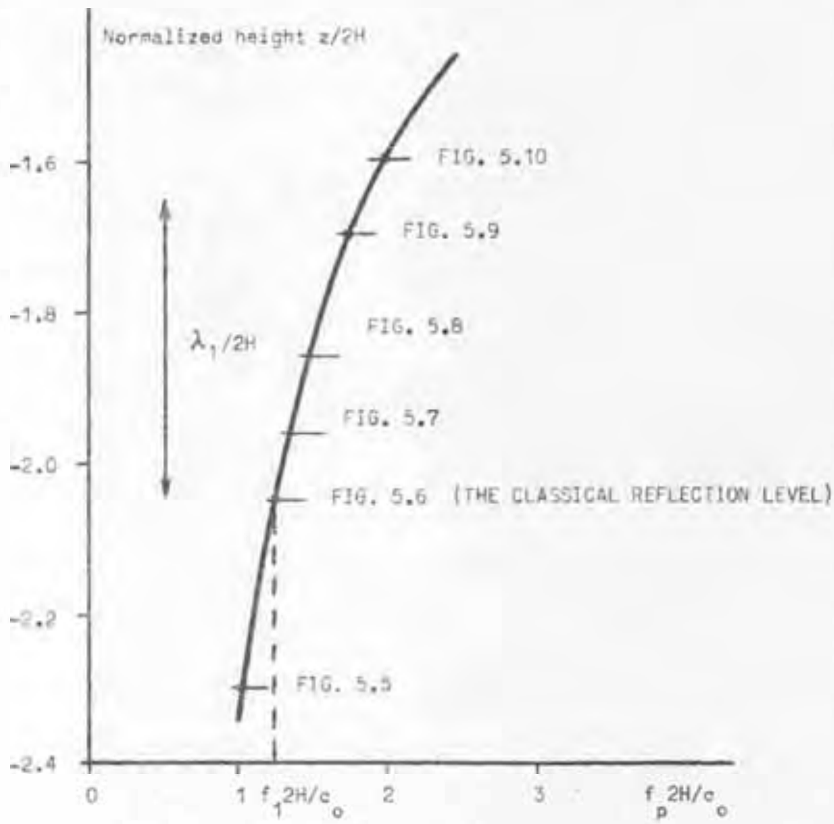

FIGURE 5.4. The observation points in the ionized Epstein layer.

frequency $f_1 = 1.25\ c_o/2H$ as the incident wave. By means of the digital computer, we have determined the transient electric field, magnetic field and the energy flow at six different levels in the layer (see figures 5.5 - 5.10). The "observation points" are shown in figure 5.4. They are situated just around the classical reflection level. This is the most interesting region.

From the energy flow, $Z_o\ S_{T,sin}$, we notice that the electromagnetic wave consists of an up-going and a returning forerunner, a transition region, which often has a very deformed waveform, and then the build-up region of the steady-state standing wave.

Although the incident electric field has an amplitude normalized to 1, the steady-state electric field amplitude is larger than 2 just outside the evanescent region (see figure 5.5). This effect is still more pronounced in figure 5.14 which shows the envelopes of the electric field and the magnetic field around the apex point of the layer when the carrier frequency is equal to the penetration frequency.

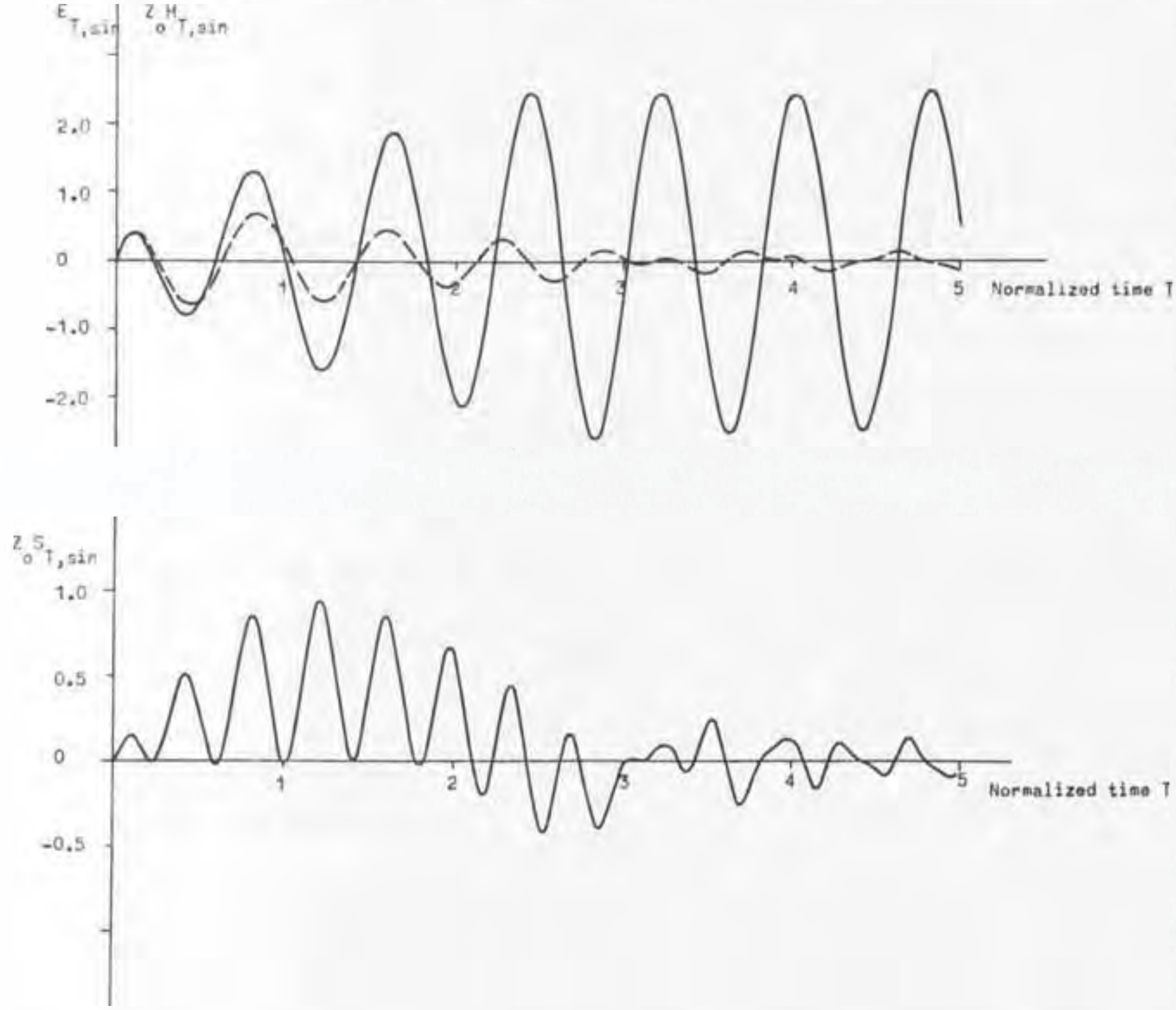

FIGURE 5.5. Electric field (———), magnetic field (- - - -) and energy flow at $z/2H = -2.30$ ($f_p = c_o/2H$). Carrier frequency $f_1 = 1.25\ c_o/2H$. Penetration frequency $f_{p,m} = 5\ c_o/2H$.

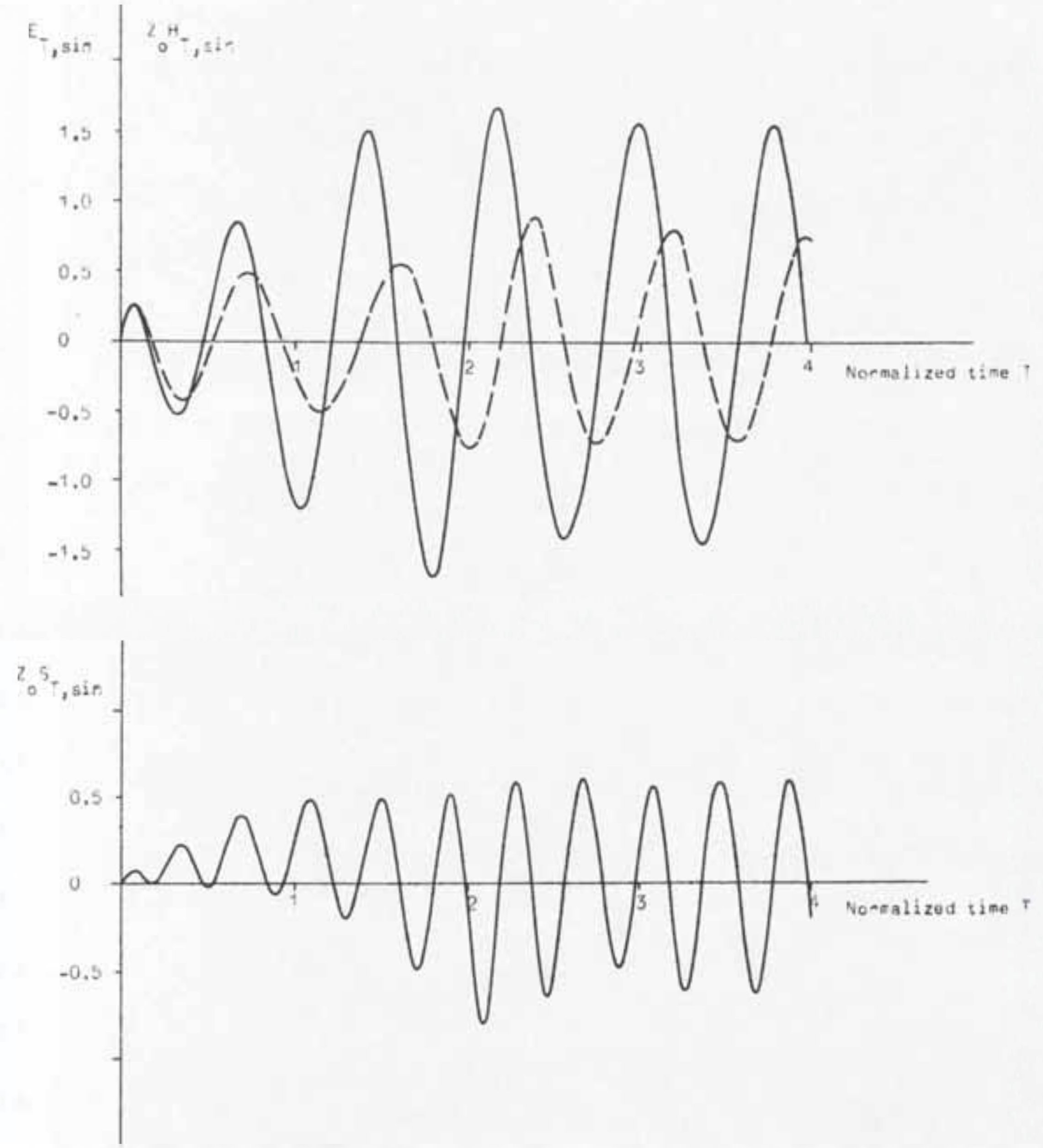

FIGURE 5.6. Electric field (———), magnetic field (- - - -) and energy flow at $z/2H = -2.05$ ($f_p = 1.25\ c_o/2H$). Carrier frequency $f_1 = 1.25\ c_o/2H$. Penetration frequency $f_{p,m} = 5\ c_o/2H$.

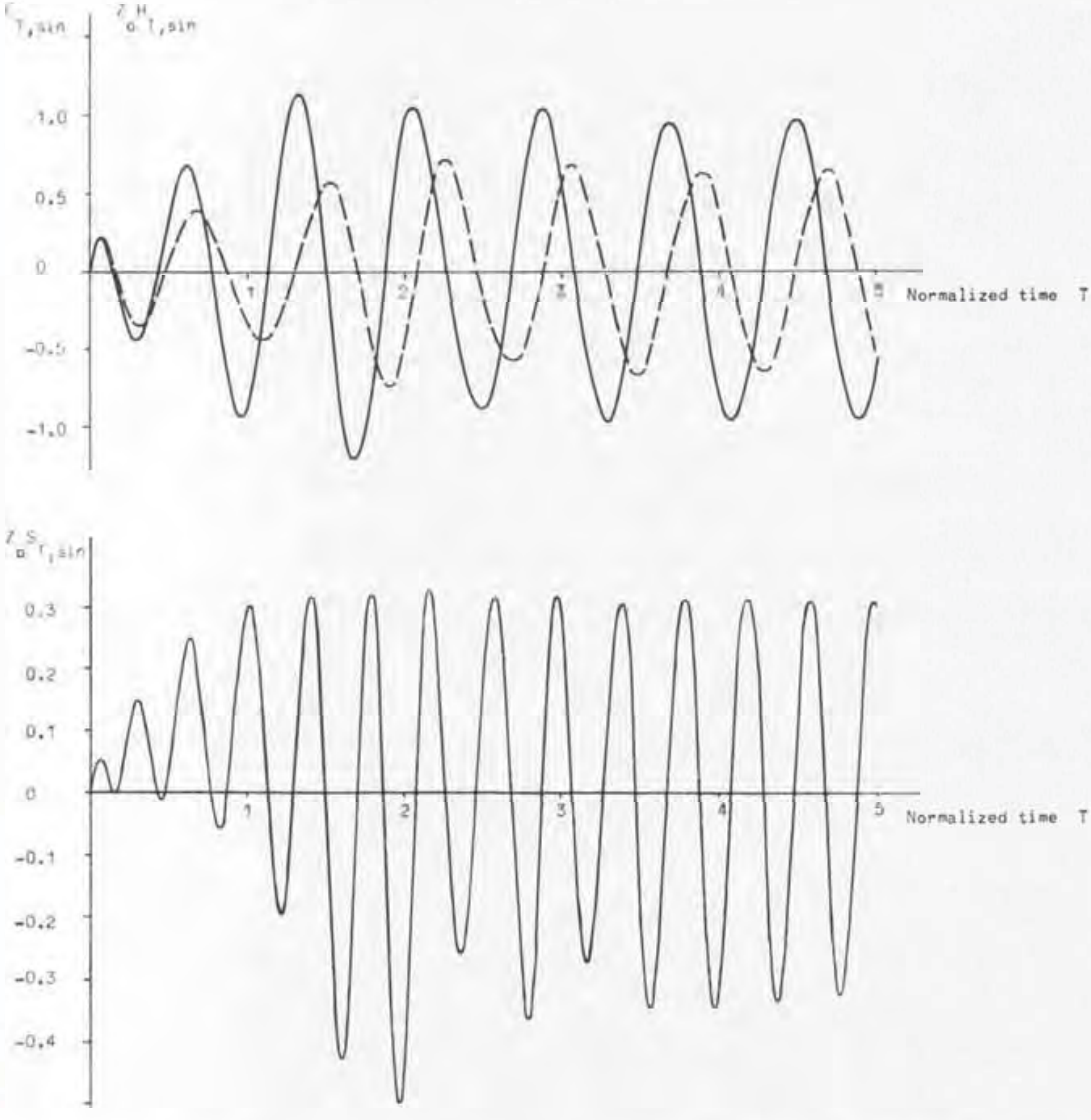

FIGURE 5.7. Electric field (———), magnetic field (- - - -) and energy flow at $z/2H = -1.96$ ($f_p = 1.38\ c_o/2H$). Carrier frequency $f_1 = 1.25\ c_o/2H$. Penetration frequency $f_{p,m} = 5\ c_o/2H$.

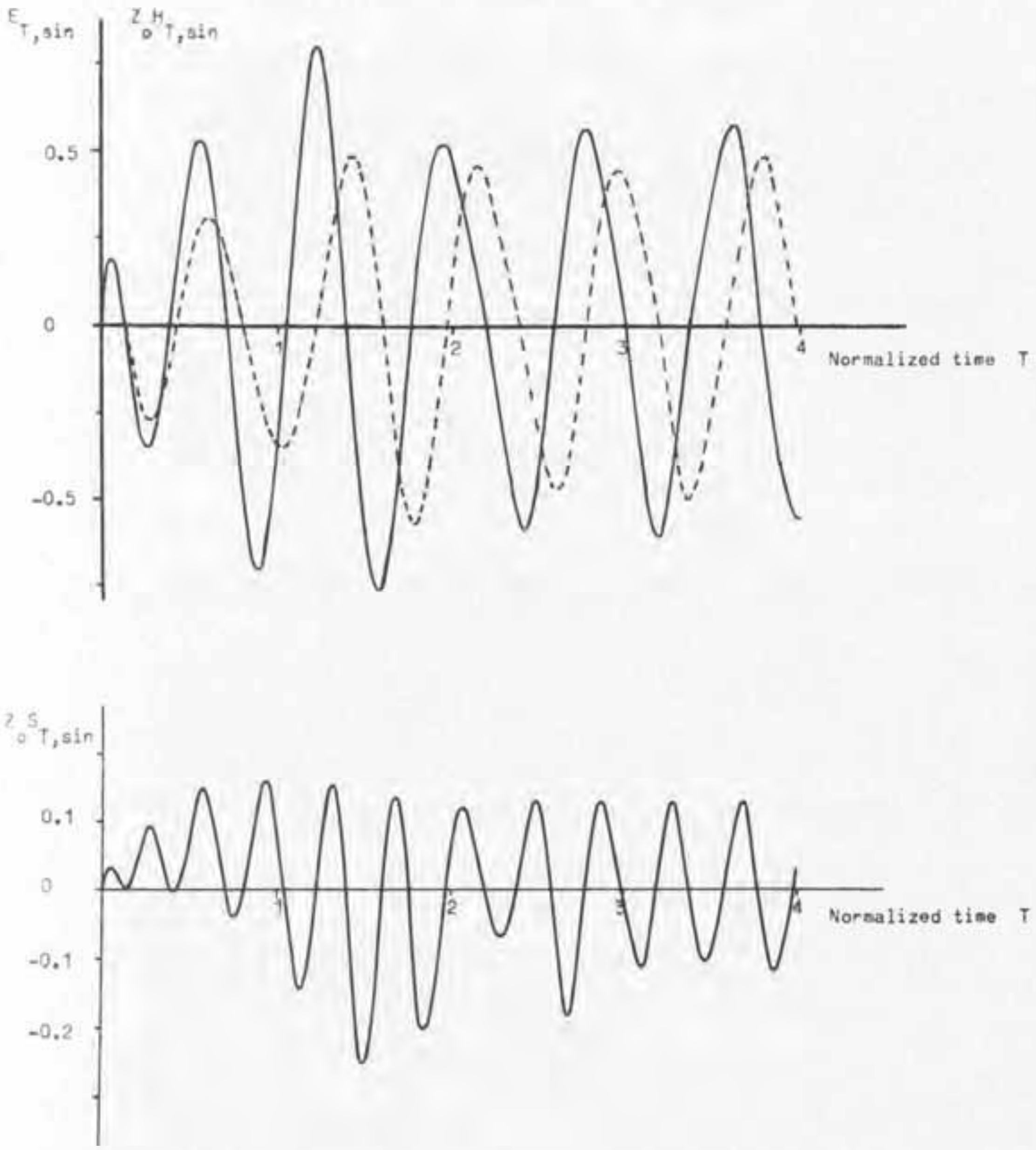

FIGURE 5.8. Electric field (———), magnetic field (- - - -) and energy flow at z/2H = -1.86 (f_p = 1.52 c_o/2H). Carrier frequency f_1 = 1.25 c_0/2H. Penetration frequency $f_{p,m}$ = 5 c_o/2H.

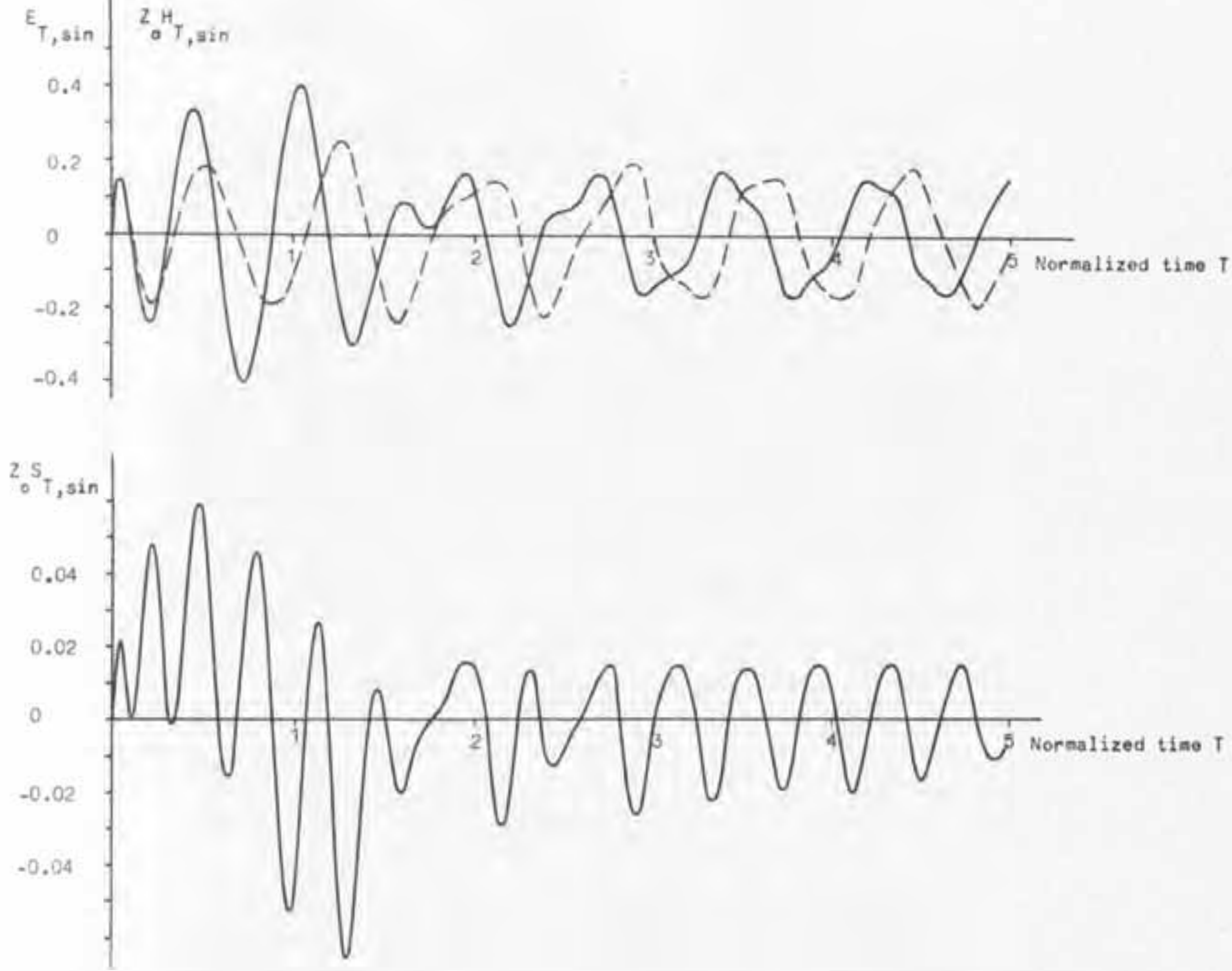

FIGURE 5.9. Electric field (——), magnetic field (- - - -) and energy flow at $z/2H = -1.70$ ($f_p = 1.77\ c_o/2H$). Carrier frequency $f_1 = 1.25\ c_o/2H$. Penetration frequency $f_{p,m} = 5\ c_o/2H$.

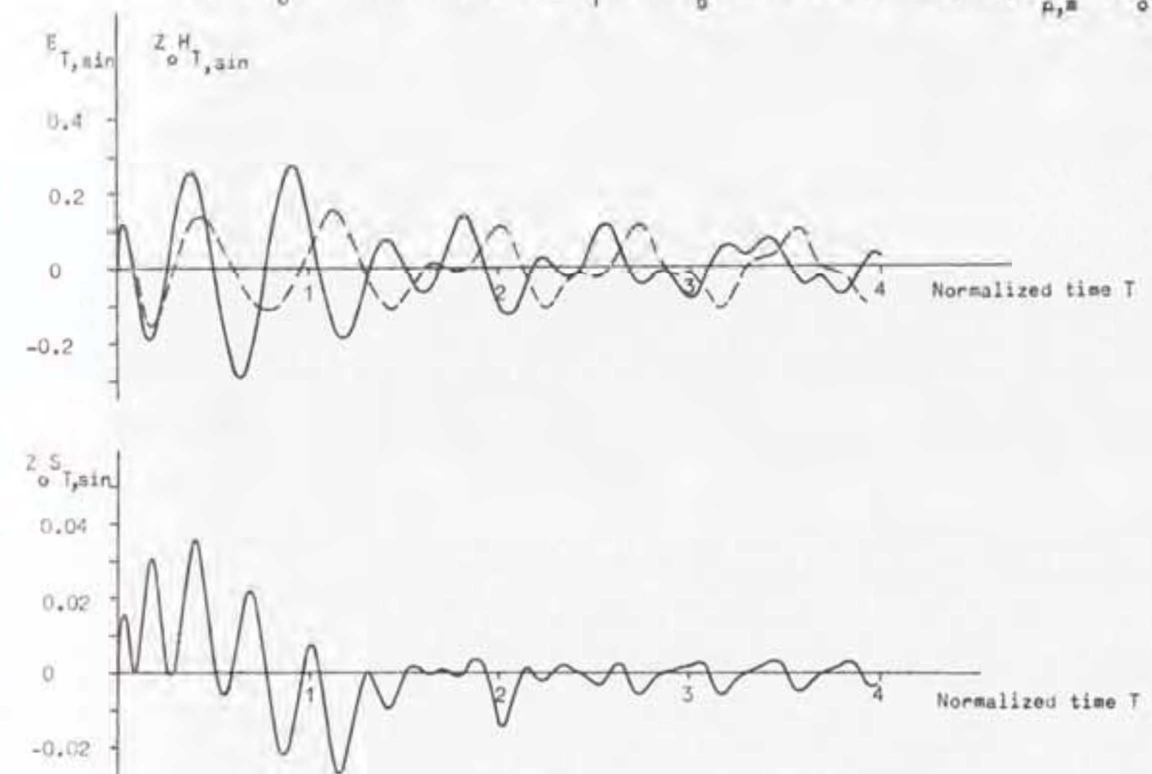

FIGURE 5.10. Electric field (——), magnetic field (- - - -) and energy flow at $z/2H = -1.60$ ($f_p = 1.94\ c_o/2H$). Carrier frequency $f_1 = 1.25\ c_o/2H$. Penetration frequency $f_{p,m} = 5\ c_o/2H$.

4b. Signal distortion when the carrier frequency is equal to or nearly equal to the penetration frequency of the layer.

When the carrier frequency of a radio signal approaches the penetration frequency of an ionized barrier, a strong distortion of the reflected or transmitted wave arises. The frequency components just around the apex plasma frequency are comparatively more time delayed. Consequently, the wave experiences a strong frequency dispersion and becomes distorted.

In most cases, the transient wave response, which gives the actual signal distortion, may be obtained by approximate method from the phase versus frequency characteristics of the system. The method to evaluate the actual Fourier integral utilizes a stationary phase principle.

If we assume the incident wave to be a unit step modulated carrier, electric field

$$E_I(t,z) = \mathrm{Im}\left\{ e^{j\,\omega_1 (t - z/c_o)} \right\} U(t - z/c_o)\ , \tag{5.58}$$

the response of the dispersive medium can be obtained from

$$E_T(t,z) = \mathrm{Im}\left\{ \frac{1}{2\pi} \int_{-\infty}^{\infty}\int_{-\infty}^{\infty} U(\hat{t} - \frac{z}{c_o})\, e^{j[(\omega_1 - \omega)\,\hat{t} + \omega t - \varphi(\omega)]} A(\omega)\, d\omega\, d\hat{t} \right\}, \tag{5.59}$$

where

$$A(\omega)\, e^{-j\varphi(\omega)}$$

is the complex transfer function of the medium.

In order to solve equation (5.59) we assume that $A(\omega)$ is slowly varying compared to $\exp[-j\,\varphi(\omega)]$ in the vincinity of the carrier frequency. We now expand $\varphi(\omega)$ in a series about ω_1 and neglect the third and higher order derivatives,

$$\varphi(\omega) \approx \varphi(\omega_1) + (\omega - \omega_1)\,\varphi'(\omega_1) + \frac{(\omega - \omega_1)^2}{2}\,\varphi''(\omega_1)\ . \tag{5.60}$$

Then we obtain the leading edge of the signal as a Fresnel integral

$$|E_T(t)| \approx \frac{A}{\sqrt{2}} \left| \int_{x}^{\infty} \exp(j\pi x^2/2)\, dx \right| , \tag{5.61}$$

where

$$x = \frac{\varphi'(\omega_1) - t}{[\pi \varphi''(\omega_1)]^{1/2}} \quad . \tag{5.62}$$

Just around the penetration frequency of the ionized barrier, we can no longer assume that the time delay, i. e. $\varphi'(\omega_1)$, varies linearly with frequency. The third derivative, $\varphi'''(\omega_1)$ should also be taken into account. A quantitative discussion of this problem has been attempted by Gershman [1952]. Furthermore a special treatment in this frequency region has been done by Fengler [1963]. He obtained the reflected signal as several infinite series, which are difficult to compute.

Using the expression for the unit step modulated carrier, eq. (5.54), computer solution can be obtained for the exact signal distortion. They will be compared with the approximate results discussed above. From the shape of $\varphi(\omega)$ one concludes that the best agreement will be in the region $(f_1/f_{p,m} - 1) \gg$ $\gg 1\%$ for the transmitted wave and in the region $(1 - f_1/f_{p,m}) \gg 1\%$ for the reflected wave. The difference $|f_1 - f_{p,m}|$ still must be so small that the time delay $\gg 1/f_1$. At these frequencies φ' varies nearly linearly with the frequency, and the reflexion or transmission coefficient is approximately constant. Accordingly, the two conditions in equation (5.61) are fulfilled.

We have determined the exact signal envelope at different carrier frequencies on both sides of the penetration frequency of a layer with $f_{p,m} = 5\, c_o / 2H$. Both the transmitted waves, figure 5.11 a, and the reflected waves, figure 5.11 b, are shown. One notices that for the largest values of the frequency difference $|\chi|$, the steepest portion of the leading edge agrees very well with the Fresnel integral. On the other hand, the exact envelope oscillates more slowly. This can be seen from figure 5.12. There we compare the approximate result with the exact envelope of the transmitted signal at $f_1 = 10\, c_o / 2H$ and $f_{p,m} = 5.4\, c_o / 2H$.

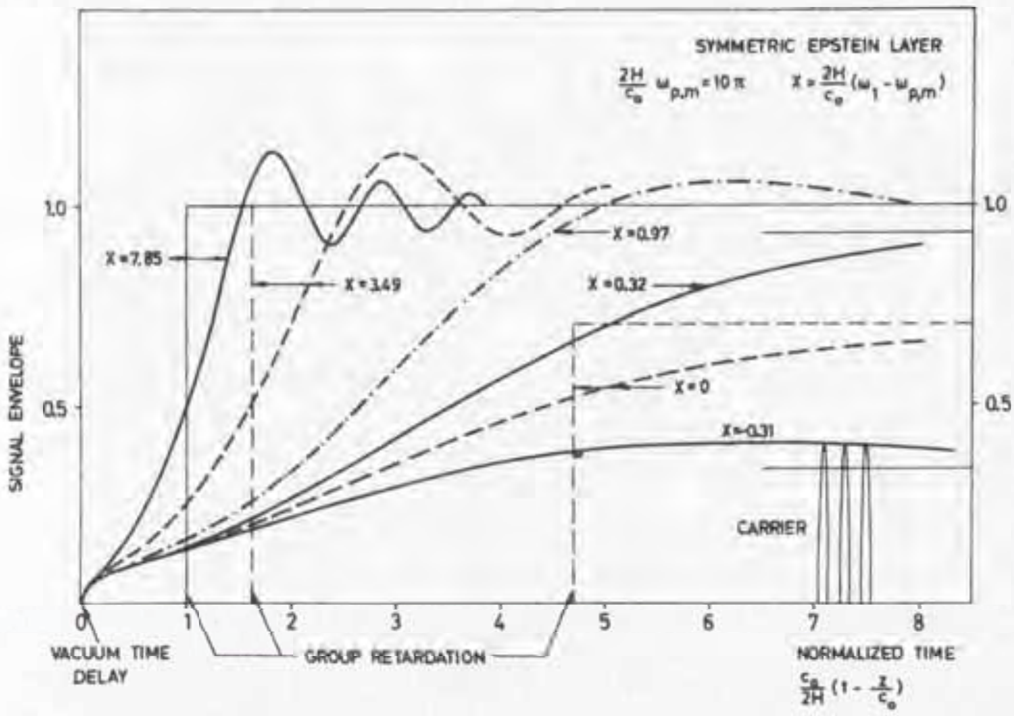

FIGURE 5.11a. The envelope of a unit step modulated carrier transmitted through a symmetrical Epstein layer with an apex plasma frequency $f_{p,m} = 5\ c_o/2H$ at six different carrier frequencies.

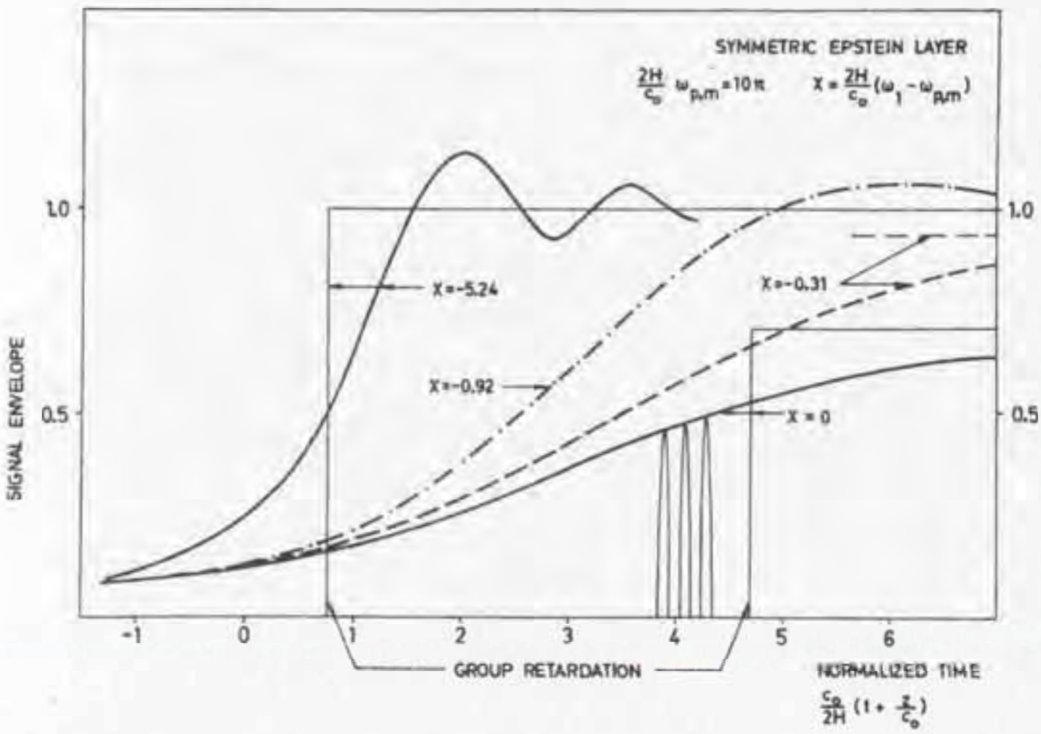

FIGURE 5.11b. The envelope of a unit step modulated carrier reflected from a symmetrical Epstein layer with an apex plasma frequency $f_{p,m} = 5\ c_o/2H$ at four different carrier frequencies.

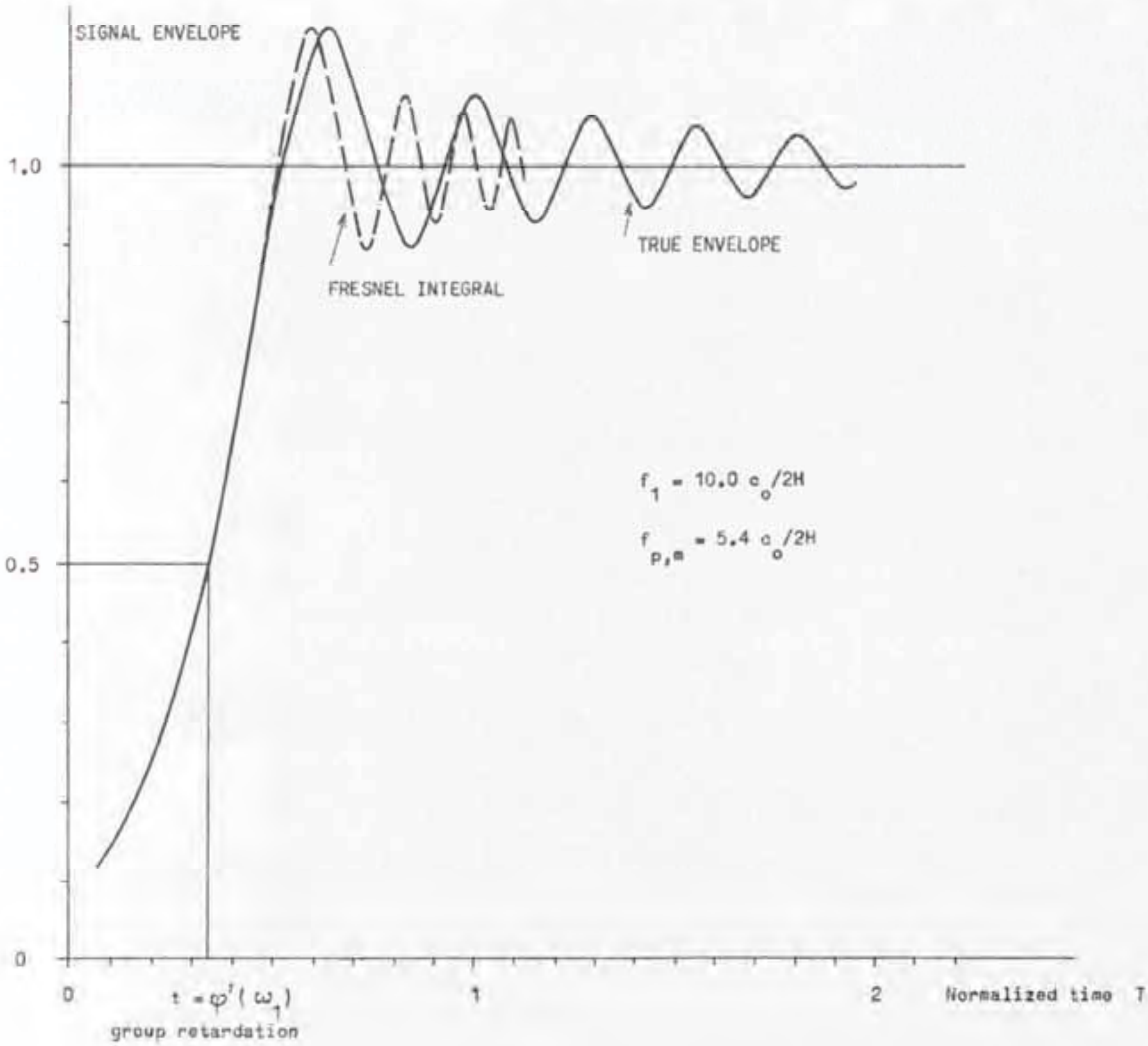

FIGURE 5.12. The true envelope of the transmitted wave compared with the Fresnel integral. Signal frequency $f_1 = 10.0\ c_o/2H$. Penetration frequency $f_{p,m} = 5.4\ c_o/2H$.

The Fresnel integrals C (x) and S (x) are defined as

$$C(x) = \int_0^x \cos \frac{\pi}{2} t^2 \, dt \tag{5.63}$$

$$S(x) = \int_0^x \sin \frac{\pi}{2} t^2 \, dt. \tag{5.64}$$

For large values of x they can be written

$$C(x) \sim \frac{1}{2} + \frac{1}{\pi x} \sin \frac{\pi}{2} x^2 \qquad (x \gg 1) \tag{5.65}$$

$$S(x) \sim \frac{1}{2} - \frac{1}{\pi x} \cos \frac{\pi}{2} x^2 . \qquad (x \gg 1) \tag{5.66}$$

By means of (5. 65) and (5. 66) we obtain the asymptotic expression for the signal envelope [eq. (5. 61)] as

$$|E(t)| \sim 1 + \frac{1}{\sqrt{2}\,\pi\,|x|} \sin\left[\frac{\pi}{2}\left(x^2 - \frac{1}{2}\right)\right], \tag{5.67}$$

$$(|x| \gg 1 , \; A = 1)$$

where x is given by eq. (5. 62).

The momentary angular frequency of the envelope oscillation can be obtained from

$$\omega_m = \frac{\partial}{\partial t}\left[\frac{\pi}{2}\left(x^2 - \frac{1}{2}\right)\right] = \frac{1}{|\varphi''(\omega_1)|}\left[t - \varphi'(\omega_1)\right]. \tag{5.68}$$

$$t \gg \varphi'(\omega_1)$$

We notice that the oscillation frequency varies linearly with time. As a matter of fact, the time variation of the lower frequency sideband of the transmitted wave is given by the actual group retardation,

$$\omega = \omega_1 - \omega_m(t) = \omega_1 - \frac{1}{|\varphi''(\omega_1)|}\left[t - \varphi'(\omega_1)\right]. \tag{5.69}$$

This can be seen from eq. (5. 60) which gives a time delay equal to

$$t = \frac{\partial \varphi}{\partial \omega} = \varphi'(\omega_1) + (\omega - \omega_1)\,\varphi''(\omega_1) , \tag{5.70}$$

i. e. the same relation as eq. (5. 69) .

Of course, corresponding results can be obtained for the upper sideband of the reflected wave.

The expansion of $\varphi(\omega)$ thus causes a serious error in the shape of the signal envelope for large values of T. Naturally, the oscillation frequency can not go to infinity. In fact, we obtain an "apex modulation" of the signal, i.e. the frequency of the envelope oscillation becomes equal to $f_{p,m}$. This can be shown by asymptotic expansion of relation (5.54).

By means of relation (5.58) we obtain

$$E_{T,\sin} = E_{T,\sin}(T_3) - \frac{2H}{c_o}\omega_1 \int_T^{T_3} \cos\left[\frac{2H}{c_o}\omega_1(T_3 - x)\right] E_T(x)\,dx\,, \tag{5.71}$$

where

$$T_3 = T + 2n\pi\frac{c_o}{2H\omega_1}\,. \qquad (n = 0, 1, 2, 3, \ldots)$$

and $E_T(x)$ is the unit step wave response. For large values of x and far above the layer we obtain

$$E_T(x) \sim A\, e^{-\frac{1}{2}x} \cos\left(\frac{2H}{c_o}\omega_{p,m} x - a\right)\,, \tag{5.72}$$

where A and a are constants given by equation (5.44).

By means of eq. (5.72) the asymptotic expression for $E_{T,\sin}$ can be written as

$$E_{T,\sin} \sim \underbrace{C_1 \cos\left(\frac{2H}{c_o}\omega_1 T - c_1\right)}_{E_{T,\text{ stationary}}} + C_2\, e^{-\frac{1}{2}T} \cos\left(\frac{2H}{c_o}\omega_{p,m} T - c_2\right)\,, \qquad (T \gg 1)$$

where C_1, C_2, c_1 and c_2 are constants.

Accordingly, the transmitted wave is modulated by the plasma oscillations sustained in the apex region. The amplitude of the modulation decreases with time as $e^{-T/2}$.

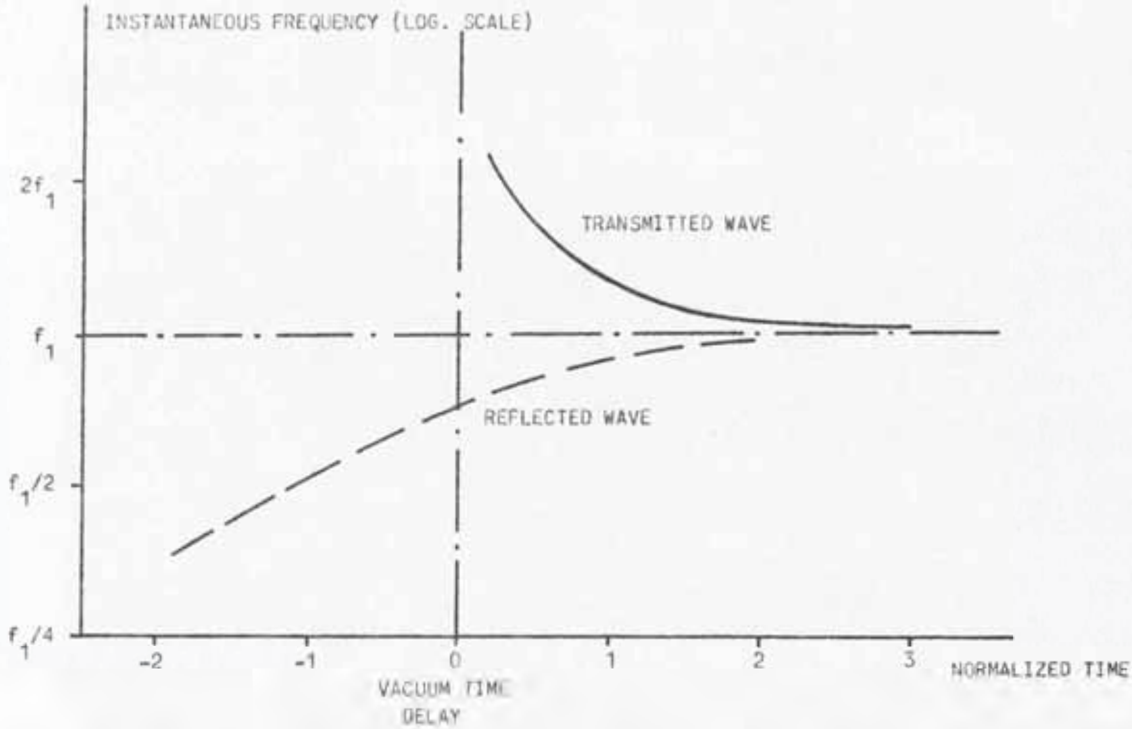

FIGURE 5.13. The instantaneous frequencies of the transmitted and reflected waves at $f_1 = f_{p,m}$.

Increasing the carrier frequency towards cutoff causes the envelope function to spread out more. We can no longer assume that the transmission or reflection factor is independent of the frequency. Besides $\varphi''(\omega_1)$ is very small and we cannot neglect the third derivative $\varphi'''(\omega_1)$, i.e. the approximate result, eq. 5.61, fails completely in this frequency region. Instead, it is perhaps possible to assume that the phase varies linearly and then to introduce a simple expression for the transmission or reflection factor which simplifies the integral.

It is interesting to study the carrier frequencies of the transmitted and reflected waves. Figure 5.13 shows the instantaneous frequencies obtained from the zero of the electric field. The instantaneous frequency is higher than f_1 for the transmitted wave and lower than f_1 for the reflected wave. The strong distortion at $f_1 \approx f_{p,m}$ makes it difficult, if not impossible, to define the time of signal travel. This fact can be seen from figures 5.11a and 5.11b where we have pointed out the group retardations obtained from the phase of the stationary full wave solutions. There are no physical reasons to assume the signal time delay to be equal to these group retardations when $f_1 \approx f_{p,m}$. It is therefore especially interesting to make an extended investigation regarding the time variations of the electric field, the magnetic field and the energy flow at different heights in the layer at tunnel transmission through the layer. This will be dealt with in next section.

Figure 5.14 shows the amplitudes of the electric field and the magnetic field at three different levels around the apex level of the layer. The signal frequency is equal to the penetration frequency, $f_1 = f_{p,m} = 5\ c_o / 2H$. At $z = 0$ the electron density gradient dN / dz is zero. Therefore, a plasma oscillation of frequency $f_{p,m}$ can be sustained there. As this oscillation has the same frequency as the incident wave, there is no signal modulation and a high steady-state electric field can be built up. The strongest field appears just below the apex, i.e. below the classical reflection level. This is in agreement with for instance the linear electron density profile, where the steady-state standing wave can be written as an Airy function.But in this case the electric field is much stronger (compared to the normalized incident wave). The amplitude of the steady-state energy flow must be equal to 0.5. Consequently, the corresponding steady-state magnetic field must be very weak. See figure 5.14.

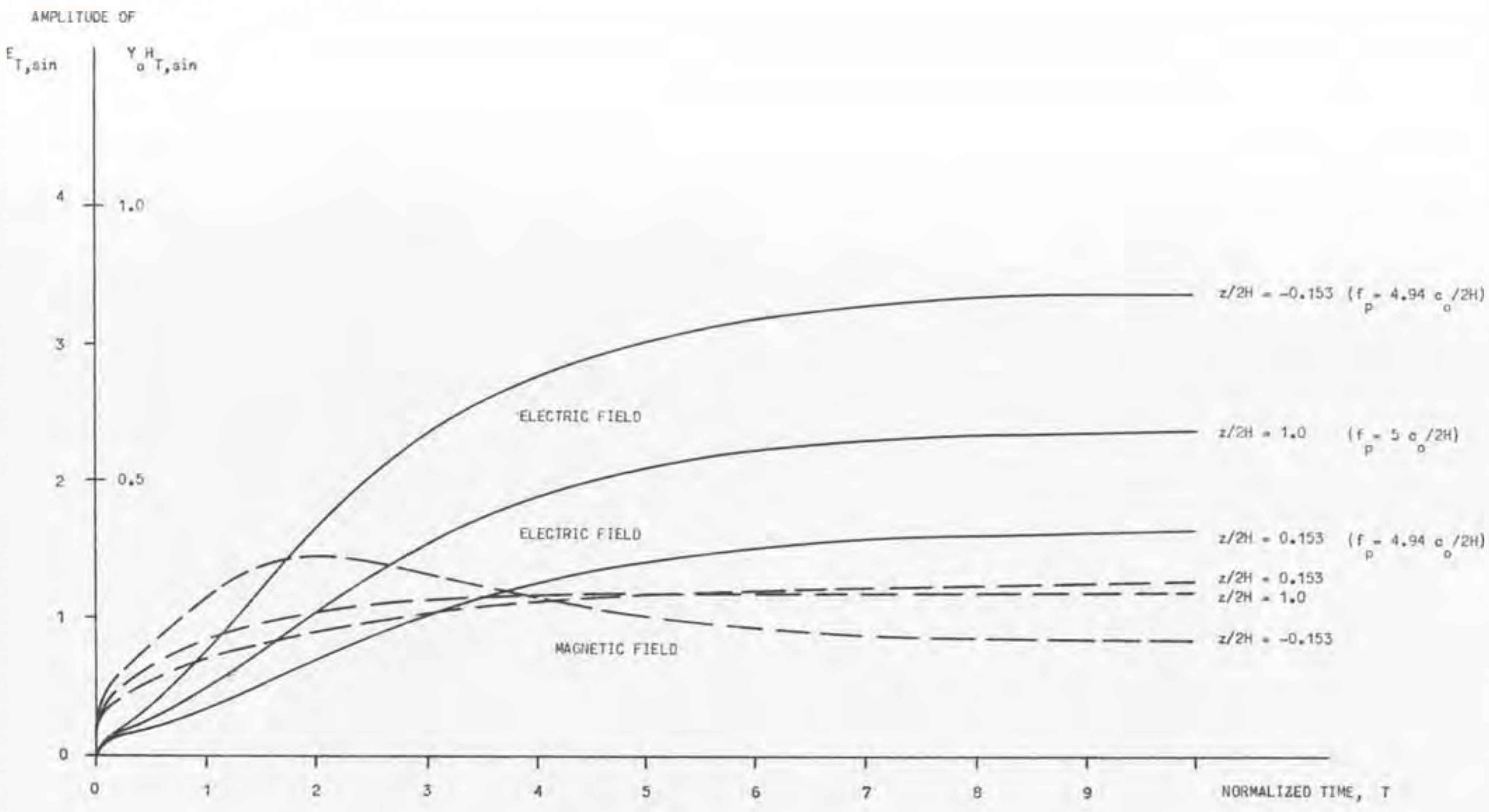

FIGURE 5.14. The amplitudes of the electric field and the magnetic field at three different levels around the apex point of a symmetrical Epstein layer. $f_1 = f_{p,m} = 5\ c_o/2H$.

4c. Transient response at tunnel transmission through a thin barrier.

From the stationary full wave solution we obtain the transmission and reflection factor as

$$|T|^2 = \frac{\cosh\left(2\pi\,\omega_1 \frac{2H}{c_o}\right) - 1}{\cos(2\pi\gamma) + \cosh\left(2\pi\,\omega_1 \frac{2H}{c_o}\right)}, \tag{5.74}$$

$$|R|^2 = \frac{\cos(2\pi\gamma) + 1}{\cos(2\pi\gamma) + \cosh\left(2\pi\,\omega_1 \frac{2H}{c_o}\right)}. \tag{5.75}$$

If $2\pi\frac{2H}{c_o}\,\omega_1 \gg 1$ and $2\pi\frac{2H}{c_o}\,\omega_{p,m} \gg 1$ they can be written

$$|T|^2 = \frac{1}{1 + \exp\left[-2\pi\frac{2H}{c_o}\left(\omega_1 - \omega_{p,m}\right)\right]}, \tag{5.76}$$

$$|R|^2 = \frac{1}{1 + \exp\left[2\pi\frac{2H}{c_o}\left(\omega_1 - \omega_{p,m}\right)\right]}. \tag{5.77}$$

$|T|$ and $|R|$ versus $\frac{2H}{c_o}\,f_1$ for a layer with $f_{p,m} = 1.75\,c_o / 2H$ are drawn in figure 5.15. We notice that $|T|$ and $|R|$ vary rapidly near the penetration frequency although the layer is thin.

We have chosen to study the transient tunnel transmission of a unit step modulated carrier at a signal frequency $f_1 = 1.5\,c_o / 2H$. Then the distance between the classical reflection levels in the layer is $1.7\,\lambda_1$ and the transmission factor, obtained from eq. (5.63), is equal to 0.007. The time variations of the electric field, the magnetic field and the energy flow have been determined at seven different heights in the medium (see figure 5.16) and are shown in figures 5.17 - 5.23. The transmission factor is very small. In the stationary state there is a negligible energy transport upwards and below the apex we nearly have a standing wave. Up to the apex level ($z = 0$), the transient wave (figures 5.17 -5.20) consists of an upgoing forerunner, a reflected forerunner decreasing with increasing height, and then the build-up region of the standing wave. Even above the apex of the layer there is a reflected forerunner with a very small amplitude.

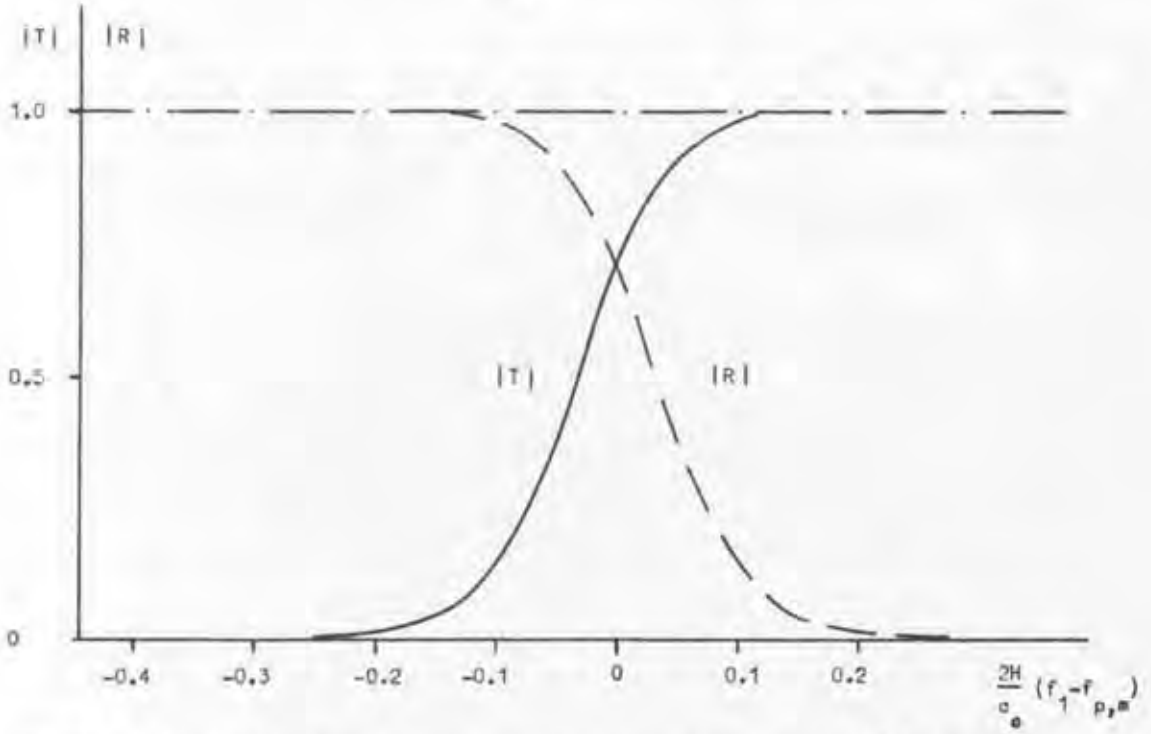

FIGURE 5.15. Transmission coefficient |T| and reflection coefficient |R| for a symmetrical Epstein layer.

In section 4b we introduced the notation "apex modulation". It would be interesting to examine if there is such a modulation in this case. Now the layer is thin and the wave is transmitted by means of the tunnel effect. The modulation frequency must be given by $f_{p,m} - f_1 = 0.25\ c_o/2H$. As a matter of fact the electric field, depicted in figure 5.19, shows a weak envelope oscillation with this frequency. Accordingly, there is an "apex modulation" even at tunnel transmission. In most cases it is, however, too weak to be discovered.

It has been pointed out by Rydbeck [1948] that a higher order approximation of the reflection and transmission coefficients can be obtained by a multiple phase integral method. The results can be interpreted in "geometrical" terms with the reflection virtually consentrated to the two branch points of the barrier (the lower and upper classical reflection points). It would be interesting to note if such a multiple reflection occurs in the evanscent region. The theory requires that the branch points are sufficiently remote. Consequently, if there are any reflected waves from the upper branch point, they will be very small and perhaps impossible to discover.

Let us look at the time variation of the energy flow at the apex point (figure 5.20). In the time interval $2.5 < T < 4.0$ we have a distinct net energy transport downwards. This is a remarkable situation. However, it is difficult to determine a single well-defined reflection level.

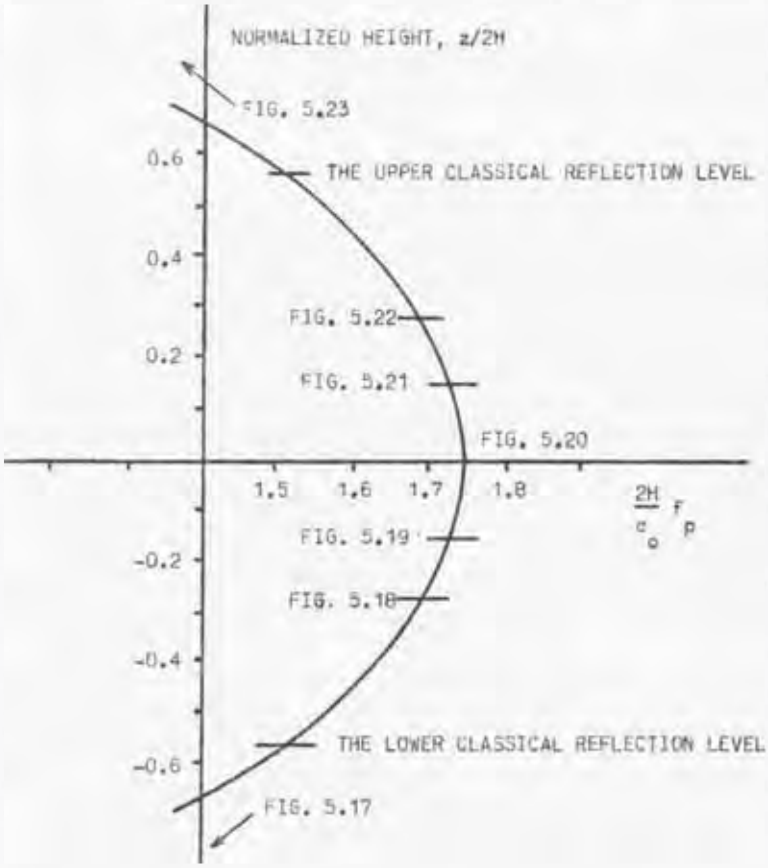

FIGURE 5.16. The apex region of the symmetrical Epstein layer

As to the group and signal velocities at tunnel transmission through the layer we at once notice from figures 5.17-5.23 that there is no relation between the two. As a matter of fact, it is difficult, if not impossible, to define a signal velocity. This velocity is a function of the barrier form, of the carrier frequency and also of the signal envelope used . In this special case the transmitted signal is deformed "beyond recognition" by the strong forerunner. Figures 5.17 - 5.23 are good illustrations of the gradual deformation. A futher analysis of the signal velocity will lead us beyond the scope of this report.

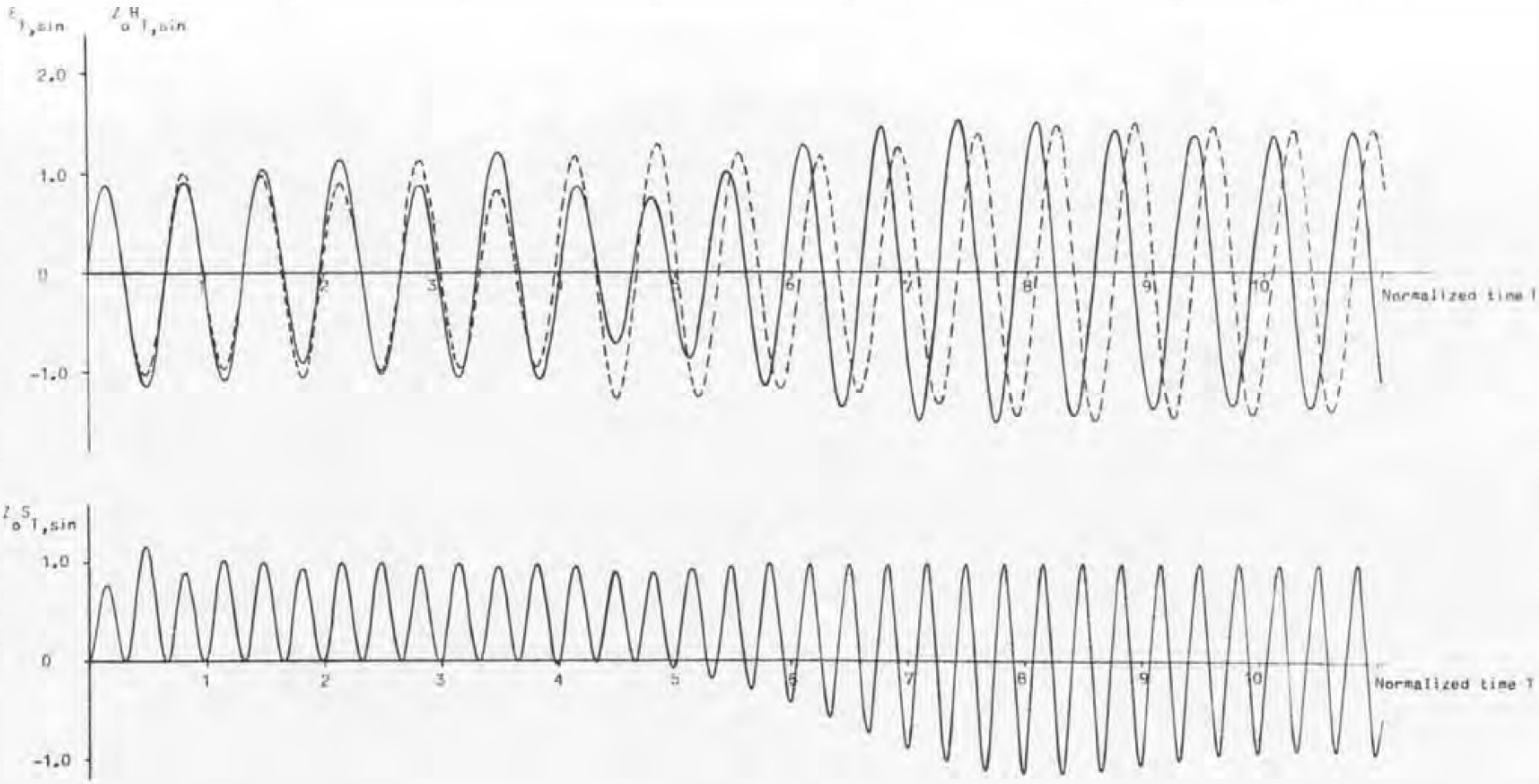

FIGURE 5.17. Electric field (——), magnetic field (- - - -) and energy flow at $z/2H = -2.30$. Carrier frequency $f_1 = 1.5\ c_o/2H$. Penetration frequency $f_{p,m} = 1.75\ c_o/2H$.

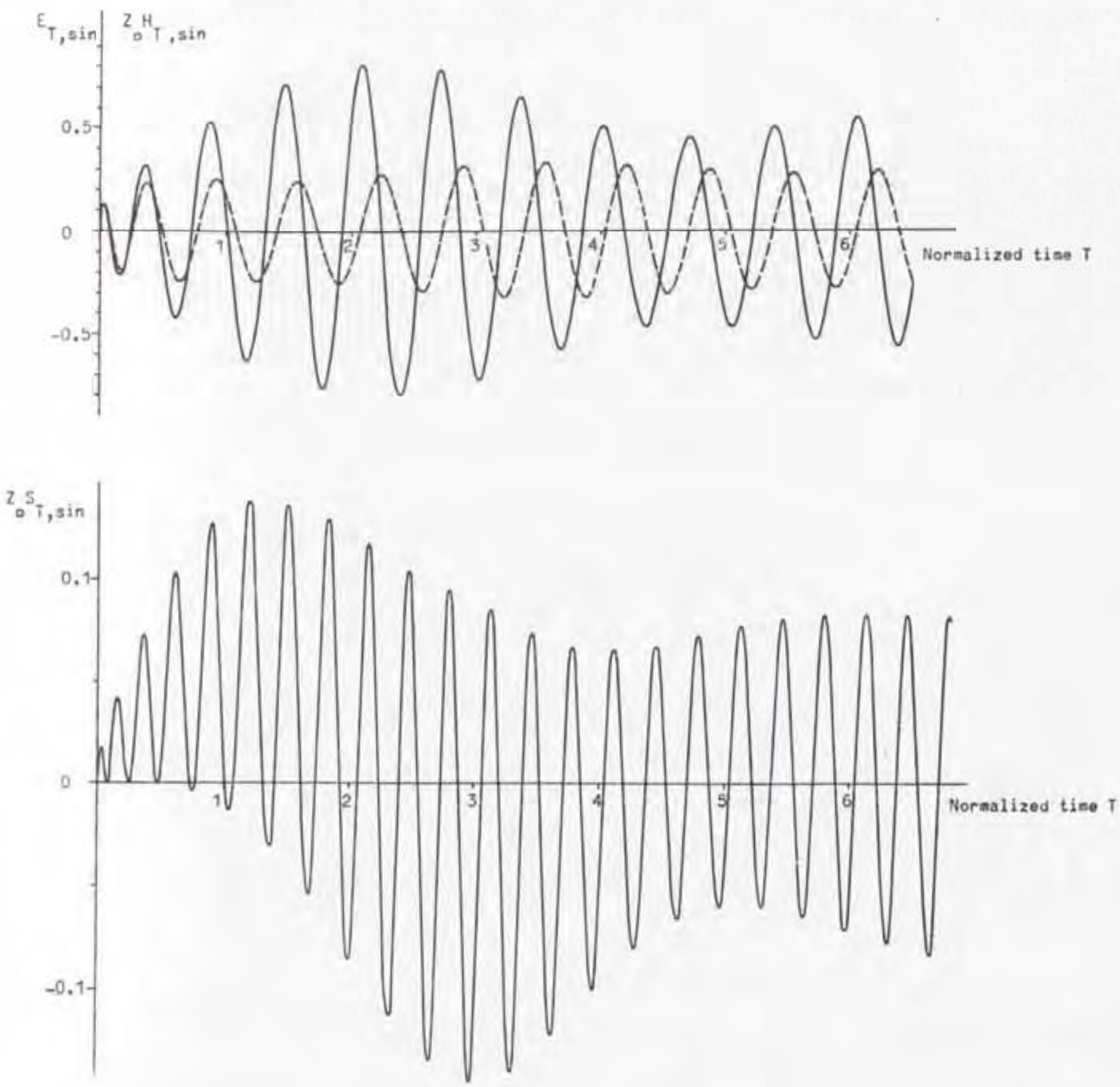

FIGURE 5.18 Electric field (———), magnetic field (- - - -) and energy flow at $z/2H = -0.285$. Carrier frequency $f_1 = 1.5\ c_o/2H$. Penetration frequency $f_{p,m} = 1.75\ c_o/2H$.

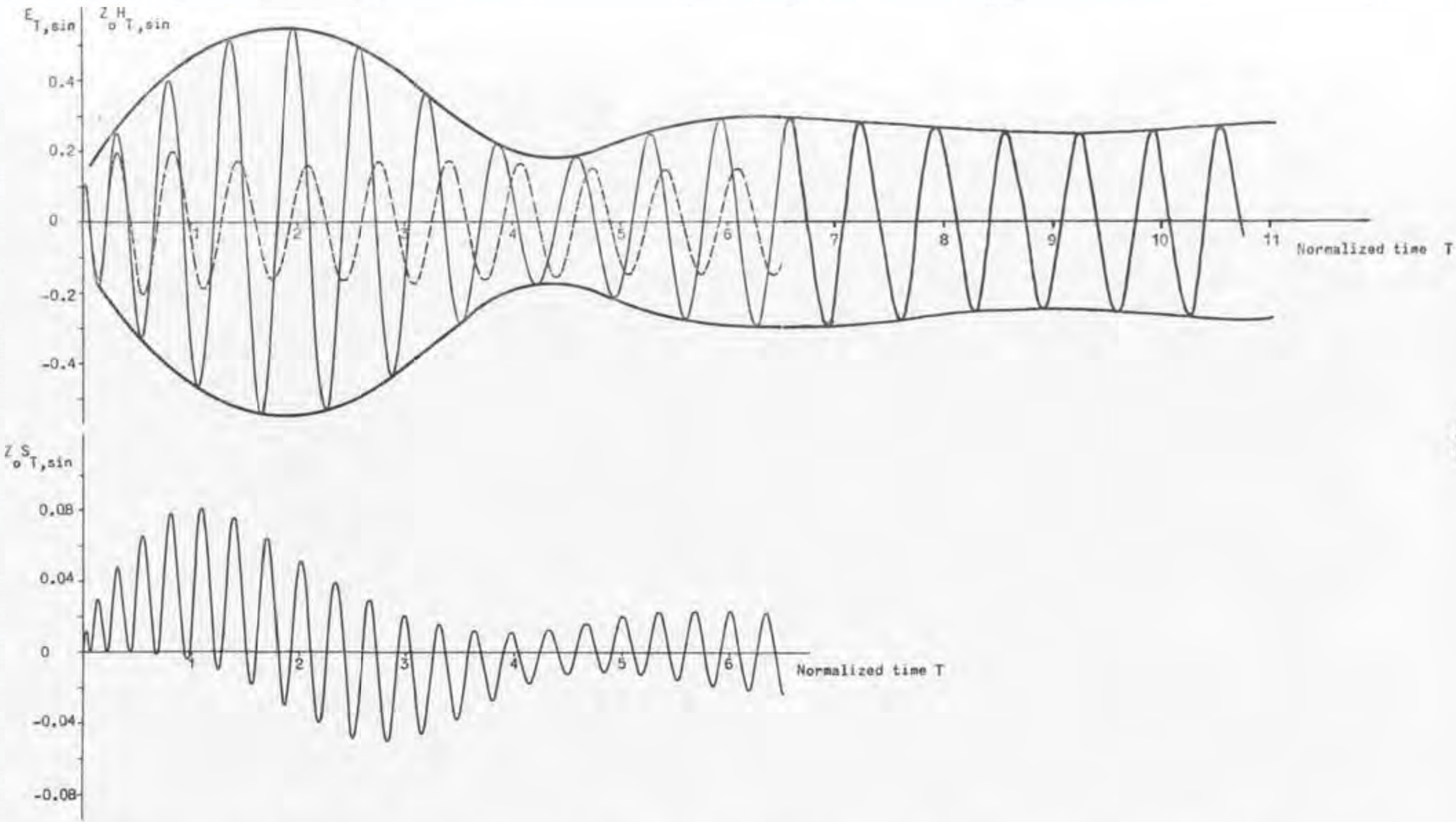

FIGURE 5.19. Electric field (——), magnetic field (- - - -) and energy flow at $z/2H = -0.153$. Carrier frequency $f_1 = 1.5\ c_o/2H$. Penetration frequency $f_{p,m} = 1.75\ c_o/2H$.

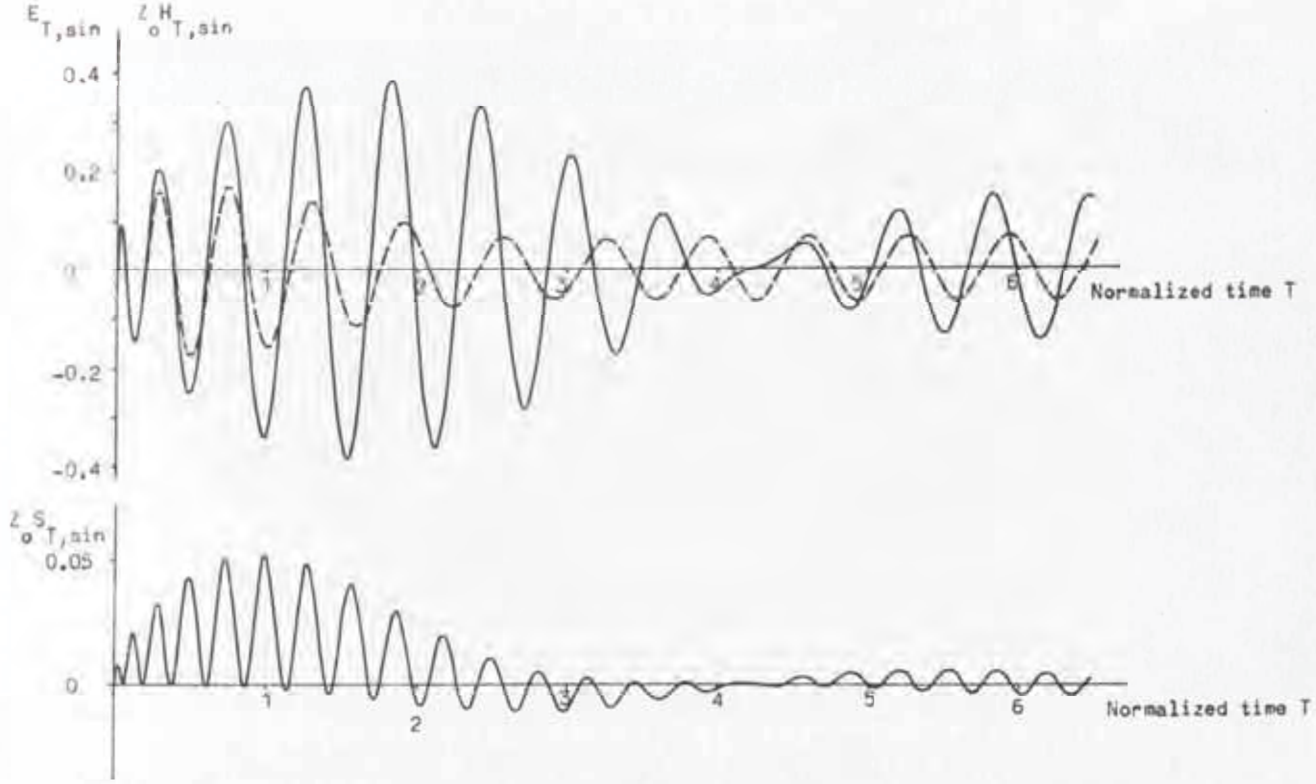

FIGURE 5.20 Electric field (——), magnetic field (- - - -) and energy flow at z/2H = 0.0. Carrier frequency $f_1 = 1.5\ c_o/2H$. Penetration frequency $f_{p,m} = 1.75\ c_o/2H$.

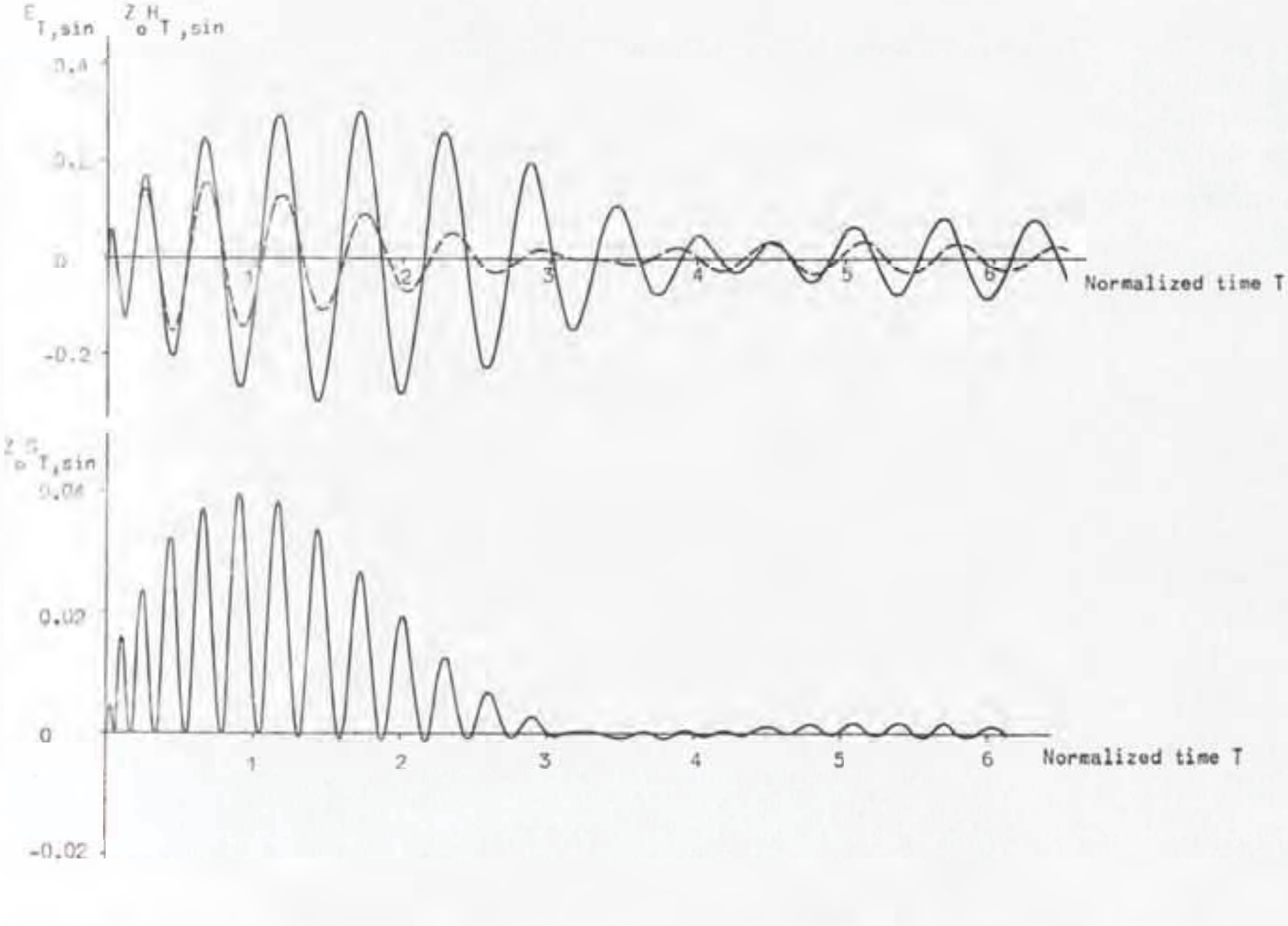

FIGURE 5.21 Electric field (——), magnetic field (- - - -) and energy flow at z/2H = 0.153. Carrier frequency $f_1 = 1.5\ c_o/2H$. Penetration frequency $f_{p,m} = 1.75\ c_o/2H$.

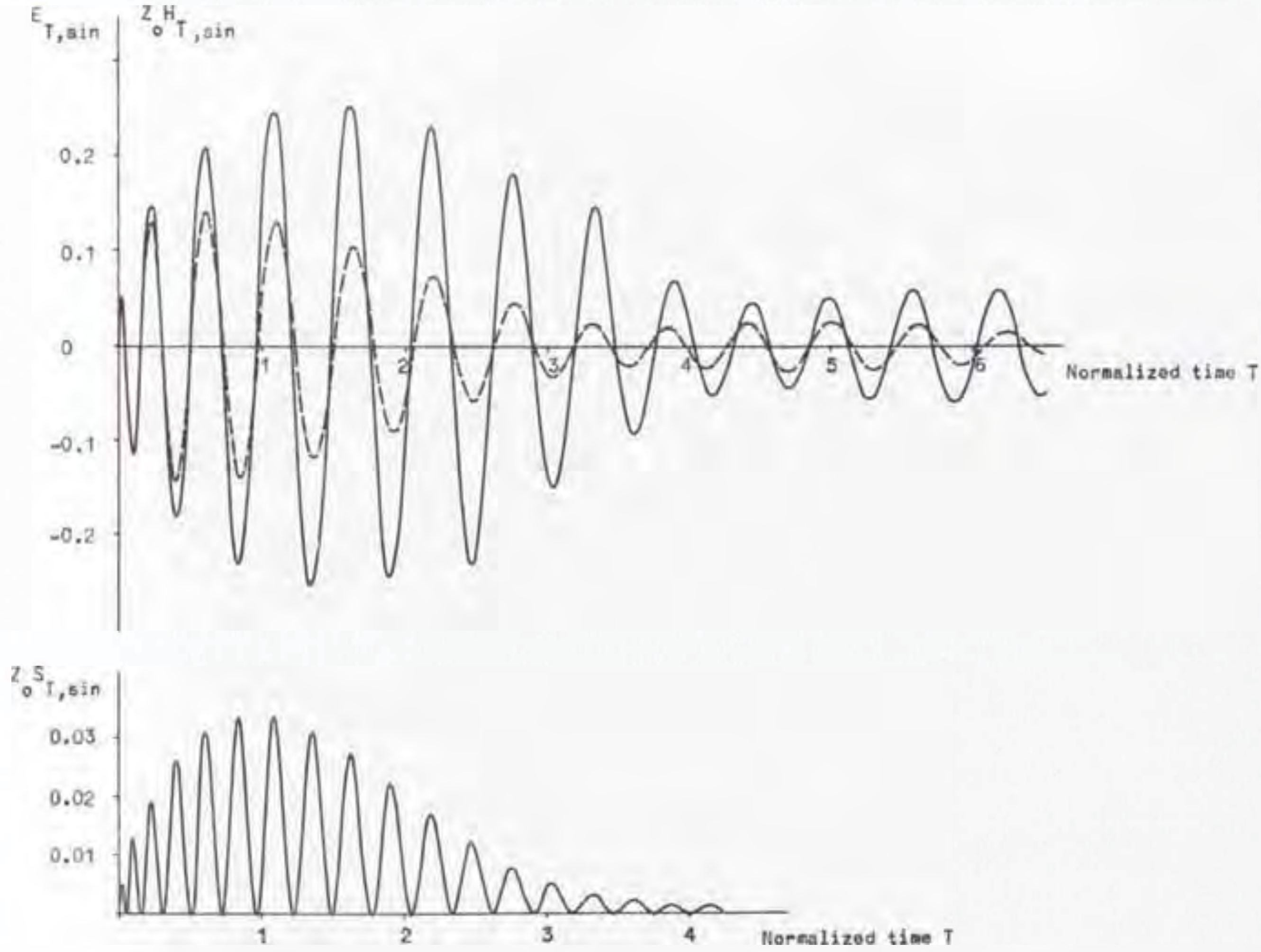

FIGURE 5.22 Electric field (——), magnetic field (- - - -) and energy flow at $z/2H = 0.285$. Carrier frequency $f_1 = 1.5\ c_o/2H$. Penetration frequency $f_{p,m} = 1.75\ c_o/2H$.

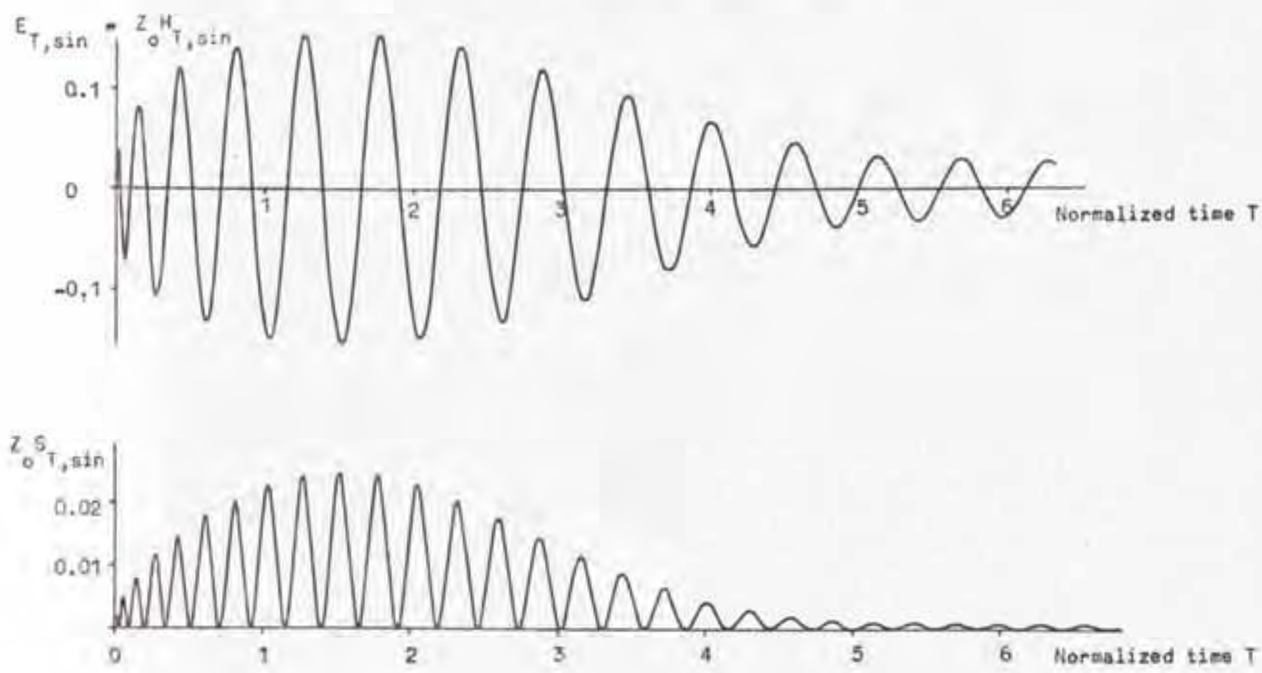

FIGURE 5.23 Electric field, magnetic field and energy flow far above the layer. Carrier frequency $f_1 = 1.5\ c_o/2H$. Penetration frequency $f_{p,m} = 1.75\ c_o/2H$.

APPENDIX I LAPLACE-TRANSFORMS OF TWO HYPERGEOMETRIC FUNCTIONS

1. The inversion of $F(\alpha, \beta; 1+p; z)$.

The bilateral Laplace integral, which will be solved, reads

$$I = \frac{1}{2\pi j} \int_{c-j\infty}^{c+j\infty} \frac{1}{p} F(\alpha, \beta;\ 1+p; z)\, e^{pt}\, dp. \qquad \text{(AI. 1)}$$

The integrand has single poles at

$$p = 0, -1, -2, \ldots .$$

and therefore we choose the real quantity $c > 0$, keeping all poles to the left of the integration contour.

The integrand goes to zero, when $|p| \to \infty$ if

$$\mathrm{Re}\{p\} > 0 \text{ and } t < 0$$

or

$$\mathrm{Re}\{p\} < 0 \quad \text{and } t > 0 .$$

We treated the two cases, $t < 0$ and $t > 0$, separately.

a. $t < 0$

We continue the integration contour at $|p| = \infty$ and $\mathrm{Re}\{p\} > 0$ (see figure AI. 1) in order to use residue calculus on the obtained, closed contour C_1. The integrand has no singlular points inside C_1 and consequently

$$I \equiv 0 \text{ when } t < 0.$$

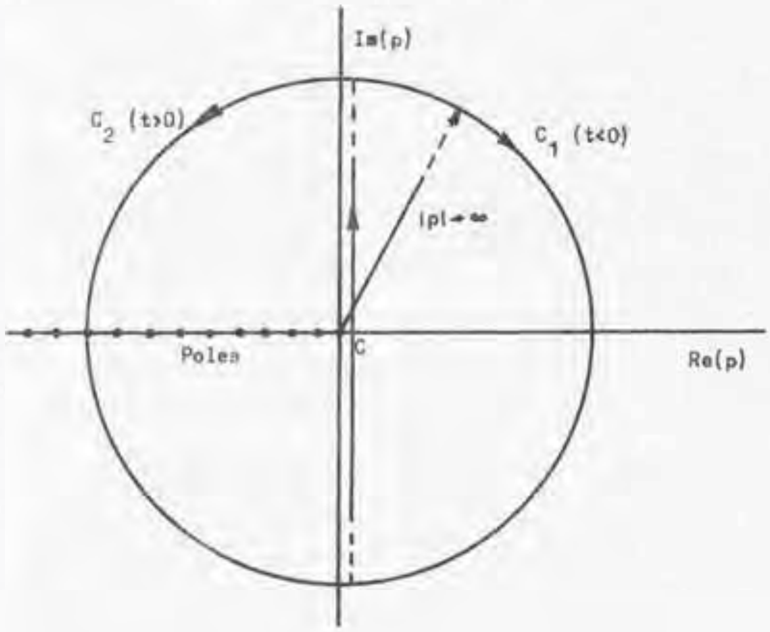

FIGURE AI.1. The integration contour.

b. $t > 0$

We now continue the integration contour at $|p| = \infty$ and $\mathrm{Re}\{p\} < 0$ then obtaining a closed contour C_2 (fig. AI.1). Inside C_2 we have single poles at

$$p = 0, -1, -2, \ \ldots$$

and

$$I = 2\pi j \ \Sigma \, \mathrm{Residues} =$$

$$= 1 + \alpha\beta \ (1 - e^{-t}) \, z + \frac{1}{2}\alpha\beta \ (\alpha + 1)(\beta + 1) \, z^2 \left(\frac{1}{2} - e^{-t} + \frac{1}{2} \, e^{-2t} \right) +$$

$$+ \frac{1}{n!} \prod_{k=0}^{n-1} \frac{(\alpha + k)(\beta + k)}{1 + k} \, z^n \, (1 - e^{-t})^n + \ldots = F[\alpha, \beta; 1; z(1-e^{-t})] \, , \tag{AI.2}$$

when $\mathrm{Re}\{p\}>0$.

Consequently

$$F[\alpha,\beta:1;z(1-e^{-t})]\ U(t) \doteq F(\alpha,\beta:1+p;z)\,. \tag{AI.3}$$

$$\mathrm{Re}\{p\}>0$$

and

$$-F\left[\frac{1}{2}+\gamma,\frac{1}{2}-\gamma:1;\frac{1}{1+e^{-z/H}}(1-e^{T})\right]\ U\left[-\left(t-\frac{z}{c_o}\right)\right] \doteq$$

$$\doteq e^{-p\frac{z}{c_o}}\ F\left[\frac{1}{2}+\gamma,\ \frac{1}{2}-\gamma\ ;1-\frac{2H}{c_o}p;\ \frac{1}{1+e^{-z/H}}\right]\,. \tag{AI.4}$$

$$\mathrm{Re}\left\{\frac{2H}{c_o}p\right\}<0$$

2. <u>The inversion of</u>

$$\frac{1}{\Gamma(-\gamma+\frac{1}{2})\,\Gamma(\gamma+\frac{1}{2})}\ \frac{\Gamma(-\frac{2H}{c_o}p)}{\Gamma(\frac{2H}{c_o}p)}\ \Gamma\left(\frac{2H}{c_o}p-\gamma+\frac{1}{2}\right)\Gamma\left(\frac{2H}{c_o}p+\gamma+\frac{1}{2}\right)\,.$$

$$\cdot\, e^{-p\frac{z}{c_o}}\ (1+e^{-z/H})^{-\frac{2H}{c_o}p}\,.$$

$$\cdot F\left[\frac{1}{2}+\gamma+\frac{2H}{c_o}p,\ \frac{1}{2}-\gamma+\frac{2H}{c_o}p;\ 1+\frac{2H}{c_o}p;\ \frac{1}{1+e^{-z/H}}\right]\,.$$

(AI.5)

From van der Pol and Bremmer [1955, p.399] we obtain

$$\frac{\Gamma(\alpha_1)\ \Gamma(\alpha_2)}{\Gamma(\gamma_1)}\ F(\alpha_1, \alpha_2; \gamma_1; -\lambda - e^{-t}) \doteqdot$$

$$\doteqdot \frac{\Gamma(p+1)\ \Gamma(\alpha_1 + p)\,\Gamma(\alpha_2 + p)}{\Gamma(\gamma_1 - p)}\ F(\alpha_1 - p\ \ \alpha_2 - p; \gamma_1 - p; -\lambda)\ ,$$

$$0 < \mathrm{Re}\left\{ p \right\} < \min\left(\mathrm{Re}\left\{\alpha_1\right\},\ \mathrm{Re}\left\{\alpha_2\right\}\right)$$

(AI. 6)

Putting

$$p = -\frac{2H}{c_o}\ p\ ,$$

$$\alpha_1 = \frac{1}{2} + \gamma\ ,$$

$$\alpha_2 = \frac{1}{2} - \gamma\ ,$$

$$\gamma_1 = 1\ ,$$

$$-\lambda = \frac{1}{1 + e^{-z/H}}\ ,$$

we at once obtain the transform of relation (AI. 5) as

$$F\left[\frac{1}{2} + \gamma\ ,\ \frac{1}{2} - \gamma\ ;\ 1\ ;\ \frac{1}{1 + e^{-z/H}}\ (1 - e^{T})\right]\ . \tag{AI. 7}$$

$$-\mathrm{Re}\left\{\frac{1}{2} - \gamma\right\} < \mathrm{Re}\left\{\frac{2H}{c_o}\ p\right\} < 0$$

REFERENCES

Abramowitz, M. , and Stegun, J. A. (1964). Handbook of Mathematical Functions, NBS. Applied Mathematics Series 55.

Bowhill, S. A. (1955). The transient response of the ionosphere at low frequencies. The Physics of the Ionosphere, The Physical Society, London.

Brillouin, L. (1914). Über die Fortpflanzung des Lichtes in dispergierenden Medien. Ann. Physik, Lpz, vol 44, p 203.

Budden, K. G. (1961). Radio waves in the ionosphere. Cambridge University Press.

Case, C. (1965). On transient wave propagation in a plasma. Proc. IEEE, vol. 53, pp. 730-73.

Case, C. and Haskell, R. E. (1966). On "Pulsed electromagnetic wave propagation in dispersive media". IEEE Trans. on Antennas and Propagation (comm.) vol. AP-14, p. 401.

Chen, S. N. C. (1963). The transient phenomenon in an isotropic plasma without collision losses. Proc. IEEE, vol. 51, pp. 1045-1046.

Деканосидзе, Е. Н. (1956). Таблицы цилиндрических функций от двух переменных. М., Издательство АН СССР.

Dekanosidze, E. N. (1960). Tables of Lommel's functions of two variables. Pergamon Press, New York.

Epstein, P. S. (1930). Reflection of waves in an inhomogeneous absorbing medium. Proc. Nat. Acad. Sci., vol. 16, pp. 627-637.

Fengler, C. (1963). The reflection of a pulse at an Epstein profile. The Ionosphere, The Institute of Physics and Physical Society, London.

Gershman, B. N. (1952). On deformation of electromagnetic pulses propagated in the ionosphere. Zh. Tekhn. Fiz. (USSR), vol. 22, pp. 101-104.

Knop, C. M. (1964). Pulsed electromagnetic wave propagation in dispersive media. Trans. IEEE, vol. AP-12, pp. 494-496.

Laddell, L. (1965/66). Private communications.

Magnus, W. and Oberhettinger, F. (1948). Formeln und Sätze für die speziellen Funktionen der mathematischen Physik, Springer-Verlag, Berlin.

Rawer, K. (1939). Elektriche Wellen in einem geschichteten Medium, Ann. Physik, Lpz., vol. 35, pp. 385-416.

Rydbeck, O. E. H. (1942). A theoretical survey of the possibilities of determining the distribution of free electrons in the upper atmosphere. Trans. Chalmers University of Technology, No. 3.

Rydbeck, O. E. H. (1944). On the propagation of radio waves. Trans. Chalmers University of Technology, No. 34.

Rydbeck, O. E. H. (1948). On the propagation of waves in an inhomogeneous medium. Trans. Chalmers University of Technology, No. 74.

Rydbeck, O. E. H. (1961). Dynamic non-linear wave propagation in ionized media. I. The isotropic case. Res. Rep. No. 27, Res. Lab. of Electronics, Chalmers University of Technology.

Rydbeck, O. E. H. and Hjalmarson Å. (1966). Coupled wave equations for multimode inhomogeneous media, Res. Rep. No. 61, Res. Lab. of Electronics, Chalmers University of Technology.

Rönnäng, B. O. (1966). Transient wave propagation in symmetric ionized Epstein layers. Res. Rep. No. 64, Res. Lab. of Electronics, Chalmers University of Technology.

Rönnäng, B. O. (1966). Transient wave propagation in symmetric ionized Epstein layers. Proc. IEEE, vol. 54, to be published.

Sommerfeld, A. (1914). Über die Fortpflanzung des Lichtes in dispergierenden Medien. Ann. Physik, Lpz., vol. 44, pp. 177-202.

Van der Pol, B. and Bremmer, H. (1955). Operational calculus based on the two-sided Laplace integral. Cambridge University Press.

Wait, J.R. (1965). Propagation of pulses in dispersive media. Radio Science, vol. 69 D, No. 11.

Earlier publications from the Research Laboratory of Electronics:

O.E.H.Rydbeck: A theoretical survey of the possibilities of determining the distribution of the free electrons in the upper atmosphere; Trans. Chalmers Univ. of Techn., No. 3, 1942.

O.E.H.Rydbeck: On the propagation of radio waves; Trans. Chalmers Univ. of Techn., No. 34, 1944.

O.E.H.Rydbeck: On the spherical and spheroidal wave functions; Trans. Chalmers Univ. of Techn., No. 43, 1945.

O.E.H.Rydbeck: A simple Kerr modulator for ionospheric recording; Trans. Chalmers Univ. of Techn., No. 44, 1945.

O.E.H.Rydbeck: Chalmers solar eclipse ionospheric expedition 1945; Trans. Chalmers Univ. of Techn., No. 53, 1946.

Reports from the Research Laboratory of Electronics:

1. O.E.H.Rydbeck: The theory of the travelling-wave tube. 1947 x).
2. J.S.A.Tomner: The experimental development of travelling-wave tubes; Trans. Chalmers Univ. of Techn., No. 67, 1948.
3. S.I.Svensson: Pulser and water load for high power magnetrons; Trans. Chalmers Univ. of Techn., No. 68, 1948.
4. U.Ingård: On the radiation of sound into a circular tube with an application to resonators; Trans. Chalmers Univ. of Techn., No. 70, 1948.
5. D.Strantz: A study of impressive wave formation in the atmosphere; Trans. Chalmers Univ. of Techn., No. 71, 1948.
6. D.Strantz: Ozonradiosonde; Trans. Chalmers Univ. of Techn., No. 72, 1948.
7. O.E.H.Rydbeck: On the propagation of waves in an inhomogeneous medium, I; Trans. Chalmers Univ. of Techn., No. 74, 1948.
8. O.E.H.Rydbeck and D.Strantz: Ionospheric effects of solar flares. Preliminary report No. 1, Trans. Chalmers Univ. of Techn., No. 83, 1949.
9. O.E.H.Rydbeck: On the forced electro-magnetic oscillations in spherical resonators. 1948 x).
10. J.S.A.Tomner: Experimental investigation of a long electron beam in an axial magnetic field; Trans. Chalmers Univ. of Techn., No. 92, 1949.
11. O.E.H.Rydbeck: The ionospheric and radio wave propagation observatory at Kiruna, 67° 50' N, 20° 14,5' E. 1949 x).
12. R.Lindquist: The panoramic ionospheric recorder. 1949 x).
13. R.Lindquist: Ionospheric effects of solar flares. Preliminary reports Nos. 2 and 3; Trans. Chalmers Univ. of Techn., No. 95, 1950.
14. O.E.H.Rydbeck: The theory of magneto ionic triple splitting; Trans. Chalmers Univ. of Techn., No. 101, 1951.
15. O.E.H.Rydbeck and S.K.H.Forsgren: On the theory of electron wave tubes; Trans. Chalmers Univ. of Techn., No. 102, 1951.
16. R.Linquist: Polar blackouts recorded at the Kiruna Observatory; Trans. Chalmers Univ. of Techn., No. 103, 1951.
17. S.K.H.Forsgren: Some calculations of ray paths in the ionosphere; Trans. Chalmers Univ, of Techn., No. 104, 1951.
18. B.N.Agdur: Experimental observations of double-stream amplification. Preliminary notes; Trans. Chalmers Univ. of Techn., No. 105, 1951.

---

x) Not published in the Chalmers Transactions.

19. B.N.Agdur and C-G.L.Åsdal: Noise measurements on a travelling wave tube; Trans. Chalmers Univ. of Techn., No. 106, 1951.

20. S.K.H.Forsgren and O.F.Perers: Vertical recording of rain by radar; Trans. Chalmers Univ. of Techn., No. 107, 1951.

21. O.F.Perers, B.K.E.Stjernberg and S.K.H.Forsgren: Microwave propagation in the optical range; Trans. Chalmers Univ. of Techn., No. 108, 1951.

22. R.Lindquist: A survey of recent ionospheric measurements at the ionospheric and radio wave propagation observatory at Kiruna, 1951 x).

23. R.Lindquist: A 16 kW panoramic ionospheric recorder; Trans. Chalmers Univ. of Techn., No. 109, 1951.

24. B.-A.Lindblad: A radar investigation of the delta aquarid meteor shower of 1950; Trans. Chalmers Univ. of Techn., No. 129, 1952.

25. G.Hellgren: The propagation of electromagnetic waves along a conical helix with variable pitch; Trans. Chalmers Univ. of Techn., No. 130, 1953.

26. G.Hellgren and J.Meos: Localization of aurorae with 10 m high power radar technique, using a rotating antenna. 1952 x).

27. O.E.H.Rydbeck: On the excitation of different space charge wave modes in travelling wave tubes; Trans. Chalmers Univ. of Techn., No. 131, 1953.

28. O.E.H.Rydbeck and B.N.Agdur: The propagation of electronic space charge waves in periodic structures; Trans. Chalmers Univ. of Techn., No. 138, 1954.

29. B.N.Agdur: Experimental investigation of noise reduction in travelling wave tubes; Trans. Chalmers Univ. of Techn., No. 139, 1954.

30. B.N.Agdur: Amplification measurements on a velocity step tube; Trans. Chalmers Univ. of Techn., No. 140, 1954.

31. O.E.H.Rydbeck and H.Wilhelmsson: A theoretical investigation of the ionospheric electron density variation during a solar eclipse; Trans. Chalmers Univ. of Techn., No. 149, 1954.

32. H.Wilhelmsson: The interaction between an obliquely incident plane electromagnetic wave and an electron beam. Part I; Trans. Chalmers Univ. of Techn., No. 155, 1954.

33. S.Olving: Electromagnetic wave propagation on helical conductors imbedded in dielectric medium; Trans. Chalmers Univ. of Techn., No. 156. 1955.

34. S.Olving: Amplification of the travelling wave tube at high beam current. Part I; Trans. Chalmers Univ. of Techn., No. 157, 1955.

35. H.Wilhelmsson: On the reflection of electromagnetic waves from a dielectric cylinder; Trans. Chalmers Univ. of Techn., No. 168, 1955.

36. B.-A.Lindblad: Combined visual and radar observations of Perseid meteors. I: Observations in 1953 x).

37. S.Olving: A new method for space charge wave interaction studies. Part I; Trans. Chalmers Univ. of Techn., No. 178, 1956.

38. V.Westberg: Measurements of noise radiation at 10 cm from glow lamps; Trans. Chalmers Univ. of Techn., No. 180, 1956.

39. S.I.Svensson, G.Hellgren and O.Perers: The swedish radioscientific solar eclipse expedition to Italy, 1952; Trans. Chalmers Univ. of Techn., No. 181, 1956.

40. N.Wax: A note on design considerations for proposed auroral radar; Trans. Chalmers Univ. of Techn., No. 182, 1957.

41. N.Wax: On the ring current hypothesis; Trans. Chalmers Univ. of Techn., No. 171, 1956.

---

x) Not published in the Chalmers Transactions.

42. G.H.Joshi: The electromagnetic interaction between two crossing electron streams. Part I; Trans. Chalmers Univ. of Techn., No. 183, 1957.

43. J.Mesa and S.Olving: On the origin of radar echoes associated with auroral activity; Trans. Chalmers Univ. of Techn., No. 195, 1958.

44. G.H.Joshi: The electromagnetic interaction between two crossing electron streams. Part II; Trans. Chalmers Univ. of Techn., No. 197, 1958.

45. H.Wilhelmsson: The interaction between an obliquely incident plane electromagnetic wave and an electron beam. Part II; Trans. Chalmers Univ. of Techn., No. 198, 1958.

46. H.Wilhelmsson: On the properties of the electron beam in the presence of an axial magnetic field of arbitrary strength; Trans. Chalmers Univ. of Techn., No. 205, 1958.

47. H.Wilhelmsson: The interaction between an obliquely incident plane electromagnetic wave and an electron beam. Part III; Trans. Chalmers Univ. of Techn., No. 206, 1958.

48. B.Höglund and V.Radhakrishnan: A radiometer for the hydrogen line; Trans. Chalmers Univ. of Techn., No. 223, 1959.

49. S.Olving: Electromagnetic and space charge waves in a sheath helix; Trans. Chalmers Univ. of Techn., No. 225, 1960.

50. H.Wilhelmsson: A survey of radio-frequency and microwave resonance lines of interest to radio astronomy. 1960 x).

51. S.Olving: A new method for space charge wave interaction studies. Part II; Trans. Chalmers Univ. of Techn., No. 228, 1960.

52. Papers presented at the fourth international conference on ionization phenomena in gases at Uppsala, August 17-21, 1959. 1960 x).

53. H.Wilhelmsson: Two problems concerning the electron ring current. 1960 x).

54. T.Orhaug: The variation of electron density in the ionosphere during a solar eclipse. 1960 x).

55. H.Wilhelmsson and M.Fischer: On the force-free magnetic fields. 1960 x).

56. O.E.H.Rydbeck: On the coupling between waves in inhomogeneous systems. 1961 x).

57. H.Wilhelmsson: The scattering of an electromagnetic wave by a dielectric-coated metallic cylinder. Reprint from Arkiv för Fysik, Band 23, nr 41 x).

58. H.Wilhelmsson: Accounting for smoothing effects in 21 cm observations. Reprint from Arkiv för Astronomi, Band 3, nr 16 x).

59. B.Höglund: 21 cm Observations in the Galactic Anti-centre. Reprint from Arkiv för Astronomi, Band 3, nr 16 x).

60. H.Gerritsen: Recent Developments in Maser Devices and Materials. Reprint from Applied Optics, Vol. 1, No 1 x)

x) Not published in the Chalmers Transactions.

Research Reports from the Research Laboratory of Electronics:

1. O.E.H.Rydbeck and K.H.B.Wilhelmsson: The influence of the electron velocity distribution on space charge waves. 1959.
2. K.H.B.Wilhelmsson: Oscillatory properties of gyromagnetic electronic cold plasmas with drift motion. 1959.
3. H.B.Hvatum: Solar radio noise measurements during the 1954 solar eclipse. 1959.
4. T.As.Orhaug: Ionospheric observations during the solar eclipse June 30, 1954. 1959.
5. K.H.B.Wilhelmsson: The electromagnetic coupling between an electron beam and incident plane waves for an axially finite interaction domain. 1960.
6. Research notes communicated at the radio scientific conference in Stockholm, February 29 - March 2, 1960. 1960.
7. O.E.H.Rydbeck: The propagation and coupling of waves in inhomogeneous media with applications to electromagnetic and space charge waves. (On the propagation of waves in an inhomogeneous medium II).
8. O.E.H.Rydbeck: Electromagnetic and space charge waves in inhomogeneous structures with applications to ionized media and microwave tubes. 1960.
9. K.H.B.Wilhelmsson: On the geometrical theory of diffraction with application to the electron beam. 1960.
10. O.E.H.Rydbeck: The Doppler effect in dispersive, inhomogeneous media with applications to electromagnetic waves in ionized media. 1960.
11. S.Olving and A.Ots: An experimental investigation of the propagation of space charge waves along radially inhomogeneous electron beams. 1960.
12. A.V.Stomberg: The rotatron - an electron tube for shift and multiplication of frequencies. 1960.
13. O.E.H.Rydbeck and M.H.Fischer: Space charge waves in an electron beam of Gaussian cross section. 1960.
14. O.E.H.Rydbeck: The integral equation of travelling wave tubes with electron beams of arbitrary cross section. 1960.
15. O.E.H.Rydbeck and A.R.Thomasson: Low frequency waves in inhomogeneous magneto ionic media. 1960.
16. T.As.Orhaug: Observations of radio star scintillations at high latitudes. 1960.
17. T.As.Orhaug: Observations of solar radio noise at 150 Mc/s. 1960.
18. O.E.H.Rydbeck and J.Askne: Whistler mode - ionized stream interactions. Part 1, 1963.
19. K.H.B.Wilhelmsson: On the problem of overtaking in a velocity distributed electron stream. 1960.
20. O.E.H.Rydbeck: On the coupling between waves in inhomogeneous systems. 1960.
21. O.E.H.Rydbeck: Research in the field of propagation and interaction of electromagnetic waves and space charge type waves in homogeneous and inhomogeneous media. 1960.
22. D.T.Farley, J.P.Dougherty and D.W.Barron: A theory of incoherent scattering of radio waves by a plasma in a uniform magnetic field. 1961.
23. L.F.Eastman: Coherent non-linearities in a mangeto-ionic medium. 1961.
24. D.T.Farley: Artificial heating of the electrons in the F-region of the ionosphere. 1961.
25. K.H.B.Wilhelmsson: Scattering of electromagnetic waves by an anisotropic medium. 1961.
26. K.H.B.Wilhelmsson: The interaction between an obliquely incident plane electromagnetic wave and an electron beam in the presence of a static magnetic field of arbitrary strength. 1961.
27. O.E.H.Rydbeck: Dynamic non-linear wave propagation in ionized media. 1. The isotropic medium. 1961.
28. O.E.H.Rydbeck: Dynamic non-linear wave propagation in ionized media. 2. The magneto-ionic medium. 1962.

29. O.E.H.Rydbeck: Dynamic non-linear wave propagation in ionized media. 3. Electromagnetic non-linear wave interaction and reflection from a plane ionized medium. 1963.

30. O.E.H.Rydbeck: Dynamic non-linear wave propagation in ionized media. 4. Non-linear electromagnetic wave propagation and harmonic radiation in magneto-ionic media. 1963.

31. K.H.B.Wilhelmsson: Dynamic non-linear wave propagation in ionized media. 5. Reflection of electromagnetic waves from an ionized stream in the presence of a high power primary wave. 1962.

32. K.H.B.Wilhelmsson: Dynamic non-linear wave propagation in ionized media. 6. Scattering of electromagnetic waves by an anisotropic medium with an harmonically time-varying dielectric tensor. 1962.

33. O.E.H.Rydbeck: Dynamic non-linear wave propagation in ionized media. 7. Non-linear plasma waves in a streaming homogeneous, cold ionized medium. 1962.

34. A.R.Thomasson: Dynamic non-linear wave propagation in ionized media. 8. Reflection of electromagnetic waves from a dielectric plane layer varying periodically in space and time. 1962.

35. K.H.B.Wilhelmsson: Dynamic non-linear wave propagation in ionized media. 9. A non-linear coupling mechanism for generation of very low frequency waves. 1963.

36. K.H.B.Wilhelmsson: Dynamic non-linear wave propagation in ionized media. 10. Non-linear interaction between an obliquely incident plane electromagnetic wave and an electron beam. 1963.

37. S.Olving: On the non-linear theory of the plane travelling wave tube. 1963.

38. K-O.Yngvesson: Observations of the Venus probe Mariner R-2 at the Onsala Space Observatory. 1963.

39. K.H.B.Wilhelmsson: Dynamic non-linear wave propagation in ionized media. 11. Non-linear excitation of hydromagnetic waves and hybrid resonances by two interacting high power primary waves. 1963.

40. S.Olving and O.Nilsson: Propagation of nonlinear Hahn-Ramo waves along an annular electron current-sheath. 1963.

41. S.Olving and M.Fischer: Small-signal nonlinear klystron waves. 1964.

42. S.Olving and S.Wallander: Nonlinear space charge wave theory of the hydrodynamic disc-electron beam. 1964.

43. O.E.H.Rydbeck: Dynamic non-linear wave propagation in ionized media. 12. Electromagnetic wave reflection from an oscillating, collision free magneto-ionic medium. 1964.

44. A.R.Thomasson: Dynamic non-linear wave propagation in ionized media. 13. Microscopic treatment of the interaction between a plane electromagnetic wave and an oscillating medium. 1964.

45. K.H.B.Wilhelmsson: Dynamic non-linear wave propagation in ionized media. 14. Generation of longitudinal plasma waves by non-linear coupling of two high-power circularly polarized transverse waves. 1964.

46. K.H.B.Wilhelmsson and A.R.Thomasson: Dynamic non-linear wave propagation in ionized media. 15. Čerenkov effect in a pre-oscillating medium. 1964.

47. K.H.B.Wilhelmsson: The magneto-ionic theory for mass-anisotropic electrons. 1964.

48. O.E.H.Rydbeck: Research in the field of propagation of high power waves in ionized media. 1964.

49. R.Tengblad: Concentration effects in a maser material. 1964.

50. O.Nilsson: Some frequency and power conversion proper ties of cyclotron waves. 1965.

51. O.Nilsson: Anomalous noise peak in Adler tubes. 1965.

52. B.Geidne: Nonlinear analysis of a microwave beamplasma amplifier. 1965.

53. J.Askne: Stimulated scattering from a semi-infinite dispersive medium periodic in time and space. 1965.

54. S.Yngvesson: Chromium-doped rutile: Maser properties at 1420 Mc/s and application to a traveling-wave maser. 1965.

55. T.M.Srinivasan: Measurements on nonlinear space charge waves. 1965.

56. O.E.H.Rydbeck: Wave coupling in multi-mode. inhomogeneous, ionized media, with applications to electron stream-whistler mode interactions. 1966.

57. P.McIsaac: Wave propagation in a dispersive medium. 1966.

58. S.Wallander: Nonlinear theory of the planar microwave vacuum diode. 1966.

59. S.Wallander: Nonlinear traveling wave tube analysis with two signal frequencies. 1966.

60. O.Nilsson: Approximate theory of the wire helix slow wave structure. 1966.

61. O.E.H.Rydbeck and Å.Hjalmarson: Coupled wave equations for multi-mode inhomogeneous media. 1966.

62. O.E.H.Rydbeck and Å.Hjalmarson: Coupled waves in magneto-ionic media. Part I. 1966.

63. J.Askne: Reflection and amplification of electromagnetic waves in an oscillating ionized medium, Part. I. 1966.

64. J.Askne: Instability properties of an ionized medium periodic in time and space.
B.Rönnäng: Transient wave propagation in symmetric, ionized Epstein layers. 1966.

65. J.I.Lindström: Measurements of nonlinearities in a traveling wave tube. 1966.

66. J.Jäderblom: Cyclotron wave amplification using self generated pump power. 1966.

67. O. Nilsson: Nonlinear distortion in traveling wave tubes. 1966.

68. S. Kronlund: Measurements on a beam-plasma microwave amplifier. 1966.

69. P.R. McIsaac: Boundary conditions for ferromagnetic media. 1966

70. B.O. Rönnäng: Transient wave propagation in inhomogeneous ionized media. 1966.

Lecture Notes from the Research Laboratory of Electronics:

1. K.H.B.Wilhelmsson: Lectures on the quantum theory of masers. 1962.

2. D.T.Farley: Lectures on the scattering of radio waves from randomly fluctuating media given 1961 at Chalmers University of Technology, Gothenburg. 1961.

3. A.Elvius: Lectures on galactic dynamics given 1961 at Chalmers University of Technology, Gothenburg. 1961.

4. K.H.B.Wilhelmsson and A.G.Lieberman: Lectures on superconductivity. 1964.

I:19

Tp

SIGNAL DISTORTION IN ANISOTROPIC HOMOGENEOUS IONIZED MEDIA

1. LONGITUDINAL MAGNETIC FIELD

BY
B. O. RÖNNÄNG

RESEARCH REPORT NO. 73
1967

RESEARCH LABORATORY OF ELECTRONICS

CHALMERS UNIVERSITY OF TECHNOLOGY

GIBRALTARGATAN 5 G

GOTHENBURG S, SWEDEN

Research Laboratory of Electronics
CHALMERS UNIVERSITY OF TECHNOLOGY
Gothenburg, Sweden

RESEARCH REPORT No. 73

SIGNAL DISTORTION IN ANISOTROPIC HOMOGENEOUS IONIZED MEDIA

Part I. Longitudinal magnetic field

By

B. O. Rönnäng

Gothenburg, March 1967

TABLE OF CONTENTS

ABSTRACT

This report deals with propagation of electromagnetic transients in anisotropic, homogeneous ionized media. Due to a longitudinal, external magnetic field an incident signal will be split up into two circularly polarized modes, which propagate independently in the homogeneous medium. By mean of the saddle-point method of integration approximate expressions for the transmitted signal in the medium have been obtained. These results have been used to calculate the distorted and time-delayed unit step modulated carrier and the distorted pulse-carrier in the layer in the isotropic as well as the anisotropic case. The split-up into a left-hand polarized and a right-hand polarized pulse is shown in a series of figures.

I INTRODUCTION

In the beginning of this century the scientists considered that the group velocity of a wave always corresponds to the velocity of energy. However, it was shown that this was in conflict to the theory of relativity since the group velocity could be larger than the velocity of light in vacuum (c_o).

This difficulty was resolved by SOMMERFELD and BRILLOUIN (1914). They investigated the distortion of a signal propagating in a homogeneous isotropic dispersive medium. Sommerfeld found that, immediately after the arrival of the front with velocity c_o , there is a disturbance of small amplitude and high frequency. Using the saddle-point method of integration Brillouin showed that, in addition to this first forerunner (precursor), there is a second one, the amplitude of which increases and the period of which decreases with time. The second forerunner joins with the main signal which propagates with the signal velocity. The term " signal velocity " refers to the travel of the head of that portion of the wave which actuates a measuring device. Except near a region of anomalous dispersion the signal velocity and the group velocity are essentially equal.

To calculate the change in form of the main part of a quasi-monochromatic pulse, which propagates in a dispersive, non-absorbing medium, a simplified stationary phase principle can be applied. This method has been used by several authors. See WAIT (1965). However, to obtain an approximate result valid always after the arrival of the wavefront (except for the immediate vincinity of the wavefront) the saddle-point method of integration must be used.

Near the front of the main signal the simple integration due to Debye can not be applied, since a pole of the integrand is near the saddle-point. A slightly modified method must be used and a solution is obtained in terms of Fresnel integrals. Referring to this method of integration two closely related works must be mentioned. In 1953 PEARSON used the method to study the transient motion of sound waves in acoustic waveguides and recently the distortion of a unit step modulated sine wave, which propagates in an isotropic homogeneous plasma, has been treated [HASKELL and CASE (1966)].

In a previous report by the author the transient wave responses of two different inhomogeneous ionized media - the exponentially stratified medium and the symmetrical Epstein layer - were studied [RÖNNÄNG (1966)]. By means of the linearized wave equations analytic expressions for the unit step wave responses were derived. In both cases they were written in closed mathematical forms, namely as a Bessel function and a Legendre function respectively. The unit step modulated sine wave responses, written as convolution integrals, were computed at different heights in the media and at different carrier frequencies. Furthermore, the strong signal distortion at tunnel transmission through a thin symmetrical Epstein layer was studied in detail.

The present report can be considered as an extension of the above work to the anisotropic case. By introducing a longitudinal static magnetic field two wave-modes can exist in the ionized medium. Consequently, the treatment becomes more complicated and we have therefore limited ourselves to the homogeneous case. Thus, we are studying transient signal propagation in a semi-infinite homogeneous ionized medium.

An incident linearly polarized wave will be split up into a left-hand polarized mode and a right-hand polarized mode. These two modes propagate independently but are coupled to each other due to the boundary conditions.

By means of the saddle-point method of integration (the method of steepest descent) the distortion of an incident unit step wave, of an incident unit step modulated sine wave and of an incident rectangular pulse carrier are studied. The individual modes as well as the total x- and y-components of the electric field have been computed for different propagation distances and for different carrier frequencies. For the isotropic case the curves are compared with corresponding results obtained earlier by other authors. It is shown that the simplified method, mentioned above, is usuable only in a narrow time region about the steepest portion of the front of the signal.

If we know the amplitude and the phase of the transmitted unit step carrier it is possible to determine the rectangular pulse carrier response. This has been done for the isotropic as well as the anisotropic medium. The interesting spit-up into two pulses, when the gyro-frequency differs from zero, is shown.

Acknowledgement.

The author's thanks are due to Professor O. E. H. Rydbeck, Director of the Research Laboratory of Electronics, for his encouraging interest in this work.

Index of symbols.

Symbol	Description
Latin alphabet	
$\bar{B}_o$	Static magnetic field
C	Fresnel cosine integral
c_o	Velocity of light in vacuum
$\bar{D}$	Displacement vector
$\bar{E}$	Electric field strength
e	Charge on the electron
erf	Error function
J_0, J_1, J_2	Bessel functions
m	Mass of electron
n	Refractive index
n'	Group refractive index
N	Number of electrons per unit volume
p	Laplace operator
$p_s = j\omega_s$	Laplace operator at the saddle-point
R	Wave polarisation
$\tilde{R}$	Laplace-transformed reflection coefficient
S	Fresnel sine integral
t	Time
$\tilde{T}$	Laplace-transformed transmission coefficient
U	Unit step function
$\bar{v}$	Electron velocity
v_g	Group velocity
w	$p\,(t - n_{+}\frac{z}{c_o})$
x, y, z	Cartesian coordinate

Greek alphabet

α	$\sqrt{\frac{1}{\pi} \mid w''(j\omega_s^+) \mid} \, (\omega_1 - \omega_s^+)$
γ	$\mid w(j\omega_s^+) \mid + \frac{1}{2} \mid w''(j\omega_s^+) \mid (\omega_1 - \omega_s^+)^2$
λ_o	Plasma wavelength
τ	z/c_o
ω	Angular frequency
ω_1	Carrier frequency
ω_p	Plasma frequency
ω_o	$\omega_p = \omega_o$ when $z > 0$
ω_H	Gyro frequency
ω_s	Imaginary part of p_s

superscript

i, t, r	Incident, transmitted, reflected
+	The positive one
-	The negative one

subscript

+	Left-hand polarized mode
-	Right-hand polarized mode
x, y	x-component, y-component

II THE REFRACTIVE INDEX OF AN IONIZED MEDIUM WITH A LONGITUDINAL STATIC MAGNETIC FIELD.

In order to derive the formula for the refractive index n of an ionized medium with a longitudinal static magnetic field we must first define certain properties of both the electromagnetic wave and the medium. For our present purpose we shall assume the following properties:

Wave properties.

(1) A plane wave travelling in positive z-direction. The Laplace-transformed* electric field $\tilde{E}(p, z)$ is proportional to e^{-npz/c_0}.

(2) Given wave polarization R defined as $R = \frac{\tilde{E}_y}{\tilde{E}_x}$.

Properties of the medium.

(3) The medium is anisotropic due to a longitudinal, uniform, external magnetic field $\bar{B}_o$, directed in positive z-direction.

(4) Electrons only are effective .

(5) No collision-losses.

(6) The medium is a cold plasma.

The forces acting on an electron, if we neglect non-linear effects, are

(1) The electric force $e \cdot \bar{E}$.

(2) The force $e\bar{v} \times \bar{B}_o$ due to the electron motion $\bar{v}$ relative to the imposed magnetic field $\bar{B}_o$.

Then the equations of motion are

---

* Throughout this report we use the bilateral Laplace transform in place of the complex Fourier integrals to make it uniform to the previous report on this subject [RÖNNÄNG, 1966].

$$m\ddot{x} = e\,E_x + e\dot{y}\,B_o$$
$$m\ddot{y} = e\,E_y - e\dot{x}\,B_o \qquad (2.1)$$

where

$$\dot{x} = \frac{\partial x}{\partial t} \text{ and } \ddot{x} = \frac{\partial^2 x}{\partial t^2}$$

Furthermore the wave propagation is defined by Maxwells equations,

$$\operatorname{div} \bar{D} = 0$$
$$\operatorname{div} \bar{B} = 0$$
$$\operatorname{curl} \bar{H} = \dot{\bar{D}} \qquad (2.2)$$
$$\operatorname{curl} \bar{E} = -\dot{\bar{B}} = -\mu\,\dot{\bar{H}}$$

where

$$\bar{D} = \varepsilon_o\,\bar{E} + Ne\bar{r} \qquad (\,\bar{r} = x\hat{x} + y\hat{y} + z\hat{z}\,) \qquad (2.3)$$

Now let us Laplace-transform relation (2. 1) and (2. 2). Since the electric and magnetic vectors of the wave do not vary in the x- and y-direction we have

$$\frac{\partial}{\partial x} = \frac{\partial}{\partial y} = 0$$

Furthermore

$$\frac{\partial}{\partial t} \doteq p, \qquad \frac{\partial^2}{\partial t^2} \doteq p^2 \qquad (2.4)$$

Introducing the wave polarization

$$R = \frac{\tilde{E}_y}{\tilde{E}_x} = -\frac{\tilde{H}_x}{\tilde{H}_y} \qquad (2.5)$$

we obtain from (2. 1) and (2. 2)

$$R = \pm j \qquad (2.6)$$

There are consequently two characteristic waves propagating in our magneto-ionic medium. Both of them are circularly polarized. $R = -j$ corresponds to the right-hand polarization and $R = j$ to the left-hand polarization.

Introducing the angular plasma frequency

$$\omega_p^{\,2} = \frac{Ne^2}{m\varepsilon_o} \tag{2.7}$$

and the gyrofrequency

$$\omega_H = \left| \frac{eB_o}{m} \right| \tag{2.8}$$

we furthermore obtained from (2. 1) and (2. 2) the refractive index of the medium as

$$n_{\pm}^{\,2}(p) = 1 + \frac{\omega_p^{\,2}}{p(p \pm j\omega_H)} \tag{2.9}$$

For the plus sign $R = +j$ and for the minus sign $R = -j$.

III THE TRANSMITTED ELECTRIC FIELD IN A SEMI-INFINITE HOMOGENEOUS MAGNETO-IONIC MEDIUM (LONGITUDINAL MAGNETIC FIELD)

We now consider the problem of transient electromagnetic wave propagation in a semi-infinite homogeneous magneto-ionic medium. The uniform magnetic field $\bar{B}_o$ is assumed to be directed in the positive z-direction according to Chapter II. The constant plasma angular frequency is equal to ω_o. See figure 3. 1.

Let us suppose that a transient, linearly polarized, plane electromagnetic wave is incident upon the magneto-ionic medium. The incident electric field is expressed

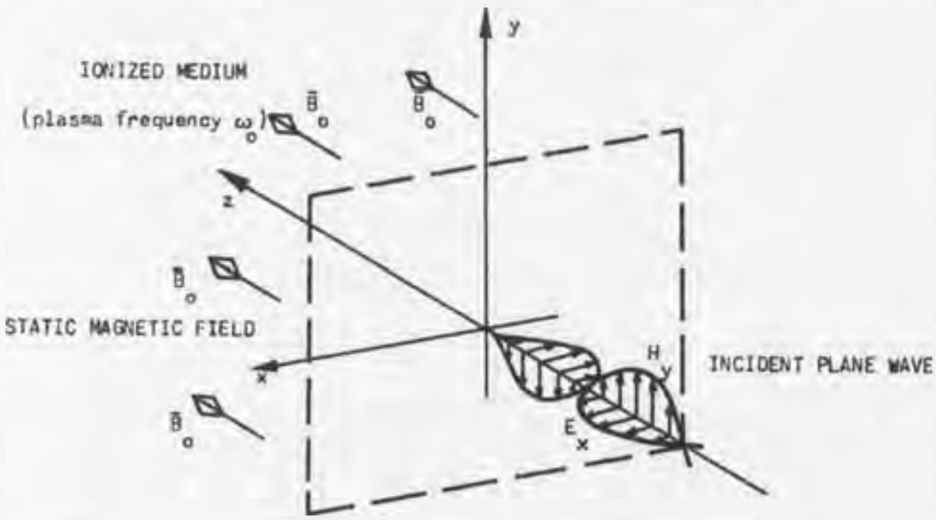

FIGURE 3. 1 The semi-infinite, magneto-ionic medium.

by means of the bilateral Laplace transform as

$$E_x^i (t, z) = \frac{1}{2\pi j} \int_{c-j\infty}^{c+j\infty} \frac{1}{p} \tilde{E}_x^i (p) e^{p (t - \frac{z}{c_o})} dp \qquad (3. 1)$$

For example, $\tilde{E}_x^i (p)$ may be a unit step wave or a unit step modulated sine wave. Then $\tilde{E}_x^i$ is equal to 1 and $\frac{\omega_1 p}{p^2 + \omega_1^2}$ respectively. ω_1 is the angular frequency of the carrier.

The x- and y-components of the reflected wave can be written as

$$E_x^r (t, z) = \frac{1}{2\pi j} \int_{c-j\infty}^{c+j\infty} \frac{1}{p} \tilde{E}_x^i (p) \tilde{R}_x (p) e^{p (t + \frac{z}{c_o})} dp \qquad (3. 2)$$

$$E_y^r(t, z) = \frac{1}{2\pi j} \int_{c-j\infty}^{c+j\infty} \frac{1}{p} \tilde{E}_x^i(p)\ \tilde{R}_y(p)\, e^{p\left(t+\frac{z}{c_o}\right)}\, dp \qquad (3.3)$$

Introducing the transmission coefficients $\tilde{T}_{x,+}(p)$ and $\tilde{T}_{x,-}(p)$ for the left-hand polarized mode and the right-hand polarized mode respectively we obtain the transmitted waves as

$$E_x^t(t, z) = \frac{1}{2\pi j} \int_{c-j\infty}^{c+j\infty} \frac{1}{p} \Big\{ \underbrace{\tilde{T}_{x,+}(p)\, \tilde{E}_x^i(p)\, e^{p\left(t-n_+\frac{z}{c_o}\right)}}_{\text{left-hand polarized mode}} +$$

$$+ \underbrace{\tilde{T}_{x,-}(p)\, \tilde{E}_x^i(p)\, e^{p\left(t-n_-\frac{z}{c_o}\right)}}_{\text{right-hand polarized mode}} \Big\}\, dp \qquad (3.4)$$

and

$$E_y^t(t, z) = \frac{1}{2\pi j} \int_{c-j\infty}^{c+j\infty} \frac{1}{p} \Big\{ j\, \tilde{T}_{x,+}(p)\, \tilde{E}_x^i(p)\, e^{p\left(t-n_+\frac{z}{c_o}\right)} -$$

$$- j\, \tilde{T}_{x,-}(p)\, \tilde{E}_x^i(p)\, e^{p\left(t-n_-\frac{z}{c_o}\right)} \Big\}\, dp \qquad (3.5)$$

where

$$n_\pm = \sqrt{1 + \frac{\omega_o^2}{p\,(p \pm j\omega_H)}} \qquad (3.6)$$

Relation (3.5) is given from (3.4) by means of the polarization conditions [eq. (2.6)].

From the boundary conditions at $z = 0$ we easily obtain the reflection and transmission coefficients

$$\tilde{R}_x(p) = \frac{1 - n_+ n_-}{(1 + n_+)(1 + n_-)} \qquad (3.7)$$

$$\tilde{R}_y(p) = -j\, \frac{n_+ - n_-}{(1 + n_+)(1 + n_-)} \qquad (3.8)$$

$$\tilde{T}_{x,+}(p) = \frac{1}{1 + n_+} \qquad (3.9)$$

$$\tilde{T}_{x,-}(p) = \frac{1}{1+n_-} = \tilde{T}^*_{x,+}(p^*) \tag{3.10}$$

Since

$$n_-(p) = n^*_+(p^*)$$

and

$$\tilde{T}_{x,-}(p) = \tilde{T}^*_{x,+}(p^*)$$

the singularities of the integrand in (3.4) and (3.5) are symmetrically distributed about the real axis of the complex p-plane. Accordingly $E^t_x(t, z)$ and $E^t_y(t, z)$ are real functions of time.

We can write the x- and y-components by means of the left-hand polarized mode as

$$\boxed{\begin{aligned} E^t_x(t, z) &= 2\,\mathrm{Re}\left\{ \frac{1}{2\pi j} \int_{c-j\infty}^{c+j\infty} \frac{\tilde{T}_{x,+}(p)}{p} \tilde{E}^i_x(p)\, e^{p\left(t - n_+ \frac{z}{c_0}\right)} dp \right\} && (3.11) \\ E^t_y(t, z) &= -2\,\mathrm{Im}\left\{ \frac{1}{2\pi j} \int_{c-j\infty}^{c+j\infty} \frac{\tilde{T}_{x,+}(p)}{p} \tilde{E}^i_x(p)\, e^{p\left(t - n_+ \frac{z}{c_0}\right)} dp \right\} && (3.12) \end{aligned}}$$

In the following chapters we are going to use these expressions in order to determine $E^t_x(t,z)$ and $E^t_y(t,z)$ for different incident signals.

IV THE SOMMERFELD PRECURSOR

Before we try to find approximate expressions for $E_x^t(t, z)$ and $E_y^t(t, z)$ we must specify the incident wave $E_x^i(t, z)$. In the following, two interesting cases are treated. We suppose that

$$E_x^i(t, z) = U\left(t - \frac{z}{c_o}\right) \qquad (4.1)$$

or

$$E_x^i(t, z) = \sin\left[\omega_1\left(t - \frac{z}{c_o}\right)\right] U\left(t - \frac{z}{c_o}\right) \qquad (4.2)$$

i.e.

$$\tilde{E}_x^i(p) = 1 \qquad (4.3)$$

or

$$\tilde{E}_x^i(p) = \frac{\omega_1 p}{p^2 + \omega_1^2} \qquad (4.4)$$

respectively.

The first part of the signal arrives when t is slightly greater than z/c_o. Its form can be found by a method given by SOMMERFELD (1914), and this part is sometimes called the " Sommerfeld Precursor ".

The contour from $c-j\infty$ to $c+j\infty$ in (3.11) may be distorted into a large semicircle in the right half of the complex p-plane. Let R be its radius, so that on the semicircle

$$p = R e^{j\alpha} \qquad -\frac{\pi}{2} < \alpha < \frac{\pi}{2} \qquad (4.5)$$

Now (3.6) shows that as $|p| \to \infty$ both n_+ and n_- tend to 1 and

$$\lim \tilde{T}_{x,+}(p) = \lim \tilde{T}_{x,-}(p) = \frac{1}{2} \qquad (4.6)$$

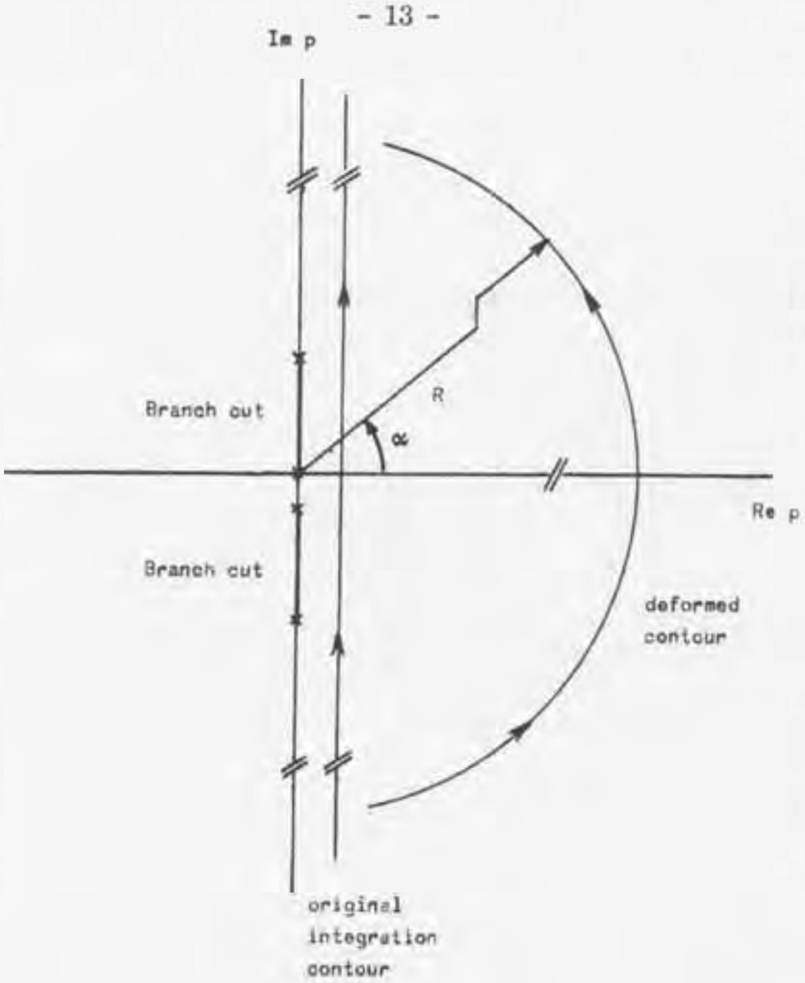

Figure 4.1. The integration contour.

Hence on the large semicircle the exponentials in (3.11) and (3.12) have the form

$$\exp\left[\, p \left(t - \frac{z}{c_o} \right) \right] \tag{4.7}$$

and if $t < z/c_o$ the real part of this exponent is negative and large. Thus the exponential term in the integral gives zero when R tends to infinity. This shows that no signal can be received when $t < z/c_o$.

Expanding n_+ for large values of $|p|$ we obtain

$$n_+ \sim 1 + \frac{1}{2}\,\frac{\omega_o^2}{p\,(p + j\omega_H)} \sim 1 + \frac{\omega_o^2}{2\,p^2} \tag{4.8}$$

Notice that with this approximation the medium is isotropic and consequently

$$E_y^t(t, z) \sim 0 \qquad \left(t - \frac{z}{c_o} << 1 \right) \tag{4.9}$$

The unit step wave response

Let us first consider the case of an incident unit step wave. Then

$$E_x^t(t, z) \sim 2\,\mathrm{Re}\left\{\frac{1}{2\pi}\int_{-\pi/2}^{\pi/2} e^{R\,(t-\frac{z}{c_o})\,2j\sin\alpha}\,d\alpha\right\} \qquad (4.10)$$

if we choose

$$R = \omega_o\left[\frac{z}{2c_o}\,\frac{1}{(t-\frac{z}{c_o})}\right]^{1/2} \qquad (4.11)$$

Now eq. (4. 10) is a standard representation of a Bessel function and

$$\boxed{E_x^t(t, z) \sim J_o\left\{\omega_o\left[\frac{2z}{c_o}\left(t-\frac{z}{c_o}\right)\right]^{1/2}\right\} U\left(t-\frac{z}{c_o}\right) \qquad \left(t-\frac{z}{c_o} << 1\right)} \qquad (4.12)$$

If we put $2\,z/c_o = t + z/c_o$ this is the first term in the exact result for the isotropic case [eq. (6. 12)].

The unit step modulated sine wave response

Assuming an incident unit step modulated carrier (sine wave) we instead obtain

$$E_x^t(t, z) \sim 2\,\mathrm{Re}\left\{\frac{\omega_1}{2\pi}\int_{-\pi/2}^{\pi/2} \frac{1}{R}\, e^{R\,(t-\frac{z}{c_o})\,2j\sin\alpha}\, e^{-j\alpha}\,d\alpha\right\} \qquad (4.13)$$

where as before

$$R = \omega_o\left[\frac{z}{2c_o}\,\frac{1}{(t-\frac{z}{c_o})}\right]^{1/2} \qquad (4.14)$$

From (4. 13)

$$E_x^t(t, z) \sim \frac{\omega_1}{\pi}\int_o^{\pi} \frac{1}{R}\sin\left[2R\left(t-\frac{z}{c_o}\right)\cos\beta + j\beta\right]d\beta \qquad (4.15)$$

Eq. (4. 15) is the integral representation of a Bessel function and

$$E_x^t(t, z) \sim \frac{2\omega_1}{\omega_o} \left\{ \frac{(t - \frac{z}{c_o})}{\frac{2z}{c_o}} \right\}^{1/2} J_1 \left\{ \omega_o \left[\frac{2z}{c_o} \left(t - \frac{z}{c_o} \right) \right]^{1/2} \right\} U\left(t - \frac{z}{c_o} \right)$$

$$\left(t - \frac{z}{c_o} << 1 \right) \qquad (4.16)$$

The same expression is obtained for the isotropic case [HASKELL and CASE (1966)] and it works well only just at the wave front where

$$t - \frac{z}{c_o} << 1$$

The wave front is composed by the highest frequency components which do not feel the anisotropy and propagate with a velocity just below the vacuum velocity c_o.

V THE SADDLE-POINT APPROXIMATION

Approximate values of the integrals in (3.11) and (3.12) will be found by means of the saddle-point method or the method of steepest descents. It is an approximate method which relies on the property that the exponential in the integrals varies much more rapidly than the other factors when p is varied.

The exponent in

$$I = \frac{1}{2\pi j} \int_{c-j\infty}^{c+j\infty} \frac{\tilde{T}_{x,+}(p)}{p} \tilde{E}_x^i(p)\, e^{p\left(t - n_+ \frac{z}{c_o}\right)} dp \qquad (5.1)$$

has saddle points where its derivative is zero, that is where

$$\frac{d}{dp}\left[p\left(t - n_+ \frac{z}{c_o}\right)\right] = 0 \qquad (5.2)$$

or

$$\frac{t}{z/c_o} = n_+ + p\frac{dn_+}{dp} = n_+' \qquad (5.3)$$

where n_+' is the group refractive index and

$$n_+ = \sqrt{1 + \frac{\omega_o^2}{p\,(p + j\omega_H)}} \qquad (5.4)$$

Introducing the angular frequency $\omega = -jp$ we obtain from equation (5.3) the instantaneous frequency versus time or the frequency dependence of the group velocity.

We obtain

$$\frac{t}{z/c} = n_+ - \frac{p}{2n_+}\left(\frac{\omega_o}{p}\right)^2 \frac{2p + j\omega_H}{(p + j\omega_H)^2} \qquad (5.5)$$

There are consequently two saddle points, both of which lie on the imaginary axis as there are no collision losses. They are unsymmetrically situated with respect to the real p-axis and move with time along the imaginary axis. At $t = z/c_o$ they are at $\pm j\infty$ and as time proceeds they approach

$$j\left\{-\frac{\omega_H}{2}+\sqrt{\frac{\omega_H^2}{4}+\omega_o^2}\right\} \tag{5.6}$$

and

$$-j\left\{\frac{\omega_H}{2}+\sqrt{\frac{\omega_H^2}{4}+\omega_o^2}\right\} \tag{5.7}$$

respectively. The branch cuts and the saddle-points are shown in figure 5.1.

The saddle points can be found by plotting $\frac{t}{z/c_o}$ against p from (5.5). An example is shown in figure 5.2. For any given t and z/c_o the horisontal line $n_+{}' = \frac{t}{z/c_o}$ is drawn in the diagram. The points where it cuts the curves give the actual p-values of the saddle points.

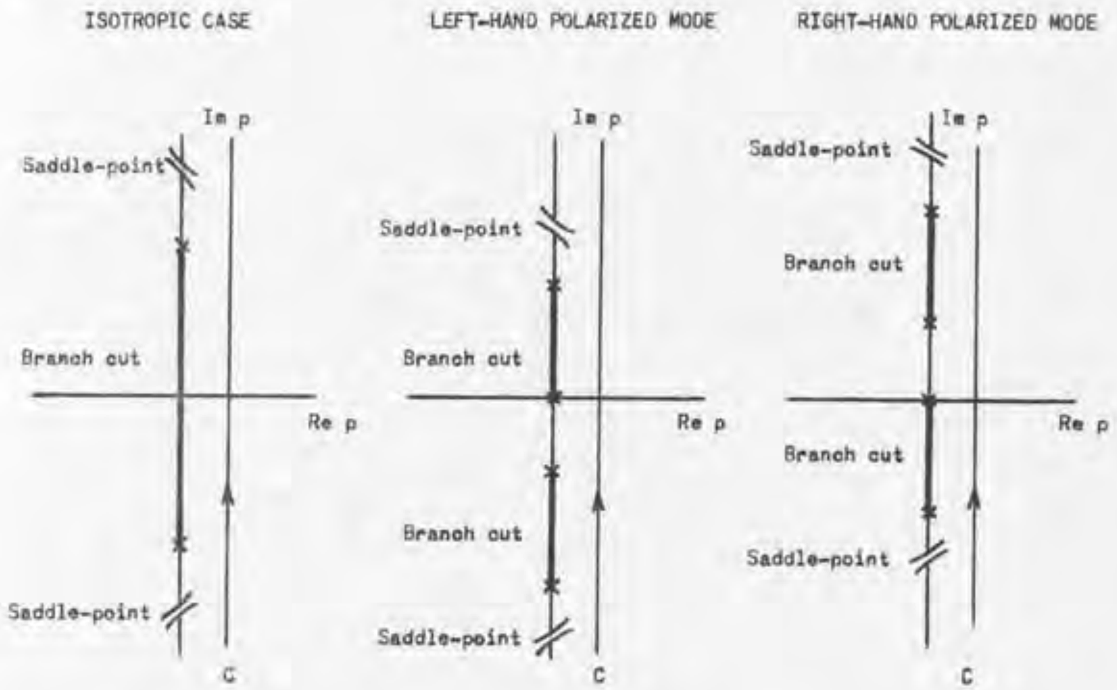

FIGURE 5.1 The branch cuts and the saddle points in the complex p-plane.

We shall now find the contribution to integral (5.1) from a saddle point at $p = p_s$. The exponent in (5.1) is therefore exponded in a Taylor series about p_s

$$p\left(t - n_+ \frac{z}{c_o}\right) = w(p) = w(p_s) + \underbrace{w'(p_s)(p - p_s)}_{=0} + \frac{1}{2} w''(p_s)(p - p_s)^2 + \ldots \tag{5.8}$$

The second term of the Taylor expansion is zero because the first derivative of the exponent w (p) is zero at the saddle point.

We obtain

$$w'' = \frac{d^2}{dp^2}\, w = \frac{d}{dp} \left\{ t - \frac{z}{c_o} \left(n_+ + p \frac{dn_+}{dp} \right) \right\} = - \frac{z}{c_o} \frac{d}{dp} \left\{ n_+ + p \frac{dn_+}{dp} \right\} \quad (5.9)$$

From figure 5.2 we notice that $w''(p_s)$ is imaginary and

$$\begin{aligned} \mathrm{Im}\{w''(p_s)\} &< 0 \quad \text{when} \quad \mathrm{Im}\{p_s\} > 0 \\ \mathrm{Im}\{w''(p_s)\} &> 0 \quad \text{when} \quad \mathrm{Im}\{p_s\} < 0 \end{aligned} \quad (5.10)$$

We obtain from one of the saddle points p_s

$$I_1 = \frac{1}{2\pi j} \int_{C_1} \frac{1}{p}\, \widetilde{T}_{x,+}(p)\, \widetilde{E}^i_x(p)\, e^{w(p_s) + \frac{1}{2} w''(p_s)(p - p_s)^2}\, dp \quad (5.11)$$

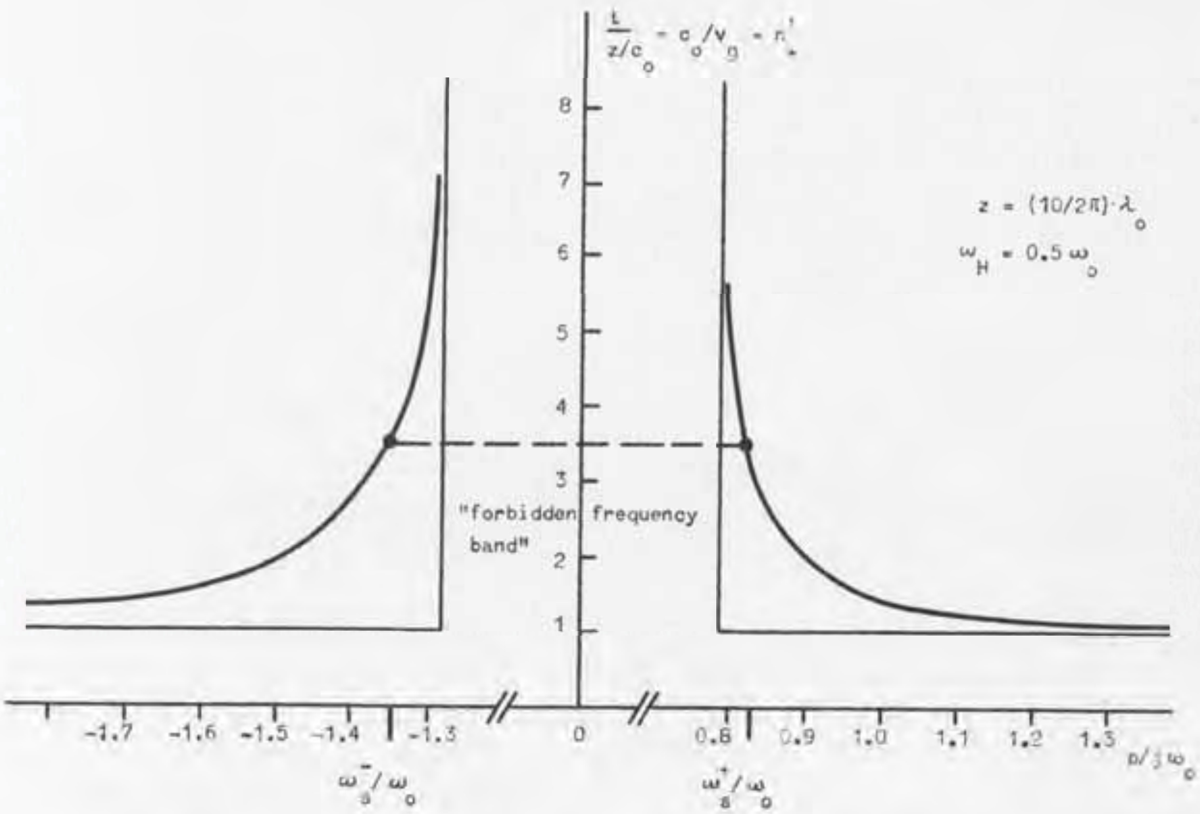

FIGURE 5.2 The dependence of the real group refractive index or the normalized time $\frac{t}{z/c_o}$ upon the situation of the saddle point.

The original contour C is here distorted to run through the saddle point in a direction which makes the second term in w (p) negative or zero. This is the direction of the most rapid change, i.e. the direction of the line of steepest descent through the saddle point.

On the contour let

$$p - p_s = r\, e^{j\alpha} \tag{5.12}$$

Then

$$\alpha = \frac{\pi}{4} \text{ and } \frac{5\pi}{4} \qquad \text{when} \qquad \mathrm{Im}\{p_s\} < 0$$

and

$$\alpha = -\frac{\pi}{4} \text{ and } \frac{3\pi}{4} \qquad \text{when} \qquad \mathrm{Im}\{p_s\} > 0$$

The integration contour is shown in figure 5.3.

Let us first study the general case

$$I = \int_C f(p)\, e^{\frac{1}{2} w''(p_s)(p - p_s)^2}\, dp \tag{5.13}$$

When f (p) is a holomorphic function in the neighborhood of the saddle point it can be expanded in a Taylor series about the saddle point. If f (p) is slowly varying it can be given its value for $p = p_s$ and placed outside the integral.

With

$$p - p_s = r\, e^{j\alpha}$$

the contribution from the saddle point is

$$I \sim f(p_s) \int_{-\infty}^{\infty} e^{-\frac{1}{2} |w''(p_s)| r^2}\, e^{j\alpha}\, dr \tag{5.14}$$

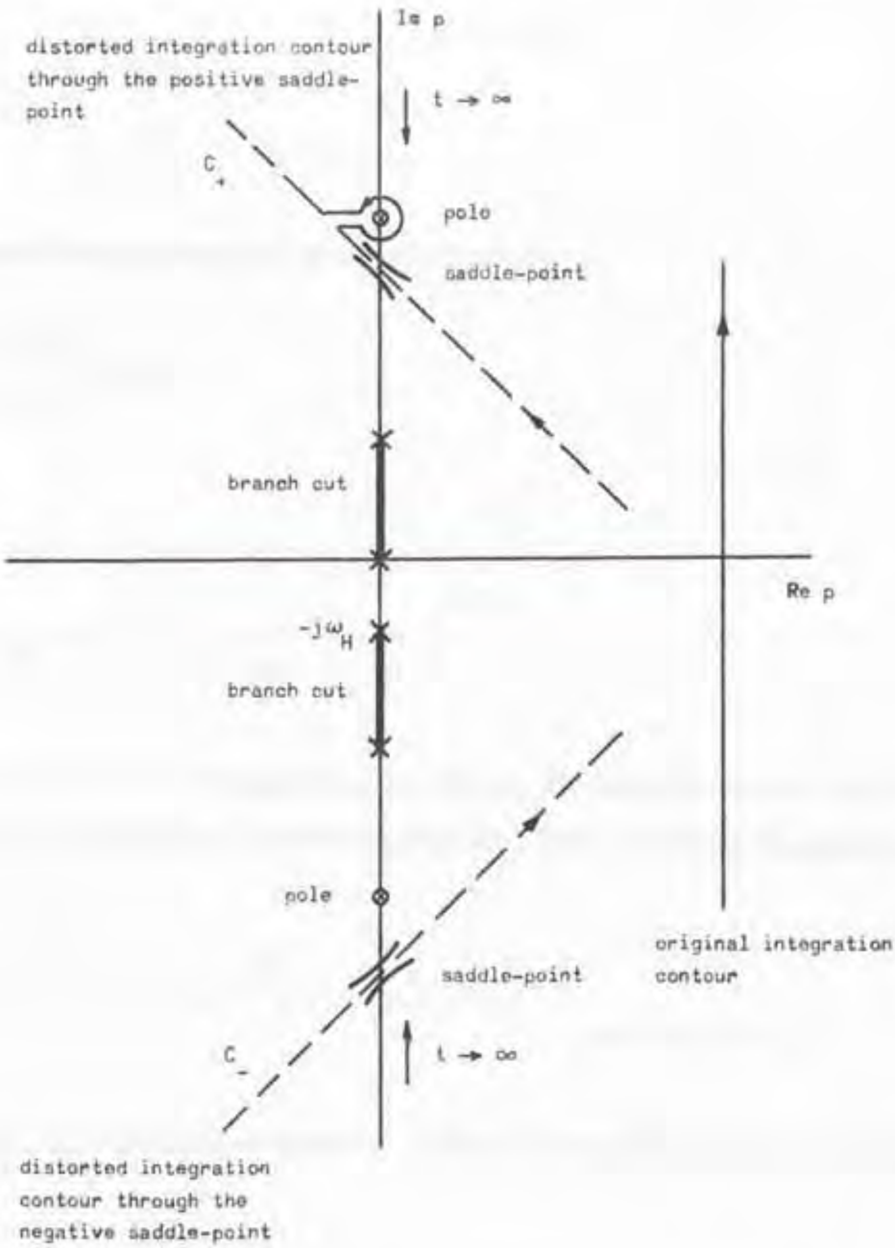

FIGURE 5.3 The integration contours through the saddle-point.

where α is chosen to get the exponent real and < 0.

Since $|w''(p_s)|$ is assumed to be large the integrand decreases rapidly as r departs from zero. The main contribution comes from very near the saddle point, where $r = 0$, and the integral limits may be set as $\pm \infty$ without serious errors.

Now

$$\int_{-\infty}^{\infty} e^{-\frac{1}{2}\,|\,w''(p_s)\,|\,r^2}\, dr \tag{5.15}$$

is a standard definite integral, which has the value

$$\frac{\sqrt{2\pi}}{|\,w''(p_s)\,|^{1/2}} \tag{5.16}$$

and

$$I \sim f(p_s)\, e^{j\alpha} \cdot \left\{ \frac{2\pi}{|\,w''(p_s)\,|} \right\}^{1/2} \tag{5.17}$$

If f (p) in (5.13) is a meromorphic function in the neighborhood of the saddle point we must instead use a Laurent expansion. Then we obtain an integral of the form

$$\int_{-\infty}^{\infty} \frac{e^{-t^2}}{t - z}\, dt = j\pi\, e^{-z^2} \left[1 - \mathrm{erf}(-jz) \right] \qquad (\mathrm{Im}\{z\} > 0) \tag{5.18}$$

where erf (- j z) is the Error function. We shall return to this case in Chapter VII.

VI THE UNIT STEP WAVE RESPONSE.

Let us assume the incident wave to be a unit step wave [eq. (4.1)].

Then

$$E_x^t\ (t, z) = 2\ \mathrm{Re}\left\{ \frac{1}{2\pi j} \int_C \frac{1}{p}\ \widetilde{T}_{x,+}\ (p)\ e^{p\,(t - n_+ \frac{z}{c_o})}\ dp \right\} \qquad (6.1)$$

and

$$E_y^t\ (t, z) = -\ 2\ \mathrm{Im}\left\{ \frac{1}{2\pi j} \int_C \frac{1}{p}\ \widetilde{T}_{x,+}\ (p)\ e^{p\,(t - n_+ \frac{z}{c_o})}\ dp \right\} \qquad (6.2)$$

There are two saddle points $p_s^+ = j\omega_s^+$ and $p_s^- = j\omega_s^-$ ($\omega_s^+ > 0$, $\omega_s^- < 0$) corresponding to the components from the left circularly polarized vector (R = j) and the right circularly polarized vector (R = - j) respectively.

We obtain by means of chapter V [rel. (5.17)]

$$E_x^t\ (t, z) \sim \frac{2\,\widetilde{T}_{x,+}\,(j\omega_s^+)}{\omega_s^+\,[\,2\pi\,|\,w''\,(j\omega_s^+)\,|\,]^{1/2}}\ \cos\left[\,|\,w\,(j\omega_s^+)\,|\ - \frac{\pi}{4}\,\right] +$$

left-hand polarized mode

$$+ \frac{2\,\widetilde{T}_{x,+}\,(j\omega_s^-)}{(-\omega_s^-)\,[\,2\pi\,|\,w''\,(j\omega_s^-)\,|\,]^{1/2}}\ \cos\left[\,|\,w\,(j\omega_s^-)\,|\ - \frac{\pi}{4}\,\right]$$

right-hand polarized mode

(6.3)

where

$$\frac{1}{\widetilde{T}_{x,+}\,(j\omega)} = 1 + \left\{ 1 - \frac{\omega_o^2}{\omega\,(\omega + \omega_H)} \right\}^{1/2} \qquad (6.4)$$

[rel. (3.9)]

From relation (6.3) the corresponding y-component can be written down at once

$$\boxed{\begin{aligned} E_y^t(t,z) \sim -\, & \frac{2\,\widetilde{T}_{x,+}(j\omega_s^+)}{\omega_s^+\left[2\pi\,|w''(j\omega_s^+)|\,\right]^{1/2}} \cos\left[\,|w(j\omega_s^+)| - \frac{3\pi}{4}\,\right] + \\ & + \frac{2\,\widetilde{T}_{x,+}(j\omega_s^-)}{(-\omega_s^-)\ \left[2\pi\,|w''(j\omega_s^-)|\right]^{1/2}} \cos\left[\,|w(j\omega_s^-)| - \frac{3\pi}{4}\,\right] \qquad (6.5) \end{aligned}}$$

When $\omega_H \to 0$ we obtain the result of the isotropic case

$$E_x^t(t,z) \sim \frac{4\,\widetilde{T}_{x,+}(j\omega_s^+)}{\omega_s^+\left[2\pi\ |w''(j\omega_s^+)|\ \right]^{1/2}} \cos\left[\,|w(j\omega_s^+)| - \frac{\pi}{4}\,\right] \qquad (6.6)$$

$$E_y^t(t,z) = 0 \qquad (6.7)$$

since the saddle points ($j\omega_s^+$ and $j\omega_s^-$) are symmetrically situated on the imaginary p-axis at

$$p_s = \pm j\,\frac{\omega_o t}{\sqrt{t^2 - \tau^2}} \qquad (6.8)$$

where

$$\tau = \frac{z}{c_o}$$

Furthermore

$$|w(j\omega_s^+)| = \omega_o \cdot \sqrt{t^2 - \tau^2} \qquad (6.9)$$

$$|w''(j\omega_s^+)| = \frac{(t^2 - \tau^2)^{3/2}}{\omega_o \cdot \tau^2} \qquad (6.10)$$

and consequently from (6.6)

$$E_x^t(t,z) \sim \left\{ \frac{2}{\pi\,\omega_o\,\sqrt{t^2 - \tau^2}} \right\}^{1/2} \frac{2\tau}{t+\tau} \cos\left(\omega_o\,\sqrt{t^2 - \tau^2} - \frac{\pi}{4}\right) \qquad (6.11)$$

in the isotropic case.

This is the first term in the asymptotic expansion of the exact expression for the transmitted wave [RÖNNÄNG, 1966]

$$E_x^t(t, z) = \left\{ J_0 \left[\omega_0 \sqrt{t^2 - \tau^2} \right] + \frac{t-\tau}{t+\tau} J_2 \left[\omega_0 \sqrt{t^2 - \tau^2} \right] \right\} U(t-\tau) \tag{6.12}$$

The range of validity of the saddle-point approximation is delimited to large values of the second derivative of the exponent w. For the isotropic case

$$| w''(j\omega_s^+) | = \frac{(t^2 - \tau^2)^{3/2}}{\omega_0 \tau^2} \tag{6.13}$$

according to eq. (6.10), which implies that the condition

$$| w(j\omega_s^+) | = \omega_0 \sqrt{t^2 - \tau^2} \gg 1 \tag{6.14}$$

must hold. Accordingly, relation (6.11) fails in the immediate vincinity of the initial wavefront.

It is instructive to examine the discrepancy between the true waveform and the saddle-point approximation immediately after the arrival of the wavefront. We have chosen a space point at $z = 10 \lambda_0 / 2\pi$ in the semi-infinite plasma. From figure 6.1 we notice that already after a few oscillations the error $\Delta E_x^t = E^t_{x,\ \text{saddle point}} - E^t_{x,\ \text{true}}$ is small. As a matter of fact

$$\Delta E_x^t \approx - \frac{2t - \frac{7}{4}\tau}{t+\tau} \left\{ \frac{2}{\pi \omega_0^3 (t^2 - \tau^2)^{3/2}} \right\}^{1/2} \sin \left[\omega_0 \sqrt{t^2 - \tau^2} - \frac{\pi}{4} \right] \tag{6.15}$$

Relation (6.15) is the second term in the asymptotic expansion of (6.12).

$E_x^t(t, z)$, $E_y^t(t, z)$ and the individual, circularly polarized modes have been tabulated for $z = 10 \lambda_0 / 2\pi$ and $\omega_H = 0.5\, \omega_0$ by means of a digital computer. The result is shown in figures 6.2 and 6.3. If we choose a fix instantaneous frequency, we notice that the left-hand polarized mode arrives earlier than the right-hand polarized mode. This is evident as the left circular mode is supported by the static magnetic field.

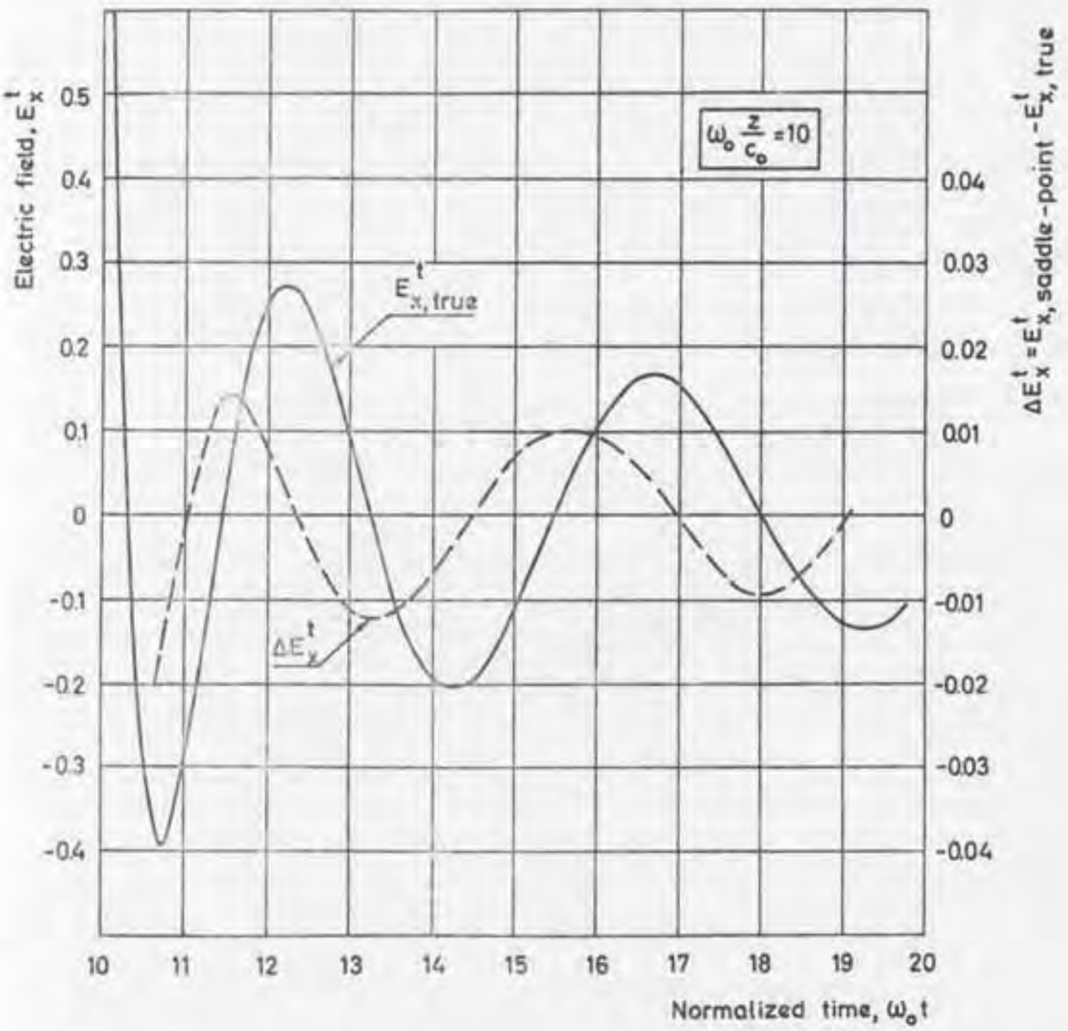

FIGURE 6. 1 The initial oscillations of the transmitted unit step wave response in the isotropic case ($\omega_H = 0$). The continuous curve is obtained from the exact expression and the dashed line depicts the discrepancy $\Delta E^t_x = E^t_{x,\text{ saddle-point}} - \Delta E^t_{x,\text{ true}}$.

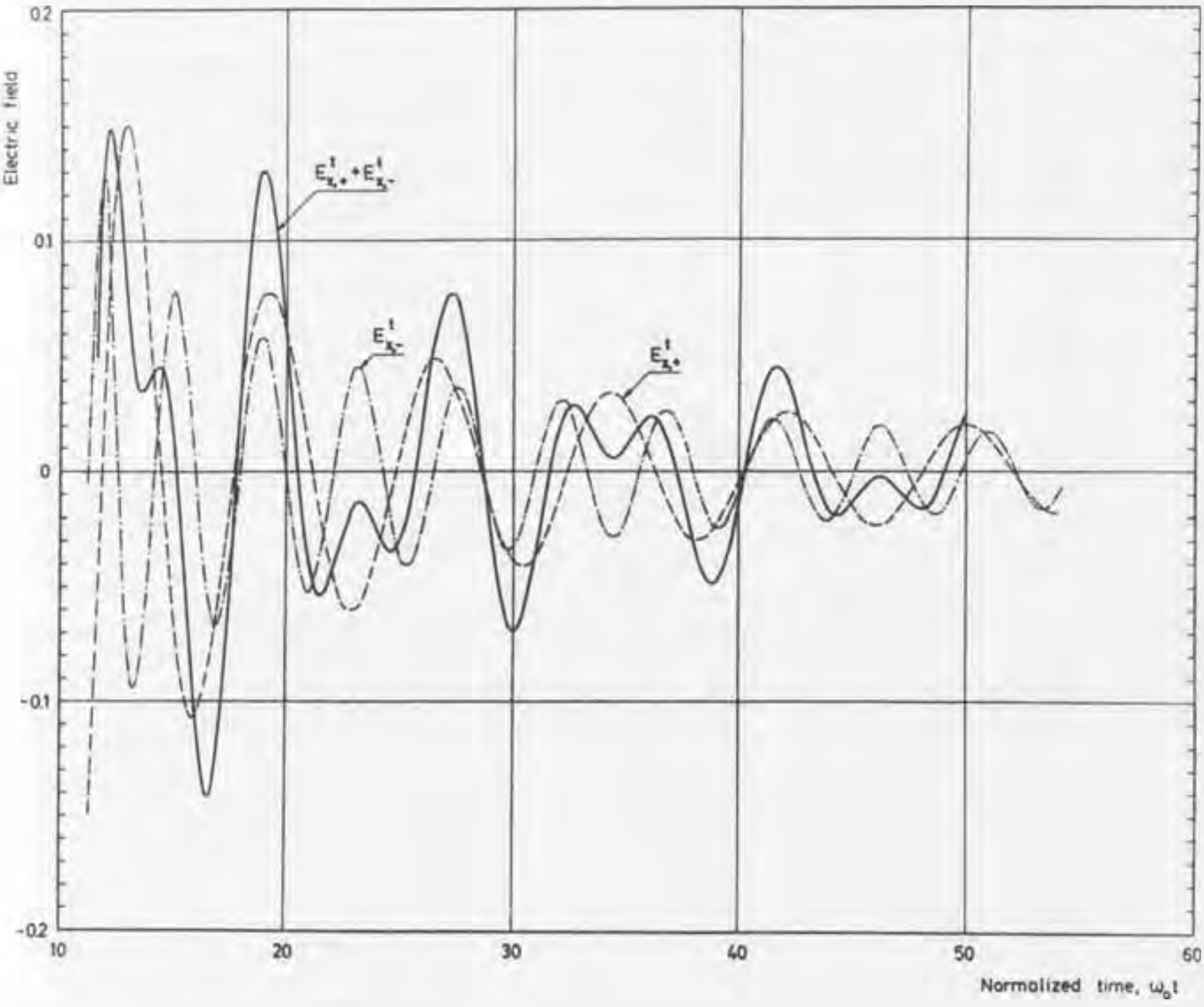

FIGURE 6. 2 The x-components of the total transmitted field and of the individual circularly polarized modes. Gyro frequency $\omega_H = 0.5\,\omega_o$. Observation point $z = 10\,\lambda_o/2\pi$.

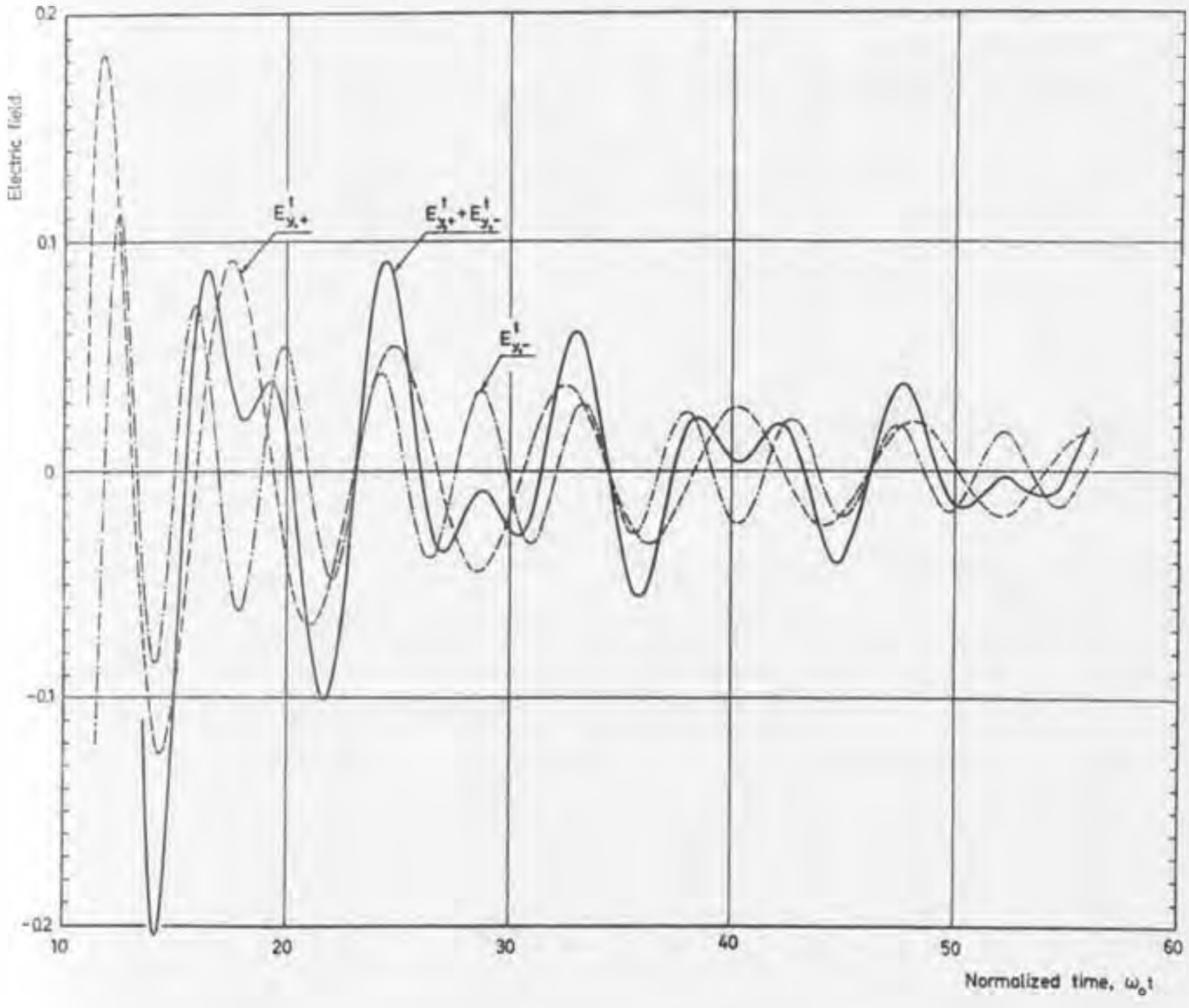

FIGURE 6.3 The y-component of the total transmitted field and of the individual circularly polarized modes. Gyro frequency $\omega_H = 0.5\,\omega_o$. Observation point $z = 10\,\lambda_o / 2\pi$.

VII THE UNIT STEP MODULATED SINE WAVE RESPONSE

When the incident wave is a unit step modulated sine wave (carrier) we obtain from relations (3.11) and (3.12)

$$E_x^t (t, z) = 2 \operatorname{Re} \left\{ \frac{1}{2 \pi j} \int_C \frac{\omega_1}{p^2 + \omega_1^2} \tilde{T}_{x,+} (p) e^{p (t - n_+ \frac{z}{c_0})} dp \right\} \tag{7.1}$$

and

$$E_y^t (t, z) = - 2 \operatorname{Im} \left\{ \frac{1}{2 \pi j} \int_C \frac{\omega_1}{p^2 + \omega_1^2} \tilde{T}_{x,+} (p) e^{p (t - n_+ \frac{z}{c_0})} dp \right\} \tag{7.2}$$

where ω_1 is the angular frequency of the carrier.

Still the integrand has two saddle points situated on the positive and negative imaginary p-axis. However, this case is more complicated as there are two singularities (poles) at $p = j \omega_1$ and $p = - j \omega_1$.

Let us therefore divide the integration contour C into two parts C_+ and C_- corresponding to C in the upper and lower half p-plane (see figure 5.3). As a matter of fact, this is the left-hand polarized mode and the right-hand polarized mode respectively. We choose to study the left-hand polarized component.

The x-component of the left-hand polarized wave.

Due to the circular polarization it is necessary only to study for instance the x-component of the left-hand polarized mode. Then the y-component can easily be obtained. Its phase is 90° displaced.

The contribution to $E_x^t (t, z)$ when we integrate along C_+ can be written

$$\left\{ E_x^t (t, z) \right\}_+ \sim 2 \operatorname{Re} \left\{ \frac{1}{2 \pi j} \int_{C_+} \frac{\omega_1}{p^2 + \omega_1^2} \tilde{T}_{x,+} (p) e^{p (t - n_+ \frac{z}{c_0})} dp \right\} \tag{7.3}$$

In solving (7.3) we must take into account three different cases corresponding to different time regions, viz.

$\omega_s^+ > \omega_1$, giving the precursor,

$\omega_s^+ \approx \omega_1$, giving the time-delayed signal build-up,

and

$\omega_s^+ < \omega_1$, giving the posterior transient solution.

The three integration contours and the resulting field versus time are sketched in figure 7. 1.

The precursor ($\omega_s^+ > \omega_1$).

By means of the unit step wave response (6. 3) we at once obtain

$$\left\{ E_x^t\ (t, z) \right\}_+ \sim \frac{2\,\omega_1\, \widetilde{T}_{x,+}(j\,\omega_s^-)}{(\omega_1^2 - \omega_s^{+\,2})\,[\, 2\pi\, |w''(j\,\omega_s^+)|\,]^{1/2}} \cos [\, |w\,(j\,\omega_s^+)| + \frac{\pi}{4}\,] \tag{7.4}$$

The result is valid as long as the amplitude

$$\left| \frac{2\,\omega_1\, \widetilde{T}_{x,+}(j\,\omega_s^+)}{(\omega_1^2 - \omega_s^{+\,2})\,[\, 2\pi\, |w''\ (j\,\omega_s^+)|\,]^{1/2}} \right| \ll 1$$

The transient precursor takes infinite values when $c_o t - z = 0$ and when $\omega_s^+ = \omega_1$, i. e. $v_g\ (\omega_1)\cdot t = z$, which correspond to the front of the precursor and the front of the main signal, respectively. Thus in the neighbourhood of these sections the asymptotic form (7. 4) becomes invalid. Near the front of the main signal the pole at $p = j\,\omega_1$ and the saddle point at $p = j\,\omega_s^+$ are close to one another and (7. 4) tends infinity. See figure 8. 1.

The main signal build-up.

At the moment when the path of integration, i. e. the saddle point, reaches the pole at $j\,\omega_1$, the intensity of the oscillation increases rapidly. Previously, it was very small [see eq. (7. 4)] and it now gets the magnitude of the final intensity. This moment defines the signal arrival and permits one to define a signal velocity [BRILLOUIN (1914)]. From (5. 3) we notice that the signal velocity normally is equal to the group velocity.

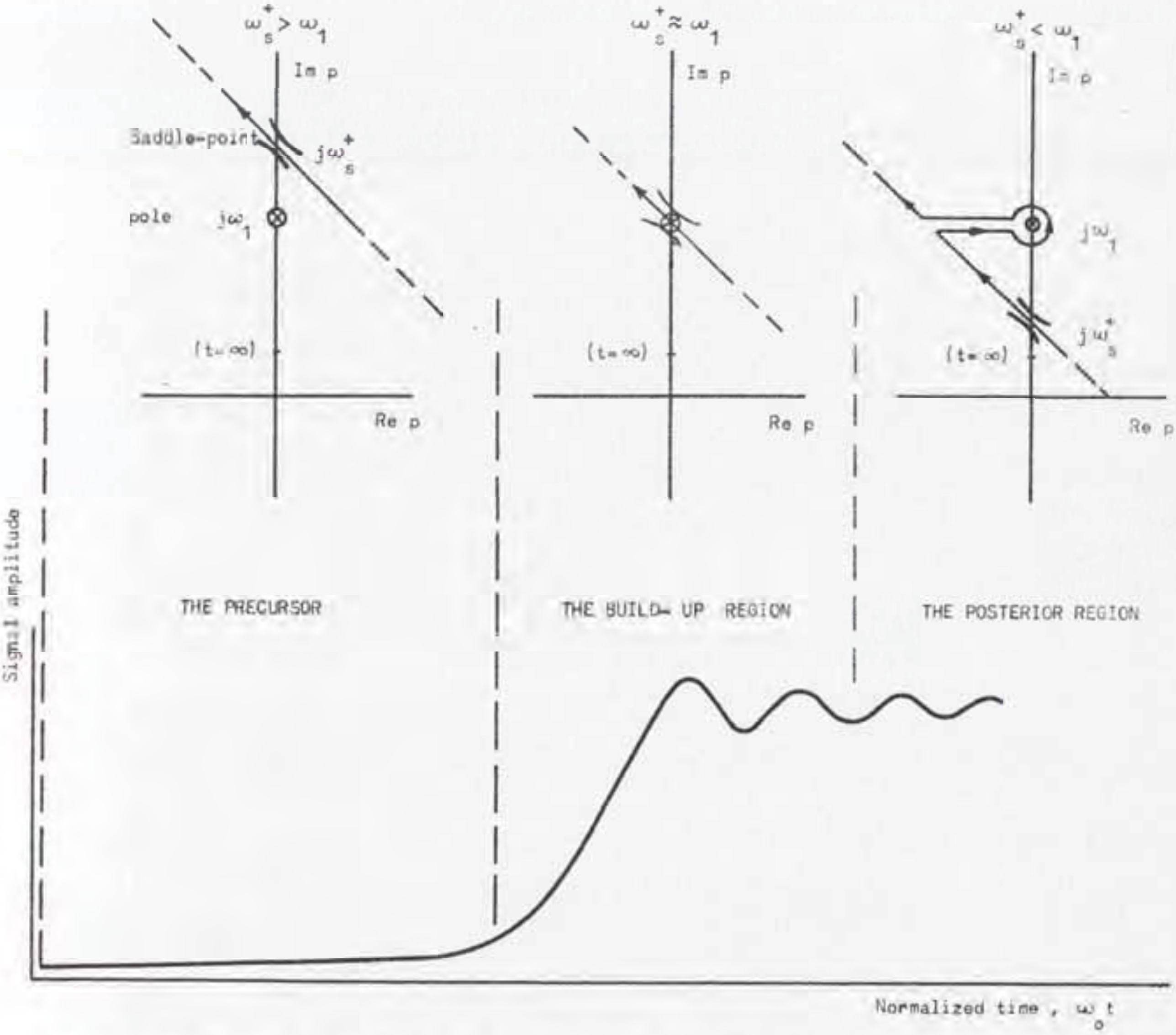

FIGURE 7.1 The position of the saddle-point and the corresponding region of the signal envelope. When $\omega_s^+ > \omega_1$ one obtains the precursor, $\omega_s^+ \approx \omega_1$ corresponds to the build-up region and the posterior is obtained when

$$\omega_1 > \omega_s^+ > -\frac{\omega_H}{2} + \sqrt{\frac{\omega_H^2}{4} + \omega_o^2} \quad .$$

Now we can write

$$\left\{ E_x^t\,(t, z) \right\}_+ \sim \mathrm{Re} \left\{ \frac{1}{2\pi} \int_{C_+} \underbrace{\frac{1}{p + j\omega_1}\, \widetilde{T}_{x,+}(p)\, e^{p\,(t - n_+ \frac{z}{c_o})}}_{I_{+,1}}\, dp \right\} -$$

$$- \mathrm{Re} \left\{ \frac{1}{2\pi} \int_{C_+} \underbrace{\frac{1}{p - j\omega_1}\, \widetilde{T}_{x,+}(p)\, e^{p\,(t - n_+ \frac{z}{c_o})}}_{I_{+,2}}\, dp \right\}$$

(7.5)

The integrand of the first integral ($I_{+,1}$) is analytic over the range of integration and we at once obtain from relation (6. 3)

$$I_{+,1} \sim \frac{\widetilde{T}_{x,+}(j\omega_s^+)}{(\omega_s^+ + \omega_1)\,[\,2\pi |w''(j\omega_s^+)|\,]^{1/2}} \cos\left[\,|w(j\omega_s^+)| + \frac{\pi}{4}\,\right] \tag{7. 6}$$

If we as before approximate the integration contour C_+ in the second integral in (7. 5) by a straight line we obtain

$$I_{+,2} \sim -\mathrm{Re}\left\{ \frac{1}{2\pi} \int_{-\infty}^{\infty} \frac{\widetilde{T}_{x,+}(j\omega_s^+)}{R + je^{-j3\pi/4}(\omega_s^+ - \omega_1)}\, e^{w(j\omega_s^+) + \frac{1}{2} w''(j\omega_s^+)\, e^{j3\pi/2} R^2}\, dR \right\} \tag{7. 7}$$

From relation (5. 18) eq. (7. 7) can be written when $\omega_s^+ > \omega_1$ as

$$I_{+,2} \sim \frac{\widetilde{T}_{x,+}(j\omega_s^+)}{2}\, \mathrm{Re}\left\{ e^{j\left\{|w(j\omega_s^+)| - \frac{\pi}{2} + \frac{1}{2}|w''(j\omega_s^+)|\cdot(\omega_s^+ - \omega_1)^2\right\}} \cdot \right.$$

$$\left. \cdot \left[\, 1 - \mathrm{erf}\left(\sqrt{\tfrac{1}{2}|w''(j\omega_s^+)|}\, (\omega_s^+ - \omega_1)\, e^{j\pi/4} \right) \right] \right\} \tag{7. 8}$$

$$(\omega_s^+ > \omega_1)$$

where

$$\mathrm{erf}\left(a\, e^{j\frac{\pi}{4}}\right) = \sqrt{2}\, e^{j\frac{\pi}{4}} \left\{ C\left(\sqrt{\tfrac{2}{\pi}}\, a\right) - j\, S\left(\sqrt{\tfrac{2}{\pi}}\, a\right) \right\}$$

C and S are the Fresnel cosine and the Fresnel sine integrals.

Introducing

$$\alpha = \sqrt{\frac{1}{\pi}\, |w''(j\omega_s^+)|}\, (\omega_1 - \omega_s^+) \tag{7. 9}$$

we obtain by relations (7.6) and (7.8)

$$\left\{E_x^t(t,z)\right\}_+ \sim \frac{\tilde{T}_{x,+}(j\omega_s^+)}{2}\left\{\left[1+C(\alpha)+S(\alpha)\right]\sin\gamma + \right.$$

$$\left. +\left[C(\alpha)-S(\alpha)\right]\cos\gamma\right\} +$$

$$+\frac{\tilde{T}_{x,+}(j\omega_s^+)}{\left[2\pi|w''(j\omega_s^+)|\right]^{1/2}(\omega_s^+ + \omega_1)}\cos\left[|w(j\omega_s^+)| + \frac{\pi}{4}\right]$$

$$(\omega_s^+ > \omega_1) \qquad (7.10)$$

where

$$\gamma = |w(j\omega_s^+)| + \frac{1}{2}|w''(j\omega_s^+)|\cdot(\omega_1 - \omega_s^+)^2 \qquad (7.11)$$

When $\omega_s^+ < \omega_1$ we must take into account the contribution from the pole at $p = j\omega_1$. The integration contour is shown in figure 7. 1.

We obtain

$$\left\{E_x^t(t,z)\right\}_+ \sim \tilde{T}_{x,+}(j\omega_1)\sin\left[|w(j\omega_1)|\right] -$$

$$-\frac{\tilde{T}_{x,+}(j\omega_s^+)}{2}\left\{\left[1-C(\alpha)-S(\alpha)\right]\sin\gamma - \right.$$

$$\left. -\left[C(\alpha)-S(\alpha)\right]\cos\gamma\right\} +$$

$$+\frac{\tilde{T}_{x,+}(j\omega_s^+)}{\left[2\pi|w''(j\omega_s^+)|\right]^{1/2}(\omega_s^+ + \omega_1)}\cos\left[|w(j\omega_s^+)| + \frac{\pi}{4}\right]$$

$$(\omega_s^+ < \omega_1) \qquad (7.12)$$

When

$$\frac{1}{2}|w''(j\omega_s^+)|\cdot(\omega_1 - \omega_s^+)^2 \ll |w(j\omega_s^+)| \qquad (7.13)$$

i. e.

$$\omega_s^+ \approx \omega_1$$

relations (7.10) and (7.12) give

$$\{E_x^t(t,z)\}_+ \sim \frac{1}{\sqrt{2}}\,\widetilde{T}_{x,+}(j\omega_1)\Big[\Big\{[\tfrac{1}{2}+C(\alpha)]^2+[\tfrac{1}{2}+S(\alpha)]^2\Big\}^{1/2}$$

$$\sin\Big\{|w(j\omega_s^+)| + \arctan\frac{C(\alpha)-S(\alpha)}{1+C(\alpha)+S(\alpha)}\Big\}\Big] +$$

$$+\frac{\widetilde{T}_{x,+}(j\omega_1)}{2\omega_1[2\pi|w''(j\omega_1)|]^{1/2}}\cos[\,|w(j\omega_s^+)|+\tfrac{\pi}{4}]$$

$$(\omega_s^+ \gtrless \omega_1) \qquad (7.14)$$

The first term in (7.14) is the well-known Fresnel diffraction pattern. The second term is normally a small correction since $|w''(j\omega_1)| >> 1$.

<u>The posterior region.</u>

When $\omega_s^+ > \omega_1$ we obtain

$$\{E_x^t(t,z)\}_+ \sim \frac{2\omega_1\widetilde{T}_{x,+}(j\omega_s^+)}{(\omega_1^2-\omega_s^{+2})[2\pi|w''(j\omega_s^+)|]^{1/2}}\cos[\,|w(j\omega_s^+)|+\tfrac{\pi}{4}]+$$

$$+\underbrace{\widetilde{T}_{x,+}(j\omega_1)\sin[\,|w(j\omega_1)|\,]}_{\text{The stationary solution}} \qquad (7.15)$$

- ooo -

Let us examine the boundary between the signal build-up region and the posterior region. Do they overlap each other? For large values of

$$\alpha = \sqrt{\frac{1}{\pi}|w''(j\omega_s^+)|}\,(\omega_1-\omega_s^+) \qquad (7.16)$$

we obtain

$$\left.\begin{aligned} C(\alpha) &\approx \frac{1}{2}+\frac{1}{\pi\alpha}\sin(\tfrac{1}{2}\pi\alpha^2)\\ S(\alpha) &\approx \frac{1}{2}-\frac{1}{\pi\alpha}\cos(\tfrac{1}{2}\pi\alpha^2)\end{aligned}\right\}(\alpha \gg 1) \qquad (7.17)$$

By expansion of sin γ and cos γ in relation (7.12) where

$$\gamma = | w (j \omega_s^+) | + \frac{1}{2} \pi \alpha^2 \tag{7.18}$$

$\{E_x^t (t, z)\}_+$ in the build-up region, eq. (7.12), becomes

$$\{E_x^t(t, z)\}_+ \sim \widetilde{T}_{x, +}(j \omega_1) \sin [| w (j \omega_1) |] + \\ + \frac{2 \omega_1 \widetilde{T}_{x, +} (j \omega_s^+)}{(\omega_1^2 - \omega_s^{+2}) [2 \pi | w'' (j \omega_s^+) |]^{1/2}} \cos [| w (j \omega_s^+) | + \frac{\pi}{4}] \\ (\alpha \gg 1) \tag{7.19}$$

This is the same expression as (7.15), i. e. the build-up region and the posterior region overlap each other. In the same way we obtain an overlaping region at the boundary between the precursor and the build-up signal.

- ooo -

Let us at last sum up our results.

An incident unit step modulated sine wave, plane-polarized in the x-direction,

$$E_x (t, z) = \sin [\omega_1 (t - \frac{z}{c_o})] U (t - \frac{z}{c_o})$$

gives rize to two transmitted signals, a left-hand circularly polarized wave and a right-hand circularly polarized wave.

The x-component of the left-hand polarized signal after it has propagate a distance z in the anisotropic medium can be written

$$\{ E_x^t(t, z)\}_+ \sim \frac{\widetilde{T}_{x, +} (j \omega_s^+)}{2} \{[1 + C (\alpha) + S (\alpha)] \sin \gamma + \\ + [C (\alpha) - S (\alpha)] \cos \gamma \} + \\ + \frac{\widetilde{T}_{x, +} (j \omega_s^+)}{[2\pi | w'' (j \omega_s^+) |]^{1/2} (\omega_s^+ + \omega_1)} \cos [| w (j \omega_s^+) | + \frac{\pi}{4}] \tag{7.20}$$

when $\omega_s^+ > \omega_1$, i.e. $t < \frac{z}{v_g(\omega_1)}$,

and

$$\left\{ E_x^t(t,z) \right\}_+ \sim \widetilde{T}_{x,+}(j\omega_1)\sin[|w(j\omega_1)|] - \\ - \frac{\widetilde{T}_{x,+}(j\omega_s^+)}{2}\left\{ [1 - C(\alpha) - S(\alpha)]\sin\gamma - \right. \\ \left. - [C(\alpha) - S(\alpha)]\cos\gamma \right\} + \\ + \frac{\widetilde{T}_{x,+}(j\omega_s^+)}{[2\pi|w''(j\omega_s^+)|]^{1/2}(\omega_s^+ + \omega_1)}\cos[|w(j\omega_s^+)| + \frac{\pi}{4}] \tag{7.21}$$

when $\omega_s^+ < \omega_1$, i.e. $t > \frac{z}{v_g(\omega_1)}$,

where

$$\gamma = |w(j\omega_s^+)| + \frac{1}{2}|w''(j\omega_s^+)|(\omega_1 - \omega_s^+)^2$$

$$\alpha = \sqrt{\frac{1}{\pi}|w''(j\omega_s^+)|}\,(\omega_1 - \omega_s^+)$$

$$w = p\left(t - n_+\frac{z}{c_o}\right)$$

$$\widetilde{T}_{x,+}(j\omega_s^+) = \frac{1}{1 + \sqrt{1 - \frac{\omega_o^2}{\omega_s^+(\omega_s^+ + \omega_H)}}}$$

From the x-component of the left-hand polarized field the corresponding right-hand polarized mode and the y-components can be obtained. The right-hand polarized wave in the x-direction by the substitution $\omega_H \to -\omega_H$ and the y-components by phase displacement 90^o.

The range of validity of (7.20) and (7.21) is determined by the condition

$|w''(j\omega_s)| \gg 1$ (see figure 5.2) which eliminates the immediate vincinity of the wavefront ($t = \frac{z}{c_o}$).

VIII NUMERICAL RESULTS.

By means of the approximate expressions (7. 20) and (7. 21) we have determined the distorted signal envelope by means of a digital computer SAAB - D 21. The unit step modulated sine wave response as well as the rectangular pulse-carrier response have been calculated. The medium is assumed to be isotropic ($\omega_H = 0$) or anisotropic ($\omega_H \neq 0$). In most cases we omit the transmission factor at the boundary $z = 0$, i. e. we assume that the medium is infinite.

1. The isotropic case.

Let us first look at the unit step modulated sine wave response. The transmitted signals at two carrier frequencies are studied.

Carrier frequency $\omega_1 = 1.1\, \omega_o$. The resulting signal envelope is shown at two different points $z = 10\, \lambda_o$ and $z = 100\, \lambda_o$. At the longer propagation path the Sommerfeld precursor [eq. (4. 16)] is inserted. Futhermore the transmitted field at a semi-infinite layer is drawn. The total transmission factor is of course larger than 1 since $n_+ < 1$. n_+ is determined by the instantaneous frequency, i. e. by the saddle-point value.

It is interesting to compare the obtained curves with the Fresnel diffraction pattern — the classical result, which is obtained if one uses a simplified stationary phase principle (Taylor expansion about $\omega = \omega_1$). In figure 8. 2 we notice that the curves agree only at the steepest portion of the leading edge. The approximate signal envelope obtained by the saddle-point method oscillates more slowly, a result which earlier has been pointed out by the author [RÖNNÄNG (1966)]. From relation (7. 15) we notice that the oscillation frequency of the envelope goes to ($\omega_1 - \omega_o$) and not to infinity which is the case for the Fresnel wriggles. As a matter of fact, the modulation is created by inteference between the strong carrier with frequency ω_1 and the delayed components with lower frequencies. The lowest frequency is equal to ω_o, the group velocity of which is zero.

Carrier frequency $\omega_1 = 1.05\, \omega_o$. As the carrier frequency approaches the plasma frequency the envelope is more dispersed and the front of the signal is more delayed. See figure 8. 1. The dashed curves are the precursor and the posterior obtained by the simple expressions (7. 4) and (7. 15). They agree very well with the complicated results (7. 20) and (7. 21) from which the continuous curve has been computed.

If we know the envelope and the phase of the distorted unit step modulated carrier it is possible to determine the pulse-carrier response.

The rectangular pulse-carrier can be written

$$E_x^i(t, z) = \sin\left[\omega_1\left(t - \frac{z}{c_o}\right)\right] U\left(t - \frac{z}{c_o}\right) - \sin\left[\omega_1\left(t - T - \frac{z}{c_o}\right)\right] U\left(t - T - \frac{z}{c_o}\right) \tag{8.1}$$

where T is the pulse duration.

If we assume that $\omega_1 \cdot T = n \cdot 2\pi$ ($n = 1, 2, 3, \ldots\ldots$), i. e. the pulse contains a whole number of wavelengths,

$$E_x^i(t, z) = \sin\left[\omega_1\left(t - \frac{z}{c_o}\right)\right]\left[U\left(t - \frac{z}{c_o}\right) - U\left(t - T - \frac{z}{c_o}\right)\right] \tag{8.2}$$

In figure 8. 3, 8. 4 and 8. 5, which show the distorted pulse at $z = 100\,\lambda_o$ for $\omega_1 = 1.1\,\omega_o$ and $\omega_1 = 1.05\,\omega_o$, $\omega_o \cdot T$ is equal to $100\,\pi$ (figure 8. 3) and $200\,\pi$. At a plasma frequency f_o of for instance 5 MHz these values of $\omega_o \cdot T$ correspond to $T = 10\,\mu s$ and $T = 20\,\mu s$ respectively.

The rapid oscillations at the signal build-up region are caused by interference with the high frequency components arised from the abrupt termation of the pulse. They start T seconds after the arrival of the wavefront. However, their amplitude is so small that it is still possible to put the pulse velocity equal to the group velocity. In figures 8. 3, 8. 4 and 8. 5 we have inserted the delayed original pulse, which arrives at $t = z / v_g$.

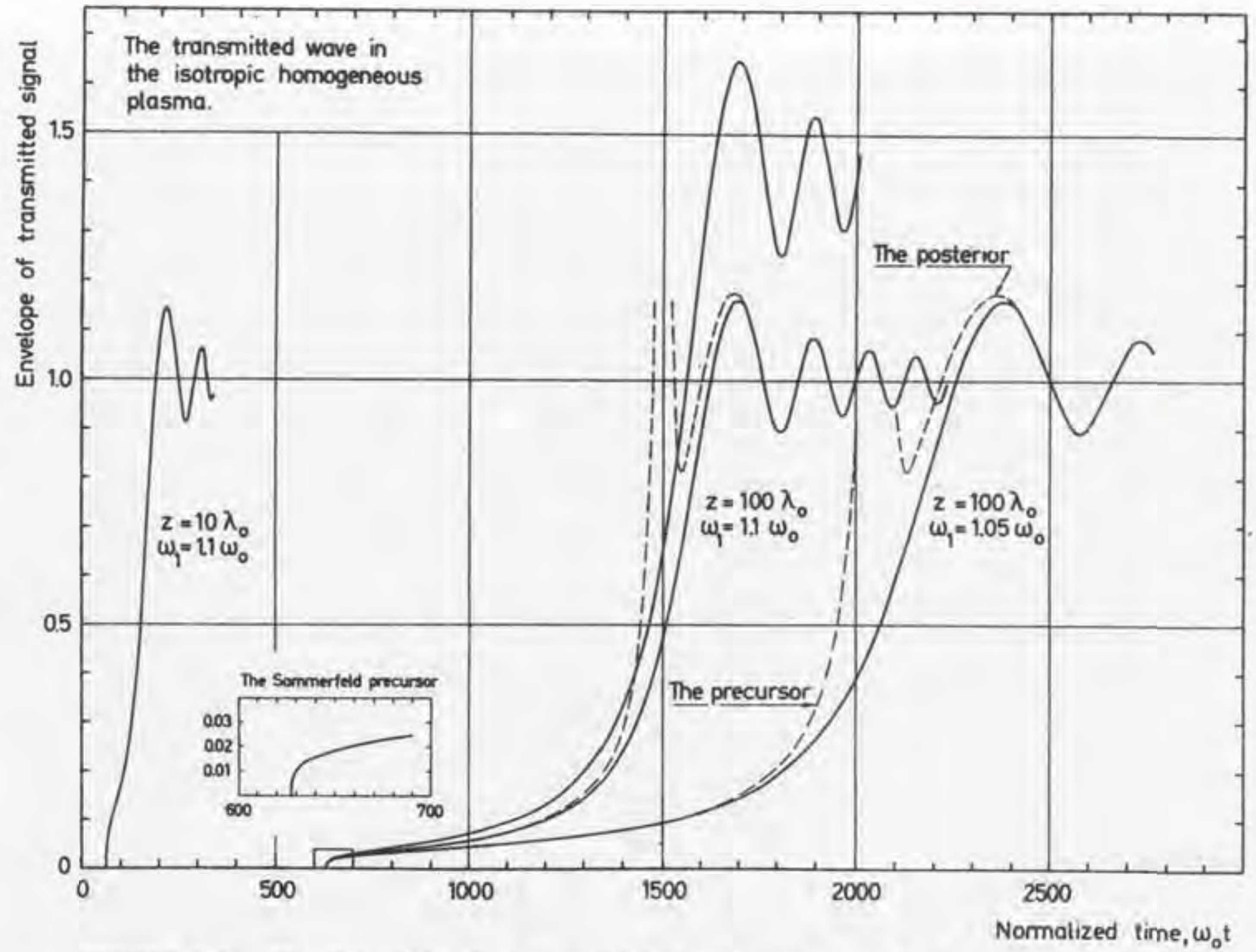

FIGURE 8.1 The distorted unit step modulated carrier observed at $z = 10\,\lambda_o$ and $z = 100\,\lambda_o$. The ionized medium is isotropic, i.e. $\omega_H = 0$. Carrier frequency $\omega_1 = 1.1\,\omega_o$ and $1.05\,\omega_o$.

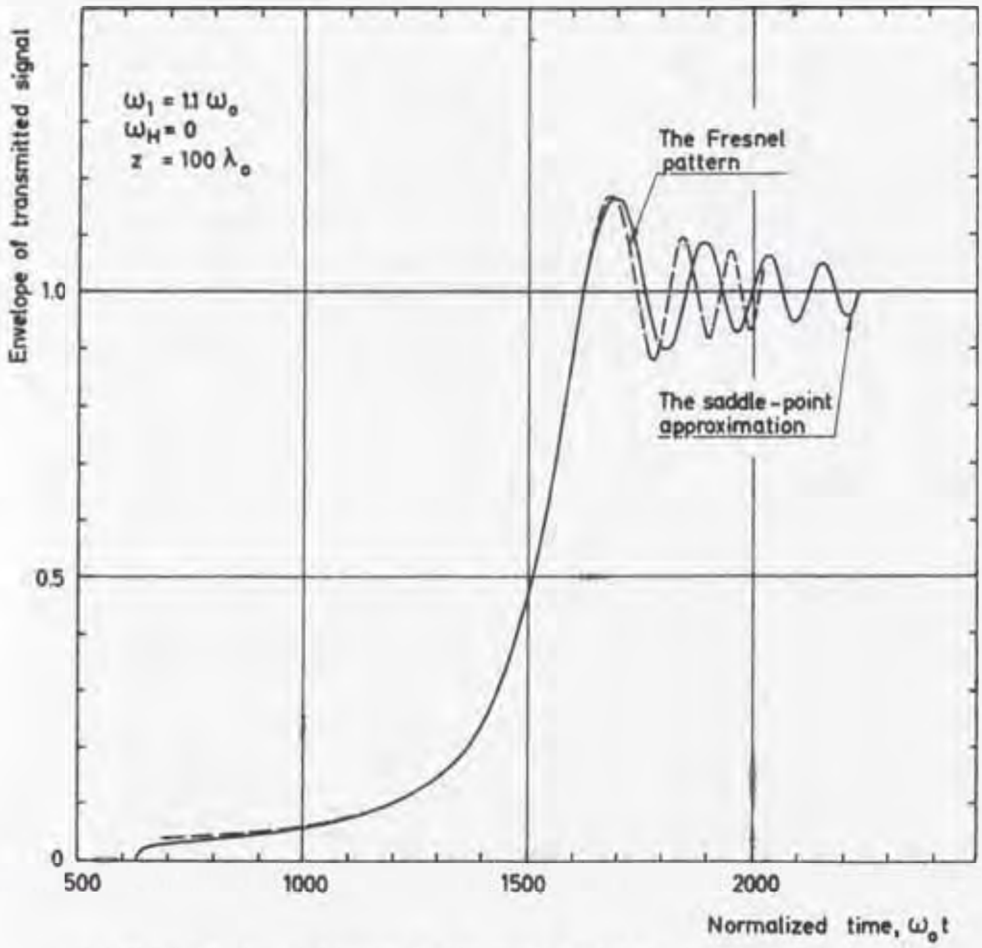

FIGURE 8.2 The unit step modulated sine wave response - obtained by the saddle-point method - compared with the classical Fresnel pattern.

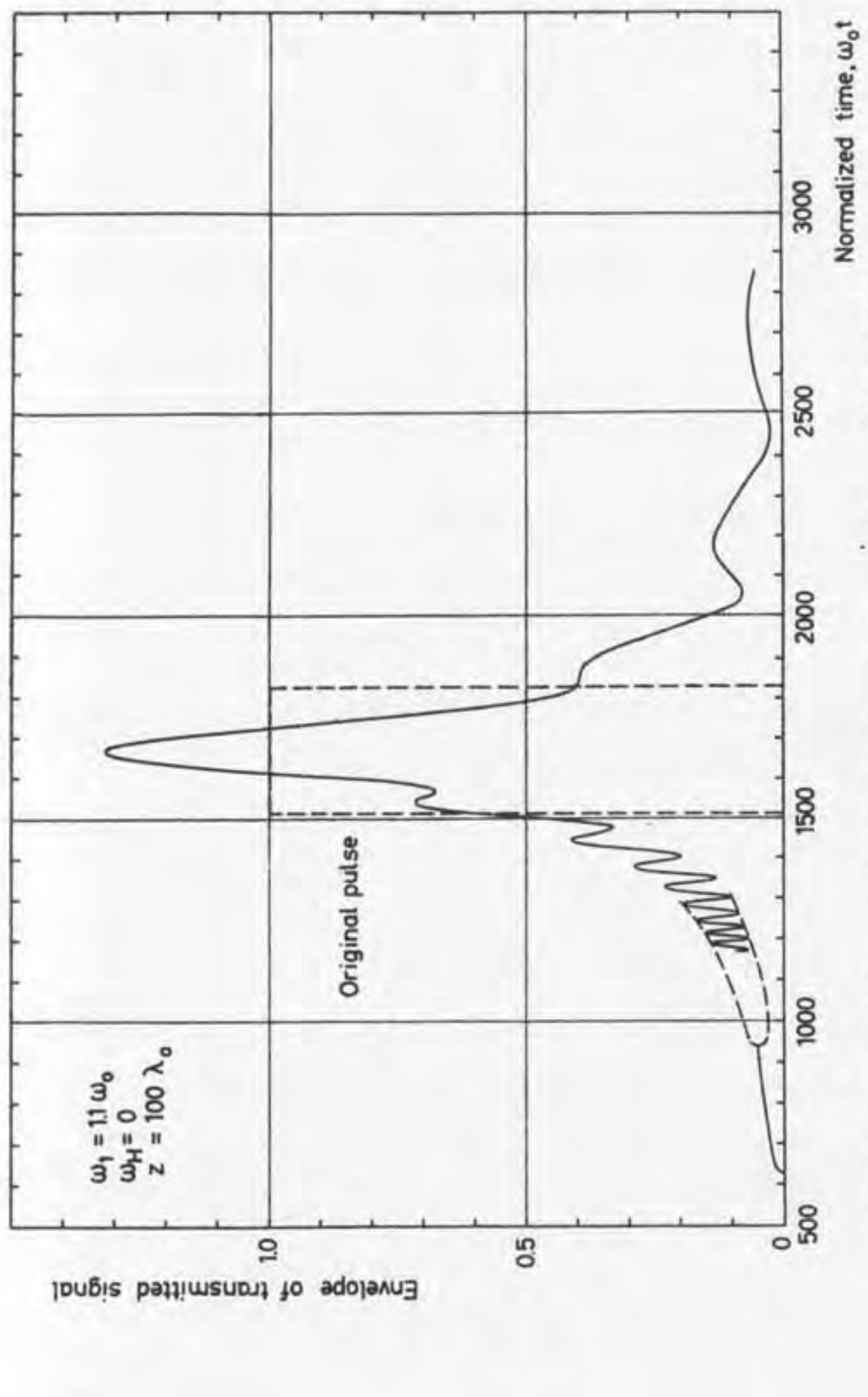

FIGURE 8.3 The transmitted pulse-carrier at $z = 100\,\lambda_o$. Pulse duration $T = 100\,\pi/\omega_o$. Carrier frequency $\omega_1 = 1.1\,\omega_o$.

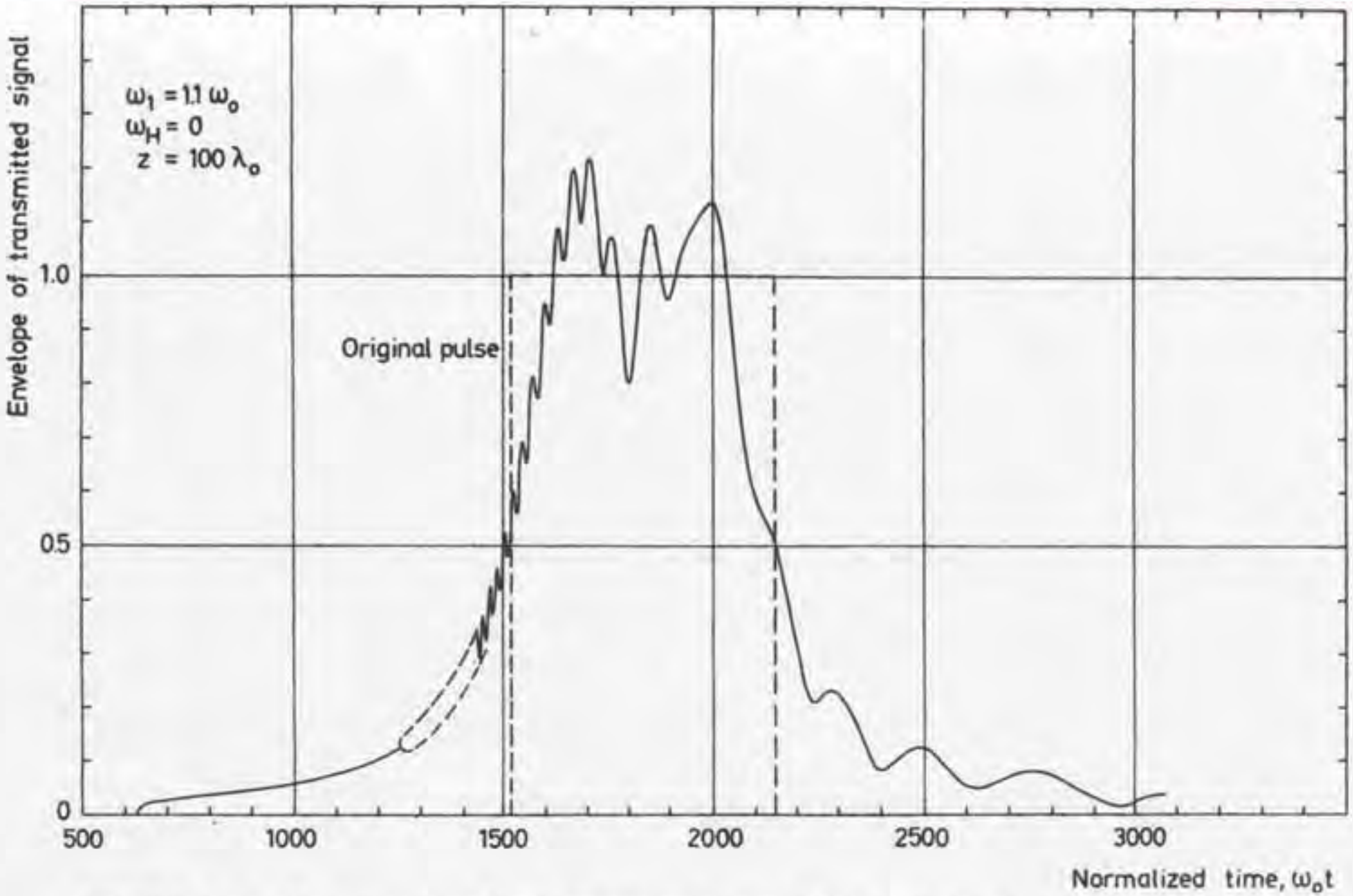

FIGURE 8.4 The transmitted pulse-carrier at $z = 100\,\lambda_o$. Pulse duration $T = 200\,\pi/\omega_o$. Carrier frequency $\omega_1 = 1.1\,\omega_o$.

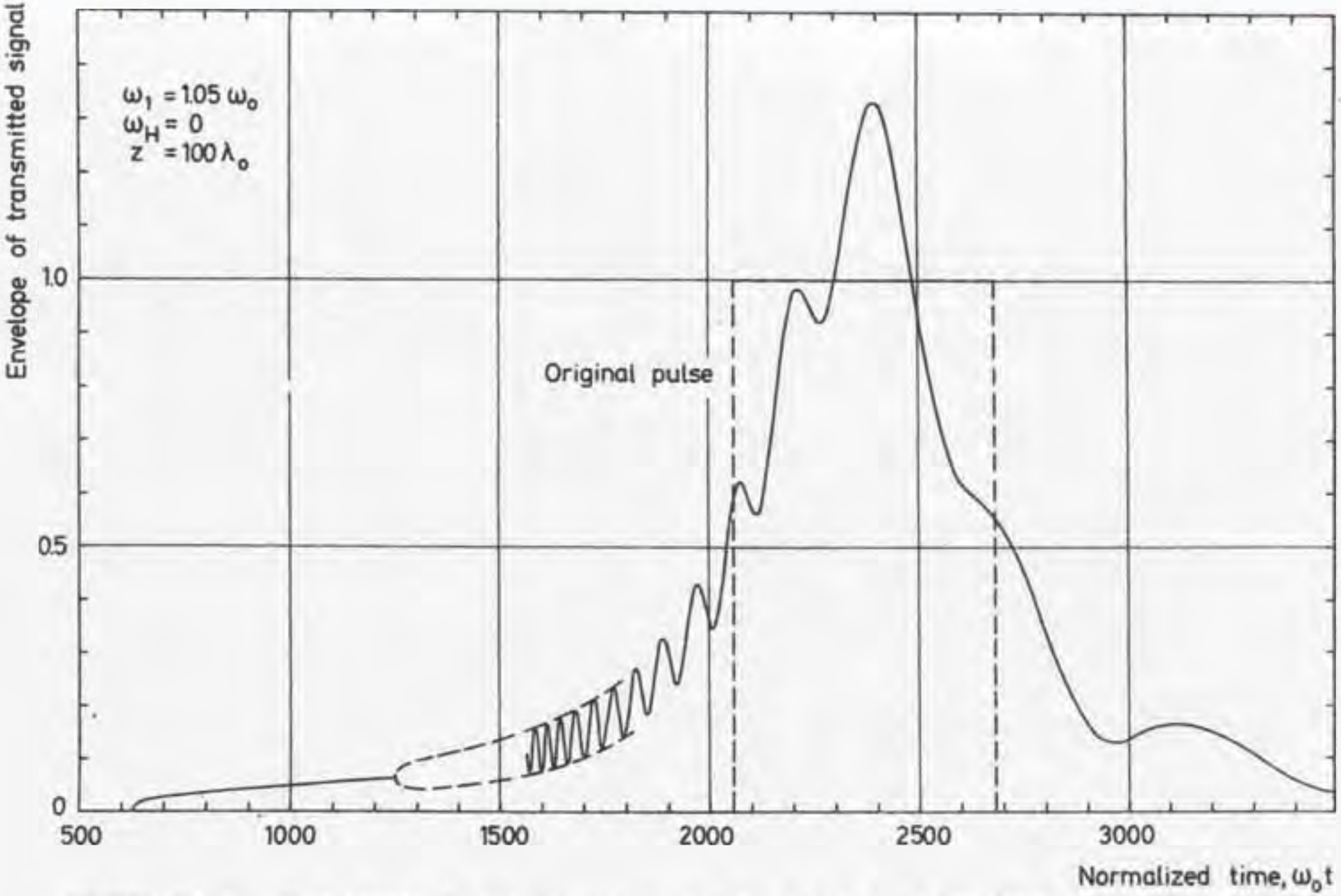

FIGURE 8.5 The transmitted pulse-carrier at $z = 100\ \lambda_o$. Pulse duration $T = 200\ \pi/\omega_o$. Carrier frequency $\omega_1 = 1.05\ \omega_o$.

2. The anisotropic case.

If we introduce a longitudinal external magnetic field the incident linearly polarized signal $E_x^i(t, z)$ is split up into two circularly polarized modes. Accordingly, we obtain a resulting component in the y-direction, too. The two modes propagate with different propagation constants and arrive at the observation point z at different times. Figures 8. 6 and 8. 7 show the x- and y-components of the transmitted unit step modulated sine wave. The following notations on the curves have been used:

1.	The total field for an infinite layer, i. e. there is no reflection at $z = 0$.
1. l	The left-hand polarized mode for the infinite layer.
1. r	The right-hand polarized mode for the infinite layer.
2. 2. l 2. r	Corresponding fields for the semi-infinite layer.

In figures 8. 6 and 8. 7 the gyro frequency has been choosen in order to get the resulting stationary field in the x-direction. This means that the Faraday rotation is equal to $n \cdot \pi$ ($n = 0, 1, 2 \ldots$). Accordingly, the y-component exists only in the time interval when the left-hand polarized mode has arrived but before the right-hand polarized mode appears. See figure 8. 7.

It is interesting to find the condition for obtaining the stationary signal in the y-direction. This is obtained if the modes are 180^o phase-displaced, i. e. if

$$|k_o z (n_+ - n_-)| = (2n+1) \cdot \pi \quad (n = 0, 1, 2, 3 \ldots .) \tag{8.2}$$

For $n = 0$ the gyro frequency $\omega_H << \omega_o$ when $z >> \lambda_o$ and $\omega_1 \gtrsim \omega_o$, and we obtain

$$\frac{\omega_H}{\omega_o} \approx \frac{\lambda_o}{2z} \frac{\omega_1}{\omega_o} \sqrt{\left(\frac{\omega_1}{\omega_o}\right)^2 - 1} \qquad (\omega_H << \omega_1) \tag{8.3}$$

We assume that

$z = 100 \lambda_o$

$\omega_1 = 1.1 \omega_o$

from which we obtain

$$\omega_H \approx 0.00252\,\omega_o$$

This case is plotted in figure 8.8. Notice that the y-component is very weak from the beginning since the momentary frequency is high and the medium is nearly isotropic.

The split-up into a left-hand polarized mode and a right-hand polarized mode becomes still more evident if we look at the pulse response. In figures 8.9 and 8.10 the x- and y-components of the transmitted signal have been plotted. The individual pulses are well separated but there is a strong irregular ripple superimposed. The arrival of the first pulse is well defined by the group velocity. However, the second pulse is spread out. If we define the pulse arrival to be the time when the envelope has reached the value 0.25, this means that the arrival is not determined by the group velocity. Of course, this is due to interference between the two modes and not to anomalous dispersion.

We have also computed the pulse response when the Faraday rotation is equal to $\pi/2$. We have already shown that the gyro frequency then is equal to $0.00252\,\omega_o$ when $\omega_1 = 1.1\,\omega_o$ and $z = 100\,\lambda_o$. The resulting x- and y-components of the transmitted pulse are depicted in figure 8.11. The dashed curve with the small and oscillating amplitude is the resulting x-component.

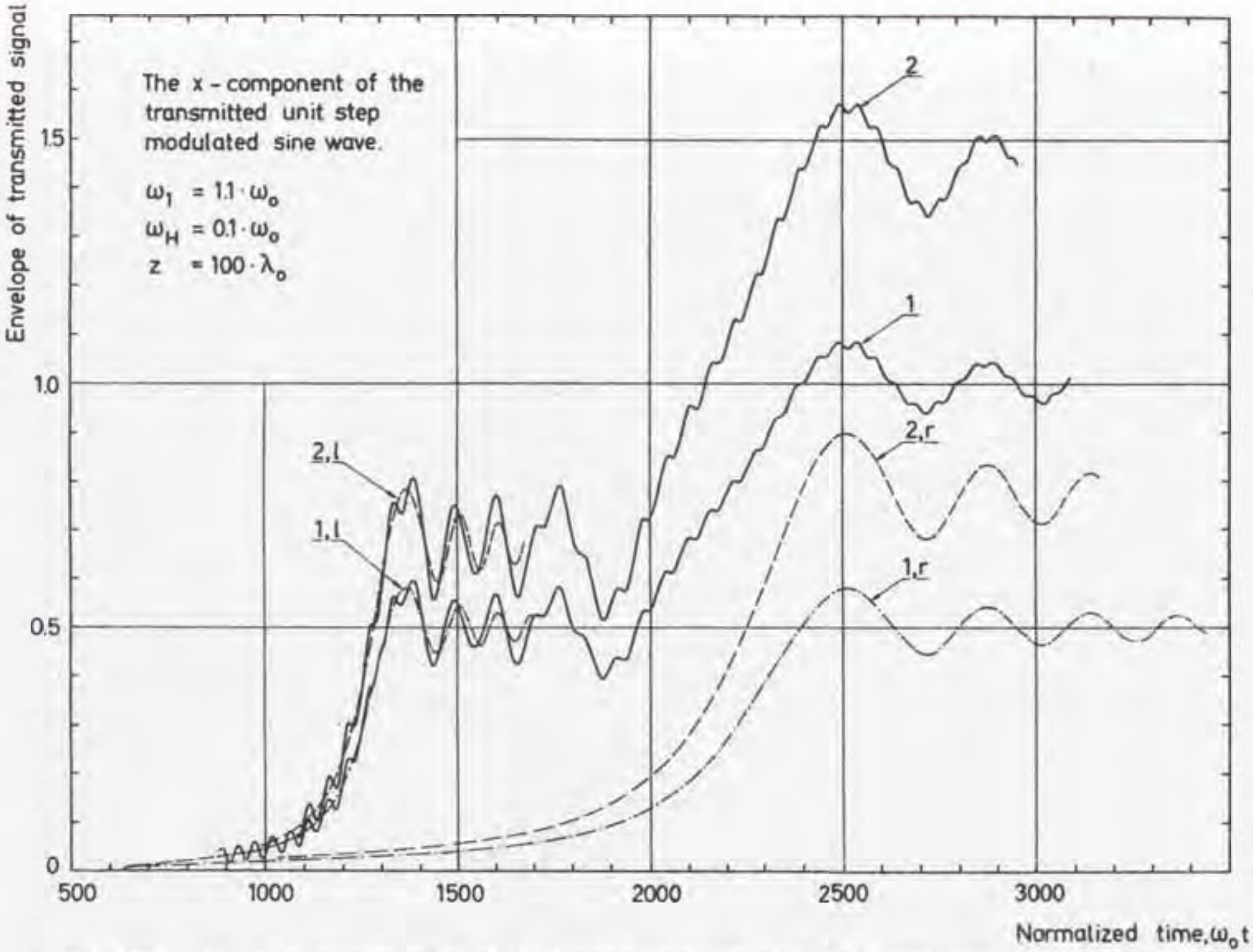

FIGURE 8, 6 The x-component of the transmitted unit step modulated carrier at $z = 100 \lambda_o$ in an anisotropic layer ($\omega_H = 0,1 \omega_o$). The notations 1., 1,1, ... are explained on page 44.

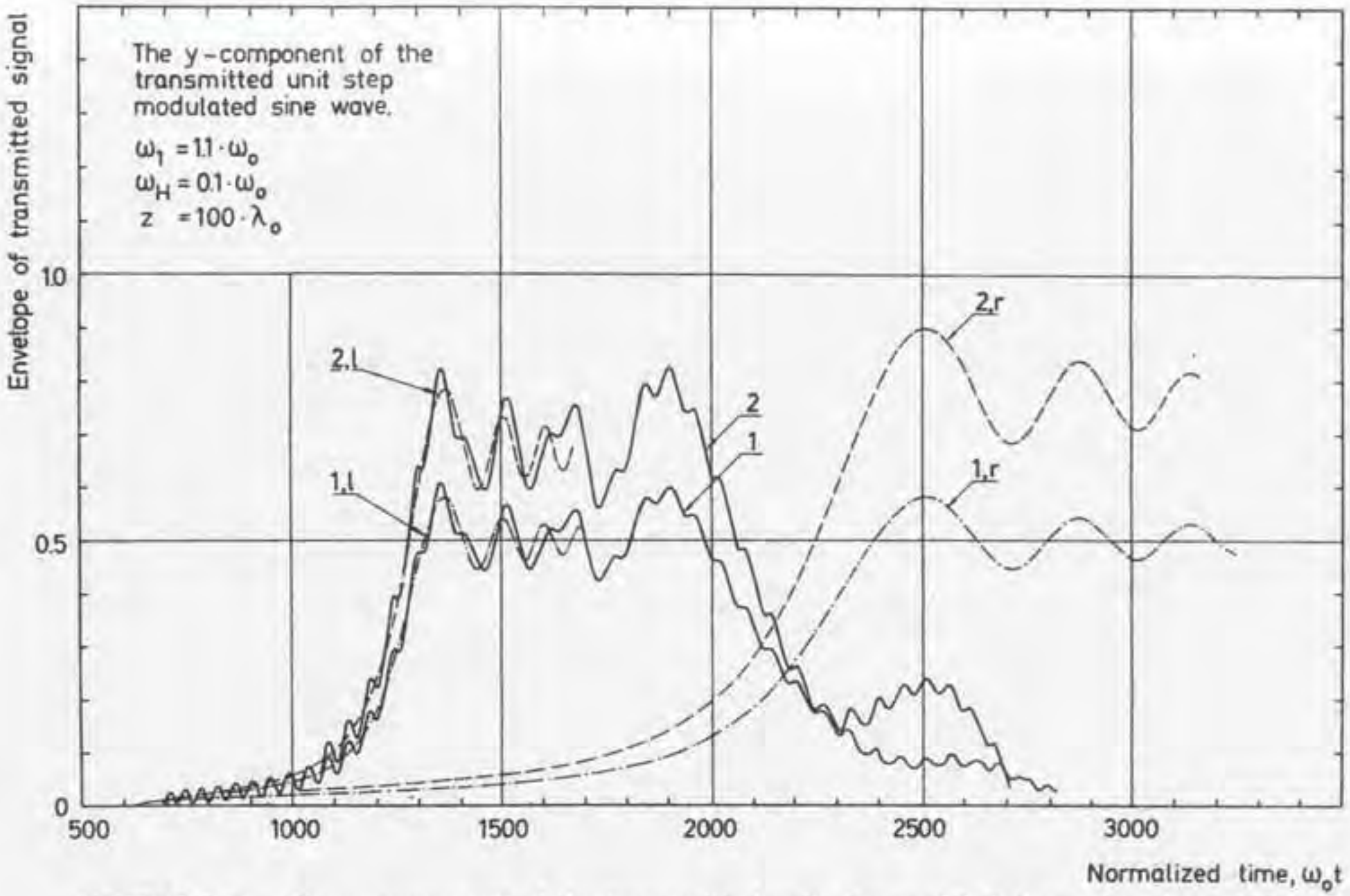

FIGURE 8. 7 The y-component of the transmitted unit step modulated carrier at $z = 100\,\lambda_o$ in an anisotropic layer ($\omega_H = 0.1\,\omega_o$). Compare with figure 8. 6.

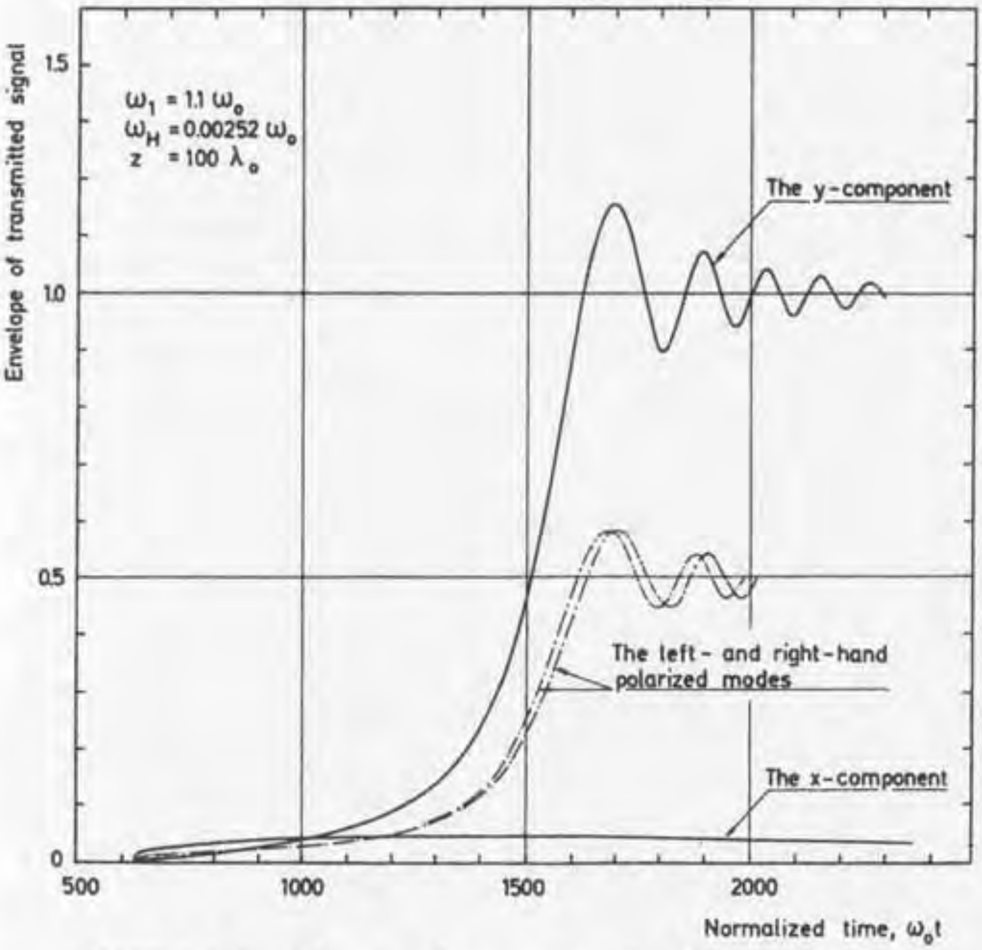

FIGURE 8. 8 The x- and y-components of the signal envelope with a weak magnetic field ($\omega_H = 0.00252\ \omega_o$).

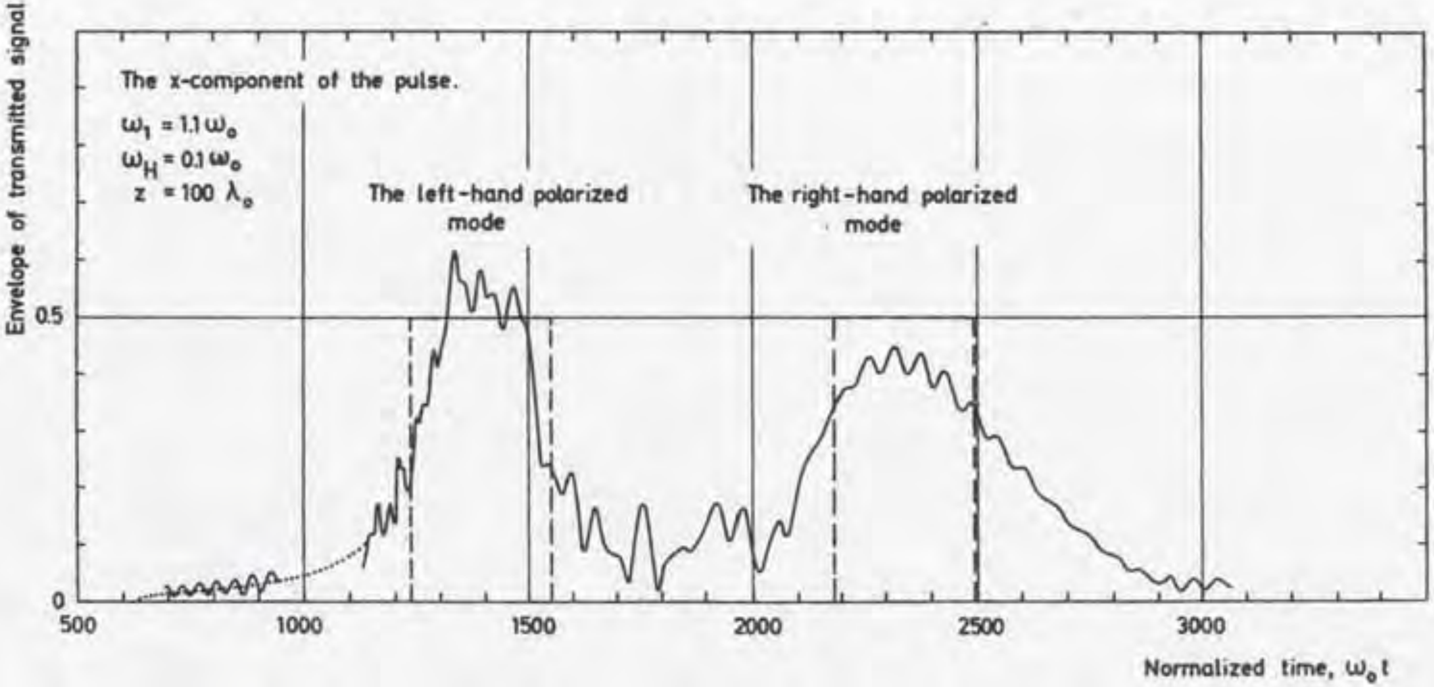

FIGURE 8.9 The x-component of the transmitted rectangular pulse-carrier at $z = 100\,\lambda_o$. Gyro-frequency $\omega_H = 0.1\,\omega_o$. Carrier frequency $\omega_1 = 1.1\,\omega_o$.

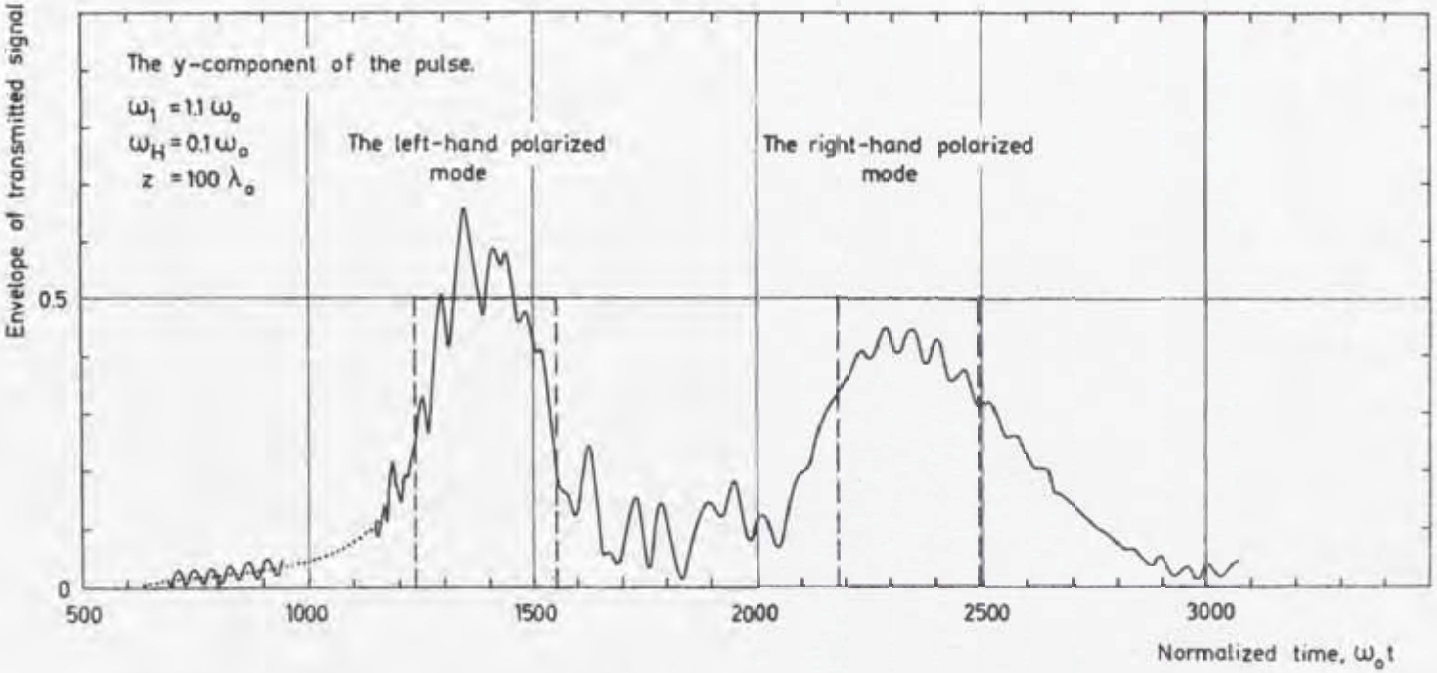

FIGURE 8.10 The y-component of the transmitted rectangular pulse-carrier at $z = 100\,\lambda_o$. Compare with figure 8.9.

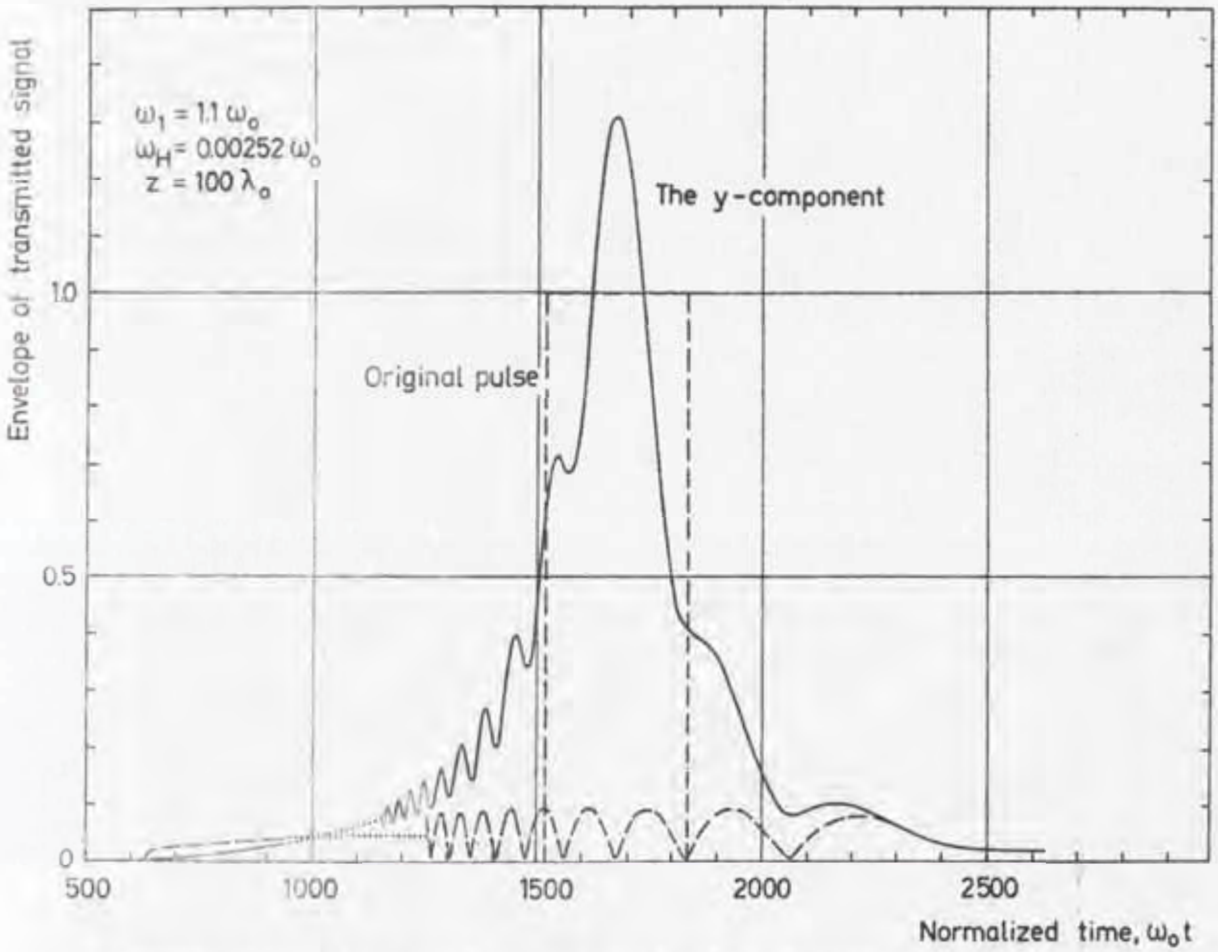

FIGURE 8.11 The x- and y-components of the transmitted rectangular pulse-carrier at a weak magnetic field. The dashed line with the small amplitude is the x-component.

IX REFERENCES

Brillouin, L. (1914). Über die Fortpflanzung des Lichtes in dispergierenden Medien. Ann. Physik, Lpz, vol.44, p.203.

See

Brillouin, L. (1960). Wave Propagation and Group Velocity. Academic Press, New York.

Denisov, N. G. (1951). Propagation of electromagnetic signals in an ionized gas. Zhurnal éksperimental'noĭ i teoreticheskoĭ fiziki, vol 21, pp. 1354-1363.

Ginzburg, V. L. (1964). The Propagation of Electromagnetic Waves in Plasmas. Pergamon Press.

Haskell, R. E. and Case, C. T. (1966). Transient Signal Propagation in Lossless, Isotropic Plasmas, Volume II. Physical Science Research Papers, No. 241, Air Force Cambridge Research Laboratories.

Pearson, J. D. (Aug., 1953). The transient motion of sound waves in tubes. Quart. J. Mech. Appl. Math., vol. 6, pp. 313-335.

Rydbeck, O. E. H. (1942). A theoretical survey of the possibilities of determining the distribution of free electrons in the upper atmosphere. Trans. Chalmers University of Technology, No. 3.

Rönnäng, B. O. (Sept. 1966). Transient wave propagation in symmetric ionized Epstein layers. Proc. IEEE, vol. 54, No. 9, pp. 1207-1209.

Rönnäng, B. O. (1966). Transient wave propagation in inhomogeneous ionized media. Res. Rep. No. 70, Res. Lab. of Electronics, Chalmers University of Technology.

Sommerfeld, A. (1914). Über die Fortpflanzung des Lichtes in dispergierenden Medien. Ann. Physik, Lpz, vol.44, pp. 177-202.

Wait, J. R. (Nov. 1965). Propagation of Pulses in Dispersive Media. Radio Science, vol. 69 D, No. 11, pp. 1387-1401.